The Role of Water in the Magmatic and Tectonic Evolution of Metamorphic Core Complexes: A Stable Isotope Study of the Southern Omineca Crystalline Belt, British Columbia, Canada

Thesis by
Gregory James Holk

In Partial Fulfillment of the Requirements
for the Degree of
Doctor of Philosophy

California Institute of Technology
Pasadena, California
1997

(Defended November 26, 1996)

ACKNOWLEDGEMENTS

There are many people that have played a role in inspiring me to pursue a career finding clues to those mysteries about the way our complex world operates. The journey from journeyman to scientist has been a long one, the fulfillment of a dream that I have had since I was a child. I very much look forward to continuing that journey exploring the wonder our world has to offer. At this time, I recognize those individuals whose influence, guidance, and friendship have made this journey a rewarding and satisfying one. To these people, I am very grateful.

First, I would like to thank and express my gratitude to my scientific mentor, Professor Hugh P. Taylor, Jr., for providing a free environment that allowed me to build up confidence in both the field and the laboratory. He was always available to provide much needed guidance, encouragement, and valuable insight into the scientific question at hand when I needed it. His sweeping, but precise, view of science is one that I strive to emulate. His enthusiasm in teaching has provided me with inspiration to be the best possible teacher and mentor I can possibly be.

During the duration of my scientific apprenticeship at Caltech I have had the opportunity to learn from, interact with, and obtain encouragement from many of the faculty that have always provided a stimulating intellectual environment. Professor Leon T. Silver has provided much guidance to me by always making himself available for consultation and providing the best advice and encouragement possible. I have also benefitted from discussions with Professors Arden Albee, Sam Epstein, George Rossman, Kerry Sieh, Gerry Wasserburg, Brian Wernicke, Peter Wyllie. I also acknowledge fruitful interactions with visiting faculty Paige Chamberlain, Geoff Davies, Ken Hsu, Tony Lasaga, and Leigh Royden.

The many interactions with and encouragement from my fellow graduate students at Caltech has made my experience an enjoyable and rewarding one. In particular, many thanks to DJ Wood, Doug Yule, my officemates Mark Abolins and Eme Burt, my labmates Diane Clemens-Knott and Carey Gazis, my roommates Brad Woods, Dave Evans, and Phil Willems. Thanks also to Paul Asimow, Lisa Grant, Liz Holt, Jean Hsieh, Tom LaTourette, Woh-Jer Lee, Elizabeth Nagy, Eve Schaffer, Edwin Schauble, Laura Wasylenki, and Judy Zachariasen.

I have been fortunate to have the opportunity to interact with and learn from many post-doctoral fellows at Caltech. I am eternally grateful to Mike Palin, the master of the laboratory, for teaching me so many valuable laboratory skills and being a wonderful collaborator while constructing the Caltech oxygen isotope laser extraction system. It was a great pleasure to spend time in the field and discuss metamorphic core complex water-rock interactions with Mark Peters. Other post-docs I would like to thank are Xiahong Feng, Marc Hirschmann, Brett McGuiness, Serge Nadeau, Geoff Nicholls, Don Porcelli, Eriks Puris, and Zeke Snow.

Discussions and interaction with my scientific colleagues have contributed greatly to the way this thesis was carried out and the development of the conclusions presented in this work. These colleagues are Georges Beaudoin, Sharon Carr, Peter Larson, Elizabeth Miller, Jean Morrison, Karlis Muehlenbachs, Bruce Nesbitt, Randy Parrish, Bruce Taylor, and Steve Wickham. I also thank Debbie Dreyfus and Jim Holk for field assistance.

Most of all, I would like to express my gratitude and love to my parents, James and Carolyn Holk, for providing me with much guidance, support, and the zest of exploration needed to pursue many of those questions our world poses to us. I look back fondly to the many explorations in the American Southwest with my family while growing up. I also thank my sister Laura for the great enthusiasm, love, and support she has given me through the years.

ABSTRACT

The oxygen isotope data in this study delineate 2 major episodes of water-rock interaction related to the metamorphic, plutonic, and tectonic development of the metamorphic core complexes in the southern Omineca belt. Episode 1 is a Paleocene pre-extensional metamorphic/magmatic-hydrothermal event. The occurrence of isotopically uniform quartz ($\delta^{18}O = 12.5 \pm 0.5‰$) and feldspar ($10.9 \pm 0.7‰$) throughout different rock types indicates that much of a 6-km-thick section of the mid-crustal Selkirk allochthon underwent internally buffered $^{18}O/^{16}O$ homogenization during Paleocene melting and decompression as it moved up the Monashee decollement thrust ramp. Areas of uniform $\delta^{18}O$ are those with the most leucogranite or those subjected to severe anatexis. Only locally, in the most impermeable (or refractory) zones did ^{18}O exchange among the rocks, leucogranite melts, and aqueous fluids fail to go to completion (*i.e.*, in the deepest parts of the section, in a marble-rich zone, around some thick amphibolites, and in most garnets). Evidence for $^{18}O/^{16}O$ heterogeneity in the protoliths of these rocks is observed in stratigraphically correlative lower-grade units elsewhere in British Columbia, as well as in garnets that coexist with isotopically homogeneous quartz. A model is introduced utilizing water as a petrologic catalyst: fluids evolved during muscovite breakdown and partial melting of pelites produce $^{18}O/^{16}O$ homogenization with only minor influx of external H_2O; this is followed by release of magmatic H_2O from these melts as they crystallize (triggering further melting of adjacent feldspathic assemblages) during and after the ~20 km uplift that occurred in the thrusting event that took place just prior to detachment faulting.

Episode 2 is a series of Eocene synextensional meteoric-hydrothermal events affecting the shallow crust along all of the major detachment faults in the region, and along some parts of the Monashee decollement; these effects were locally enhanced by added heat from some synextensional alkaline intrusions (the Coryell plutons). Very large quartz-feldspar $^{18}O/^{16}O$ disequilibrium effects were imprinted upon the rocks during exchange with hot meteoric waters (initial $\delta^{18}O \sim -15$); the mineral most affected was feldspar ($\delta^{18}O$ down to -5.0). In the Valhalla core complex, the hanging wall rocks above the Slocan Lake fault are sufficiently uniform to allow us to apply open-system kinetic oxygen isotope exchange modeling, thereby placing constraints on the duration (1-3 Ma) and integrated fluid flux ($\geq 10^7$ $cm^3{}_{H_2O}/cm^2{}_{rock}$) for this hydrothermal metamorphism.

TABLE OF CONTENTS

LIST OF FIGURES

Chapter 5.

Chapter 6.

Appendix A.

LIST OF TABLES

Chapter 1. Introduction

1.1 Nature and Purpose of Study

1.1.1 General Statement

This thesis represents a stable isotope study of some of the metamorphic core complexes that comprise the southern Omineca Crystalline Belt of southeastern British Columbia, Canada. The study was initiated as an attempt to investigate one of the most favorable localities on Earth where definitive stable isotope studies of fossil meteoric-hydrothermal systems can be combined and integrated with well-mapped exposures of some classic metamorphic core complexes.

The southern Omineca belt in British Columbia is arguably one of the best locations to address the role of H_2O in the evolution of metamorphic core complexes. There are excellent exposures of a very complete, well-mapped, dated, and correlated mid-crustal section at the southern Thor-Odin complex. Road-cuts along the southeastern shore of

Slocan Lake afford continuous exposure of a complete upper- to lower-plate section through the Slocan Lake detachment fault. Erosion has exposed a series of deep, early compressive shear zones which separate the basement rocks from the overlying zones of anatexis in the mid-crust. However, the most important reason for selecting these areas is their high-latitude location in North America where meteoric waters are known to have been very low in $\delta^{18}O$ and δD during the Mesozoic and Cenozoic (Magaritz and Taylor, 1986). The degree of water-rock interaction during meteoric-hydrothermal metamorphism is much easier to quantify when there is a large isotopic contrast between water and rock.

The scope of the project changed and expanded during the course of this study from 1991 to the present, as new directions were pursued. A number of the following questions regarding the role of aqueous fluids in the development of metamorphic core complexes were formulated as part of the initial project; others arose during this period, and are addressed within the body of this thesis to varying degrees of success:

1. What types of hydrothermal systems developed during the evolutionary history of the core complexes?
2. What was the duration and intensity of water-rock interaction at various levels in the crust?
3. Is it possible to define the location and depth of the transition from metamorphic/magmatic hydrothermal systems at lithostatic pressure to meteoric systems at hydrostatic pressure?
4. What is the role of water in the generation of lower-plate syntectonic magmas?

5. What was the temperature contrast between the upper and lower plates during the evolution of the core complexes, and specifically during the meteoric-hydrothermal activity?
6. To what extent did the presence or absence of synextensional lower-plate magmas drive the hydrothermal alteration of the upper plate?
7. Did the earlier compressional history of this terrane have any impact on the various deep-level hydrothermal processes?
8. Are aqueous fluids the primary agent that produced wholesale weakening of the crust in this area, perhaps triggering the development of detachment faults in the middle part of the continental crust?
9. What are the tectonic controls governing the behavior of the various hydrothermal systems?
10. How much water is needed to drive decompression-driven dehydration melting of the middle crust?
11. Was the exsolution of, and/or the dissolving of, aqueous fluids in high-silica partial melt phases an important process in the evolution of these core complexes?

1.1.2 Importance of Study

This kind of study is important because it provides information about the hydrothermal evolution of metamorphic core complexes. The determination of the structure, geometry, and type of hydrothermal system(s) that has evolved in these terranes will result in a better understanding of the thermal state of the lower plate as it is uplifted and as it approaches the crustal depths where meteoric water circulation takes place.

Variations in the intensity of the upper-plate hydrothermal systems are very likely dependent on the thermal state of the lower plate. For example, the intensity and scale of meteoric-hydrothermal systems in the upper plate ought to be greater at locations containing syndeformational plutons than at locations where these plutons are absent.

Tectonic models describing the evolution of regions of large-scale extension (Wernicke, 1981; 1990; Gans, 1987; Miller et al., 1988) predict different crustal heat distributions during deformation. Wernicke's (1981) simple shear model, with detachment faults rooting in the upper mantle, predicts heating of lower crustal levels as a result of the influx of hotter mantle material. The effects of this thermal perturbation of the lower crust will reach mid-to-upper crustal levels, either in the late stages of extension, or once extension has ceased. The pure-shear model proposed by Miller et al. (1988) suggests that wholesale remobilization of lower crustal material to shallower crustal levels occurs during this type of extension. The thermal imprint of the pure shear mode of deformation should be much more intense than the Wernicke model, because large amounts of heat can be readily advected from the lower crust to the middle and upper crust during extension.

Previous stable isotope studies in the southern Omineca belt have demonstrated that hydrostatic meteoric water circulation is focused along some of the N-trending detachment faults (Magaritz and Taylor, 1986), and it has been suggested that these effects may have reached depths of 15 km or more in these zones (Nesbitt and Muehlenbachs, 1989). If meteoric waters actually reach these proposed depths, this will have profound implications on disciplines as diverse as metamorphic petrology and seismology. It is typically assumed that fluids involved in regional metamorphic dehydration reactions are at lithostatic pressure. If meteoric waters at hydrostatic pressure reach great depths, then previous estimates of the temperatures at which these dehydration reactions take place will be in error. Transient effects associated with earthquakes (*e.g.*, seismic pumping) may have great impact on the crustal hydrology of systems of this type (Sibson et al., 1975; McCaig et al., 1990).

1.1.3 Field Work and Sampling in the Southern Omineca Crystalline Belt

This research involved three field seasons in British Columbia. During the first, five-week, field season in the summer of 1991, rock samples were collected for a regional reconnaissance $^{18}O/^{16}O$ study in order to best determine the prime localities for more detailed future studies. During the second, ten-week, field season in the summer of 1992, attention was focused on studying detachment fault-related processes at the Valhalla complex, and lower-plate aqueous fluid processes related to mid-crustal anatexis at the southern Thor-Odin complex. In the third, three-week, field season in the summer of 1994, samples were collected from deep in the basement in order to investigate water-rock interaction beneath the deep-seated thrust faults of the Monashee complex; in addition, numerous samples were collected from the Late Precambrian-to-Mesozoic stratigraphic sequence in the Purcell and Selkirk mountains for the purpose of determining initial oxygen isotope heterogeneity in these lower-grade units that are interpreted as the stratigraphic equivalents of the section investigated at the Thor-Odin complex.

1.2 Metamorphic Core Complexes

1.2.1 General Description

Metamorphic core complexes are domal uplifts of ductilely deformed metamorphic and plutonic rocks tectonically overlain by imbricately faulted unmetamorphosed sedimentary and/or volcanic cover rocks (Coney, 1973; 1980; Davis and Coney, 1979; Crittenden et al., 1980; Armstrong, 1982; Davis, 1983; Davis and Lister, 1985). Low-angle normal faults, termed detachment faults, separate the ductile lower plates from the brittle upper plates. These complexes are usually formed in regimes that underwent an early episode of compression followed by a later episode of uplift and extension.

The lower plate (Figure 1.1, Zone A) of a typical core complex is comprised of high-grade metasedimentary rocks, older intrusive gneisses, and synextensional plutonic rocks. Commonly, there is evidence that the lower-plate rocks were multiply deformed and metamorphosed, although such evidence may be transposed and obliterated by mylonitic deformation immediately beneath the detachment zones. Metamorphism and migmatization of the lower plate can take place either during crustal thickening in the hinterland of an early compressional orogenic episode, or in response to the emplacement of mantle-derived magmas into the middle and lower crust during extension.

A typical upper plate (Figure 1.1, Zone B) is comprised of older low-grade (or unmetamorphosed) sedimentary and volcanic rocks intruded by granitic plutonic rocks; these rocks are broken up by listric brittle faults that root into the basal detachment zone that separates the upper and lower plates. The tilted fault blocks of the upper plate are juxtaposed against clastic sedimentary and/or volcanic rocks deposited in synextensional basins (h on Figure 1.1), and the lower plate can be shown to be the source for much of the detritus shed into these extensional basins. These coarse clastic rocks may be interlayered with thick sequences of tuffaceous volcanic rocks erupted during extension.

The detachment faults can be clearly shown to be extensional (Figure 1.1, Zone C), based on younger-on-older stratigraphic juxtaposition, brittle overprinting of early ductile fabrics, normal shear-sense kinematic indicators, and occurrence of coeval listric normal

Figure 1.1 -- Structural domains of metamorphic core complexes (modified after Crittenden et al., 1980). The lower plate (A) is comprised of: (a) high-grade metasedimentary rocks, (b) gneissic older intrusive rocks, and (c) young, synextensional plutonic rocks. The upper plate (B) is made up of: (g) low-grade (or unmetamorphosed) sedimentary and volcanic rocks, (h) clastic sedimentary rocks or volcanic rocks deposited in tilted synextensional basins, and (i) brittle, listric faults which root into the basal detachment fault that separates the upper and lower plates. The detachment fault zone (C) has (d) mylonitic lower plate rocks overlain and overprinted by (e) brittle and extremely hydrothermally altered rocks of the detachment surface, and (f) syntectonic mylonitic carbonate. Synextensional plutonic rocks commonly intrude into detachment faults and are subsequently deformed.

Figure 1.1 Structural Domains of Metamorphic Core Complexes

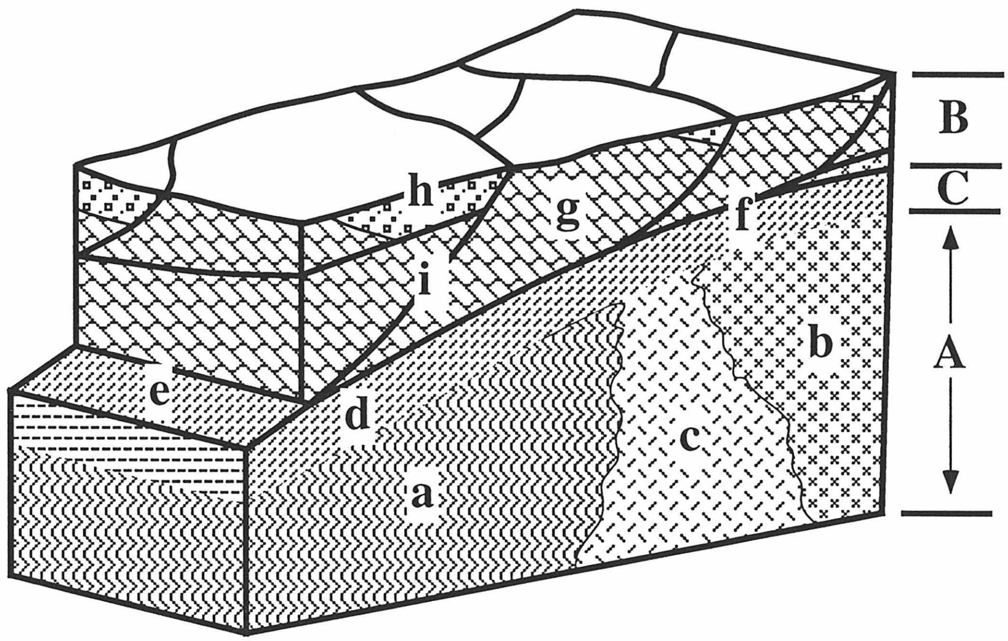

faults in the normal faults of the upper plate. Syntectonic mylonitic carbonate is commonly found within the detachment zones, and synextensional granitic plutonic rocks generally intrude these zones; both features provide time constraints and record information about the deformational history of these fault zones. Zones of intense chloritization, sericitization, and brecciation mark the upper levels of the detachment faults, indicating a history of hydrothermal metamorphism.

1.2.2 Geologic Importance

Metamorphic core complexes provide a window into the middle and lower continental crust, and studies of such complexes provide clues to deformational, magmatic, metamorphic, and hydrothermal processes active in the middle crust during orogeny (Coney, 1980; Armstrong, 1982; and Wernicke, 1992). In western North America these features are associated with anatexis in crust thickened during the Columbian, Sevier, and Laramide orogenies (Coney and Harms, 1984; Patino Douce et al., 1990; and Armstrong and Ward, 1991). This crustal melting probably plays a significant role in weakening the continental crust in such areas (Wickham, 1987; Hollister, 1993), and understanding this phenomenon in its petrologic and tectonic context is important in understanding how and why the onset of detachment faulting is triggered in the interval between the waning stages of outboard thrusting (*e.g.*, Parrish et al., 1988; Carr, 1992) and the attainment of crustal thermal equilibrium following the termination of thrusting (*e.g.*, Dewey, 1988; Miller et al., 1989).

Rapid exhumation of the lower plate can cause an isothermal decompression of the middle crust (Anderson et al., 1988; Spear and Parrish, 1996). This extension-driven decompression of the lithosphere also may be an important agent driving anatexis in the mantle (McKenzie and Bickle, 1988; Latin and White, 1990) and in the lower and middle crust (Gans, 1987; Gans et al., 1989; and Carr, 1992). Lower-crustal underplating by mantle-derived magmas can add heat to the lower and middle crust, further driving melting of these layers (Gans, 1987; Gans et al., 1989; Bergantz, 1989; Grunder and Wickham, 1991).

During detachment faulting, the profound thermal contrast that results from the rapid denudation and uncovering of a hot, lower plate from its original position beneath a cold, upper plate (in association with the presence of melted rock in the lower plate) can provide a favorable environment for convective circulation of hydrothermal fluids in the upper plate (Spencer and Welty, 1986; Kerrich and Hyndman, 1986; and Reynolds and Lister, 1987). These hydrothermal systems may provide clues into extension-related mineralization processes (Spencer and Welty, 1986; Nesbitt et al., 1989; Beaudoin et al., 1991, 1992).

Controversy still exists concerning the origin and nature of detachment faults – are these features simply exhumed exposures of the paleo brittle-ductile transition (Miller et al., 1983), or are they through-going, shallow-dipping normal faults (Wernicke, 1981)? Fluids at lithostatic pressure reduce normal stress and frictional sliding resistance (Hubbert and Rubey, 1959), creating conditions suitable for the formation and development of low-angle normal faults. Detailed analysis of brecciated detachment surfaces strongly suggests that the presence and circulation of water plays an essential role in the formation of detachment faults (Davis and Coney, 1979; Bartley and Glazner, 1985). These fluid-rich environments are fundamentally weak because water pressure typically exceeds the tensile strength of the rock (Axen, 1992; Axen and Selverstone, 1994). Nevertheless, the observed seismicity along an active detachment fault at the Woodlark-D'Entrecasteaux extensional province of Papua New Guinea (Abers, 1991) provides strong evidence that these faults are capable of accumulating stresses sufficiently large to generate moderate earthquakes. However, much more work is required to gain an understanding of the effect of water on the mechanics of detachment faulting, and this can be done by studying the fossil hydrothermal systems associated with metamorphic core complexes.

1.2.3 Occurrence

Metamorphic core complexes and similar extensional zones have been recognized in orogenic belts throughout the world (Figure 1.2). This structural association typically occurs in regions where extensional collapse of mountain belts is superimposed upon a previous episode of compressional orogeny (Coney and Harms, 1984; Dewey, 1988). Such complexes are found in the Aegean Sea (Lister et al., 1984), the Himalayan orogen (Burchfiel and Royden, 1985), the Alpine orogen (Selverstone, 1988), the Andean orogen (Dalziel and Brown, 1989), the Variscan orogen (Echtler and Malevieille, 1990), the Scandinavian Caledonides (Fossen and Tykkelid, 1992), and the New England Appalachians (Getty and Gromet, 1992), and one is probably forming right now in the Woodlark basin-D'Entrecasteaux islands, Papua New Guinea (Baldwin, 1993). However, the first-recognized and most intensively studied metamorphic core complexes are those of the North American Cordillera (Figure 1.3), where they define a sinuous belt that stretches for at least 3000 km from northwestern Mexico to southwestern Canada (*see* Crittenden et al., 1980).

In North America (*see* Figure 1.3), metamorphic core complexes are usually found about 100 km inboard (*i.e.*, in the hinterland) of the Cordilleran fold and thrust belt (Crittenden, 1980), in the vicinity of the zone of greatest crustal thickening (Coney and

Figure 1.2 -- The worldwide distribution of Tertiary collapsed orogenic belts (after Dewey, 1988). Metamorphic core complexes are common features of these belts, forming in response to gravitational instability imposed on the crustal system as it is overthickened by compression. Collapse occurs either during the waning stages of compression or immediately following the compressive stage of orogeny.

Figure 1.3 -- Map of Cordilleran metamorphic core complexes (after Armstrong, 1982). Core complexes are denoted by the dark shading. Tertiary volcanic rocks are shown with a "V" pattern. The Cretaceous Cordilleran batholith belt is shown with a cross-hatch stipple pattern. The metamorphic core complexes are typically located in the hinterland of the Mesozoic-Early Tertiary Sevier-Rocky Mountain fold and thrust belt. Core complexes formed as the result of the exhumation of the middle crust during detachment faulting. Giant ignimbrite eruptions commonly occurred simultaneously with the formation of metamorphic core complexes.

Figure 1.2 Collapsed Orogenic Belts

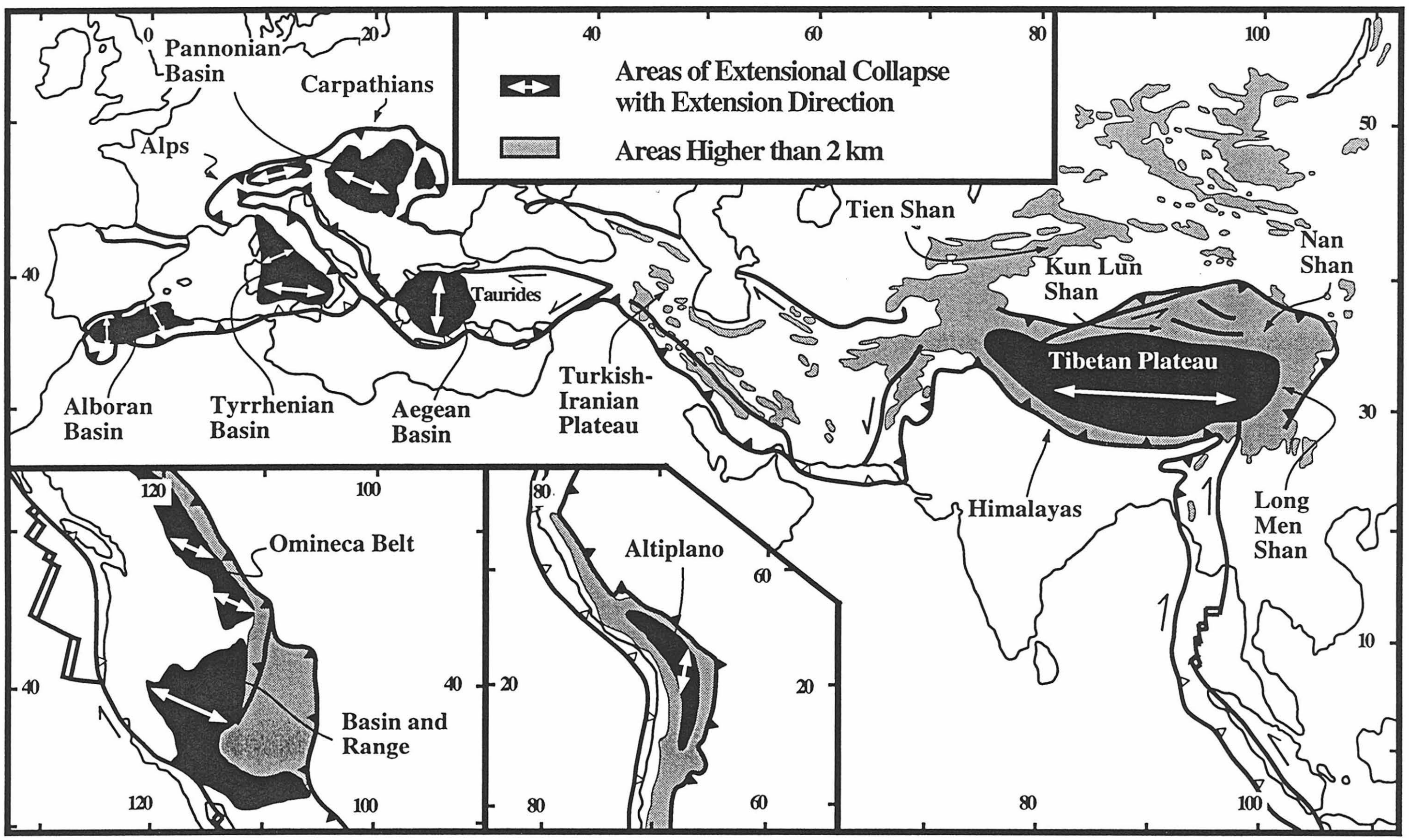

Figure 1.3
Cordilleran Metamorphic Core Complexes

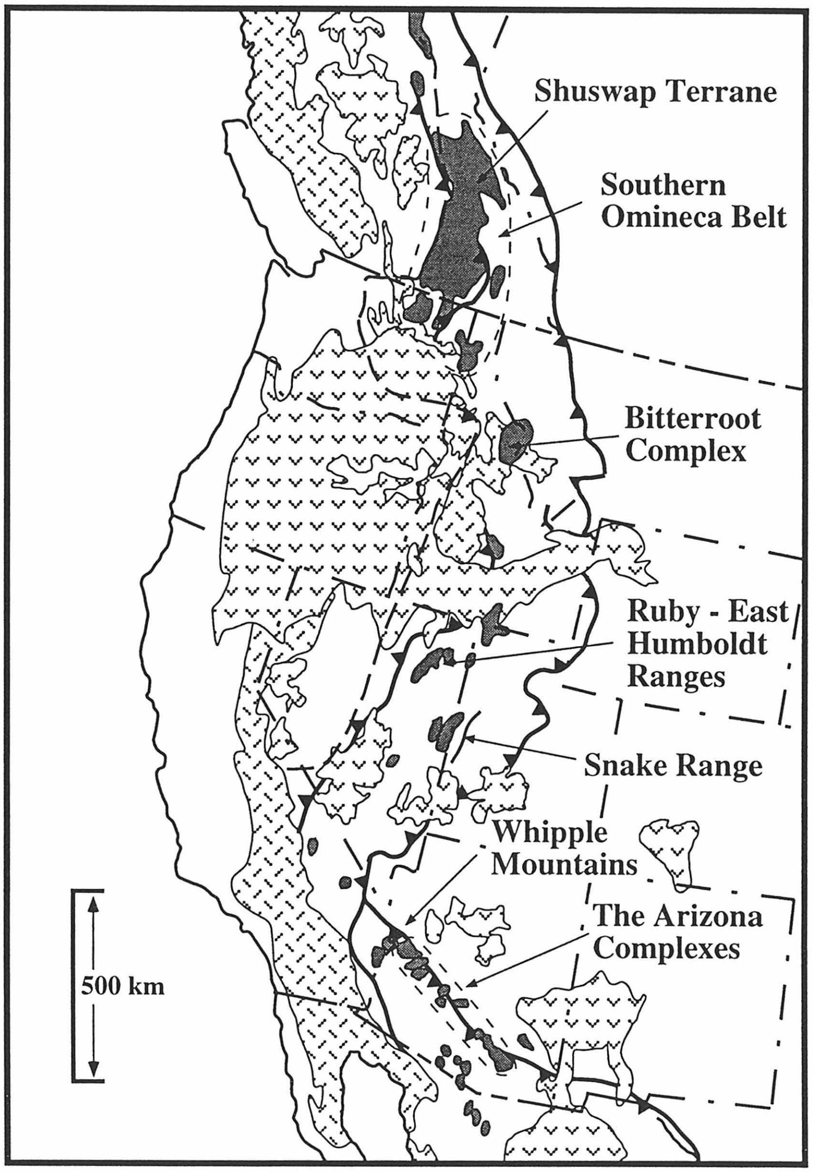

Harms, 1984). These features are located east of the $^{87}Sr/^{86}Sr = 0.706$ line of Kistler and Peterman (1973), indicating a crustal affinity for the plutonic igneous rocks that comprise these structures. The core complexes are also about 200-400 km east of the Mesozoic-to-Early Cenozoic Cordilleran batholith belt that was emplaced along the continental margin. A belt of high-^{18}O Cenozoic volcanic rocks (Larson and Taylor, 1986; Grunder and Wickham, 1991) and high-^{18}O Cretaceous and Cenozoic "S-type" plutonic rocks (Solomon and Taylor, 1989; Miller and Bradfish, 1980) overlaps the metamorphic core complex belt. These complexes are also located at the site of the most intense deformation and regional metamorphism (Anderson et al., 1988; Parrish et al., 1988; Miller and Gans, 1989).

1.3 Historical Development of our Understanding of Core Complexes

1.3.1 Recognition and Definition

The importance of metamorphic core complexes in the development of the current crustal architecture of the North American Cordillera was first recognized in the eastern Great Basin (Misch, 1960; Armstrong and Hansen, 1966; Moores et al., 1968; Armstrong, 1972). Major subhorizontal dislocation planes displaying large displacements and separating unmetamorphosed cover rocks from underlying metamorphosed rocks were discovered by Misch (1960) in the Snake Range, Nevada. Initially, this flat-lying discontinuity was interpreted to be the deep decollement root zone for the Mesozoic fold and thrust belt 100 km to the east (Misch, 1960), but it was later found to be an extensional structure with the realization that this decollement omitted stratigraphy and was kinematically associated with younger-on-older normal faults in its hanging wall (Armstrong, 1972).

Intense shearing and steep metamorphic gradients distinguish the decollement zone, which served to accommodate ductile mobilization and separation of the metamorphic infrastructure out from beneath a rigid suprastructure (Armstrong and Hansen, 1966). K-Ar geochronology demonstrated that Mesozoic metamorphism of the infrastructure and final cooling during the Tertiary were two separate events representing different stages of the orogenic development of these complexes (Armstrong and Hansen, 1966).

These early contributions firmly established the extensional nature of metamorphic core complexes as well as a recognition that they represent ubiquitous and important features of the eastern portions of the Cordilleran orogen. Numerous examples of this tectonic association were soon recognized in a belt that extended from northwestern Mexico to southern Canada (*see* Crittenden et al., 1980). It was firmly established that exhumation of these core complexes followed Mesozoic-to-Early Tertiary Columbian-Sevier-Laramide thrusting, but preceded Tertiary Basin and Range block faulting (Coney, 1980). However, much controversy remained concerning the crustal mechanics involved in the initiation and evolution of the associated detachment faults, and with the mid-to-lower crustal processes associated with this style of extension.

1.3.2 Three Models of Detachment Faulting

Three models of crustal extension have been proposed to account for the formation of detachment faults and the consequent development of metamorphic core complexes (see Figure 1.4). These are the mega-landslide model, the in situ ductile-stretching model, and the rooted, low-angle normal fault model.

Gravitational spreading of overthickened crust (Figure 1.4a) is a necessary condition for the mega-landslide model to operate (Price and Mountjoy, 1970; Coney and Harms,

Figure 1.4 -- Three models of crustal extension associated with the development of metamorphic core complexes (from Wernicke, 1981). (a) The megalandslide model with coeval extension of overthickened crust and shortening in the foreland due to gravitational collapse. (b) The in-situ ductile stretching model with penetrative ductile thinning (pure shear) of the lower and middle crust accompanied by domino-style tilting of brittle upper crustal blocks. (c) The rooted low-angle normal fault model in which extension is accommodated by crustal-scale simple shear.

Figure 1.5 -- End-member kinematic models for the development of detachment fault systems (from Wernicke, 1992). (a) Domino-style fault block rotation. This model operates with simultaneous rotation of fault blocks that comprise the upper plate. Blocks are subsequently cut by successive generations of faults, and this results in further rotation. (b) A rolling hinge. This model operates by sequential detachment of thin slices of crust from the distal block (on the right) as the proximal block (on the left) moves away. Model (a) predicts prolonged simultaneous block rotation and continuous, slow exhumation across the entire zone of extension while model (b) predicts localized rotation and rapid exhumation of detached distal blocks in the hinge zone over a short period of time. A hinge migrates (and rolls) through the lower plate in model (b) while a hinge is not a necessary element of the alternate model. The rolling hinge (b) scenario predicts more rapid and localized decompression at the zone of basal detachment than does the domino fault-block rotation (a) scenario. This makes the rolling hinge model a more efficient means of transporting hot middle crustal material to shallow crustal depths, possibly along an adiabat.

Figure 1.4 Models for Extension

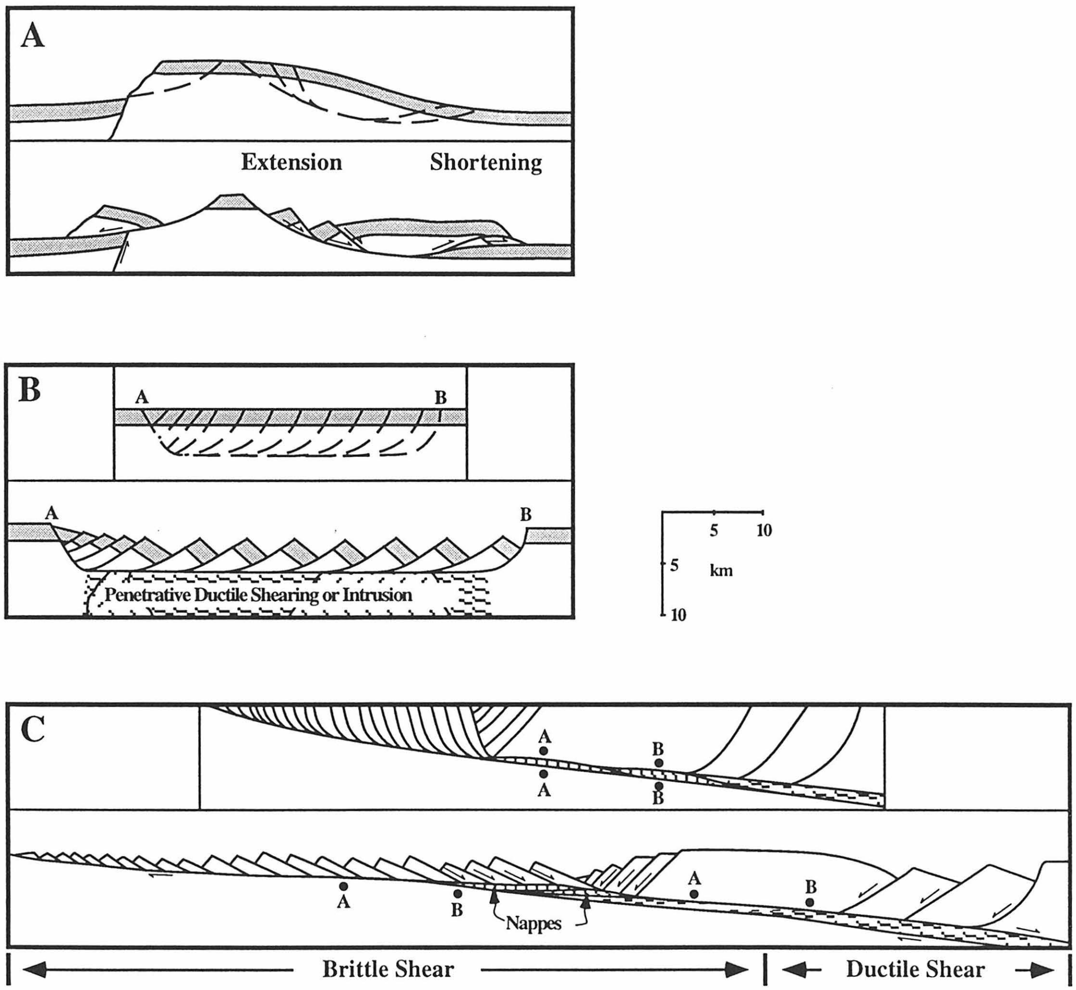

Figure 1.5 Endmember Kinematic Models For Detachment Faults

a) Synchronous, Domino-Style Fault Block Rotation

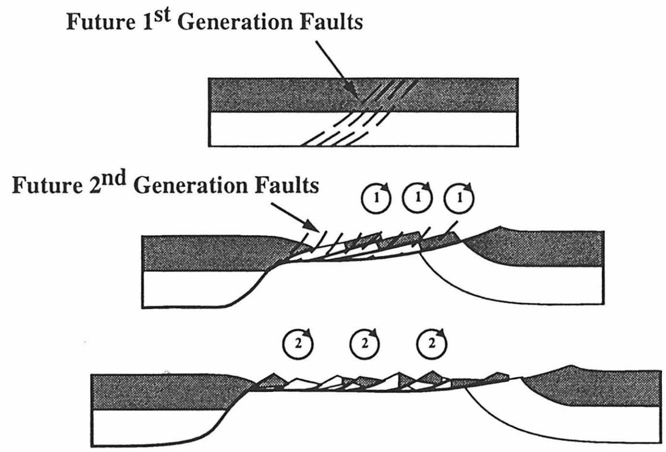

b) Sequential Detachment From Distal Block, Migrating Flexure

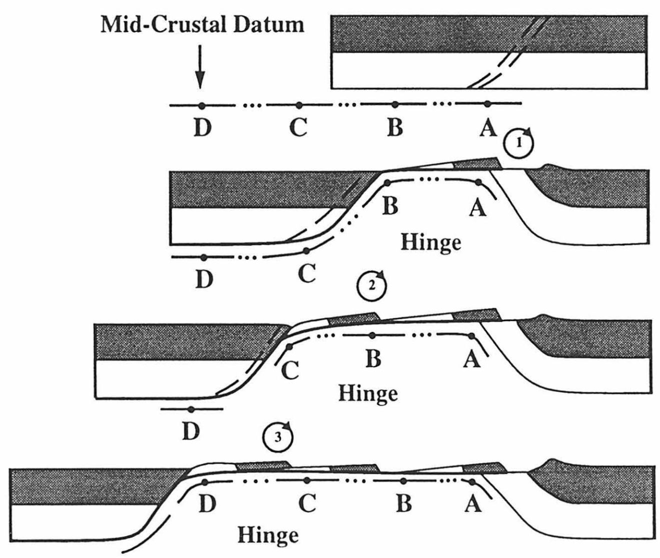

1984). Applying this case to the Cordilleran examples, the metamorphic core rocks are assumed to rise buoyantly, driving synchronous eastward thrusting of the foreland thrust belt by gravity sliding, with normal faults related to spreading merging into root decollement zones of the outboard fold and thrust belt (Price and Mountjoy, 1970). It was initially thought that extension in the southern Omineca belt (Figure 1.3) was driven by this process (Price and Mountjoy, 1970; Coney, 1973). It was later proposed that most tectonic denudation occurred through eastward obduction and telescoping of allochthons, with extension playing a minor (and late) role in the formation of these complexes (Brown and Read, 1983). Palinspastic restoration of regions that have undergone large amounts of extension led Coney and Harms (1984) to conclude that crust overthickened by earlier compression underwent lateral spreading, collapse, and deep-seated crustal extension driven by gravitational instabilities generated as a result of internal heating, anatexis, and/or thermal perturbation by addition of heat from below.

The in situ ductile-stretching model (Figure 1.4b) operates through the weakening of the crust in response to the intrusion of large amounts of magma (Anderson, 1971; Proffett, 1977; and Gans, 1987). Upper-plate normal faults produce domino-like tilted fault blocks (Proffett, 1977; Miller et al., 1983), and these faults root into a basal detachment zone that serves to decouple the brittle upper plate from a ductile lower plate deforming in pure shear (Anderson, 1971; Miller et al., 1983; Gans, 1987). The brittle-ductile transition is brought to the Earth's surface as extension reaches very high magnitudes (up to 500%; Miller et al., 1983).

In the third model (Wernicke, 1981), extension is accommodated by simple-shear deformation along a deep-rooting low-angle normal fault (Figure 1.4c). Early ductile fabrics and brittle deformation are kinematically coordinated, with the ductile fabrics being reworked in the brittle regime (Wernicke, 1981; Davis et al., 1986). Lower-plate warping and tectonic denudation driven by extension-related isostasy (Spencer, 1984) results in the cessation of movement along earlier detachment faults (Davis and Lister, 1988). This model is an extension of an earlier model that suggested metamorphic core complexes essentially represent a crustal-scale mega-boudinage formed by the ductile stretching and necking of basement rocks accompanied by detachment along zones of weakness, such as the basement-cover unconformity and/or zones of high pore fluid pressure (Davis and Coney, 1979).

1.3.3 Current Models of Crustal Extension

Current models of crustal extension are summarized by Wernicke (1992). These models are not mutually exclusive, but represent end-member situations that incorporate many of the concepts discussed in the previous two sections. Summarized below are two models pertaining to detachment faulting processes (Figure 1.5) – the domino-style fault rotation model and the rolling hinge model, together with a description of two possible modes of deep-crustal extension (Figure 1.6) – uniform deep-crustal stretching and mid-crustal flow of crustal material laterally from unextended domains into extended domains.

The domino fault-block rotation model operates by the simultaneous rotation of upper-plate fault blocks (Figure 1.5a). These blocks are subsequently cut by successive generations of faults, which drive further block rotation, resulting in continued shallowing of the dips of faults from the earlier generation. Most of the dip-shallowing happens when these faults are inactive. Random and multiple generations of faulting result in widely varying amounts of rotation for these upper-plate blocks. This model predicts slow exhumation of the lower plate across the entire zone of extension.

Figure 1.6 -- Modes of deep-crustal response to extension (from Wernicke, 1992). (a) Unstrained crust. (b) Uniform deep-crustal stretching. Magmatic flux from the mantle is concentrated beneath the extended domain, injecting basaltic melt and driving large-scale anatexis of the deep crust. The stretched layer is displaced from beneath stable blocks and into extended domains. (c) A mobile (fluid) crustal layer. Ductile flow of a weak middle crust takes place from unextended into extended domains, and is accompanied by shearing of the strong, mafic lower crust in order to accommodate crustal extension. Both models predict a low-relief Moho, but the addition of mantle-derived material into the extended domain is necessary in the uniform deep-crustal stretching model, whereas magmatic input from the mantle directly beneath unroofed areas is not required in the mobile fluid crust model.

Figure 1.6 Contrasting Modes of Deep-Crustal Response to Extension

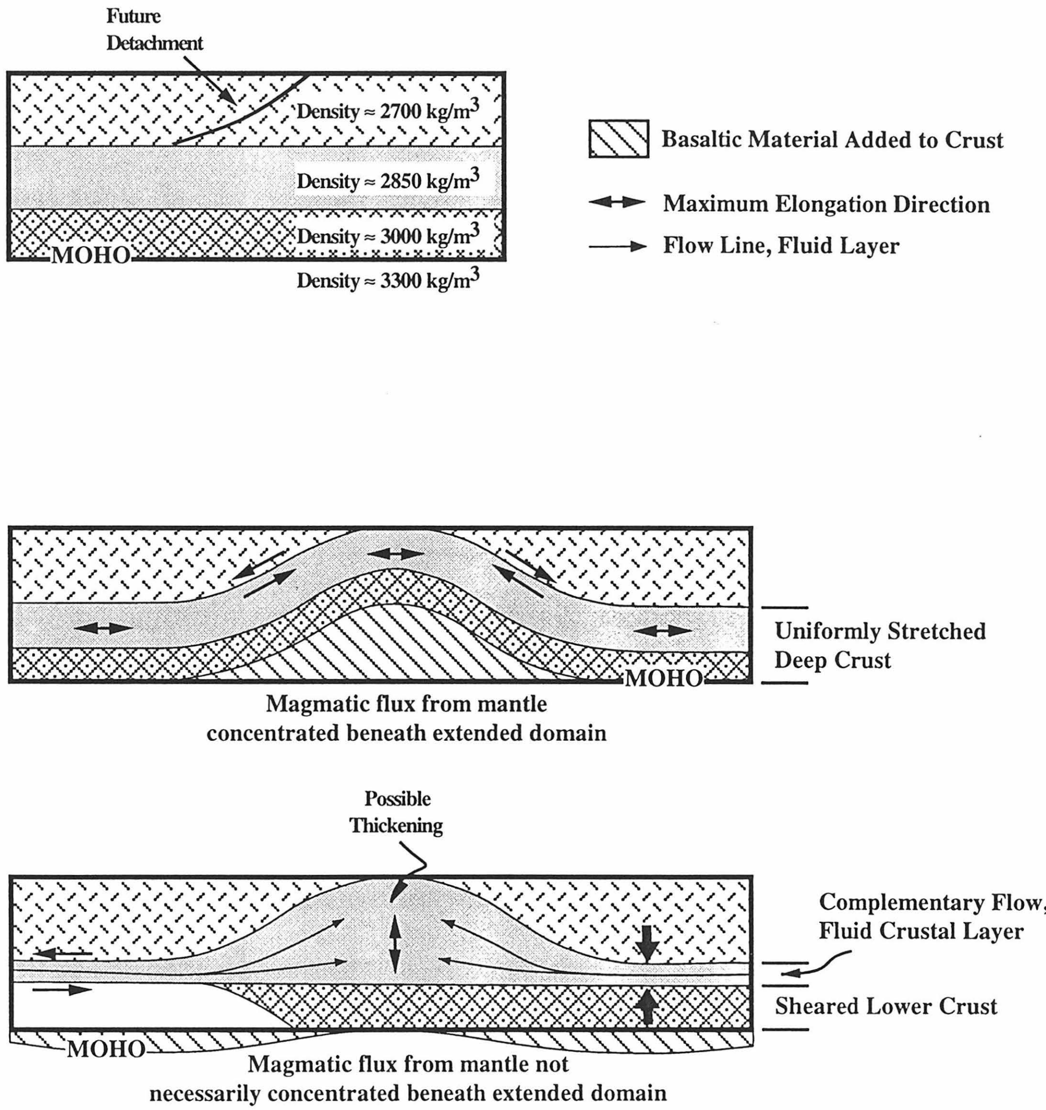

The rolling hinge model operates by sequential detachment of discrete fault blocks from the upper plate as the lower plate moves away and upward towards the Earth's surface (Figure 1.5b). Upper-plate block rotation is localized within a monoclinally warped hinge zone where rapid exhumation of the lower plate takes place during isostatic rebound at the site of greatest unloading. A cessation of faulting then occurs between the detached blocks and the lower-plate terrane in a direction away from the original breakaway zone. In this scenario, only one generation of faulting is necessary for each block to complete its rotation. The hinge migrates and rolls through the lower plate with continued extension. This scenario predicts rapid and localized decompression at the zone of basal detachment, providing a more efficient means of transporting hot mid-crustal material to shallow depths, possibly along an adiabat if the rate of denudation is sufficiently high.

During uniform deep-crustal stretching, redistribution of crustal mass is accomplished by magma transport (Figure 1.6b). Basaltic magma is added to the lower crust beneath the extended domain, providing the heat necessary for large-scale anatexis, which in turn weakens the crust and keeps the Moho flat. There is uniform thinning of the middle and lower crust, but minimal displacement between these layers. Kinematically, there will be a passive displacement of the stretched layer from beneath the stable blocks into the extended domains.

The model involving fluid-layer flow of weak, quartzose middle crustal material from unextended to extended domains (Figure 1.5c) requires a rheologically layered lithosphere with a strong upper and lower crust, combined with a relatively weak middle crust. Extension in the lower crust is accommodated by shearing of that strong, mafic layer. This wholesale mobilization of the mid-crust results in thickening of the middle crustal layer beneath the zone of greatest extension, whereas this layer is thinned beneath unextended domains. Magma input from the mantle directly under extensional terrains is not a necessary component for this mechanism to work, especially in crust overthickened by previous orogenic events. Nevertheless, advection of heat due to magmatism may be required to kep the middle crust weak (Wernicke, 1990; 1992). This model is similar to an earlier model by Block and Royden (1990) which proposes the wholesale mobilization of the lower crust into the zone of extension.

1.4 The Role of Aqueous Fluids in Metamorphic Core Complexes

1.4.1 General Statement

Aqueous fluids play a prominent role in the development of metamorphic core complexes at all structural levels. Lower-plate aqueous fluids are probably important in the generation of lower-plate magmas (Patino-Douce et al., 1990; Carr, 1992; Brown, 1994; and Peters and Wickham, 1995) and in the overall weakening of the crust (Davis and Coney, 1979; Bartley and Glazner, 1985; Axen, 1992; and Hollister, 1993). They are also important in producing the conditions needed for the formation of detachment faults (Hubbert and Rubey, 1959; Bartley and Glazner, 1985; Yin, 1989; 1991).

The aqueous fluid regimes of metamorphic core complexes are probably similar to those active in low pressure metamorphic terranes described by Wickham (1990; see Figure 1.7). Extensional metamorphic terranes are characterized by low-pressure regional metamorphism, involvement of large amounts of surface-derived water in the metamorphic process (Wickham and Taylor, 1985, 1987; Nesbitt and Muehlenbachs, 1989), and extensive partial melting at mid-crustal levels (Wickham and Oxburgh, 1985; Sandiford and Powell, 1986; Wickham, 1987; McKenzie and Bickle, 1988; Wickham,

Figure 1.7 -- Regimes of fluid flow in an extensional metamorphic terrane such as the Hercynian of the Pyrenees (modified after Wickham and Taylor, 1987). This type of extensional metamorphic terrane is characterized by low-pressure regional metamorphism, the involvement of large amounts of surface-derived water in the metamorphic process, and extensive partial melting at middle-crustal levels. Mid-crustal melting is driven by heat introduced into the crust by mafic intrusions emplaced in the deep crust during extension. These mafic melts drive melting in the lower crust, producing granodioritic and alkalic magmas which intrude into shallower crustal levels during later stages of crustal extension. The flux of surface-derived pore fluids is very high in the shallower, younger metasedimentary sequence, but is much lower in the underlying, and mostly older, gneisses. Homogeneous $\delta^{18}O$ values typify the mid-crustal metasedimentary rocks while the deep gneisses are heterogeneous in $^{18}O/^{16}O$.

Figure 1.7 Regimes of Fluid Flow in an Extensional Metamorphic Terrane

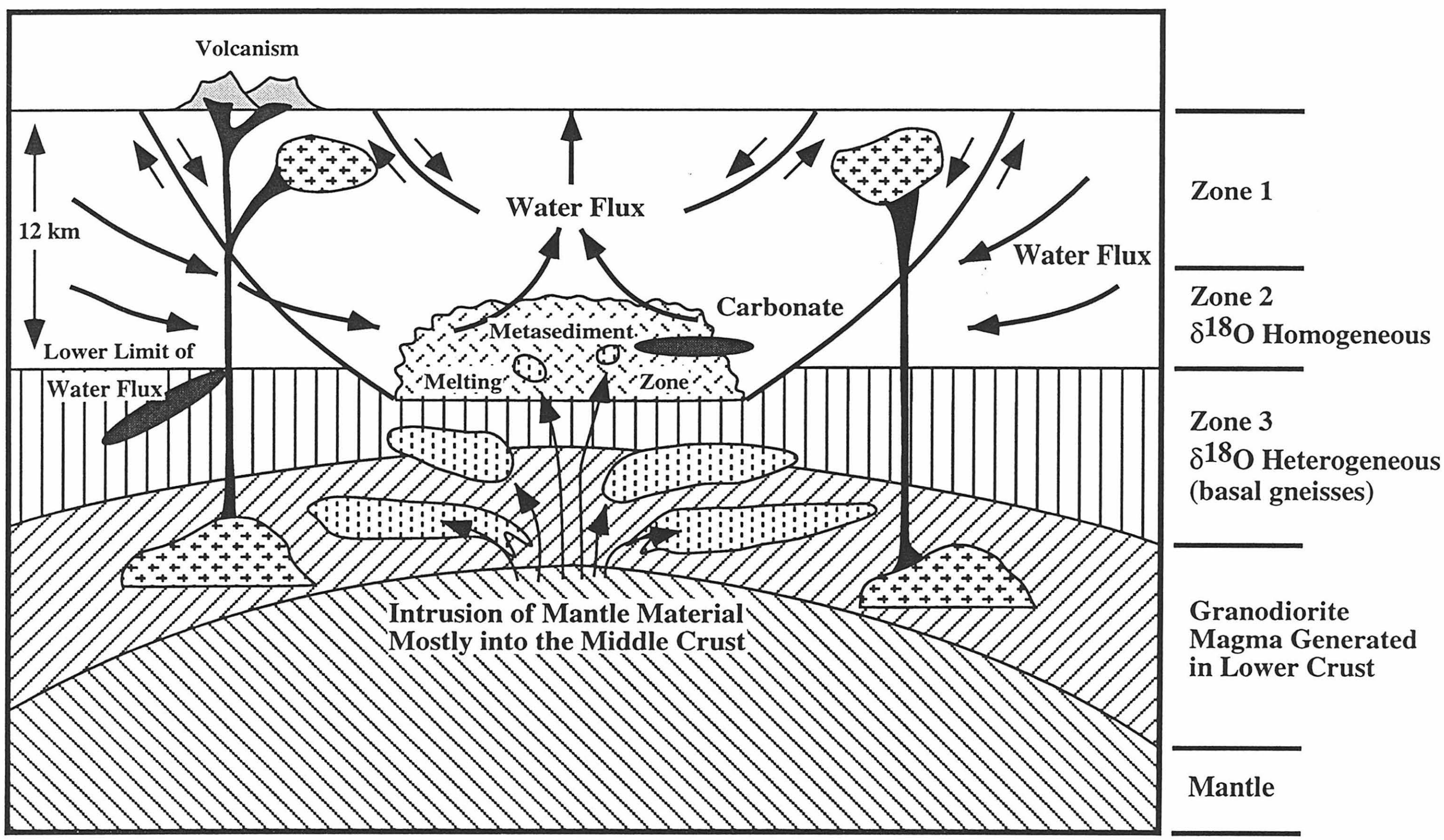

1990). This mid-crustal melting is driven by heat introduced into the crust by mafic intrusions intruded during extension (Wickham and Oxburgh, 1985; Gans, 1987; Sandiford and Powell, 1988). These mafic magmas also drive melting in the lower crust, producing granodiorites and granites that intrude into shallower crustal levels during the later stages of extension (Wickham and Taylor, 1990). The release of magmatic H_2O from these mantle-derived magmas may be an important factor fluxing partial melting of the heated lower and middle crust (Newton et al., 1980; Wickham and Peters, 1990; 1992; Peters and Wickham, 1995). However, melts generated by this rift-related anatectic event may also be an important agent of large-scale crustal dehydration (Valley et al., 1990). The flux of surface-derived pore fluids is typically very high at shallow levels and decreases with depth (Gregory and Taylor, 1981; Wickham and Taylor, 1985; 1987). Wickham and Taylor (1985, 1987) found that in these kinds of terranes in the Pyrenees the mid-crustal metasedimentary rocks typically have homogeneous $\delta^{18}O$ values while the deep gneisses are heterogeneous in $^{18}O/^{16}O$.

At least two modes of hydrothermal activity (see Figure 1.8) are active during detachment faulting (Kerrich and Hyndman, 1986; Kerrich and Rehrig, 1987; Reynolds and Lister, 1987): (1) A convective system involving meteoric waters or formation waters at hydrostatic pressure at shallow crustal levels within the brittle regime. (2) A low water/rock ratio system involving metamorphic and/or magmatic water at lithostatic pressures active at deep crustal levels in the ductile regime. Effects of the deep-seated hydrothermal alteration may be overprinted and obscured by later interaction of these rocks with meteoric water as these formerly ductile rocks enter the brittle regime during denudation (Reynolds and Lister, 1987; Fricke et al., 1992; Morrison, 1994).

Figure 1.8 -- Detachment fault fluid flow regimes (from Reynolds and Lister, 1987). Two modes of hydrothermal activity are active during detachment faulting: (a) a hydrostatic convective upper-plate system involving mostly meteoric water, and (b) a deeper, lithostatic lower-plate system involving magmatic and/or metamorphic water from below. The upper plate meteoric-hydrothermal system overprints the effects of the deep-level hydrothermal system as the lower plate is transported into the regime of brittle deformation.

Figure 1.8 Detachment Fault Fluid Flow Regimes

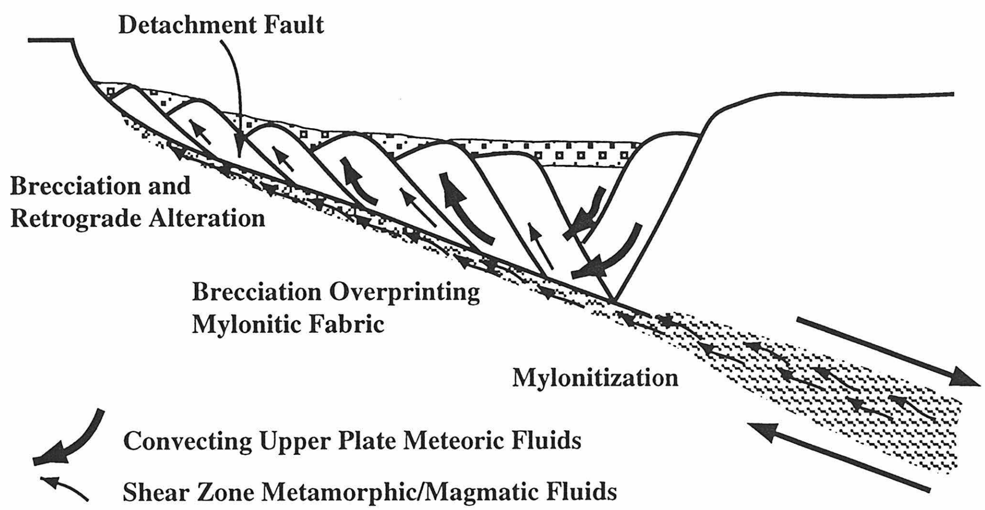

The meteoric-hydrothermal systems may be active throughout the brittle portion of the crust during extension, perhaps to depths of 15 km (Nesbitt and Muehlenbachs, 1989, 1991). Seismic pumping (Sibson et al., 1975) also could be an important fluid transport mechanism allowing local infiltration of surface-derived formation waters into ductile portions of the lower plate adjacent to detachment surfaces (Reynolds and Lister, 1987; Fricke et al., 1992). Mixing between these two types of fluids may be an important mineralizing process in the upper plate (Spencer and Welty, 1986; Nesbitt and Muehlenbachs, 1989; Beaudoin et al., 1991, 1992). Evolved saline meteoric waters caused large-scale K-metasomatism in upper plate volcanic sections of the Arizona complexes (Brooks, 1986; Roddy et al., 1988).

1.4.2 Stable Isotope Studies of Detachment Faults and the Upper Plate

Stable isotope studies have proved essential in understanding hydrothermal systems operating during the development of metamorphic core complexes. Initially, these studies focused on water-rock interaction associated with detachment faulting, and very few studies have dealt with the deep-seated lithostatic systems. One of the goals of the present study is to codify and unify the attributes of the various kinds of hydrothermal systems associated with the development of metamorphic core complexes.

Many stable isotope studies have shown that rift zones and extensional settings are the most favorable sites for deep penetration and convective circulation of meteoric-hydrothermal fluids (Taylor, 1974; 1977; 1978; Taylor and Forester, 1979; Taylor et al., 1991). Similar studies have also demonstrated that during extension, detachment faults can serve as conduits for the movement of large amounts of meteoric-hydrothermal fluids as the lower plate is brought to shallower crustal levels. Lee et al. (1982, 1984) made the first discovery of the involvement of meteoric water affecting plutonic rocks cataclastically deformed along a detachment fault, namely in the Snake Range decollement in eastern Nevada.

Magaritz and Taylor (1986) in their $^{18}O/^{16}O$ survey of plutonic rocks of the southern Canadian Cordillera discovered that the most intense hydrothermal alteration was localized along major N-trending lineaments (subsequently proved to be major detachment faults; Templeman-Kluit and Parkinson, 1986; Carr et al, 1987; Parrish et al, 1988). Magaritz and Taylor (1986) proposed that the emplacement of early Tertiary dikes and sills into these lineaments provided the heat source which drove the convective circulation of meteoric-hydrothermal fluids.

Much of our understanding of detachment-related hydrothermal processes came from research by Kerrich and his colleagues (1986, 1987, and 1988) at the Bitterroot complex in Montana, and in numerous core complexes in Arizona. These studies delineated the dual nature of hydrothermal processes active during core complex formation, where magmatic and/or metamorphic fluids interact with the ductilely deforming lower-plate rocks followed by an overprinting of these rocks by late meteoric-hydrothermal activity as the lower plate makes its way into the brittle regime. These studies also determined that the temperatures at which $^{18}O/^{16}O$ exchange takes place decrease towards the surface. Follow-up studies by Roddy et al. (1988) found that low-temperature, upper-plate, meteoric-hydrothermal systems involving saline brines are responsible for the profound mobility of potassium, first reported by Brooks (1986), as well as for the Cu-Au-Ag mineralization observed at the Harcuvar Mountains complex in Arizona. On the other hand, stable isotope studies at South Mountain, Arizona, by Smith et al. (1991) were interpreted as indicating that meteoric-hydrothermal effects are absent from the mylonitic and brittle rocks of that detachment fault, and that magmatic waters played the main role in chloritization and mineralization at this location.

In their regional stable isotope survey of gold-quartz veins from the Canadian Cordillera, Nesbitt and Muehlenbachs (1989) suggested that meteoric waters at hydrostatic pressure reach depths of at least 15 km in regions of strike-slip and extensional faulting. In a subsequent paper (1991), these workers postulated that regional structural style is the main controlling factor determining the depth of penetration of meteoric waters, with deep movement of meteoric waters happening only in extensional environments. These workers went further to speculate that most gold-quartz veins hosted by greenschist and lower-grade rocks in the southern Omineca belt were formed within the outflow limbs of meteoric water convection cells, and that these meteoric waters were the dominant aqueous fluid involved in the extension-related metamorphism of these rocks (Nesbitt and Muehlenbachs, 1995). Nesbitt et al. (1995b) carried this further to propose that this large-scale meteoric water-rock interaction drove decarbonation of pelites and calc-silicates, and may even have been responsible for an apparent increase in atmospheric CO_2 concentration and the associated greenhouse warming during the Eocene.

At the Ruby-East Humboldt Range complex, Fricke et al. (1992) found that meteoric waters infiltrated into the ductile mylonite zone at least 70 meters beneath the Secret Pass detachment zone. Seismic pumping (Sibson et al., 1975) was proposed as the mechanism of fluid infiltration into the mylonites during a time interval in which ductile flow and brittle fracturing were alternately happening. D/H measurements of biotite from various levels of this complex provided evidence for the infiltration of meteoric waters as deep as 2 km beneath the detachment surface (Wickham et al., 1993).

In the upper plate of the Slocan Lake fault in British Columbia, Beaudoin et al. (1991, 1992) documented the formation of Ag-Pb-Zn-Au vein and replacement deposits during the Eocene unroofing of the Valhalla complex. They proposed that mineralization took place during mixing between a deep-seated high-salinity fluid isotopically equilibrated with the crust and a low-salinity upper-crustal meteoric water. The Slocan Lake fault may also have served as the transport avenue for the migration of CO_2-rich mantle-derived fluids upward to the shallow crustal depths at which mineralization occurred.

1.4.3 Stable Isotope Studies of the Lower Plate

At the East Humboldt Range, Nevada, Wickham and Peters (1990) documented an oxygen isotope discontinuity in high-grade lower-plate rocks of this metamorphic core complex. This discontinuity separates a low-^{18}O, isotopically homogeneous zone at the deepest structural levels from an overlying zone that is heterogeneous in $^{18}O/^{16}O$. These observations were interpreted to be the result of upward infiltration of large amounts of deep-seated magmatic water. Grunder and Wickham (1991) discovered that extension-related magmas which erupted in these areas became successively lower in $^{18}O/^{16}O$ with time, indicating that a similar homogenization process was probably active in the mid-crustal source regions of these magmas (but one that involved a mantle-source fluid). Numerical modeling of oxygen isotope profiles across marble and silicate layers from the deepest sections of this complex were utilized to argue that mantle-derived magmas crystallizing and releasing volatiles at depth were sufficient to account for the homogeneous low-^{18}O section (Wickham and Peters, 1992).

Subsequent studies by Peters and Wickham (1995) found a correlation between the abundance of leucogranite and both the degree of ^{18}O-lowering of metasediments, and the $^{18}O/^{16}O$ homogeneity on the outcrop scale. Marble-rich sections were found to have an opposite correlation. They proposed an $^{18}O/^{16}O$ exchange mechanism involving convective recirculation of magmatic fluids introduced into the system by the intruding leucogranites.

Deep levels of the lower plate of the Whipple Mountain complex in southeastern California experienced meteoric water-rock interaction as the result of the juxtaposition of the lower plate against the base of the faulted upper plate (Morrison, 1994). Morrison (1994) found evidence for dual fluid regimes in these lower plate rocks with mylonitic dikes in $^{18}O/^{16}O$ equilibrium with magmatic or metamorphic fluid at >600°C while non-mylonitic dikes showed evidence for $^{18}O/^{16}O$ exchange with meteoric waters at ~ 350°C. Fracturing associated with the emplacement of these late, non-mylonitic dikes apparently served as the mechanism allowing for ingress of meteoric water as deep as 4 km into the lower plate.

1.5 Description of Thesis Chapters

The chapters of this thesis are structured to represent the work I have done in each structural domain in order to answer some of the questions posed above. Chapter 2 is an overview of the tectonic and geologic setting of the southern Omineca Crystalline Belt; it includes descriptions of the sedimentary, volcanic and plutonic rocks, a discussion of the metamorphic history of the terrane, a tectonic synthesis, and a summary of the regional-scale stable isotope geochemistry of southern British Columbia.

Chapter 3 presents results of $^{18}O/^{16}O$ studies of basement-zone rocks of the Monashee Complex that lie underneath the Monashee decollement. Chapter 4 is a detailed discussion of $^{13}C/^{12}C$ and $^{18}O/^{16}O$ data on rocks and minerals from the middle crustal zone of the southern Thor-Odin complex and from the underlying Monashee decollement. Included in Chapter 4 is the presentation of a material-balance model invoking multiple stages of $^{18}O/^{16}O$ exchange during decompression-related anatexis as a way to account for the observed oxygen isotope homogenization in the allochthonous middle crustal layer in the southern Thor-Odin complex. Portions of the contents of Chapters 3 and 4 have been written up with co-author Hugh P. Taylor, Jr., and already submitted for publication; that manuscript is in press and included in Chapter 4.

Chapter 5 is a summary of $^{18}O/^{16}O$ studies of detachment faults throughout the southern Omineca belt, but most of this chapter describes work done at the Valhalla complex, and particularly the Slocan Lake detachment fault. The appendix describes analytical methods: (A) a description of analytical procedures incorporated in this work, and (B) a description of the Caltech oxygen isotope laser extraction system, built in collaboration with Michael Palin, which was used to obtain much of the mineral separate $^{18}O/^{16}O$ data obtained in this study (including all of the garnet data).

Chapter 2. Geologic Setting

2.1 The Cordilleran Orogen in Canada

The tectonic architecture of the Canadian Cordillera can best be described in terms of morphogeologic belts and terranes (Monger et al., 1982; Wheeler et al., 1991; Gabrielse et al., 1991; Monger, 1993). A morphogeologic belt is a physiographic and geologic domain which is the product of an integrated series of geologic processes that created a distinct petrologic and tectonic framework. Terranes are fault-bounded packages of rock that preserve a geologic record different from those of neighboring terranes (Coney et al., 1980; Saleeby, 1984). The morphogeologic belts of the Canadian Cordillera are the physiographic product of the amalgamation of such terranes into superterranes, as for example, by the collision and accretion of the Intermontane Superterrane against North America in the Middle Jurassic, followed by the Cretaceous to Early Tertiary collision and accretion of the Insular Superterrane along the western margin of North America (Monger et al., 1982).

2.1.1 Morphogeological Belts of the Canadian Cordillera

The Canadian Cordillera is comprised of five morphogeological belts (Figure 2.1). From east to west, these are: the Foreland Rocky Mountain fold and thrust belt, the Omineca belt, the Intermontane belt, the Coast belt, and the Insular belt (Monger et al., 1982; Gabrielse et al., 1991). The Coast and Omineca belts were formed along the metamorphic and plutonic sutures that juxtaposed the Intermontane and Insular superterranes against ancestral North America (Monger et al., 1982).

The Foreland belt, or Rocky Mountain fold and thrust belt, is comprised of miogeoclinal strata deposited in a subsiding, passive environment at the continental margin (Bond and Kominz, 1983; Ricketts 1989). These rocks were imbricately thrust eastward between the Jurassic and the early Eocene (Price and Mountjoy, 1970; McMechan and Thompson, 1989). The Omineca belt is the product of metamorphism and plutonism associated with the accretion of the Intermontane Superterrane to North America during the middle Jurassic (Monger et al., 1982; Brown et al., 1986; Brown and Read, 1983). Metamorphism and anatexis continued into the Cretaceous and early Tertiary (Brown et al., 1986; Carr et al., 1987; Armstrong, 1988; Parrish et al., 1988; Carr, 1991; 1992; 1995; Spear and Parrish, 1996). The metamorphic and plutonic rocks of this belt were exhumed during the Cretaceous and Paleocene by eastward-directed, basement-cored thrusting (Brown et al., 1986; Brown and Journeay, 1987; McNicoll and Brown, 1994), followed by Eocene extension (Templeman-Kluit and Parkinson, 1986; Carr et al., 1987; Parrish et al., 1988, Carr, 1992). However, it has been suggested that much of the unroofing of the middle crust in this terrain may have occurred as the result of synchronous thrusting and extension during the Cretaceous (Hodges and Walker, 1992). The Intermontane belt is comprised of unmetamorphosed Paleozoic to Mesozoic sedimentary and volcanic rocks of island arc and deep ocean basin affinity (Gabrielse et al., 1991). Numerous Cretaceous to Eocene right-lateral strike-slip faults having great displacement (~ 1000 km) cut the Intermontane belt (Price and Carmichael, 1986; Monger, 1993).

The Coast belt is a zone of intense metamorphism and plutonism that formed during the Cretaceous-to-Early Tertiary accretion of the Insular Superterrane to the continental margin (Gabrielse et al., 1991). The principal feature of the Coast belt is the Jurassic-Paleocene Coast Range batholith, a magmatic arc comprised of numerous, large tonalitic to granodioritic plutons, and their associated metamorphosed country rocks (Roddick, 1983; Armstrong, 1988). The Insular belt includes the modern Pacific continental margin and comprises Paleozoic, Mesozoic, and Cenozoic volcanic arc, oceanic and clastic wedge assemblages (Gabrielse et al., 1991). These rocks are disrupted by west-verging thrust faults, plutons, and right-lateral strike-slip faults (Rubin et al., 1990; McClelland et al., 1992).

2.1.2 Terranes of the Canadian Cordillera

The present crustal architecture of the southern Canadian Cordillera is dominated by ancestral North America and two superterranes, the Intermontane and Insular superterranes (Figure 2.2). These superterranes are an amalgamation of numerous subsidiary terranes (that can be divided into subterranes), including some pericratonic terranes (Coney et al., 1980; Jones et al., 1983; Saleeby, 1984).

The Intermontane superterrane was established as a separate entity by the latest Triassic, and was accreted to North America during the Jurassic (Coney et al., 1980; Gabrielse et al., 1991). The Slide Mountain, Quesnel, Cache Creek, and Stikine terranes comprise the Intermontane superterrane (Figures 2.2 and 2.3) in the southern Canadian Cordillera (Wheeler et al., 1991). In the following discussion, the Slide Mountain and

Figure 2.1 -- Morphogeologic belts of the Canadian Cordillera (after Gabrielse et al., 1991). The Coast and Omineca belts are metamorphic and plutonic culminations formed during the collision and accretion of the Intermontane and Insular Superterranes to North America. The Foreland belt is the Rocky Mountain fold and thrust belt. The Intermontane and Insular belts are composed of volcanic, sedimentary, and plutonic rocks belonging to the Intermontane and Insular Superterranes, respectively.

Figure 2.2 -- Terrane map of the Canadian Cordillera (modified after Gabrielse et al., 1991). The Insular Superterrane is comprised of Wrangellia (WR) and the Alexander Terrane (AX). The Intermonatane Superterrane is made up of the Cache Creek terrane (CC), Stikinia (ST), Quesnellia (QN), and the minor terranes to the southwest. The Coast Plutonic complex (CPC) and the Nisling Terrane (NS) are also shown.

Figure 2.3 -- The distribution of terranes and regional structures in the southern Omineca belt (after Tempelman-Kluit et al., 1991). The Selkirk Allochthon is comprised of rocks from several terranes, including part of ancestral North America, the Kootenay Terrane, Quesnellia, and the Slide Mountain Terrane, and all of these were thrust as a package over the Monashee Terrane along the Monashee decollement between the Middle Jurassic and Paleocene.

Figure 2.1 Morphogeologic Belts of the Canadian Cordillera

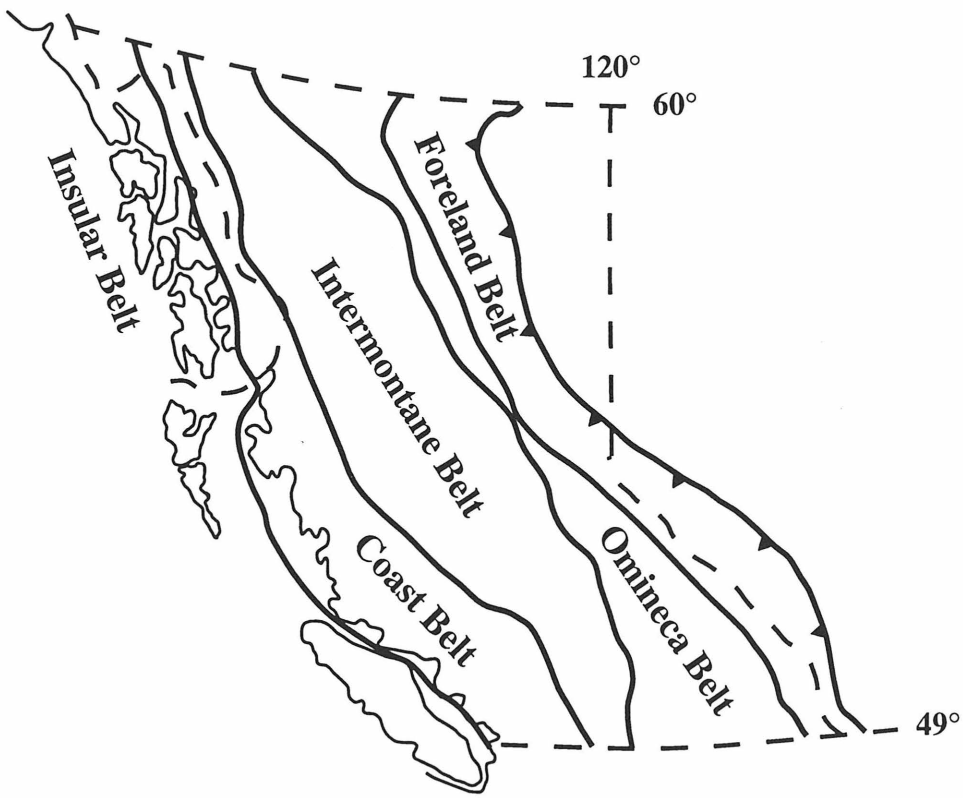

Figure 2.2 Terrane Map of the Canadian Cordillera

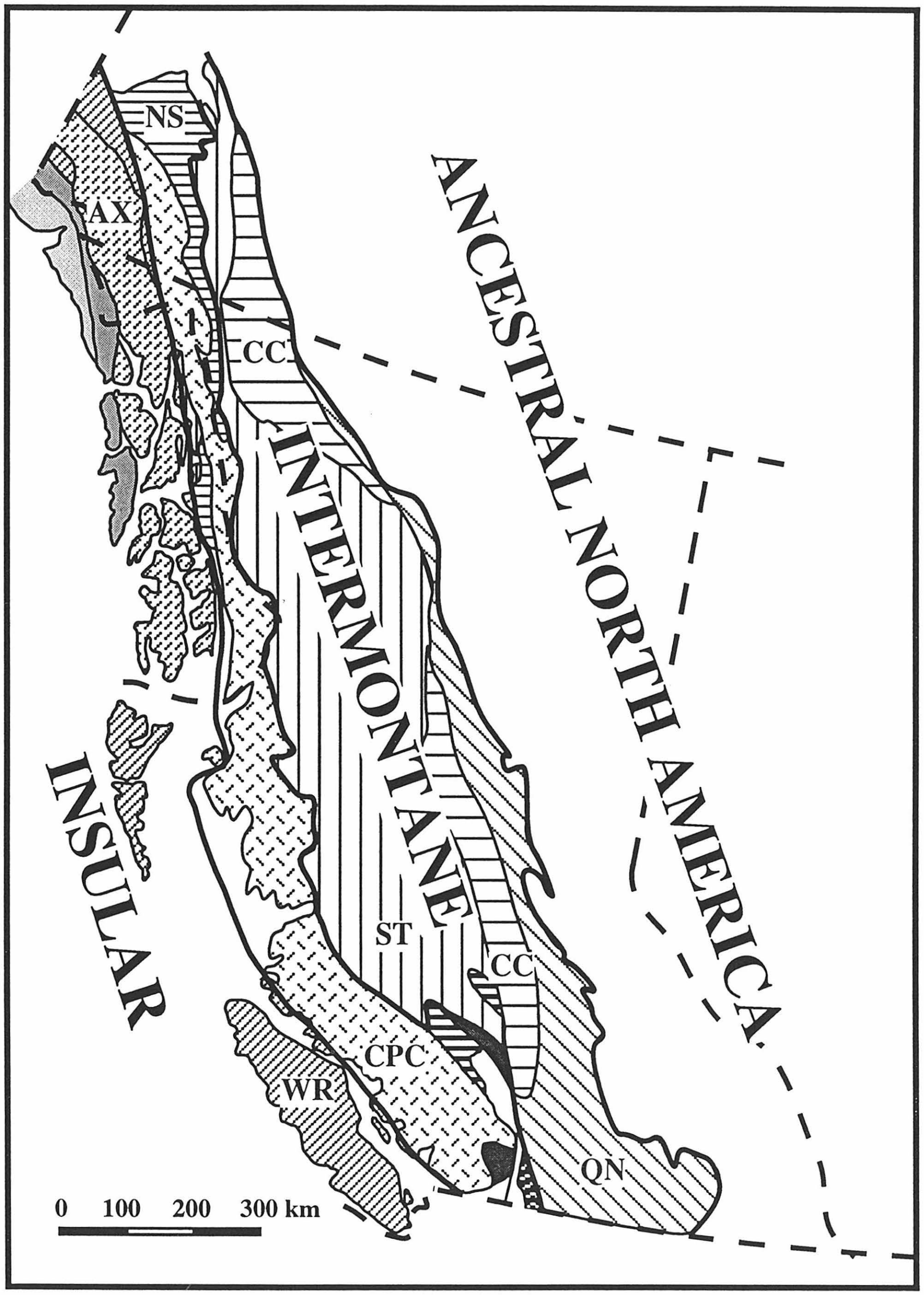

Figure 2.3 The Selkirk Allochthon

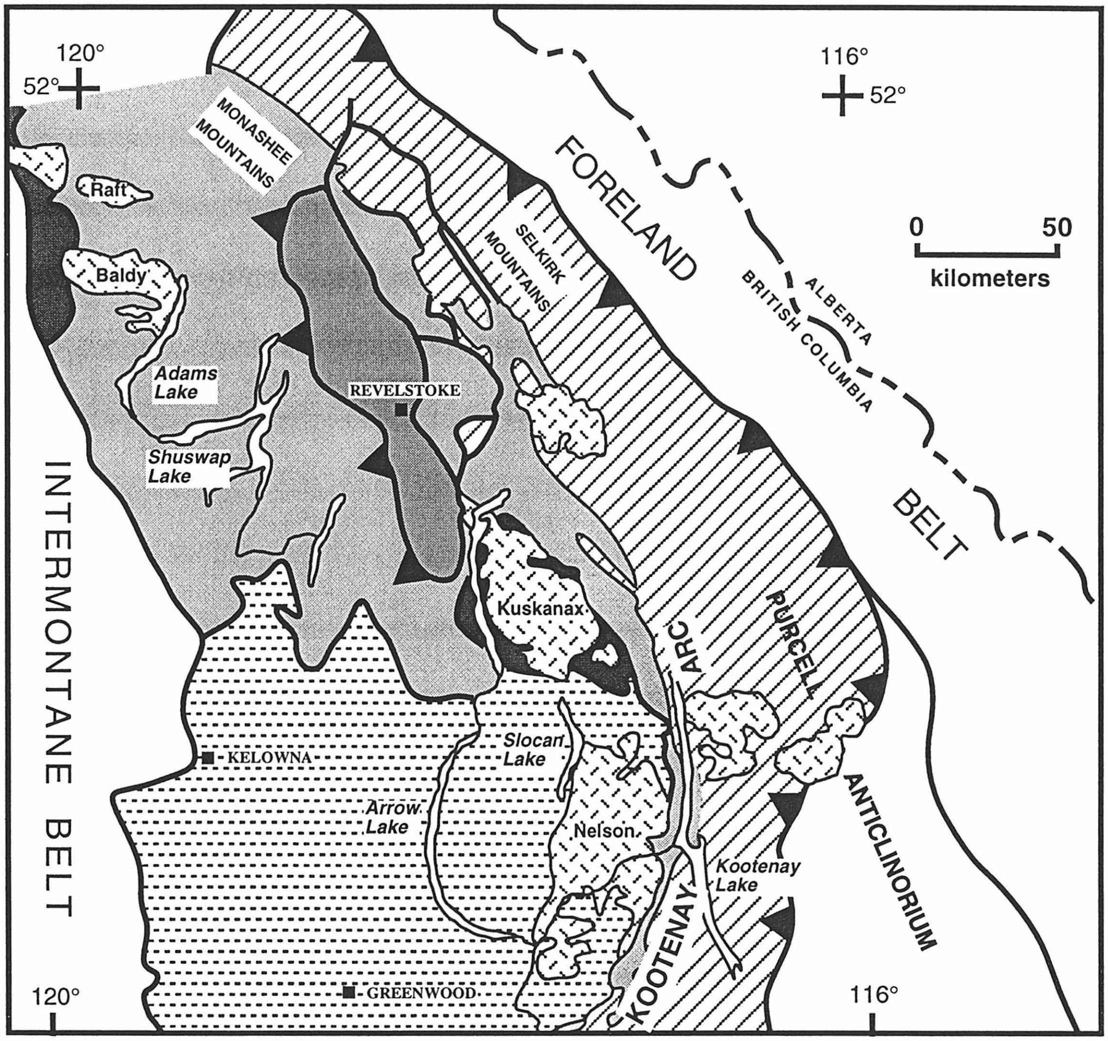

Mesozoic Intrusions

INTERMONTANE SUPERTERRANE

Quesnellia Terrane

Slide Mountain Terrane

NORTH AMERICAN AFFINITY

Ancestral North America

Kootenay Terrane

Monashee Terrane

Quesnel Terranes are described in detail, but only a few general features of the Stikine and Cache Creek Terranes will be discussed. The two latter terranes lie well to the northwest of the study area of this thesis, whereas the Slide Mountain and Quesnel Terranes crop out in the area of interest, namely the southern Omineca Belt.

The Insular Superterrane is comprised of the Alexander Terrane, Wrangellia, and numerous minor terranes of oceanic affinity (Monger et al., 1982). These terranes were amalgamated by the time of accretion onto the western margin of the Intermontane Superterrane during the mid-Cretaceous, as indicated by plutons of the Coast batholith that cross cut this suture zone (Saleeby, 1984; Armstrong, 1988; Woodsworth et al., 1991). No further details of the Insular Superterrane are discussed because it lies far to the west of the study area.

2.1.3 Geologic Framework of the Southern Omineca Belt

From deepest to shallowest, the southern Omineca belt is divided into three tectonic zones (Figures 2.3 and 2.4): (1) the basement zone of the Monashee Terrane, (2) the middle crustal infrastructure of the Selkirk Allochthon, and (3) the upper crustal Selkirk Allochthon (Parrish et al., 1988; Carr, 1991; 1995; Cook et al., 1992; Parrish, 1995). The Selkirk Allochthon is a 25-km-thick thrust sheet that was displaced at least 200 km over the Monashee Terrane during ductile shearing along the Monashee decollement (Brown et al., 1986; 1992; see Figure 2.4). The deep, high-grade infrastructure of the Selkirk Allochthon was detached from the upper-crustal suprastructure and rapidly denuded by displacements along the numerous north-trending Eocene detachment faults found throughout the region (Parrish, 1984; Lane et al., 1984; Templeman-Kluit and Parkinson, 1986; Parrish et al., 1988). These events produced a crustal architecture consisting of three distinct zones that have experienced separate depositional, magmatic,

Figure 2.4 -- Tectonic map of the southern Omineca belt (after Carr, 1991). The basement zone is shown in the light shading. Dark shading denotes the middle-crustal infrastructure of the Selkirk Allochthon. These basement and middle crustal zones represent the lower plate rocks of the metamorphic core complexes. The suture between the Intermontane Superterrane (white pattern) and ancestral North America (diagonal striped pattern) roughly corresponds to the Kootenay Arc (see Figure 2.3). The line A-B indicates the location of the cross sections in Figure 2.4. Deep, ductile Jurassic-Paleocene compressive structures form the upper boundaries of the basement zone; two of these are shown, Monashee Decollement (MD) and Gwillim Creek Shear zone (GCSZ) and indicated with teeth in the hanging wall. Extensional detachment faults, Columbia River fault (CRF), Slocan Lake fault (SLF), Valkyr shear zone (VSZ), Okanagan fault (OF), Newport fault (NF), Granby fault (GF), Kettle fault (KF), and Priest River fault (PRF), form the boundaries between the upper plates and the middle crustal zones.

Figure 2.4 Tectonic Map of the Southern Omineca Belt

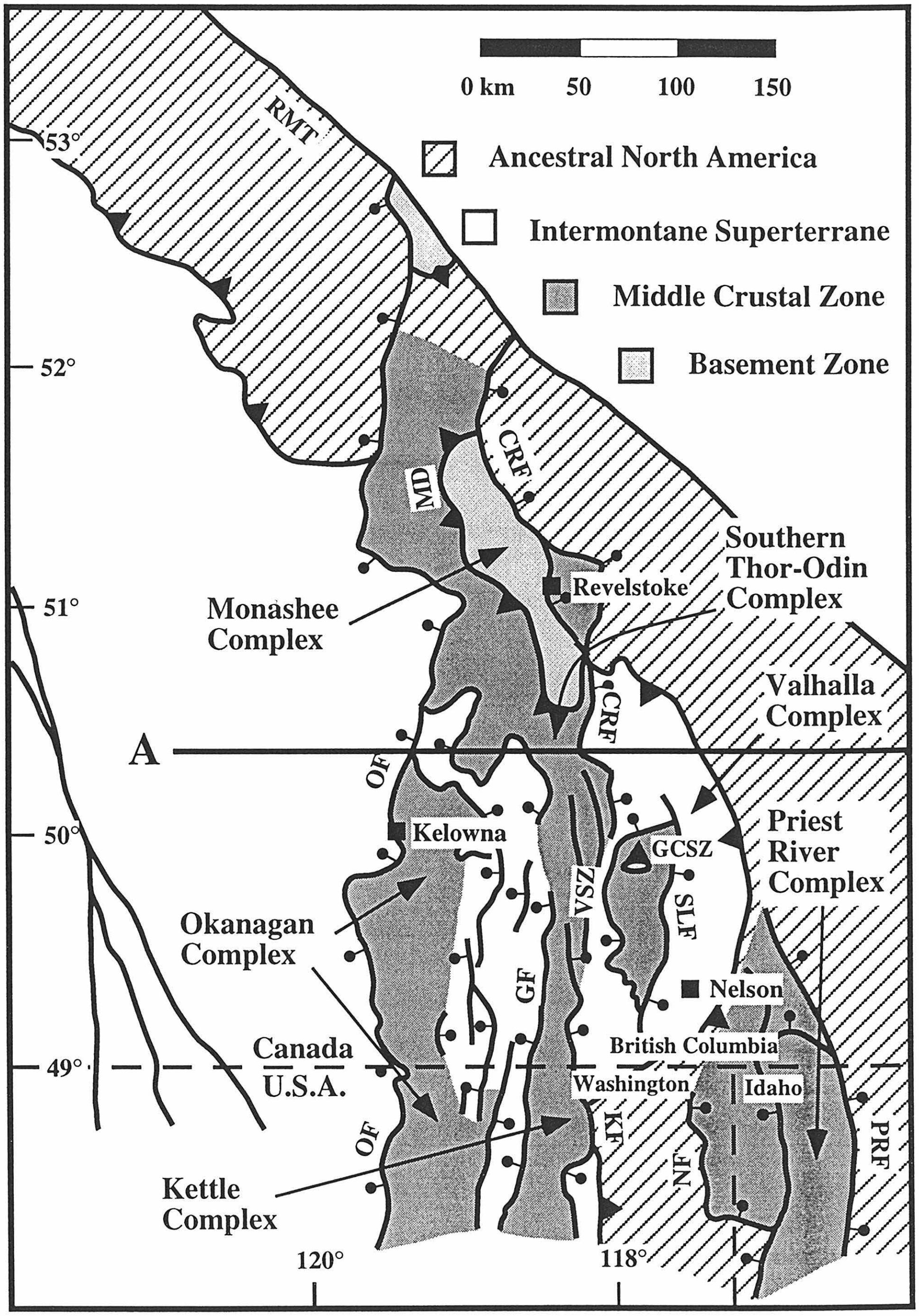

Figure 2.5 -- Interpretive cross-sections showing the tectonic evolution of the southern Omineca belt (after Cook et al., 1992). The miogeocline is denoted by the diagonal pattern. The North America basement is shown with the dark pattern. Accreted rocks of the Quesnellia and Slide Mountain terranes are shown in the horizontal lined pattern. The location of this cross section at the latitude of the southern Thor-Odin complex is shown on Figure 2.4. The heavy dashed curves denote the inferred pre-deformation locations of major faults active during the episode depicted in each sucessively younger panel, whereas the opposite is true for the light dotted curves. The Jurassic panel shows the inferred state of this part of the western margin of North America just before the accretion of the Intermontane Superterrane. The Paleocene section shows the thickened crust built during Middle Jurassic to Paleocene thrust faulting and obduction, and it represents the state of the system just prior to Eocene extension. The present day current crustal section shows crustal thinning due to Eocene extension.

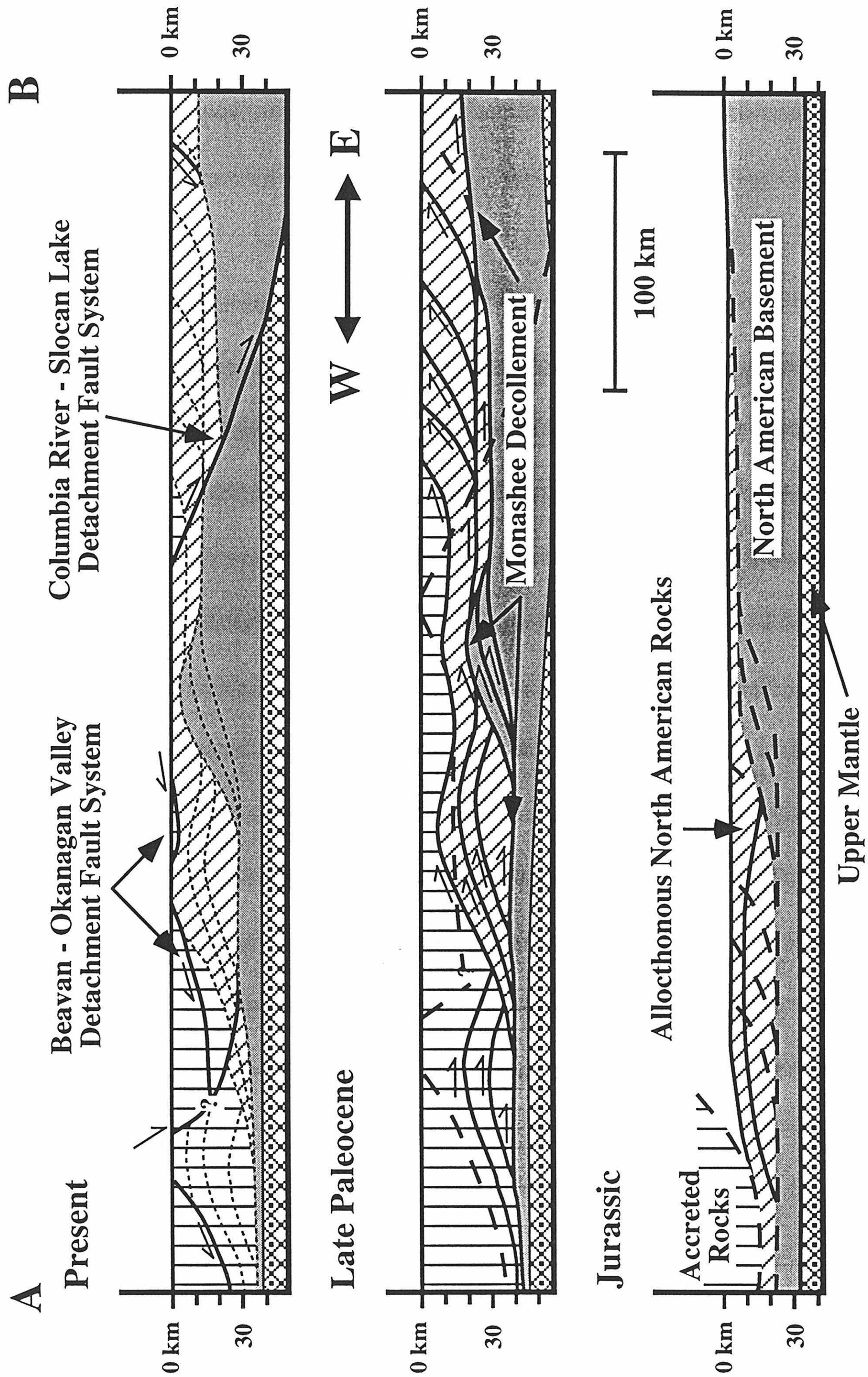

Figure 2.5 Tectonic Evolution of the Southern Omineca Belt

metamorphic, and plutonic histories (Parrish et al., 1988; Carr, 1991; 1995; Parrish, 1995). Taken as a whole, this geologic history of the study area of this thesis also applies in general to the overall evolution of the Mesozoic and early Cenozoic orogenic events that affected the southern Canadian Cordillera, as described in more detail in the following sections.

2.2 Ancestral North America

Ancestral North America by definition consists of rocks that are autocthonous to the ancient North American craton (Figure 2.3 and 2.4). In the southern Omineca belt, rocks belonging to Ancestral North America are exposed in the Purcell Anticlinorium and the eastern part of the study area. Between the Middle Proterozoic and the accretion of outboard terranes in the Middle Jurassic, the evolution of ancestral North America is marked by rifting, followed by subsidence and associated passive-margin sedimentation (Bond and Kominz, 1983; Ricketts, 1989; Gabrielse et al., 1991; Fritz et al., 1991). In the southern Omineca belt, the volcanic and sedimentary rock units that comprise ancestral North America are exposed in the Purcell Anticlinorium and the eastern part of the study area; these are the Middle Proterozoic Purcell Supergroup, the Late Proterozoic Windermere Supergroup, the Lower Cambrian Hamill Group, the Mohican and Badshot Formations, and the Middle Cambrian Index Formation, which is the base of the Lardeau Group.

2.2.1 The Middle Proterozoic Purcell Supergroup

The Middle Proterozoic (1700-1200 Ma) Purcell (or Belt) Supergroup is exposed in southeastern British Columbia and southwestern Alberta, as well as in Montana and Idaho. Sedimentary facies and thickness (up to 20 km-thick) patterns have been used to interpret this assemblage as an embayment in the continental margin (McMechan, 1981); however, a two-sided intracratonal basinal origin for the Purcell has also been argued (Winston et al., 1984). Virtually all units that comprise the Purcell Supergroup are intruded by a series of 1430-1340 Ma mafic sills (Zartman et al., 1982) and granodiorites (J.K. Mortenson, *cited in* Woodsworth et al., 1991), indicating deposition in a rift setting.

Principal divisions of the Purcell Supergroup are the basal, lower, middle carbonate, and upper divisions (Price, 1964; Aitken and McMechan, 1991). Turbiditic sequences of 4200 m of thinly-bedded quartzite, argillaceous quartzite, siltite, and argillite comprise the Alridge Formation, the basal division (Reesor, 1958). The lower division Creston Formation, a 900-2400 m-thick sequence of siltite, argillite, and quartz arenite, grades into the lower Kitchener Formation, 17-500 m of dolomitic argillite (McMechan, 1981). The middle carbonate division is comprised of up to 1900 m of basinal-facies subtidal carbonates and clastics of the upper Kitchener and Coppery Creek Formations (Reesor, 1983; Aitken and McMechan, 1991).

The upper division of the Purcell Supergroup has been divided into the eastern and western facies series (Aitken and McMechan, 1991). The eastern facies series in the eastern Purcell Mountains is made up of 1300-3000 m of siltite, argillite, basalt, dolomite, sandstone, and volcaniclastics of the Van Creek, Nicol Creek, Sheppard, Gateway, Phillips, and Roseville Formations (McMechan et al., 1980). This sequence was deposited in a tidal flat environment and punctuated by basaltic volcanism (McMechan, 1981). In the western Purcell Mountains, the western-facies series consists of an unknown thickness of deformed and metamorphosed siltite, quartzite, phyllite, and carbonate belonging to the La France Creek Group and the Mount Nelson Formation (Reesor, 1958).

2.2.2 *The Upper Proterozoic Windermere Supergroup*

The Upper Proterozoic Windermere Supergroup crops out throughout the eastern part of the study area. These strata (Figure 2.6) record a history of rifting, uplift, erosion, glaciation, and volcanism (Gabrielse and Campbell, 1991). Analogous rift-related late Precambrian clastic rocks are found along the entire length of the North American Cordillera (Stewart, 1972). In order to properly describe this unit and to show along-strike facies variations, sections from the southern Purcell Mountains, the northern Selkirk Mountains, and the southern Cariboo Mountains are described. Stratigraphic sequences correlated with the Windermere comprise much of the middle-crustal infrastructure of the southern Omineca belt (Hoy, 1977; 1988; Scammell and Brown, 1980; Carr, 1991) studied in this work (Figure 2.6).

At the southern Purcell Mountains, the Windermere is made up of the Toby Formation diamictites, the Irene Volcanics, and the clastic rocks of the Horsethief Creek Group (Little, 1960; Reesor, 1973). The Toby Formation is a (up to 500 m-thick) polymictic conglomerate containing angular to subangular pebbles, cobbles, and boulders of dolostone, quartzite, and slate derived from the underlying Purcell Supergroup. The Irene Volcanics are a 700 m-thick sequence of fine-grained mafic tuff and massive schistose greenstone having a Nd/Sr apparent age of 762±40 Ma (W. J. Devlin, *cited in* Gabrielse and Campbell, 1991). The Horsethief Creek Group is a 1000-3000 m-thick sequence of slate, argillite, and phyllite with lesser amounts of quartzite, greywacke, arkosic grit, pebble conglomerate, and limestone. This stratigraphic group is split into three parts: a lower argillite and slate unit containing minor limestone; a middle unit composed of quartzite, arkosic grit, and pebble conglomerate; and an upper unit of slate and siltstone with minor carbonate. The upper and lower units are locally turbiditic.

Figure 2.6 -- A stratigraphic column of sedimentary and volcanic rocks that comprise ancestral North America and the Kootenay Terrane (see Figure 2.3) in the southern Omineca belt (compiled from Fyles and Eastwood, 1962; Fyles, 1964; Klepacki and Wheeler, 1985; Pell and Simony, 1987). The stratigraphic boundary between ancestral North America and the Kootenay Terrane is the upper contact of the Index Formation in the Lardeau Group. This section is correlative with the middle crustal sequence at the southern Thor-Odin metamorphic core complex (Carr, 1992).

Figure 2.6 Stratigraphy of Southern Omineca Belt

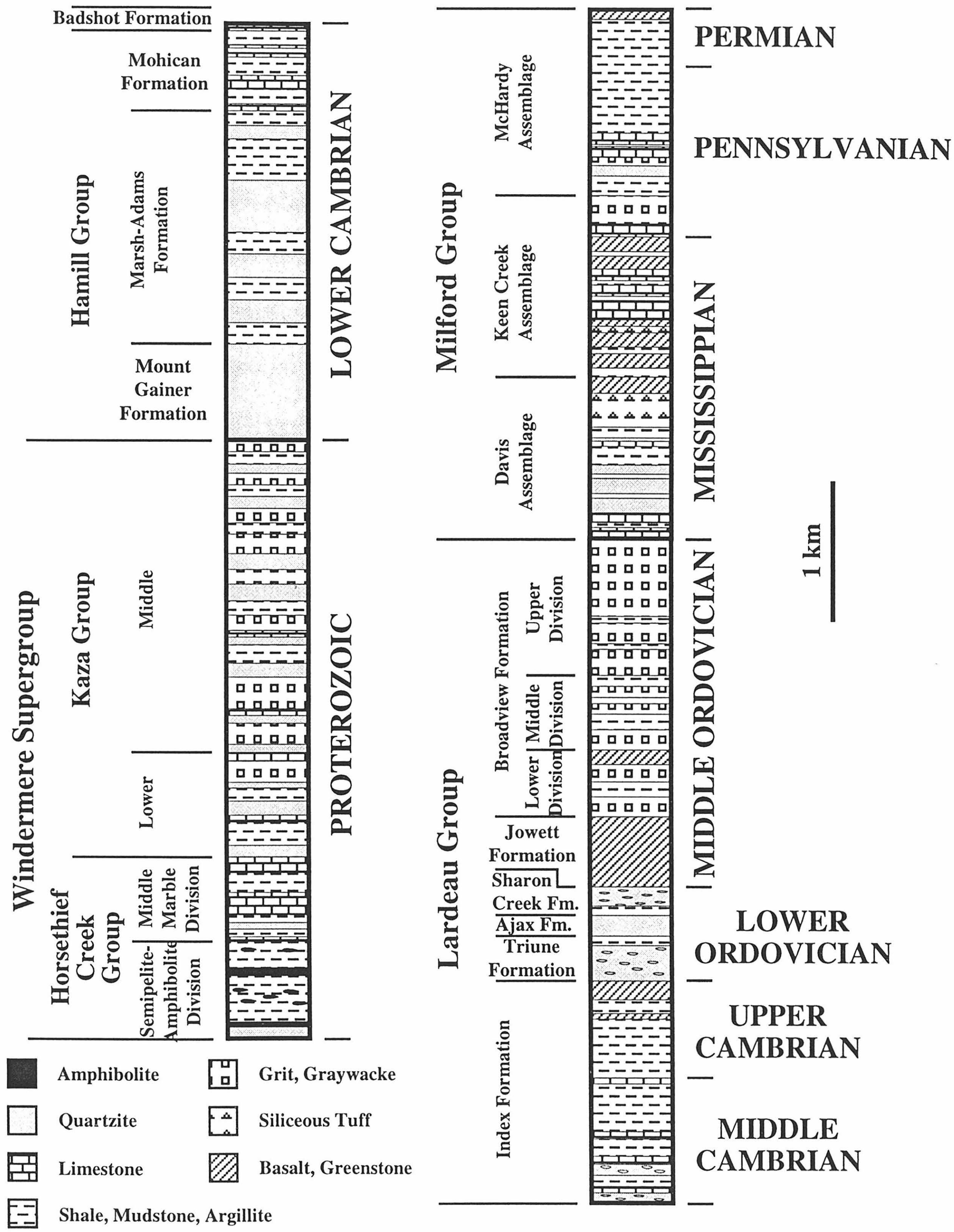

Pebble conglomerates of the middle unit interfinger with quartzite and grit where they occur as channel fill.

Up to 6000 m of the the Horsethief Creek Group are exposed in the northern Selkirk Mountains (Brown et al., 1978; Poulton and Simony, 1980). The Toby Formation and the Irene Volcanics are absent in this area. From older to younger, this unit is divided into the lower grit, lower slate, lower calcareous, upper slate, carbonate, and upper clastic divisions. The basal lower grit division is composed of 100 m of metasandstone and granule conglomerate, grit, pelite, and minor limestone. The lower slate division is made up of 700-800 m of slate. Impure carbonate, phyllite, and rusty schist comprise the lower calcareous division. 1200 m of slate and minor calcareous clastic rocks make up the upper slate division. Massive carbonates of the carbonate division overlie the upper slate division. The upper clastic division caps the sequence and comformably underlies the Cambrian Hamill Formation. This unit is comprised of up to 3300 m of feldspathic sandstone, granule and cobble conglomerate, and pelite, and it becomes more calcareous to the west. The facies changes in these stacked sequences vary from a basal submarine fan environment to shallow-water accumulation facies conditions, and have been interpreted to be two superposed clastic wedges (Pell and Simony, 1986), but it also has been argued that this association was formed by thrust stacking (Struik, 1986).

The Horsethief Creek Group and the Kaza Group (Figure 2.6) make up the Windermere Supergroup in the northwestern part of the study area in the southern Cariboo Mountains (Pell and Simony, 1986; Struik, 1986). The Horsethief Creek Group is subdivided into the semipelite-amphibolite division, the middle marble zone, and the upper clastic unit. The basal semipelite-amphibolite division is comprised of a 500-100 m-thick sequence of micaceous pelitic and psammitic schist interlayered with garnetiferous amphibolite overlain by a few tens of meters of carbonate and calc-silicate which is beneath 100 m of pelitic schist. The middle marble unit consists of 5-100 m of gray marble containing intervening thin layers of micaceous schist. The upper clastic unit is gradational into the Kaza Group and is made up of 150-100 meters of alternating metasandstone and pelitic schist with minor gritty sandstone. The Kaza Group is a 3500 m-thick, well-bedded clastic sequence of graded gritty sandstone and pebble conglomerate interlayered with argillite, slate, and phyllite. The depositional facies of this sequence is a submarine fan environment that records gradual shallowing with time. The clastic detritus that fed these submarine fans was probably derived from crystalline rocks being eroded from a rifted continental margin.

2.2.3 Cambrian Stratigraphy

The Cambrian evolution of the western margin of ancestral North America is marked by the deposition of miogeoclinal sediments in a subsiding (Bond and Kominz, 1984) passive margin (the Columbia Basin). Cambrian units from this sequence are preserved, and are located in the Kootenay Arc (Figure 2.3). These are the Hamill Group and the Mohican, Badshot, and Index Formations (Fyles and Eastwood, 1962; Fyles, 1964; Hoy, 1977; Brown et al., 1978; Figure 2.5). Sporadic occurrences of volcanic rocks and local anomalous thicknesses and facies changes suggest repeated episodes of extension (Devlin, 1984). These rocks are highly deformed and metamorphosed at high grade throughout the southern Omineca Belt, making stratigraphic correlation and paleogeographic interpretation difficult (Crosby, 1968; Brown et al., 1978; Archibald et al., 1983; 1984).

In most places, the Hamill Group unconformably overlies the Windermere Supergroup (Fyles and Eastwood, 1962; Fyles, 1964; Hoy, 1977; Pell and Simony, 1987), but there are places where this contact is conformable in the northern Selkirk

Mountains (Brown et al., 1978). Basal sections of the Hamill Group consist of cobble-sized clasts in a clean, light-colored quartzite. Sandstone and coarse clastic rocks of the Hamill are 1300-2000 m thick. Occasional occurrences of greenstone and coarse clastics in this unit suggest repeated episodes of rifting. In the west Kootenay Arc, upper portions of the Hamill Group laterally grade into phyllite and interbedded limestone of the Mohican Formation (Fritz et al., 1991). The Mohican Formation varies from a 5-10 m to 600 m in thickness. These thickness variations are probably tectonic in origin.

The Badshot Formation is a distinctive shallow-water carbonate unit in a clastic succession that conformably overlies the Mohican Formation and Hamill Group (Fyles and Eastwood, 1962; Fyles, 1964; Hoy, 1977). It is comprised of a 50-300 m-thick package of thin to massive beds of light to dark gray limestone that may be locally altered to white marble and dolomite. This is an excellent marker unit for use in correlating stratigraphy in sections that have undergone high-grade metamorphism. Numerous small stratiform Pb-Zn-Ag deposits are hosted in the Badshot (Hoy, 1977a; Fritz et al., 1991).

The Index Formation was deposited during the Upper Cambrian and conformably overlies the Badshot Formation (Fyles and Eastwood, 1962; Fyles, 1964; Hoy, 1977). This unit is a 450-750 m-thick sequence of dark gray, locally black and greenish-gray rhythmically bedded phyllite with interlayers of limestone, and minor calcite-cemented quartzite (Fritz et al., 1991). Near the top of this unit are local occurrences of greenish colored volcanic rocks. Distinctive talc-schist layers mark the upper boundary of the Index Formation (Zanzwig, 1973). These talc-schist layers are exposed for 100 km along strike and they may represent remnants of Early Paleozoic oceanic crust. This distinctive marker unit marks the boundary between ancestral North America and the Kootenay Terrane (see Figure 2.3).

2.3 The Monashee Terrane

The Monashee Terrane (Figure 2.3) is the basement zone for the southern Omineca belt, and is very likely part of Ancestral North America (Read and Brown, 1983; Brown and Journeay, 1987; Hoy, 1988). It lies in the footwall of the Monashee Decollement, and is comprised of Precambrian basement exposed in the Thor-Odin (Reesor and Moore, 1971; Duncan, 1984; Parkinson, 1991) and Frenchman Cap gneiss domes (Fyles, 1970; McMillan, 1971; Brown and Read, 1983; Brown and Journeay, 1987; Armstrong et al., 1991). These domes are made up of Early Proterozoic augen orthogneiss and layered quartzofeldspathic paragneiss (Armstrong et al., 1991; Parkinson, 1991) unconformably overlain by clastic sediments of probable Late Proterozoic to Middle Cambrian age (Scammell and Brown, 1990; Hoy, 1988). Another occurrence of Proterozoic basement is the Vaseaux Formation, a foliated granitic gneiss unit in the footwall of the Okanagan Valley fault (Ross, 1973; Armstrong et al., 1991; Parrish, 1991).

The Early Proterozoic basement rocks of the Monashee Terrane are divided into two orthogneiss units and one paragneiss unit that comprise the oldest rocks found in the southern Omineca belt (Reesor and Moore, 1971). These rocks are metamorphosed in the upper amphibolite facies and are exposed in the cores of large northeast-verging nappes that are transposed by the Columbia River detachment fault (Reesor and Moore, 1971; Duncan, 1984). Parkinson (1991) suggested that Early Proterozoic events recorded in these rocks may be correlative with the Wopmay orogen to the northeast.

The mantling gneiss division of the Monashee Terrane is a thick and laterally extensive sucession of metasedimentary rocks intercalated with volcanic and intrusive rocks (Bosdachin and Harrap, 1988; Scammell and Brown, 1990). The 740 Ma Mount Copeland syenite complex (Parrish, 1991) intrudes the lower part of the section (Fyles, 1970), placing a maximum age constraint on the deposition of units that unconformably overlie this intrusion. An early Cambrian stratiform Pb-Zn deposit in the upper part of the section places a minimum age constraint on the rocks below this stratigraphic level (Hoy, 1988). These geochronologic constraints along with lithological similarity imply that the gneisses that unconformably overlie these core gneisses are correlative with the Windermere Supergroup (Scammell and Brown, 1990).

2.4 The Kootenay Terrane

The Kootenay terrane (Figure 2.3) is pericratonal to the ancestral North American plate margin. There is no record of significant displacement, but rocks of the Kootenay terrane have a different depositional and structural history than the ancient continental margin of North America (Gabrielse et al., 1991). This terrane consists of intensely deformed, variably metamorphosed, and poorly dated Proterozoic to Triassic siliceous clastic sediments with subordinate volcanics and limestones. These rocks are intruded by Ordovician, Devonian, and Mississippian granitoid plutons (Okulitch, 1985). Deformed Lower Paleozoic strata seem to be stratigraphically related to ancient North America, but younger, less deformed rocks are not. In southern British Columbia, this terrane is separated from ancestral North America by the Purcell and Esplanade thrust faults (Wheeler et al., 1991).

2.4.1 The Middle Cambrian – Middle Ordovician Lardeau Group

The Lardeau Group is a complex belt of Middle Cambrian to Middle Ordovician phyllite, grit, mafic volcanics, and carbonate (Fyles and Eastwood, 1962; Fyles, 1964; Smith and Gehrels, 1992; see Figure 2.6). Formation units of the Lardeau Group in the Kootenay Terrane are the Triune, Ajax, Sharon Creek, Jowett, and Broadview Formations. This sequence overlies the Badshot Formation and is unconformably overlain by the Mississippian-Permian Milford Group. The defined boundary between the Kootenay Terrane and ancestral North America is within the Lardeau Group (the talc-schist zone; Zwanzig, 1973). This boundary is a pre-Mississippian thrust fault termed the Lardeau shear zone by Smith and Gehrels (1992). Portions of this sequence below this boundary are discussed above in the section on ancestral North America. The Lardeau Group was deformed and metamorphosed to greenschist facies sometime between the Middle Ordovician and the Mississippian (Smith and Gehrels, 1992).

The three basal units consist of outer basinal sediments deposited along the margin of ancestral North America (Fyles and Eastwood, 1962; Read and Wheeler, 1977). The Triune Formation is a 250 m-thick greyish-black siliceous argillite. Thickly bedded quartzite with limy concretions comprise the 250 m-thick Ajax Formation. The Ajax Formation is overlain by greyish-black siliceous argillites and recrystallized ribbon cherts of the Sharon Creek Formation. The Jowett Formation is an 800 m-thick massive and pillowed tholeiitic lava, aquagene tuff, and volcanic breccia sequence.

The Broadview Formation may be the western facies of the clastic Triune to Sharon Creek sucession (Read and Wheeler, 1977). Quartz and feldspar grit, quartzite, phyllite, and limestone make up this thick (>1000 m) clastic sequence. The provenance of these rocks was likely from crystalline rock outcrops to the west at the time of deposition. Boulders of the Broadview Formation in the basal conglomerate of the overlying Milford Group have a Rb-Sr isochron date of 479±17 Ma.

2.4.2 The Mississippian – Permian Milford Group

The Milford Group is an intensely deformed sequence of Mississippian-Permian pericratonal marginal basin sediments and oceanic volcanics that unconformably overlie the Lardeau Group (Fyles and Eastwood, 1962; Klepacki and Wheeler, 1985; see Figure

2.6). Three main facies series of this unit have been distinguished: (1) the Davis assemblage, an eastern near-shore facies, (2) the Keen Creek assemblage, a westerly volcanic facies, and (3) the McHardy assemblage, a westernmost facies. The Mount Roberts Group are rocks that are correlative with the Milford Group that outcrop in the region between Kootenay Lake and Greenwood.

Each of these facies series is up to 600 m-thick. The eastern facies is an ascending series of basal conglomerate, limestone, sandstone, shale, cherty tuff, and greenstone. Interbedded limestones, and tholeiitic volcanics overlying a basal conglomerate comprise the westerly volcanic facies. Farthest to the west, in ascending order, is a series of limestones and calcareous sandstones, tuffaceous sandstones, boulder conglomerates, limestones, and black siliceous argillites with minor tholeiitic flows. Siliceous argillite of the westernmost facies is conformably overlain by Permian tholeiites of the Kaslo Formation, the oldest unit that overlaps the Slide Mountain and Kootenay Terranes (Klepacki and Wheeler, 1985).

2.4.3 Stratigraphy of the Western Kootenay Terrane

In the Adams Lake area, the Eagle Bay Assemblage occurs in southwest- and west-verging thrust sheets (Schriazza and Preto, 1984). Within this highly metamorphosed and poorly dated sequence is a Lower Cambrian limestone unit similar to the Badshot Formation intercalated with green calcareous chlorite schist, mafic and intermediate volcanics, and volcaniclastic fragmental schist. This sequence is overlain by black graphitic, siliceous and calcareous phyllite similar to the Index Formation. The Sicamous Formation is grey and green phyllitic sandstone, grit, phyllite, and quartzite with minor limestone and greenstone which may correlate with the lower part of the Lardeau Group. There is a sharp metamorphic transition at the uppermost greenstone unit of this sequence with higher metamorphic grades recorded in the older rocks. Early Devonian (387 Ma) granite and granodiorite, and Late Ordovician granitic plutons (452±17 Ma U-Pb zircon) intrude this sequence in the Adams-Shuswap Lake area (Okulitch, 1985). These plutons are made up of well foliated and lineated orthogneiss. Thin Mississippian and Permian limestones are present along with a sequence of Mississippian grey phyllite, siltstone, sandstone, and grit with minor limestone, conglomerate, and tuff similar to the near-shore facies of the Milford Group.

2.5 The Slide Mountain Terrane

The Slide Mountain Terrane (Figure 2.3) is the easternmost terrane exotic to North America in the southern Omineca belt (Coney et al., 1980; Gabrielse et al., 1991; Monger et al., 1991). Permian fusulinid faunas indicate a depositional site far to the south for these rocks (Carter et al., 1991). Rocks belonging to the Slide Mountain Terrane outcrop in the Goat Range, the immediate hanging wall of the Columbia River fault along the east shore of northern Arrow Lake, and in the Greenwood area. The Late Paleozoic marginal ocean basin rocks of the Kaslo Formation comprise the Slide Mountain Terrane in the Goat Range (Klepacki and Wheeler, 1985). This terrane was eastwardly thrust over Paleozoic rocks of the Kootenay Terrane during the Permian. The Upper Permian basal conglomerate of the Slocan Group is an overlap unit between the Slide Mountain and Quesnellia Terranes.

The ocean basin rocks of the Kaslo Group are divided into two assemblages that are separated by a Permian thrust fault (Klepacki and Wheeler, 1985). The upper sheet assemblage consists of tholeiitic pillow lava with minor greywacke and volcanic conglomerate floored by ultramafic rock. The lower sheet is made up of pyroxene-porphyry pillow lava flows, and tuffaceous greenstone interbedded with green and white cherty tuff. These cherts yield late-Early and early-Late Permian conodonts. The lower sheet overlies the McHardy assemblage of the Milford Group.

2.6 The Quesnellia Terrane

Quesnellia is an island arc terrane (Figure 2.3) formed during the late Paleozoic and early Mesozoic offshore from ancestral North America and far to the south of its current latitude (Gabrielse et al., 1991; Carter et al., 1991). This terrane consists of upper Paleozoic and lower Mesozoic volcanic and sedimentary strata and associated plutonic rocks that stratigraphically and structurally overlie the Slide Mountain and Kootenay Terranes (Monger et al., 1991). The mostly Paleozoic basement of Quesnellia is divided into the the Harper Ranch subterrane and the Okanagan subterrane (Monger et al., 1991). Overlapping Triassic volcanic rocks of the Nicola Group that overlap these subterranes is evidence of their amalgamation into the Quesnel Terrane by that time (Read and Okulitch, 1977). Volcanic, volcaniclastic, and clastic rocks of the Jurassic Rossland and Slocan Groups comprise the youngest components of Quesnellia deposited before accretion to North America (Monger et al., 1991).

2.6.1 The Harper Ranch Subterrane

The Harper Ranch subterrane is made up of latest Devonian to late Permian arc-related clastic, volcanic, and carbonate rocks that crop out near northern Okanagan Lake (Monger et al., 1991). Rocks of this subterrane are highly folded and faulted, preventing the preservation of a continuous stratigraphic section. Thinly interbedded argillite, laminated argillite, and siltstone are the most abundant rock types, but sequences of graded, turbiditic volcanigenic sandstone are also common. Thin carbonate beds are interlayered in this clastic succession. Fossiliferous late Devonian to late Permian carbonate olistrostromes (some as large as 2 km) punctuate these strata. These lithologic associations imply that the Harper Ranch Group represents the distal portion of a basin related to an active volcanic island arc (Monger et al., 1991).

2.6.2 The Okanagan Subterrane

The Okanagan subterrane is composed of Ordovician to Triassic oceanic or marginal basinal volcanic and sedimentary rocks that may be correlative with similar rocks in the Slide Mountain Terrane (Monger, 1977). An angular unconformity separates the mostly Paleozoic strata of the Okanagan subterrane from the overlying Middle to Upper Triassic rocks of the Nicola Group (Read and Okulitch, 1977). Stratigraphic sequences and correlative aspects of the rock units that comprise this terrane are poorly understood due to their structural complexity.

The Carboniferous to Permian Anarchist, Chapperon, and Kubau Groups, the Carboniferous or Permian Attwood Formation and Knob Hill Group, and the Ordovician to Late Triassic Shoemaker Assemblage are the rock units that comprise the Okanagan Subterrane (Monger et al., 1991). The Anarchist, Chapperon, and Kubau Groups are a sequence of massive quartzite, chloritic phyllite and schist, greenstone, and marble (Jones, 1959). The Attwood Formation is a limestone and argillite unit that occurs near Greenwood (Little, 1983). Associated with the Attwood are cherts and greenstones of the Knob Hill Group (Little, 1983). The Shoemaker Assemblage consists of intermixed strata of greenstone, silicified tuff, minor limestone, and chert breccia that outcrops west of the Okanagan fault near the international border. The upper parts of the Shoemaker may correlate with the Nicola Group to the west. Ultramafic intrusions and dikes intrude the Chapperon and Knob Hill Groups. This suite of rocks probably represents an ancient subduction complex or marginal basin (Monger, 1977; Monger et al., 1991).

2.6.3 The Late Triassic – Early Jurassic Nicola Group and Guichon Batholith

The Nicola Group is a suite of Upper Triassic and Lower Jurassic arc volcanic rocks intruded by the Guichon batholith. There are four main facies series for this group of rocks that unconformably overlie and overlap Paleozoic rocks of the Harper Ranch and Okanagan subterranes (Monger et al., 1991). The western facies series is a preserved emergent arc succession of calc-alkaline acidic-to-intermediate flows, breccias, and volcaniclastics. A back-arc facies series of intermediate feldspar and feldspar-augite porphyry volcaniclastic rocks are adjacent to the western facies series to the east. The eastern facies series is an easterly thickening pile of alkaline augite porphyry, pillows, and volcaniclastics. The eastern volcanic facies series grades eastward into the Slocan Group; a sequence of argillite and siltstone, with local volcaniclastic lenses, limestone, and breccia beds. The volcano-stratigraphic associations among these four facies series, along with the presence of subvolcanic intrusions in the western suite, indicate that the Nicola Group was erupted and deposited above an east-dipping subduction zone active along the western margin of Quesnellia.

The late Triassic to early Jurassic was a time of extensive, but scattered plutonism in Quesnellia. The Guichon Batholith is the best studied member of this plutonic suite. Large plutons of this 200-210 Ma batholith were emplaced into synvolcanic faults cutting the synplutonic Nicola Group (McMillan, 1985). This calc-alkaline suite of hornblende-biotite granodiorite, quartz diorite, pyroxene-hornblende diorite, and minor quartz monzonite, leucogranodiorite, and syenodiorite is low in initial $^{87}Sr/^{86}Sr$ (0.7028–0.7037; Armstrong, 1988; Ghosh, 1995) and $\delta^{18}O$ (7.3–7.5; Magaritz and Taylor, 1986), and high in ε_{Nd} (+4.2 to +7.3; Ghosh, 1995). These radiogenic and stable isotope data indicate a depleted mantle source for this island-arc plutonic suite. Numerous porphyry Cu and Mo deposits are associated with this plutonic suite (McMillan, 1985).

An early Jurassic syenite pluton of the Copper Mountain suite is found in the southern Okanagan Valley.

2.6.4 The Jurassic Rossland Group

The Early Jurassic Rossland Group consists of the Archibald, Elise, and Hall Formations in the west and the Rossland volcanics in the east (Little, 1960; Monger et al., 1991). The Archibald Formation as a lowermost Jurassic sequence of sandstone, argillite, and tuff that grades into augite and augite-feldspar porphyry of the flows and pyroclastics of the Elise Formation. The Hall Formation unconformably rests on the Elise Formation. This >300 meter thick sequence of black shale and argilliceous sandstone with minor siltstone and conglomerate had a likely source to the north and northeast, probably the margin of North America. These rocks represent the final marine incursion into Quesnellia.

To the east, the Early Jurassic Rossland Group consists of variably metamorphosed agglomerate, conglomerate, lavas and volcaniclastics intercalated with marine shale and siltstone (Beddoe-Stephens and Lambert, 1981; Beddoe-Stephens, 1982). The lavas are augite-rich ankaramites to plagioclase-phyric andesite, with some augite porphyry basalts; this was an island arc setting. The lavas have an upper mantle parent magma that experienced initial melting at 20 kb and experienced later crystal fractionation. This volcanic front migrated eastward toward the continent and by Middle Jurassic time it was encroaching onto the Slide Mountain Terrane and Ancestral North America.

2.7 Tertiary Volcanic and Sedimentary Rocks

There was intense and pervasive volcanism between 55 and 36 Ma in the southern Omineca belt. The Challis-Kamloops volcanic belt extends through Idaho, Wyoming, Montana, and into central British Columbia (Souther, 1991). In British Columbia, these rocks are the Kamloops, Penticton, and Coryell volcanic assemblages (Church, 1973; Ewing, 1981). These magmas were generated above an east-dipping subduction zone. The Kamloops Group is calc-alkaline. The Penticton-Coryell suite consists of alkaline rhomb porphyries and syenites.

The Kamloops Group is preserved in fault-bounded basins, and was erupted during a time of subsidence. The Tranquille Formation is a 450 m-thick sequence of lacustrine sediments and andesitic bedded tuffs. These grade upward into complexly interlayered andesitic and basaltic tuffs and flows, tuffaceous lacustrine sediments, phreatic breccias, mudflows and pillowed andesite flanked by hyaloclastic breccia. The Dewdrop Formation is a 1000 m-thick sequence of basaltic andesite flows and pyroclastics. The lower part of this unit is subaqueous with palagonite breccia mudflows and phreatic breccia. The upper part of this unit is subaerial with basaltic to andesitic subaerial flows and pyroclastics. These rocks are an alkali-rich calc-alkaline suite with little or no Fe-enrichment, with $^{87}Sr/^{86}Sr$ initial values of 0.704 to the west and 0.706 to the east. K_2O and SiO_2 also increase eastward. This cogenetic suite is probably a subduction-related continental arc (Armstrong, 1988).

The Penticton Group crops out in the Okanagan Valley, where it makes up the White Lake basin (Church, 1973). This sequence is up to 2400 m-thick and the basin is bounded by normal faults. The Marron Formation is a 1500 m-thick unit of highly alkaline, mainly rhomb porphyry lavas and breccias. The Marama Formation is a 200 m-thick sequence of rhyolite and rhyodacite. These units are overlain by conglomerate and epiclastic volcanic breccia slide deposits from the lower plate of the Okanagan Valley Fault. The White Lake basin is cut by at least 3 intrusive phases of rhomb porphyry, or augite porphyry sills and dikes which probably served as feeders. The highly potassic rhomb porphyries of the Marron Formation are chemically similar and peripheral to the Coryell epizonal plutonic rocks to the east to make up a coeval and comagmatic alkaline assemblage. This assemblage involved much continental crust. These volcanic rocks may have been transported as much as 100 km from their plutonic roots (Tempelman-Kluit and Parkinson, 1986).

2.8 Compressional Deformation and Tectonism

Numerous pulses of compressional tectonism affected all crustal levels of the southern Omineca belt between the late Paleozoic and early Cenozoic (Tempelman-Kluit et al., 1991; Monger, 1993). The most regionally extensive of these episodes is associated with the collision of the Intermontane Superterrane against North America during the Middle Jurassic. The other important collisional event took place in the Late Cretaceous to Paleocene as the Insular Superterrane was accreted to North America. The Monashee decollement served as a detachment structure separating deep basement rocks of the Monashee Complex from the overlying middle and upper crustal rocks of the Selkirk Allochthon. It is estimated that crustal shortening exceeded 75% and crustal thickening exceeded 20 km during the interval between the Middle Jurassic and the Paleocene (Parrish et al., 1988; Cook et al., 1992; Cook and Varsek, 1994).

2.8.1 The Monashee Decollement and the Basement Layer

The Monashee decollement is a fundamental boundary structure in the southern Omineca belt that accommodated the eastward overthrusting of uniformly high-grade migmatitic gneisses and semiconcordant leucogranites (the infrastructure) of the Selkirk Allochthon over the basement rocks of the Monashee complex (Brown et al., 1986; 1992). This major pre-extensional structure is a 1250-1500 m-thick network of annealed mylonitic shear zones whose planar and linear fabrics grade into synmetamorphic foliations in both the upper and lower plates (McNicoll and Brown, 1995). Two major episodes of displacement are preserved at the Monashee decollement: (1) Middle Jurassic movements that predate early arching and uplift of the underlying basement, and (2) Late Cretaceous to Early Tertiary movement associated with as much as 20 km of thrust ramping as the Selkirk Allochthon was transported over the arched and uplifted basement (Cook et al., 1992). This deep-level shear zone has been interpreted to represent the basal decollement surface of the Rocky Mountain fold and thrust belt to the east. It is estimated that displacement along the Monashee decollement may be as great as 200 km.

The Monashee complex comprises the basement core zone of the southern Omineca belt. It is an exhumed antiformal duplex system of basement-cored horses (Brown and Read, 1983). The main constituents of this complex are the Frenchman Cap and Thor-Odin domes (Wheeler, 1964; Reesor and Moore, 1971); these are second order culminations along the axis of the antiformal complex that are the product of at least three generations of non-coaxial folding (Fyles, 1970; Duncan, 1984). The oldest folding episode involved east-verging fold nappes and associated low-angle thrust faults. This was followed by the east-to-northeast directed isoclinal folding linked with the first stage of deformation at the Monashee decollement. The last folding event involved the formation of north-trending late-to-post-metamorphic folds formed during late-stage uplift and arching associated with thrust ramping and extensional unroofing. Similar deformational styles are observed in probable Precambrian gneiss basement in the footwall of the Okanagan Valley fault in the southern Okanagan Valley (Ross, 1973).

2.8.2 The Selkirk Allochthon

The Selkirk Allochthon envelops the Monashee complex and extends east to the southern Rocky Mountain Trench (Figure 2.3). It is a 25 km-thick composite thrust nappe consisting of pre-Eocene plutonic rocks and strata from ancestral North America, the Kootenay Terrane, and the eastern portion of the Intermontane Superterrane (Brown et al., 1986). Modes of deformation vary with depth (Simony et al., 1980). Ductile deformation is prevalent in the middle crustal infrastructure exposed beneath Eocene detachment faults (Brown and Murphy, 1982; Parrish et al., 1988). Brittle deformation is characteristic of the upper crustal suprastructure exposed in the Kootenay Arc and Purcell Anticlinorium. The infrastructure-suprastructure transition is preserved in a 15 km-thick section in the northern Selkirk and Monashee Mountains (Simony et al., 1980).

The middle crustal infrastructure of the Selkirk Allochthon is exposed in the lower plate of the regional network of north-trending Eocene detachment faults and in the hanging wall of the Monashee decollement (Parrish et al., 1988; Carr, 1991). These deep parts of the allocthon have been metamorphosed to near-granulite conditions during the development of late Cretaceous to Paleocene penetrative deformation and anatectic plutonism. These rocks were at the peak of metamorphism in the Paleocene, and were rapidly quenched during tectonic denudation in the Eocene. The Paleocene-Eocene Ladybird granitic suite is a characteristic component of this middle-crustal portion of the southern Omineca belt. Older structures have been transposed and erased by late-Cretaceous to Paleocene penetrative compression and large-scale anatexis as this deep, hot portion of the Selkirk Allochthon was transported up the 20 km ramp developed in the Monashee decollement by Cretaceous time (Cook et al., 1992). Numerous compressional shear zones kinematically related to the Monashee decollement occur in the infrastructure.

High-grade, ductile middle crustal rocks are exposed in the lower plates of detachment faults at the Valhalla, southern Thor-Odin, and Okanagan metamorphic core complexes and in the Shuswap Complex (Carr et al., 1987; Parrish, 1981; Parrish et al., 1988). Structural styles are complex west of the Kootenay Arc. Southwest verging folds and thrust faults make up the dominant Mesozoic structures. To the east, eastward verging structures culminate in complex, duplex style thrust sheets at the Monashee and Valhalla complexes. Northwest verging structures dominate the southern part of the Kootenay Arc. The occurrence of late or post-metamorphic eastward verging folds in both the upper and lower plates of the Monashee decollement suggests similar histories for the Monashee Complex and Selkirk Allochthon during uplift and eastward telescoping of the southern Omineca belt during the Mesozoic and Early Cenozoic.

A 15 km-thick section through the Selkirk Allochthon is provided by structures that display a gentle west-northwest plunge within the Cariboo Mountains and a regional southeast plunge within the Selkirk and northern Purcell Mountains (Simony et al., 1980; Raeside and Simony, 1983). This section is comprised of structures that vary from ductile, polyphase, and recumbent at depth, to brittle and upright at high structural levels. Metamorphic grade and intensity also increase with depth. Three major phases of deformation are recognized in this transitional zone that encompasses the middle- to upper-crustal layers of the Northern Selkirk Allochthon. Large ductile southwest-verging nappes (up to 50 kilometers in amplitude) deformed at garnet-grade conditions occur in deep levels of this terrane and comprise the first stage of deformation. The Middle Jurassic second stage involves as much as 12 km of burial during folding and thrust faulting coeval with the climax of regional metamorphism. Folds and faults are northeast-verging in the hanging wall of the Purcell Thrust Fault, but these structures are southwest-verging in the footwall rocks of the Selkirk Mountains. At depth, these high-grade schistose structures have erased evidence of the first stage. Fold amplitudes are large (>6 kilometers) and wavelengths are small (<2 kilometers) at deep levels; but at higher structural levels these fold amplitudes decrease, folds become more open, and more brittle cleavage becomes common. Northeast-verging thrust faults may merge with the Monashee decollement at depth. The late Cretaceous to early Tertiary third stage involves 6-12 km of burial during post-metamorphic northeastward folding and faulting (Simony et al., 1980). This phase is coeval and kinematically related with the west-to-east progression of thrusting in the Foreland Belt as an eastward-tapering wedge was obducted onto ancestral North America (Brown et al., 1986).

The Kootenay Arc is a north-trending arcuate structural arc characterized by intense polyphase deformation and local high-grade regional metamorphism along the boundary between terranes of North American affinity and the Intermontane Superterrane (Fyles and Eastwood, 1962; Fyles, 1964; 1967; Crosby, 1968; Hoy, 1977). A late Paleozoic to early Cenozoic deformational history of the eastern part of the upper crustal layer of the southern Omineca belt is preserved in this arc and in the Purcell Anticlinorium to the east.

Intermittent periods of deformation, metamorphism, and plutonism have affected the Kootenay Arc, including: (1) Deformation occurred prior to the deposition of the Milford Group in the Mississippian (Smith and Gehrels, 1992). (2) The Slide Mountain Terrane was thrust onto the Kootenay Terrane during the Permian (Klepacki and Wheeler, 1985). (3) The Intermontane Superterrane collided and was accreted to North America in the middle Jurassic (Price et al., 1986; Archibald et al., 1983). (4) The Kootenay Arc was transported eastward during late Cretaceous to early Tertiary thrusting in the Foreland Belt and Purcell Anticlinorium (Price et al., 1986; Archibald et al., 1984). Metamorphic isograd patterns in northward-plunging thermal culminations at Kootenay Lake, the Clachnaculainn Slice, and Shuswap Lake suggest that much of the deformation was post-metamorphic (Crosby, 1968; Hoy, 1977; 1980). Isograds are obliquely truncated by the Monashee decollement and the Purcell Thrust Fault (Greenwood et al., 1991).

At least four stages of deformation are recognized in the Kootenay Arc (Fyles 1964; 1967; Hoy, 1977; 1980). The earliest structures are overturned to the west, originally east-verging pre-Mississippian recumbent isoclinal folds in the Lardeau Group. This was followed by the southeastward thrusting of deep-water facies rocks of the Permian-Carboniferous Kaslo Group onto near-shore facies rocks of the same sequence. These faults are cut by a Permian diorite pluton in the Goat Range (Klepacki and Wheeler, 1985). The third stage of deformation is associated with the formation of pre- to syn-metamorphic folds and faults that define a structural fan near the eastern margin of the allochthon. West of the fan-axis are mostly west-verging structures, with east-verging structures to the east. This generation of structures is cut by the Middle Jurassic Nelson and Kuskanax batholiths (Read and Wheeler, 1977). The fourth stage of deformation is associated with the development of the curvature of the arc as it was transported during the Jurassic-Paleocene eastward movement of the Selkirk Allochthon. This deformation is localized and cannot be correlated across the Kootenay Arc, but it is well developed along its eastern margin where it merges into structures of the Purcell Anticlinorium.

The Purcell Anticlinorium is a large north-plunging asymmetric box fold cored by the middle Proterozoic Purcell Supergroup (Price, 1986). This anticlinorium formed above a basal detachment fault in response to ramping in late Cretaceous to Paleocene time. Strain increases and minor folds become more common to the west where structures merge with those of the Kootenay Arc. Most structures are the product of Mesozoic deformation, but some minor folds may be Middle Proterozoic in age. The east limb of the anticlinorium is disrupted by the Rocky Mountain Trench fault system. Early north-trending faults are cut by Middle Cretaceous granitoids.

2.8.3 The Intermontane Superterrane and the Adams-Shuswap Lake Area

Most structures in the Intermontane Superterrane verge westward away from the southern Omineca belt (Brown and Read, 1983). The Mesozoic structural evolution of this region is complex and poorly understood. Much of the deformation in this terrane is the product of the early-middle Jurassic agglomeration of the Cache Creek, Stikine, Quesnellia, and Slide Mountain terranes to form the composite Intermontane Superterrane (Monger et al., 1982). West-directed late-early to middle Jurassic overturned folds in the Harper Ranch Group and the eastern sedimentary facies of the Nicola Group are related to the northeast-directed thrusting of Quesnellia onto North America. To the northeast, syn- or post-metamorphic middle Jurassic southwest-verging structures formed following the 171-164 Ma accretion of the Intermontane Superterrane to North America. Early Cretaceous westward thrusting in the eastern part of this terrane is related to uplift in the southern Omineca belt (Johnson, 1989).

The oldest structures in the Adams and Shuswap Lake areas are pervasive foliations subparallel to bedding with north to east-northeast foliation axes (Okulitch, 1984; Schairizza and Preto, 1984). These structures are overprinted by west-northwest to northwest trending southwest verging folds and thrust faults. There are four thrust sheets from this episode of deformation. This system is cut by the Middle Jurassic Raft batholith and the Middle Cretaceous Baldy batholith.

2.9 Plutonic Rocks

The southern Omineca belt has a long, multi-stage history of plutonism extending from the Early Proterozoic up to the Eocene (Armstrong, 1988). Pre-Middle Jurassic magmatic events that affected the Monashee Complex, the Kootenay Terrane, and Quesnellia are discussed in previous sections. Between the Middle Jurassic and the

Figure 2.7 -- Plutonic and volcanic rocks of the southern Omineca belt (from Parrish et al., 1988). At least eight episodes of plutonism are recognized in this region. The tectonic context of the Precambrian orthogneiss and Paleozoic granitic rocks of the Kootenay terrane are poorly understood. Jurassic plutonism is related to island arc magmatism above an east-dipping subduction zone and the melting of eugeoclinal sediments following the accretion of the Insular Superterrane. Cretaceous plutonism is associated with anatexis of sedimentary source material at deep crustal levels (Brandon and Lambert, 1993, 1994). The Eocene Ladybird granitic suite is the product of large-scale anatexis of the middle crust (Carr, 1992). Melting of the very deep crust and mantle lithosphere in response to asthenospheric upwelling probably produced the alkaline Coryell suite (Bevier, 1987).

Figure 2.7 Plutonic Rocks of the Southern Omineca Belt

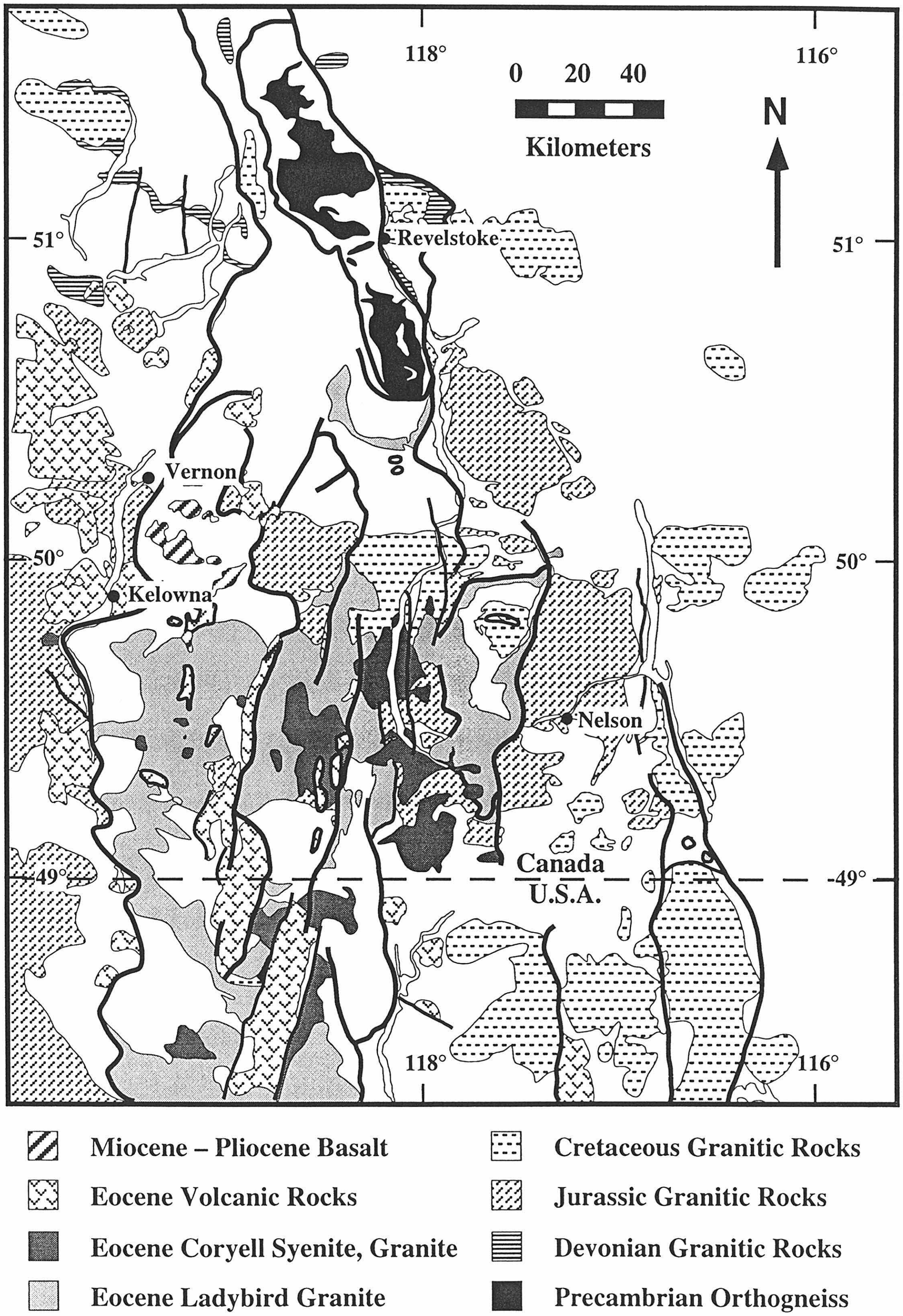

Eocene, plutonism was related to events related to the accretion of the superterranes and the extension that followed it.

2.9.1 Jurassic Plutonic Rocks

Middle Jurassic plutonic rocks are widespread across all terranes that comprise the southern Omineca belt (Figure 2.7). Four suites of the Mid-Jurassic plutons intrude the eastern part of the southern Omineca belt in the western part of the Kootenay Arc (Armstrong, 1988). These plutonic suites record a change from alkaline plutonism from about 170-180 Ma to calc-alkaline from about 160-170 Ma, to two-mica granites from about 150-160 Ma. Numerous poorly studied plutonic complexes similar to the Nelson Batholith are found between Okanagan Lake and the Columbia River. The age of the Okanagan composite batholith, west of the Okanagan valley, is poorly known, but is most likely Jurassic.

The Kuskanax suite is the oldest of the well-dated Mid-Jurassic plutonic suites. This batholith intrudes the metamorphosed and deformed Kootenay Arc (Read and Wheeler, 1977). These rocks are leucocratic quartz monzonite containing 40-70% microcline megacrysts, 10-30% aegerine-augite, and minor quartz and albite. Some satellite stocks contain magmatic epidote and andradite. These magmas were emplaced during the main compressive stage of deformation. Thus, the 173±5 Ma U-Pb zircon date provides constraints on the timing of deformation in this part of the Kootenay Arc (Parrish, 1992). Emplacement of this alkalic plutonic suite in a compressive tectonic setting is perplexing in that this style of magmatism typically occurs in an anorogenic, extensional environment.

The 159-170 Ma calc-alkaline Nelson plutonic suite was emplaced during or after the waning stages of regional metamorphism and deformation in the Kootenay Arc (Little, 1960; Fyles, 1967). This suite is composed of medium- to coarse-grained granite to granodiorite. Mafic minerals are hornblende and biotite. K-feldspar megacrysts are common. Contact relations are controversial due to a complex post-emplacement deformational history (Fyles, 1967). These plutons occur in the hanging wall of the Slocan Lake and Valkyr shear zones and have been extensively affected by hydrothermal alteration associated with extension (Beaudoin er al., 1992). These magmas cooled rapidly, as indicated by 160-170 Ma K-Ar cooling ages (Parrish et al., 1988).

The 167-170 Ma Adamant pluton and Mount Toby stock intrude the Horsethief Creek Group in the Purcell and Selkirk Mountains (Woodsworth et al., 1991). The Adamant pluton is composite with a hypersthene-augite core that grades outward to hornblende granite. The pluton is foliated concordant with deformation in the country rocks, implying that it is pretectonic. The post-tectonic Galena Bay stock is located in the immediate hanging wall of the Columbia River detachment fault. It is a 162 Ma, unfoliated, leucocratic biotite-muscovite granite (Armstrong, 1988).

The Okanagan composite batholith consists of at least seven plutonic units that intruded the Upper Triassic Nicola Group (Peto, 1973; Medford et al., 1982). It is subdivided into the Pennask batholith to the north and the Similkameen batholith to the south. These batholiths display a crude zonation with quartz diorite-rich cores and granodiorite-rich margins. Rocks of this suite are hornblende-rich with subordinate biotite. Pink granodiorite to granite of the 162.5 Ma Osprey Lakes pluton intrudes the core of this composite batholith.

Middle Jurassic plutonic rocks in the western part of the southern Omineca belt have $\varepsilon_{Nd} > 0$, but plutons of this generation along the eastern belt all have $\varepsilon_{Nd} = -3.0$ to -9.1 (the Kuskanax, Nelson, and Bonnington batholiths; Brandon and Smith, 1994; Ghosh, 1995). Virtually all initial $^{87}Sr/^{86}Sr$ values are < 0.710, indicating that highly radiogenic basement was unlikely to have been involved in the generation of these magmas (Armstrong, 1988; Ghosh, 1995). $^{87}Sr/^{86}Sr$ increases to the east from 0.7036 to 0.7083, indicating assimilation by these magmas of greater amounts of volcanigenic material that had undergone oceanic-hydrothermal alteration (Ghosh, 1995). These magmas have similar isotopic charateristics to the volcanigenic central zone as defined by Solomon and Taylor (1989).

2.9.2 Cretaceous Plutonic Rocks

The mid-Cretaceous was another important episode of plutonism in the southern Omineca belt (Armstrong, 1988). Large granite and granodiorite plutons of the Bayonne suite were intruded into a belt east of the Kootenay Arc in the Purcell Mountains (Figure 2.7). Granitoids of this suite are also present in the Shuswap Lake region. These plutons postdate metamorphism and are strongly discordant with country rocks. Coeval volcanic rocks are absent.

Lithological, geochemical, and isotopic data indicate that this plutonic suite is the product of continental anatexis (Brandon and Lambert, 1993; 1994). Lithologies are biotite- and biotite-muscovite leucogranite and granodiorite, and biotite-hornblende granodiorite and granite. K-feldspar megacrysts are abundant. The plutons are felsic, S-type, large-ion-lithophile element enriched, and initial $^{87}Sr/^{86}Sr$ ranges from 0.710 to 0.740 (Armstrong, 1988).

The White Creek batholith is the best studied unit in this suite (Reesor, 1958; Brandon and Lambert, 1994). It is a compositionally zoned batholith with a rim of biotite granodiorite grading inward to hornblende-biotite granodiorite and K-feldspar megacrystic granite. The core is composed of muscovite-biotite leucogranite which intrudes the outer units. Internal foliation parallels the outer contact. Initial $^{87}Sr/^{86}Sr$ values of 0.7250 at the

Figure 2.8 -- ε_{Nd} vs initial $^{87}Sr/^{86}Sr$ of plutonic rocks of the southern Omineca belt (compiled from Sevigny et al., 1989; Armstrong, 1991; Sevigny and Parrish, 1993; Brandon and Lambert, 1993; 1994; Brandon and Smith, 1994; Ghosh, 1995). Data are from the Triassic-Early Jurassic Nicola and Guichon batholiths in Quesnellia (solid dots), the middle Jurassic batholiths (*e.g.*, Nelson, Kuskanax) near the Kootenay Arc (open dots), the Cretaceous batholiths (closed squares) east of the Kootenay Arc (*e.g.*, Bayonne, White Creek), the Eocene Ladybird suite (diamonds), the Eocene Coryell alkaline suite (open squares), and Jurassic-Cretaceous plutonic rocks of the western Omineca belt and the Intermontane Superterrane (plus signs).

Figure 2.8 Radiogenic Isotopes of Plutonic Rocks

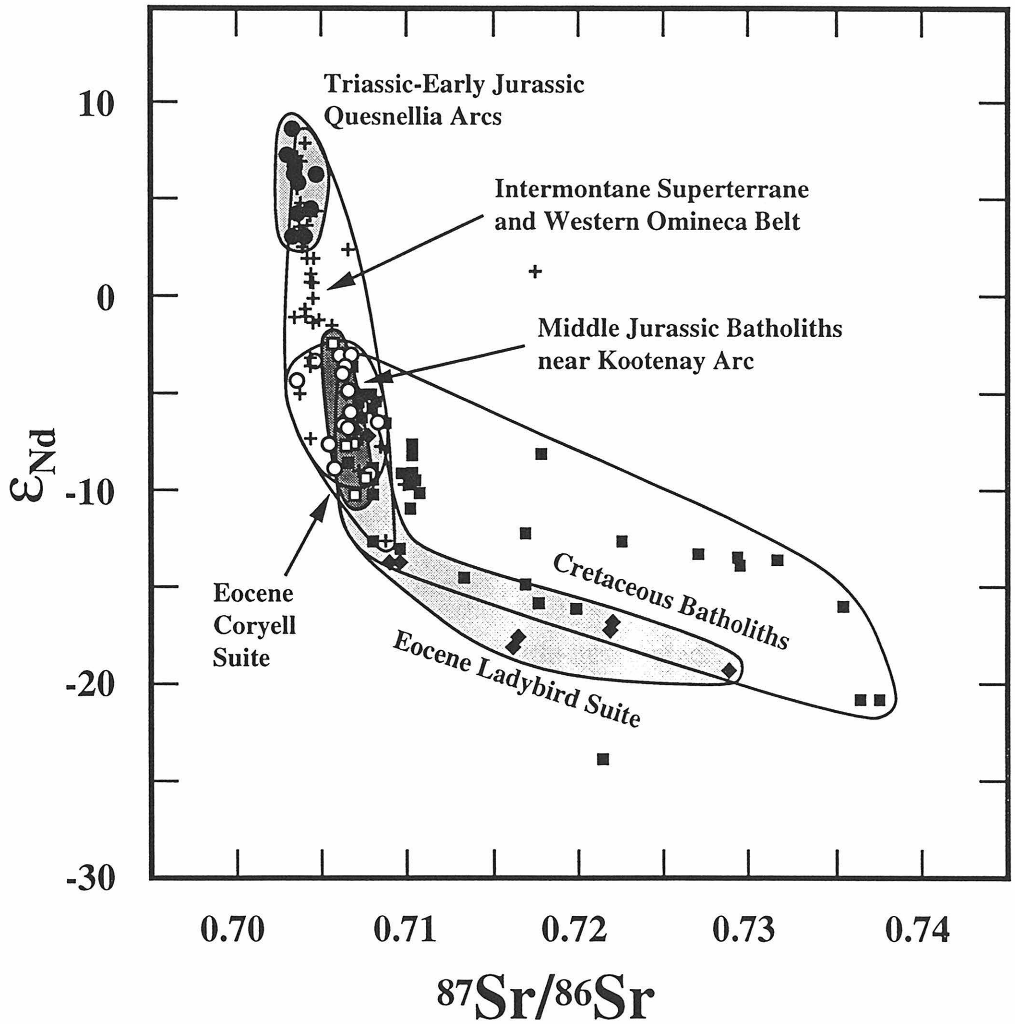

core and 0.7077 along the margin indicate that this batholith is the product of differing degrees of crustal assimilation. Contact metamorphic assembleges imply an emplacement depth of 15 km (Reesor, 1958).

The Cretaceous plutonic suite, like the Middle Jurassic suite, has regional-scale radiogenic isotope trends that indicate a greater amount of assimilation of materials of continental affinity to the east (Armstrong, 1988; Brandon and Lambert, 1993; 1994; Brandon and Smith, 1994; Ghosh, 1995). The large batholith-scale bodies in the Purcell Mountains have initial $^{87}Sr/^{86}Sr$ between 0.7065 and 0.7375 and ε_{Nd} between –3.5 and –20.8 (Brandon and Lambert, 1993; 1994); this indicates that these plutons are the product of the melting of cratonal basement and the miogeocline, similar to Solomon and Taylor's (1989) miogeoclinal subzone "S" in their central zone for Great Basin granitoids. Plutons having these isotopic characteristics extend west to the Okanagan Fault, but it should be noted that there are numerous small plutons having more primitive radiogenic isotopic signatures (initial $^{87}Sr/^{86}Sr < 0.7060$ and $\varepsilon_{Nd} > 0$) within this zone (Ghosh, 1995). This indicates the involvement of mantle-derived magma in the formation of these magmas to the west; note that these plutons are emplaced into the Quesnellia island arc.

2.9.3 The Paleocene – Eocene Ladybird Leucogranite Suite

The Ladybird leucogranite suite (or Valhalla series) is exposed in the footwall of regional-scale detachment faults thoughout the southern Omineca belt (Parrish et al., 1988; Figure 2.7). It has been best studied in the Adams River area (Sevigny et al., 1989), the southern Thor-Odin complex (Reesor and Moore, 1971; Carr, 1992), and at the Valhalla complex (Reesor, 1965; Carr et al., 1987). The Paleocene-Eocene emplacement of this plutonic suite brackets the transition between compressional and extensional tectonic regimes (Parrish et al., 1988; Carr, 1992).

At the Valhalla complex, emplacement of a homogeneous Paleocene I-type hornblende-biotite megacrystic quartz monzonite was followed by the intrusion of an Early Eocene leucocratic biotite quartz monzonite (Reesor, 1965; Carr et al., 1987). These sheet-like bodies intrude and structurally overlie Late Cretaceous and older plutonic and metamorphic rocks, and then are extensively mylonitized.

Initial $^{87}Sr/^{86}Sr$ values (0.7153 to 0.74181) from the Ladybird plutons north of Adams Lake are very radiogenic (Sevigny et al., 1989); this indicates anatexis of a metapelitic source, most likely the Horsethief Creek Group metapelites. In the Valhalla complex, the Ladybird is much less radiogenic in $^{87}Sr/^{86}Sr$ (0.7064 to 0.7096), but ε_{Nd} for these rocks is –4.9 to –13.7 (Ghosh, 1995), indicating a basement, or miogeoclinal source for these magmas.

2.9.4 The Late Eocene Sheppard – Coryell Suite

The syn- to post-extensional Coryell suite is a distinctive group of strongly alkaline high-level batholiths, plutons, and stocks found between Okanagan Lake and the Columbia River (Armstrong, 1988; Tempelman-Kluit, 1989; Figure 2.7). This suite is comprised of pink, variably textured, commonly porphyritic syenite with lesser amounts of granite, shonkinite, diorite, and monzonite. Mafic minerals are biotite and hornblende with local occurrences of pyroxene. These intrusive rocks are associated with the Marron Formation in the White Lake basin (Church, 1973; Little, 1983). The strongly alkaline chemistry of this suite indicates a continental rift setting for the generation of these magmas (Woodsworth et al., 1991). The Shingle Creek porphyry is a calc-alkaline coarsely porphyritic granite that is exposed west of the Okanagan shear zone.

The 47 Ma Sheppard intrusions are exposed south of Trail, where they crosscut the Valkyr shear zone and are deformed by the Slocan Lake fault (Carr et al., 1987). These are composed of intensely sheared and mylonitized biotite granite with subordinate syenite. These intrusions may be related to calc-alkaline volcanic rocks in the upper part of the White Lake basin or possibly the Kettle River Formation. Initial $^{87}Sr/^{86}Sr$ values (0.7067 to 0.7069) and ε_{Nd} values (–6.8 to –10.2) from the Coryell suite indicate that these magmas are probably the product of large-scale melting of the deep continental basement (Ghosh, 1995).

2.10 Metamorphism

Two major phases of metamorphism affected the southern Omineca belt since the Middle Jurassic (Greenwood et al., 1991). Middle Jurassic regional metamorphism is associated with the collision of the Intermontane Superterrane with the western margin of ancestral North America (Figure 2.9). This metamorphism is the product of intense crustal contraction and burial during the formation of the Kootenay Arc (Crosby, 1968; Hoy, 1977; 1980). This was followed by extensive Cretaceous-Paleocene high-grade metamorphism that affected the deep infrastructure of the Selkirk allochthon as it was thrust over the Monashee complex along the Monashee decollement (Froese, 1970; Reesor and Moore, 1971; Carr et al., 1987; Parrish et al., 1988). Large-scale anatexis is associated with this event, as large portions of the allochthon were heated to temperatuers above the stability of muscovite (Carr, 1992).

2.10.1 The Monashee Complex – Basement Zone

Mantling gneisses of the Monashee Terrane record a two-stage Mesozoic history of prograde metamorphism, a Jurassic event and a Cretaceous-Paleocene event (Journeay, 1988). These episodes of metamorphism are related to the eastward thrusting of the Selkirk Allochthon and coeval folding and imbrication in the Monashee complex (Brown

Figure 2.9 -- Variations in grade of metamorphism in the southern Omineca belt (from Read et al., 1991). The basement and middle-crustal infrastructure are typically metamorphosed to amphibolite grade while much of the upper-crustal suprastructure is metamorphosed to greenschist grade. The heavy solid lines represent major faults, and it can be seen that sharp breaks in metamorphic grade typically occur at most of the detachment faults. Granitic plutons in this map are shown by the dense heavy stipple pattern. The major lakes in this region are typically arcuate or elongate in a N-S direction, and from upper left to lower right, these are: Adams and Shuswap Lakes, Arrow Lake, Slocan Lake, and Kootenay Lake (compare with Figure 2.3).

Figure 2.10 -- K-Ar cooling ages for the southern Omineca belt (after Armstrong, 1988). The heavy solid lines represent major structural boundaries, including detachment faults and thrust faults. The dark shading represents areas having cooling ages of less than 60 Ma. The horizontal ruling denotes places with cooling ages greater than 150 Ma. The white areas have cooling ages intermediate between 60 Ma and 150 Ma. The 100 Ma chrontour is shown with a dashed line. Note that the dark shaded areas closely correspond with lower-plate outcrops (compare with Figure 2.4), indicating that the cooling ages of lower plate rocks are generally less than 60 million years. The early Tertiary thermal high at Kootenay Lake is shown by the < 60 million year shaded zone in the extreme southeast part of the diagram.

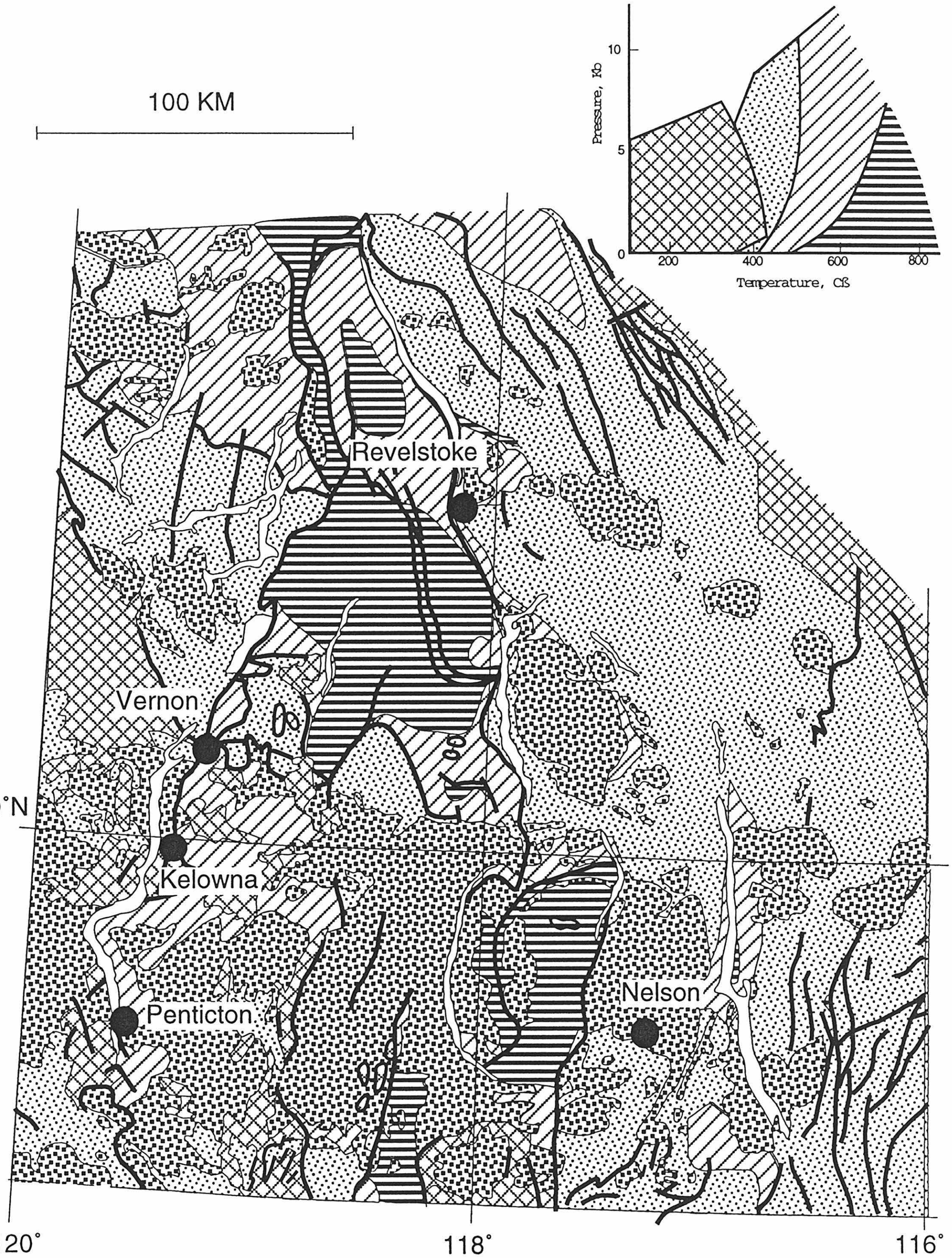

Figure 2.9 Isograd Map of the Southern Omineca Belt

Figure 2.10 K-Ar Cooling Ages

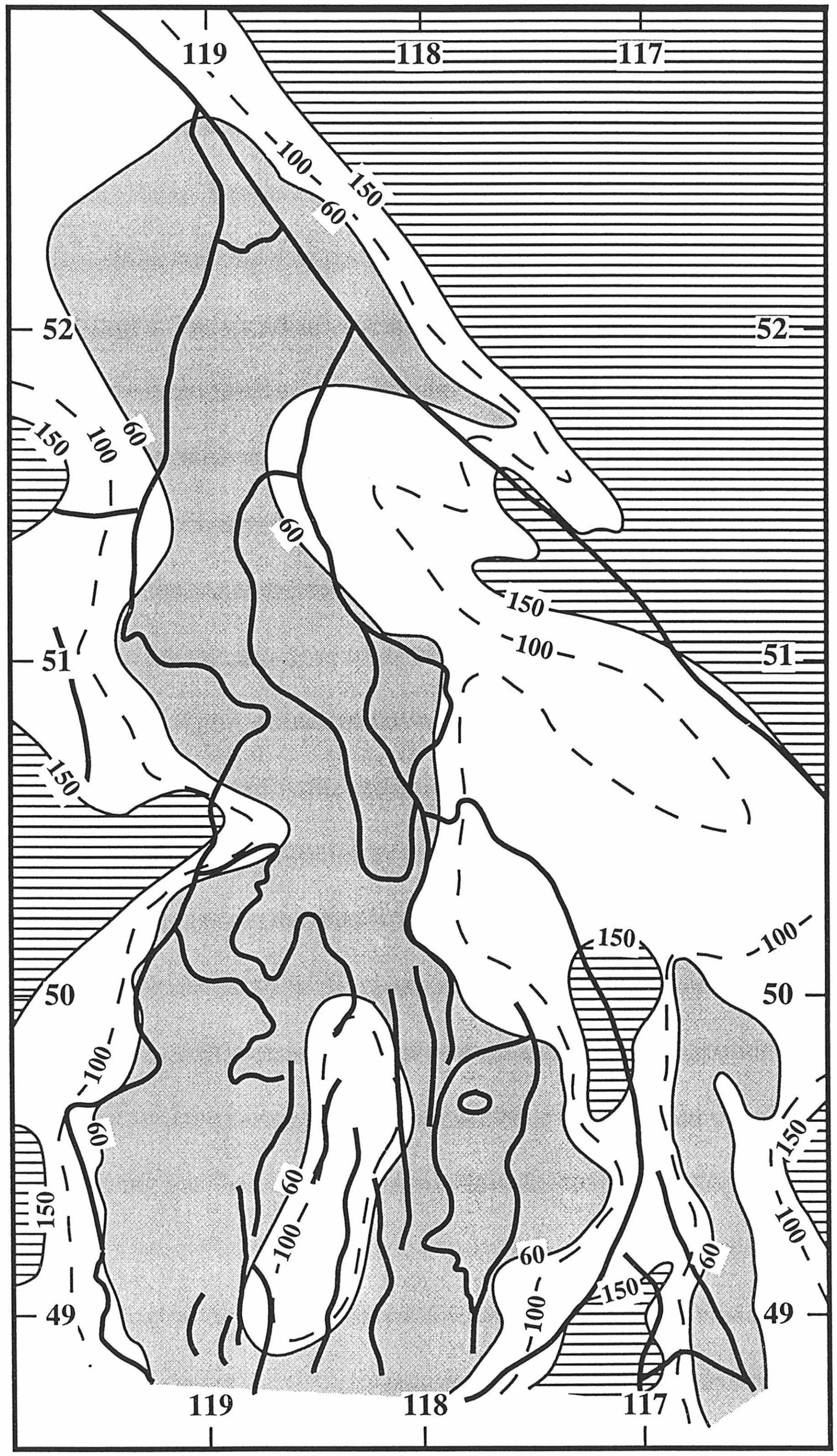

and Journeay, 1983). The Jurassic metamorphic belt is a "hot-side-down" sequence that goes from middle amphibolite facies (640 °C, 6.4 kb) to lower granulite facies (685 °C, 7.5 kb). Antiformal isograds cut early shear zones related to the Monashee Decollement.

The second metamorphic event to affect the mantling gneisses of the Monashee complex is associated with renewed thrusting along the Monashee Decollement during the Cretaceous and Early Teritary (Journeay, 1988; 1989). This metamorphic sequence is inverted in a hot-side-up configuration. Metamorphic grade increases upward from greenschist facies (450 °C, 3.5 kb) to upper amphibolite facies (650-680 °C, 2.5 kb) at the Frenchman Cap dome. This inverted gradient formed in response to the emplacement of high-grade metamorphic and plutonic rocks of the Selkirk Allochthon onto uplifted and previously metamorphosed rocks of the Monashee complex. Preservation of the inversion was possible with the immediate rapid denudation during Eocene detachment faulting.

Reesor and Moore (1971) report similar, but much higher grade inverted isograd patterns at the Thor-Odin dome in the southern Monashee complex. This metamorphic sequence increases upward from the sillimanite+muscovite zone to the sillimanite+K-feldspar zone. Rocks immediately adjacent to the Monashee Decollement have experienced decompression-related retrogression involving the reaction of aluminosilicates to cordierite. Kyanite is an early phase and is overprinted by reactions to sillimanite. Nyman and Ghent (1995) report granulite-facies conditions (720-820 °C, 7.5-9.0 kb) and high degrees of partial melting in mantling gneisses situated 100 m beneath the Monashee Decollement along the Trans Canada Highway west of Revelstoke.

2.10.2 The Infrastructure of the Selkirk Allochthon – Middle Crustal Zone

The second major episode of metamorphism affected the southern Omineca belt during the final stages of crustal thickening and contraction associated with the collision between the Insular Superterrane and ancestral North America. These rocks were rapidly brought close to the surface and cooled by tectonic denudation during extension immediately following contraction. Metamorphic culminations at sillimanite+K-feldspar temperature conditions are in the footwalls of detachment faults and these zones are bound by these faults.

The Valhalla complex is an Eocene metamorphic culmination with sillimanite+K-feldspar zone rocks and associated leucocratic granitoids (Reesor, 1965; Carr et al., 1987). The Slocan Lake fault separates these high-grade lower plate rocks from the chlorite-grade upper plate.

2.10.3 The Kootenay Arc Suprastructure – The Upper Crustal Zone

In ancestral North America, metamorphic grade increases westward from the chlorite to biotite zones across the Purcell Anticlinorium (Crosby, 1968; Reesor, 1958; 1973). This increase in metamorphic grade is independent of stratigraphic depth and is coeval with higher-grade metamorphism to the west, suggesting a post-deformational mode of metamorphism. There are local occurrences of Jurassic contact metamorphism near the Kootenay Arc (Crosby, 1968), the Summit Creek area (Archibald et al., 1983), and the contact zone of the Kuskanax batholith (Klepacki and Wheeler, 1985).

There is a gradual westward increase in metamorphic grade in the Kootenay Arc. Burial depth varies along strike (Archibald et al., 1983; 1984), with the Windermere Supergroup buried down to depths as great as 15-20 kilometers (5-6 kb) whereas the Lardeau Group in the Riondel area were buried to approximately 13 kilometers (4.5 kb). Metamorphic grade (probably Jurassic) of rocks north of the Valhalla complex gradually and continuously decrease form the staurolite-sillimanite zone (630-680 $^{\circ}$C, 5.0 – 6.8 kb) to the chlorite zone in the Slocan metamorphic low (Parrish, 1981).

A narrow northerly-oriented metamorphic high is located at Kootenay Lake (Crosby, 1968; Hoy, 1977; 1980; Archibald et al., 1983; 1984). Metamorphic grade increases from the biotite or chlorite zone to the sillimanite+K-feldspar zone over a distance of less than 5 kilometers. A zone of biotite K-Ar ages < 60 Ma (Archibald et al., 1984; see Figure 2.10) along Kootenay Lake indicates that this isograd trend may be due to a localization of heat flow beneath this zone during Eocene extension.

2.11 Eocene Extension

Eocene extension and detachment faulting comprise the final stage in the tectonic development of metamorphic core complexes in the southern Omineca belt (Parrish et al., 1988). These extensional structures represent the gravitational collapse (Price and Mountjoy, 1970; Armstrong, 1982; Coney and Harms, 1984) of at least a 50 km-thick crustal sequence comprised of the Monashee Complex and Selkirk Allochthon, two crustal sections stacked during the Jurassic–Paleocene compressional orogeny (Brown and Read, 1983; Brown et al., 1986; 1992; Brown and Journeay, 1987; Cook et al., 1992). This collapse was probably initiated by a change in plate motion that set up a regional stress regime conducive to dextral transpression. This is the time at which detachment of the suprastructure from the infrastructure of the Selkirk Allochthon took place. The magnitude of extension across the southern Omineca belt is estimated to be 60-80% (Parrish et al., 1988).

Extensional detachment faults, shear zones, and high-angle normal faults occur in a southward-widening wedge that goes from north of the Monashee Complex to beyond the U.S.A.-Canada border into Washington and Idaho (Hansen and Goodge, 1988; Rhodes and Hyndman, 1988; Parrish et al., 1988; Fox, 1994). From west-to-east, this extensional zone extends from Okanagan Lake to Kootenay Lake. Extension is associated with widespread magmatism beginning with Paleocene-early Eocene anatexis and intrusion of the Ladybird leucogranite suite (Carr et al., 1987; Parrish et al., 1988; Armstrong et al., 1991; Carr, 1991; 1992; 1995), followed by intrusion and eruption of alkaline magmas of the Coryell-Penticton suite in the middle to late Eocene (Church, 1973; Carr and Parkinson, 1989). K-Ar cooling ages of less than 60 Ma of lower plate rocks indicate that final cooling occurred during extension (Medford, 1975; Matthews, 1981; 1983; Carr et al., 1987; Armstrong, 1988; Figure 2.10). This contrasts with K-Ar cooling ages of 165-70 Ma from the upper plate (Medford, 1975; Matthews, 1981; Armstrong, 1988). A north-south axis centered on the Monashee Complex is the boundary between an east-dipping detachment fault domain to the east and a domain of west-dipping detachment faults to the west. The east-dipping faults were active at 58-52 Ma while the west-dipping fault were active at 52-47 Ma (Parrish et al., 1988).

Final exhumation of the Monashee Complex and the surrounding high-grade migmatites at deep levels of the Selkirk Allochthon took place as the result of displacements along the Columbia River and Eagle River detachment faults (Lane, 1984; Lane et al., 1989; Carr, 1991; 1992; 1995). Subsidiary high-angle normal faults, shear fractures, and dike-filled extension joints account for 4-5 km of extension across this area. The north-trending Columbia River fault is 150 km long and comprises the eastern boundary of the lower plate in this extensional domain. This fault is a 1 km thick 20-30° east-dipping, top-to-the-east mylonitic shear zone which has been overprinted by brittle deformation near the detachment surface. The southwest-trending Eagle River Fault is a west-dipping, top-to-the-west detachment fault similar to the Columbia River Fault (Johnson, 1989). To the southwest, the Eagle River Fault becomes the Okanagan Valley Fault (Parrish et al., 1988). Displacements along both of these detachment faults are estimated to be at 10-15 km.

The Okanagan Valley Fault is a south-southwest-trending 300 km-long detachment fault that extends from the Monashee Complex to the northern Washington (Templeman-Kluit and Parkinson, 1986; Parrish et al., 1988; Hansen and Goodge, 1988; Fox, 1994). This gently (10-20°) west-dipping, top-to-the-northwest shear zone is the western boundary of the Okanagan Complex (Bardoux, 1985; Parrish et al., 1988). Displacement along this shear zone is estimated to be 60-80 km (Templeman-Kluit and Parkinson, 1986). A 1-2 km-thick downward thickening bottom-to-the-top sequence of coarsely crystalline granodiorite, fine-grained mylonitic gneiss, augen gneiss, mylonite, and microbreccia comprises this shear zone (Bardoux, 1985). The upper plate contains numerous steeply and gently-dipping extensional faults, gravity slide blocks, and fault-bound basins filled with synextensional volcanic rocks and debris shed from the lower plate (Church, 1973; Bardoux, 1985).

The Valhalla Complex is a tectonic window of penetratively deformed Paleocene to early Eocene granitoids and older metasedimentary rocks exposed by displacements along the Valkyr shear zone and the Slocan Lake Fault (Parrish, 1984; Carr et al., 1987). The west-dipping, top-to-the-east Valkyr shear zone is a 1-3 km-thick amphibolite grade shear zone that bounds the northern, western, and southern margins of the Valhalla Complex. The east-dipping, top-to-the-east Slocan Lake fault is the eastern bounding structure of the Valhalla Complex. Lower to middle greenschist grade deformation along the Slocan Lake Fault postdates movement along the Valkyr shear zone. These two loci of deformation are interpreted to have been part of a middle-crustal normal fault or shear zone whose western limb was deactivated during doming and uplift of the lower plate during extension through isostatic rebound (Carr et al., 1987).

Other complexes with similar structural and plutonic associations are the Kettle-Grand Forks (Cheney, 1980), Priest River (Rhodes and Hyndman, 1988), and

Clachnachudainn complexes. Eocene normal, reverse, and dextral strike-slip faults in the Intermontane belt are related to right-lateral transform motions associated with regional oblique extension and clockwise rotation of the Intermontane Belt (Price, 1979). These faults are a system of northeast-, northwest-, and north-directed faults that cross-cut contractional structures formed during the Mesozoic. The Nicola horst is a north-northeast trending horst containing rocks of the Nicola batholith and possible Tertiary plutonic rocks and metamorphic rocks with Early Tertiary K-Ar cooling ages (Armstrong, 1988).

2.12 Oxygen and Hydrogen Isotope Geochemistry

One of the principal reasons why southern British Columbia was chosen for this study is the fact that it is a northerly region where the $\delta^{18}O$ values of meteoric ground waters are very low, thereby providing a striking contrast with the much higher $\delta^{18}O$ values of magmatic and metamorphic waters. It is also a mountainous region in which the topographic barriers are subparallel to the Pacific Coast. This kind of topography, combined with the northerly latitude, leads to a pronounced shift in the $\delta^{18}O$ and δD values of the rain and snow that falls in this region, as shown on Figure 2.11. Note that there is a marked decrease in δD and $\delta^{18}O$ in such meteoric waters moving inland from the Pacific Coast, as well as a decrease as one moves north from the U.S.A.-Canada border to the Yukon.

The δD contours for present-day meteoric waters shown on Figure 2.11 can be transformed into $\delta^{18}O$ contours, simply by applying the meteoric water equation of Craig (1961):

$$\delta D = 8\delta^{18}O + 10$$

Thus, in the area of interest for the present study around the southern Omineca belt in southeastern British Columbia, present-day meteoric waters vary approximately from $\delta D = -110$ and $\delta^{18}O = -15$ to $\delta D = -150$ and $\delta^{18}O = -20$. These represent approximate annual averages; the δD and $\delta^{18}O$ values of local precipitation can be significantly higher in the summer and lower in the winter.

Magaritz and Taylor (1986) measured the hydrogen and oxygen isotope ratios of more than 500 samples, mainly from granitic plutons, along a 700-km, E-W traverse across the accreted terranes of southern British Columbia (latitudes 49° - 52°N). Their sample localities are shown on Figure 2.12. Despite the geological complexity and range of intrusive ages (Late Triassic to Tertiary), and although there are "steps" in the isotopic values at some geologic boundaries, two clear patterns emerged from their work: (1) The $^{18}O/^{16}O$ and D/H values of the waters involved in hydrothermal interactions with the granitic rocks during the late Mesozoic and early Tertiary exhibited a regular eastward trend of depletion in both D and ^{18}O. Enormous areas were affected by the hydrothermal processes, but the most intense ^{18}O depletions were observed in the mineral feldspar, and were localized along major north-trending fracture zones or lineaments (*e.g.*, the Okanagan Lake and Slocan Lake faults). (2) Independent of hydrothermal effects, the primary $\delta^{18}O$ values of the granitic rocks also were found to change systematically eastward, from +7.5 to +8.5 in Vancouver Island, reaching a minimum of +5.5 to +7.0 in the western and central Coast Plutonic Complex, then increasing progressively from the eastern Coast batholith to the Okanagan batholith, and attaining a maximum $\delta^{18}O$ of +10.0 to +12.0 in the Nelson batholith. Two older, geographically isolated batholiths (Guichon and Thuya) were found to be unique in their high δD values, and they apparently were

Figure 2.11 -- Map of British Columbia (modified after Magaritz and Taylor, 1986) showing in a generalized fashion the range of δD values in present-day meteoric waters (lakes, streams, rivers, groundwaters, etc.) in this region, based on data from Friedman et al. (1964), Yapp and Epstein (1982), Hitchon and Krouse (1972), and Clark et al. (1982). These δD contours can be exactly converted to the analogous $\delta^{18}O$ contours by applying the meteoric water equation of Craig (1961). Thus, $\delta D = -70$ is $\delta^{18}O = -10$, $\delta D = -90$ is $\delta^{18}O = -12.5$, $\delta D = -110$ is $\delta^{18}O = -15$, $\delta D = -130$ is $\delta^{18}O = -17.5$, $\delta D = -150$ is $\delta^{18}O = -20$, and $\delta D = -170$ is $\delta^{18}O = -22.5$.

Figure 2.12 -- Generalized geologic map of southern British Columbia, showing the locations of samples analyzed for $^{18}O/^{16}O$ and D/H by Magaritz and Taylor (1986), as well as major granitic batholiths (Coast Range, Thuya, Guichon, Raft, Okanagan, and Nelson) and the tectonostratigraphic terrane boundaries of Monger and Berg (1984): WR, Wrangellia; NK, Nooksack; QN, Quesnel; MT, Methow-Tyaughton; P, Pacific Rim; C, Crescent; KO, Kootenay; SK, Skagit; HZ, Hozameen; MO, Monashee; CR, craton; CC, Cache Creek; BR, Bridge River; S, Stikine; TA, Tracy Arm.

Figure 2.13 -- Graph from Magaritz and Taylor (1986) showing the δD values of biotite, hornblende, and/or chlorite from the various kinds of rocks from the sample localities indicated in Figure 2.12, plotted versus distance eastward from the Pacific Coast of Vancouver Island.

Figure 2.11 British Columbia Meteoric Waters

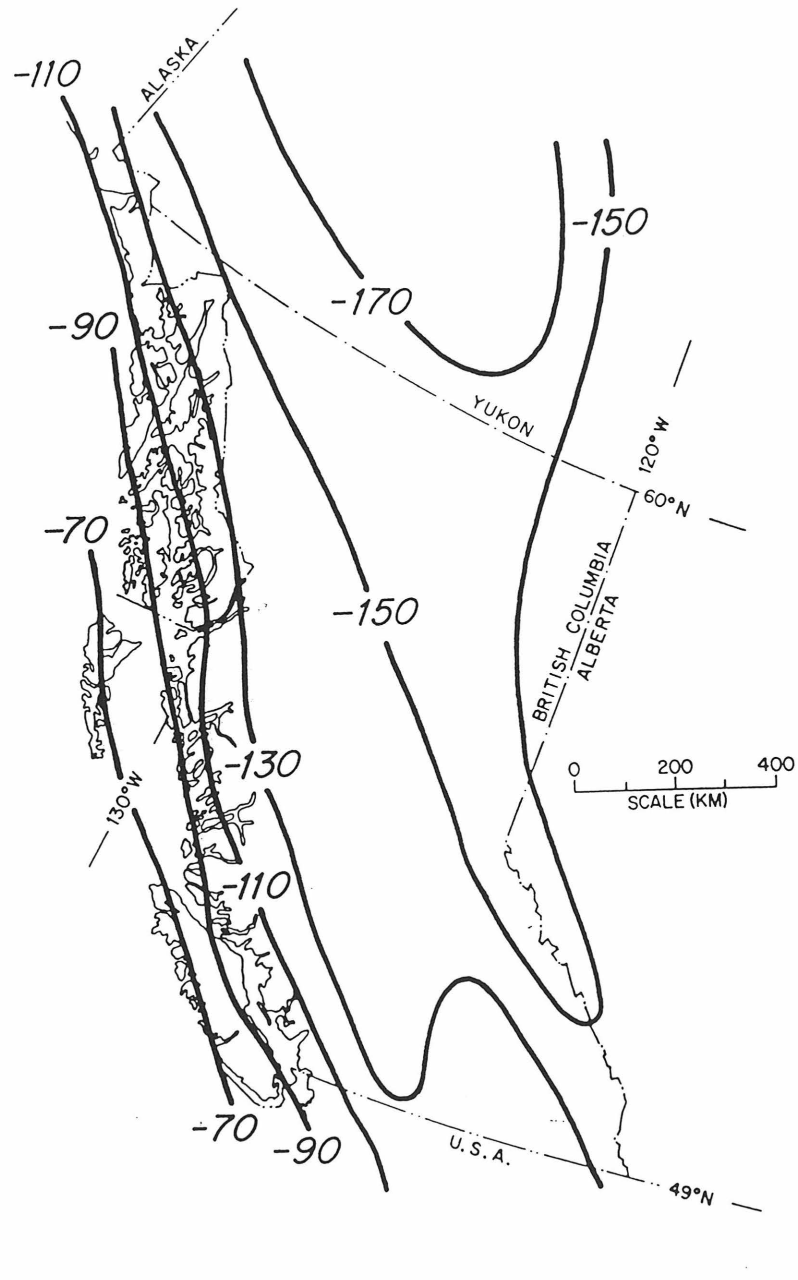

Figure 2.12 Sample Locations for Magaritz and Taylor (1986) Study

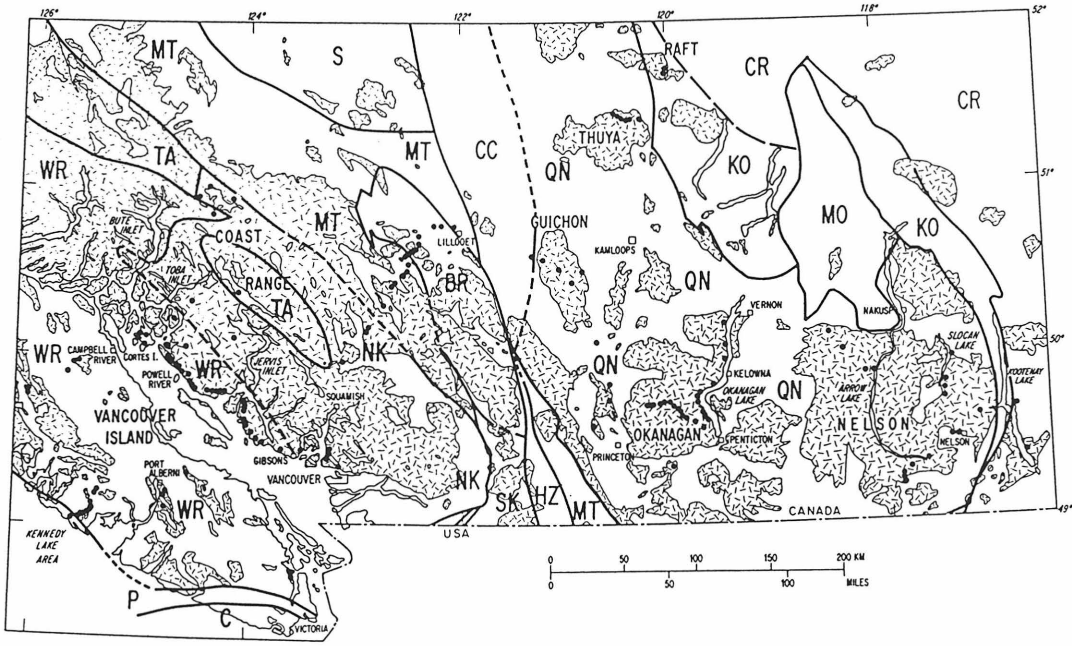

Figure 2.13 δD Values from Southern British Columbia Batholiths

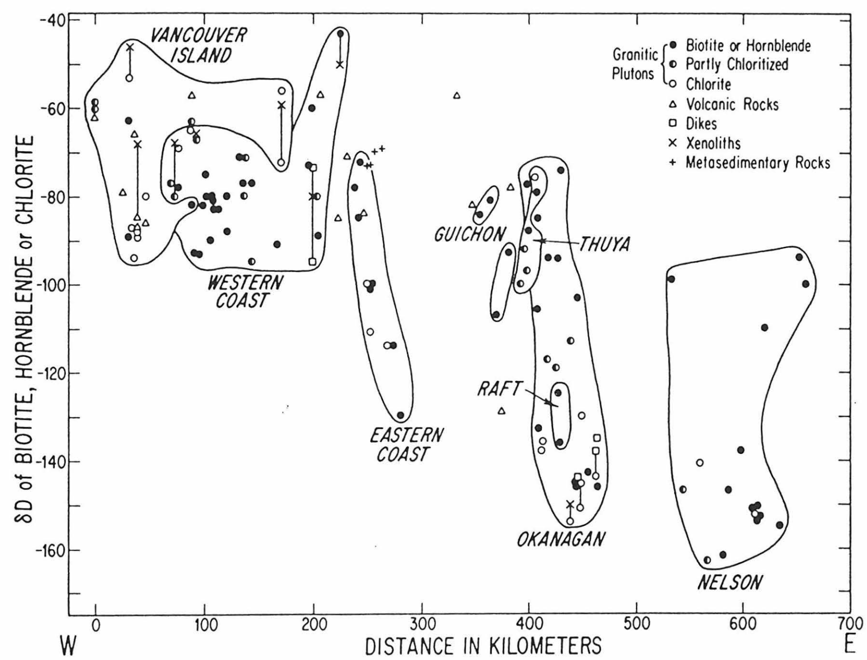

not strongly affected by the early Tertiary meteoric-hydrothermal systems; this is perhaps why these older batholiths preserved their early Jurassic to Triassic K/Ar ages.

The D/H variations observed by Magaritz and Taylor (1986) for each of the individual batholithic terranes in southern British Columbia display some interesting regional systematics; these west-to-east D/H variations are best shown by projecting the data on a latitudinal cross section (Figure 2.13). Although the freshest, least altered samples in each terrane typically have δD values close to or within the presently accepted "primary magmatic" δD range of –65 to –85, the subset of heavily altered granitic rocks exhibits steadily decreasing δD values from west to east. If we confine the discussion just to samples that show hydrothermal $^{18}O/^{16}O$ effects (*i.e.*, those with ^{18}O-depleted feldspars or whole rocks that must have experienced very high water/rock ratios), the measured δD values change systematically from west to east, going from Vancouver Island (–45 to –65), to the main Coast Range batholith (–115 to –130), to the Okanagan batholith (–130 to –150), and finally to the easternmost area that was sampled, the Nelson batholith (–145 to –165).

The above-described effects are nicely shown by the relatively uniform δD values of the horizontal arms of each of the inverted "L" patterns on diagrams like those shown in Figure 2.14, from Magaritz and Taylor (1986). The geographic variations of δD and $\delta^{18}O$ throughout British Columbia show up as a series of these L-shaped patterns, each one characteristic of a specific geographic area. These effects show up when δD is plotted against either $\delta^{18}O$ feldspar or against $\Delta^{18}O$ quartz-feldspar. On both kinds of diagrams, the horizontal arms of each "L" represent the samples that have been subjected to the highest water/rock ratios; in each case, the horizontal arm displays an approximately constant δD value characteristic of that particular geographic area.

Figure 2.14 -- (**Top**) Plot of δD versus $\delta^{18}O$ feldspar (modified after Magaritz and Taylor, 1986), showing data-points obtained on samples from the granitic batholiths of southern British Columbia. The stippled area labeled 200 m.y. indicates samples from the Triassic Thuya and Guichon batholiths (see text). (**Bottom**) Another plot of δD versus $\delta^{18}O$ feldspar from Magaritz and Taylor (1986), showing the various batholith fields shown above, together with the meteoric water line of Craig (1961), and the calculated δD and $\delta^{18}O$ values of the pristine, unexchanged meteoric waters that were the source of the hydrothermal fluids that produced the various "inverted-L" patterns.

Figure 2.14 Southern British Columbia Batholiths, δD versus $\delta^{18}O$ Feldspar

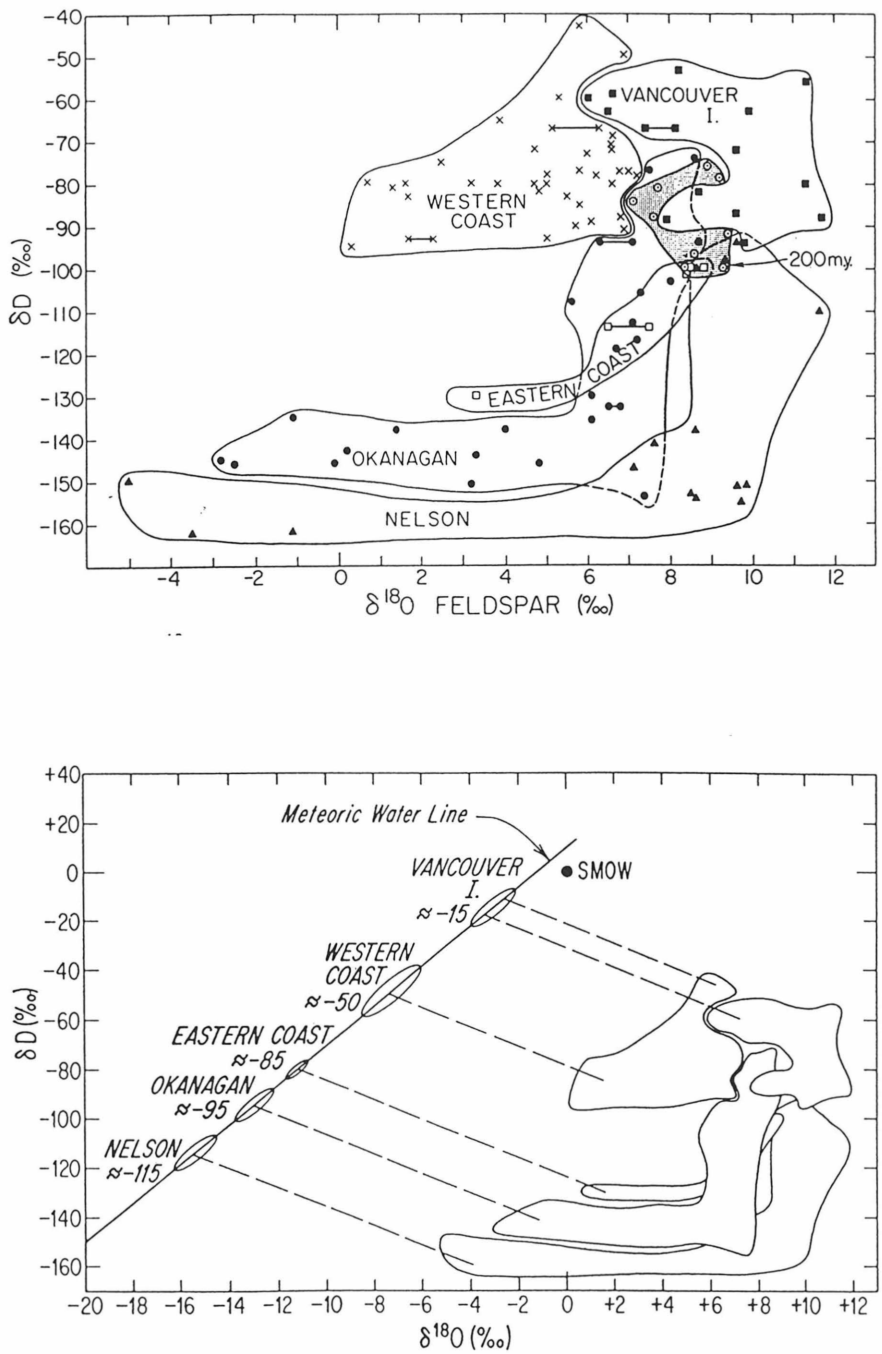

Making certain assumptions about the temperature and other parameters (see Taylor, 1974), Magaritz and Taylor (1986) calculated the δD values of the H_2O that coexisted with the hydrothermal chlorites and biotites in the most heavily altered samples, as shown on the bottom diagram of Figure 2.14. Such a δD value will represent the original δD value of the surface waters involved in the hydrothermal convective systems at the time of alteration, so by plotting this value on the meteoric water line (Craig, 1961), we can obtain a complete picture of the original isotopic compositions of these waters prior to their entrance into each hydrothermal system.

Figure 2.14 shows that in direction, but not in magnitude, the same general west-to-east pattern of D/H and $^{18}O/^{16}O$ that exists in the meteoric waters of southern British Columbia today (Figure 2.11) also must have existed when the bulk of the hydrothermal alteration occurred in the late Mesozoic and early Cenozoic. In all these localities, the calculated δD values of the hydrothermal fluids are about 20‰ higher than those of present-day local groundwaters. This is equivalent to a $\delta^{18}O$ value about 2.5‰ higher than the $\delta^{18}O$ of present-day meteoric waters. These isotopic data are thus nicely compatible with the types of northward translations of the batholithic terranes suggested by various workers (*e.g.*, Coney et al., 1980; Monger et al., 1991; Monger, 1993). However, they are also compatible simply with an overall shift away from a somewhat warmer and less continental climate everywhere in southern British Columbia during the late Mesozoic and early Cenozoic. The similarities of the patterns today and in the early Tertiary imply that the general topography at that time must have been somewhat similar to the present-day topography (*e.g.*, a mountain chain parallel to the Pacific Coast).

The present $^{18}O/^{16}O$ study represents the first systematic follow-up to the studies of Magaritz and Taylor (1986), outlined above. Note that the work to be described below mainly focuses on more detailed studies of some of the regions around the Nelson, Okanagan, Raft, Guichon, and Thuya batholiths shown on Figures 2.13 and 2.14, namely those with the lowest $\delta^{18}O$ and δD values delineated by Magaritz and Taylor (1986).

Chapter 3. The Monashee Complex: Hydrothermal Processes in the Basement Zone

3.1 Introduction

The main subject of this chapter is the metamorphic-hydrothermal evolution of the Monashee basement complex and the implications of this water-rock interaction to local anatexis and the thermal evolution of the footwall of the Monashee decollement. The Monashee complex (Figure 3.1) is a window into the depths of the southern Omineca belt, and it preserves a deformational history distinct from the overlying crustal zones. The lack of abundant early Tertiary leucogranite (Carr, 1992) and the preservation of an inverted metamorphic sequence beneath the Monashee decollement (Journeay, 1988) contrasts with the pervasive anatectic phenomena observed in the deepest levels of the overlying Selkirk allochthon. These differences indicate a much different overall metamorphic-hydrothermal history for this terrane as it was underthrust beneath the Selkirk allochthon, although water-rock interaction in this basement terrane suite must also have affected the overlying crustal layers (*e.g.*, Selkirk allochthon, detachment faults) at least locally. It is likely that changes in the rheological competence of rocks along the Monashee decollement took place in response to these hydrothermal processes.

Thermal inversions, or inverted metamorphic sequences, can be created by the overthrusting of a hot thrust sheet over colder autochthonous rocks (Graham and England, 1976; England and Thompson, 1984). This type of metamorphic association, distinguished by upwardly increasing metamorphic grade, forms during overthrusting in subduction zones (Cloos, 1985; Peacock, 1987), magmatic arcs (Crawford et al., 1987; Himmelberg et al., 1991), and orogenic belts (Graham and England, 1976; Molnar and England, 1990; Allen and Chamberlain, 1991). These thermal perturbations are short lived because conductive and advective heating of the lower plate will return it to a state of approximate thermal equilibrium with the upper plate within a few million years following the emplacement of the hot upper plate (England and Thompson, 1984; Peacock, 1988). Thus, such metamorphic inversions are preserved only when rapid uplift and cooling immediately follows overthrusting.

A situation that is possibly analogous to the Monashee Complex is found in the Himalayan orogen, where dehydration fluids may have migrated upward into the hanging wall of the Main Central thrust to drive anatexis, forming the High Himilayan leucogranite suite (Le Fort et al., 1988). Anatexis near the thrust zone itself can induce rapid tectonic movements through reduced friction as the elastic strength of this zone is sapped by the accumulating melt (Crawford and Hollister, 1986). This can provide a mechanism for rapid uplift and swift transport of hot packages of rock to shallow crustal levels, thus allowing for the required rapid quenching of these rocks.

3.2 Geologic Setting

The Monashee complex is the basement core zone of the southern Omineca belt exposed as a tectonic window beneath the Monashee decollement and Columbia River detachment fault (Figure 3.1). This basement zone is tectonically overlain by high-grade

Figure 3.1 -- Simplified geology (modified from Brown and Journeay, 1987; and Parkinson, 1991) of the Monashee complex and environs showing sample locations. Frenchman Cap (FC) and Thor-Odin (TO) gneiss domes represent second-order culminations of the Monashee complex (see text). The thick dashed curve is the Trans-Canada highway. The Columbia River detachment fault (CRF) separates the Monashee complex from the Selkirk allochthon suprastructure to the east. The Monashee decollement (MD) separates the basement from the Selkirk allochthon infrastructure to the west and south. The Eagle River detachment fault (ERF) separates the upper-crustal zone from the mid-crustal Selkirk allochthon. Also shown are a few of the steeply-dipping normal faults that occur in the area (*e.g.*, Victor Lake fault, VF). The 7 sample localities < 200 m below the Monashee decollement (MD) are denoted by open squares. The 4 ^{18}O-depleted sample localities from the allochthon and the 3 ^{18}O-depleted samples from the vicinity of the Columbia River fault are shown by open triangles. The 3 CRF samples are discussed in Chapter 5 (these are GH-74 and GH-66, just south and just north of Revelstoke, respectively, and GH-31 30 km farther north). All other samples are indicated by solid squares (including the outcrop locality labelled Blattner in the southern part of the Thor-Odin dome). MC-2 and MC-3 are localities discussed in detail in the text.

Figure 3.2 Thermal Evolution of Selkirk Allochthon and Monashee Complex

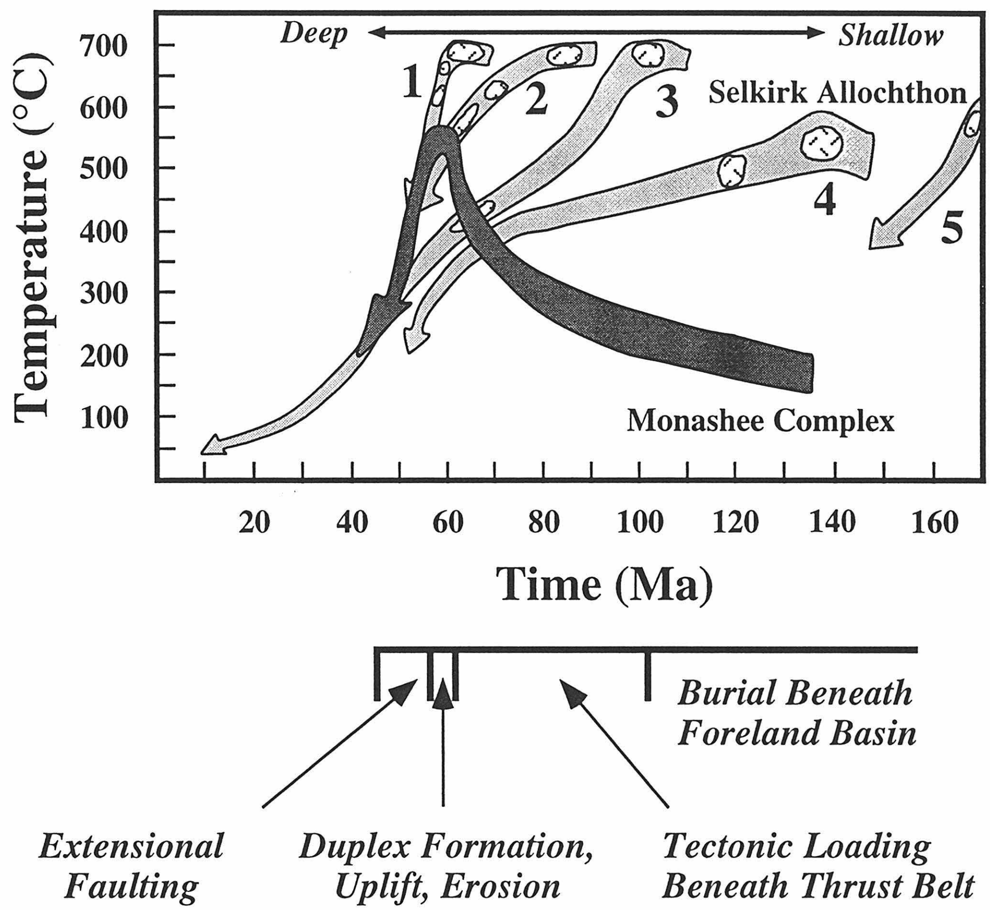

mid-crustal rocks of the Selkirk allochthon. The complex can be subdivided into a core zone of Early Proterozoic orthogneiss and paragneiss basement rocks, overlain by a mantling sequence of Late Proterozoic to Paleozoic metasedimentary rocks.

The Monashee complex is thus an antiformal, basement-cored complex that has been exhumed during late Cretaceous-Paleocene obduction, backfolding, and "piggy-back" thrust-stacking (Brown et al., 1986); this was in turn followed by Eocene extensional denudation along the Columbia River fault (Parrish et al., 1988). The Frenchman Cap and Thor-Odin gneiss domes can be considered to be regional interference structures that are second order culminations of the antiformal Monashee complex (Fyles, 1970; Mcmillan, 1971; Reesor and Moore, 1971; Duncan, 1984; Brown and Journeay, 1987, and Hoy, 1988). At least three folding events are recognized: (1) east-vergent fold nappes and detachment faults, (2) east-to-northeast directed isoclinal folding linked to northeast-directed thrusting along the Monashee decollement, and (3) late-to-post-metamorphic folds formed during the final stages of unroofing of the complex.

The Monashee decollement is a fundamental boundary structure with as much as 200 km displacement that served as the basal decollement for the Rocky Mountain fold and thrust belt to the east (Brown et al., 1992; Cook and Varsek, 1994). This thrust zone is a 1-3 km thick network of annealed mylonitic shear zones and imbricated fault blocks that separate the Monashee complex from the high-grade migmatitic rocks of the Selkirk allochthon (Brown and Journeay, 1987; Carr, 1991; McNicoll and Brown, 1994). Planar and linear fabrics merge into synmetamorphic foliations on both sides of the decollement. Two major episodes of displacement are recognized: (1) eastward movement of the upper plate during the middle Jurassic, cross cutting the early fold nappes and predating the uplift and arching of the complex; and (2) late Cretaceous to Paleocene northeastward displacement of the Selkirk Allochthon following arching and uplift of Frenchman Cap and Thor-Odin domes. The Monashee thrust ramp formed as a result of arching of the Monashee complex, developed in response to stacking of fault sheets deeper in the basement during the Cretaceous (Brown et al., 1986).

The basement paragneiss unit consists of intermixed and interlayered biotite-quartz-feldspar gneiss, quartzitic gneiss, biotite-quartz-plagioclase gneiss and minor aluminosilicate schist and amphibolite (Fyles, 1970; Reesor and Moore, 1971; McMillan, 1973). Nd and Sr isotope data (Armstrong et al., 1991; Parkinson, 1991) and U/Pb apparent ages of detrital zircons (Parkinson, 1991) imply a 2200 Ma protolith for these paragneisses. Migmatization and much of the metamorphism of these rocks took place during the Proterozoic (Okulitch, 1984; Hoy, 1988; Armstrong et al., 1991; Parrish, 1995).

The basement core orthogneiss consists of granodiorite gneiss cut by a younger, compositionally variable granitoid gneiss (Reesor and Moore, 1971). The deformed and foliated granodiorite gneiss contains hornblende, biotite, augen of K-feldspar and plagioclase, and occurs as lenses in paragneiss; it is locally migmatized. This intrusive suite has apparent U/Pb zircon ages of 1960±40 Ma (Wanless and Reesor, 1975) and 1934±6 Ma (Parkinson, 1991), and Nd-isotopes suggest some interaction with 2800 Ma Archean crust (Parkinson, 1991). The biotite-bearing granitoid gneiss is medium-grained and texturally more homogeneous and less deformed than the older gneiss; it occurs as pods, lenticles, and layers in the older paragneiss. Granitoid compositions range from granodiorite and tonalite to leuco-quartz monzonite. These late granitoids have an apparent U/Pb zircon age of 1874±21 Ma, and Nd-isotope data suggest a source rock having an age similar to the paragneiss unit (Parkinson, 1991).

The mantling gneiss is a sequence (up to 2300 m-thick) of amphibolite, quartzite, metapelite, and arkosic grit with minor calc-silicate and marble that unconformably overlies the basement units (Hoy, 1988; Scammell and Brown, 1990). The stratigraphic sequence from bottom to top is: (1) 30 m of basal quartzite, (2) 150-500 m of interlayered quartzite, metapelite, arkosic grit, and quartzofeldspathic gneiss, (3) 200 m of layered amphibolite, hornblende gneiss, and pyroclastic carbonatite, (4) up to 800 m of quartzite with thin layers of mafic and pelitic rocks, and (5) a 120-200 m complex sequence of metapelite, amphibolite, and calcareous schist. This sequence was correlated with rift-related rocks of the Windermere Supergroup by Hoy (1988) and Scammell and Brown (1990), but it has also been suggested that these rocks belong to the older Purcell Supergroup (Armstrong et al., 1991).

Mantling gneisses of the Monashee Terrane record a two-stage Mesozoic-early Cenozoic history of prograde metamorphism; both episodes are related to the eastward thrusting of the Selkirk Allochthon (Brown and Journeay, 1987; Journeay, 1988; Lane et al., 1989). The "hot-side-down" Jurassic metamorphic sequence ranges from middle amphibolite facies (640 °C, 6.4 kb) to lower granulite facies (685 °C, 7.5 kb). Isograds cut early shear zones related to the Monashee decollement and are antiformal. This event is probably coeval with the regional Barrovian metamorphic event that affected the Kootenay Arc and Cariboo Mountains (Greenwood et al., 1991).

Mapped isograd patterns in the footwall of the Monashee decollement in the northern part of Frenchman Cap dome indicate an inverted metamorphic sequence overprinting the earlier Barrovian metamorphism (Journeay, 1988). Metamorphic grade increases upward from greenschist facies (450 °C, 3.4 kbar) to upper amphibolite facies (650-680 °C, 2.5 kbar). Isograds mapped by Reesor and Moore (1971) in the Thor-Odin dome indicate a similar, but higher-temperature and more subtle thermal inversion, with metamorphic conditions increasing upward from the sillimanite+muscovite zone to the sillimanite+K-feldspar zone just beneath the Monashee decollement. Granulite facies conditions (720-820 °C, 7.5-9.0 kbar) are reported for migmatitic mantling gneiss just beneath the Monashee decollement along the Trans-Canada highway west of Revelstoke (Nyman et al., 1995).

Parrish (1995) applied the accepted blocking temperatures of several radiogenic isotope systems to determine the Mesozoic to early Cenozoic thermal evolution of the Monashee complex (Figure 3.2). These geochronological data indicate that heating of the Monashee complex was rapid as it was buried beneath the hot Selkirk allochthon at about 80-60 Ma. Maximum temperatures (> 600 °C) were reached at about 58-60 Ma. This thermal climax was followed by extremely rapid cooling (> 600 °C to < 250 °C) in less than 10 million years as tectonic denudation occurred due to duplex formation, uplift, erosion, and extensional unloading. This contrasts with the thermal evolution of the base of the Selkirk allochthon: the latter terrane that was approximately held at T > 600 °C for much of the Mesozoic, although it also experienced thermal quenching in the Eocene.

3.3 Samples Studied

A reconaissance suite of 19 samples from most of the rock units described above was collected from virtually all accessible parts of the Monashee complex. Sample and outcrop locations are shown on Figure 3.1, and the $^{18}O/^{16}O$ data are given in Table 3.1. Access to this basement zone was inhibited by very rough glaciated alpine terrain; much of it is above timberline and only accessible by helicopter and mountaineering techniques. Five analyzed samples from the deepest exposed structural level of the Thor-Odin dome from an earlier study by Blattner (1971) round out this reconnaissance coverage of rocks beneath the Monashee decollement.

The Trans-Canada highway transects the Monashee complex through the structural low between the Frenchman Cap and Thor-Odin domes. Logging roads that radiate out from this highway provided access to the lower-grade northwestern margin of the complex and to the early Proterozoic basement rocks at the southern margin of the

Figure 3.2 -- Temperature-time diagram comparing a plausible thermal evolution for parts of the Selkirk allochthon (light shading) with that of the Monashee complex (dark shading), as derived from geochronological data (from Parrish, 1995). Patterned blobs in the paths indicate episodes of felsic magmatism. Temperature-time plots labeled 1-5 are for different levels within the allochthon in order of their structural position from lowest (1) to highest (5) relative to the Monashee decollement. The Monashee complex was rapidly heated during tectonic loading as hot rocks of the Selkirk allochthon were thrust over the arched basement complex at about 60-70 Ma. Rapid cooling took place during duplex formation, uplift, and erosion, followed by extensional denudation. The short duration of heating in the Monashee complex made possible the preservation of the inverted metamorphic sequence beneath the Monashee decollement.

Figure 3.2 Thermal Evolution of Selkirk Allochthon and Monashee Complex

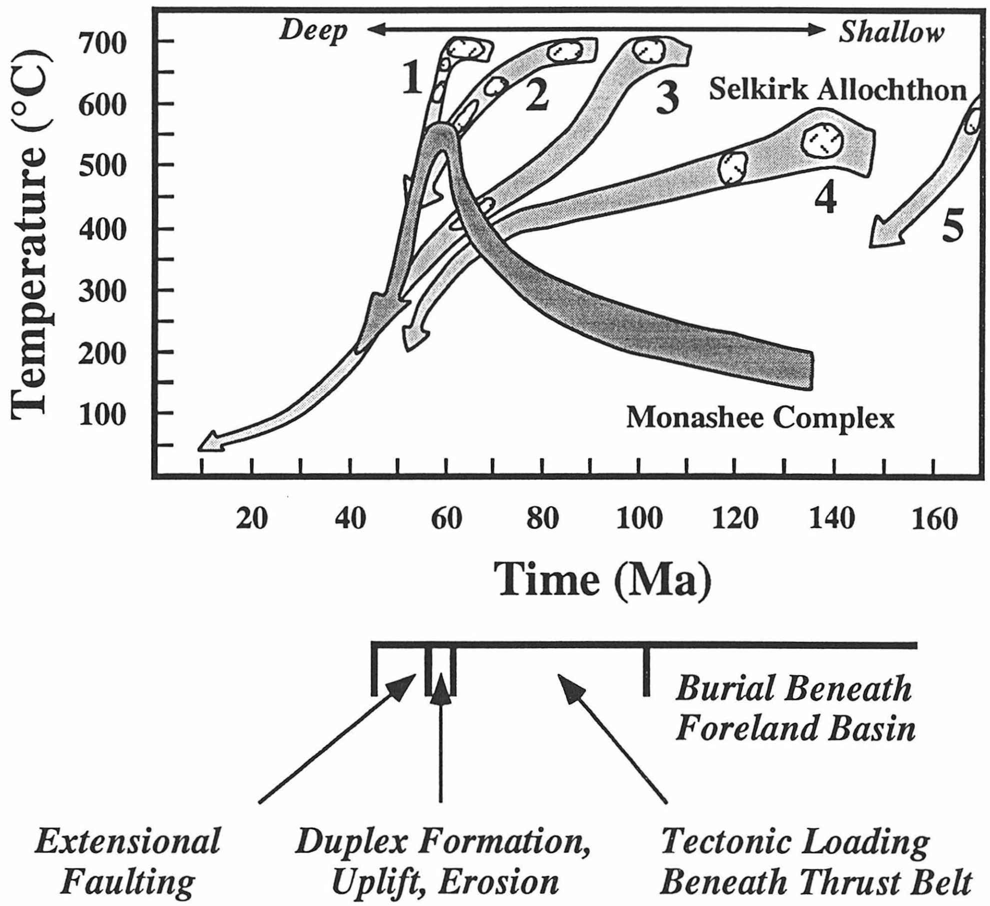

Frenchman Cap gneiss dome. Very limited access to the easternmost margin of the Thor-Odin dome was provided by short logging roads that meet the highway along the western shore of Arrow Lake.

Mineral separates from four samples of basement gneiss were analyzed for $^{18}O/^{16}O$; these include two orthogneisses and two paragneisses. Mineral separates in 15 metasedimentary rocks and leucogranites from 11 separate outcrops of the mantling gneiss unit were also analyzed for $^{18}O/^{16}O$. Three samples were collected from each of two outcrops in the deepest accessible part of the mantling gneiss at Frenchman Cap dome. At location MC-2, mineral separates were analyzed from samples that are less than a meter apart in a sequence consisting of 0.1-1.0 m-thick layers of calcic metapelite, metapelite, and calc-silicate. Metapelite, psammite, and quartzite samples were also collected from a similarly layered sequence (MC-3) about 1 km from MC-2.

Also included in this discussion are eight whole-rock and quartz $\delta^{18}O$ analyses of metapelite, leucogranite, and calc-silicate from the Selkirk allochthon west of the northern Monashee complex, and three samples from the Columbia River fault zone. Other isotopic results from the Selkirk allochthon and the Columbia River fault zone are discussed in detail below in Chapters 4 and 5.

3.4 Stable Isotope Results

3.4.1 Deepest Exposures of Thor-Odin Gneiss Dome (Blattner, 1971)

Blattner (1971) studied variations in $\delta^{18}O$ and mineral chemistry of early Proterozoic migmatites from the deepest exposed level of the Thor-Odin gneiss dome. These rocks are from the veined granodiorite gneiss described by Reesor and Moore (1971), a unit that underwent migmatization and was intruded by granite at about 1874-1934 Ma (Parkinson, 1991). A pegmatoid vein concordant with a hornblende-bearing granitoid biotite flasergneiss displays the following $\delta^{18}O$ values: quartz = +8.0, K-

TABLE 3.1. $^{18}O/^{16}O$ DATA ON ROCKS AND MINERALS FROM THE MONASHEE COMPLEX

Sample*	Rock Type	WR†	Qz†	Fs†	Gr†§	Am†	Bi†	Cc†#
MONASHEE COMPLEX								
Early Proterozoic Basement Gneiss								
3099**	Granodiorite gneiss					3.8		
3100**	Pegmatoid vein		8.0	6.5			2.5	
3117**	Granite		8.4	6.7		4.3	2.7	
3118**	Amphibolite					4.1		
?**††	Metaconglomerate			8.8				
GH-49	Metapelite gneiss		10.2	7.7				
GH-669	Granodiorite gneiss		9.7	8.1	7.1			
MC-4	Granite gneiss		9.3	2.7				
MC-5	Quartzite		12.0					
Late Proterozoic Mantling Gneiss								
> 200 m below Monashee decollement								
GH-76	Metapelite		14.0					
GH-556	Calc-silicate gneiss		16.4					
MC-2	Pelitic calc-silicate		14.7					
MC-2a	Metapelite		13.6	12.1				
MC-2b	Calc-silicate		13.4					
MC-3a	Psammite		12.2					
MC-3b	Quartzite		12.2					
MC-3c	Metapelite		14.7					
< 200 m below Monashee decollement								
GH-75	Migmatitic metapelite	10.7	11.0	9.0				
GH-552	Metapelite		10.6					
GH-553	Metapelite		11.6	9.6				
GH-555	Metapelite		11.3					
GH-841	Granodiorite gneiss		10.6	9.0				
GH-842	Leucogranite gneiss		11.0	8.4				
GH-843	Migmatitic leucogranite		11.1	9.1				
SELKIRK ALLOCHTHON§§								
GH-557	Metapelite		12.0					
GH-77	Metapelite	12.4	12.4					
GH-78	Metapelite	8.7						
GH-81	Metapelite	-1.0						
GH-79	Leucogranite	9.6						
GH-83	Biotite Schist	2.9						
GH-80	Calc-silicate	12.4						
GH-190	Metapelite	-1.7						
COLUMBIA RIVER FAULT								
GH-31	Marble							7.6##
GH-66	Granodiorite		10.8	4.5				
GH-74	Metapelite	7.1						

Note: Mineral separates were hand-picked under the microscope. Some quartz separates were treated with HF to remove impurities. Oxygen was liberated from quartz and feldspar by reaction with F_2 in Ni reaction vessels at 550 °C, converted to CO_2, and analyzed on a Finnegan MAT 252 mass spectrometer (Taylor and Epstein, 1962).

TABLE 3.1 (Continued)

Data are from sample localitites shown on Figure 3.1. See Chapter 4 for data from other portions of the Selkirk allochthon and Columbia River fault not shown on this map.

*Numbers refer to samples archived at the Division of Geological and Planetary Sciences, California Institute of Technology, Pasadena, California.

†The oxygen isotope data for whole rocks (WR), quartz (Qz), feldspar (Fs), almandine garnet (Gr), amphibole (Am), biotite (Bi), and calcite (Cc) are reported in the δ notation, where δ is the relative difference in parts per thousand in $^{18}O/^{16}O$ between the sample and a standard. The standard is V-SMOW (Vienna standard mean ocean water). NBS-28 has a $\delta^{18}O = +9.60$ on this scale. Replicate analyses of samples and the Caltech rose quartz working standard ($\delta^{18}O = +8.45$) have an analytical error of ± 0.2‰.

§The garnet oxygen isotope data were also acquired by a fluorination procedure, but one using the Caltech oxygen isotope laser extraction system, instead of externally heated Ni reaction vessels. Caltech rose quartz ($\delta^{18}O = +8.45 \pm 0.10$; N = 25) and Hualalai olivine ($\delta^{18}O = +5.37 \pm 0.10$; N = 42) laboratory standards were analyzed each operating day during collection of garnet $^{18}O/^{16}O$ data. Duplicate laser analyses of randomly chosen, hand picked, inclusion-free grains of crushed garnet (typically two to three 0.5-1.0 mg grains were analyzed in each run) display an analytical uncertainty of ≤ 0.3‰. Comparison of laser and conventional quartz analyses agreed to within ± 0.2 ‰.

#The calcite stable isotope data were acquired by reaction with H_3PO_4 (McCrea, 1950), and corrected using the fractionation factor of 1.01008 (Sharma and Clayton, 1965).

**These data are from Blattner (1971).

††Neither a sample number, nor an actual $\delta^{18}O$ value was given by Blattner (1971) for this metaconglomerate. This feldspar $\delta^{18}O$ value is based on the description given by Blattner (1971, p. 168): "However, in accordance with its metasedimentary origin, the plagioclase was found to be heavier by 2.2‰ $\delta^{18}O$ than the K-feldspar." K-feldspar (6.6‰) values are from data from the migmatites 100 m structurally below the metaconglomerate.

§§Data from the Selkirk allochthon are listed in structural order from lowest to highest.

##$\delta^{13}C = -0.1$

Figure 3.3 -- Plot showing whole-rock and mineral $\delta^{18}O$ values from the Monashee complex, the Selkirk allochthon, and the Columbia River detachment fault within the map area shown in Figure 3.1. Data are from this study and Blattner (1971). From left to right, sample groups are listed in order from deepest to shallowest crustal level. Complex structural relations in the Monashee complex prevent the listing of those particular samples in any structural and/or stratigraphic order. Samples from the Selkirk allochthon are listed according to increasing distance from the Monashee decollement. Note the 8‰ variation in quartz $\delta^{18}O$ in the basement gneiss and mantling gneiss > 200 m below the Monashee decollement, contrasting with uniform quartz $\delta^{18}O$ values of 11.0 ± 0.3 just beneath this thrust fault.

Figure 3.3 Monashee Complex Data

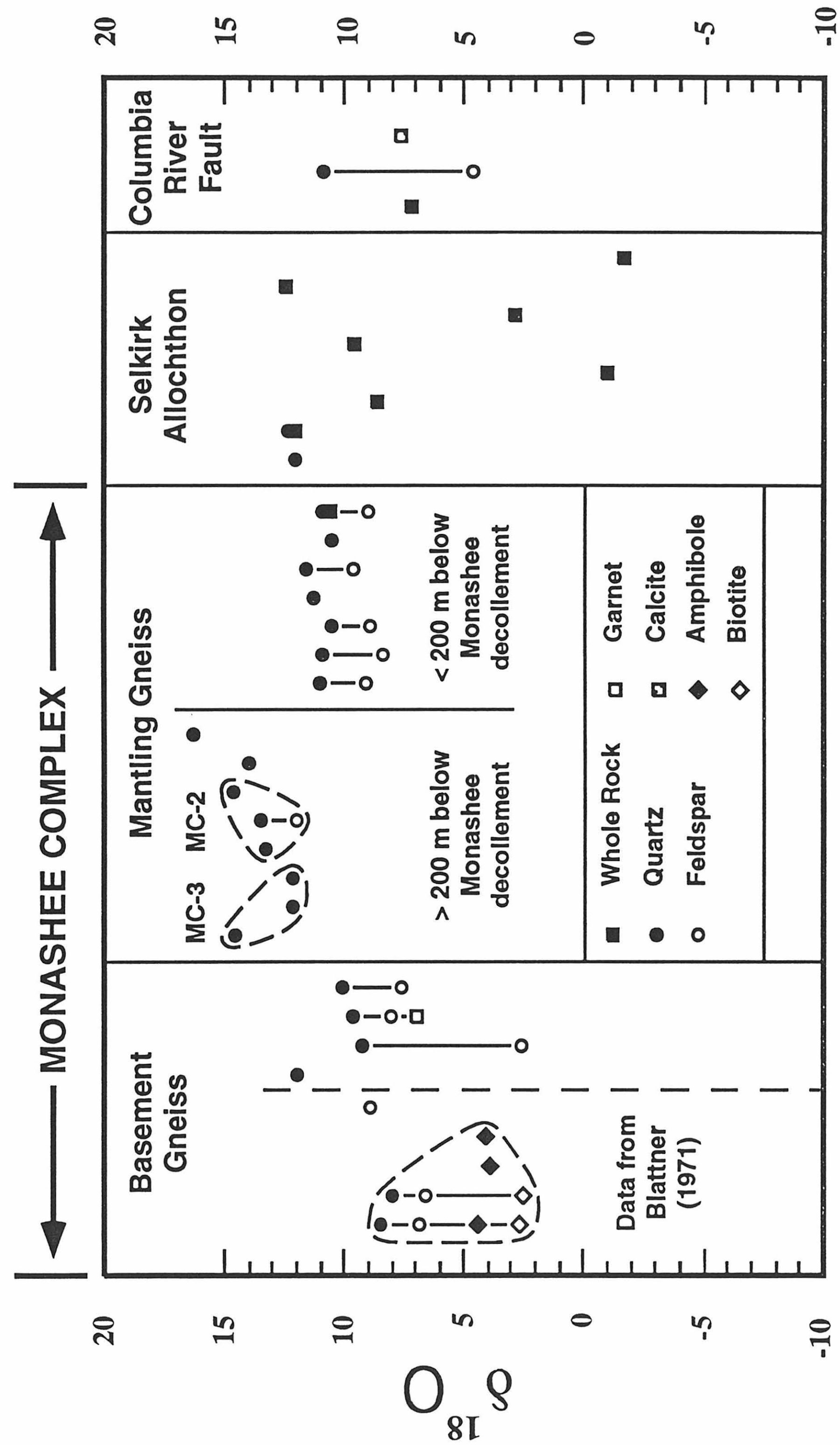

feldspar = +6.5, and biotite = +2.5 (Figure 3.3). These data, using the $^{18}O/^{16}O$ fractionations of Javoy (1977) and Clayton and Kieffer (1991), indicate apparent isotopic equilibrium at 500-600 °C. Selvages of mafic minerals are observed around the pegmatoid veins, suggesting that veins formed during partial melting of the flaser gneiss. Hornblende from the host flasergneiss has $\delta^{18}O$ = +3.8, compatible with equilibrium with minerals of the pegmatoid vein at 550 °C. Amphibolite inclusions occur as stringers in the flasergneiss, and hornblende from one of these inclusions has $\delta^{18}O$ = +4.1. Cross-cutting pegmatites, amphibolites, and flasergneiss display mineral $\delta^{18}O$ values that are also in apparent near-equilibrium with minerals in the other rocks (quartz = +8.4, K-feldspar = +6.7, biotite = +2.7, amphibole = +4.3).

These data from early Proterozoic migmatites indicate $^{18}O/^{16}O$ equilibrium on the outcrop scale, most probably during anatexis in the early Proterozoic. A metaconglomerate 100 m structurally above the migmatites has a feldspar $\delta^{18}O$ value 2.2‰ higher (~ +8.8) than the feldspars from the migmatites, indicating that homogenization did not extend that far. However, no information is provided by Blattner (1971) about the stratigraphic context of this metaconglomerate (it may belong to the mantling gneiss); thus, it is possible that deposition of the conglomerate could have happened subsequent to the anatexis of the orthogneiss and paragneiss. These relations indicate that either the effects of Proterozoic anatexis of basement core rocks were limited to the scale of an outcrop, or that the metaconglomerate was not even part of the system at the time of initial migmatization of the basement gneisses.

3.4.2 Samples Analyzed in this Study

If one excludes rocks immediately below the Monashee decollement, it is clear that throughout the Monashee Complex minerals in basement orthogneiss and paragneiss, and in the mantling gneiss are all very heterogeneous in ^{18}O (Figure 3.3). Early Paleozoic basement gneiss has quartz $\delta^{18}O$ = +8.0 to +12.0 (N = 6), feldspar $\delta^{18}O$ = +2.7 to +8.1 (N = 6), and garnet $\delta^{18}O$ = +7.1. Metasediments from the mantling gneiss > 200 m below the Monashee decollement are heterogeneous in $^{18}O/^{16}O$ with quartz $\delta^{18}O$ = +12.2 to +16.4 (N = 7). Nesbitt and Muehlenbachs (1995) also report whole rock $^{18}O/^{16}O$ heterogeneity of at least 5‰ for these rocks. The very large 8.4‰ range in quartz $\delta^{18}O$ suggests relatively low water/rock ratios during prograde metamorphism; otherwise, some degree of isotopic homogenization would be expected. Four $\Delta_{Q\text{-}F}$ values of ~ 1.5‰ indicate $^{18}O/^{16}O$ equilibrium at T ~ 600 °C, but in two other samples the $\Delta_{Q\text{-}F}$ values of 2.5‰ and 6.6‰ clearly indicate disequilibrium (Figure 3.4); this is almost certainly the result of meteoric-hydrothermal alteration (see Criss and Taylor, 1986), an event related to Eocene extensional faulting (see Magaritz and Taylor, 1986; Nesbitt and Muehlenbachs, 1995; and Chapter 5).

The mantling gneiss is also very heterogeneous in $^{18}O/^{16}O$ on the outcrop scale. At MC-2, metapelite, pelitic calc-silicate, and calc-silicate samples collected from the same outcrop less than 1 m apart have quartz $\delta^{18}O$ values of +13.6, +14.7, and +13.4 respectively (see Figure 3.3). Feldspar from the metapelite at this site has $\delta^{18}O$ = +12.1. At outcrop MC-3, $^{18}O/^{16}O$ heterogeneity is also observed between 0.1-1.0 m-thick layers of psammite, quartzite, and metapelite (quartz $\delta^{18}O$ = +12.2, +12.2, and +14.7, respectively). The other two outcrops from the mantling gneiss may be from the imbricate thrust zone of the Monashee decollement; these rocks have quartz $\delta^{18}O$ = +16.4 and +14.0, indicating that they may have been impermeable and therefore dry during shearing along the Monashee decollement (see discussion below in Chapter 4 and Holk and Taylor, in press).

In striking contrast to the rocks described above, rocks < 200 m below the Monashee decollement are remarkably uniform in $^{18}O/^{16}O$ (quartz $\delta^{18}O$ = +11.0 ± 0.3‰, N = 7; feldspar $\delta^{18}O$ = +9.0 ± 0.4‰, N = 5; see Figures 3.3 and 3.4). Isotopic

Figure 3.4 -- Plot of $\delta^{18}O$ quartz vs. coexisting $\delta^{18}O$ feldspar for the Monashee complex. Data are from this study and Blattner (1971). Dashed lines at $\Delta_{Q\text{-}F} = 1.0‰$ and $\Delta_{Q\text{-}F} = 2.0‰$ represent the generally accepted constraining boundaries for $^{18}O/^{16}O$ equilibrium at near magmatic temperatures. Feldspar ^{18}O depletions down to $\delta^{18}O < +5$ in two samples are the result of late-stage meteoric-hydrothermal exchange during extension along high-angle normal faults and detachment faults (*e.g.*, Columbia River fault). Mantling gneisses < 200 m beneath the Monashee decollement have uniform quartz $\delta^{18}O = 11.0 \pm 0.3‰$ and feldspar $\delta^{18}O = 9.2 \pm 0.4‰$. Basement gneiss and the remainder of the mantling gneiss are very heterogeneous in ^{18}O.

Figure 3.2 Quartz vs. Feldspar

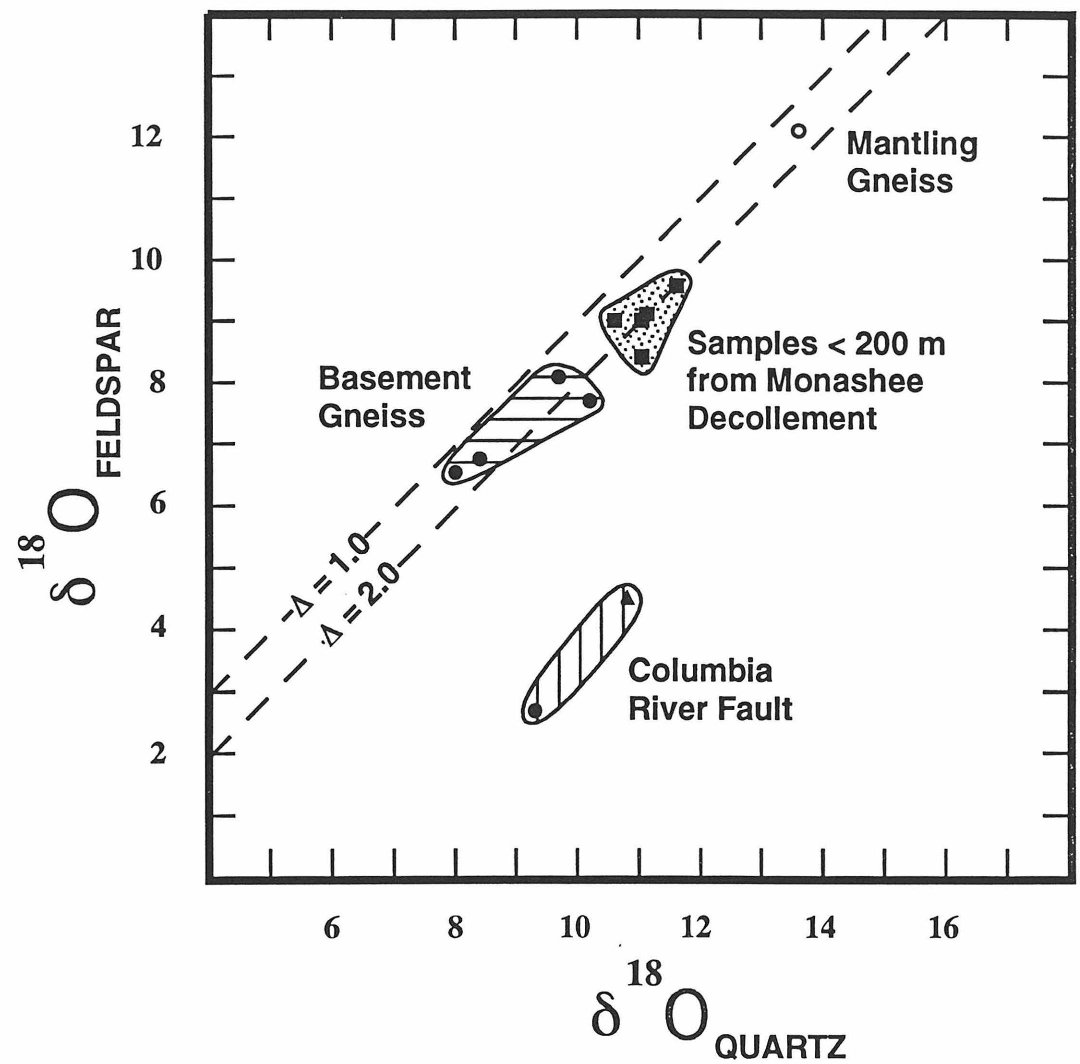

equilibrium at magmatic temperatures is indicated by $\Delta_{Q\text{-}F}$ = 1.6-2.6‰. Water in equilibrium with these quartz separates at 700 °C has $\delta^{18}O$ ~ +10.5 (Clayton et al., 1972). It is important to note in this connection that Nyman et al. (1995) showed that these rocks underwent as much as 50 vol. % melting during thrusting along the Monashee decollement. An even more compelling correlation between anatexis and $^{18}O/^{16}O$ homogeneity is observed in the immediately overlying Selkirk allochthon throughout the southern Thor-Odin complex (Holk and Taylor, in press; Chapter 4).

As will be described in detail below in Chapter 5, the middle crustal rocks of the Selkirk allochthon locally show evidence of meteoric-hydrothermal alteration, and this was in many places preceded by the $^{18}O/^{16}O$ homogenization event described in detail in Chapter 4. Whole-rock $\delta^{18}O$ analyses of these mid-crustal rocks were found to range from –1.7 to +12.4. The low-^{18}O samples are located either near detachment faults (Eagle River fault) or the steeply-dipping Eocene normal faults (or their projected locations, see Figure 3.1), indicating that meteoric-hydrothermal activity in these zones was related to this extensional faulting (see Chapter 5 for more discussion of these phenomena in the area delineated in Figure 3.1). Two samples from the immediate hanging wall of the Monashee decollement along the Trans-Canada highway have quartz $\delta^{18}O$ = +12.2 ±0.2‰; these values are within the range of homogenized quartz $\delta^{18}O$ values observed at an analogous structural position in the southern Thor-Odin complex (Chapter 4). This homogeneity is interpreted to be the product of multiple stages of $^{18}O/^{16}O$ exchange involving H_2O, leucogranite melt, and unmelted rock during anatexis of the Selkirk Allochthon (see Chapter 4 and Holk and Taylor, in press).

The three samples from the Columbia River fault zone indicate $^{18}O/^{16}O$ disequilibrium due to exchange with low-^{18}O meteoric water during detachment faulting (*e.g.*, see Figure 3.4). Metapelite from the immediate footwall has whole rock $\delta^{18}O$ = +7.1. Marble from the hanging wall has $\delta^{18}O$ = +7.6 and $\delta^{18}O$ = –0.1. A granodiorite from the fault zone has quartz and feldspar $\delta^{18}O$ values of +10.8 and +4.5, respectively. Each of these rocks has been strongly depleted in ^{18}O by meteoric-hydrothermal activity (see Chapter 5 for more details). Meteoric-hydrothermal activity that affected the two low-^{18}O samples from the basement gneiss also may be related to the Columbia River fault, or perhaps to unmapped steeply-dipping Eocene normal faults.

3.5 Discussion

The heterogeneous $^{18}O/^{16}O$ data from the Monashee complex indicate relatively low water/rock ratios for this deep section of the southern Omineca belt at the time of prograde metamorphism. However, there must have been enough H_2O in the system to drive anatexis and $^{18}O/^{16}O$ homogenization in the immediate footwall of the Monashee decollement. The questions we need to pose about this system are: (1) How and why did the zone just beneath the Monashee decollement homogenize quartz $\delta^{18}O$ values at +11.0? (2) Was there enough H_2O in the system to account for the up to 50 vol % partial melting of pelites near the Monashee decollement, as proposed by Nyman et al. (1995)? (3) Why are deeper parts of the section heterogeneous in $^{18}O/^{16}O$ while the migmatitic rocks just beneath the decollement are so uniform?

The most likely source of aqueous fluids in this system is the dehydration of hydrous minerals as the lower-plate rocks heat up. Metamorphic dehydration fronts (*e.g.*, muscovite-out, chlorite-out) move downward with time in this thermal environment (England and Thompson, 1984; Peacock, 1987). Aqueous fluids released by these dehydration reactions will move upward to shallower depths (*e.g.*, Walther and Orville, 1982); in this case this means up-temperature toward the ductile Monashee decollement. In general, rocks undergoing ductile flow are known to be relatively impermeable to metamorphic pore fluids (Rye et al., 1976; Taylor and Forester, 1979). Thus the impermeable ductile layer along the decollement will focus fluid flow in an up-dip direction along the sole of the shear zone, causing water/rock ratios to be higher in this zone relative to the underlying rocks. It is possible that aqueous fluids could be trapped beneath ductile shear zones, as is proposed for the western margin of the Coast Ranges batholith in southeastern Alaska during the Eocene (Goldfarb et al., 1991). Goldfarb et al. (1991) document rapid dewatering of subducted metamorphic rocks during thermal inversion in a magmatic arc setting; these fluids are thought to be responsible for extensive gold mineralization along the 200 km length of the Juneau gold belt.

Eventually, during the heating process, the wet melting temperature of pelite (750 °C at 8 kbar; Vielzeuf and Hollaway, 1988) and arkosic grit will be reached. The rocks just beneath the Monashee decollement will be the first to undergo migmatization and anatexis, inasmuch as this is the hottest part of the Monashee complex at the time of overthrusting. The introduction of a melt phase into the system drastically changes the behavior of aqueous fluids in the vicinity of these melts. Water will partition into the melt phase if it is H_2O-undersaturated (Brown, 1994; Holtz and Johannes, 1994), resulting in a drying out of the system and providing a sink whereby devolatilized fluids from below can be locally trapped, thus maintaining low water/rock ratios for the system as a whole. These pockets of melt along the sole of the Monashee decollement will enhance its function as an impermeable barrier that inhibits the transport of aqueous fluids from the basement zone across and into the overlying Selkirk allochthon. However, focused fluid flow along this boundary will also be inhibited as H_2O is absorbed by the leucogranite melts.

Most of the rocks that comprise the Monashee complex are early Proterozoic basement gneisses that experienced a previous cycle of metamorphism and migmatization during the Proterozoic (Armstrong et al., 1991; Parkinson, 1991). Blattner's (1971) data demonstrate $^{18}O/^{16}O$ homogeneity on at most an outcrop scale during that event. This earlier dehydration event may have exhausted the ability of these rocks to contribute H_2O to the system during subsequent episodes of metamorphism. Thus, the only component of the Monashee complex able to contribute H_2O to the system during the Cretaceous to early Tertiary episodes would be the mantling gneisses. This situation may be analogous to that observed in the Alps, where the only rocks contributing H_2O to the Alpine metamorphic-hydrothermal system are those deposited after the Hercynian, because the older rocks had already been devolatilized during this late Paleozoic event (Hoernes and Friedrichsen, 1980).

Lithologic proportions of the 2.4 km-thick mantling gneiss sequence are (Table 3.2): 17% pelite, 8% arkosic grit, 40% quartzite, and 35% amphibolite (Scammell and Brown, 1990). A rough material-balance calculation using these lithologic proportions indicates a bulk $\delta^{18}O = +11.2$, a value just a little bit higher than the whole-rock $\delta^{18}O$ of rocks just beneath the Monashee decollement. This indicates that the migmatites were probably homogenized as basically a closed system to the average bulk $\delta^{18}O$ of the mantling gneiss reservoir during anatexis. Only 25% of this section, namely the pelites and arkosic grits, is probably available for anatexis at the peak temperatures inferred for this complex. Anatexis of this section will be further inhibited because the pelites are the only lithologies in the mantling gneiss sequence able to contribute H_2O to the system to drive melting.

The amount of water introduced into the system during the formation of the thermal inversion can be estimated by calculating the amount of H_2O released by the dehydration of metapelite during the heating of the lower plate. The major sources of H_2O in a system of this type are dehydration of muscovite and chlorite. A metapelite containing 35 vol. % muscovite and 20 vol. % chlorite contains about 4.5 wt. % H_2O. Fluids released during dehydration of these minerals are enough to drive ~ 40 vol. % melting of these pelites (assuming melt containing 10 wt. % H_2O). This estimate is nearly consistent with that of Nyman et al. (1995) for migmatites along the sole of the Monashee decollement. The remaining 10% melting can be driven by the introduction of aqueous fluid from below, as described in the preceding discussion. Journeay (1988) reports a minimum temperature of

TABLE 3.2. BULK $\delta^{18}O$ CALCULATION OF THE MANTLING GNEISS

Lithology	$\delta^{18}O$	Percent of Section
Arkosic Grit	+12	8
Pelite	+16	17
Quartzite	+11	40
Amphibolite	+9	35
Bulk $\delta^{18}O$		+11.2

Note: Lithologic proportions are from Scammell and Brown (1990)

The $\delta^{18}O$ value used for arkosic grit in the material balance calculation is based on $^{18}O/^{16}O$ results of quartz ($\delta^{18}O$ +10.5) and feldspar ($\delta^{18}O$ = +13.0) from low-grade arkosic grits of the Windermere Supergroup in the Purcell Mountains.

The model pelite $\delta^{18}O$ value is taken from the approximate average whole-rock $\delta^{18}O$ (+15.8) of argillites from the Belt (Purcell) Supergroup, Montana (Eslinger and Savin, 1973).

Figure 3.5 -- Cartoon showing plausible relationships required along the Monashee decollement that are required to explain the $^{18}O/^{16}O$ and petrologic data. This model involves the formation of a thermal inversion during late Cretaceous-Paleocene overthrusting of the Selkirk allochthon, dehydration of the Monashee terrane, and anatexis just below the Monashee decollement. The inset is a depth vs. temperature diagram showing plausible steady-state geotherms for the base (curve 1) and top (curve 2) of the Monashee thrust ramp. These geotherms take into account the accumulation of radiogenic heat-producing elements during overthrusting (Huerta et al., 1996) along with heat produced during frictional sliding (Molnar and England, 1990) during movements along the Monashee decollement. The frictional heating component was calculated assuming a shear stress of 50 MPa, a fault dip of 15°, a slip rate of 20 km/my, and thermal conductivity of 2.5 W/m^2K. The wet solidus for granite (Wyllie, 1977) also is shown (curve a). Note that both the top and base of the Monashee thrust ramp are at temperatures above the granite solidus, allowing anatexis at both of these levels. Low water/rock ratios in most of the Monashee complex are indicated by heterogeneous quartz $\delta^{18}O$ values. $^{18}O/^{16}O$ homogenization near the Monashee decollement probably happened during partial melting as these rocks reached the melting temperature of wet pelite and arkosic grit. The ingress of fluids from below and continued heating from above drove further partial melting of the uppermost part of the Monashee complex. These leucogranite melts would have acted as sinks for aqueous fluids. Prior to melting, aqueous fluid flow was probably focused along the sole of the ductile Monashee decollement. These melts formed an extremely weak zone in the crust that accommodated large and rapid displacements along the Monashee thrust ramp, providing an effective mechanism for quick, nearly isothermal uplift of the Selkirk allochthon.

Figure 3.5 Model for Fluid Flow – Monashee Complex

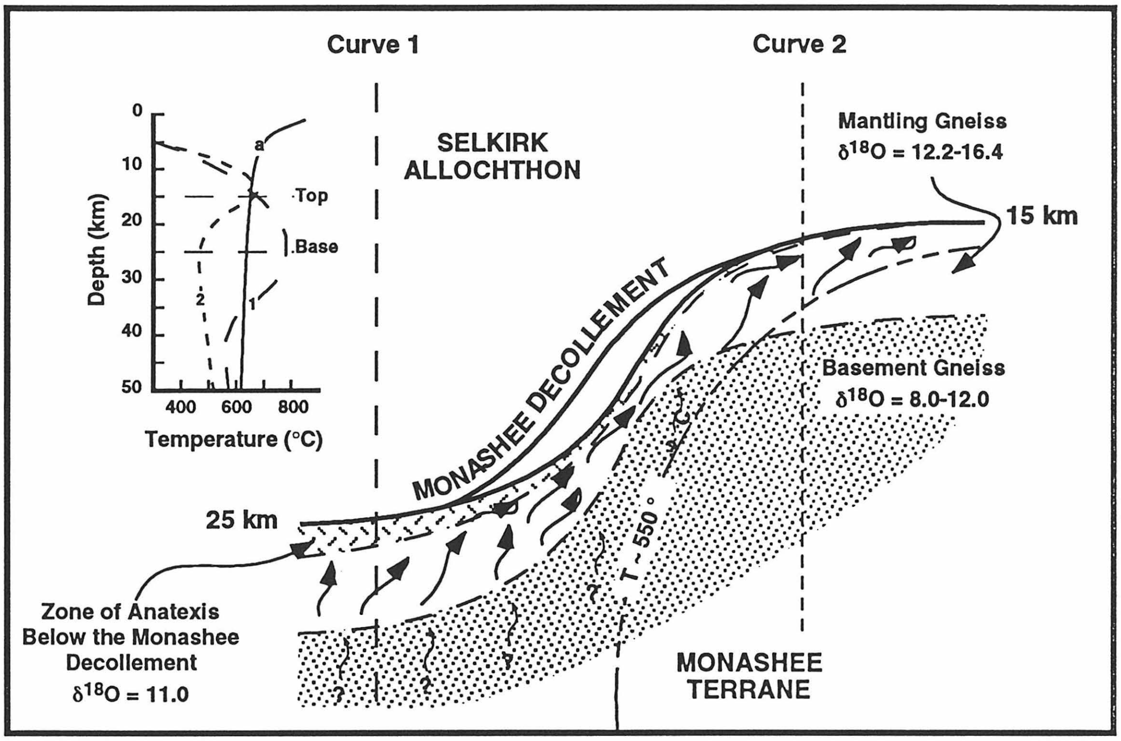

~ 450 °C, a temperature well within the stablility of chlorite, for the deepest parts of this inverted sequence. However, the extent to which the mantling gneiss sequence escaped chlorite dehydration during the Jurassic Barrovian event is uncertain.

Wickham and Taylor (1987) observed whole-rock $^{18}O/^{16}O$ heterogeneity ($\delta^{18}O$ = +6 to +22) at deep levels of the Hercynian Pyrenees. They concluded that this deep zone was infiltrated by much smaller amounts of metamorphic pore fluid than at shallower mid-crustal levels. The overlying zone had been subjected to large-scale infiltration of marine pore waters (Wickham and Taylor, 1985), and it was proposed that interconnected porosity was greatly reduced at these great depths. Extensive partial melting at the base of the overlying zone may have provided a ductile layer that was impermeable to downward fluid penetration. Similar stable isotope heterogeneities are also observed at deep levels of other orogenic belts (Wickham and Taylor, 1987; Valley and O'Neil, 1984).

The primary mode of $^{18}O/^{16}O$ exchange and fluid transport in this kind of high-grade metamorphic terrane may be the movement of leucogranite melts as they become buoyant and intrude upward into the Selkirk allochthon after breaking through the Monashee decollement. As will be discussed in Chapter 4, some addition of water to the Selkirk Allochthon is probably needed to account for the amount of leucogranite observed in that section. Perhaps this metamorphic H_2O has its ultimate source in the deep-seated Monashee terrane.

This reconnaissance regional-scale $^{18}O/^{16}O$ study of the Monashee terrane provides neither a sufficiently detailed sample suite nor sufficiently confident structural controls on the sample suite to conclusively prove the model proposed in this chapter. However, an excellent location for the further testing these ideas would be an area in the northernmost Monashee complex studied by Scammell and Brown (1990).

Chapter 4. The Selkirk Allochthon at the Southern Thor-Odin Complex: Anatexis in the Middle Crustal Zone

4.1 Manuscript in Press in *Geology*

$^{18}O/^{16}O$ homogenization of the middle crust during anatexis: The Thor-Odin metamorphic core complex, British Columbia

Gregory J. Holk* Division of Geological and Planetary Sciences, Caltech 170-25, Pasadena, California 91125

Hugh P. Taylor, Jr. Division of Geological and Planetary Sciences, Caltech 170-25, Pasadena, California 91125

*Present address: Geological Survey of Canada, 601 Booth Street, Ottawa, Ontario, Canada K1A 0E8

Data Repository item #### contains additional material related to this article.

ABSTRACT

The occurrence of isotopically uniform quartz ($\delta^{18}O = 12.5 \pm 0.5‰$) and feldspar ($10.9 \pm 0.7‰$) throughout different rock types indicates that much of a 6-km-thick section of the mid-crustal Selkirk allochthon underwent internally buffered $^{18}O/^{16}O$ homogenization during Paleocene melting and decompression as it moved up the Monashee thrust ramp. Areas of uniform $\delta^{18}O$ are those with the most leucogranite or those subjected to severe anatexis. Only locally, in the most impermeable (or refractory) zones did ^{18}O exchange among the rocks, leucogranite melts, and aqueous fluids fail to go to completion (*i. e.*, in the deepest parts of the section, in a marble-rich zone, around some thick amphibolites, and in most garnets). Evidence for $^{18}O/^{16}O$ heterogeneity in the protoliths of these rocks is observed in stratigraphically correlative lower-grade units elsewhere in British Columbia, as well as in garnets that coexist with isotopically homogeneous quartz. In our model, $^{18}O/^{16}O$ homogenization accompanied muscovite dehydration and partial melting of pelites with only minor influx of external H_2O, followed by release of magmatic H_2O from these melts (triggering further melting of adjacent feldspathic assemblages) as they were uplifted 20 km during thrusting just prior to onset of detachment faulting. Locally, low $\delta^{18}O$ in feldspar (down to –3.8) and profound quartz-feldspar $^{18}O/^{16}O$ disequilibrium were imprinted at shallow levels during meteoric-hydrothermal alteration associated with Eocene detachment faulting.

INTRODUCTION

Metamorphic core complexes represent ductilely deformed middle crust uplifted and exposed in an extensional setting (Armstrong, 1982). This is commonly associated with anatexis in crust thickened during orogenesis (Coney and Harms, 1984). Processes involving H_2O are known to play a prominent role in the development of core complexes at virtually all structural levels (Reynolds and Lister, 1987), and thus stable isotope studies are essential in understanding these features (Nesbitt and Muehlenbachs, 1989; Peters and Wickham, 1995).

Here we evaluate ^{18}O exchange, hydrothermal metamorphism, and partial melting in the Thor-Odin complex, British Columbia. This is an ideal location for understanding the role of H_2O in the evolution of core complexes because of (1) excellent exposures of a well-mapped and dated mid-crustal section (Carr, 1991, 1992), and (2) at this high latitude in the late Mesozoic and early Tertiary there were clear-cut isotopic contrasts between local meteoric ground waters and metamorphic or magmatic H_2O (Magaritz and Taylor, 1986; Nesbitt and Muehlenbachs, 1989).

GEOLOGIC SETTING AND SAMPLE LOCALITIES

The Thor-Odin complex is the product of late Mesozoic to Paleocene compression followed by Eocene extension (Carr, 1991). It consists of three fault-bounded zones (Figure 1) that are typical of core complexes in the southern Omineca belt (Parrish et al., 1988), namely Precambrian basement, mid-crustal amphibolite facies rocks, and a brittle upper zone.

The Monashee decollement is a northeast-vergent ductile shear zone that separates the mid-crustal zone of the Selkirk allochthon from basement. LITHOPROBE seismic profiles establish this shear zone as a west-dipping ramp with 20 km of vertical relief (Cook et al., 1992). Peak temperature and pressure conditions during Paleocene thrusting were > 750 $^{\circ}C$ and > 6 kbar (Carr, 1995; Nyman et al., 1995). Mylonitic and brittle deformation along the Columbia River and Beavan detachment faults completed the exhumation of the complex (Parrish et al., 1988).

In the allochthon, leucogranite sheets are synkinematic with Paleocene metamorphism; their outcrop abundance increases from 30% just above the decollement to 100% in the 3-km-thick, sill-like South Fosthall pluton (Carr, 1991). U-Pb zircon ages (55-62 Ma) on these granites bracket the latest deformation of the Monashee decollement and earliest stages of detachment faulting (Carr, 1992; 1995). Carr (1992) cited Wyllie (1977) and Whitney (1988) in proposing an anatectic origin for the leucogranites during decompression associated with tectonic shortening as the allochthon moved up the thrust ramp. In this paper we integrate these models with our $^{18}O/^{16}O$ data.

Traverse 1 is a suite of samples collected across the imbricate thrust zone (Figure 1) and into an overlying amphibolite-rich zone that is correlative with a Proterozoic rift sequence (Carr, 1991). The amphibolite-rich zone is lithologically heterogeneous, consisting of 0.1–40-m-thick layers of metapelite, calc-silicate, quartzite, marble, and amphibolite intruded by 0.2– 30-m-thick leucogranite sheets. Traverse 2 crosses an equally heterogeneous, but more marble-rich zone comprised of thin layers (< 1 m) of all of the above lithologies except amphibolite; these are intercalated with thick (up to 50 m) marble units (Cambrian Empress marble). Traverse 3 passes through the lower part of a leucogranite-rich zone (Figure 1); here, sequences of lower Paleozoic metapelite, amphibolite, and calc-silicate occur as discrete layers within the dominant leucogranite. Several additional samples were collected higher in the leucogranite-rich zone and throughout the basement.

OXYGEN ISOTOPE DATA

Throughout the allochthon, but particularly within the uppermost 4-km-thick leucogranite-rich zone, minerals in the metasediments and leucogranites are characteristically uniform in ^{18}O (Figure 2) and in approximate isotopic equilibrium at high temperatures. For example, in the leucogranite-rich zone and in most of the amphibolite-rich zone, quartz $\delta^{18}O = 12.5 \pm 0.5‰$ (1σ std. dev.) for metapelite (N = 11), $12.2 \pm 0.1‰$ for quartzite (N = 2), and $12.3 \pm 0.4‰$ (N = 24) for the concordant leucogranites. Within the leucogranite-rich zone, no exceptions have been found to this remarkable $^{18}O/^{16}O$ homogeneity; this includes even the garnets (see below) and a 1-m-thick marble unit, which has calcite $\delta^{18}O = 12.4$. Ignoring a few low-^{18}O feldspars that are the result of a late-stage meteoric-hydrothermal event associated with detachment faulting (Holk and Taylor, 1994b), the quartz-feldspar $^{18}O/^{16}O$ fractionations (*i.e.*, $\Delta_{Q\text{-}F}$ values) from all igneous and metamorphic lithologies within this zone are typical of granitic plutons throughout the world ($\Delta_{Q\text{-}F} = 1.5 \pm 0.6‰$, N = 28). Using the calibrations of Clayton et al. (1972) and Clayton and Kieffer (1991), the above data imply apparent equilibrium temperatures of 550-650 °C and a coexisting aqueous fluid with $\delta^{18}O \approx +11.0$, which is at least 20‰ higher than the coeval meteoric surface water associated with detachment faulting (Magaritz and Taylor, 1986).

Amphibolite quartz is isotopically variable, but trends are systematic (Figure 3); relatively low $\delta^{18}O$ values (9.7) occur in two thick layers (10-40 m) of undeformed amphibolite within a narrow interval in the upper part of the amphibolite-rich zone. Elsewhere in this zone, homogenized quartz $\delta^{18}O$ values of $12.8 \pm 0.6‰$ (N = 4) are observed in the numerous thin (< 1m) amphibolite layers; in contrast to the thick amphibolites, these typically contain abundant quartzo-feldspathic veins or melt segregations. Quartz in metapelitic paragneiss directly adjacent to the thick amphibolites is 0.5-1.5‰ lower in ^{18}O than the characteristic homogenized quartz found in all lithologies throughout the rest of the 900-m-thick amphibolite-rich zone (Figure 2).

Quartz $\delta^{18}O$ values in the marble-rich zone (Figure 2) are higher and more variable than in any other part of the allochthon: 13.9-16.2 (N = 8) for metapelite, 13.6-16.2 (N = 3) for quartzite, 12.4-15.9 (N = 3) for calc-silicate, and 14.3-18.8 (N = 5) for leucogranite. These relict high $\delta^{18}O$ values are readily attributable to exchange with the intercalated ^{18}O-rich marble layers (calcite $\delta^{18}O$ = 15.9-22.0, N = 9), whose protoliths probably had $\delta^{18}O$ = 20-28 (Veizer and Hoefs, 1976). This lack of ^{18}O homogenization was not unexpected, because ductile, pure marble layers such as these are typically impermeable to metamorphic pore waters (*e.g.*, Rye et al., 1976).

The Δ_{Q-F} values in the imbricate thrust zone (Figure 2) display an enormous range (1.0‰ to 14.0‰), indicating that a meteoric-hydrothermal event affected these highly fractured rocks; this event is probably correlative with analogous phenomena observed nearby in the vicinity of detachment faults. Concordant leucogranite sheets are totally absent in the imbricate thrust zone, and quartz $\delta^{18}O$ values of metapelite, quartzite, gneiss, and calc-silicate display a wide range, 10.2-14.6 (N = 7), 11.9-15.0 (N = 7), 11.0-13.4 (N = 4), and 16.3, respectively. Although some of these lower $\delta^{18}O$ values can be attributed to the late-stage meteoric-hydrothermal activity, all quartz $\delta^{18}O$ values significantly higher than 12.3 must represent relict metasedimentary values. The only leucogranitic materials in the imbricate thrust zone are rare, late-stage dikes that have undergone meteoric-hydrothermal ^{18}O-depletion (with feldspar $\delta^{18}O$ as low as –3.8); these post-kinematic leucogranite magmas must have been more ^{18}O-rich than the typical concordant leucogranites in the allochthon, because they retain quartz $\delta^{18}O$ values as high as 13.2-14.4 (N = 3).

Basement rocks beneath the Monashee decollement contain virtually no early Tertiary leucogranite (Carr, 1992), and as in the zone of imbricate thrusting, quartz $\delta^{18}O$ values (Figure 2) are highly variable (8.0-16.4, Blattner, 1971; this study). However, the above statements do not apply to the rocks within 200 m of the decollement. Nyman et al. (1995) showed that these underwent as much as 50 vol. % melting, and our data show that they contain isotopically homogeneous quartz ($\delta^{18}O = 11.0 \pm 0.3‰$, N = 7); note that these homogeneous $\delta^{18}O$ values are 1.0-1.5‰ lower than those from homogeneous zones in the overlying allochthon (Figure 2).

In contrast to quartz, coexisting almandine garnet is isotopically variable in all parts of the allochthon except the leucogranite-rich zone, where garnet $\delta^{18}O = 9.8 \pm 0.5$ (N = 8) in all lithologies (Figure 3). In samples from homogeneous parts of the amphibolite-rich zone, garnet $\delta^{18}O = 9.5 \pm 1.0‰$ (N = 13), whereas coexisting quartz is more uniform at $\delta^{18}O = 12.6 \pm 0.5‰$. Garnets from metapelites in the marble-rich zone have $\delta^{18}O$ = 12.4-13.5 (N = 4). Quartz-garnet fractionations ($\Delta_{Q\text{-}G}$ values) are relatively constant at $2.7 \pm 0.4‰$ (N = 7) in all lithologies of the leucogranite-rich zone. Using the calibration of Javoy (1977), these values indicate equilibrium at $700 \pm 100\ ^{\circ}C$, compatible with the thermochronologic estimates of Carr (1995). Inasmuch as all these rocks were metamorphosed at similar grade, the variable $\Delta_{Q\text{-}G}$ values in the amphibolite-rich (1.8-4.1‰) and marble-rich zones (1.4-2.7‰) clearly indicate isotopic disequilibrium.

DISCUSSION

Oxygen diffusion in garnet is slow (Fortier and Gilletti, 1989), and it is well known that during prograde metamorphism, garnet oxygen is often effectively isolated from fluid exchange processes that affect other silicate minerals (*e.g.*, Chamberlain and Conrad, 1991). Thus, garnet can record information about pre-existing whole-rock $^{18}O/^{16}O$ heterogeneity, or about $\delta^{18}O$ changes in the local environment around the growing garnet crystals. Also, because garnets can preserve evidence of an earlier, low-temperature stage, $\Delta_{Q\text{-}G}$ values can be larger than those set at peak metamorphic grade. Small $\Delta_{Q\text{-}G}$ values (1.4-2.1‰) in two metapelites from the high-^{18}O marble-rich zone (Figure 3) thus imply that garnet growth occurred before these rocks were partially homogenized and depleted in ^{18}O. In contrast, large $\Delta_{Q\text{-}G}$ values (3.8-4.0‰) in metapelite and leucogranite at the contact of a thick amphibolite layer are more equivocal. It is likely that these rocks underwent incipient homogenization and ^{18}O enrichment after the garnets acquired the low $\delta^{18}O$ signature of the adjacent mafic-volcanic(?) protolith; however, the $\Delta_{Q\text{-}G}$ values could also indicate a lower-temperature prehistory. In the garnets of the leucogranite-rich zone, all such ^{18}O evidence of prograde metamorphic or lithologic prehistory has been obliterated.

The profound $^{18}O/^{16}O$ homogeneity of the Thor-Odin mid-crustal layer could be due to (1) initial protolith homogeneity, (2) influx and exchange with external oxygen-bearing fluids, and/or (3) internal closed-system homogenization during anatexis. Mechanism (1) clearly cannot represent a general explanation, because of the known $^{18}O/^{16}O$ heterogeneity observed in similar metasedimentary sections elsewhere on Earth, particularly noting the extreme $\delta^{18}O$ values exhibited by protoliths of amphibolite and marble. In the leucogranite-rich and amphibolite-rich zones, quartz $\delta^{18}O$ values in calcsilicates and thin amphibolites are almost as homogeneous as those in the intercalated leucogranites and metapelites. Note that mechanism (1) also requires that the Proterozoic and Paleozoic sections by coincidence both start out with exactly the same, uniform $\delta^{18}O$ values, and this can be refuted because quartz $\delta^{18}O$ = 12.7-15.6 (N = 14) in analogous (but lower grade) Late Proterozoic metapelites 180 km to the north (Bowman and Ghent, 1986; O'Neil and Ghent, 1975); those rocks are stratigraphically correlative with metapelites from the Thor-Odin amphibolite-rich zone (where quartz $\delta^{18}O = 12.5 \pm 0.5$, N = 6). Our own data set provides evidence of original $^{18}O/^{16}O$ heterogeneity. Zones that were a priori expected to be relatively impermeable or refractory (the marble-rich zone, the thick amphibolites, and the garnets) are in fact the only parts of the allochthon that display marked $^{18}O/^{16}O$ heterogeneity. Also, the $\delta^{18}O$ heterogeneity in quartz from the deepest and most deformed allochthonous assemblages (*i.e.*, imbricate thrust zone) is similar to that displayed by garnets coexisting with homogeneous quartz higher in the section; this implies an original whole-rock $\delta^{18}O$ variation of at least 4.5‰.

We can also rule out mechanism (2), unless the hypothesized external H_2O by coincidence already had a $\delta^{18}O$ in equilibrium with the bulk average material of the allochthon. Excluding the marble-rich zone, a rough material-balance calculation utilizing $^{18}O/^{16}O$ data on analogous and/or correlative lower-grade protoliths shows that there cannot have been any more than a 0.5-1.0‰ lowering in the bulk $\delta^{18}O$ of the metasedimentary section (by dehydration?). This contrasts with other localities where it has been shown that the bulk crust was strongly depleted in ^{18}O by exchange with externally derived aqueous fluids during metamorphism (*e.g.*, Shieh and Schwarcz, 1974; Wickham and Taylor, 1985; Peters and Wickham, 1995).

The portions of the core complex that are most (least) homogenized in $^{18}O/^{16}O$ are either those that are most (least) leucogranite-rich or the ones that have undergone the most (least) extensive anatexis; this implies that the anatectic melts themselves facilitated $^{18}O/^{16}O$ exchange with the unmelted rocks, and/or that they served as a source of aqueous fluids that promoted such exchange. This is the basis for the following semiquantitative model. A first stage of $^{18}O/^{16}O$ exchange is inferred to have occurred during melting of metapelite, fluxed by H_2O released by upper amphibolite facies muscovite dehydration, perhaps supplemented by small amounts of external H_2O. Dehydration at 750 °C and 8 kbar of such a pelite (containing ~ 3.5 wt. % H_2O, mainly as OH in muscovite) can produce > 30 % partial melting, liberating a leucogranite melt that contains ~ 10 wt. % H_2O (Clemens and Vielzeuf, 1987). Because the solubility of H_2O in granitic melt decreases during its ascent (Whitney, 1988), H_2O is released as these peraluminous melts reach saturation during their migration to shallow crustal depth, either passively due to displacements along the underlying decollement or actively in response to buoyant forces. This H_2O is then available to further exchange $^{18}O/^{16}O$ with adjacent rocks infertile to melting (paragneiss, amphibolite, quartzite, calc-silicate), as well as to drive more melting of those still fertile portions of the section (arkosic grit and pelite) that previously escaped anatexis. In addition, the migrating melts themselves serve as agents of $^{18}O/^{16}O$ exchange. Thus, in our model concurrent crystallization and melting occur during decompression of these leucogranite melts, and release of latent heat of crystallization also contributes energy for continued melting and hydrothermal circulation. This cyclic process of melting, H_2O release, crystallization, and $^{18}O/^{16}O$ exchange can in principle continue until the system cools to temperatures below the wet granite solidus (*i.e.*, ~ 680 °C at 2 kbar, Wyllie, 1977).

Holk and Taylor (1994a) quantitatively modeled this multi-stage H_2O influx-exsolution-release cycle that produces, releases, and rereleases magmatic and/or metamorphic pore fluids at several stages of anatexis of the rising allochthon, allowing the same H_2O to be used over and over again as a petrologic catalyst. This adequately explains both the degree of melting and the extent and localization of $^{18}O/^{16}O$ homogenization observed in the Thor-Odin core complex.

ACKNOWLEDGMENTS

This research was supported by NSF grant EAR 93-17036 and GSA grant 4951-92. We thank S. Carr, P. Larson, B. Nesbitt, M. Palin, R. Parrish, M. Peters, L. Silver, B. Wernicke, S. Wickham, and P. Wyllie for discussions, and J. Holk for field assistance. Reviews by A. Grunder, Z. Sharp, and S. Wickham substantially improved the manuscript. Division of Geological and Planetary Sciences, California Institute of Technology. Contribution 5609.

REFERENCES CITED

Armstrong, R.L., 1982, Cordilleran metamorphic core complexes – from Arizona to southern Canada: Annual Reviews in Earth and Planetary Sciences, v. 10, p. 129-154.

Blattner, P., 1971, Migmatite by partial fusion and short range hydrothermal transfer, British Columbia: Schweizerische Mineralogische un Petrographische Mitteilungen, v. 51, p. 155-177.

Bowman, J. R., and Ghent, E. D., 1986, Oxygen and hydrogen isotope study of minerals from metapelitic rocks, staurolite to sillimanite zones, Mica Creek, British Columbia: Journal of Metamorphic Geology, v. 4, p. 131-141.

Carr, S. D., 1991, Three crustal zones in the Thor-Odin - Pinnacles area, southern Omineca Belt, British Columbia: Canadian Journal of Earth Sciences, v. 28, p. 2003-2023.

Carr, S. D., 1992, Tectonic setting and U-Pb geochronology of the early Tertiary Ladybird leucogranite suite, Thor-Odin - Pinnacles area, southern Omineca belt, British Columbia: Tectonics, v. 11, p. 258-278.

Carr, S. D., 1995, The southern Omineca belt, British Columbia: New perspectives from the LITHOPROBE geoscience program: Canadian Journal of Earth Sciences, v. 32, p. 1720-1739.

Chamberlain, C. P., and Conrad, M. E., 1991, Oxygen isotope zoning in garnet: Science, v. 254, p. 403-406.

Clayton, R. N., and Kieffer, S. W., 1991, Oxygen isotopic thermometer calculations, in Taylor, H. P., Jr., et al., eds., Stable isotope geochemistry: A tribute to Samuel Epstein, San Antonio, Geochemical Society, p. 3-10.

Clayton, R. N., O'Neil, J. R., and Mayeda, T. K., 1972, Oxygen isotope exchange between quartz and water: Journal of Geophysical Research, v. 77, p. 3057-3067.

Clemens, J. D., and Vielzeuf, D., 1987, Constraints on melting and magma production in the crust: Earth and Planetary Science Letters, v. 86, p. 287-306.

Coney, P. J., and Harms, T., 1984, Cordilleran metamorphic core complexes: Cenozoic extensional relics of Mesozoic compression: Geology, v. 12, p. 550-554.

Cook, F. A., and nine others, 1992, Lithoprobe crustal reflection cross section of the southern Canadian Cordillera, 1, Foreland thrust and fold belt to Fraser River fault: Tectonics, v. 11, p. 12-35.

Fortier, S. M., and Giletti, B. J., 1989, An empirical model for predicting diffusion coefficients in silicate minerals: Science, v. 245, p. 1481-1484.

Holk, G. H., and Taylor, H. P., Jr., 1994a, Multiple stages of influx and exsolution of H_2O from anatectic melt during adiabatic decompression, a petrologic catalyst responsible for $^{18}O/^{16}O$ homogenization of metamorphic core complexes: Geological Society of America Abstracts with Programs, v. 26, no. 7, p. 280.

Holk, G. H., and Taylor, H. P., Jr., 1994b, $^{18}O/^{16}O$ data on contrasting crustal-scale aqueous fluid regimes before and during Eocene extension in the Southern Omineca Crystalline Belt, British Columbia: United States Geological Survey Circular 1107, p. 140.

Javoy, M., 1977, Stable isotopes and geothermometry: Geological Society of London Journal, v. 133, p. 609-636.

Magaritz, M., and Taylor, H. P., Jr., 1986, Oxygen 18/Oxygen 16 and D/H studies of plutonic, granitic, and metamorphic rocks across the Cordilleran batholiths of southern British Columbia: Journal of Geophysical Research, v. 91, p. 2193-2217.

Nesbitt, B. E., and Muehlenbachs, K., 1989, Origins and movement of fluids during deformation and metamorphism in the Canadian Cordillera: Science, v. 245, p. 733-736.

Nyman, M. W., Pattison, D. R. M., and Ghent, E. D., 1995, Melt extraction during formation of K-feldspar + sillimanite migmatites, west of Revelstoke, British Columbia: Journal of Petrology, v. 36, p. 351-372.

O'Neil, J. R., and Ghent, E. D., 1975, Stable isotope study of coexisting metamorphic minerals from the Esplanade Range, British Columbia: Geological Society of America Bulletin, v. 86, p. 1708-1712.

Parrish, R. R., Carr, S. D., and Parkinson, D. L., 1988, Eocene extensional tectonics and geochronology of the southern Omineca belt, British Columbia and Washington: Tectonics, v. 7, p. 181-212.

Peters, M. T., and Wickham, S. M., 1995, On the causes of ^{18}O-depletion and $^{18}O/^{16}O$ homogenization during regional metamorphism; the East Humboldt Range core complex, Nevada: Contributions to Mineralogy and Petrology, v. 119, p. 68-82.

Reynolds, S. J., and Lister, G. S., 1987, Structural aspects of fluid-rock interactions in detachment zones: Geology, v. 15, p. 362-366.

Rye, R. O., Schuiling, R. D., Rye, D. M., and Jansen, J., 1976, Carbon, hydrogen, and oxygen isotope studies of the regional metamorphic complex at Naxos, Greece: Geochimica et Cosmochimica Acta, v. 40, p. 1031-1049.

Shieh, Y. N., and Schwarcz, H. P., 1974, Oxygen isotope studies of granite and migmatite, Grenville province of Ontario, Canada: Geochimica et Cosmochimica Acta, v. 38, p. 21-45.

Veizer, J., and Hoefs, J., 1976, The nature of $^{18}O/^{16}O$ and $^{13}C/^{12}C$ secular trends in sedimentary carbonate rocks: Geochimica et Cosmochimica Acta, v. 40, p. 1387-1395.

Whitney, J. A., 1988, The origin of granite: The role and source of water in the evolution of granitic magmas: Geological Society of America Bulletin, v. 100, p. 886-1897.

Wickham, S. M., and Taylor, H. P., Jr., 1985, Stable isotopic evidence for large-scale seawater infiltration in a regional metamorphic terrane; the Trois Seigneurs Massif, Pyrenees, France: Contributions to Mineralogy and Petrology, v. 91, p. 122-137.

Wyllie, P. J., 1977, Crustal anatexis: An experimental review: Tectonophysics, v. 43, p. 41-71.

FOOTNOTE

[1]GSA Data Repository item ####, $^{18}O/^{16}O$ data on coexisting minerals in rocks from the southern Thor-Odin metamorphic core complex, is available on request from Documents Secretary, GSA, P.O. Box 9140, Boulder, CO 80301. E-mail: editing@geosociety.org

FIGURE CAPTIONS

Figure 1. Location of study area in British Columbia (inset) and simplified geology of southern Thor-Odin metamorphic core complex (modified from Carr, 1992) showing traverses 1, 2, and 3, and other sample locations (squares). Monashee decollement (MD) separates basement from middle crustal zone of Selkirk allochthon. Columbia River fault (CRF) and Beavan fault (BF) are Eocene detachment faults that separate middle and upper crustal zones. Dashed line beneath MD indicates boundary of a 200-m-thick basement zone that is homogeneous in $^{18}O/^{16}O$ (see text).

Figure 2. Quartz and feldspar $\delta^{18}O$ vs. structural height. $\delta^{18}O$ values are relative to V-SMOW (Vienna Standard Mean Ocean Water). All of the data[1] from 115 rock specimens that we analyzed from Thor-Odin are plotted on diagram except for three thick low-^{18}O amphibolites (see Fig. 3) and six late-stage leucocratic dikes. Note that quartz and

feldspar are each uniform in ^{18}O and in apparent equilibrium at near-magmatic temperatures throughout much of the mid-crustal zone, suggesting pervasive homogenization with aqueous fluid having $\delta^{18}O \approx +11.0$. High $\delta^{18}O$ in marble-rich zone is likely due to incomplete isotopic homogenization with initially ^{18}O-rich, relatively impermeable marble. Low $\delta^{18}O$ values of quartz from amphibolite-rich zone are from two pelites and a leucogranite collected adjacent to thick low-^{18}O amphibolite layers. Feldspar ^{18}O depletions (down to $\delta^{18}O = -3.8$) within imbricate thrust and amphibolite-rich zones are the result of late-stage meteoric-hydrothermal exchange. Marked variability of quartz $\delta^{18}O$ within basement and imbricate thrust zone indicates that these deeper parts of the complex did not undergo oxygen isotope homogenization, except for zone of anatexis within 200 m of Monashee decollement. There, the $\delta^{18}O$ of quartz is uniform at a level 1.0-1.5‰ lower than homogeneous quartz in the overlying allochthon, as shown by two patterned vertical bands. Basement samples are from wider area than shown on Figure 1, and two of the plotted quartz-feldspar pairs are from Blattner (1971).

Figure 3. $\delta^{18}O$ quartz vs. coexisting $\delta^{18}O$ garnet (almandine) from Thor-Odin complex. Dashed line at $\Delta = 2.5‰$ represents equilibrium at 750 °C (Javoy, 1977). Heterogeneous $\Delta_{Q\text{-}G}$ values of 1.8-4.1‰ within amphibolite-rich zone, large $\Delta_{Q\text{-}G} \geq 2.5‰$ in low-^{18}O thick amphibolite outcrops, and small $\Delta_{Q\text{-}G} \leq 2.5‰$ within high-^{18}O marble-rich zone all indicate systematic $^{18}O/^{16}O$ disequilibrium effects in which garnet has preserved evidence of pre-metamorphic $^{18}O/^{16}O$ heterogeneity (note that this statement does not apply to garnets from the thoroughly homogenized leucogranite-rich zone, which display uniform $\Delta_{Q\text{-}G} \sim 2.7‰$).

Figure 1

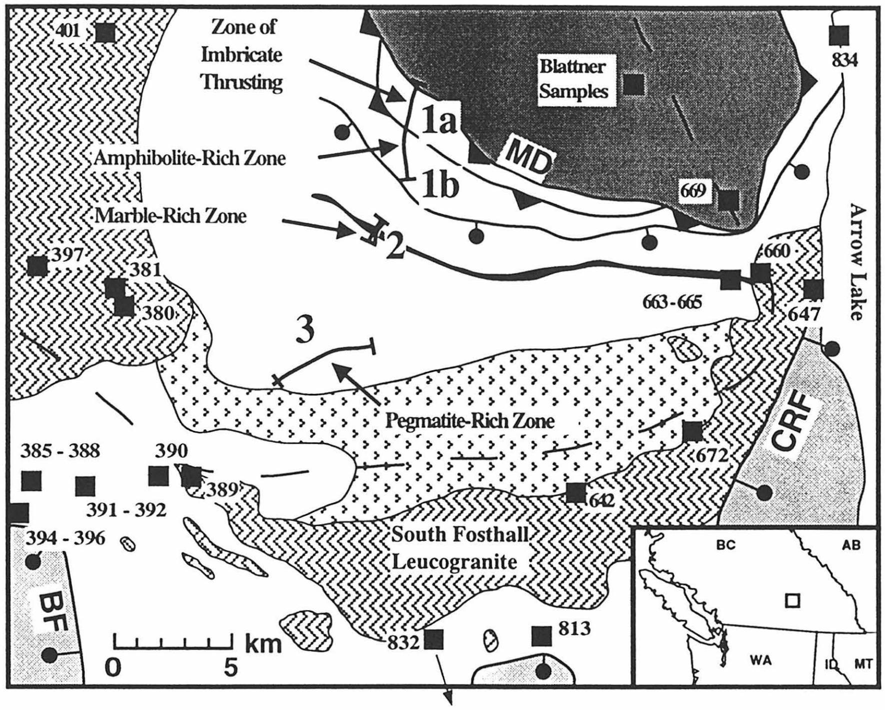

Thrust Fault
(Teeth on Hanging Wall)

Normal Fault
(Pegs on Hanging Wall)

Middle Crustal Zone
(Lower Plate of Normal Faults)

South Fosthall Leucogranite
(Late Paleocene to Eocene)

< 50% Metamorphic Rocks

> 50% Metamorphic Rocks
(Late Proterozoic to Permian)

Empress Marble
(Early Cambrian)

Upper Crustal Zone
(Upper Plate of Normal Faults)

Stratified Rocks
(Paleozoic to Lower Jurassic)

Basement Zone
(Lower Plate of Monashee Decollement)

Paragneiss and Orthogneiss
(Proterozoic)

Figure 2

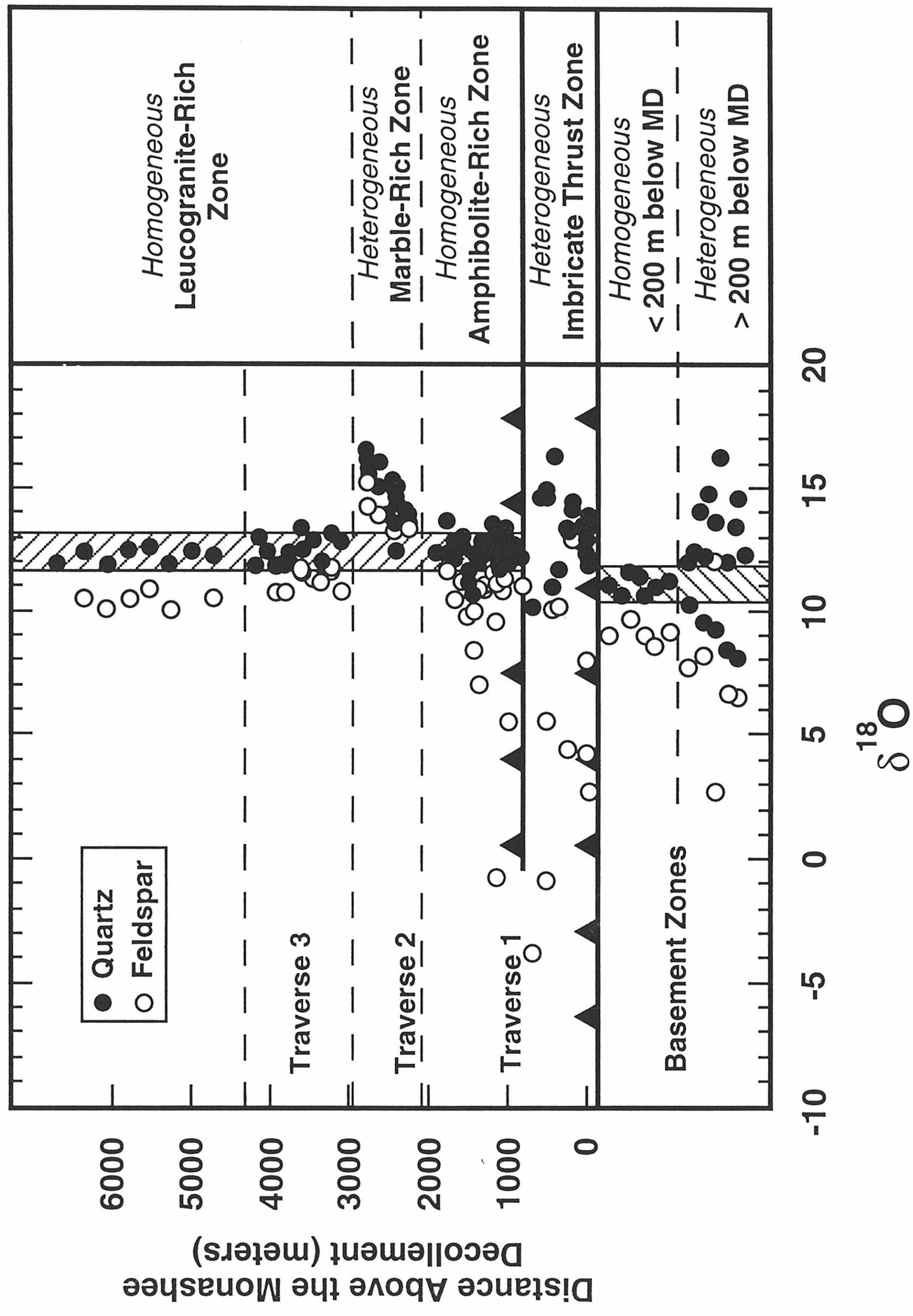
Quartz
Feldspar
Homogeneous
Leucogranite-Rich Zone
Heterogeneous
Marble-Rich Zone
Homogeneous
Amphibolite-Rich Zone
Heterogeneous
Imbricate Thrust Zone
Homogeneous
< 200 m below MD
Heterogeneous
> 200 m below MD
Traverse 3
Traverse 2
Traverse 1
Basement Zones
Distance Above the Monashee Decollement (meters)
6000
5000
4000
3000
2000
1000
0
-10
-5
0
5
10
15
20
$\delta^{18}O$

Figure 3

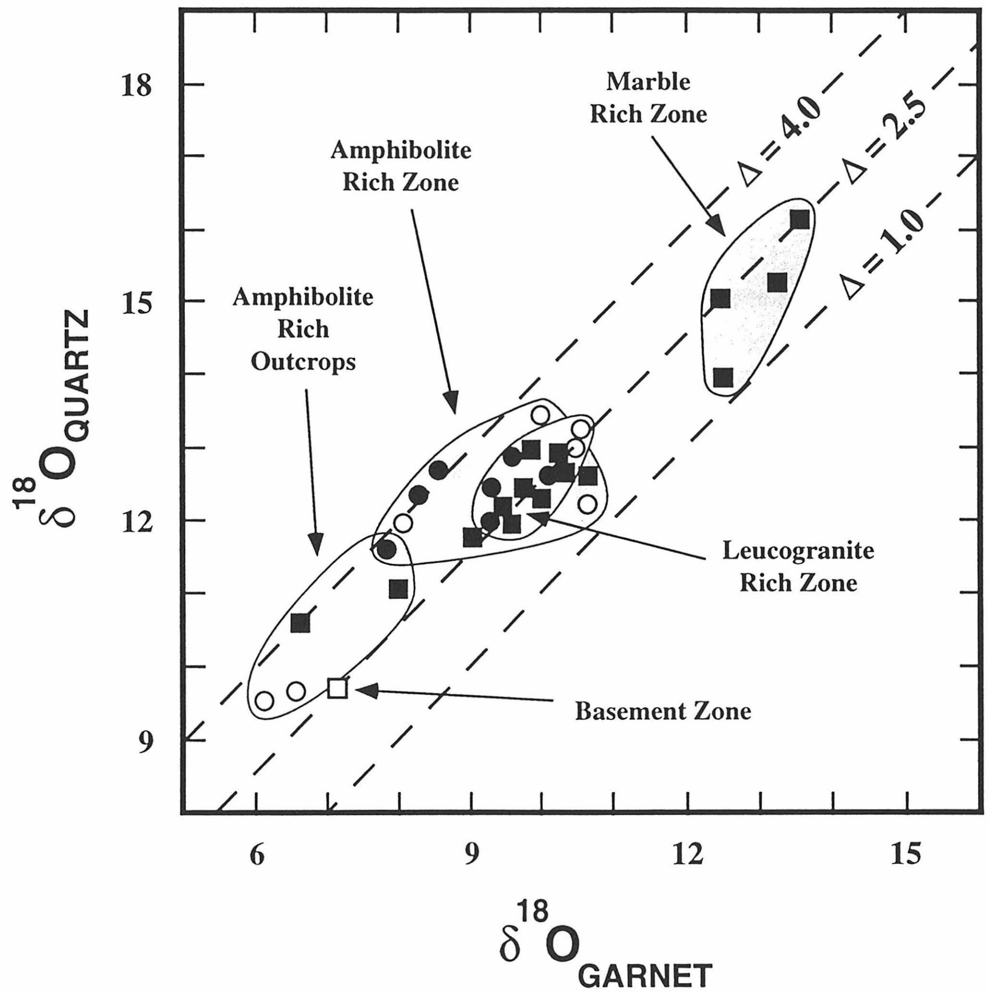
18
15
12
9
6
9
12
15
δ18O QUARTZ
δ18O GARNET
Marble
Rich Zone
Amphibolite
Rich Zone
Amphibolite
Rich
Outcrops
Leucogranite
Rich Zone
Basement Zone
Δ = 4.0
Δ = 2.5
Δ = 1.0

TABLE 1. $^{18}O/^{16}O$ DATA ON COEXISTING MINERALS IN ROCKS FROM THE SOUTHERN THOR-ODIN METAMORPHIC CORE COMPLEX (Except for the basement zone, samples are listed in stratigraphic order from deepest to shallowest)

Sample*	Rock Type	Qz†	Fs†	Grt†§
THE BASEMENT ZONE				
> 200 m below Monashee decollement				
GH-49	Basement Gneiss	10.2	7.7	
GH-556	Calc-Silicate	16.4		
GH-669	Basement Gneiss	9.7	8.1	7.1
MC-2	Psammite	14.7		
MC-2a	Pelite	13.6	12.1	
MC-2b	Calc-Silicate	13.4		
MC-3a	Quartzite	12.2		
MC-3b	Calc-Silicate	12.2		
MC-3c	Pelite	14.7		
MC-4	Basement Gneiss	9.3	2.7	
MC-5	Basement Gneiss	12.0		
< 200 m below Monashee decollement				
GH-75	Leucogranite	11.0	9.0	
GH-552	Pelite	10.6		
GH-553	Pelite	11.6	9.6	
GH-555	Pelite	11.3		
GH-841	Leucogranite	10.6	9.0	
GH-842	Leucogranite	11.0	8.4	
GH-843	Leucogranite	11.1	9.1	
MONASHEE DECOLLEMENT				
Zone of imbricate thrusting				
MD-1	Gneiss	13.4	2.7	
Thrust				
MD-2	Quartzite	11.9		
MD-3	Pelite	13.9		
MD-4	Quartzite	12.1		
MD-5	Pelite	13.1	4.2	
MD-6	Pelite	12.3	8.0	
MD-6a	Aluminous Schist	12.9		
MD-7	Gneiss	12.9		
MD-14	Quartzite	13.5		
Thrust				
MD-17a	Leucocratic Dike	14.4	12.9	
MD-17b	Quartzite	14.2		
Thrust				
MD-19b	Leucocratic Dike	13.2	4.4	
MD-20a	Quartzite	13.5		
Thrust				
MD-24	Gneiss	11.7	10.2	
Thrust				
MD-26a	Calc-Silicate	16.4		
MD-27	Gneiss	11.0	10.0	
MD-29	Quartzite	14.9		
MD-29a	Pelite	14.6	–0.9	
MD-29b	Amphibolite		5.5	8.6
Thrust				
MD-30	Quartzite	14.7		
MD-31	Pelite	10.2	–3.8	
MD-32	Pelite	12.1		9.3
Thrust				
SELKIRK ALLOCHTHON				
Amphibolite-rich zone				
MD-33a	Leucocratic Sheet	12.3	11.0	
MD-35	Pelite	12.7		10.3
MD-35a	Leucocratic Dike	13.4	–3.8	
MD-37	Pelite	11.8		9.1
MD-38	Leucocratic Sheet	12.1	5.4	
MD-38a	Pelite	13.3	11.3	
MD-38b	Amphibolite	13.0		
MD-39a	Leucocratic Sheet	12.2	10.8	
MD-40	Amphibolite		–0.8	
MD-40a	Leucocratic Sheet	11.7	11.1	
MD-40b	Pelite	11.8	9.6	
MD-41	Quartzite	12.3		
MD-41a	Leucocratic Sheet	12.9	11.5	9.7
MD-41b	Amphibolite	13.6		10.0
MD-50	Pelite	12.4	10.9	
MD-50a	Leucocratic Sheet	12.7	11.0	8.6
MD-49	Pelite	12.8	7.0	10.5
MD-49a	Quartzite	12.1		
MD-48	Pelite		10.9	8.7
MD-48a	Amphibolite	11.9		8.1
MD-48b	Leucocratic Sheet	12.3	10.0	8.3
MD-47a	Amphibolite#	9.7		6.6
MD-47	Pelite#	10.7	8.4	6.7
MD-46b	Leucocratic Sheet#	11.7		7.8
MD-46	Amphibolite#	9.7	8.1	6.1
MD-46a	Pelite#	11.1	9.8	8.0
MD-45	Amphibolite	13.0		10.4
MD-45a	Leucocratic Sheet	12.7	11.2	10.2
MD-44	Calc-Silicate	12.9		10.4
MD-44a	Leucocratic Sheet	12.1	10.4	
MD-43	Leucocratic Sheet	12.3	11.5	
MD-43a	Calc-Silicate	13.8		
MD-42	Amphibolite#		9.1	6.8
NF-3	Amphibolite	12.3		10.5
Normal Fault				

TABLE 1 (continued).

Sample*	Rock Type	Qz†	Fs†	Gr†§	Sample*	Rock Type	Qz†	Fs†	Gr†§
Marble-rich zone					**Leucogranite-rich zone**				
MD-57	Quartzite	13.6			MD-59	Leucocratic Dike	11.1	10.3	
MD-57a	Pelite	13.9	13.3		MD-60a	Leucocratic Sheet	12.8	10.7	
MD-57b	Psammite	14.0			MD-63	Pelite	13.1	11.7	
MD-58	Pelite	14.5	13.7		MD-63a	Amphibolite		11.7	10.3
MD-58a	Leucocratic Sheet	14.3	13.9		MD-66	Leucocratic Sheet	11.8	11.1	
MD-58b	Psammite	15.1	13.7		MD-68	Leucocratic Sheet	12.9	11.2	
MD-58d	Calc-Silicate	12.4			MD-70	Leucocratic Sheet	12.4	11.4	
MD-58f	Leucocratic Sheet	15.0	13.3		MD-70a	Amphibolite	13.3	11.6	10.5
MD-58g	Pelite	15.3		13.2	MD-71a	Pelite	12.3		9.8
MD-58h	Quartzite	13.6			MD-73	Leucogranite	11.9	10.6	
MD-56a	Leucocratic Dike	18.8	17.0		MD-81	Leucogranite	11.9	10.6	
MD-56c	Leucocratic Dike	17.4	16.8		MD-80a	Pelite	12.3		10.0
MD-55	Pelite	13.9	13.2	12.5	MD-78	Pelite	13.0		9.8
MD-53	Quartzite	16.1			MD-77a	Pelite	11.9		9.6
MD-53a	Pelite	15.1	13.9	12.4	GH-380	Leucogranite	12.2	10.5	
MD-51	Calc-Silicate	15.7			GH-381	Leucogranite	12.5		9.2
MD-51a	Calc-Silicate	15.9			GH-401	Leucogranite	11.9	10.1	
MD-51b	Leucocratic Sheet	16.3	14.2		GH-389	Leucogranite	12.6	10.8	
MD-51d	Pelite	16.2	15.3	13.5	GH-397	Leucogranite	12.5	10.5	
					GH-642	Leucogranite	11.8	10.1	
					GH-660	Leucogranite	12.6	10.5	
					GH-834	Leucogranite	11.9		9.2

Note: Mineral separates were hand-picked under the microscope. Some quartz separates were treated with HF to remove impurities. Oxygen was liberated from quartz and feldspar by reaction with F_2 in Ni reaction vessels at 550 °C, converted to CO_2, and analyzed on a Finnegan MAT 252 mass spectrometer.

The leucocratic sheets and dikes are essentially leucogranitic in composition, but they are from smaller bodies and they typically display more variable grain size than the rocks labeled leucogranite.

*Numbers refer to samples archived at the Division of Geological and Planetary Sciences, California Institute of Technology, Pasadena, California.

†The oxygen isotope data for quartz (Qz), feldspar (Fs), and almandine garnet (Gr) are reported in the δ notation, where δ is the relative difference in parts per thousand in $^{18}O/^{16}O$ between the sample and a standard. The standard is V-SMOW (Vienna standard mean ocean water). NBS-28 has a $\delta^{18}O = +9.60$ on this scale. Replicate analyses of samples and the Caltech rose quartz working standard ($\delta^{18}O = +8.45$) have an analytical error of ± 0.2‰.

§The garnet oxygen isotope data were also acquired by a fluorination procedure, but one using the Caltech oxygen isotope laser extraction system, instead of externally heated Ni reaction vessels. Caltech rose quartz ($\delta^{18}O = +8.45 \pm 0.10$; N = 25) and Hualalai olivine ($\delta^{18}O = +5.37 \pm 0.10$; N = 42) laboratory standards were analyzed each operating day during collection of garnet $^{18}O/^{16}O$ data. Duplicate laser analyses of randomly chosen, hand picked, inclusion-free grains of crushed garnet (typically two to three 0.5-1.0 mg grains were analyzed in each run) display an analytical uncertainty of ≤ 0.3‰. Comparison of laser and conventional quartz analyses agreed to within ± 0.2 ‰.

#These samples are from the three thick, massive amphibolite outcrops mentioned in the text. Pelites and leucogranites were collected within 0.1 meters of the contacts of these 2–40-m-thick amphibolites.

4.2 General Statement

Metamorphic core complexes represent ductilely deformed middle crust uplifted and exposed in an extensional setting (Armstrong, 1982). In western North America these features are associated with extensive magmatism (Armstrong and Ward, 1991) in crust thickened during Mesozoic orogenesis (Coney and Harms, 1984). Extension may be compensated by flow of rock material from unextended areas (Block and Royden, 1990; Wernicke, 1990), possibly driven by the weakening of the middle and/or lower crust by anatexis (Patino Douce et al., 1990) and/or injection of basaltic magma into the lower crust (Gans, 1987).

It is now clear that processes involving H_2O play a prominent role in the development of metamorphic core complexes at all structural levels, and also that stable isotope studies are essential in understanding these kinds of water/rock interactions. The influence of H_2O is clearly paramount in the production of crustal melts (Tuttle and Bowen, 1958; Wyllie, 1977; Taylor, 1988). These melts are a likely agent of H_2O transport and $^{18}O/^{16}O$ exchange during the early events that affected the ductile, deeper portions of metamorphic core complexes (Reynolds and Lister, 1987; Wickham and Peters, 1990; Wickham et al., 1991; Morrison, 1994; Holk and Taylor, 1993, 1994; Peters and Wickham, 1995). At later stages, it is well known that large-scale meteoric-hydrothermal systems have penetrated both the upper and lower plates along major detachment faults throughout the North American Cordillera (Kerrich, 1987; Beaudoin et al., 1991; Holk and Taylor, 1991; Fricke et al., 1992; Morrison, 1994; Nesbitt and Muehlenbachs, 1995).

In this chapter we quantitatively evaluate the hydrothermal processes associated with metamorphism and partial melting that produced the homogenization of $\delta^{18}O$ values in deep portions of the southern Thor-Odin complex in southern British Columbia (Holk and

Taylor, 1994). We specifically address the coupling between protolith stratigraphy, thermotectonic evolution, and aqueous fluid-rock interaction in the formation of the Ladybird leucogranite suite. The Thor-Odin complex arguably represents the optimum location for addressing the role of water in the tectonic and petrologic evolution of these Cordilleran metamorphic core complexes, because: (1) This is a very large system in which deep-seated pre-extensional thrust faults are exposed for as much as 100 km at the surface, and major uplifts have provided a complete mid-crustal section below the detachment faults. (2) Exposures are excellent, and structures are well mapped and dated (Reesor and Moore, 1971; Duncan, 1984; and Carr, 1991). (3) Stratigraphic units are well defined (Reesor and Moore, 1971) and reliably correlated (Hoy, 1977; Carr, 1991). (4) However, the most compelling reason for singling out the Thor-Odin complex for isotopic study is its high latitude location relative to other metamorphic core complexes in North America; meteoric water is known to have been very low in ^{18}O and deuterium during the Eocene development of the metamorphic core complexes in British Columbia (Magaritz and Taylor, 1986; Beaudoin et al., 1991; Nesbitt and Muehlenbachs, 1995), providing a very clear-cut isotopic contrast between meteoric waters and either metamorphic or magmatic waters (*e.g.*, Taylor and Sheppard, 1986). This allows us to quantitatively sort out the extent of the meteoric-hydrothermal overprint that is ubiquitous in all of these tectonic systems, particularly in the vicinity of the detachment faults.

4.3 Geologic Setting

The Thor-Odin complex is the product of late Mesozoic to Paleocene compression followed by Eocene extension (Carr, 1991). It consists of three fault-bounded zones (Figures 4.1 and 4.2) that are typical of core complexes in the southern Omineca belt

(Parrish et al., 1988), namely Precambrian basement, mid-crustal amphibolite-facies rocks, and a brittle upper zone.

The middle crustal zone and adjoining bounding structures preserve evidence of Mesozoic-to-Early Tertiary deformation, metamorphism, and anatexis. A thick sequence at least 6000 meters thick of metapelite, quartzite, psammite, amphibolite, calc-silicate, and marble makes up the middle crustal zone (Reesor and Moore, 1971; Carr, 1991). This section is correlated with the Late Precambrian-to-Mississippian clastic, post-rift, pericratonic sequence of the Kootenay terrane, and Permian-to-Triassic deep ocean basin and island arc sediments of the Slide Mountain and Quesnallia terranes (Hoy 1977; Carr, 1991). Interlayered within this sequence are cm-to-km thick sheets of Eocene (Ladybird) leucogranite. Cross-cutting dikes, stocks, and plutons of this leucogranite are also common.

The Monashee decollement is a ductile shear zone, active up to 58-59 Ma (Carr, 1992), responsible for the northeastward transport of mid-crustal rocks of the Selkirk Allochthon over the basement zone. In the study area, this shear zone is a duplex containing imbricate slices of basement and supracrustal gneisses (McNicoll and Brown, 1995). Lithoprobe crustal seismic profiles establish the Monashee decollement as a west-dipping crustal-scale ramp with 20 km of vertical relief (Cook et al., 1992), which served as the root thrust of the Rocky Mountain Foreland Thrust Belt (and is proposed to have at least 100 km displacement, Brown et al., 1991). North of the study area, apparent temperature and pressure conditions during shearing were > 650° C and > 6 kb (Lane et al., 1989; Nyman et al., 1995). The overall thermal history of this terrane, as proposed by Carr (1995), is shown on Figure 4.3.

Mylonitic and brittle deformation along the low-angle Columbia River and Beavan detachment faults accommodated the respective eastward and westward movement of the

Figure 4.1 -- Location of study area in British Columbia (inset), showing the simplified geology of the southern Thor-Odin metamorphic core complex (modified from Carr, 1992) and the locations of Traverses 1, 2, and 3, and other sample locations (squares). The Monashee decollement (MD) separates the basement from the middle crustal zone of Selkirk allochthon. The Columbia River fault (CRF) and Beavan fault (BF) are Eocene detachment faults that separate the middle and upper crustal zones. The dashed line beneath the MD indicates the boundary of a 200-m-thick basement zone that is homogeneous in $^{18}O/^{16}O$ (see text). Sample localities 385-388 and 391-396 in the southwest corner of the map are associated with the Beavan fault and are discussed in Chapter 5. Sample localities 647-665, 672, and 813-834 along the east side of the map are associated with the Columbia River fault, and are discussed in Chapter 5.

Figure 4.1 Thor-Odin Complex

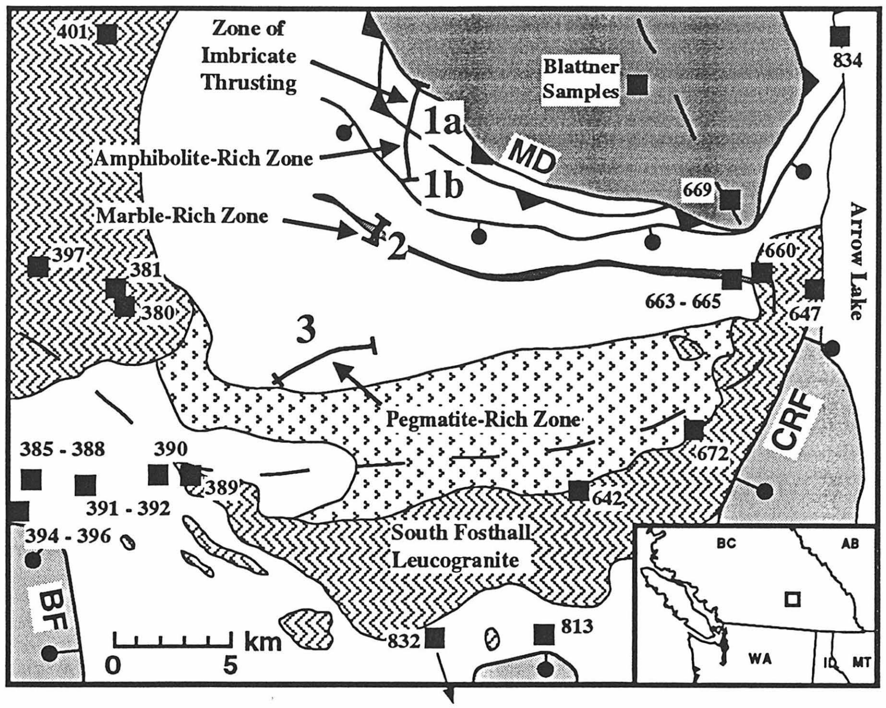

Thrust Fault
(Teeth on Hanging Wall)

Normal Fault
(Pegs on Hanging Wall)

Middle Crustal Zone
(Lower Plate of Normal Faults)

South Fosthall Leucogranite
(Late Paleocene to Eocene)

< 50% Metamorphic Rocks

> 50% Metamorphic Rocks
(Late Proterozoic to Permian)

Empress Marble
(Early Cambrian)

Upper Crustal Zone
(Upper Plate of Normal Faults)

Stratified Rocks
(Paleozoic to Lower Jurassic)

Basement Zone
(Lower Plate of Monashee Decollement)

Paragneiss and Orthogneiss
(Proterozoic)

Figure 4.2 -- North-south cross-section of the southern Thor-Odin metamorphic core complex, modified after Carr (1992). Sample traverses and sample locations from Figure 4.1 are projected onto this cross section at their correct structural locations. Traverse 1 includes the zone of imbricate thrusting zone and an overlying amphibolite-rich zone. Traverse 2 corresponds to a portion of the marble-rich zone. Traverse 3 is the pegmatite-rich and leucogranite-rich zone beneath the Ladybird granite pluton. Crystallization of the Ladybird granite pluton and associated underlying leucocratic sheets occurred during latest movement along the Monashee decollement and earliest stages of deformation along the Columbia River fault (Carr, 1992). Standard symbols indicating the direction of slip on the Columbia River fault are shown on the right-hand-side of the cross section by the plus sign (movement away from viewer) and open circle (toward the viewer).

Figure 4.3 -- Thermal evolution of Thor-Odin complex (after Carr, 1995) as determined from closure temperatures of geochronometers. The stippled pattern indicates episodes of plutonism. The thermal maximum occurred at about 60-70 Ma, and is associated with anatexis and the petrogenesis of the Ladybird plutonic suite during the waning stages of compressional deformation. Rapid cooling from > 700 °C to ~ 300 °C occurred during the extensional denudation of the complex at about 58-45 Ma.

Figure 4.2 Cross Section Thor-Odin Complex

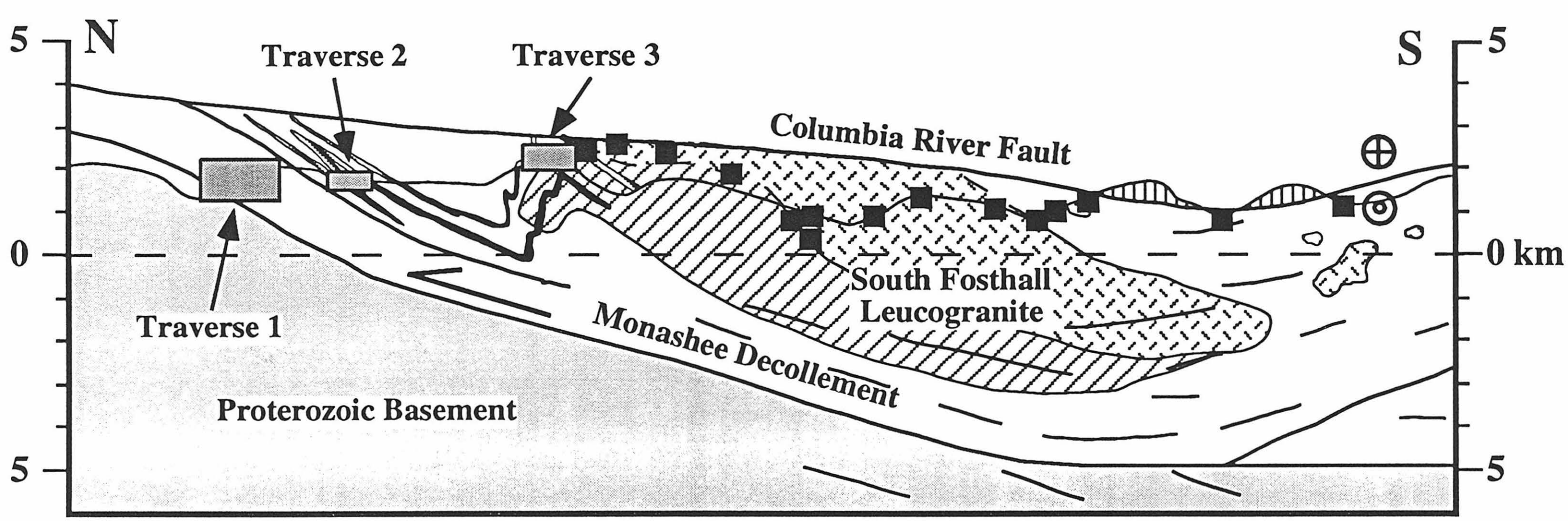

Figure 4.3 Southern Thor-Odin Complex: Thermal History

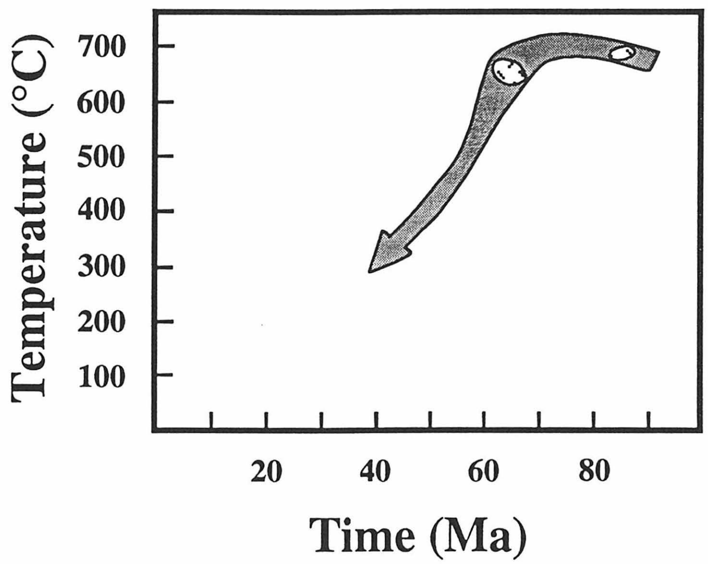

upper crustal zone during the Eocene exhumation of the mid-crustal zone (Parrish et al., 1988; Carr, 1992). The Columbia River fault was definitely active at 55 Ma, but may have been active as early as 59.7 Ma (Parrish et al., 1988). Displacement along the Columbia River fault at the latitude of the Thor-Odin complex is estimated to be 20-30 km (Read, 1979; Parrish et al., 1988).

In the southern Thor-Odin complex Ladybird leucogranite sheets are synkinematic with deformation associated with the latest stages of upper amphibolite-facies metamorphism (Reesor and Moore, 1971; Duncan, 1984; Carr, 1991; 1992). The outcrop abundance of leucogranite increases from 30% immediately above the Monashee decollement to nearly 100% at the 3-km-thick, sill-like South Fosthall pluton just below the Columbia River fault (Carr, 1991). U-Pb zircon ages (55-62 Ma) constrain the time of crystallization of these granites to be concurrent with the latest deformation along the Monashee decollement and the earliest stages of movement along the Columbia River fault (Carr, 1992; 1995). Carr (1992) cited Wyllie (1977) and Whitney (1988) in proposing an anatectic origin for these leucogranites during decompression melting associated with tectonic shortening as the Selkirk Allochthon was carried up the Monashee thrust ramp. In this chapter I expand upon, and quantify this model, and propose that the movement and redistribution of aqueous fluids between these melts and adjacent lithologies played a major role in the decompression melting and hydrothermal metamorphism of this terrane.

4.4 Samples Studied

Sample localities and sample traverses are shown on the simplified geologic map of the southern Thor-Odin complex (Figure 4.1). Traverse 1 is a suite of samples collected across the imbricate thrust zone and into an overlying amphibolite-rich zone that is correlative with a Proterozoic rift sequence, namely the semipelitic amphibolite division of the Horsethief Creek Group, a subdivision of the Windermere Supergroup (Carr, 1991). The amphibolite-rich zone is lithologically heterogeneous, consisting of 0.1–40-m-thick layers of metapelite, calc-silicate, quartzite, marble, and amphibolite intruded by 0.2–30-m-thick leucogranite sheets. Traverse 2 crosses an equally heterogeneous, but more marble-rich zone comprised of thin layers (< 1 m) of all of the above lithologies except amphibolite; these are intercalated with thick (up to 50 m) marble units (Cambrian Empress marble). This marble-rich zone is correlated with intercalated marble and quartzite of the Cambrian Mohican and Badshot Formations (Carr, 1991). Traverse 3 passes through a leucogranite-rich zone just beneath a large Ladybird Series pluton (the South Fosthall pluton; Figure 4.1); here, sequences of metapelite, amphibolite, and calc-silicate correlated with the Cambrian-Ordovician Lardeau Group occur as discrete layers within the dominant leucogranite. Several samples of leucogranite from the South Fosthall pluton were collected.

4.5 Stable Isotope Results

Throughout the Selkirk allochthon, but particularly within the uppermost 4-km-thick leucogranite-rich zone, minerals in the metasediments and leucogranites are characteristically uniform in ^{18}O (Figure 4.4 and Table 4.1), and in approximate isotopic equilibrium at high temperatures. For example, in the leucogranite-rich zone and in most of the amphibolite-rich zone, quartz $\delta^{18}O = 12.5 \pm 0.5‰$ (1σ std. dev.) for metapelite (N = 11), $12.2 \pm 0.1‰$ for quartzite (N = 2), and $12.3 \pm 0.4‰$ (N = 24) for the concordant leucogranites. Within the leucogranite-rich zone, no exceptions have been found to this remarkable $^{18}O/^{16}O$ homogeneity; this includes even the garnets (see below) and a 1-m-thick marble unit, which has calcite $\delta^{18}O = 12.4$. Ignoring a few low-^{18}O feldspars that are the result of a late-stage meteoric-hydrothermal event associated with detachment

Figure 4.4 -- Quartz and feldspar $\delta^{18}O$ vs. structural height. $\delta^{18}O$ values are relative to SMOW (Standard Mean Ocean Water). All of the data from 115 rock specimens analyzed in the present study from the southern Thor-Odin complex are plotted on this diagram, except for three thick low-^{18}O amphibolites (see Figure 4.6) and 5 late-stage leucocratic dikes (sample numbers MD-35a, MD-17a, MD-19b, MD-56c, and MD-59). Note that quartz and feldspar are each uniform in ^{18}O and in apparent equilibrium at near-magmatic temperatures throughout much of the mid-crustal zone, suggesting pervasive homogenization with aqueous fluid having $\delta^{18}O \approx +11.0$. The high $\delta^{18}O$ values in the marble-rich zone are likely due to incomplete isotopic homogenization with the initially ^{18}O-rich, relatively impermeable marble layers. The low $\delta^{18}O$ values of quartz from the amphibolite-rich zone are from two pelites and a leucogranite collected adjacent to thick low-^{18}O amphibolite layers. Feldspar ^{18}O depletions (down to $\delta^{18}O = -3.8$) within the imbricate thrust and amphibolite-rich zones are the result of late-stage meteoric-hydrothermal exchange. Marked variability of quartz $\delta^{18}O$ within the basement and the imbricate thrust zone indicates that these deeper parts of the complex did not undergo oxygen isotope homogenization, except for a zone of anatexis within 200 m of Monashee decollement (see Chapter 3). There, the $\delta^{18}O$ of quartz is uniform at a level 1.0-1.5‰ lower than homogeneous quartz in the overlying allochthon, as shown by the two patterned vertical bands. Basement samples are from wider area than shown on Figure 4.4, and two of the plotted quartz-feldspar pairs are from Blattner (1971).

Figure 4.4 Thor-Odin $\delta^{18}O$ vs. Height

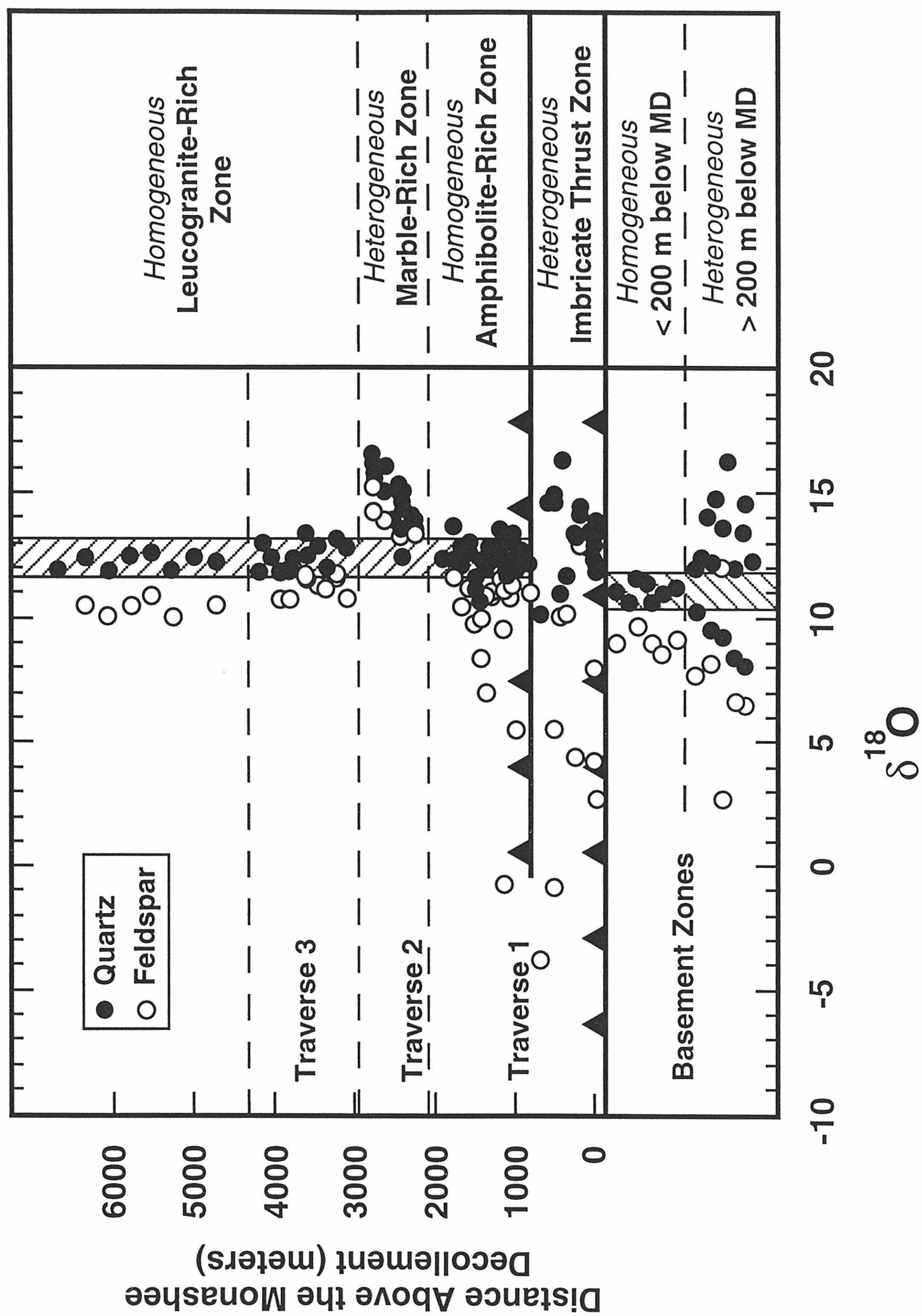

TABLE 4.1. $^{18}O/^{16}O$ DATA ON ROCKS AND MINERALS FROM THE SELKIRK ALLOCHTHON

Sample*	Rock Type	Qz†	Fs†	Gar§	Other	Cc# $\delta^{18}O$	Cc# $\delta^{13}C$
Amphibolite-Rich Zone							
MD-33a	Leucogranite Sheet	12.3	11.0				
MD-35	Pelitic Gneiss	12.7		10.3			
MD-35a	Leucogranite Dike	13.4	–3.8				
MD-36a	Calc-Silicate					15.2	–3.5
MD-36b	Marble					18.8	8.5
MD-37	Pelitic Gneiss	11.8		9.1			
MD-38	Leucogranite Sheet	12.1	5.4				
MD-38a	Quartzofeldspathic Gneiss	13.3	11.3		7.5a		
					7.4b		
MD-38b	Amphibolite	13.0			10.3a		
					8.0b		
MD-39a	Leucogranite Sheet	12.2	10.8				
MD-40	Amphibolite		–0.8		4.3a		
MD-40a	Leucogranite Sheet	11.7	11.1				
MD-40b	Pelitic Gneiss	11.8	9.6		4.2b		
MD-41	Quartzite	12.3					
MD-41a	Leucocratic Sheet	12.9	11.5	9.7			
MD-41b	Amphibolite	13.6		10.0	10.7a		
					9.7b		
MD-50	Pelitic Gneiss	12.4	10.9				
MD-50a	Leucocratic Sheet	12.7	11.0	8.6			
MD-49	Pelitic Gneiss	12.8	7.0	10.5	4.1b		
MD-49a	Quartz Vein	12.1					
MD-48	Feldspathic Gneiss		10.9	8.7			
MD-48a	Amphibolite	11.9		8.1	8.1a		
					6.2b		
MD-48b	Leucocratic Sheet	12.3	10.0	8.3	7.3b		
Thick Amphibolite Outcrops							
MD-47	Pelitic Gneiss	10.7	8.4	6.7			
MD-47a	Amphibolite	9.7		6.6			
MD-46	Amphibolite	9.7	8.1	6.1	7.8a		
					3.1b		
MD-46a	Pelitic Gneiss	11.1	9.8	8.0			
MD-46b	Leucogranite Sheet	11.7		7.8			
MD-45	Amphibolite	13.0		10.4	9.6a		
MD-45a	Leucocratic Sheet	12.7	11.2	10.2	9.0b		
MD-44	Calc-Silicate	12.9		10.4			
MD-44a	Leucocratic Sheet	12.1	10.4				
MD-43	Leucocratic Sheet	12.3	11.5				
MD-43a	Calc-Silicate	13.8					
MD-42	Amphibolite		9.1	6.8	6.3a		
NF-3	Amphibolite	12.3		10.5			

TABLE 4.1 (Continued)

Sample*	Rock Type	Qz†	Fs†	Gar§	Other	Cc# $\delta^{18}O$	Cc# $\delta^{13}C$
Marble-Rich Zone							
MD-57	Quartzite	13.6					
MD-57a	Semi-Pelitic Gneiss	13.9	13.3				
MD-57b	Psammitic Gneiss	14.0					
MD-58	Pelitic Gneiss	14.5	13.7		9.6b		
MD-58a	Leucogranite Sheet	14.3	13.9				
MD-58b	Psammitic Gneiss	15.1	13.7				
MD-58c	Marble					21.0	−1.9
MD-58d	Calc-Silicate	12.4			12.5p		
MD-58e	Marble					18.2	0.9
MD-58f	Leucogranite Sheet	15.0	13.3				
MD-58g	Semi-Pelitic Gneiss	15.3		13.2	11.8b		
MD-58h	Quartzite	13.6					
MD-56a	Leucogranite Sheet	18.8	17.0				
MD-56b	Marble					20.6	0.3
MD-56c	Leucogranite Dike	17.4	16.8				
MD-55	Pelitic Gneiss	13.9	13.2	12.5			
MD-54	Marble					21.7	−0.4
MD-53	Quartzite	16.1					
MD-53a	Pelitic Gneiss	15.1	13.9	12.4			
MD-53b	Marble					19.3	1.9
MD-51	Calc-Silicate	15.7				15.2	−4.0
MD-51W	Marble: Whole Rock					21.5	2.3
MD-51C	Marble: Coarse Fraction					22.0	2.4
MD-51M	Marble: Matrix Fraction					21.5	2.2
MD-51a	Calc-Silicate	15.9				15.5	−5.2
MD-51b	Leucocratic Sheet	16.3	14.2				
MD-51c	Marble					15.9	2.0
MD-51d	Pelitic Gneiss	16.2	15.3	13.5			
Leucogranite-Rich Zone							
MD-59	Leucogranite Dike	11.1	10.3				
MD-60a	Leucogranite Sheet	12.8	10.7				
MD-63	Pelitic Gneiss	13.1	11.7				
MD-63a	Amphibolite		11.7	10.3	10.1a		
MD-66	Leucogranite Sheet	11.8	11.1				
MD-68	Leucogranite Sheet	12.9	11.2				
MD-70	Leucogranite Sheet	12.4	11.4				
MD-70a	Amphibolite	13.3	11.6	10.5	9.0b		
MD-71a	Pelitic Gneiss	12.3		9.8			
MD-73	Leucogranite	11.9	10.6				
MD-74a	Marble					12.4	0.2
MD-74b	Calc-Silicate					9.6	−6.4
MD-77a	Pelitic Gneiss	11.9		9.6			
MD-78	Pelitic Gneiss	13.0		9.8			
MD-80a	Pelitic Gneiss	12.3		10.0			
MD-81	Leucogranite	11.9	10.6				

TABLE 4.1 (Continued)

Sample*	Rock Type	Qz†	Fs†	Gar§	Other	Cc# $\delta^{18}O$	Cc# $\delta^{13}C$
South Fosthall Pluton							
GH-380	Leucogranite	12.2	10.5				
GH-381	Leucogranite	12.5		9.2			
GH-389	Leucogranite	12.6	10.8				
GH-397	Leucogranite	12.5	10.5				
GH-401	Leucogranite	11.9	10.1				
GH-642	Leucogranite	11.8	10.1				

Note: Mineral separates were hand-picked under the microscope. Some quartz separates were treated with HF to remove impurities. Oxygen was liberated from quartz and feldspar by reaction with F_2 in Ni reaction vessels at 550 °C, converted to CO_2, and analyzed on a Finnegan MAT 252 mass spectrometer (Taylor and Epstein, 1962).

*Numbers refer to samples archived at the Division of Geological and Planetary Sciences, California Institute of Technology, Pasadena, California. Data are from sample localities and traverses shown on Figure 4.1.

†The oxygen isotope data for whole rocks (WR), quartz (Qz), feldspar (Fs), almandine garnet (Gar) and calcite (Cc) are reported in the δ notation, where δ is the relative difference in parts per thousand in $^{18}O/^{16}O$ between the sample and a standard. The standard is V-SMOW (Vienna standard mean ocean water). NBS-28 has a $\delta^{18}O$ = +9.60 on this scale. Replicate analyses of samples and the Caltech rose quartz working standard ($\delta^{18}O$ = +8.45) have an analytical error of ± 0.2‰.

§The garnet oxygen isotope data were also acquired by a fluorination procedure, but one using the Caltech oxygen isotope laser extraction system, instead of externally heated Ni reaction vessels. Caltech rose quartz ($\delta^{18}O$ = +8.45 ± 0.10; N = 25) and Hualalai olivine ($\delta^{18}O$ = +5.37 ± 0.10; N = 42) laboratory standards were analyzed each operating day during collection of garnet $^{18}O/^{16}O$ data. Duplicate laser analyses of randomly chosen, hand picked, inclusion-free grains of crushed garnet (typically two to three 0.5-1.0 mg grains were analyzed in each run) display an analytical uncertainty of ≤ 0.3‰. Comparison of laser and conventional quartz analyses agreed to within ± 0.2 ‰.

#The calcite stable isotope data were carried out using the standard analytical procedure involving reaction with H_3PO_4 (McCrea, 1950), and corrected using the fractionation factor of 1.01008 (Sharma and Clayton, 1965).

The symbols a and b in the column labeled "Other" represent, respectively, analyses of amphibole (hornblende) and biotite.

TABLE 4.2. $^{18}O/^{16}O$ DATA ON MINERALS FROM THE ZONE OF IMBRICATE THRUSTING ASSOCIATED WITH THE MONASHEE DECOLLEMENT

Sample*	Rock Type	Qz†	Fs†	Other	Cc $\delta^{18}O$	Cc $\delta^{13}C$
Lower Plate Basement						
MD-1	Basement Gneiss	13.4	2.7			
Zone of Imbricate Thrusting						
MD-2	Quartzite	11.9				
MD-3	Pelitic Schist	13.9				
MD-4	Quartzite	12.1				
MD-5	Pelitic Schist	13.1	4.2			
MD-6	Pelitic Schist	12.3	8.0			
MD-6a	Aluminous Schist	12.9				
MD-7	Basement Gneiss	12.9				
MD-14	Quartzite	13.5				
Thrust						
MD-17	Calc-Silicate				15.7	−7.6
MD-17a	Leucogranite Dike	14.4	12.9			
MD-17b	Quartz Vein	14.2				
Thrust						
MD-19b	Leucogranite Dike	13.2	4.4			
MD-20a	Quartz Vein	13.5				
Thrust						
MD-24	Basement Gneiss	11.7	10.2			
Thrust						
MD-26a	Calc-Silicate	16.4			15.4	−4.9
MD-27	Pelitic Schist	11.0	10.0			
MD-29	Quartzite	14.9				
MD-29a	Pelitic Schist	14.6	−0.9	4.4b		
MD-29b	Amphibolite		5.5	8.6g 8.8a		
Thrust						
MD-30	Quartzite w/Late Calcite Veins	14.7			12.8	−1.7
MD-31	Pelitic Schist w/Late Calcite	10.2	−3.8		−2.1	−7.9
MD-32	Pelitic Schist	12.1		9.3g		

Note: See footnote to Table 4.1 for explanation of terms and symbols; note that g in the column labelled "other" represents garnet (almandine).

faulting (Holk and Taylor, 1994b), the quartz-feldspar $^{18}O/^{16}O$ fractionations (*i.e.*, $\Delta_{Q\text{-}F}$ values) from all igneous and metamorphic lithologies within this zone are typical of granitic plutons throughout the world ($\Delta_{Q\text{-}F}$ = 1.5 ± 0.6‰, N = 28). Using the calibrations of Clayton et al. (1972) and Clayton and Kieffer (1991), the above data imply apparent equilibrium temperatures of 550-650 °C and a coexisting aqueous fluid with $\delta^{18}O$ ≈ +11.0, which is at least 20‰ higher than the coeval meteoric surface water associated with detachment faulting (Magaritz and Taylor, 1986).

Amphibolite quartz is isotopically variable, but trends are systematic (Figure 4.5 and 4.6); relatively low $\delta^{18}O$ values (+9.7) occur in two thick layers (10-40 m) of undeformed amphibolite within a narrow interval in the upper part of the amphibolite-rich zone. Elsewhere in this zone, homogenized quartz $\delta^{18}O$ values of +12.8 ± 0.6‰ (N = 4) are observed in the numerous thin (< 1m) amphibolite layers; in contrast to the thick amphibolites these typically contain abundant quartzo-feldspathic veins or melt segregations. Quartz in metapelitic paragneiss directly adjacent to the thick amphibolites is 0.5-1.5‰ lower in ^{18}O than the characteristic homogenized quartz found in all lithologies throughout the rest of the 900-m-thick amphibolite-rich zone (Figure 4.4); this indicates local $^{18}O/^{16}O$ exchange involving these amphibolites, aqueous fluid, and the adjacent rocks.

Quartz $\delta^{18}O$ values in the marble-rich zone (Figures 4.4, 4.5, and 4.6) are higher and more variable than in any other part of the allochthon: +13.9 to +16.2 (N = 8) for metapelite, +13.6 to +16.2 (N = 3) for quartzite, +12.4 to +15.9 (N = 3) for calc-silicate, and +14.3 to +18.8 (N = 5) for leucogranite. Quartz-feldspar fractionations are generally less than 1‰ and indicative of disequilibrium, as they give unrealistically high temperatures for these rocks. These relict high $\delta^{18}O$ values and anomalous $\Delta_{Q\text{-}F}$ values are readily attributable to exchange with the intercalated ^{18}O-rich marble layers (calcite $\delta^{18}O$ = +15.9-+22.0, N = 9), whose protoliths probably had $\delta^{18}O$ = +20 to +28 (Veizer and Hoefs, 1976). This lack of ^{18}O homogenization was not unexpected, because ductile, pure marble layers such as these are typically impermeable to metamorphic pore waters (e.g., Rye et al., 1976).

The Δ_{Q-F} values in the imbricate thrust zone (Figure 4.4) display an enormous range (1.0‰ to 14.0‰), indicating that a meteoric-hydrothermal event affected these highly fractured rocks; this event is probably correlative with analogous phenomena observed nearby in the vicinity of detachment faults, and discussed in detail in Chapter 5. Concordant leucogranite sheets are totally absent in the imbricate thrust zone, and quartz $\delta^{18}O$ values of metapelite, quartzite, gneiss, and calc-silicate display a wide range, +10.2 to +14.6 (N = 7), +11.9 to +15.0 (N = 7), +11.0 to +13.4 (N = 4), and +16.3, respectively. Although some of these lower $\delta^{18}O$ values can be attributed to the late-stage meteoric-hydrothermal activity, all quartz $\delta^{18}O$ values significantly higher than +12.3 must represent relict metasedimentary values.

The only leucogranitic materials in the imbricate thrust zone are rare, late-stage dikes that have undergone meteoric-hydrothermal ^{18}O-depletion (with feldspar $\delta^{18}O$ as low as –3.8); these post-kinematic leucogranite magmas must have been more ^{18}O-rich than the typical concordant leucogranites in the allochthon, because they retain quartz $\delta^{18}O$ values as high as +13.2 to +14.4 (N = 3).

In contrast to quartz, coexisting almandine garnet is isotopically variable in all parts of the allochthon except the leucogranite-rich zone, where garnet $\delta^{18}O = +9.8 \pm 0.5$ (N = 8) in all lithologies (Figure 4.6). In samples from homogeneous parts of the amphibolite-rich zone, garnet $\delta^{18}O = +9.5 \pm 1.0$‰ (N = 13), whereas coexisting quartz is more uniform at $\delta^{18}O = +12.6 \pm 0.5$‰. Garnets from metapelites in the marble-rich zone have

$\delta^{18}O$ = +12.4 to +13.5 (N = 4). Quartz-garnet fractionations ($\Delta_{Q\text{-}G}$ values) are relatively constant at 2.7 ± 0.4‰ (N = 7) in all lithologies of the leucogranite-rich zone. Using the calibration of Javoy (1977), these values indicate equilibrium at 700 ± 100 °C, compatible with the thermochronologic estimates of Carr (1995). Inasmuch as all these rocks were metamorphosed at similar grade, the variable $\Delta_{Q\text{-}G}$ values in the amphibolite-rich (1.8-4.1‰) and marble-rich zones (1.4-2.7‰) clearly indicate isotopic disequilibrium.

Oxygen diffusion in garnet is slow (Fortier and Gilletti, 1989), and it is well known that during prograde metamorphism, garnet oxygen is often effectively isolated from fluid exchange processes that affect other silicate minerals (*e.g.*, Chamberlain and Conrad, 1991). Thus, garnet can record information about pre-existing whole-rock $^{18}O/^{16}O$ heterogeneity, or about $\delta^{18}O$ changes in the local environment around the growing garnet crystals. Also, because garnets can preserve evidence of an earlier, low-temperature stage, $\Delta_{Q\text{-}G}$ values can be larger than those set at peak metamorphic grade. Small $\Delta_{Q\text{-}G}$ values (1.4-2.1‰) in two metapelites from the high-^{18}O marble-rich zone (Figure 4.6) thus imply that garnet growth occurred before these rocks were partially homogenized and depleted in ^{18}O. In contrast, large $\Delta_{Q\text{-}G}$ values (3.8-4.0‰) in metapelite and leucogranite at the contact of a thick amphibolite layer are more equivocal. It is likely that these rocks underwent incipient homogenization and ^{18}O enrichment after the garnets acquired the low $\delta^{18}O$ signature of the adjacent mafic-volcanic(?) protolith; however, the $\Delta_{Q\text{-}G}$ values could also indicate a lower-temperature prehistory. In the garnets of the leucogranite-rich zone, all such ^{18}O evidence of prograde metamorphic or lithologic prehistory has been obliterated.

Biotite from quartzofeldspathic gneiss, metapelite, amphibolite, and leucogranite from the amphibolite-rich zone has a 5.6‰ range in $^{18}O/^{16}O$ ($\delta^{18}O$ = +4.1 to +9.7; N = 8). Quartz-biotite oxygen isotope fractionations (Figure 4.7) indicate disequilibrium

Figure 4.5 -- Plot of $\delta^{18}O$ quartz versus coexisting $\delta^{18}O$ feldspar from the Selkirk Allocthon, the Monashee Decollement, and the Columbia River fault for samples collected from the area shown in Figure 4.1. The dashed 45° diagonal line at $\Delta = 1.5$ represents a typical quartz-feldspar $^{18}O/^{16}O$ fractionation observed in plutonic granitic rocks. Coexisting quartz and feldspar from the Monashee decollement define a steep array in δ-δ space, indicative of extreme isotopic disequilibrium imposed on the system during a short-lived (~ 10^5-10^6 yr) meteoric-hydrothermal ($\delta^{18}O_{water} \leq -11.0$) event at $T < 350$ °C. The shallower slope of the array defined by data from the Columbia River fault suggests a longer-lived and/or higher temperature meteoric-hydrothermal event than that affecting the Monashee Decollement. Rocks of the middle crustal zone appear to be in apparent isotopic equilibrium at magmatic temperatures. Data from the marble-rich zone are 1-3 ‰ heavier in ^{18}O than the isotopically homogenized rocks from other parts of the middle crustal zone, a result of local exchange between H_2O-rich fluid and isotopically heavy impermeable marble. Note that the isotopic composition of the leucogranite sample from the amphibolite-rich outcrop is within the range of homogeneous values. The solid dots = leucogranites, solid squares = pelites, open dots = amphibolites, open squares = Monashee decollement, open diamonds = Columbia River fault. The arrow on the y-axis indicates a sample with $\delta^{18}O$ quartz = +4.6. The data point labelled 834 is a somewhat ambiguous sample; it lies near the trace of the Monashee decollement, but it actually lies on the projection of the Columbia River fault along the west shore of Arrow Lake.

Figure 4.5 Thor-Odin Quartz vs. Feldspar

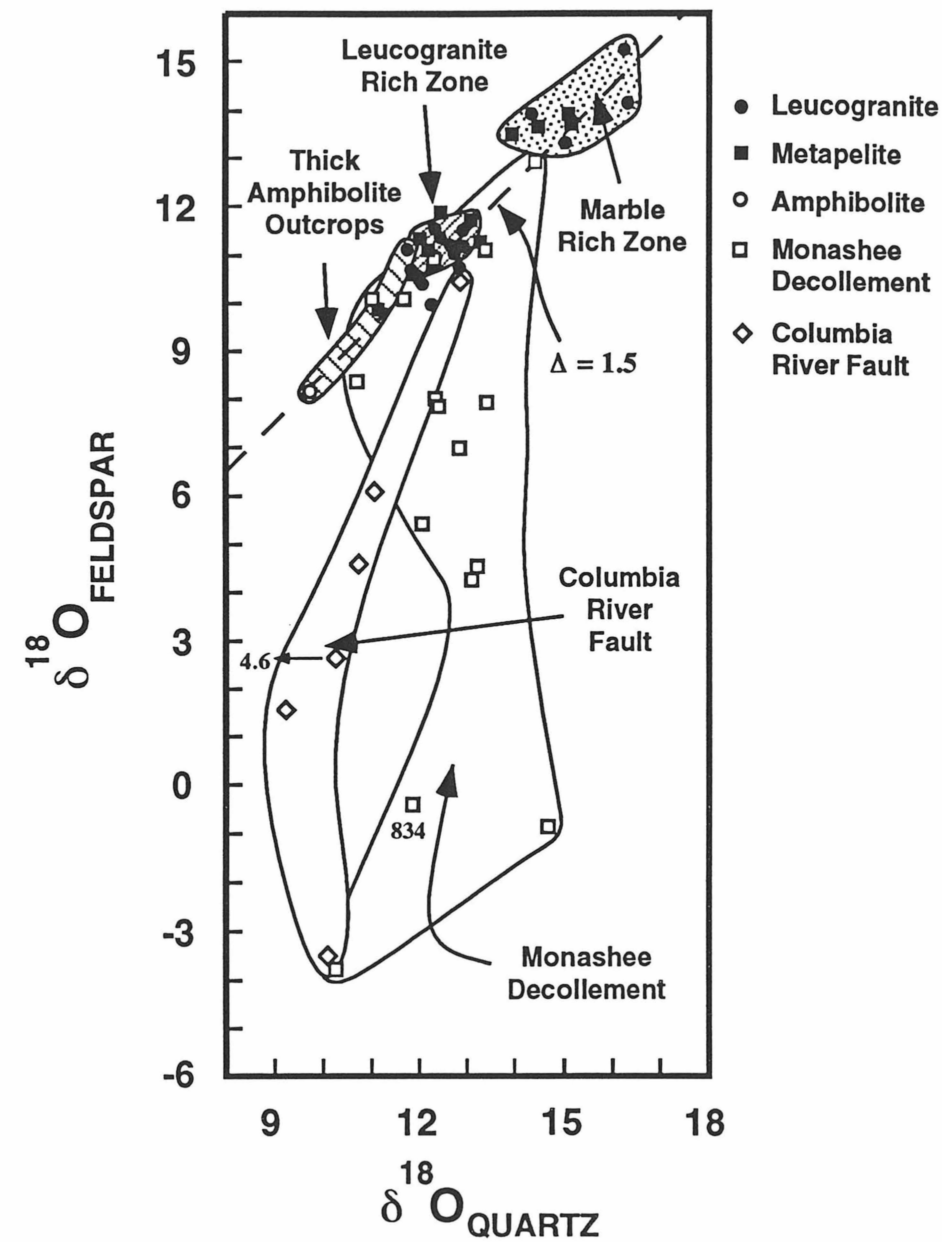

Figure 4.6 -- $\delta^{18}O$ quartz vs. coexisting $\delta^{18}O$ garnet (almandine) from Thor-Odin complex. Dashed line at $\Delta = 2.5‰$ represents equilibrium at 750 °C (Javoy, 1977). The heterogeneous $\Delta_{Q\text{-}G}$ values of 1.8-4.1‰ within amphibolite-rich zone, the large $\Delta_{Q\text{-}G} \geq 2.5‰$ in low-^{18}O thick amphibolite outcrops, and the small $\Delta_{Q\text{-}G} \leq 2.5‰$ within high-^{18}O marble-rich zone all indicate systematic $^{18}O/^{16}O$ disequilibrium effects in which garnet has preserved evidence of pre-metamorphic $^{18}O/^{16}O$ heterogeneity (note that this statement does not apply to garnets from the thoroughly homogenized leucogranite-rich zone, which display uniform $\Delta_{Q\text{-}G} \sim 2.7‰$). The symbols are the same as ones listed in the caption of Figure 4.5.

Figure 4.6 Thor-Odin Quartz vs. Garnet

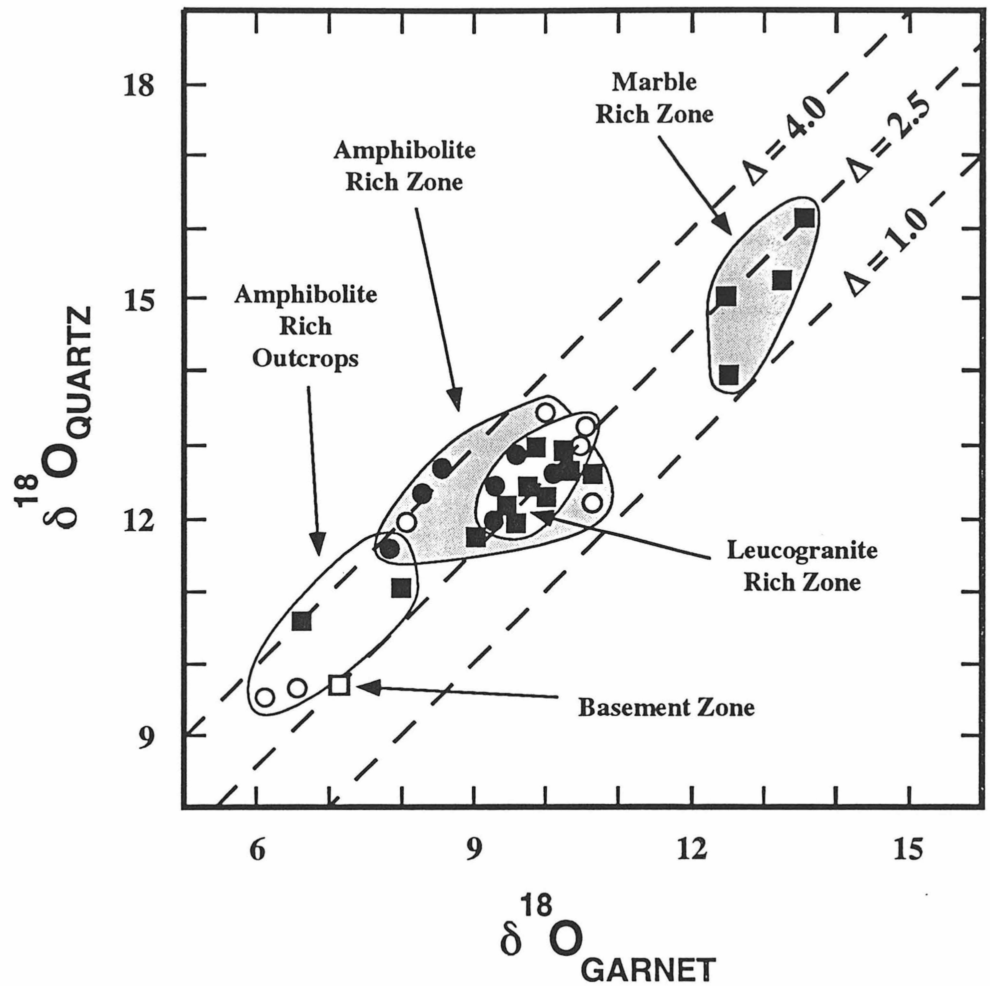

($\Delta_{Q\text{-}B}$ = 3.7‰ to 8.7‰); this is most likely the product of late-stage chloritization during the meteoric-hydrothermal event that affected the imbricate thrust zone and the lower parts of the amphibolite-rich zone. It has been shown that biotite is extremely susceptible to these late-stage effects (Criss and Taylor, 1983). Biotite from a thick amphibolite (Figure 4.7) has $\delta^{18}O$ = +3.1 and $\Delta_{Q\text{-}B}$ = 6.6‰, a fractionation much larger than that expected at the high temperatures experienced by this terrane; this indicates that even these thick amphibolites were affected by the meteoric event. A metapelite from the imbricate thrust zone has $\Delta_{Q\text{-}B}$ = 10.2‰. This is labelled Monashee decollement on Figure 4.7; it is noteworthy that this sample has feldspar $\delta^{18}O$ = –0.9, and it also exhibits the largest observed quartz-biotite isotopic disequilibrium yet seen. Quartz-biotite fractionations observed in metapelites from the marble-rich zone ($\delta^{18}O$ = +9.6 and +11.8) and an amphibolite from the leucogranite-rich zone ($\delta^{18}O$ = +9.0) range from 3.5‰ to 4.9‰ (N = 3); these fractionations are typical of most high grade metamorphic rocks (Garlick and Epstein, 1967; Satir and Friedrichsen, 1986).

Most $\delta^{18}O$ values of amphibole from amphibolite of the amphibolite-rich and leucogranite-rich zones range from +8.1 to +10.7 (N = 5). Amphibole-quartz $^{18}O/^{16}O$ fractionations for these amphibolites are 2.7‰ to 3.6‰, indicating equilibrium at 650-750 °C using the fractionation factors of Javoy (1977). However, it should be noted that one amphibolite from this zone has amphibole $\delta^{18}O$ = –4.3; the feldspar $\delta^{18}O$ from this rock is –0.8, clearly indicating that the feldspar and the amphibole were both strongly affected by the meteoric event affecting areas near the imbricate thrust zone. A quartzofeldspathic gneiss 100 m from this ^{18}O-depleted amphibolite has amphibole $\delta^{18}O$ = +7.5, but the $\Delta_{Q\text{-}A}$ of this sample is 5.8‰. Amphiboles from the thick amphibolite layers have $\delta^{18}O$ = +6.3 and +7.8 and one has a $\Delta_{Q\text{-}A}$ value of 1.9‰.

Figure 4.7 -- $\delta^{18}O$ quartz vs. coexisting $\delta^{18}O$ biotite from Thor-Odin complex. Data from this study (solid dots and squares) are compared with data from lower grade pelites and quartzofeldspathic metasediments of the Windermere Supergroup at Mica Creek (Bowman and Ghent, 1986) and the Esplanade Range (O'Neil and Ghent, 1975), as shown by the crosses and by the shaded envelope. Dashed lines at $\Delta = 4‰$ and $\Delta = 6‰$ represent equilibrium at 625 °C and 475 °C, respectively (Javoy, 1977). The lower grade Windermere assemblages appear to be in approximate isotopic equilibrium at plausible metamorphic temperatures; they also display at least a 6‰ variation in bulk $\delta^{18}O$; this indicates that the stratigraphically equivalent amphibolite-rich zone of the Selkirk Allochthon had a similar degree of ^{18}O heterogeneity prior to Paleocene anatexis. Large $^{18}O/^{16}O$ fractionations within the imbricate thrust zone and in the amphibolite-rich zone indicate late-stage exchange with hot meteoric waters. The large $\Delta_{Q\text{-}B}$ (6.6‰) from the thick amphibolite outcrop probably is the result of infiltration of meteoric waters as much as 700 m into the hanging wall of the imbricate thrust zone of the Monashee decollement.

Figure 4.8 -- $\delta^{18}O$ quartz vs. coexisting $\delta^{18}O$ amphibole from Thor-Odin complex. Data from this study are compared with data from lower-grade rocks of the Windermere Supergroup at the Esplanade Range (O'Neil and Ghent, 1975). Dashed lines at $\Delta = 3‰$ and $\Delta = 5‰$ represent equilibrium at 700 °C and 500 °C, respectively (Javoy, 1977). Most samples seem to be in $^{18}O/^{16}O$ equilibrium at their inferred peak metamorphic temperatures. The large $\Delta_{Q\text{-}A}$ (5.8‰) and the presence of heavily fractured and chloritized amphibole in the quartzofeldspathic gneiss sample suggest that isotopic disequilibrium is the product of meteoric water/rock interaction.

Figure 4.7 Thor-Odin Quartz vs. Biotite

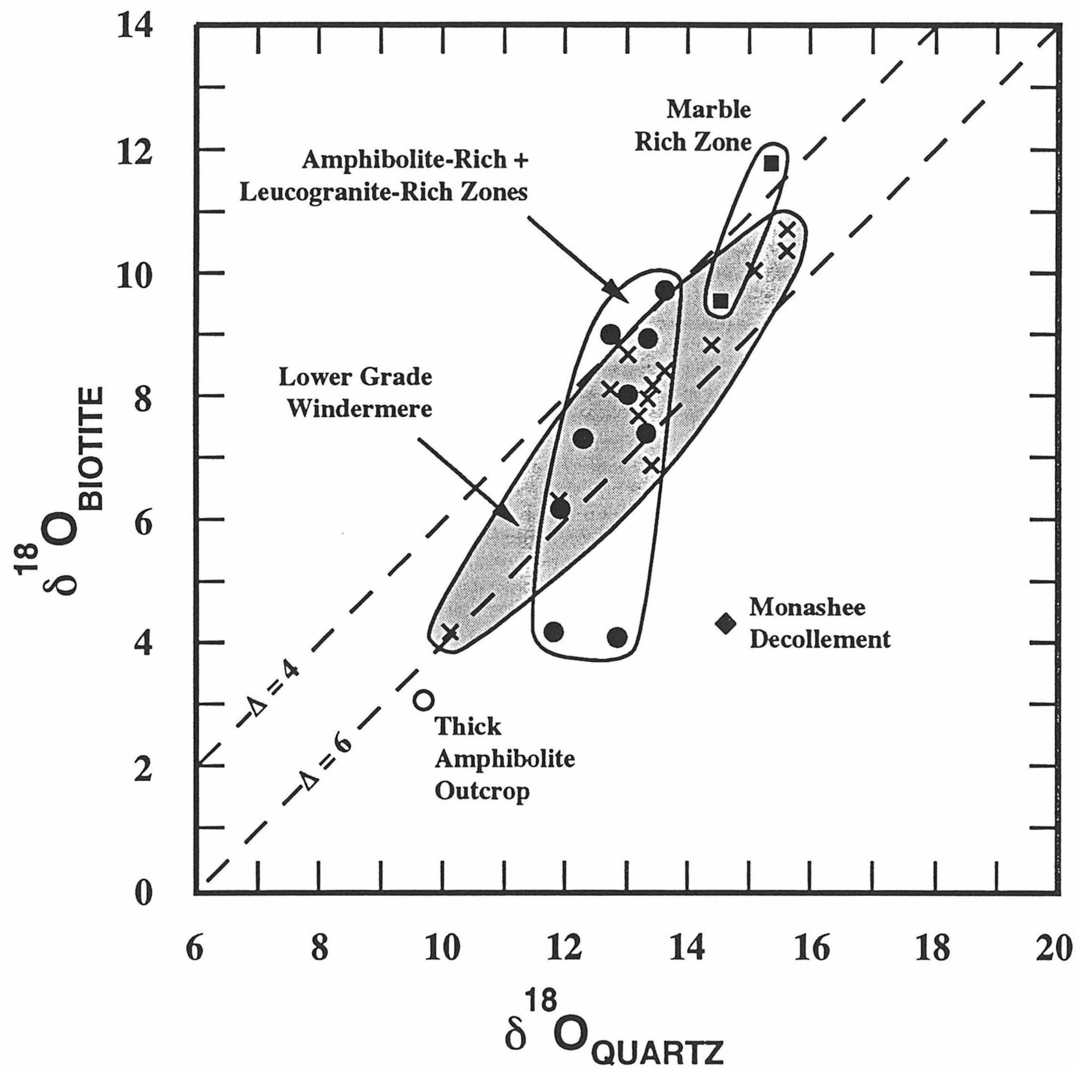

Figure 4.8 Thor-Odin Quartz vs. Amphibole

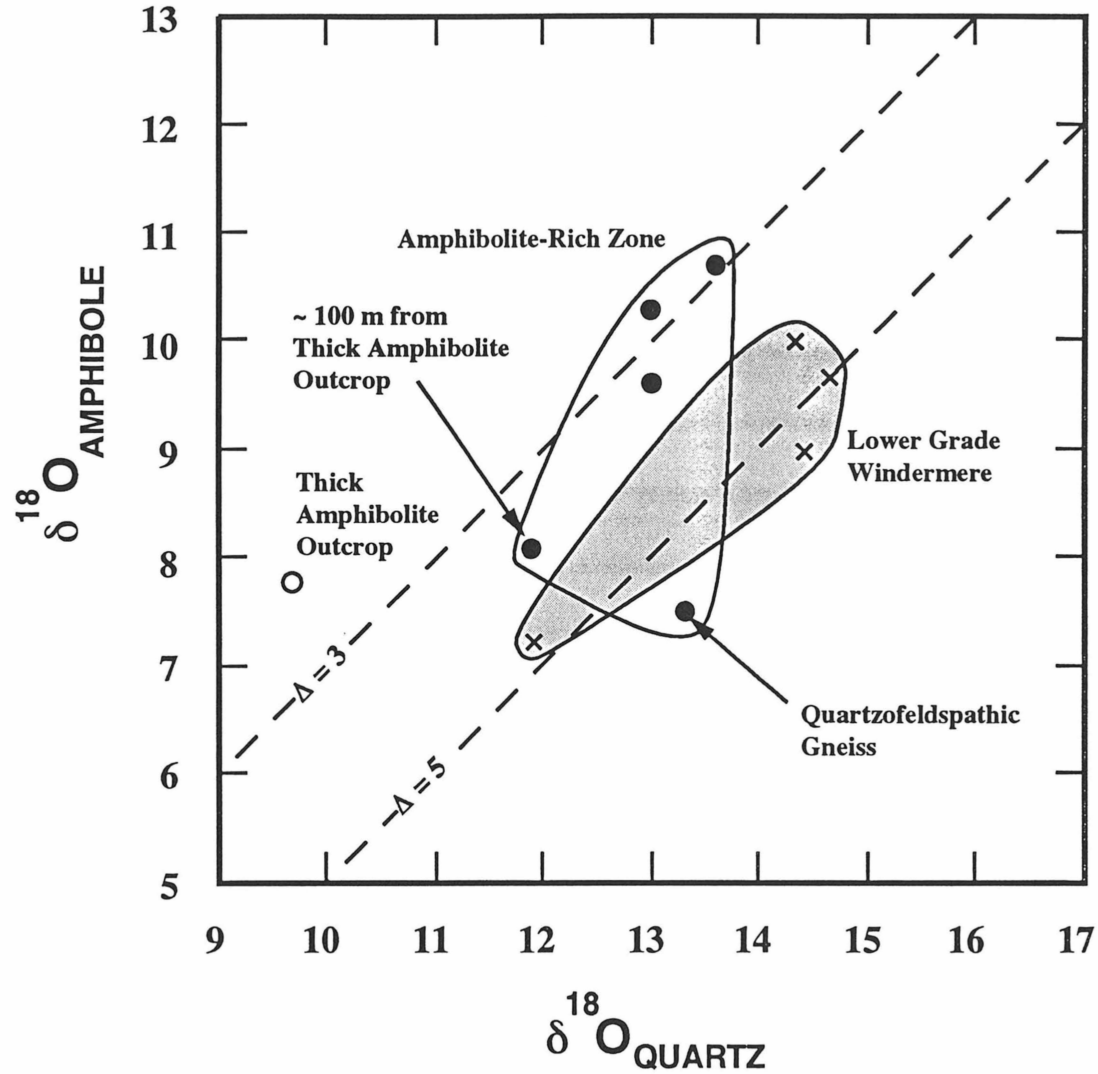

Stable isotope analyses of marble and calc-silicate from the Selkirk Allochthon exhibit systematic variations indicative of H_2O-driven decarbonation. Zoisite-bearing calc-silicates from the imbricate thrust zone, the amphibolite-rich zone, and the marble-rich zone are very uniform in ^{18}O ($\delta^{18}O = +15.4 \pm 0.2$; N = 5) and variable in ^{13}C ($\delta^{13}C =$ –3.5 to –7.6); this indicates decarbonation in equilibrium with a fluid of constant oxygen isotope composition. Calcite from marble of the marble-rich zone has $\delta^{18}O = +15.9$ to +22.0 (N = 8) and $\delta^{13}C = -1.9$ to +2.4; these values indicate that these marbles may have exchanged $^{18}O/^{16}O$ with aqueous fluids with limited decarbonation. One marble from the amphibolite-rich zone has $\delta^{18}O = +18.8$ and $\delta^{13}C = +8.5$; this high ^{13}C marble is typical of carbonates of Late Precambrian age (Knoll et al., 1986; Wickham and Peters, 1993) and rocks such as these are widespread in the Windermere sequence in southeastern British Columbia (Ghent and O'Neil, 1985). One marble from the leucogranite-rich zone has $\delta^{18}O = +12.4$ and $\delta^{13}C = +0.2$; this indicates complete $^{18}O/^{16}O$ homogenization of this leucogranite-rich zone. Calc-silicate collected within a centimeter of this homogenized marble has $\delta^{18}O = +9.6$ and $\delta^{13}C = -6.4$; the low-^{18}O and low-^{13}C calc-silicate implies Rayleigh fractionation of oxygen and carbon during decarbonation of this calc-silicate at low fluid/rock ratio (*e.g.*, Valley, 1986).

4.6 $^{18}O/^{16}O$ Homogenization of the Selkirk Allochthon During Anatexis

The profound $^{18}O/^{16}O$ homogeneity of the Thor-Odin mid-crustal layer could be due to (1) initial protolith homogeneity, (2) influx and exchange with large amounts of external oxygen-bearing fluids, and/or (3) an internal closed-system homogenization process involving multiple stages of $^{18}O/^{16}O$ exchange involving leucogranite melt, internally-derived aqueous fluid, and unmelted rock. Mechanism (1) clearly cannot represent a general explanation, because of the known $^{18}O/^{16}O$ heterogeneity observed in similar metasedimentary sections elsewhere on Earth, particularly noting the extreme $\delta^{18}O$ values exhibited by protoliths of amphibolite ($\delta^{18}O \sim +6$) and marble ($\delta^{18}O \sim +25$-30). In the leucogranite-rich and amphibolite-rich zones, quartz $\delta^{18}O$ values in calc-silicates and thin amphibolites are almost as homogeneous as those in the intercalated leucogranites and metapelites. Note that mechanism (1) also requires that the Proterozoic and Paleozoic sections by coincidence both start out with exactly the same, uniform $\delta^{18}O$ values, and this can be refuted because quartz $\delta^{18}O = +12.7$ to $+15.6$ ($N = 14$) in analogous (but lower grade) Late Proterozoic metapelites 180 km to the north (Bowman and Ghent, 1986; O'Neil and Ghent, 1975); those rocks are stratigraphically correlative with metapelites from the Thor-Odin amphibolite-rich zone (where quartz $\delta^{18}O = +12.5 \pm 0.5$, $N = 6$). Our own data set provides evidence of original $^{18}O/^{16}O$ heterogeneity. Zones that were a priori expected to be relatively impermeable or refractory (the marble-rich zone, the thick amphibolites, and the garnets) are in fact the only parts of the allochthon that display marked $^{18}O/^{16}O$ heterogeneity. Also, the $\delta^{18}O$ heterogeneity in quartz from the deepest and most deformed allochthonous assemblages (*i.e.*, imbricate thrust zone) is similar to that displayed by garnets coexisting with homogeneous quartz higher in the section; this implies an original whole-rock $\delta^{18}O$ variation of at least 4.5‰.

We can also rule out mechanism (2), unless the hypothesized external H_2O by coincidence already had a $\delta^{18}O$ in equilibrium with the bulk average material of the allochthon. Excluding the marble-rich zone, a rough material-balance calculation utilizing $^{18}O/^{16}O$ data on analogous and/or correlative lower-grade protoliths (Table 4.3) shows that there cannot have been any more than a 0.5-1.0‰ lowering in the bulk $\delta^{18}O$ of the metasedimentary section (by dehydration?). This contrasts with other localities where it has been shown that the bulk crust was strongly depleted in ^{18}O by exchange with

TABLE 4.3 CALCULATION OF BULK $\delta^{18}O$ OF THE SOUTHERN THOR-ODIN COMPLEX

		Horsethief Creek Group	Hamill Group	Mohican – Badshot Formations	Lardeau Group
Lithology	$\delta^{18}O$	amphibolite-rich zone		marble-rich zone	leucogranite-rich zone
Arkosic Grit	+12				35
Pelite	+16	52	34	59	30
Quartzite	+11	16	66	14	16
Amphibolite	+9	19			17
Marble	+22	3		27	2
Bulk $\delta^{18}O$		+12.4	+12.7	+16.9	+12.6

Note: Lithologic proportions are from the following sources, Horsethief Creek Group – Pell and Simony (1986), Hamill Group and Mohican-Badshot Formations – Fyles and Eastwood (1962), and Lardeau Group – Fyles (1964).

See Table 3.2 for information about the $\delta^{18}O$ values used in this calculation.

externally derived aqueous fluids during metamorphism (*e.g.*, Shieh and Schwarcz, 1974; Wickham and Taylor, 1985; Peters and Wickham, 1995).

The portions of the core complex that are most (least) homogenized in $^{18}O/^{16}O$ are either those that are most (least) leucogranite-rich or the ones that have undergone the most (least) extensive anatexis; this implies that the anatectic melts themselves facilitated $^{18}O/^{16}O$ exchange with the unmelted rocks, and/or that they served as a source of aqueous fluids that promoted such exchange. Thus, the multi-stage exchange model is preferred because: (1) Most non-leucogranite lithologies have mineral $\delta^{18}O$ values identical to those of the leucogranites. (2) Local $^{18}O/^{16}O$ variability in the relatively impermeable parts of the section (*e.g.*, marbles and thick amphibolite layers) suggests a limited amount of aqueous fluid present in the system at any one time (*i.e.*, an essentially rock-buffered system).

It is possible, but unlikely, that the protolith rocks of the mid-crustal section were initially homogeneous in $^{18}O/^{16}O$. The quartz $\delta^{18}O$ values from lower grade rocks belonging to the Windermere Supergroup do not display the same degree of oxygen isotope homogeneity (Bowman and Ghent, 1986; O'Neil and Ghent, 1975) as that observed in the stratigraphically equivalent higher-grade rocks of the Selkirk Allochthon at the Thor-Odin complex (*e.g.*, compare Figure 4.4 with Figures 4.7 and 4.8). Nonetheless, Bowman and Ghent (1986) interpreted these data as being the product of a protolith that was fairly uniform in ^{18}O. Note that the oxygen isotope homogeneity that does exist in these staurolite to sillimanite grade rocks in the footwall of the Columbia River fault at Mica Creek might also be interpreted to be the product of large-scale exchange with metamorphic pore fluid having a fairly uniform $\delta^{18}O \sim +11.0$ at $T = 500$ °C. Also, note that quartz $\delta^{18}O$ values from rocks of similar metamorphic grade in the hanging wall of the Columbia River fault (upper crustal layer) are indeed variable in

$^{18}O/^{16}O$ (Bowman and Ghent, 1986). This is consistent with the metamorphic/magmatic hydrothermal event associated with ^{18}O homogenization and anatexis being restricted to the mid-crustal layer. Furthermore, these data are all from units of approximately the same bulk composition and stratigraphic position, making the conclusion concerning original homogeneity likely to be true for those particular rocks, but not necessarily for the entire section. Based on the available data, it seems inconceivable that the entire Precambrian-to-Cambrian post-rift clastic sequence was initially uniform in $^{18}O/^{16}O$ at the onset of metamorphism. However, this is a sufficiently important problem to justify doing many more $^{18}O/^{16}O$ analyses of lower-grade rocks from these units elsewhere in British Columbia.

The influx of large amounts of externally-derived meteoric-hydrothermal fluids conceivably could be responsible for at least some of the observed oxygen isotope uniformity of the mid-crustal layer. Detachment faults and the upper crustal zone underwent large-scale meteoric-hydrothermal water-rock interaction during the Eocene (Magaritz and Taylor, 1986; Nesbitt and Muehlenbachs, 1989, 1995; Holk and Taylor, 1992, 1994); these effects are also observed at the Monashee decollement. This meteoric event had local impact on the basement and mid-crustal zones along late-stage brittle normal faults associated with the extensional event related to detachment faulting (see Chapter 5). However, meteoric-hydrothermal systems typically produce $^{18}O/^{16}O$ disequilibrium between coexisting quartz and feldspar because such systems rarely reach temperatures of 600 $^{\circ}C$ or more, except within large cumulate gabbro bodies. Also, it has been demonstrated that meteoric water infiltrates no more than a few hundred meters into the lower plate of detachment faults, due to the low permeability of the plastically deforming mylonites (Fricke et al., 1992; Holk and Taylor, 1992). Massive lowering of $\delta^{18}O$ usually accompanies large-scale infiltration of externally-derived magmatic or

Figure 4.9 -- $\delta^{13}C$ and $\delta^{18}O$ of carbonates from the middle crustal layer of the southern Thor-Odin complex. Paleozoic marbles (> 95 % calcite) show a 12 per mil downward shift in ^{18}O ($\delta^{18}O$ = +24.0 to +12.0), but are unchanged in ^{13}C ($\delta^{13}C$ = –0.4 to +2.7). Below the Ladybird-series pluton, calcite from calc-silicates is uniform in ^{18}O ($\delta^{18}O$ = +15.4 ± 0.2), but variable in ^{13}C ($\delta^{13}C$ = –7.6 to +1.2). Zoisite is present in the calc-silicates. The presence of zoisite, and the oxygen isotope uniformity combined with simultaneous large-scale variability in carbon isotopes both strongly imply that large amounts of H_2O-rich fluid drove decarbonation of these calc-silicates. Calc-silicate calcite from above and within the Ladybird-series pluton is not uniform in ^{18}O or ^{13}C ($\delta^{18}O$ = +9.6 to +20.3, $\delta^{13}C$ = –6.4 to +0.3). Late-stage calcite from veins and fractures at the Monashee decollement and above the Ladybird-suite pluton are variable and light in ^{18}O and ^{13}C ($\delta^{18}O$ = –2.1 to +12.8, $\delta^{13}C$ = –8.3 to –1.2). These data suggest contrasting styles of water-rock interaction fixed by position about the pluton. The Ladybird-series pluton may have acted as an impermeable barrier to the downward circulation of meteoric H_2O during detachment faulting along the overlying Columbia River fault. Solid dots = marbles, pluses = late calcite veins, open and solid squares = calcites from calc-silicate rocks, respectively, above and below the pluton.

Figure 4.9 Carbonates

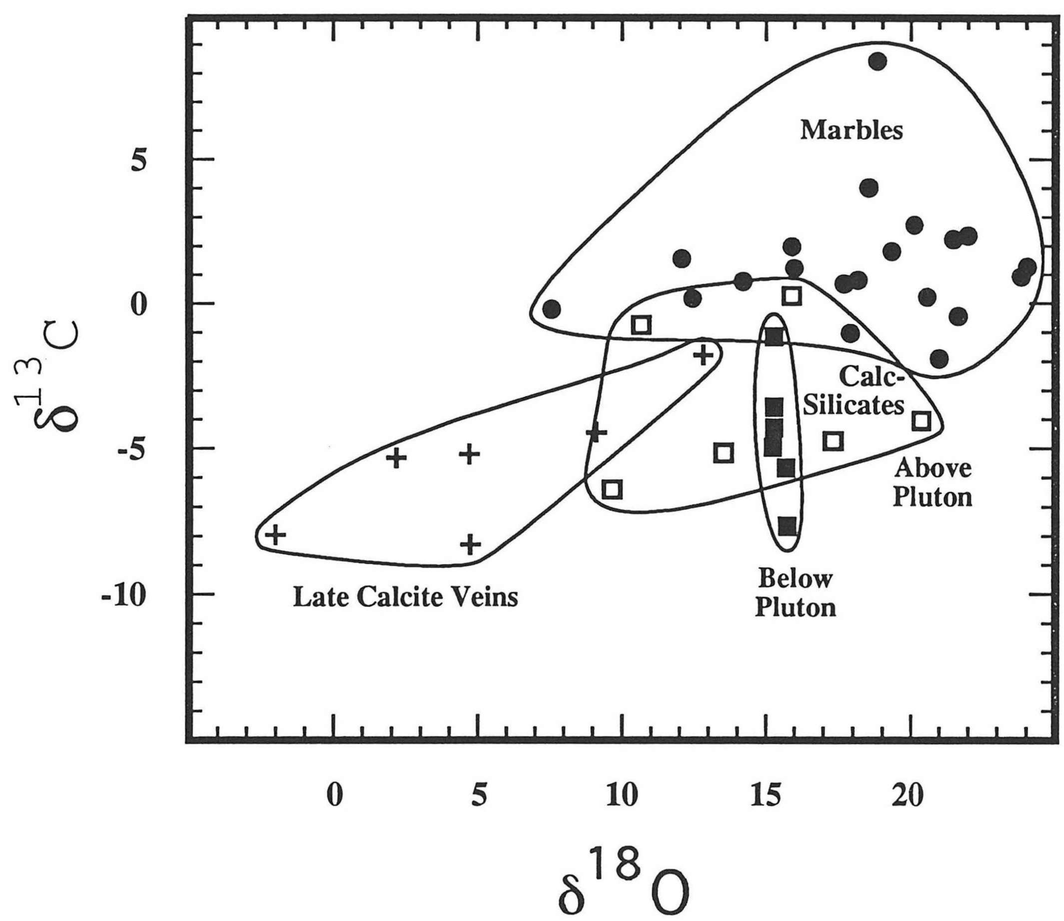

Figure 4.10 -- Plot showing outcrop-scale variations in mineral and whole rock $\delta^{18}O$ at site MD-58 in the marble-rich zone. For the metapelites and leucogranites, $\delta^{18}O$ values of quartz (+14.8; N = 5), feldspar (+13.7; N = 4), and whole rock (+14.2; N = 5) are homogeneous, even across the up to 0.5-m-thick, high-^{18}O marbles ($\delta^{18}O$ = +18.2 and +21.0). The preservation of high $\delta^{18}O$ values in these marbles indicates that they were relatively impermeable to aqueous fluid during anatexis and high-grade metamorphism. Quartz from a calc-silicate layer between the two thick marbles has $\delta^{18}O$ = +12.4, within the range of homogeneous quartz $\delta^{18}O$ found throughout the rest of the Selkirk Allochthon; this is consistent with the highly permeable state of calc-silicate lithologies during prograde metamorphism. Quartz from the quartzite layer is lower in ^{18}O than the other parts of this section; this implies that quartzites of this type may have been less permeable than other lithologies.

Figure 4.10 Marble-Rich Zone Outcrop

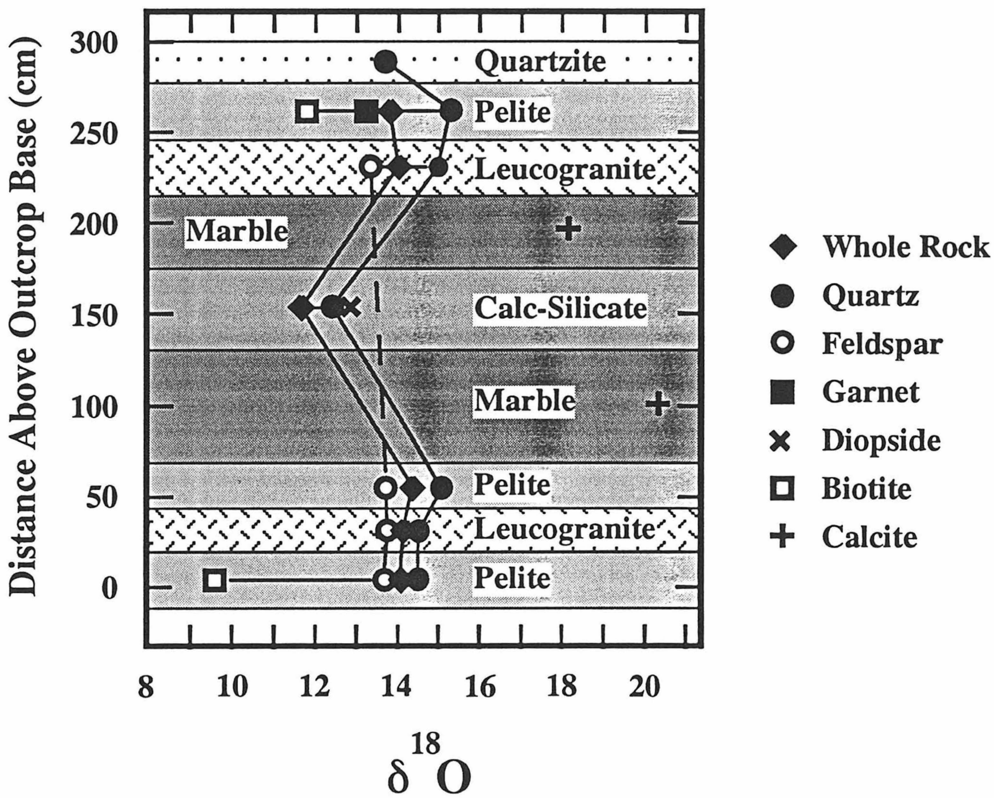

Figure 4.11 -- Distance vs. $\delta^{18}O$ plot comparing quartz and feldspar $\delta^{18}O$ from the Thor-Odin complex with quartz and whole rock $\delta^{18}O$ from the East Humboldt Range, Nevada (data from Wickham and Peters, 1992; Peters and Wickham, 1995). Quartz $\delta^{18}O$ is equally homogeneous for the Thor-Odin middle crust as it is for the upper zone of Lizzies Basin at the East Humboldt Range. The Thor-Odin data become more homogeneous upsection; this contrasts with the greater degree of ^{18}O-heterogeneity in an upward direction at the East Humboldt Range. Beneath the Monashee decollement, the section becomes heterogeneous in ^{18}O; this contrasts with the deepest parts of the East Humboldt Range, a section that is still isotopically homogeneous, but which gradually becomes more depleted in ^{18}O with depth. These systems contrast in that the aqueous fluids at Thor-Odin were apparently supplied internally and homogenization occurred in response to decompression-related anatexis, whereas the aqueous fluids had an external source (from below?) at the East Humboldt Range where water/rock ratios apparently increase downsection. Deep parts of the East Humboldt range section apparently escaped the meteoric-hydrothermal effects that affected the highest parts of that section; this contrasts with the meteoric-hydrothermal effects associated with the Monashee decollement at Thor-Odin. Whole rock $\delta^{18}O$ at the East Humboldt Range is more variable than that of quartz in the Thor-Odin core complex.

Figure 4.11

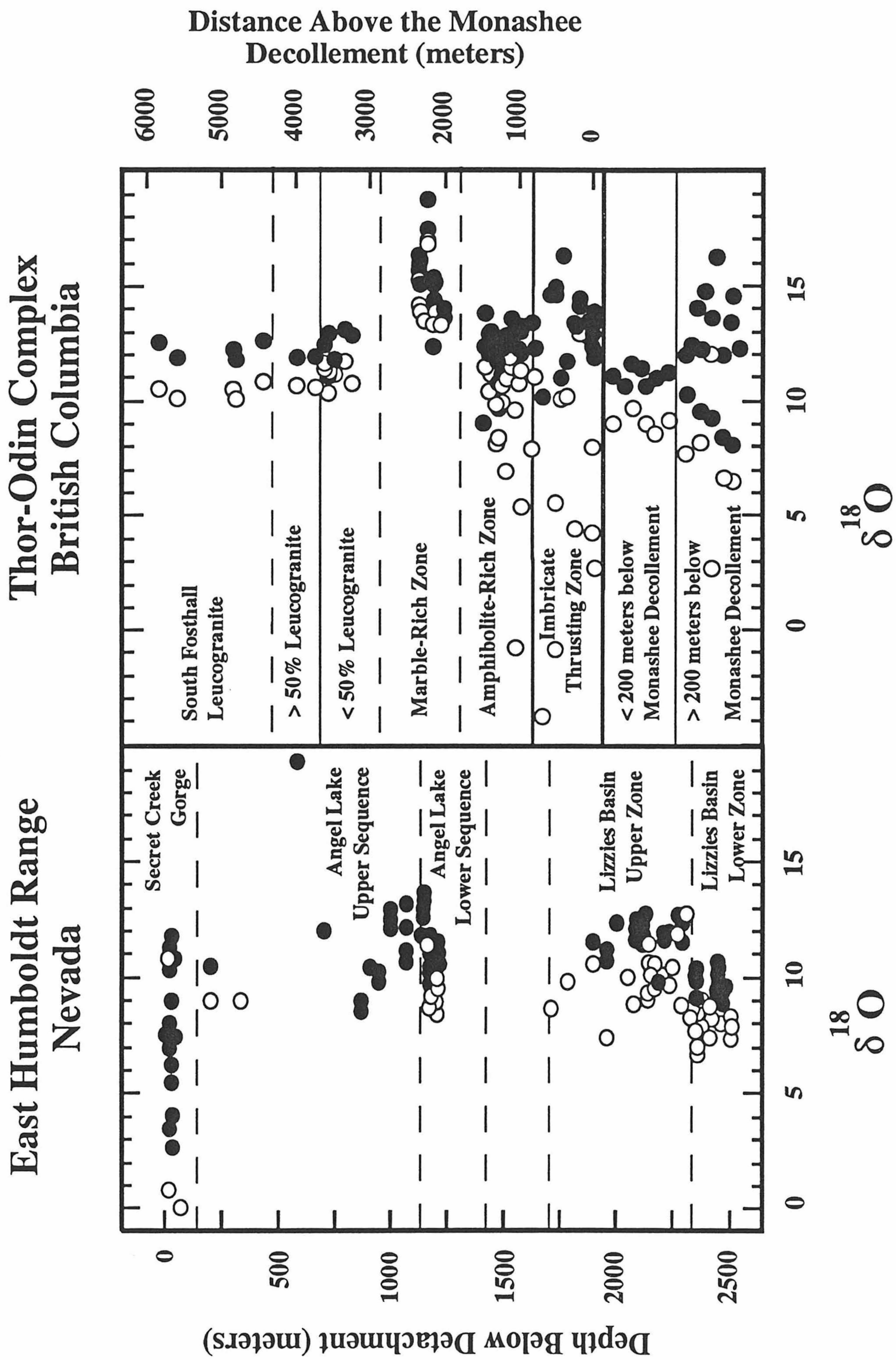

East Humboldt Range
Nevada
Thor-Odin Complex
British Columbia
Distance Above the Monashee
Decollement (meters)
6000
5000
4000
3000
2000
1000
0
Depth Below Detachment (meters)
0
500
1000
1500
2000
2500
Secret Creek
Gorge
Angel Lake
Upper Sequence
Angel Lake
Lower Sequence
Lizzies Basin
Upper Zone
Lizzies Basin
Lower Zone
South Fosthall
Leucogranite
> 50% Leucogranite
< 50% Leucogranite
Marble-Rich Zone
Amphibolite-Rich Zone
Imbricate
Thrusting Zone
< 200 meters below
Monashee Decollement
> 200 meters below
Monashee Decollement
0
5
10
15
$\delta^{18}O$
0
5
10
15
$\delta^{18}O$

Figure 4.12 -- $\delta^{18}O$ values of coexisting minerals from the present study, plotted on a cross section through the imbricate thrust zone of the Monashee decollement and the overlying amphibolite-rich zone (modified from McNicoll and Brown, 1995). The imbricate thrust blocks of basement gneiss are denoted by the densely stippled pattern, the blocks of mantling gneiss are shown without shading, and the amphibolite-rich zone is shown as the light dotted pattern that comprises the hanging wall of the Cariboo thrust. Generalized orientations of folds associated with thrusting are shown. The thick amphibolites are drawn and denoted in black. Quartz $\delta^{18}O$ values (solid dots) exhibit a range of 6.2‰ that is independent of the magnitude of quartz-feldspar $^{18}O/^{16}O$ disequilibrium; this variation is similar to that observed in correlative units beneath the Monashee decollement in the Monashee Complex, ans is therefore probably a primary metamorphic feature. Most samples with low-^{18}O feldspars are associated with mapped faults (*e.g.*, Cariboo thrust) in the imbricate thrust zone. A low-^{18}O feldspar ($\delta^{18}O$ = +4.4) from an undeformed dike that crosscuts a thrust fault associated with the Monashee decollement indicates that meteoric-hydrothermal fluids infiltrated this zone after reverse faulting in this zone ceased; brittle faults associated with extension, like those to the north, were the most likely avenues for meteoric fluid flow in this system. Local quartz-feldspar, quartz-biotite, and quartz-amphibole $^{18}O/^{16}O$ disequilibrium in the amphibolite-rich zone beneath the thick amphibolites indicate that meteoric waters affected some of these rocks, as well. Except for the thick amphibolites, the amphibolite-rich zone is homogeneous in quartz $\delta^{18}O$, but heterogeneous in garnet $\delta^{18}O$.

Figure 4.12 Imbricate Thrusting and Amphibolite-Rich Zones

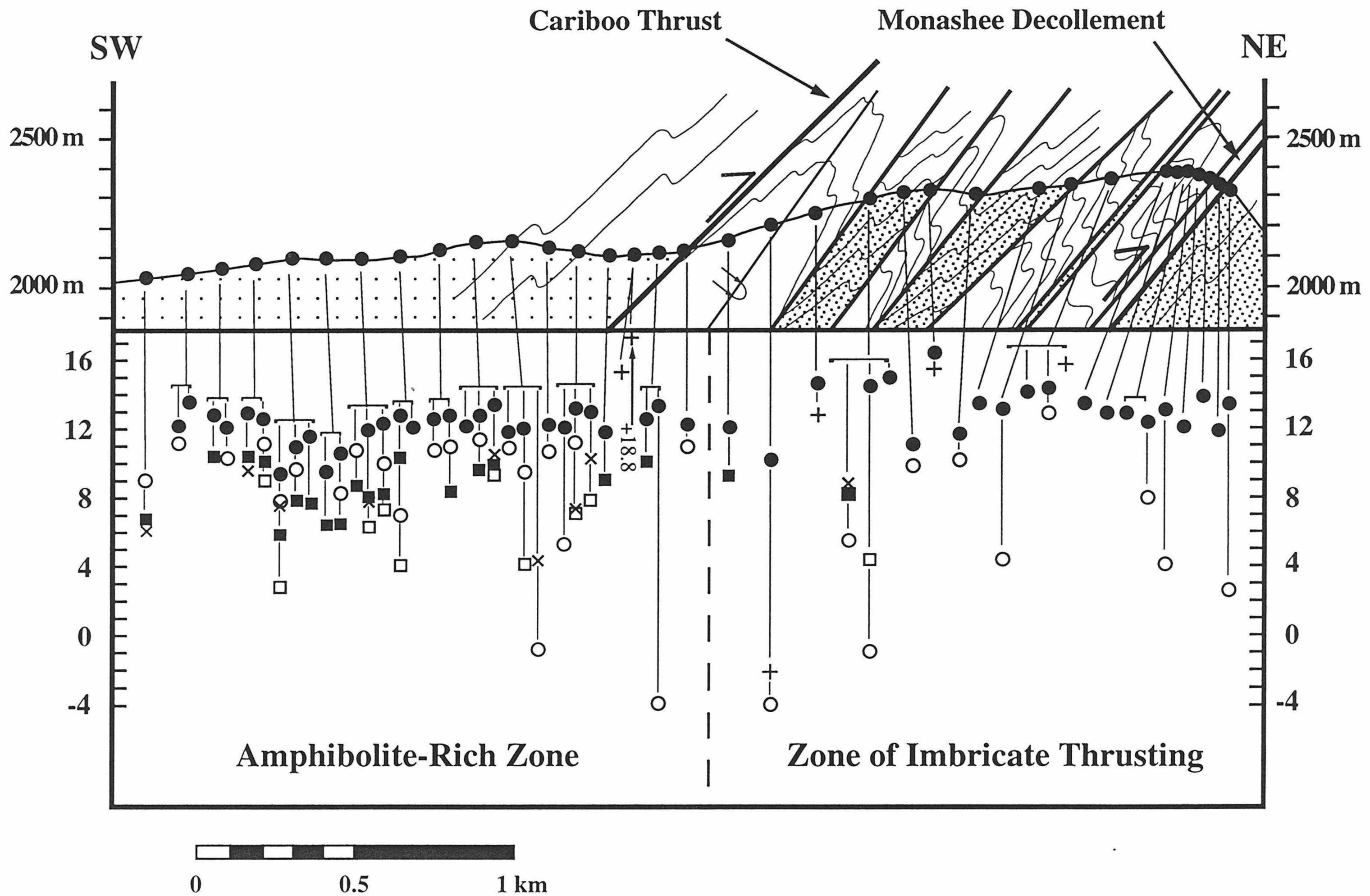

Figure 4.13 -- Quartz $\delta^{18}O$ vs. stratigraphic position in the amphibolite-rich zone. The generalized stratigraphy is from measured stratigraphic sections described in Reesor and Moore (1971). This section is comprised of ~ 30% leucogranite as sheets, pods, and lit-par-lit segregations, ~ 10% amphibolite, ~ 20% quartzite, ~ 30% paragneiss, ~ 20% metapelite, and <1% calc-silicate. This section was correlated by Carr (1991) with the Late Precambrian semipelite-amphibolite division of the Horsethief Creek Group (Windermere Supergroup). Except for the thick amphibolite outcrops, quartz is homogeneous in $\delta^{18}O$ (+12.4) for essentially all lithologies. The patterns of layers on the stratigraphic column are the same as those indicated for the data points. The vertical band indicates the range in $\delta^{18}O$ in the leucogranites.

Figure 4.13 Quartz Data versus Stratigraphy

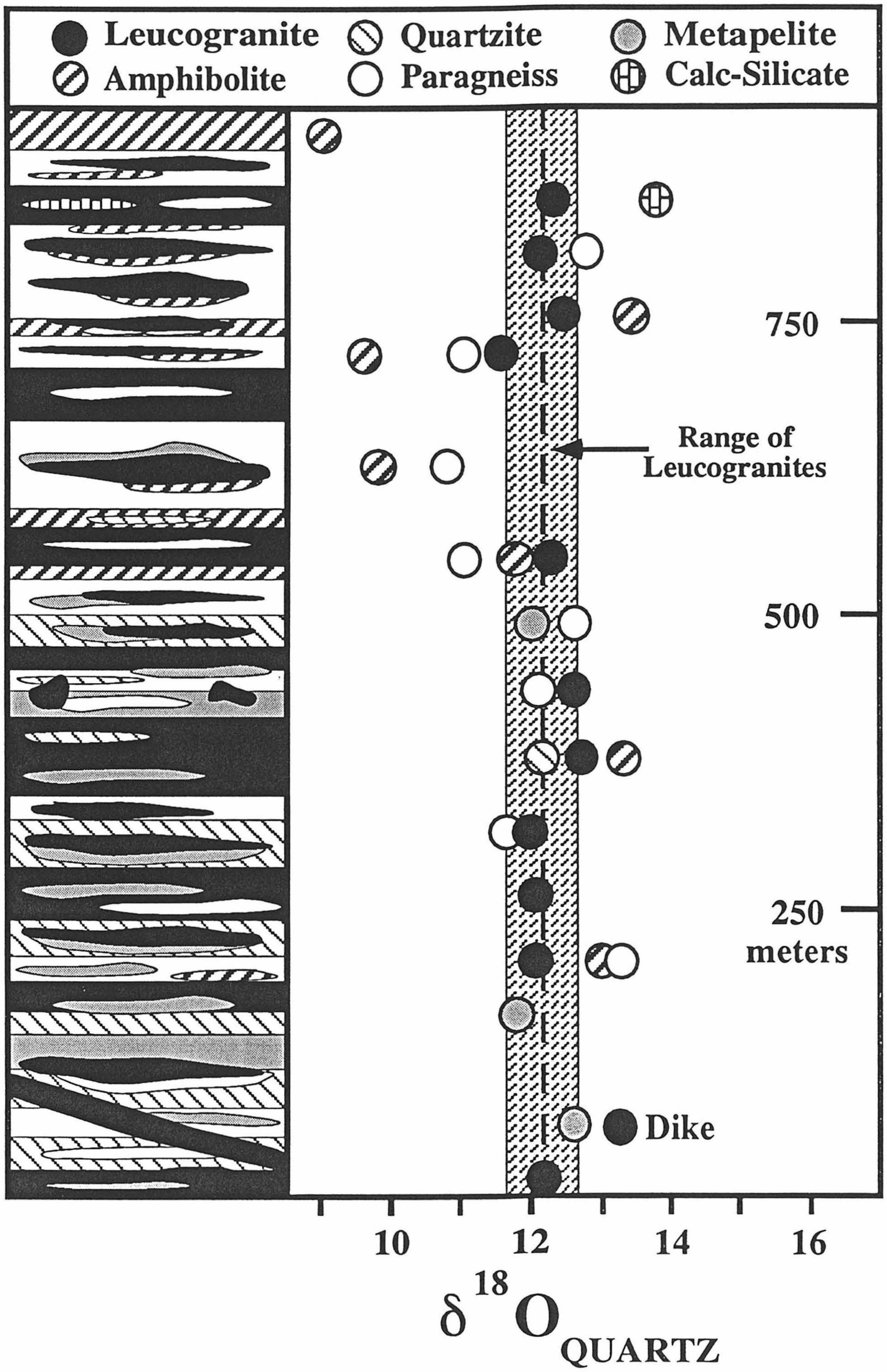

surface H_2O (Wickham and Taylor, 1987; Wickham and Peters, 1990; Peters and Wickham, 1995) into portions of the mid-crust undergoing high-grade metamorphism during extension. That type of lowering of $^{18}O/^{16}O$ is not observed at the Thor-Odin complex. Furthermore, the Monashee decollement and the basement are variable in oxygen isotopic composition, and the zone of uniform $\delta^{18}O$ is restricted to the middle crustal layer.

Thus, meteoric-hydrothermal fluids cannot be responsible for the observed degree of $^{18}O/^{16}O$ homogenization in the mid-crustal layer shown in Figure 4.4. Therefore, the source of the external fluid must be: a) volatiles produced during dehydration of the mid-crustal layer at depth, or b) H_2O-rich basement-derived leucogranite melt which intruded through the Monashee decollement during the thrusting stage. Nyman et al. (1995) concluded that a 2-km thick section of metapelite in the immediate footwall of the Monashee decollement underwent 41-54 vol.% partial melting during thrusting. Numerous leucogranite dikes having variable $\delta^{18}O$ and displaying diverse degrees of deformation crosscut the imbricate thrusting zone. This suggests that at least a small amount of H_2O-rich leucogranite migrated from the basement to the mid-crustal layer through the Monashee decollement during thrusting.

These processes of large-scale hydrothermal anatexis of thick sequences of clastic metasediments during crustal-scale thrust ramping are likely to play a pivotal role in determining the susceptibility of an orogen to subsequent wholesale extensional collapse along detachment faults.

Oxygen isotopic homogeneity is observed in many locations that have experienced orogenic collapse. In the East Humboldt Range of Eastern Nevada, Wickham and Peters (1990; 1993) and Peters and Wickham (1995) observed homogeneity in ^{18}O in the deepest portions of this metamorphic core complex. They attributed this homogeneity to be the result of large-scale isotopic exchange between infiltrating magmatically derived water ($\delta^{18}O \sim +7$) and the high-grade metamorphic rocks during the intrusion of leucogranites during extension. Also, Wickham and Taylor (1987) observed large-scale isotopic uniformity at mid-crustal levels at the Trois Seigneurs massif of the Pyrenees, and Hoernes and Friedrechsen (1980) observed similar uniformity in ^{18}O in the basement rocks of the Alps that were metamorphosed during the Hercynian.

4.7 $^{18}O/^{16}O$ Homogenization Using H_2O as a Petrologic Catalyst

To address the above considerations, a material-balance model has been formulated that follows the forward progress of partial melting of arkosic grits and pelites from a hypothetical 1 km-thick section representative of the amphibolite-rich zone. The model stratigraphic section prior to melting (Figure 4.16) is a schematic representation of a reconstructed amphibolite-rich zone stratigraphic section (after Pell and Simony, 1987). Before anatexis, this section is assumed to be composed of 35 vol. % arkosic grit, 35% pelite, 20% quartzite, and 10% amphibolite. The lower portion of the section is composed of mainly pelite and quartzite while arkosic grit and amphibolite make up most of the upper part of the section. The stratigraphic section for the amphibolite-rich zone (Reesor and Moore, 1971) was correlated by Carr (1991) to the semipelite-amphibolite subdivision of the Horsethief Creek Group (Pell and Simony, 1987) and is shown in Figure 4.13. Quartzite and amphibolite are assumed to be inert to partial melting, and the assumed pre-melt mineralogical compositions are: pelite: quartz - 30%, plagioclase(An_{25}) - 5%, muscovite - 35%, biotite - 20%, Al_2SiO_5 - 10%; arkosic grit: quartz - 45%, plagioclase (An_{25}) - 25%, muscovite - 5%, K-feldspar - 20%, biotite - 5%. Initial pelite composition is approximated from Shaw (1956), while the initial arkosic grit composition is similar to lower grade rocks to the north (Raeside and Ghent, 1983).

Figure 4.14 -- Pressure-temperature plot (modified from Vielzeuf and Holloway, 1988) showing phase relations for the (a) kyanite-sillimanite phase boundary (Holdaway et al., 1971), (b) the solidus curve for the minimum melt eutectic (Wyllie, 1977), (c) the dehydration melting curve for wet pelite (Vielzeuf and Holloway, 1988), (d) the H_2O-absent breakdown of muscovite (Althaus et al., 1970), (e) the H_2O-present breakdown of muscovite (Althaus et al., 1970), (f) the H_2O-absent breakdown of biotite, and (g) the H_2O-present breakdown of biotite (Vielzeuf and Holloway, 1988). The inferred P-T path for the amphibolite-rich zone of the Selkirk Allochthon during thrust ramping and decompression-related anatexis is shown by the arrows from [1] initial melting to [2] end of muscovite dehydration, [3] end of decompresion, and [4] final crystallization (see text). The occurrence of relict kyanite in the imbricate thrust zone and the absence of primary muscovite in the amphibolite-rich zone indicates $P_{max} \geq 8$ kb and $T_{max} \geq 765$ °C. Biotite is stable throughout the section, implying $T_{max} < 800$ °C. 20 km of vertical relief on the Monashee ramp imply 6 kb of decompression. Primary muscovite is absent in the leucogranites; this suggests that the leucogranites crystallized at low pressure.

Figure 4.14 Phase Relations

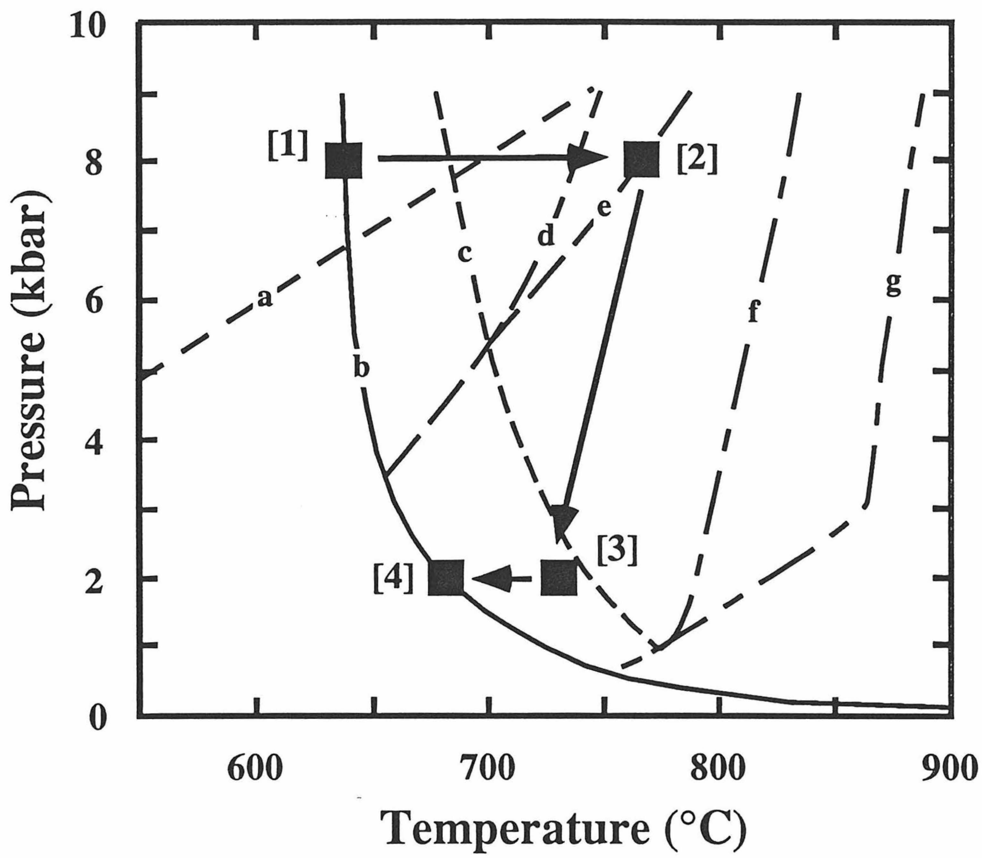

Figure 4.15 -- Plot showing liquidus phase relations and H_2O solubilities in the system Qz-Ab-Or-H_2O for minimum and eutectic compositions from Holtz and Johannes (1994), and the approximate P-T path from Figure 4.14 for the amphibolite-rich zone of the Selkirk allochthon. The heavy solid curve (b) is the solidus of the minimum melt eutectic from Figure 4.14. The lighter solid lines denote liquidus curves at various values of wt.% H_2O from 12% to 2%. The subhorizontal dashed curves represent solubility of H_2O (wt.%) in the granitic melts. These H_2O solubilities decrease with decreasing pressure. The H_2O contents on the liquidus decrease with increasing temperature and decreasing pressure. The presence of H_2O-undersaturated melt keeps H_2O activity low because all H_2O is incorporated into the melt. At a given P and T, the H_2O content on the liquidus curves provide minimum possible H_2O concentrations for the melt, whereas the intersecting solubility curves provide maximum constraints on this parameter. The intersections of these two sets of curves are used to constrain the H_2O contents of the hypothetical melts utilized in the forward progress material-balance melting model (see text) that is constructed in Figures 4.17 to 4.20 to account for the $^{18}O/^{16}O$ homogeneity observed in the Selkirk Allochthon.

Figure 4.15 Water Solubility in Magmas

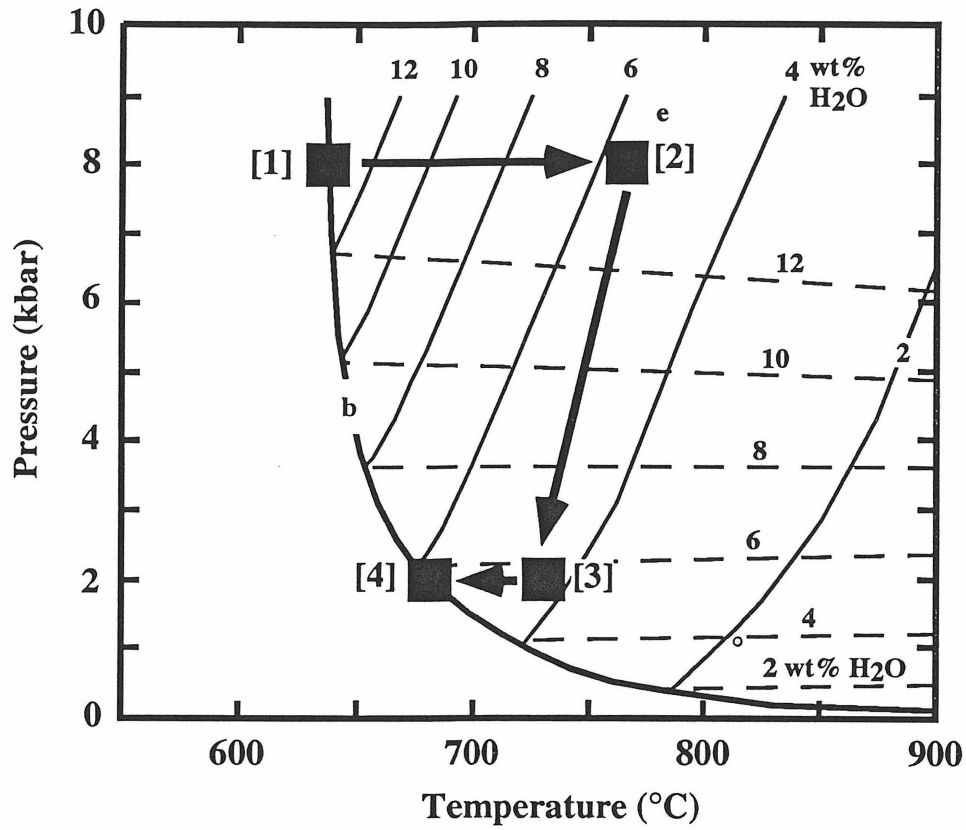

The pressure-temperature path for the Selkirk Allochthon (see Figures 4.14 and 4.15) was constructed from field and petrographic observations. The presence of kyanite (as inclusions in garnet) in the imbricate thrusting zone together with the lack of primary muscovite in the amphibolite-rich zone constrain $P_{max} \geq 8$kb and $T_{max} \geq 765\ ^{\circ}C$ (Althaus et al., 1970; Holdaway et al., 1971), whereas the presence of stable biotite indicates $T_{max} < 800^{\circ}C$ (see Vielzeuf and Holloway, 1988, and references within). A six kb decompression is inferred from 20 km of vertical relief on the Monashee ramp (Cook et al., 1992). The presence of retrograde cordierite (Reesor and Moore, 1971) in the vicinity of the Monashee decollement indicates rapid decompression (Hollister, 1977; Chamberlain and Selverstone, 1990) for these rocks, at least through 4 kb.

Melt H_2O contents are constrained using the model of Holtz and Johannes (1994). When H_2O-undersaturated melt is present, it is assumed that all locally available metamorphic pore H_2O eventually will be incorporated into this melt.

Assumptions and controls of this influx-exsolution-release model are concerned with the H_2O content of the melts, the amounts of partial melting, melt compositions, and the thermal history during decompression. Melt H_2O contents are determined by the amount of available water in the source rock for the melts. The H_2O content of the pelite-derived melt is nearly H_2O saturated while the arkosic grit-derived melt is H_2O undersaturated. The H_2O content of the grit-derived melt is that on the liquidus for a haplogranitic melt having a composition near that of the eutectic for a given pressure and temperature. The pelite-derived melts will contain an H_2O abundance occurring at saturation for that pressure and temperature. Solubility of H_2O decreases with decreasing pressure from 10 wt. % at 8 kb to 5.5 wt. % at 2 kb (see Figure 4.15). The H_2O content of melts on the

Figure 4.16 -- Ternary isobaric equilibrium diagrams for granitic melt in the system albite+orthoclase+quartz+H_2O at (a) 10 kb (Luth et al., 1964) and (b) 2 kb (Tuttle and Bowen, 1958). The bulk compositions of samples of Ladybird leucogranite from the Thor-Odin complex (data from Reesor and Moore, 1971) are plotted on these diagrams. These data imply that these leucogranites are the product of the melting of a K-rich source; this is consistent with the anatexis and crystallization at temperatures within the range of 700-780 $^{\circ}$C (Tuttle and Bowen, 1958; Luth et al., 1964). The upper compositional bound with respect to quartz content appears to be the eutectic curve between the alkali feldspar solid solution and quartz phase regions.

Figure 4.16 Granite Phase Equilibria

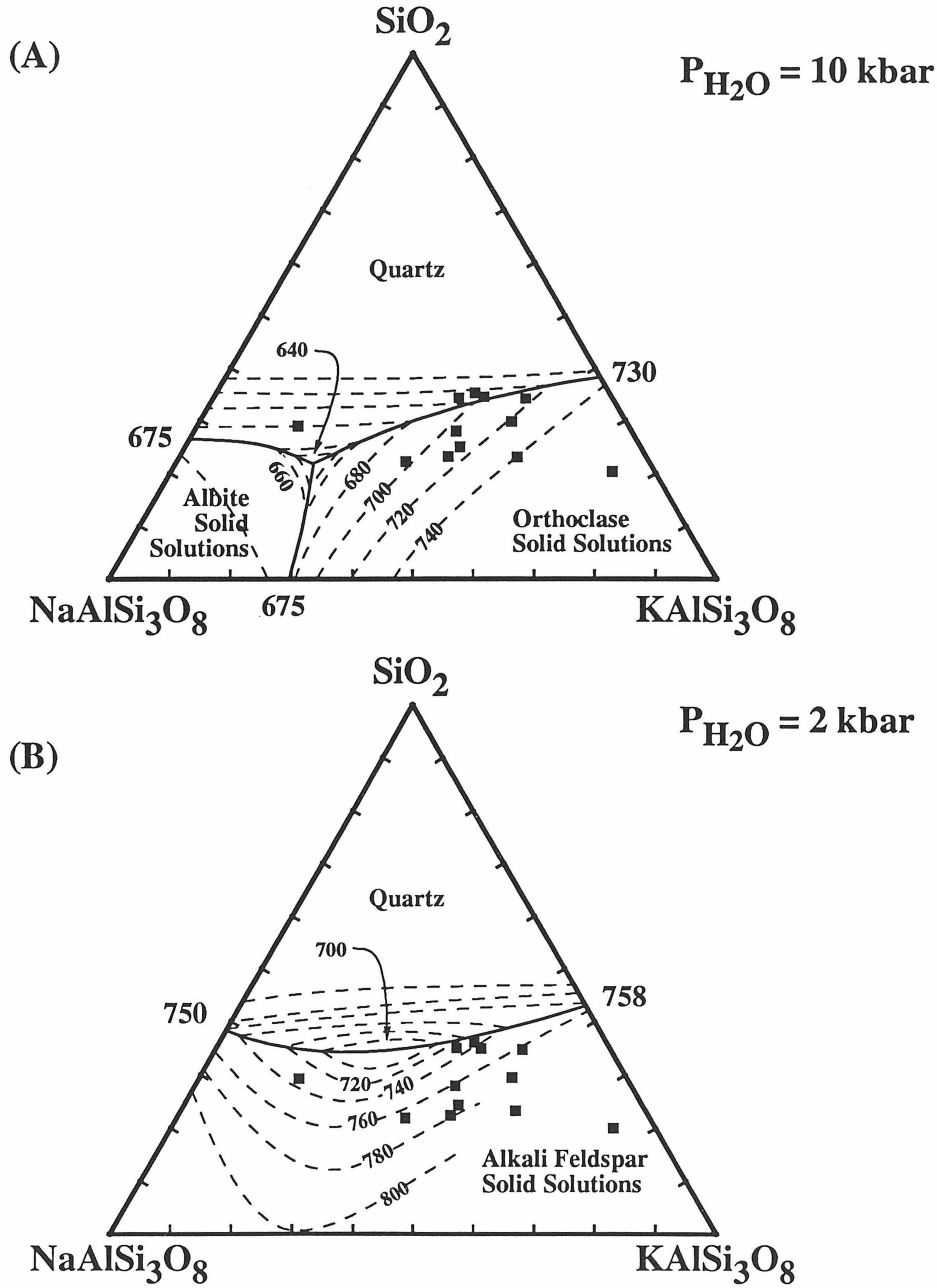

liquidus decreases with increasing temperature. At 8 kbar the H_2O at the liquidus is 14 wt. % at 630 °C and decreases to 5.5 wt. % at 765 °C (see Johannes and Holtz, 1994; and references within).

There are two modes of partial melting of crustal rocks: 1) water-saturated melting and 2) dehydration melting (*e.g.*, see Wyllie, 1977). Water-saturated melting occurs when the water-saturated solidus temperature is attained for a given lithology (about 650 °C for most lithologies). Melts produced from this style of partial melting are close to water saturation. Melt compositions are constrained by experimentally-derived phase equilibria (Tuttle and Bowen, 1958; Luth, Jahns, and Tuttle, 1964; Vielzeuf and Holloway, 1988) and petrographic observations (Reesor and Moore, 1971; and this study).

The model assumes that all H_2O goes into the melt phase when melt is present, unless all of the melt is H_2O-saturated. The presence of H_2O-undersaturated melt (*e.g.*, grit-derived melt) keeps the H_2O-activity low in portions of the system in communication with these melts. Once some melt portions become saturated, transport of H_2O from saturated to unsaturated melts through lithologies infertile to melting occurs. Since this is the case envisioned in this general scenario, some H_2O exsolved from the saturated pelite-derived melts will indeed eventually end up in nearby grit-derived melts. At these temperatures, any exsolved waters will certainly exchange $^{18}O/^{16}O$ with all lithologies infertile to melting as the water is transported through them (along fractures and grain boundaries).

The initial partial melting of metapelites and arkosic grits is assumed to occur at 8 kb and 630 °C in response to the addition (from below?) of small amounts of external H_2O (1400 mol/m^3), equivalent to a material balance W/R = 0.015 for the entire section. This represents the minimum amount of H_2O required to locally produce the observed amount of leucogranite. Initial melt composition is taken to be the minimum melt eutectic composition at 8 kb (*i.e.*, quartz - 24%, plagioclase (An_{25}) - 52%, K-feldspar - 24%; Luth et al., 1964). All available H_2O enters the initially water-saturated melt (~ 14 wt.% H_2O; Holtz and Johannes, 1994). In this scenario, pelites undergo 9 vol.% partial melting and grits experience 8 vol.% partial melting.

Muscovite dehydration is probably complete by the time these rocks reach the base of the Monashee ramp having produced (950 mol/m^3, or a W/R = 0.010). The controlling agents for the production of granitic melt in such rocks are the supply of volatiles and the amount and distribution of feldspars in the source rock (*e.g.*, Clemens and Vielzeuf, 1987). Metapelites are volatile-rich (~ 3.5 wt. % H_2O, mainly as OH in muscovite), but feldspar-poor (< 5 vol.%); the converse applies to the grit lithologies (< 1 wt. % H_2O, mainly as OH in biotite and as much as 50 vol. % feldspar). Thus, at the base of the Monashee ramp, muscovite dehydration triggers large-scale (27%) partial melting of the muscovite-bearing metapelite units, producing peraluminous granitic magmas that are nearly H_2O-saturated (11 wt.%). Because they start out chemically more similar to granites, the feldspathic grits coincidentally undergo a similar degree of partial melting; however, at this temperature (~ 750 °C) and pressure (8 kb) those melts are less potassic and have lower H_2O contents (5.5 wt.%). The calculated extents of partial melting are based upon the chemical compositions of the two types of melt at the stage of muscovite breakdown, as inferred from the actually observed end-member leucogranite compositions of the Ladybird suite at Thor-Odin (Reesor and Moore, 1971), namely: (a) pelite-derived melt: quartz - 30%, plagioclase(An_{25}) - 17%, K-feldspar - 50%, biotite - 3%, and (b) arkosic grit-derived melt: quartz - 30%, plagioclase(An_{25}) - 28%, K-feldspar - 39%, biotite - 3%. These melts are within the compositional range of possible melts in

Figure 4.17 -- The pre-melting schematic stratigraphic section utilized in the forward progress material-balance model. This is a simplified representation of the semipelite-amphibolite division of the Horsethief Creek Group of the Windermere Supergroup as documented by Pell and Simony (1987). The model operates by partial melting of metapelite and arkosic grit layers in response to the influx of small amounts of external H_2O, muscovite dehydration, and decompression, together with cycling of H_2O out of H_2O-saturated melts and into newly formed melts.

Figure 4.18 -- Changes in the section during the muscovite dehydration interval (635 °C to 765 °C at 8 kb). [1] Initial melting is inferred to occur in response to the addition of 1400 mol/m^3 H_2O into the system. Limited melting (~8%) of metapelite and arkosic grit occurs. [2] 950 mol/m^3 H_2O is released by muscovite dehydration to drive further melting (27%) of the fertile lithologies. 19% of the section is leucogranite melt when muscovite dehydration is complete. The black arrows denote the migration of the less viscous, nearly H_2O saturated, metapelite-derived melts once they become mobile. In this and subsequent diagrams, the solid black layers = leucogranite melt, the white areas are paragneiss (*i. e.* restite from melting of pelite), and other patterns are the same as on Figure 4.17.

Figure 4.17 Before Melting
T < 630 °C and P = 8 kbar

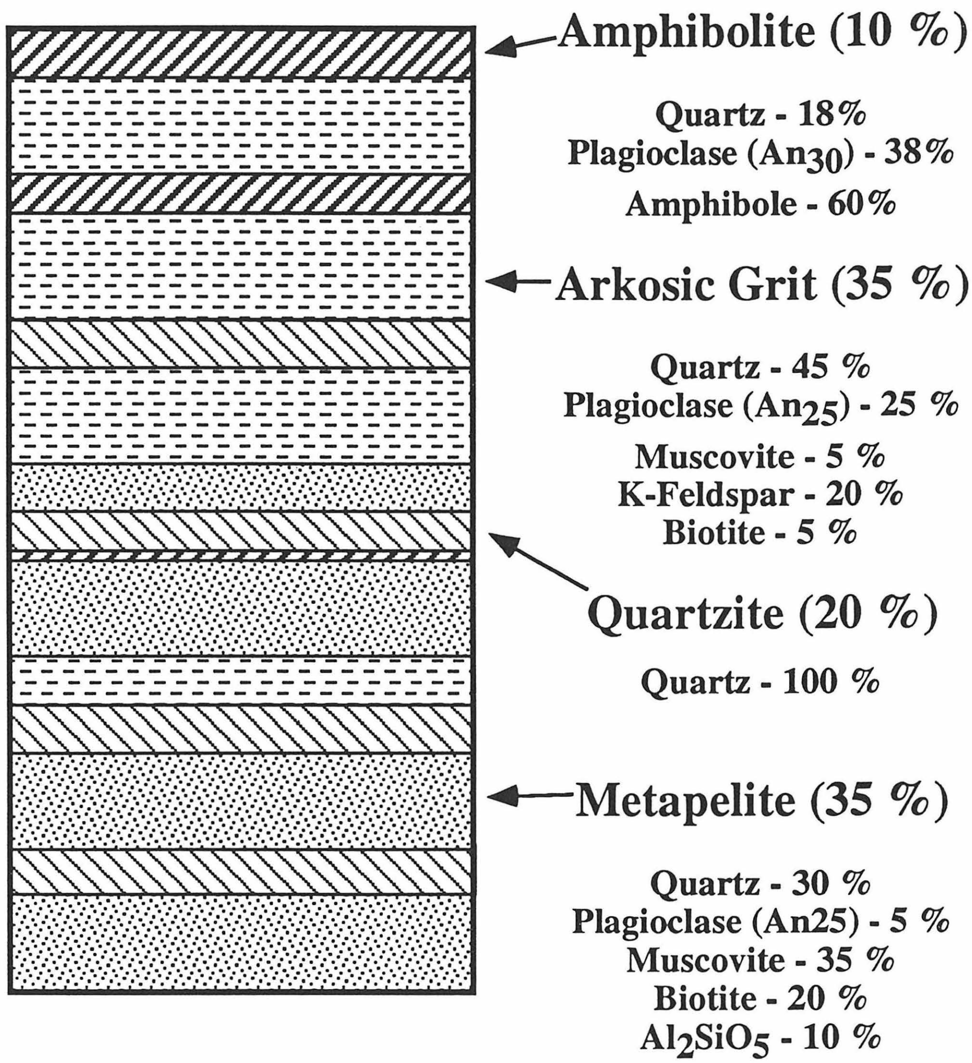

Figure 4.18

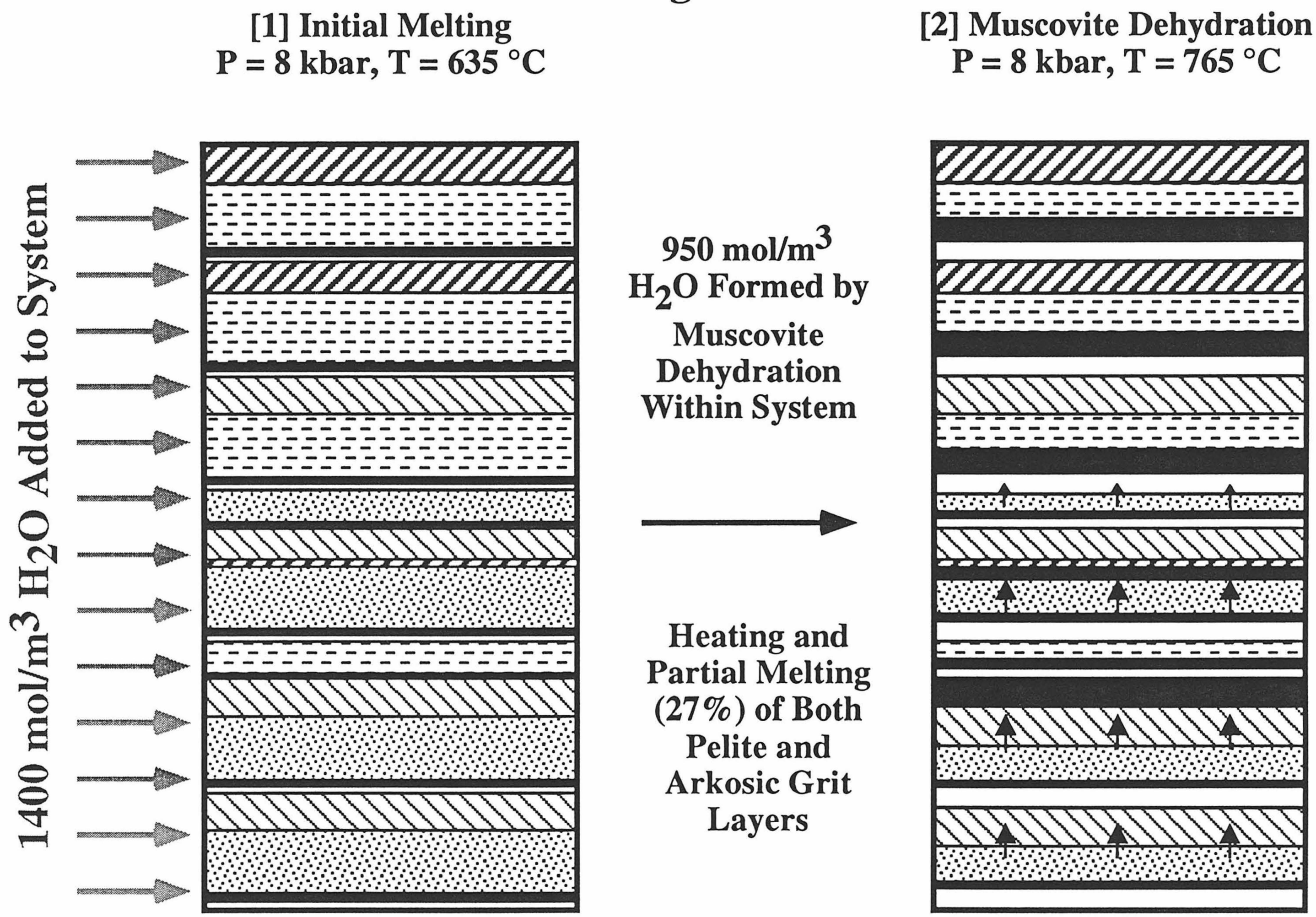
[1] Initial Melting
P = 8 kbar, T = 635 °C
[2] Muscovite Dehydration
P = 8 kbar, T = 765 °C
1400 mol/m^3 H_2O Added to System
950 mol/m^3
H_2O Formed by
Muscovite
Dehydration
Within System
Heating and
Partial Melting
(27%) of Both
Pelite and
Arkosic Grit
Layers

Figure 4.19 -- The evolution of the system during decompression from 8 kb to 2 kb. Temperature drops from 765 °C to 730 °C. Melt migration is denoted by black arrows. Aqueous fluid migration is expressed as gray arrows. Exsolution of H_2O (900 mol/m^3) from the saturated pelite-derived melts drives further melting (up to 58%) of arkosic grit. Exsolved H_2O exchanges $^{18}O/^{16}O$ with lithologies infertile to melting as it moves through the system. At the end of decompression, 27% of the section is melted rock.

Figure 4.20 -- Cooling and final crystallization of leucogranite melt. Continued release of H_2O from the crystallizing pelite-derived melt drives further melting of the arkosic grits (up to 63%). The maximum amount of melt present in the section during this stage is 26%. The arkosic grit-derived melts are assumed to reach H_2O saturation during this stage and release 100 mol/m^3 H_2O that leaves the system. Final crystallization and the release of 2250 mol/m^3 H_2O happens at 2 kb, 680 °C. At the end of crystallization, 32% of the section is leucogranite, similar to that actually observed in the amphibolite-rich zone section of the southern Thor-Odin complex. Inferred fluid flow paths are denoted by the gray arrows.

Figure 4.19

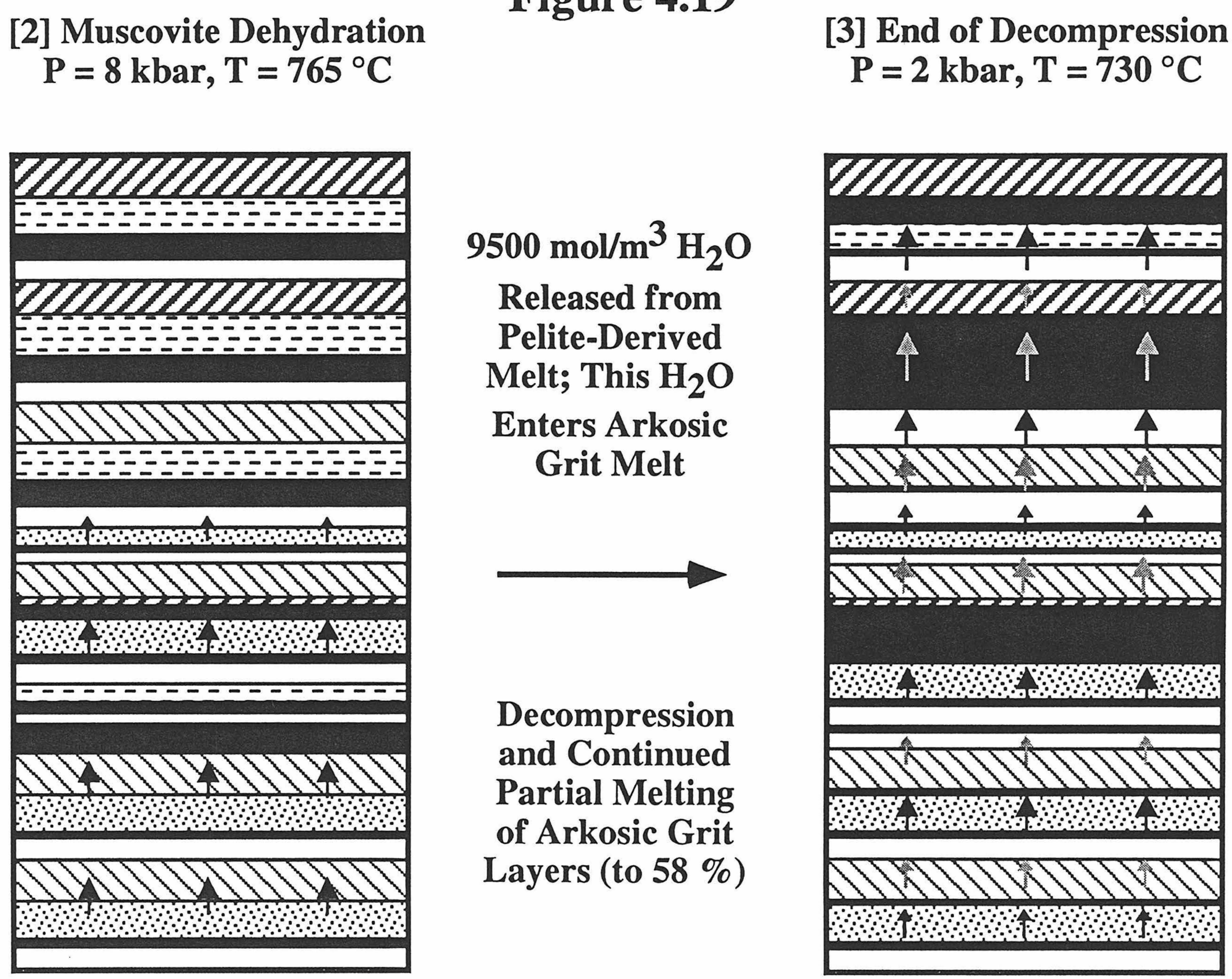
[2] Muscovite Dehydration
P = 8 kbar, T = 765 °C
[3] End of Decompression
P = 2 kbar, T = 730 °C
9500 mol/m^3 H_2O
Released from
Pelite-Derived
Melt; This H_2O
Enters Arkosic
Grit Melt
Decompression
and Continued
Partial Melting
of Arkosic Grit
Layers (to 58 %)

Figure 4.20

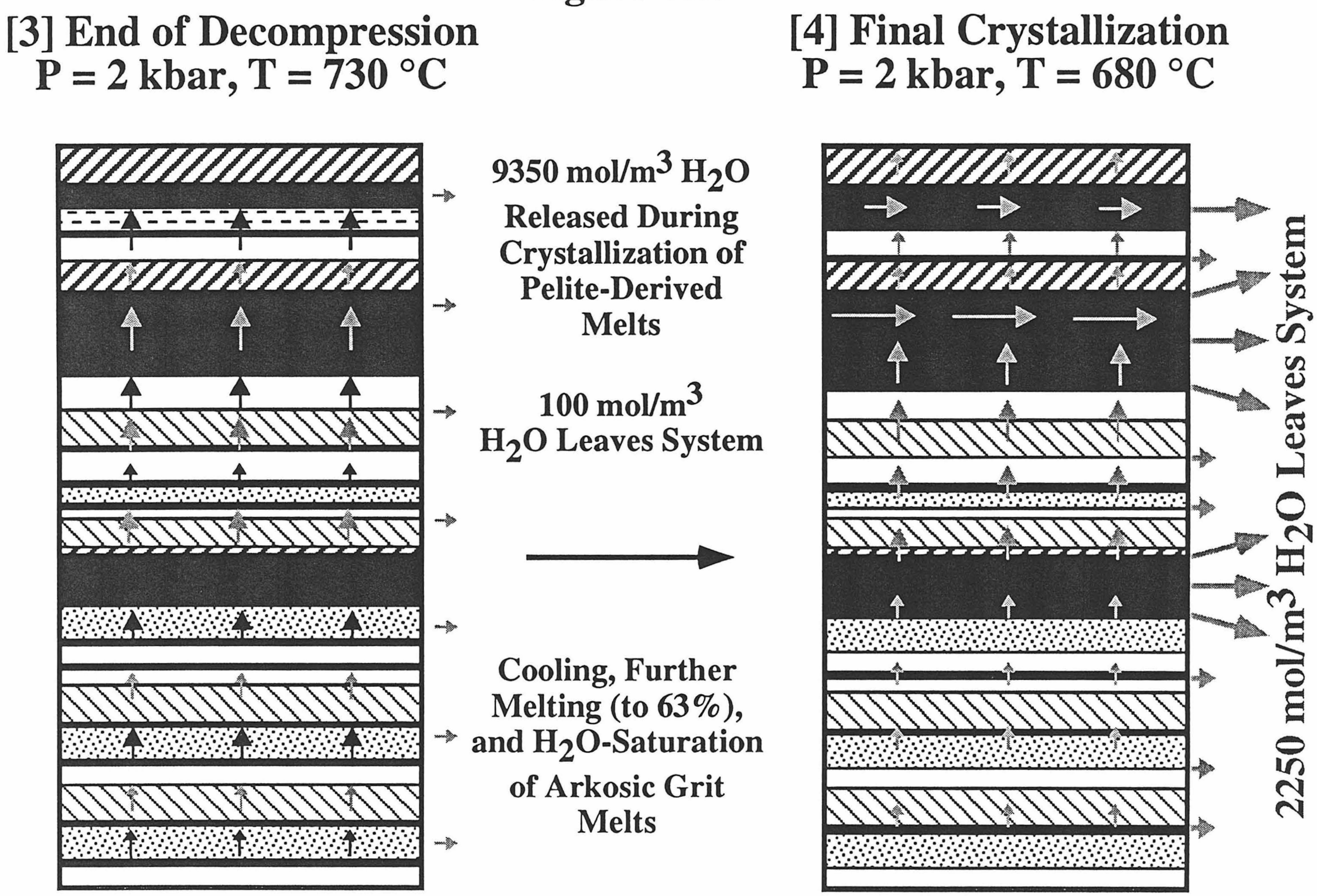
[3] End of Decompression
P = 2 kbar, T = 730 °C
[4] Final Crystallization
P = 2 kbar, T = 680 °C
9350 mol/m^3 H_2O Released During Crystallization of Pelite-Derived Melts
100 mol/m^3 H_2O Leaves System
Cooling, Further Melting (to 63%), and H_2O-Saturation of Arkosic Grit Melts
2250 mol/m^3 H_2O Leaves System

the KNASH system (Thompson and Algor, 1977). At this stage, 16 vol. % of the Windermere section is leucogranite melt.

Because the solubility of H_2O in granitic melt decreases during its ascent (Whitney, 1988), H_2O is released as these peraluminous melts reach saturation during their migration to shallower crustal depths, either passively due to displacements along the underlying decollement or actively in response to buoyant forces. The H_2O-rich pelite-derived melts are probably much less viscous than the drier grit-derived melts, and in combination with thrust ramping, these magma bodies may become mobile and migrate to shallower depths, cooling adiabatically, producing decompressive exsolution of H_2O, and allowing $^{18}O/^{16}O$ exchange to occur with rocks that come into direct communication with these melts. The net release of 900 mol/m^3 H_2O through decompression (W/R = 0.010) also promotes oxygen exchange with adjacent lithologies infertile to melting (paragneiss, amphibolite, quartzite, calc-silicate). However, this H_2O does not leave the system. Instead, it can concurrently act as a catalyst driving continued hydrothermal melting of any feldspathic grit layers that it encounters as it moves through the system. Aqueous fluid transport is assumed to be generally upward and sub-parallel to the leucocratic melt layers because the H_2O-saturated magmas will act as impermeable barriers to the transport of aqueous fluids. Eventually, partial melting of the grit units exceeds the critical melt fraction and these packets of melt also begin migrating up the Monashee ramp, exchanging $^{18}O/^{16}O$ with any rocks that they come into contact with. Thus, in our model, concurrent crystallization and melting occur during decompression of these leucogranite melts, and release of latent heat of crystallization also contributes energy for continued melting and hydrothermal circulation. The post-decompression H_2O contents at 2 kb and 730 °C are calculated to be 5.5 wt.% for the pelite-derived melt and 4.5 wt.% for the grit-derived melt. At the end of decompression, 27 vol. % of the Windermere section is leucogranite melt.

The anhydrous composition of the pelite-derived melt at 730 °C is assumed to be on the eutectic for the qtz-ab-or-H_2O system of Tuttle and Bowen (1958); namely, quartz - 36%, plagioclase (An_{25}) - 19%, K-feldspar - 42%, and biotite - 3%. The pelite-derived melt experienced 11% (27 to 24%) crystallization as K-feldspar crystallized and as the melt became more quartz-rich. The arkosic grit-derived melt has an anhydrous composition of 32 vol. % quartz, 29% plagioclase (An_{25}), 36% K-feldspar, and 3% biotite. The proportion of melted arkosic grit is assumed to have increased to 52% from 26% during this 6 km of decompression.

During cooling at 2 kb, the post-decompression compositional evolution of the two types of melt follow the phase relations for the Qz-Ab-Or-H_2O system given in Tuttle and Bowen (1958). Crystallization of the H_2O-saturated (5.5 wt.%) pelite-derived melt (from 24% to 12%) during cooling releases 800 mol/m^3 of H_2O (equivalent to a W/R = 0.009), thus driving further melting of nearby grit layers (up to 63%), as well as further $^{18}O/^{16}O$ exchange. The grit-derived melts become H_2O saturated (5.5 wt.%) at T = 730 °C and P = 2 kb near the time of final crystallization, at which stage a small amount of H_2O (100 mol/m^3, W/R = 0.001) is released to the system. This process goes on until final crystallization of the leucogranites (*i.e.*, 680 °C at 2 kbar; Wyllie, 1977), which releases all of the remaining melt H_2O (2250 mol/m^3, W/R = 0.024) except the tiny amount that is ultimately incorporated into biotite, thus producing the final episode of $^{18}O/^{16}O$ exchange among the various igneous and metamorphic lithologies. This H_2O is then assumed to leave our model section, but it should be noted that such a pore fluid would obviously be available for continued $^{18}O/^{16}O$ exchange with overlying lithologies. The maximum amount of leucogranite melt present in this section is 26 vol%, but the total amount of material that has experienced partial melting increases, and as much as 30 vol.% of the total section may have consisted of melt or melt products during this anatectic process.

Final crystallization of the melts occurs at a pressure of 2 kb and a temperature of 680 °C. Of the Windermere section, 26% is melt just prior to the final crystallization stage. At the onset of final crystallization, both types of melt have the following anhydrous composition: quartz - 33%, plagioclase (An_{25}) - 39%, K-feldspar - 25%, and biotite - 3%. Crystallization of K-feldspar and further melting of quartz and plagioclase account for the compositional change in the arkosic grit-derived melt as its composition changes during cooling (Tuttle and Bowen, 1958).

These repeated episodes of H_2O influx, dehydration, exchange, incorporation, and exsolution in leucogranite melts and rocks in the hanging wall of the MD, together with the effects of direct interaction and $^{18}O/^{16}O$ exchange between the metasedimentary rocks and the migrating partial melts, appear to be adequate to explain the pervasive $^{18}O/^{16}O$ homogenization observed in this core complex. The amounts of H_2O utilized in the model are also sufficient to produce the observed amount of leucogranite in the final section, as well as most of the material that migrated upward and coalesced to form the South Fosthall pluton. The overall amount of H_2O that passes into and through our model system integrated over the entire time period of metamorphism, partial melting, and final crystallization is 6400 mol/m^3 (equivalent to an overall W/R = 0.07). Note, however, that in the model there is actually a negative net influx of H_2O into the overall system (—950 mol/m^3) because of the early-stage dehydration of muscovite. The above model readily accounts for the observed 30% partial melting of this section of the Windermere Supergroup, and we believe that the cyclic use and re-use of H_2O as an exchange catalyst, together with processes of direct oxygen communication between rocks and leucogranite melts, are sufficient to impose the observed degree of $^{18}O/^{16}O$ homogenization, including the effects observed at higher levels in this 6-km-thick section. These processes of large-scale hydrothermal anatexis of thick sequences of clastic metasediments during crustal-scale thrust ramping are likely to play a pivotal role in determining the susceptibility of an orogen to subsequent wholesale extensional collapse along detachment faults.

The model of Podlachikov and Wickham (1994) predicts that approximately 10 meters of a 1 km-thick section will exchange $^{18}O/^{16}O$ and be in oxygen isotope equilibrium with the melts given the amount of H_2O-saturated pelite-derived melt present. However, the abundance of pelite-derived melt was likely above the reduced critical melt fraction (Arzi, 1978), as these bodies could have separated from their source and begun migrating toward higher parts of the thrust ramp. Simultaneously, the fluid transport likely occurred parallel to the long dimensions of these sheetlike leucogranite bodies, because an H_2O-saturated melt would behave as an impermeable barrier, preventing the transport of aqueous fluids across it. Intimate exchange of $^{18}O/^{16}O$ among the rocks, melts, and aqueous fluids likely occurred during this migration of melt and aqueous fluid through the rocks.

Figure 4.21 -- Comparison of the stratigraphic section before and after melting. Arkosic grit is removed from the column, the proportion of amphibolite and quartzite is unchanged. Leucogranite now comprises 32% of the section, while metapelite and paragneiss together restite comprise 38% of the section.

Figure 4.22 -- The influx-exsolution-transfer-release model for the partial melting and H_2O-melt-rock interaction of the middle crust at the southern Thor-Odin metamorphic core complex. The pre-melting section is a schematic representation of the Horsethief Creek Group as documented by Pell and Simony (1987). This section consists of arkosic grit (horizontal dashes - 35%), pelite (stippled - 35%), quartzite (light diagonal lines - 20%), and amphibolite (heavy diagonal lines - 10%). The modal compositions of these lithologies are given in the text. This material-balance model follows the forward progress of partial melting (solid black) of arkosic grit and pelite layers that occurs in response to the initial influx of 1400 mol/m^3 of H_2O into the system and the production of 950 mol/m^3 H_2O during muscovite breakdown. The residues of partial melting are shown as paragneiss layers (solid white). This dissolved H_2O is then released from the pelite-derived melts as they reach H_2O saturation during decompression, as the system moves up the Monashee ramp. These advecting H_2O-rich pore fluids exchange $^{18}O/^{16}O$ with adjacent quartzites and amphibolites, but drive further melting of nearby arkosic grit layers. During post-decompression cooling there is continued release of H_2O from all of these anatectic melts as they finally crystallize at about 680 °C, allowing this H_2O to be used once again to imprint a terminal episode of $^{18}O/^{16}O$ homogenization upon the section.

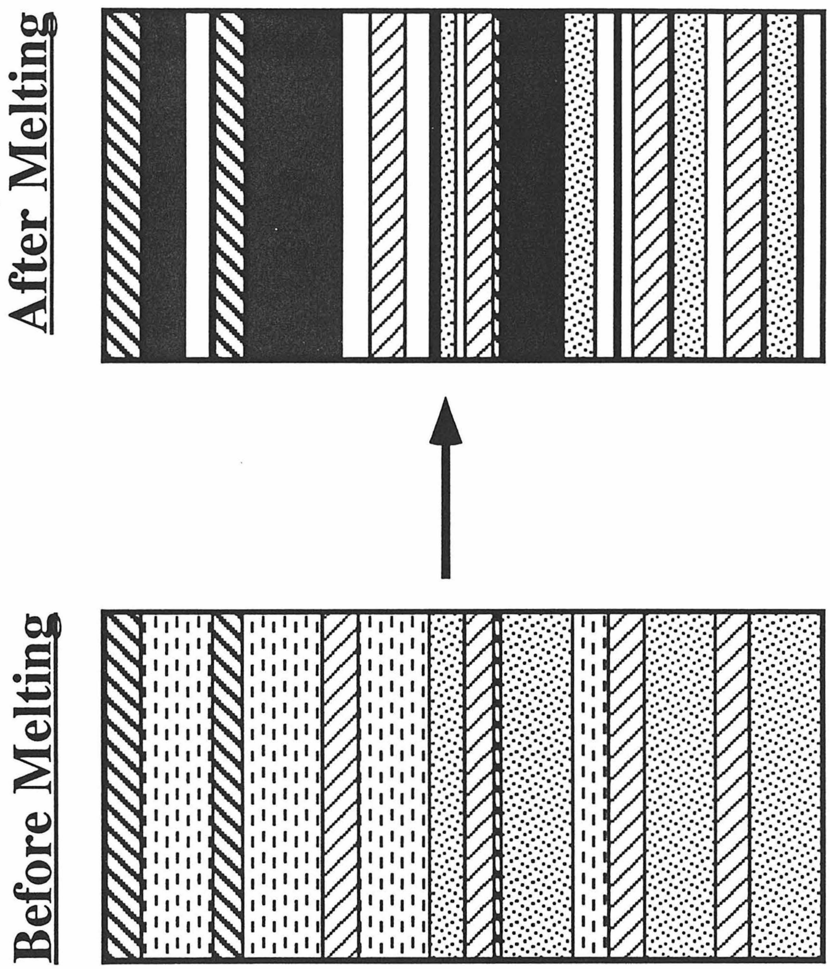

Figure 4.21

FIGURE 4.22

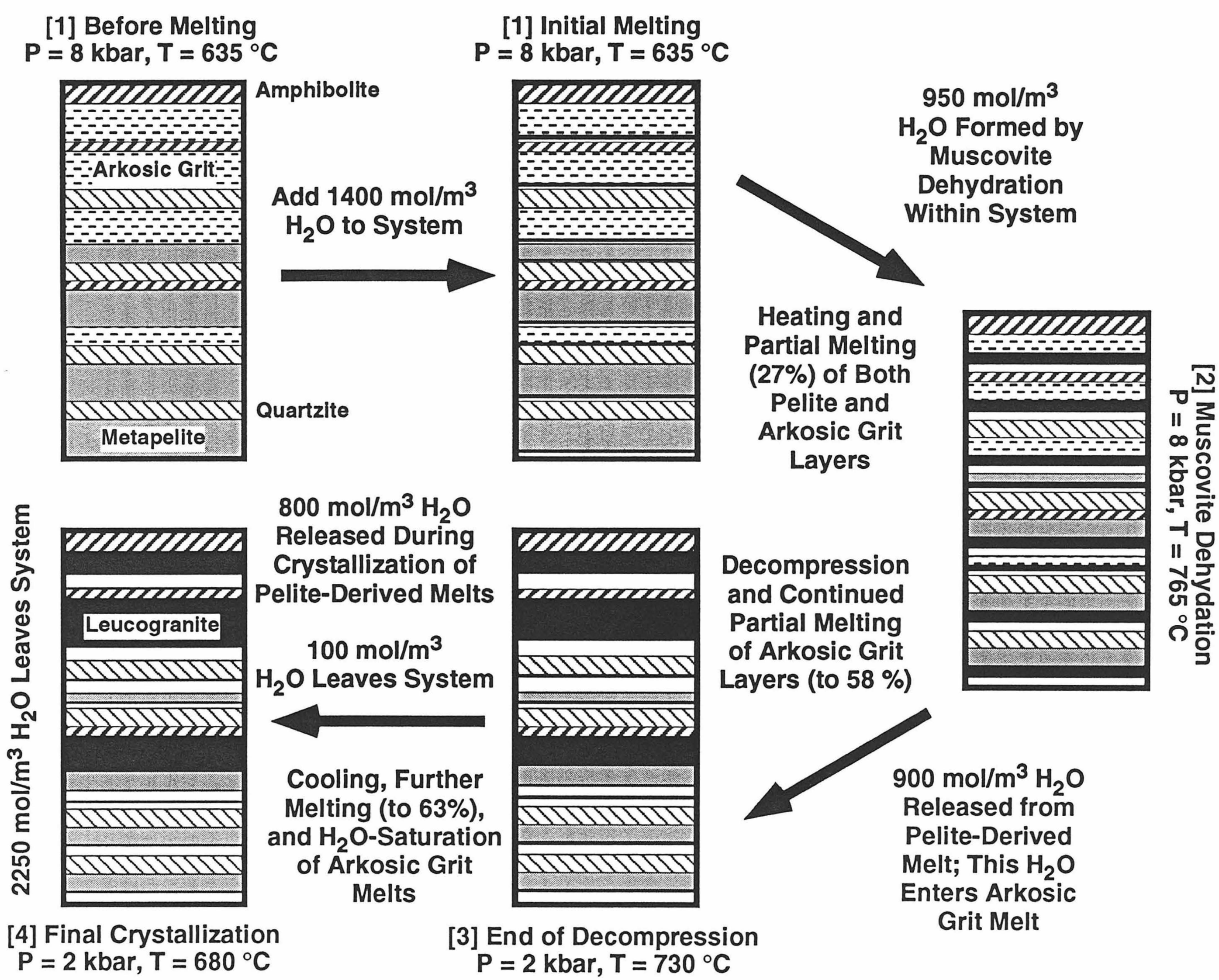
[1] Before Melting
P = 8 kbar, T = 635 °C
Amphibolite
Arkosic Grit
Quartzite
Metapelite
Add 1400 mol/m^3 H_2O to System
[1] Initial Melting
P = 8 kbar, T = 635 °C
950 mol/m^3 H_2O Formed by Muscovite Dehydration Within System
Heating and Partial Melting (27%) of Both Pelite and Arkosic Grit Layers
[2] Muscovite Dehydation
P = 8 kbar, T = 765 °C
Decompression and Continued Partial Melting of Arkosic Grit Layers (to 58 %)
900 mol/m^3 H_2O Released from Pelite-Derived Melt; This H_2O Enters Arkosic Grit Melt
[3] End of Decompression
P = 2 kbar, T = 730 °C
800 mol/m^3 H_2O Released During Crystallization of Pelite-Derived Melts
100 mol/m^3 H_2O Leaves System
Cooling, Further Melting (to 63%), and H_2O-Saturation of Arkosic Grit Melts
Leucogranite
2250 mol/m^3 H_2O Leaves System
[4] Final Crystallization
P = 2 kbar, T = 680 °C

Chapter 5. Hydrothermal Systems Related to Detachment Faults

5.1 General Statement

Many stable isotope studies (Kerrich and Hyndman, 1986; Kerrich and Rehrig, 1987; Roddy et al., 1988; Nesbitt and Muehlenbachs, 1989, 1995; Beaudoin et al., 1991, 1992; Smith et al., 1991; Fricke at al., 1992; Wickham et al., 1993; and Morrison, 1994) have shown that the detachment faults of metamorphic core complexes are major conduits for transport of meteoric water through continental crust that is undergoing extension. In these systems, meteoric-hydrothermal circulation principally affects the detachment zone and the upper plate (Smith et al., 1991; Fricke et al., 1992), but locally, such effects are also observed in parts of the lower plate intruded by late dikes emplaced after the lower plate was uplifted into the brittle deformational regime (Morrison, 1994). In addition, in British Columbia it has been suggested that very large amounts of evolved meteoric water circulated down to depths of more than 15 km in the lower plate during the Eocene extension of the southern Omineca belt (Nesbitt and Muehlenbachs, 1995).

Rapid tectonic denudation of an uplifted hot lower plate results in a zone of steep thermal gradients in the vicinity of the detachment zone (Wernicke, 1985). The occurrence of synextensional plutonic rocks in the lower plate is a common association in these core complexes (Armstrong, 1982; Armstrong and Ward, 1992). These magmas can play a prominent role in determining the thermal state of the lower plate during extension, and the presence or absence of lower plate magmas thus may be an important parameter in determining the extent of meteoric-hydrothermal activity.

Magaritz and Taylor (1986) suggested that the regional-scale meteoric-hydrothermal systems in southeastern British Columbia were related to the emplacement of Eocene magmas, a scenario similar to that observed in the Idaho batholith (Criss and Taylor, 1983). However, Nesbitt and Muehlenbachs (1989, 1995) present an alternative view; they propose that the driving force for convective circulation of meteoric fluids in British Columbia was principally the ambient heat contained within the lower plate itself. These authors discount the role of synextensional magmas in providing the heat necessary to allow for this large-scale convective circulation of meteoric water during the Eocene. Thus, new assessments of the relative roles of both magmatism and extensional detachment faulting are needed in order to fully understand the hydrothermal systems that have affected such large areas in southeastern British Columbia.

This chapter attempts to quantify the effects of meteoric-hydrothermal metamorphism in the southern Omineca belt, and to show how these effects are influenced by Eocene extension and detachment faulting, and to the emplacement of synextensional plutonic bodies. The Valhalla metamorphic core complex (Figures 5.1 and 5.2) appears to be one of the best localities in which to study these hydrothermal processes, because of excellent outcrop exposures and because at least four separate domains of water-rock interaction can be delineated there. These domains are: (1) deep-seated metamorphic/magmatic interactions in the lower-plate rocks analogous to those discussed

Figure 5.1 -- Tectonic map of part of southeastern British Columbia showing the southern Omineca belt (after Parrish et al., 1988) showing the major crustal layers, detachment faults, and deep-seated thrust faults. The detailed study areas for the detachment faults studied for $^{18}O/^{16}O$ in this work are indicated by the rectangular outlines shown on the map. These detachment faults are the older, east-dipping Slocan Lake and Columbia River (CRF) faults, the mylonitic Valkyr shear zone, the younger, west-dipping Okanagan (OF) and Beavan faults, and the Eagle River fault and steep normal faults in the basement of the Monashee complex. Meteoric-hydrothermal water-rock interaction was also discovered along the Monashee decollement in the southern Thor-Odin complex (see Chapters 3 and 4). Other detachment faults singled out on this map are the Purcell Trench fault (PTF), the Newport fault (NF), the Granby fault (GF).

Figure 5.2 -- Simplified geologic map of the Valhalla complex and surrounding areas (modified after Carr et al., 1987) showing sample locations studied in this work. This area extends from latitude 49°05' N on the south, just north of the U.S.A.-Canada border, to 50°05' N, and from longitude 117°05' to 118°22' W. Sample locations are numbered and the $\delta^{18}O$ and $\delta^{13}C$ values are keyed to these samples on Tables 5.1, 5.2, 5.3, and 5.4. The locations of the 15 samples of the Slocan Lake fault (SLF) study area are shown on a more detailed map in Figure 5.6. Ladybird leucogranite samples considered in the discussion of the Valkyr shear zone (VSZ) are denoted by the two rectangular areas that straddle the VSZ on the western margin of the Valhalla complex. Results from the Valhalla core and upper-plate intrusive rocks, the Slocan Lake fault, the Valkyr shear zone, and the Coryell intrusive suite are discussed separately. The Valhalla core is the area in the footwall of the Slocan Lake fault and the Valkyr shear zone. The Coryell intrusions are west and southwest of the Valhalla complex.

Figure 5.1 Detachment Fault Study Areas

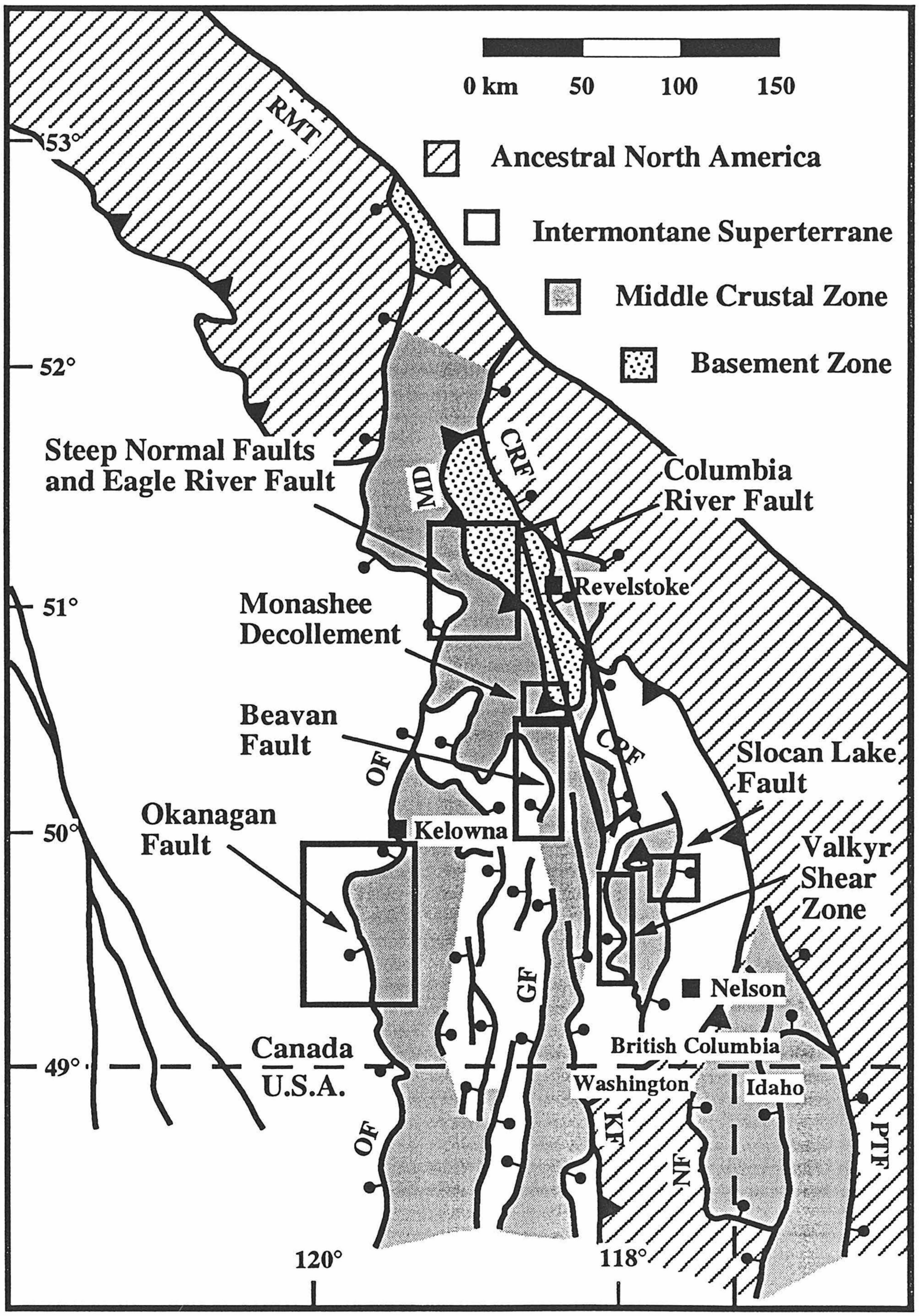

Figure 5.2 Valhalla Complex

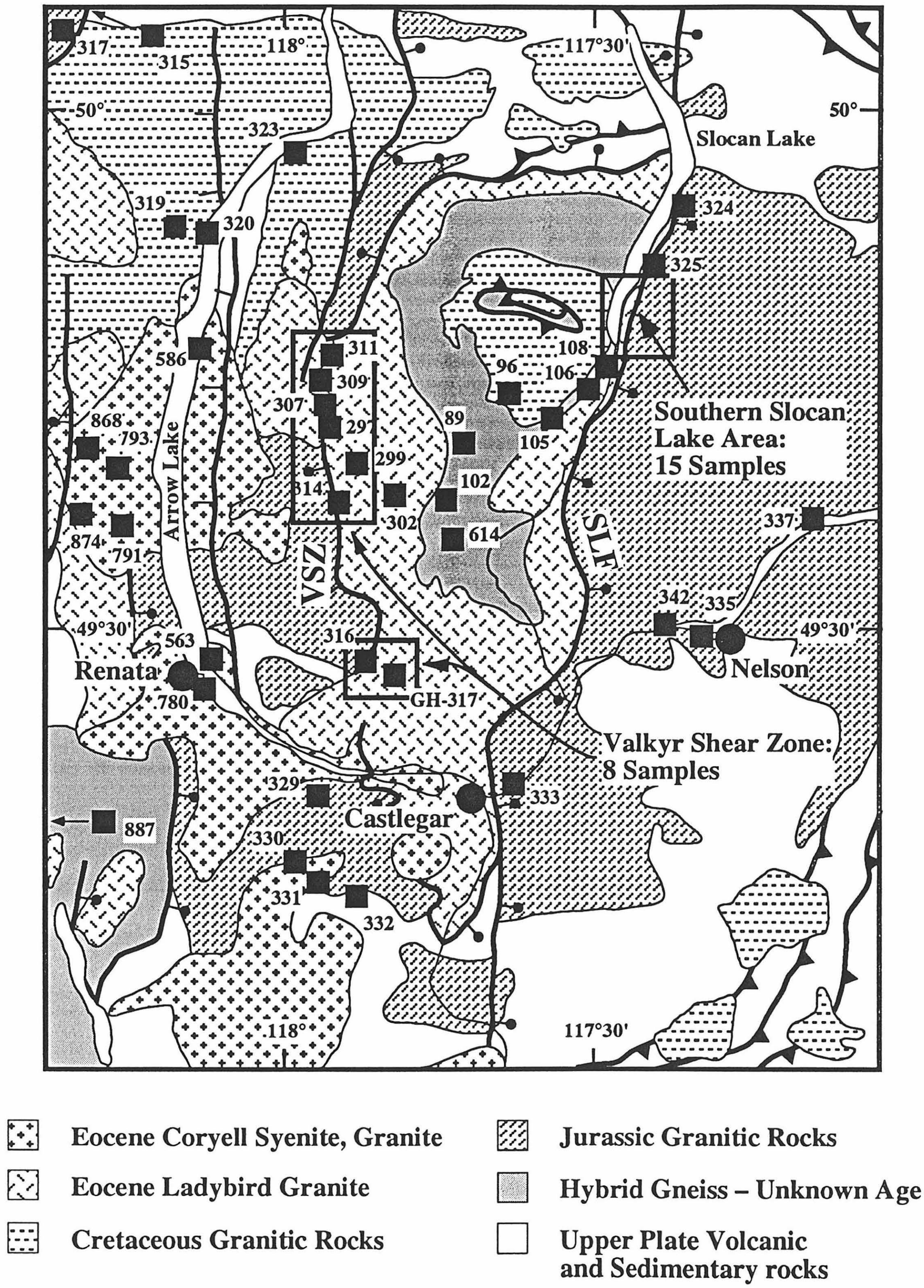

in Chapter 4; (2) detachment fault-related meteoric water-rock interaction along the Slocan Lake fault; (3) post-deformational hydrothermal activity along the Valkyr shear zone; and (4) syn-emplacement meteoric-hydrothermal metamorphism associated with the Eocene Coryell alkaline intrusions.

The Slocan Lake fault hydrothermal system is examined in detail below and modeled using the kinetic oxygen isotope exchange model for a two mineral-water system (Criss et al., 1987; Gregory et al., 1989). This modeling provides a comparative and conceptual framework within which these other hydrothermal systems can be compared. Variations in the style and intensity of meteoric-hydrothermal metamorphism are considered according to local structural environment, the thermal state of the lower plate as it relates to syntectonic plutonism, displacement and timing of detachment faulting, and lithologic controls. This detailed isotopic investigation of the Valhalla complex is then contrasted and compared with reconnaissance studies of other detachment-fault hydrothermal systems along the Columbia River fault, the Beavan-Cherryville fault system, and the Okanagan fault.

5.2 The Valhalla Complex

Detachment fault-related hydrothermal processes can be well characterized throughout the Valhalla complex (Figure 5.2). For purposes of discussion, the stable isotope data from this core complex are separated into four groups: (1) the deep rocks of the Valhalla core, (2) the Slocan Lake fault, (3) the Valkyr shear zone, and (4) the Coryell intrusive suite. These four groups provide distinct geologic and $^{18}O/^{16}O$ domains that are related to, and controlled by, the diverse tectonoplutonic phenomena that formed this complex. Note that the deep rocks studied in this work from the Valhalla core only include samples from the middle crust (*i.e.*, those generally thought to be correlative with the Selkirk allochthon of the Thor-Odin complex); no rocks equivalent to the basement rocks beneath the Monashee decollement were analyzed.

Numerous $^{18}O/^{16}O$ data from Magaritz and Taylor (1986), particularly their "Nelson batholith" sample suite, are included in the following discussion of the Valhalla complex. These data provide a regional framework for the Valhalla data, allowing the entire data set to be reinterpreted in light of recent advances in our understanding of the tectonic development of these metamorphic core complexes and environs. The main conclusion of Magaritz and Taylor (1986) was that large depletions in $\delta^{18}O$ and δD throughout southern British Columbia were the result of meteoric-hydrothermal metamorphism associated with the emplacement of Tertiary plutons along large, lake-filled, north-trending fracture zones. These fracture zones have subsequently all been found to be detachment faults related to the exhumation of high-grade lower plate rocks of the numerous metamorphic core complexes that comprise the southern Omineca belt (Carr et al., 1987; Parrish et al., 1988).

5.2.1 Geologic Setting

The Valhalla complex is one of the many metamorphic culminations in the southern Omineca belt exposed as the result of Eocene extension (Parrish et al., 1988). This metamorphic core complex was exhumed as a result of Cretaceous deep-level thrusting and obduction, followed by Eocene extension (Carr et al., 1987; Parrish, 1995; Spear and Parrish, 1996). Fundamental geologic relationships at this complex (Figures 5.2 and 5.3) are similar to those of the southern Thor-Odin complex described in Chapter 4: (1) there are Cretaceous-Paleocene compressional ductile shear zones, the Gwillim Creek shear zone, exposed in the deepest part of the complex (Carr et al., 1987; Parrish et al., 1988); (2) the middle crustal section between the thrust faults and detachment faults is characterized by large volumes of syntectonic anatectic leucogranite (Reesor, 1965; Carr et al., 1987); and (3) final exhumation and cooling of the lower plate took place during

Figure 5.3 -- ENE-trending cross section (no vertical exaggeration) across Figure 5.2 of the Valhalla metamorphic core complex (modified after Carr et al., 1987), showing by projection the relative structural positions of samples studied in this work (solid squares). These samples provide $^{18}O/^{16}O$ data through at least 5 km of section going from deep in the lower plate up to 2 km above the detachment fault in the upper-plate Nelson granodiorite. This cross section shows the layered and domed structure of this metamorphic core complex.

Figure 5.4 -- Thermal evolution of the Valhalla complex (from Spear and Parrish, 1996). Peak metamorphic temperatures and pressures in the Valhalla lower plate were $820 \pm 30\ ^{\circ}C$ and 8 ± 1 kbar. The metamorphic peak at 67-72 Ma and a cooling rate of ~25 $^{\circ}C/Ma$ are shown. The metamorphic peak occurred while the complex was still within the compressional deformational regime.

Figure 5.3 Generalized Cross Section of the Valhalla Complex

(No Vertical Exaggeration)

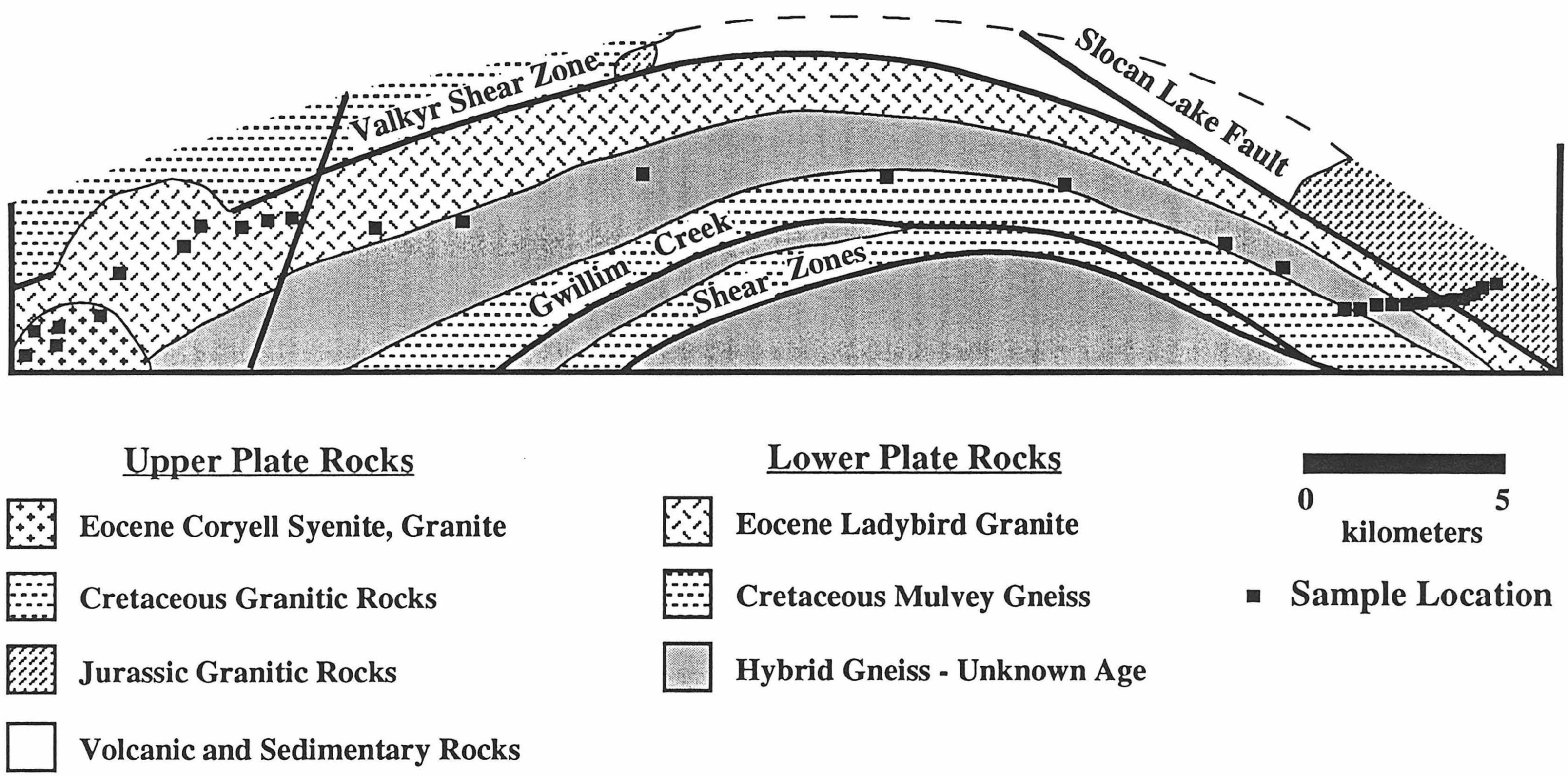

Figure 5.4 Valhalla Complex Thermal History

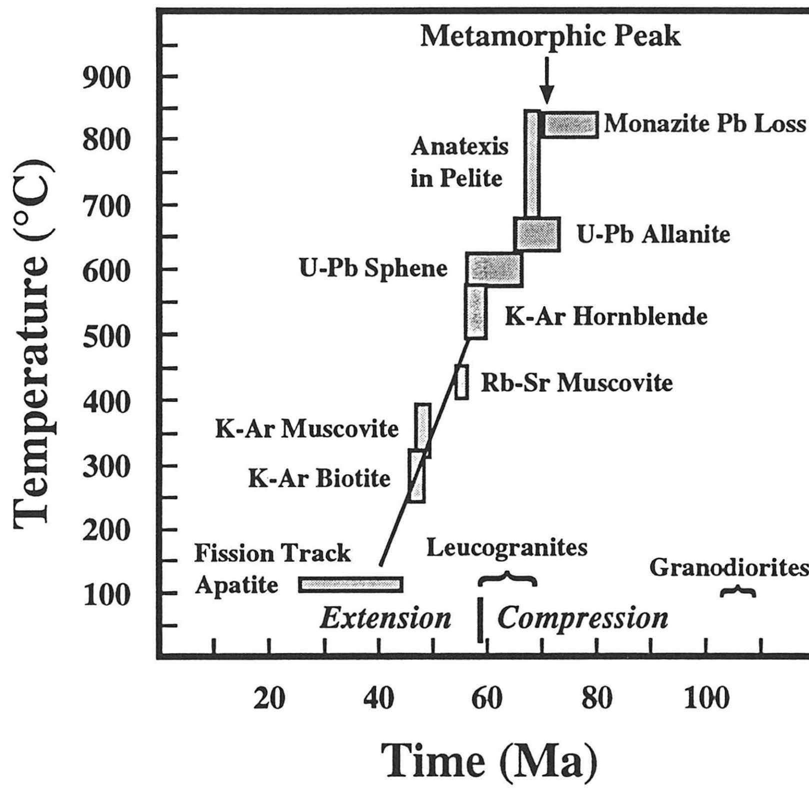

Eocene detachment faulting, principally along the Slocan Lake fault (Parrish, 1984; Carr et al., 1987).

The Valhalla complex differs from the Thor-Odin complex in several ways: (1) detachment fault kinematics are more complex, with cessation of deformation along the ductile Valkyr shear zone early in the extensional history (> 56 Ma; Carr et al., 1987), analogous to the "mylonitic front" at the Whipple Mountains complex (Davis and Lister, 1988); (2) there are two distinct intrusive phases of the Paleocene-Eocene Ladybird plutonic suite, namely the Airy quartz monzonite and the main part of the Ladybird granitic suite (Reesor 1965; Carr et al., 1987); (3) Cretaceous metaplutonic rocks comprise the immediate hanging wall of the Gwillim Creek shear zone (Carr et al., 1987); and (4) as mentioned above, outcrops of deep-seated basement gneiss are rare at Valhalla, and also relatively inaccessible.

The lower plate of the Valhalla complex is comprised of a thick anatectic hybrid gneiss sequence intruded by the Cretaceous Mulvey orthogneiss, and overlain by the Paleocene Airy quartz monzonite, which is in turn overlain by Ladybird series leucogranites. The Mulvey gneiss is a 110 Ma (Spear and Parrish, 1996), melanocratic, megacrystic K-feldspar hornblende-biotite granodiorite gneiss cut by leucocratic veins. The Airy quartz monzonite is a 62 Ma (Carr et al., 1987), megacrystic K-feldspar biotite-hornblende granitic gneiss. The Ladybird granite is the unit that provides our best data constraining the timing of extension at this core complex. A variably deformed and mylonitized leucocratic biotite quartz monzonite from the Ladybird suite has been dated at 59 Ma; and an undeformed pegmatitic granite that is post-tectonic to the Valkyr shear zone has been dated at 56.5 Ma (Carr et al., 1987). All of these plutonic gneisses are sheet-like units that appear to become younger in an upward direction (see Figures 5.2 and 5.3).

The Valhalla lower-plate hybrid gneiss is a highly deformed and mylonitized paragneiss unit of unknown age. The intensity of deformation in this unit increases toward the detachment faults. Dominant lithologies include quartzofeldspathic gneiss, metapelitic schist and gneiss, amphibolite, calc-silicate gneiss, and minor quartzite. These rocks are highly migmatitic and locally contain up to 75% lit-par-lit pegmatitic leucogranite (Reesor, 1965; Carr et al., 1987). This hybrid gneiss unit is the uppermost of three sheets of metasedimentary rocks at this complex; the other two sheets lie beneath the Gwillim Creek shear zone.

For the deep lower plate, peak granulite facies metamorphic pressure and temperature estimates of 820 ± 30 °C and 8 ± 1 kbar were obtained by garnet-biotite Fe-Mg exchange thermometry and the consideration of dehydration melting phase equilibria (Spear and Parrish, 1996). As shown in Figure 5.4, cooling from 820 °C to ~ 600 °C is inferred to be rapid (>500 °C/Ma), perhaps in response to Paleocene thrusting of the complex over cooler basement rocks along the Gwillim Creek shear zone. Geochronometers having different diffusive closure temperatures provide a ~ 25 °C/Ma cooling rate from 600 °C to ~ 150 °C between 60 and 45 Ma (Parrish, 1995; Spear and Parrish, 1996).

5.2.2 Samples Studied

Mineral separates from nine metasedimentary and metaplutonic rocks from the mid-crustal core of the Valhalla complex were analyzed to determine the degree of $^{18}O/^{16}O$ homogeneity in these rocks, for the purpose of using these data as a baseline whereby one can evaluate changes in oxygen isotopic composition of the lower plate rocks involved in detachment faulting and hydrothermal alteration. A total of seven samples of the hybrid gneiss were collected along logging roads that traverse the deep sections of this metamorphic core complex. Lithologies collected from this unit include amphibolite, calc-silicate, marble, quartzofeldspathic gneiss, metapelite, and leucogranite. One sample each of the Airy quartz monzonite and the Mulvey melanocratic granodiorite gneiss round out this reconnaissance suite of samples from the core-zone of the Valhalla complex.

Mineralogical evidence of hydrothermal alteration is limited to local replacement of biotite by chlorite and plagioclase by sericite. The amphibolite (GH-89) is comprised of hornblende+garnet+biotite+ pyroxene+quartz+plagioclase; pyroxene overgrows biotite. The plagioclase and K-feldspar of the leucocratic segregation at this outcrop (GH-89a) is slightly altered to sericite; this alteration is most likely the result of the release of water from the adjacent leucogranite as it crystallized. Alteration of feldspar to sericite is minor in the highly deformed quartzofeldspathic gneiss, metapelite, and calc-silicate that lie just beneath the Slocan Lake fault (GH-105, 106, and 108); these rocks are highly sheared, with the quartz displaying ribbon textures and grain-size reduction of biotite and feldspar, as well as parallel preferred orientation of biotite and sillimanite. The Airy quartz monzonite (GH-302) contains megacrysts of K- feldspar (with plagioclase inclusions); mafic minerals in this rock include biotite and hornblende, with the biotite altered to chlorite+opaques, and with seritization of feldspar being more prominent than in the samples mentioned above. The Mulvey granodiorite gneiss (GH-96) is a recrystallized hornblende+biotite melanocratic rock with no observed alteration; mafic minerals comprise ~30% of this rock.

5.2.3 Results

As shown in Figure 5.5, metapelite, calc-silicate, amphibolite, and leucogranites from the hybrid gneiss unit have quartz $\delta^{18}O$ values of +11.4 ± 0.9‰ (N = 6) and feldspar $\delta^{18}O$ = +10.2 ± 0.2‰ (N = 3). An amphibolite and a leucogranite sheet collected within 1 m of each other have whole rock $\delta^{18}O$ = +9.0 and +9.3, respectively. One very highly strained graphitic, siliceous calc-silicate just beneath the mylonitic shear zone associated with the Slocan Lake fault has quartz $\delta^{18}O$ = +16.5. One sample of the

TABLE 5.1. $^{18}O/^{16}O$ DATA ON ROCKS AND MINERALS FROM THE VALHALLA METAMORPHIC CORE COMPLEX

Sample*	Rock Type	WR†	Qz†	Fs†	Water/Rock Ratio§	Cc# $\delta^{18}O$	Cc# $\delta^{13}C$
UPPER PLATE							
Upper Plate Marbles							
GH-342	Marble					17.9	−1.0
GH-887a	Marble					14.2	0.8
Cretaceous Quartz Monzonite Stock							
MT-323	Quartz Monzonite		9.6	8.5			
MT-323a	Aplite Dike	9.2					
MT-323b	Late Mafic Dike	−5.3					
Jurassic Nelson Batholith							
Distal to Slocan Lake Fault							
MT-333	Quartz Diorite		10.3	8.6			
MT-335	Quartz Diorite			8.6			
MT-336	Quartz Diorite		13.3	11.6			
MT-337	Quartz Diorite		12.0	9.7			
Proximal to Slocan Lake Fault							
GH-118	Slightly Altered Granodiorite	5.5	11.5	7.0	0.14	2.0	−4.8
GH-120	Fresh Granodiorite	8.4	12.1	9.0	0.05	1.2	−5.8
MT-325	Fresh Granodiorite		11.4	9.6	0.04		
GH-122	Fresh Granodiorite	7.9	11.9	8.7	0.07	2.1	−5.5
GH-123	Altered Granodiorite			2.9	0.34		
GH-124a	Highly Altered Granodiorite	−0.2	11.3	−1.4	0.63	−3.0	−4.9
MT-324	Highly Altered Granodiorite		9.1	−5.0	1.05		
ZONE OF BRECCIATION							
GH-125	Carbonate-rich breccia	0.2			0.73	−2.1	−5.6
GH-127	Very altered granitoid	0.9			0.66	−3.2	−2.9
GH-150	Chloritic granitoid	3.3	11.4	0.5	0.49	2.5	−1.1
LOWER PLATE MYLONITE							
GH-151	Ladybird mylonite w/muscovite	7.6	11.0	6.6	0.16		
GH-154	Brittle shear zone in granite	5.3			0.31		
GH-155	Leucogranite mylonite	10.0	11.3	8.9			
GH-159	Mylonitic paragneiss		12.6	10.3			
GH-140	Mylonitic leucocratic sheet	9.6	11.6	9.1			
GH-134	Mylonitic augen gniess	10.1	11.2	8.6			
MT-326	Migmatite in hybrid gneiss			9.8			
DEEP LOWER PLATE - VALHALLA CORE							
Hybrid Gneiss							
GH-89	Amphibolite	9.0	11.2				
GH-89a	Leucogranite Sheet	9.3	10.4	10.2			
GH-102a	Calc-silicate		12.6	10.5			
GH-105	Quartzofeldspathic Gneiss		12.0	10.0			
GH-106	Metapelite		10.7				
GH-108	Graphitic Calc-silicate		16.5				
GH-614	Marble					20.6	2.2

TABLE 5.1 (Continued)

Sample*	Rock Type	WR†	Qz†	Fs†	Water/Rock Ratio§	Cc# $\delta^{18}O$	Cc# $\delta^{13}C$
DEEP LOWER PLATE - VALHALLA CORE							
Paleocene Airy Quartz Monzonite							
GH-302	Quartz Monzonite	9.2	10.1	9.0			
Cretaceous Mulvey Granodiorite Gneiss							
GH-96	Melanocratic Gneiss	8.4	9.8	9.0			
THE VALKYR SHEAR ZONE							
Eocene Ladybird Quartz Monzonite							
GH-297	Protomylonite Granite		10.8	8.1	0.05		
GH-307	Undeformed Granite	1.0	7.8	0.2	0.59		
GH-309	Quartz Monzonite		11.2	7.9	0.06		
GH-309a	Quartz + Feldspar Vein		10.9	7.0	0.11		
GH-311	Quartz Monzonite		10.5	7.7 6.0s	0.08		
GH-314	Quartz Monzonite		10.9	8.8	0.02		
GH-316	Undeformed Granite		10.8	8.8	0.02		
GH-317	Mylonitic Quartz Monzonite		9.7	4.6	0.25		
Late-Stage Mafic Dike							
GH-299	Lamprophyre	–5.1				–1.3	–2.4

Note: Mineral separates were hand-picked under the microscope. Some quartz separates were treated with HF to remove impurities. Oxygen was liberated from quartz and feldspar by reaction with F_2 in Ni reaction vessels at 550 °C (Taylor and Epstein, 1962), converted to CO_2, and analyzed on a Finnegan MAT 252 mass spectrometer.

*Numbers refer to samples archived at the Division of Geological and Planetary Sciences, California Institute of Technology, Pasadena, California. Data are from sample localities on Figure 5.2 and 5.6.

†The oxygen isotope data for whole rocks (WR), quartz (Qz), feldspar (Fs), and calcite (Cc) are reported in the δ notation, where δ is the relative difference in parts per thousand in $^{18}O/^{16}O$ between the sample and a standard. The standard is V-SMOW (Vienna standard mean ocean water). NBS-28 has a $\delta^{18}O$ = +9.60 on this scale. Replicate analyses of samples and the Caltech rose quartz working standard ($\delta^{18}O$ = +8.45) have an analytical error of ± 0.2‰.

Water/rock ratios are calculated using the open-system water/rock ratio equation of Taylor (1977), initial feldspar $\delta^{18}O$ = +10.5, initial H_2O $\delta^{18}O$ = –15, the equilibrium feldspar-H_2O oxygen isotope fractionation equation of O'Neil and Taylor (1967) at T = 300 °C for the Slocan Lake fault and T = 450 °C for the Valkyr shear zone. These calculated values were multiplied by the 0.75 to account for the proportion of feldspar in the rock.

#The calcite stable isotope data were acquired utilizing the standard reaction with H_3PO_4 (McCrea, 1950), and corrected using the fractionation factor of 1.01008 (Sharma and Clayton, 1965).

Figure 5.5 -- Plot of mineral and whole rock $\delta^{18}O$ data from the Valhalla core gneisses, the Nelson batholith distal to detachment faults, the Spruce Grove batholith, the Whatshan batholith, and upper plate marbles. Sample locations are plotted on Figure 5.2, excluding MT-315 and GH-887. $\delta^{18}O$ values are shown for whole rock (solid squares), quartz (solid dots), feldspar (open dots), and calcite (open squares). Data from the present study are denoted by the GH designation and the Magaritz and Taylor (1986) data are numbered with the MT designation. The data from the Valhalla core and the Nelson batholith are compared with data from the Slocan Lake detachment fault and the Valkyr shear zone. The Spruce Grove batholith comprises the hanging wall of the Beavan fault. The samples from the Whatshan batholith have all been affected to a certain extent by meteoric-hydrothermal alteration focused along the Columbia River and Beavan faults.

Figure 5.5 Data From the Valhalla Lower Plate and Surrounding Batholiths

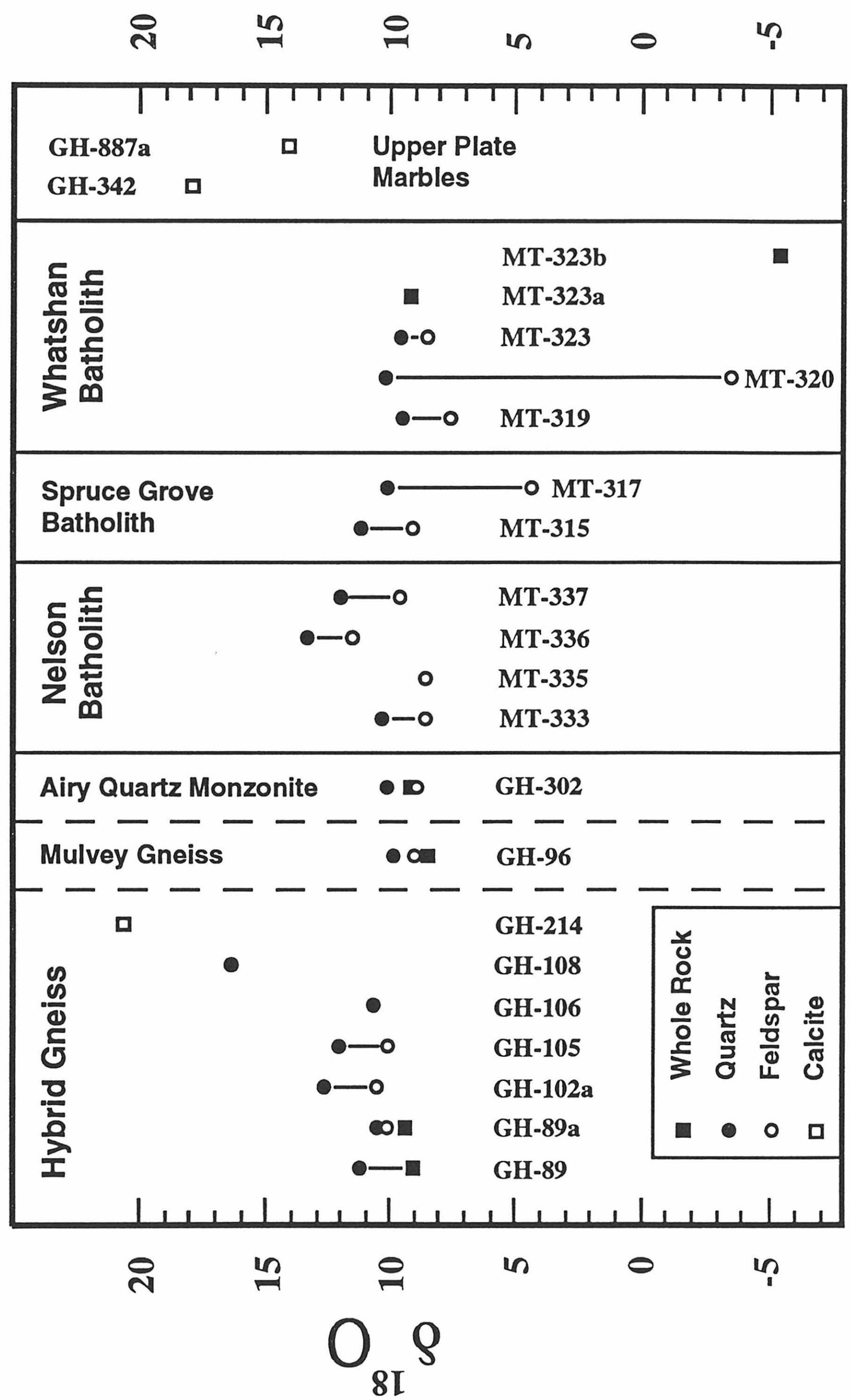

Paleocene Airy quartz monzonite has whole rock, quartz, and feldspar $\delta^{18}O$ values of +9.2, +10.1, and +9.0, respectively. A melanocratic granodiorite belonging to the Mulvey orthogneiss unit has whole rock, quartz, and feldspar $\delta^{18}O$ values of +8.4, +9.8, and +9.0, respectively. Quartz-feldspar oxygen isotope fractionations (~ 1.5‰) in these samples from the core of the Valhalla complex indicate magmatic $^{18}O/^{16}O$ equilibrium temperatures. The overall range in $\delta^{18}O$ for these Valhalla mid-crustal lower-plate rocks is similar to the range ($\delta^{18}O$ = +8 to +11) observed by Nesbitt and Muehlenbachs (1995) in whole rocks from this terrane. One dolomitic marble has $\delta^{18}O$ = +20.6 and $\delta^{13}C$ = +2.2; both values are typical of marbles throughout the region (Ohmoto and Rye, 1970; Ghent and O'Neil, 1985; Nesbitt and Muehlenbachs, 1995; Holk and Taylor, 1996).

5.2.4 Discussion

Quartz and feldspar $\delta^{18}O$ values from the mid-crustal, lower-plate rocks of the Valhalla complex show a degree of oxygen isotope homogeneity similar to that observed in analogous rocks of the Selkirk allochthon in the southern Thor-Odin complex discussed in Chapter 4. The $\delta^{18}O$ values of the homogenized rocks at Valhalla are, however, about 1‰ lower than similar rocks in the southern Thor-Odin complex; this probably reflects an original lower-^{18}O bulk composition for the Valhalla protolith, compatible with the fact that marbles and calc-silicate rocks are much less abundant at Valhalla compared to Thor-Odin (Reesor, 1965; Reesor and Moore, 1971). Quartz $\delta^{18}O$ values of the Mulvey orthogneiss and the Airy quartz monzonite are, respectively, 1.3‰ and 1.6‰ lower in ^{18}O than the average hybrid gneiss quartz $\delta^{18}O$ value (+11.4), another indication of an overall lower $\delta^{18}O$ value for the Valhalla mid-crustal section as compared to the Thor-Odin mid-crustal section.

Except for the fact that the mid-crustal section is about 1‰ lower in ^{18}O in the Valhalla core complex than it is in the southern Thor-Odin core complex, all of the discussion of the latter concerning $^{18}O/^{16}O$ homogenization and its relationship to the abundant associated anatectic leucogranite also basically applies to the Valhalla rocks. However, to a greater extent than was the case at Thor-Odin, $^{18}O/^{16}O$ homogenization at Valhalla was locally incomplete, as it did not markedly affect the extremely rare samples of dolomitic marble ($\delta^{18}O = +20.6$) and highly strained calc-silicate ($\delta^{18}O = +16.5$). Again, as discussed above in Chapter 4, these rock types were probably relatively impermeable to aqueous fluids during deformation; marbles are known to be impermeable at these high temperatures and pressures (*e.g.*, Rye et al., 1977), and the calc-silicate is a true mylonite consisting mainly of ribbon quartz and lacking late fractures.

Water/rock ratios were probably very low during high-grade metamorphism of the Valhalla hybrid gneiss at temperatures of up to 820 °C. This is consistent with the absence of late-stage muscovite throughout the complex, probably a signal that this complex was almost completely dewatered at temperatures above the wet granite solidus (Spear and Parrish, 1996). The Valhalla complex thus apparently experienced slightly higher temperatures (>800 °C) than the Thor-Odin complex (~750 °C); this is also reflected in the contrasting temperatures of these Paleocene-Eocene leucocratic magmas (hornblende is absent from the Ladybird suite at Thor-Odin, but is present at Valhalla).

5.3 The Slocan Lake Fault: A Case Study

5.3.1 Geologic Setting

The Slocan Lake fault (Figure 5.2) is the detachment fault that separates high-grade metasedimentary and metavolcanic gneisses of the Valhalla complex from unmetamorphosed (but hydrothermally altered) plutonic rocks of the Nelson batholith (Parrish, 1984). This structure is a gently east-dipping (30-40°), ductile to brittle, normal fault that was active at 54 - 45 Ma (Carr et al., 1987). The final stages of uplift of the Valhalla complex were accommodated by movement along this fault (Parrish, 1984; Carr et al., 1987; Parrish et al., 1988; Parrish, 1995; Spear and Parrish, 1996). Cooling rates during the detachment faulting were ~ 25 $^{\circ}$C (Spear and Parrish, 1996).

The Slocan Lake fault is arguably one of the best locations in the world for examining the characteristics of hydrothermal systems associated with detachment faulting. The lithologically homogeneous parts of the Nelson batholith appear to have originally been isotopically fairly uniform, thus providing a reliable baseline for monitoring stable isotopic changes in the upper plate. Furthermore, a continuous upper-to-lower plate cross section is exposed through the Slocan Lake detachment fault, allowing for a confident evaluation of changes in hydrothermal regimes according to deformational style, lithology, and structural position. These excellent exposures afford both spatial and temporal delineation of discrete fluid flow paths. However, in this connection, the most important attribute of the Slocan Lake detachment fault, and of other such faults in the southern Omineca belt, is its high latitude location during the Eocene. Meteoric waters are known to have been very low in $\delta^{18}O$ and δD in this region during detachment faulting (Magaritz and Taylor, 1986; Nesbitt and Muehlenbachs, 1995), meaning that there were enormous isotopic differences between these fluids and either magmatic or metamorphic waters, thereby allowing for a more solid assessment of the degree of water-rock interactions of various types that affected these rocks.

The 159-170 Ma Nelson batholith (Nguyen et al., 1968; Parrish, 1992; Ghosh, 1995), intrusive into low-grade black shales, volcaniclastics, and siltstones of the Triassic Slocan Group and early Jurassic Rossland Group, comprises the upper plate of the Slocan Lake fault. The Nelson plutonic suite is made up of massive porphyritic granodiorite, leucocratic hornblende-quartz syenite, and granite (Little, 1960; Reesor, 1965). Only the most abundant phase of this batholith, namely the granodiorite, was chosen for study, providing a monolithologic medium for use in quantifying $^{18}O/^{16}O$ exchange processes in the upper plate. This hornblende granodiorite is megacrystic with K-feldspar megacrysts up to 3 cm in length making up ~15 vol % of the rock. The modal mineralogy (in vol %) of this unit is: ~15% quartz, ~15% K-feldspar, ~45% plagioclase (An_{30}), ~10% hornblende, ~10% biotite, ~2% pyroxene, and ~3% accessory minerals. Numerous Ag-Pb-Zn mineral deposits formed during detachment faulting along the Slocan Lake fault are hosted by these upper plate rock units (Beaudoin et al., 1992).

A zone of brecciation separates the upper-plate Nelson batholith from the mylonitic lower-plate Ladybird leucogranite (Reesor, 1965; Parrish, 1984; Carr et al., 1987). This zone consists of brecciated mylonitic leucogranite and fractured, brecciated granodiorite that experienced intense chloritic and sericitic hydrothermal alteration. Fault gouge zones are common, and all coherence of prexisting rock fabric has been destroyed by overprinting brittle deformation (Parrish, 1984).

The uppermost part of the mylonitic lower plate is a foliated biotite quartz monzonite belonging to the Eocene Ladybird plutonic suite. These rocks have ~30% quartz, ~35% K-feldspar, ~30% plagioclase (An_{25}), ~5% biotite, and <1% accessory minerals. Mylonitic rocks are slightly porphyritic with ~ 2-5 mm rotated K-feldspar phenocrysts (or porphyroblasts ?). Fabrics are all consistent with an east-dipping stretching lineation and foliation, and indicate increasing strain toward the contact with the zone of brecciation (Carr et al., 1987). Just below the brittle zone, discrete zones of pseudotachylite and brittle shear zones crosscut the earlier mylonitic fabrics at a low angle (Parrish, 1984; Carr et al., 1987).

Beneath the leucogranite is the highly strained hybrid gneiss, a unit comprised of metasedimentary rocks that have been lit-par-lit intruded by leucogranite (Reesor, 1965; Carr et al., 1987). Within the mylonite zone is a ductilely-sheared, diopside-bearing, calcareous mylonite (Parrish, 1984). The hybrid gneiss has many transposed folds with east-trending axes. The Mulvey orthogneiss (Figure 5.6) is a veined biotite-hornblende

Figure 5.6 -- Geologic map of the Slocan Lake fault near Slocan, British Columbia (modified after Parrish, 1984). Sample locations are shown and numbered. The upper plate (right hand side of the figure) is comprised of the middle Jurassic Nelson granodiorite. Mylonitic rocks of the lower plate (along both sides of Slocan Lake) are the Eocene Ladybird leucogranite, hybrid gneiss of unknown protolith age, and the late Cretaceous Mulvey orthogneiss. A zone of brittle deformation (Slocan Lake fault gouge) marks the boundary between the upper and lower plates. Samples MT-323, 324, and 325 are located 20, 10, and 5 kilometers north of sample GH-150 along the east side of the lake (also see Figure 5.2).

Figure 5.7 -- Quartz and feldspar $\delta^{18}O$ vs. structural height relative to the Slocan Lake fault. The ranges of homogeneous quartz and feldspar $\delta^{18}O$ values from samples that escaped $^{18}O/^{16}O$ exchange with large amounts of meteoric water are shown by the two different diagonal patterns. Feldspar ^{18}O-depletions (down to a minimum $\delta^{18}O = -5.0$) are observed in most samples collected within the 1 km-thick zone that encompasses the brittle part of the Slocan Lake fault zone; this includes the upper 300 m of the quartz monzonite mylonite beneath the fault, and the lower 700 m of the Nelson granodiorite above the fault, indicating that the meteoric-hydrothermal exchange effects are related to the episode of detachment faulting. The localization of these ^{18}O-depleted feldspars at the fault zone indicates channelization of meteoric fluids along it. The location of the greatest isotopic shift from unaltered values is at the boundary between the Nelson granodiorite and the zone of brecciation and fault gouging.

Figure 5.6 The Southern Slocan Lake Area

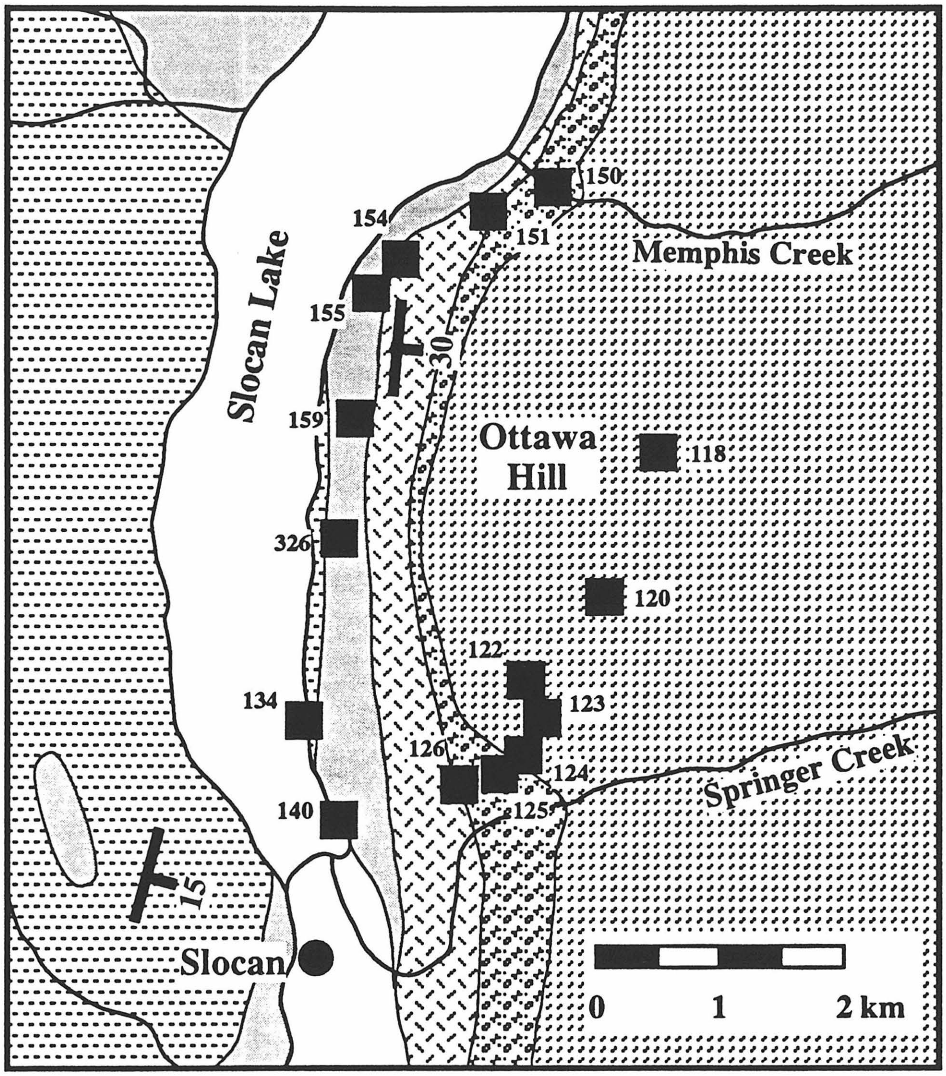

Upper Plate

Jurassic Nelson Granodiorite

Slocan Lake Fault

Eocene Slocan Lake Fault Gouge

Lower Plate

Eocene Ladybird Granite, Mylonitic

Cretaceous Mulvey Orthogneiss

Hybrid Gneiss - Unknown Age

Figure 5.7 Slocan Lake Fault and Valhalla Complex

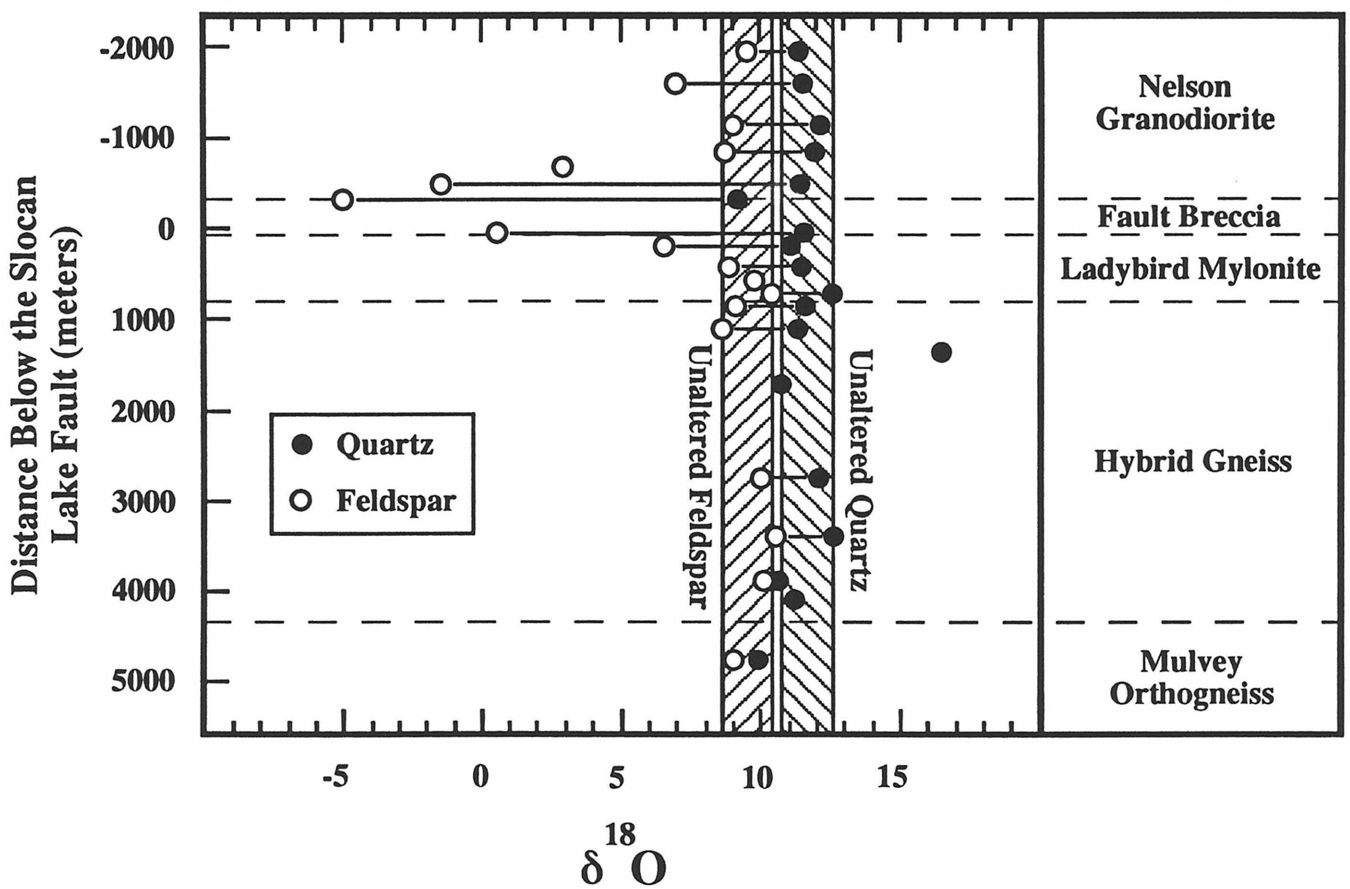

K-feldspar augen granodiorite gneiss that makes up the base of the mylonitic sequence. These orthogneisses crop out along the eastern shore of Slocan Lake in the study area.

5.3.2 Samples Studied

Mineral separates were studied from 14 samples collected near the Slocan Lake fault in the vicinity of the village of Slocan, British Columbia, in order to assess meteoric-hydrothermal water-rock interaction through a 2.5 km-thick cross section through this detachment fault (Figure 5.6). Three samples collected by Magaritz and Taylor (1986) along the eastern shore of Slocan Lake supplement these data (see Figure 5.2 for locations). These earlier localities were re-visited during the present study and geologic observations were recorded. Access to this fault zone was provided by the highway that follows the eastern shore of Slocan Lake. Roadcuts along this highway provide up to 3 km of continuous exposure, going from the upper plate granodiorites down to the deepest lower-plate orthogneiss unit.

Seven samples of Nelson granodiorite were collected from the upper plate along a logging road that traverses up Ottawa Hill and connects with the main highway at the Slocan townsite (Figure 5.6). As the Slocan Lake fault zone is approached, the granodiorite grades from an apparently undeformed state to heavily fractured, oxidized, and hydrothermally altered. Calcite-filled fractures become common within 500 m of the zone of intense brecciation. Hornblende and biotite alter to chlorite and opaques (probably ilmenite); the intensity of this alteration increases toward the brittle zone with biotite-out at ~ 400 m and hornblende-out at ~ 100 m above the brittle zone. Sericite alteration of feldspar increases downward, but K-feldspar is less affected than plagioclase, with sericitization occurring mostly along cracks in K-feldspar, whereas plagioclases are all cloudy and apparently pervasively altered to disseminated sericite.

Three samples from the zone of brittle deformation and brecciation were collected along the main highway and the Ottawa Hill logging road. These ground-up and shattered rocks are the most intensely altered of the entire section, with only remnants of the protolith mineralogy preserved. All mafic minerals have been hydrothermally obliterated and replaced by sericite and opaques. Most plagioclase is also gone, but some remnants of sericitized K-feldspar remain. Muscovite porphyroblasts are observed at the base of this unit. Calcite alteration is pervasive. This intense alteration makes it difficult to decide whether these rocks were originally Nelson granodiorite or Ladybird leucogranite.

Six lower-plate mylonites were collected along the main highway and a trail that follows the east shore of Slocan Lake. One Magaritz and Taylor (1986) sample (326) was added to this set. These samples provide a > 1 km traverse into the lower plate beneath the brittle zone through the mylonitic Ladybird granite, hybrid gneiss, and Mulvey granodiorite gneiss. No late calcite was observed. Biotite is altered to chlorite and randomly oriented leucoxene. Chlorite locally replaces garnet. However, the most distinctive aspect of this zone is the presence of muscovite prophyroblasts formed during ductile shearing; kinematic indicators defined by the preferred orientation of these phyllosilicates (Simpson and Schmid, 1983) indicate a top-to-the-east shear. Quartz is completely recrystallized, with fabrics indicating shear strain increasing upward. One sample (GH-154) is from a late-stage brittle shear zone ~300 m below the brittle zone that crosscuts the mylonitic fabrics in the Ladybird leucogranite; this has alteration mineralogy similar to the basal portions of the zone of brittle deformation.

Data from these samples are compared to the previously discussed results from the deep mid-crustal section of the lower plate of the Valhalla complex, as well as to the Nelson batholith away from known detachment faults. These data provide baselines for a comparison between altered and unaltered rocks.

5.3.3 *Integration of Results with Earlier Studies*

Whole-rock and mineral $\delta^{18}O$ values of samples from the Slocan Lake fault indicate oxygen isotope disequilibrium as the result of exchange with meteoric-hydrothermal fluids during detachment faulting (Figures 5.7 and 5.8). $\delta^{18}O$ and $\delta^{13}C$ values of calcite from the late fractures indicate meteoric water circulation continued late into the deformational history of this fault zone (Figure 5.8).

Results from the upper plate of the Slocan Lake fault are compared to data (Magaritz and Taylor, 1986) from the Nelson batholith located far from this detachment fault. These data far from the fault display variable quartz $\delta^{18}O$ (+10.3 to +13.3, N = 3) and feldspar $\delta^{18}O$ (+8.6 to +11.6, N = 4). $\Delta_{Q\text{-}F}$ ranges from 1.7‰ to 2.3‰, typical of granitic plutonic rocks (Taylor, 1986). It is noted that the combination of these "normal" $\delta^{18}O$ values with the low δD values of biotite and hornblende (–110 to –155) in these rocks indicates the involvement of a relatively small degree of meteoric-hydrothermal alteration of these rocks following the crystallization of the granodioritic magmas. This batholith covers a wide area (Figure 5.2) where there is a large range (Ghosh, 1995) in ε_{Nd} (–3.2 to –9.1) and initial $^{87}Sr/^{86}Sr$ (0.7040 to 0.7098); thus the observed variations in $\delta^{18}O$ also very likely represent regional-scale variations in the magma sources. These isotopic characteristics are similar to the eugeoclinal V-type central zone source for the Cretaceous granitoid plutons in the Great Basin, as defined by Solomon and Taylor (1989).

The hanging wall rocks of the Nelson Batholith show evidence for increasing water/rock ratios toward the Slocan Lake fault. Except for one sample ($\delta^{18}O$ = +9.1) collected right at the contact with the brittle zone of the Slocan Lake fault, quartz $\delta^{18}O$ values in the hanging wall rocks of the Nelson batholith (Figure 5.7) are homogeneous at +11.6 ± 0.3 (N = 5). However, the feldspars in these rocks become progressively more and more depleted in ^{18}O toward the Slocan Lake fault, with $\delta^{18}O$ ranging from +9.6 to –5.0. The quartz-feldspar $^{18}O/^{16}O$ fractionations also change systematically from

Figure 5.8 -- Quartz, whole rock, and calcite $\delta^{18}O$ vs. structural height in the immediate vicinity of the Slocan Lake fault. Also shown are $\delta^{13}C$ values of calcite from this zone. Very low whole-rock $\delta^{18}O$ values in the fault breccia zone as compared to other zones indicate channelization of meteoric waters along this zone of enhanced permeability. Homogeneous $\delta^{13}C$ values in the upper plate indicate precipitation of calcite filling late fractures in equilibrium with a uniform carbon reservior ($\delta^{13}C \sim -5$). The low calcite $\delta^{18}O$ values in the brittle zone indicate precipitation either at higher temperatures or from an aqueous fluid 4-5‰ lower in ^{18}O than the fluids that affected the upper plate.

Figure 5.8 Slocan Lake Fault

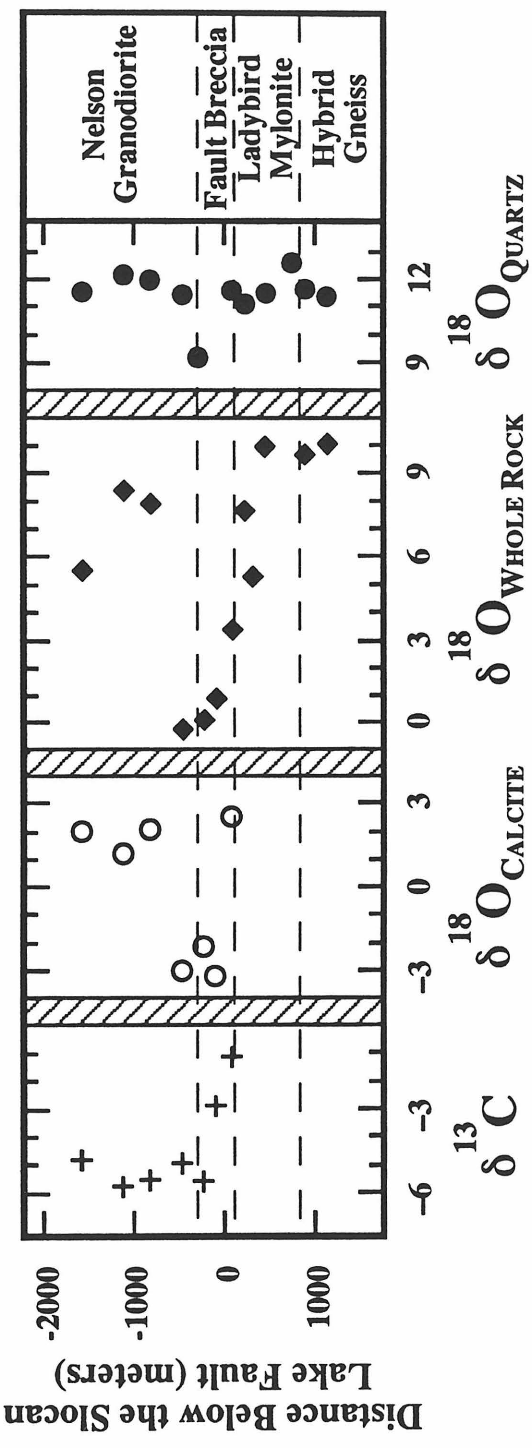

Δ_{Q-F} = 1.8‰ to 14.1‰ (Figure 5.9), with highest values nearest the fault zone, indicating marked isotopic disequilibrium, and indicating that the feldspars exchanged with much larger amounts of meteoric water than did the coexisting quartz. Low $\delta^{18}O$ values (–3.0 to +2.1, N = 4) of late fracture-filling calcite also reveal the presence of meteoric-hydrothermal fluids during the waning stages of this hydrothermal system. These calcites have homogeneous $\delta^{13}C$ values (–5.3 ± 0.4‰), suggesting that the calcites were precipitated in approximate $^{13}C/^{12}C$ equilibrium with a homogeneous carbon reservoir (aqueous bicarbonate ion?) having $\delta^{13}C \sim -5$, using the equilibrium fractionation factor of Bottinga (1969), and assuming T ~ 200 °C. Meteoric-hydrothermal effects are obviously also responsible for the δD values of –150 in the biotite+chlorite separates from the two granodiorite samples analyzed by Magaritz and Taylor (1986).

In the upper plate, whole-rock $\delta^{18}O$ ranges from –0.2 to +8.4 (N = 4); these values are lower than the feldspar $\delta^{18}O$ values for most of these rocks, indicating that some of the $\delta^{18}O$ lowering in these rocks is attributable to meteoric-hydrothermal alteration of the mafic minerals (up to 25 %) in these rocks (dominantly to chlorite). The maximum whole-rock $\delta^{18}O$ values (+7.9 and +8.4) are similar to those reported by Beaudoin and others (1992) for this phase of the Nelson batholith ($\delta^{18}O$ = +8.1). However, it should be noted that even these "normal"-^{18}O Nelson batholith rocks have relatively large Δ_{Q-F} = 3.1‰, clearly indicating that their feldspars have been slightly lowered in ^{18}O by exchange with hot meteoric waters. To the south, away from the Slocan Lake fault, whole-rock $\delta^{18}O$ values of the Bonnington pluton are +7.2; however, right at the fault, $\delta^{18}O$ = +2.6 (Nesbitt and Muehlenbachs, 1995), indicating that meteoric-hydrothermal fluids affected this fault along virtually its entire length.

All altered granitoids from the zone of brecciation show evidence of $^{18}O/^{16}O$ exchange with heated meteoric water. The three analyzed samples from this zone have very low whole-rock $\delta^{18}O$ values (+0.2 to +3.3); these data are similar to the whole-rock

$\delta^{18}O$ values (+0.1 to +3.6) reported by Beaudoin and others (1992) for samples collected 100-300 m above the Slocan Lake fault. Quartz and feldspar $\delta^{18}O$ values (+11.4 and +0.5) from a sample collected just above the mylonitic leucogranite indicate extreme $^{18}O/^{16}O$ disequilibrium ($\Delta_{Q\text{-}F}$ = 10.9‰). As is the case in the upper plate, calcite $\delta^{18}O$ (–3.2 to +2.5) values indicate precipitation from hot meteoric waters, and $\delta^{13}C$ values (–5.6 to – 1.1) decrease upward. These analyses are supplemented by some data by Beaudoin et al. (1992), who obtained $\delta^{18}O$ and $\delta^{13}C$ values of +3.5 and –3.5, respectively, for a calcite vein from this zone.

Lower-plate mylonites locally show evidence of ^{18}O exchange with meteoric-hydrothermal fluids, but this is restricted to the uppermost 300 m. Quartz $\delta^{18}O$ values are homogeneous at +11.5 ± 0.6‰, a value nearly identical to the similarly uniform $\delta^{18}O$ values observed deeper in the lower plate (where homogeneous quartz $\delta^{18}O$ = +11.2). Only one coexisting quartz-feldspar pair (~ 150 m below the detachment surface) was found to be demonstrably out of $^{18}O/^{16}O$ equilibrium ($\Delta_{Q\text{-}F}$ = 4.4‰). Also, a sheared and fractured leucogranite collected ~ 250 m below the base of the brittle zone is slightly ^{18}O-depleted, with whole rock $\delta^{18}O$ = +5.3. These data indicate that hot meteoric waters locally infiltrated the lower plate through such brittle shear zones. These observations are similar to those of Beaudoin and others (1992) for the uppermost 400 m of the Ladybird mylonitic gneiss section, namely: (1) there is a down-section increase in whole-rock $\delta^{18}O$ from +1.0 to +5.1 over 400 m, and (2) a low-^{18}O mylonitic gneiss (whole-rock $\delta^{18}O$ = +0.7) formed near a cross-cutting brittle shear zone.

$^{18}O/^{16}O$ exchange equilibrium at T ~ 450 °C (Clayton and Keiffer, 1991) is indicated by the nearly uniform feldspar $\delta^{18}O$ values (+9.3 ± 0.7‰) and $\Delta_{Q\text{-}F}$ values (2.4 ± 0.2‰) in mylonites that apparently escaped any marked exchange with low-^{18}O meteoric waters. Using the feldspar-H_2O oxygen isotope fractionations of O'Neil and Taylor (1967), water in equilibrium with these mylonites at 450 °C would have had $\delta^{18}O$

~ +8.0. Water having this $\delta^{18}O$ can be either magmatic water or evolved meteoric water. The δD of biotite from MT-326 is –151 (Magaritz and Taylor, 1986), conclusively indicating that at least small amounts of meteoric water were involved in the mylonitization. This low-δD sample is ~ 500 m below the base of the brittle zone, demonstrating that small quantities of hot meteoric waters managed to infiltrate this deep into the lower plate, presumably during detachment faulting. It should be noted that in the lower plate mylonite section, Beaudoin et al. (1992) observed greater variation in quartz and feldspar $\delta^{18}O$ (+9.6 to +12.2 and +7.4 to +9.8, respectively) than was observed in the present study. These workers also report $\Delta_{Q\text{-}F}$ values of 1.8‰ and 2.3‰, but they erroneously imply isotopic equilibrium temperatures of 240 °C and 180 °C for these fractionations (when in fact they indicate T ≥ 500 °C, if the more up-to-date calibration of Clayton and Keiffer (1992) is applied.

Beaudoin et al. (1992) measured $\delta^{18}O$ and $\delta^{13}C$ of gangue carbonate and quartz from synextensional Ag-Pb-Zn deposits from the upper plate of the Slocan Lake fault. Their data from these deposits hosted in the Nelson batholith within 10 km of the study area are summarized below. Gangue quartz has $\delta^{18}O$ between –2.2 and +11.6, but these data have a bimodal distribution about +11.3 and –1.3; this probably indicates the involvement of at least two kinds of hydrothermal fluids having different $^{18}O/^{16}O$ compositions during this Eocene mineralization event. A locality on the Slocan Lake fault has quartz $\delta^{18}O$ values of +9.8 and –1.4, another indication of multiple stages of fluid-rock interaction and channelization of fluid flow on the outcrop scale. Vein calcite and dolomite display a similar range in $\delta^{18}O$ (–2.0 to +3.5), but a smaller range in $\delta^{13}C$ (–3.2 to –5.1) than the previously mentioned carbonate results.

5.3.4 Discussion and Comparison with Previous Work

It is clear from the isotopic data that heated meteoric water was the dominant aqueous fluid medium that affected the Slocan Lake fault zone during extension. Homogeneous, relatively low δD values from both the upper and lower plate indicate the presence of at least small amounts of meteoric-hydrothermal fluids in all of the sampled deformational regimes, and this presumably occurred during the time period when the fault was active. However, these fluids were in general rock-buffered at low water/rock ratios, retaining their meteoric $^{18}O/^{16}O$ signatures only locally, where water/rock ratios were high enough, mainly along the fault, in the uppermost part of the mylonite section, and in proximal portions of the granodiorite upper plate.

Questions remain concerning the nature of the waters involved in mylonitization. Could some magmatic water or metamorphic water have been mixed with meteoric water, analogous to the situation proposed by Beaudoin et al. (1992) for the upper plate Ag-Pb-Zn deposits in the Kokanee Range? Can this alteration have occurred at sufficiently low W/R that the meteoric water signature has been lost during exchange of $^{18}O/^{16}O$ with the mylonites, even though the original D/H of the meteoric waters remained unchanged?

Rocks from deeper levels of the Valhalla lower plate are homogeneous in ^{18}O and the mineral assemblages indicate apparent $^{18}O/^{16}O$ equilibrium at $T \sim 600\ ^{\circ}C$ with aqueous fluids having $\delta^{18}O \sim +10.0$; this is compatible with $^{18}O/^{16}O$ equilibrium with metamorphic and/or magmatic waters during high-grade metamorphism, similar to the situation described for the southern Thor-Odin complex in Chapter 4. Thus, if magmatic or metamorphic fluids entered the Slocan Lake fault from below, they likely would have been imprinted with the isotopic characteristics of these lower-plate metamorphic/magmatic rocks. The aqueous fluids involved in mylonitization ($\delta^{18}O \sim +8.0$), however, are at least 2‰ lower in ^{18}O than those deep-level metamorphic/magmatic fluids in the Valhalla lower plate. It is also noteworthy that the overall bulk $\delta^{18}O$ (~ 10.0) of the mylonitic rocks seems to be unchanged from analogous rocks deeper in this crustal section. This suggests that rock-buffered conditions prevailed in the mylonites, with temperature of $^{18}O/^{16}O$ exchange perhaps being the principal parameter determining fluid $\delta^{18}O$; this is consistent with the 2‰ difference in the quartz-water and feldspar-water equilibrium fractionation factors between 450 °C and 600 °C (O'Neil and Taylor, 1967; Clayton et al., 1972). However, the very low δD value from this zone indicates that the hydrogen budget of these rocks was controlled by the small amounts of meteoric water that apparently entered this zone of ductile deformation. The D/H systematics of the rock-water system, even at low water/rock ratio, are controlled by the δD of water, because the mass proportion of hydrogen in water (11 %) is far greater than that for rock (still < 0.1% for a rock with 10 vol. % biotite). Thus, it is concluded that small amounts of meteoric water migrated at least 800 m deep into the lower plate during detachment faulting. Comparing these data with observations in another Cordilleran metamorphic core complex, note that they are consistent with the steady downward increase in δD (–150 to –60) through the upper two km of the Ruby Mountains-East Humboldt Range core complex 1000 km to the south (Wickham et al., 1993).

Only the uppermost part of the lower-plate mylonite section was exposed to enough meteoric-hydrothermal fluid to measurably lower the feldspar $\delta^{18}O$ relative to mylonites deeper in the section. The low $\delta^{18}O$ values observed in the late brittle shear zone indicate that shear zones like these were open and permeable, providing pathways for meteoric fluids to come in laterally or from above, perhaps during episodes of fracturing (earthquakes?). During times of low strain rate, these shear zones probably deform ductilely and thus are relatively impermeable, with their porosity perhaps even decreasing sufficiently to drive fluids out of these zones and into the adjacent rocks. This mechanism is analogous to the seismic pumping process, first suggested by Sibson and coworkers

(1975), operating at the brittle-ductile transition (~10-15 km depth) in fault zones. This seismic pumping process appears to be a common mode of fluid transport employed in bringing surface-derived water deep down into the ductile portions of faults, as evidenced by data from Alpine shear zones in the Pyrenees (McCaig et al., 1990), from the detachment fault at the Ruby Mountains-East Humboldt Range metamorphic core complex (Fricke et al., 1992), and perhaps from the Mother Lode gold deposits in California (Sibson 1987), to name only a few. The resulting increase in fluid pressure by this process may be an important mechanism of fault weakening, allowing for normal slip to be mechanically possible along shallow-dipping normal faults (Bartley and Glazner, 1985; Axen, 1992; Axen and Selverstone, 1994).

Low $\delta^{18}O$ values in the brittle zone and the rocks near it indicate that these more permeable rocks served as the main channelway for the transport of water into the detachment system and adjacent parts of the lower plate during extension at this metamorphic core complex. The extreme $^{18}O/^{16}O$ disequilibrium observed at the Slocan Lake fault indicates open-system exchange with low-^{18}O meteoric-hydrothermal fluids. Open system material-balance water-rock ratios can be calculated if the initial $\delta^{18}O$ of the rock and water, and the temperature of exchange is known (Taylor, 1977). The three homogeneous δD values of biotite and chlorite from strongly ^{18}O-depleted samples provide a baseline from which the $\delta^{18}O$ of this water can be calculated, inasmuch as the δD of water will be unchanged during water-rock interactions that involve such a large amount of water.

The temperature can be estimated from liquid-vapor homogenization temperatures of fluid inclusions. Beaudoin et al. (1992) report homogenization temperatues of ~ 300 °C from fluid inclusions in synextensional Eocene quartz and calcite veins collected within 10 km of the study area. This temperature is consistent with the alteration mineralogy observed in these rocks. Much of the D/H exchange between hydrous minerals and hot meteoric water is related to the transformation of biotite and hornblende to chlorite during hydrothermal activity. The chlorite-H_2O equilibrium hydrogen isotope fractionation factor at 300 °C is estimated to be ~ 40‰ (Taylor, 1974; Suzuoki and Epstein, 1976); thus H_2O in D/H equilibrium with a chlorite having $\delta D = -150$ would have a $\delta D = -110$. The $\delta^{18}O$ of original, unexchanged meteoric water can be calculated using the equation for the meteoric water line (Craig, 1961):

$$(1) \qquad \delta D = 8\delta^{18}O + 10‰.$$

Using this equation, the δD value of -110 for the water would imply a $\delta^{18}O$ value of -15 for the pristine meteoric water, prior to its entering the hydrothermal flow system and being heated.

It should be noted that the lowest $\delta^{18}O$ value obtained for feldspar in this region is -5.0, and that the quartz $\delta^{18}O$ value (+9.1) from the particular sample that exhibits this minimum feldspar $\delta^{18}O$ value also happens to be the only instance where quartz $\delta^{18}O$ deviates from the homogeneous quartz ($\delta^{18}O = +11.4$) observed throughout the rest of the section. At 300 °C, water in equilibrium with this minimum feldspar $\delta^{18}O = -5.0$ would have $\delta^{18}O = -9.8$, using the feldspar-water equilibrium oxygen isotope fractionation factor of O'Neil and Taylor (1967). This meteoric water $\delta^{18}O$ value is close to being in oxygen isotope equilibrium at 300 °C with the lowest-^{18}O quartz vein ($\delta^{18}O = -2.2$) from the immediately surrounding area (Beaudoin et al., 1992), using the quartz-water equilibrium oxygen isotope fractionation factor of Clayton et al. (1972).

Nevertheless, locally there is evidence that even lower-^{18}O meteoric-hydrothermal fluids were active in the region during Eocene extension. Beaudoin et al. (1992) report $\delta^{18}O = -12.2$ for a vein calcite located 30 km east of the study area, indicating that meteoric water with $\delta^{18}O$ as low as -16.0 may have been involved in Eocene hydrothermal metamorphism in this region. There are no implications here that such ^{18}O-depleted waters affected the Slocan Lake fault, especially if these fluids didn't directly enter the fault from above, but instead percolated into it at depth following a lengthy period of $^{18}O/^{16}O$ exchange with the upper plate Nelson batholith. Magaritz and Taylor (1986) report consistently very low hydrous mineral δD values (–138 to –163) from the Nelson batholith throughout the southern Omineca extensional zone. Farther east, at the Bluebell Pb-Zn deposit, vein quartz $\delta^{18}O$ values as low as –6.2 (Ohmoto et al., 1971) provide further indication of the involvement of very ^{18}O-depleted meteoric-hydrothermal fluids. Nesbitt and Muehlenbachs (1995) proposed that the zones of low-^{18}O quartz veins are major fluid recharge areas where large quantities of fresh, unexchanged meteoric water entered deep fracture systems in the crust, and were locally partitioned into myriads of shallow convective systems. Perhaps the elevated $\delta^{18}O$ of meteoric waters at the Slocan Lake fault may be the result of those waters having an earlier history of oxygen isotope exchange as they passed deep into the crust, with the fault itself serving as a discharge zone for this major hydrothermal system.

Beaudoin et al. (1992a) document a 15 million year history of hydrothermal activity, going from 59 to 44 Ma in the hanging wall of this detachment fault. It is likely that the isotopic compositions of the meteoric waters themselves may have changed over this prolonged period of time. The oxygen isotope record of benthic foraminifera (Douglas and Woodruff, 1981) indicate that the Eocene was a time of profound climate change. It has been suggested that large-scale decarbonation at the onset of metamorphism associated with the Himalayan orogen released CO_2 into the atmosphere to drive 4-5 °C global warning between 59 and 53 Ma (Kerrick and Caldiera, 1993, 1994). This time coincides with the early stages of extension in southeastern British Columbia (Parrish et al., 1988); it has been proposed that decarbonation of shales by meteoric-hydrothermal metamorphism during this time in the southern Omineca belt may be the cause of this global warming (Nesbitt et al., 1995). Such a warming could account for a ~ 3-4‰ increase in meteoric water $\delta^{18}O$, using the estimate that meteoric water $\delta^{18}O$ changes at the rate of +0.7 ‰/°C (Baadsgaard, 1964). It should also be noted that gabbroic dikes in the Kootenay Lake area have $^{40}Ar/^{39}Ar$ apparent ages of 26-30 Ma (Beaudoin et al., 1992a). The interval 53-28 Ma was a period of global cooling with global average temperatures dropping 9 °C (Douglas and Woodruff, 1981). Cooling of this magnitude would result in a lowering of meteoric water $\delta^{18}O$ of ~ 6‰ over this interval; this is similar to the inferred variation in meteoric water $\delta^{18}O$ (–16 to –10) along the eastern part of the southern Omineca belt.

5.3.5 Calculation of Water/Rock Ratios

Taylor's (1977) open-system material-balance water/rock ratio model describes a plausible end-member hydrothermal process, namely a dynamic single-pass open-system where a succession of infintesimal packets of water of fixed $\delta^{18}O$ react completely with the rock (Taylor, 1977). Each water packet immediately leaves the system once its interaction is complete, and this continues throughout the entire process. This system is simplified to a two-component system consisting of just rock and water, and $^{18}O/^{16}O$ exchange is assumed to be isothermal. This model contrasts with another plausible end-member process, namely the "closed" system water/rock ratio model, in which each exchanged water packet is re-cycled back into the same reservoir of water from which the water packets are being supplied, which in principle allows the exchanged water to be used over and over again during the entire episode of water-rock interaction (Taylor, 1977). In general, hydrothermal systems in nature probably most closely approach the single-pass, open-system, end-member model, and the profound $^{18}O/^{16}O$ disequilibrium between quartz and feldspar at the Slocan Lake fault indicates that this dynamic open-system water/rock ratio model is the best simple model to use in describing the style of hydrothermal metamorphism in this shear zone.

Open-system water/rock ratios are calculated using the equation of Taylor (1977):

$$(2) \qquad (W/R)_{open} = \ln\left(\frac{\Delta + \delta^{in}_{fluid} - \delta^{in}_{rock}}{\Delta + \delta^{in}_{fluid} - \delta^{f}_{rock}}\right)$$

where Δ is the rock-water $^{18}O/^{16}O$ fractionation factor (assumed to be constant during the exchange process), δ^{in}_{fluid} is the initial $\delta^{18}O$ of the (meteoric) water, δ^{in}_{rock} is the initial $\delta^{18}O$ of the rock, and δ^{f}_{rock} is the final (measured) $\delta^{18}O$ of the rock after exchange. For this system, water-rock ratios are calculated mainly using the changes in feldspar $\delta^{18}O$. At 300 °C $\Delta_{F\text{-}H_2O}$ = 4.5‰, using the feldspar-H_2O equilibrium fractionation factor of O'Neil and Taylor (1967). δ^{in}_{rock} will then be the feldspar $\delta^{18}O$ in the original rock before any interaction with meteoric water; the feldspar $\delta^{18}O$ is calculated by taking the average quartz $\delta^{18}O$ for the upper plate granodiorites and assuming a "normal magmatic" quartz-feldspar oxygen isotope fractionation of 1.5 ‰ for these rocks (*e.g.*, Taylor and Sheppard, 1986). Similarly, δ^{f}_{rock} is then simply the measured feldspar $\delta^{18}O$ value for that rock. The initial water $\delta^{18}O$ is assumed to be –15, equivalent to a pristine meteoric water having δD = –110 (see Figure 2.14 and Magaritz and Taylor, 1986). These calculated water/feldspar ratios are then converted into water/rock ratios by multiplying by the volume fraction of feldspar in the feldspar-quartz assemblage (typically 0.75), and assuming that the coexisting quartz was inert during hydrothermal alteration. These water/rock ratios are tabulated in Table 5.1. Water/rock ratios for samples lacking feldspar $\delta^{18}O$ analyses in the zone of brecciation and the lower plate mylonite zone were estimated using an initial whole-rock $\delta^{18}O$ value = +11.0 and a $\Delta_{WR\text{-}H_2O}$ = 6.0‰.

Material balance water/rock ratios in the zone of brecciation and the lower 350 m of the Nelson granodiorite are all greater than 0.50, whereas this parameter decreases to near zero in the mylonite zone, and ranges from 0.04 to 0.34 higher in the upper plate (Table 5.1). It should be noted that this model calculation inherently represents a minimum estimate of the amount of meteoric water/rock interaction (Taylor, 1977), and it is also a minimum because the model does not take into account the up to 25% mafic minerals that have locally experienced intense $^{18}O/^{16}O$ and mineralogical alteration in response to the influx of these meteoric waters (and whose $\delta^{18}O$ values in general were not measured in this study).

5.3.6 Open-System Kinetic Exchange Modeling of the Slocan Lake Fault

The lithologic homogeneity of the upper plate granodiorite makes it feasible to carry out a more detailed modeling of $^{18}O/^{16}O$ exchange processes active during the history of this hydrothermal system. For this purpose, the general open-system kinetic oxygen isotope exchange model of Criss et al. (1987) is employed to track the evolution of quartz, feldspar, and water $\delta^{18}O$ as water/rock ratios increase with time. Gregory et al. (1989) examined this in detail in various two-mineral hydrothermal systems in which the two minerals exchange with H_2O at markedly different rates. In such systems, the slopes of the data arrays where the $\delta^{18}O$ of one mineral is plotted versus the $\delta^{18}O$ of its coexisting counterpart provide information about the intensity, duration, and temperature of meteoric-hydrothermal activity. If the slow-exchanging mineral is plotted on the horizontal axis, and the fast-exchanging mineral on the vertical axis, and if the temperature of the $^{18}O/^{16}O$ exchange event can be eliminated as a variable, then the slope of this data array defines an isochron (*i.e.*, the duration of hydrothermal activity), where short-lived systems produce δ-δ arrays having very steep slopes, while shallow arrays indicate a longer-lived system (*e.g.*, see Figure 5.9). Inasmuch as rates of $^{18}O/^{16}O$ exchange are more rapid at higher

Figure 5.9 -- $\delta^{18}O$ of quartz vs. $\delta^{18}O$ of coexisting feldspar for the Slocan Lake fault zone. Data are compared to our best available estimates of the $\delta^{18}O$ values of the minerals in the unaltered protoliths, namely, samples from the lower plate Valhalla complex (plus signs) and "unaltered" samples (Magaritz and Taylor, 1986) from the Nelson batholith (open squares). Note that there is very little difference in the $\delta^{18}O$ of these two protoliths. These rocks from the Valhalla lower plate and from the "unaltered" Nelson batholith appear to be in apparent $^{18}O/^{16}O$ equilibrium at magmatic temperatures. The dashed 45° diagonal lines at $\Delta = 0$ and $\Delta = 2.0$ represent the range of "normal" quartz-feldspar $^{18}O/^{16}O$ fractionations in plutonic granitic rocks (Taylor, 1968). Coexisting quartz and feldspar from the upper plate Nelson batholith (filled circles) define a steep array in δ-δ space, indicative of extreme $^{18}O/^{16}O$ disequilibrium imposed on this system as it underwent brittle fracturing and extension during a short-lived (~ 5×10^5 to 3×10^6 yr) meteoric-hydrothermal event at T ~ 300 °C (see text). A much lesser degree of $^{18}O/^{16}O$ disequilibrium is observed in the lower plate mylonites (open circles), implying much smaller W/R ratios for these highly deformed rocks and limited infiltration of meteoric water into them, presumably because they were undergoing ductile deformation during much of the hydrothermal episode (see text). Quartz $\delta^{18}O$ values from these lower plate mylonites span most of the range of $\delta^{18}O$ values observed in the Valhalla lower plate. Note that $\Delta_{Q\text{-}F} = 2.4$ ‰ for most of the lower plate mylonites would be compatible with $^{18}O/^{16}O$ equilibrium at T ~ 450 °C.

Figure 5.9 Slocan Lake Fault

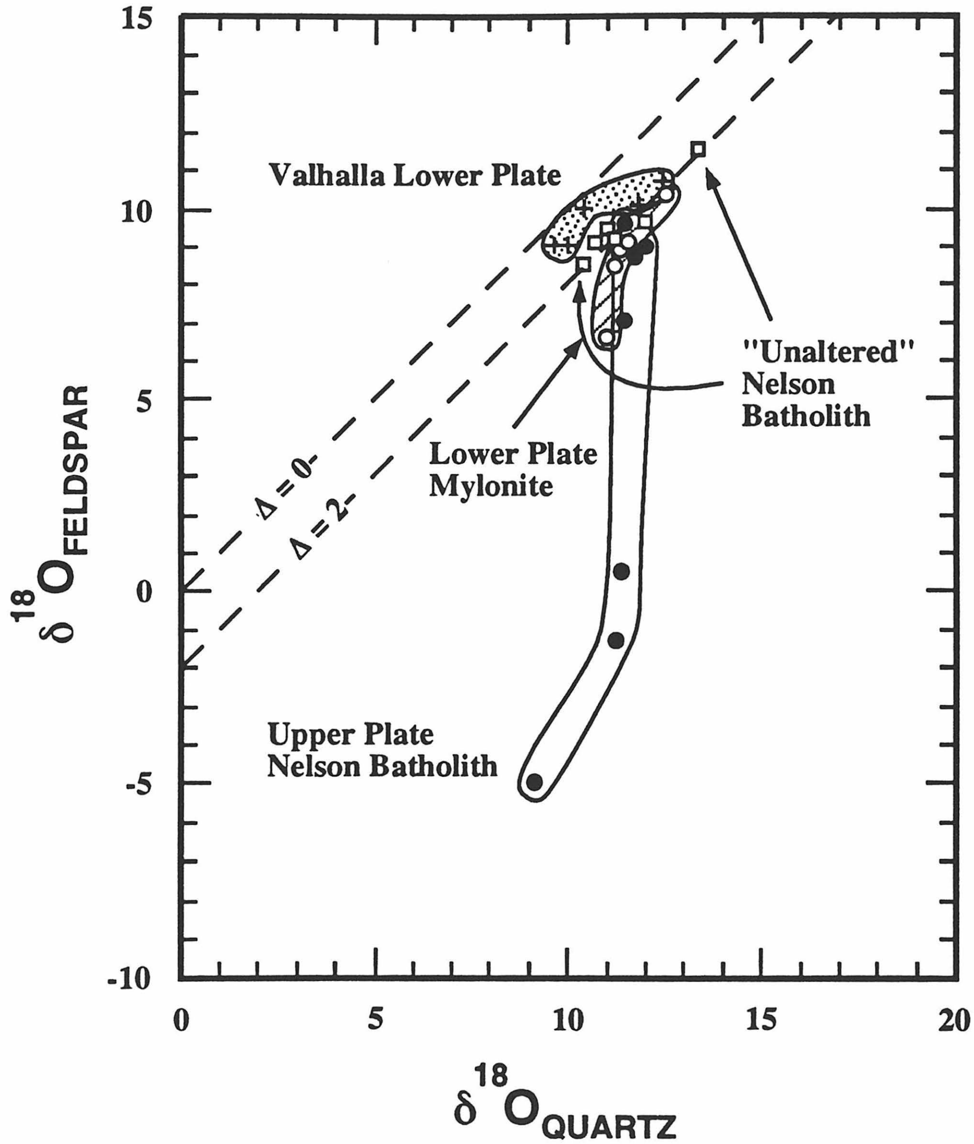

temperatures (Cole and Ohmoto, 1986; Giletti, 1988), then other things being equal (*i.e.*, duration of hydrothermal activity) a high-temperature system will also lead to a data array with a shallower slope compared to that of a lower-temperature system. The suitability of this model is dependent on there being marked differences in oxygen exchange rates between water and the two minerals of interest; feldspar-quartz pairs have turned out to be the best in this respect, both because they are (1) abundant rock-forming minerals, and (2) feldspar is known to exchange with H_2O much faster than quartz (Taylor, 1977). In order for this type of modeling to be most effective, it is useful if the fast-exchanging mineral rapidly attains $^{18}O/^{16}O$ equilibrium with the hydrothermal fluids before any noticeable effects of exchange with these waters are observed in the slow-exchanging mineral. This seems to be the case with quartz and feldspar in typical hydrothermal systems at 200°-400 °C (Gregory et al., 1989).

In granitoid rocks, the dominant oxygen-bearing phases are the feldspars and quartz. The rate of diffusive oxygen isotope exchange in feldspar is approximately four orders of magnitude greater than that for quartz at 300 °C (Giletti, 1988). A solution of Dodson's (1973) equation for diffusive closure temperatures, utilizing the diffusion parameters summarized by Giletti (1988) applied to typical quartz and feldspar samples from the Nelson batholith, together with a cooling rate of 25 °C/Ma (Spear and Parrish, 1996), indicates closure temperatures for these minerals much higher (~ 500 °C for quartz, and ~ 350 °C for feldspar) than the temperature of meteoric-hydrothermal water-rock interaction (~ 300 °C) for this hydrothermal system, making it unlikely that diffusion is the mode of $^{18}O/^{16}O$ exchange in this system.

O'Neil and Taylor (1967) noted that the morphology of a feldspar grain is unaffected by oxygen isotope and cation exchange during the fine-scale solution-redeposition processes that are observed during hydrothermal exchange of feldspars in the laboratory. Furthermore, some of the $^{18}O/^{16}O$ exchange that takes place in nature between hydrothermal fluids and these minerals and rocks is undoubtedly related to mineralogic changes associated with the sericitization of feldspar and the chloritization of mafic minerals. Thus, the dominant mechanism of oxygen isotope exchange in the systems investigated in this study was most likely recrystallization or fine-scale solution-redeposition, not simple solid-state diffusion.

The Criss et al. (1987) model involves the simultaneous solution of the following differential equations:

$$(3) \qquad \frac{dR_i}{dt} = k_{iw}\left(\alpha_{iw}R_w - R_i\right)$$

$$(4) \qquad X_w \cdot dR_w = \left(R_w^{in} - R_w\right)u \cdot dt - \sum_{n=1}^{n} x_i \cdot dR_i$$

where R_i is the $^{18}O/^{16}O$ ratio of the mineral i, R_w is the $^{18}O/^{16}O$ ratio of water w, t is time, k_{iw} is the isotopic exchange rate of the mineral i with H_2O, α_{iw} is the mineral-water isotopic fractionation factor, u is the normalized flow rate in s^{-1}, X_w is the mole fraction of water, and x_i is the mole fraction of the mineral i. Equation 3 assumes that the rate of $^{18}O/^{16}O$ exchange is proportional to the differences between the initial $\delta^{18}O$ values in the system and their final equilibrium values. Equation 4 is basically just a statement of material balance, but assuming a uniformly constant fluid flux entering and then leaving the system.

A system of n crystalline phases plus water is described by $n+1$ differential equations which must be simultaneously solved. For quartz (Q), feldspar (F), and water (W), these equations are:

$$(5) \qquad \frac{dR_Q}{dt} = k_{Q-W}\left(\alpha_{Q-W}R_w - R_Q\right)$$

$$(6) \qquad \frac{dR_F}{dt} = k_{F-W}\left(\alpha_{F-W}R_w - R_F\right)$$

$$(7) \qquad X_w\frac{dR_w}{dt} = \left(R_w^{in} - R_w\right)u - \frac{X_Q\left(dR_Q\right)}{dt} - \frac{X_F\left(dR_F\right)}{dt}$$

The following matrix equation was used by Criss et al. (1987) as a solution to the above equations:

(8)

$$\begin{bmatrix} R_Q \\ R_F \\ R_W \end{bmatrix} = \begin{bmatrix} \frac{\alpha_{Q-W}k_Q}{k_Q-\lambda_1} & \frac{\alpha_{Q-W}k_Q}{k_Q-\lambda_2} & \frac{\alpha_{Q-W}k_Q}{k_Q-\lambda_3} \\ \frac{\alpha_{F-W}k_F}{k_F-\lambda_1} & \frac{\alpha_{F-W}k_F}{k_F-\lambda_2} & \frac{\alpha_{F-W}k_F}{k_F-\lambda_3} \\ 1 & 1 & 1 \end{bmatrix} \times \begin{bmatrix} e^{-\lambda_1 t} & 0 & 0 \\ 0 & e^{-\lambda_2 t} & 0 \\ 0 & 0 & e^{-\lambda_3 t} \end{bmatrix} \begin{bmatrix} C_1 \\ C_2 \\ C_3 \end{bmatrix} + \begin{bmatrix} R_Q^{eq} \\ R_F^{eq} \\ R_W^{eq} \end{bmatrix}$$

The eigenvalues (λ) are the roots of the following equation:

$$(9) \qquad 0 = x_w\lambda^3 - M\lambda^2 + N\lambda - k_1k_2u$$

where

$$(10) \qquad M = k_Q\left(\alpha_{Q-W}X_Q + X_W\right) + k_F\left(\alpha_{F-W}X_F + X_W\right) + u$$

and

$$(11) \qquad N = k_Qk_F\left(\alpha_{Q-W}X_Q + \alpha_{F-W}X_F + X_W\right) + u\left(k_Q + k_F\right)$$

In the above equations, initial constants (C_1, C_2, C_3) are determined by solving the matrix equation, after determining the eigenvalues from the initial and boundary conditions.

The values of the kinetic exchange rate constants for quartz and feldspar (k_Q and k_F) that are utilized in the present model are taken from the measured slope of the array of coexisting $\delta^{18}O$ quartz and $\delta^{18}O$ feldspar in samples from the Slocan Lake fault, with feldspar plotted on the y-axis (Figure 5.10). This steep array has a slope of 25; this can be assumed to give us the relative rates of mineral-water oxygen isotope exchange for these two minerals in this system. Because almost all of the early $^{18}O/^{16}O$ water/rock exchange is taken up by the fast exchanging mineral, Gregory et al. (1989) were able to demonstrate that the constant defined by the ratio of the rates of exchange of the fast- and slow-exchanging minerals corresponds to the slope of the array defined by the data at relatively low water/rock ratios. For large k_Q/k_F, quartz will retain its initial $\delta^{18}O$ value during virtually the entire early part of the $^{18}O/^{16}O$ exchange history, even as the $\delta^{18}O$ of the faster-exchanging feldspar becomes markedly altered. It should be noted that these calculations can only be approximations because the vagaries of the exchange processes between these minerals and water in nature are only loosely constrained (*e.g.*, these exchange parameters are dependent on grain size, surface area, temperature, point defect density, rate of solution-redeposition, etc.; see Gregory et al., 1989).

The value of k_Q used in the present study is the same as that determined empirically by Gregory et al. (1989) in their study of quartz and meteoric water in well-characterized fossil hydrothermal systems. The supply of heat to such systems is the main controlling factor in determining their lifetimes, and given the time constraints and the preservation of steep arrays in δ-δ space for systems similar to those studied in the present work, k_Q was determined by Gregory et al. (1989) to be ~10^{-14} s^{-1}, based on numerical modeling studies of analogous hydrothermal systems (Norton and Taylor, 1979; Cathles, 1983;

Figure 5.10 -- Open system kinetic $^{18}O/^{16}O$ exchange model for the upper plate Nelson granodiorite. The dashed line is the array in δ-δ space defined by most of the $\delta^{18}O$ data-points (black dots) from the upper plate rocks. The asterisk represents a sample in which the feldspar $\delta^{18}O$ was measured, but the quartz was not; based on the uniformity of quartz $\delta^{18}O$ in other samples, it is assumed that the data-point for this sample would plot near the asterisk. The solid curve is the exchange trajectory for quartz and feldspar calculated by the methods of Criss et al. (1987) using the parameters listed in the upper left of the diagram (see text), together with equations 3 to 11.

Figure 5.10 **Open-System Kinetic Isotope Exchange Model for the Upper Plate Nelson Granodiorite at the Slocan Lake Fault**

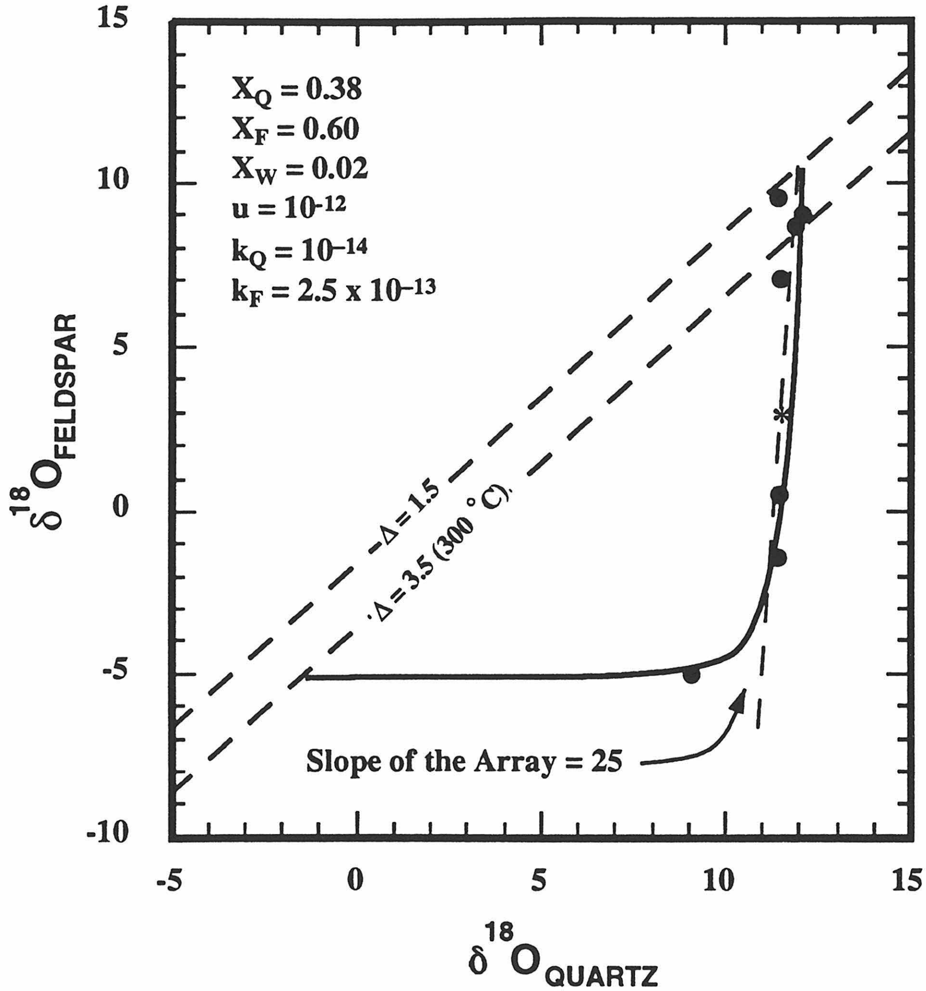

Norton, 1984). The k_F value of 2.5 X 10^{-13} used in this work derives directly from this choice of k_Q and the fact that the array slope in Figure 5.10 is 25 (= k_F/k_Q).

The other parameters and initial conditions are determined by the modal proportions of quartz and feldspar in the granodiorite, the limitations provided by the isotopic data from the study area, and the constraint imposed by the minimum feldspar $\delta^{18}O$ value in the study area (and the fact that the coexisting quartz in this same sample also has undergone a measurable lowering of $\delta^{18}O$, implying significant $^{18}O/^{16}O$ exchange with the meteoric-hydrothermal fluids. The initial quartz and feldspar $\delta^{18}O$ values are found by projecting the data array upward along the exchange trajectory to the $\Delta_{Q\text{-}F}$ = 1.5‰ line, as shown on Figure 5.10. The initial water $\delta^{18}O$ is assumed to be –15.0 because this is the best determined water $\delta^{18}O$ value for this general region during the Eocene (see above; Magaritz and Taylor, 1986; Nesbitt and Muehlenbachs, 1995). From these constraints, X_Q = 0.38 (25 modal % quartz), X_F = 0.60 (75 modal % feldspar), X_W = 0.02, initial water $\delta^{18}O$ = –15.0, initial quartz $\delta^{18}O$ = +12.0, and initial feldspar $\delta^{18}O$ = +10.5.

This model was solved numerous times to obtain a minimum estimate of the normalized flow rate u . A u value of 10^{-12} s^{-1} produced the best fit trajectory for the Slocan Lake fault data, but values of 10^{-13} to 10^{-11} are also very plausible given the lack of datapoints in the critical region where the curvature is most pronounced. Smaller flow rates result in a leftward shift of the exchange trajectory, because quartz $\delta^{18}O$ will start dropping before complete attainment of $^{18}O/^{16}O$ equilibrium between feldspar and water. Greater flow rates result in a rightward shift of the exchange trajectory, and in the limit of extremely large u-values the initial exchange trajectory will be vertical (slope $\rightarrow \infty$). Increasing the flow rate increases the curvature of the exchange trajectory to virtually a right angle, signifying complete attainment of feldspar-water equilibrium before there is any drop whatsoever in quartz $\delta^{18}O$ values.

Solution of equation 8 for quartz, feldspar, and water $\delta^{18}O$ with respect to time (Figure 5.11) demonstrates the degree of $^{18}O/^{16}O$ exchange with time for each mineral, as well as the overall interdependence of the three phases involved in this system. Water $\delta^{18}O$ begins to increase immediately as oxygen isotope exchange with the rocks (*i.e.*, principally the feldspar) begins. Over the first 3,000 years, the water $\delta^{18}O$ increases by about 8‰ to a value of –7.0; during this time there is no noticeable change in feldspar $\delta^{18}O$ (<0.1‰) because the water/rock ratios are very small, as is the amount of feldspar that has actually exchanged ^{18}O with these waters. A pronounced decrease in feldspar $\delta^{18}O$ begins soon after the water $\delta^{18}O$ reaches its maximum value. Then, as the feldspar decreases in ^{18}O (as ultimately the quartz does, as well), the equilibrated H_2O also must decrease slightly, even though the H_2O soon becomes the dominant part of the system. It takes approximately 300,000 years for the feldspar $\delta^{18}O$ to go down from its initial value to its minimum value of –5.0. During this time, water $\delta^{18}O$ decreases by about 2.5‰ to –9.5. For the first 300,000 years isotopic exchange between quartz and water is negligible. It would take about 10 Ma for quartz $\delta^{18}O$ to drop from its initial value down to –1.4. During the bulk of the time when quartz is the only mineral changing in $^{18}O/^{16}O$, water $\delta^{18}O$ is unchanged; this is because the normalized flow rate ($u = 10^{-12}\ sec^{-1}$) is so much larger than the rate of isotopic exchange involving quartz ($k_Q = 10^{-14} sec^{-1}$) and water. At each step, a fresh new packet of water is added to the rock before the quartz has much of a chance to alter its isotopic composition. It should be noted that the final $\delta^{18}O$ of the water is constrained by the oxygen isotopic observations at this detachment fault, specifically the minimum feldspar $\delta^{18}O$ (–5.0) and the δD values of hydrous minerals.

Figure 5.12 shows the change in oxygen isotope fractionations between minerals and water as a function of time. Both $\Delta_{Q\text{-}W}$ and $\Delta_{F\text{-}W}$ initially decrease by 7.5‰ as water $\delta^{18}O$ increases to –7.5 during the initial stages of exchange in a system that is "rock buffered" at these time scales. As exchange proceeds between feldspar and quartz, $\Delta_{Q\text{-}W}$

Figure 5.11 -- Evolution of quartz, feldspar, and water $\delta^{18}O$ with time for the kinetic open-system oxygen isotope exchange model. Water $\delta^{18}O$ increases to –7.0 during the first 3000 yrs of activity in this hydrothermal system, as these waters evolve toward a final steady state value at $\delta^{18}O = -9.5$. Feldspar $\delta^{18}O$ begins to decrease once the water has reached its maximum $\delta^{18}O$. The lowering of feldspar $\delta^{18}O$ from an initial value of +10.5 to the minimum observed value of –5.0 takes place over a time period of 300,000 yrs. During this time, water $\delta^{18}O$ gradually decreases to its final steady state value of –9.5. This final steady state water $\delta^{18}O$ value is dependent on the initial $\delta^{18}O$ of the water and the relative difference between flow rate and the exchange rate of the slowest exchanging mineral (namely quartz, in this case). The lowering of quartz $\delta^{18}O$ from +12.0 to –1.5 occurs from 200,000 yrs to ~ 10 Ma. Water $\delta^{18}O$ remains constant at its steady state value of –9.5 for the duration of ^{18}O depletion of the quartz, because the exchange rates of quartz are so small relative to the flow rate.

Figure 5.12 -- Evolution of Δ values with time for the kinetic open-system exchange model. $\Delta_{Q\text{-}W}$ and $\Delta_{F\text{-}W}$ values both decrease 7.3‰ as water $\delta^{18}O$ increases 7.5‰ from its initial value due to exchange of small amounts of water with feldspar at the onset of $^{18}O/^{16}O$ exchange during the first 3 ka of this hydrothermal system. $\Delta_{Q\text{-}W}$ gradually increases by about 2‰ between 3,000 yrs and 200,000 yrs during $^{18}O/^{16}O$ shift in feldspar becomes pronounced as feldspar $\delta^{18}O$ drops to –5.0 and $\Delta_{Q\text{-}W}$ drops to the equilibrium value at 300 °C over a 300 ka period. The time of maximum $^{18}O/^{16}O$ disequilibrium between quartz and feldspar coincides with the time at which feldspar $\delta^{18}O$ values reach their final state in equilibrium with the steady state water $\delta^{18}O$ composition.

Figure 5.11 Time versus $\delta^{18}O$ for the Kinetic Open-System Exchange Model

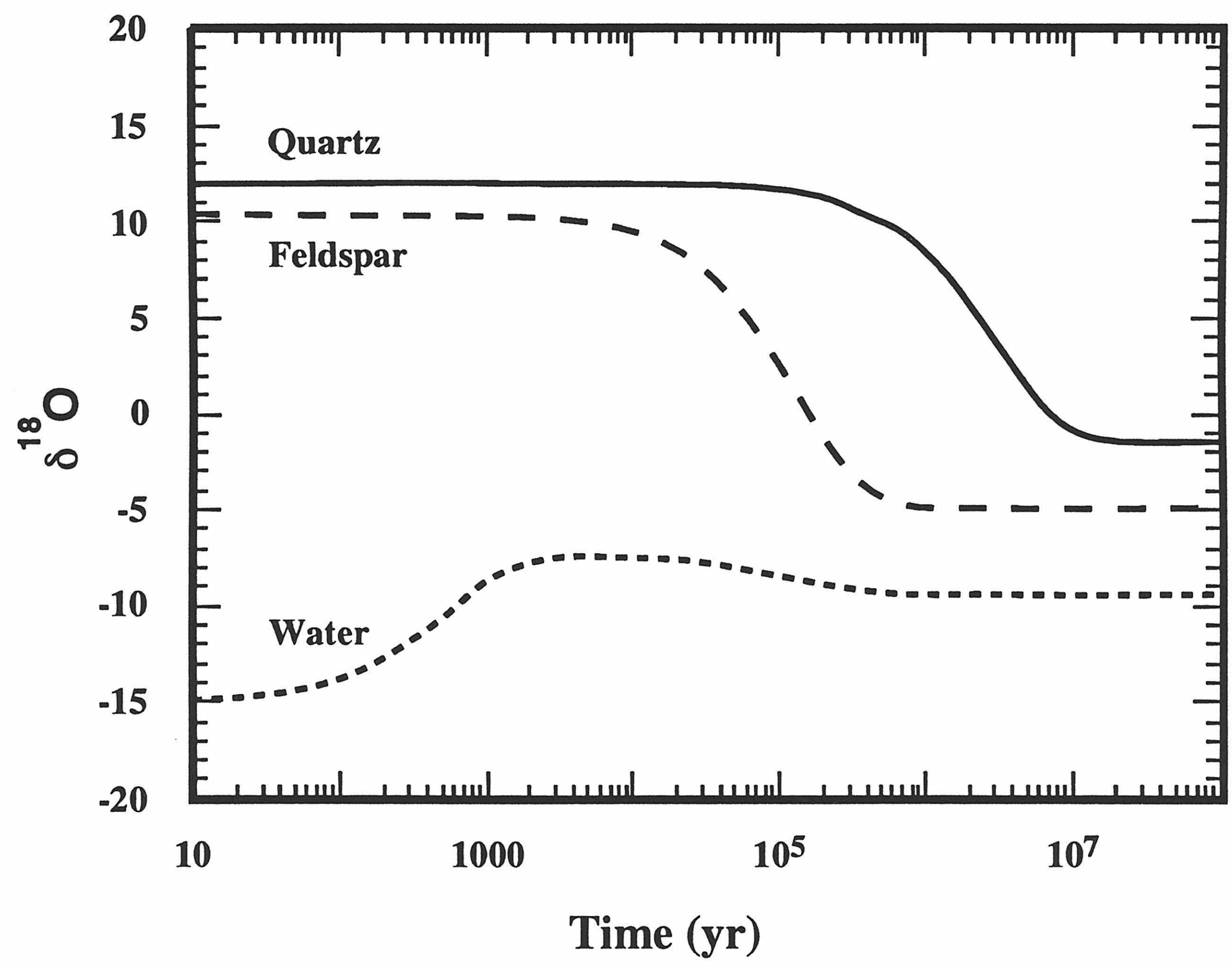

Figure 5.12 Oxygen Isotope Fractionations versus Time for the Kinetic Open-System Exchange Model

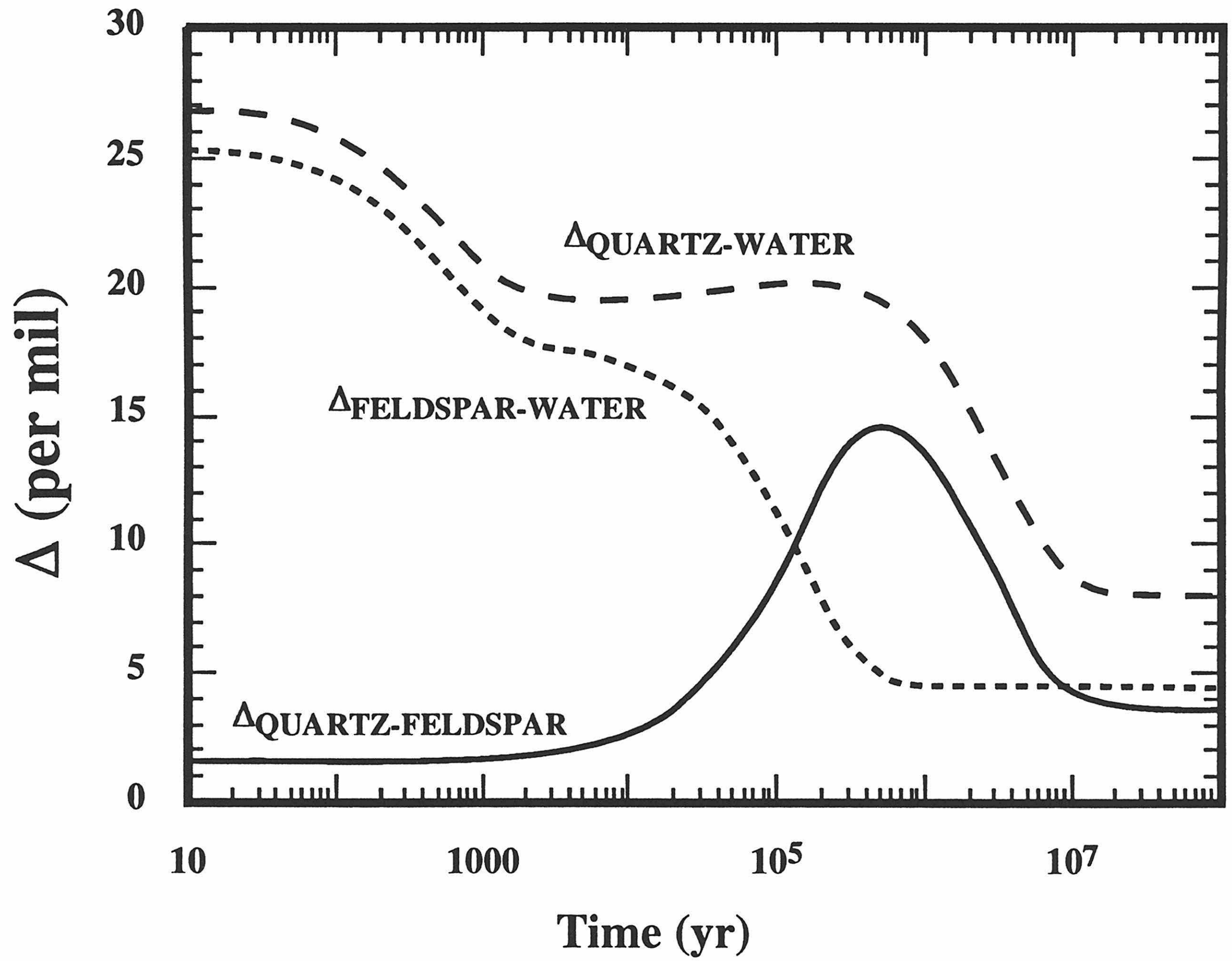

values gradually increase by 2‰ as water $\delta^{18}O$ is lowered by that amount and as the feldspar $\delta^{18}O$ reaches its final equilibrium $\delta^{18}O$ value. As shown by the peak of the $\Delta_{Q\text{-}F}$ curve on Figure 5.12, the time of maximum quartz-feldspar oxygen isotope disequilibrium occurs at about 500,000 yrs in this system; this is the time at which feldspar is close to the completion of the exchange cycle with meteoric fluid, but where quartz is just beginning to become markedly lowered in ^{18}O. Following this time, assuming the hydrothermal system continued to operate, $\Delta_{Q\text{-}W}$ would gradually decrease to its equilibrium value over a period of about 10 Ma, assuming T ~ 300 °C. However, in the particular data set being modeled, there is no evidence that hydrothermal alteration continued past the time at which the lowest-^{18}O quartz had been formed (*i.e.*, about 750,000 yrs in the model).

This simplistic model obviously should not be applied as a description of the actual oxygen isotope exchange history of the upper plate Nelson granodiorite at the Slocan Lake fault (Figures 5.9 and 5.10). Nevertheless, the model is internally consistent, and does provide a good correlation between the measured quartz and feldspar $\delta^{18}O$ values and the exchange trajectory calculated for these rocks. The success of the model calculation is probably attributable to (1) the simple flow geometry of the Slocan Lake hydrothermal system; (2) the probable presence of only one type of hydrothermal fluid here; and (3) the lithologically homogeneous medium involved in meteoric-hydrothermal metamorphism throughout the hanging wall of the detachment fault at this locality. Had these rocks been lithologically heterogeneous, or if there were evidence for influx of more than one type of water, there would have been much scatter in the data and the system would have been very difficult, or impossible, to model.

The above modeling provides us with some information about the time scale of the meteoric-hydrothermal event that affected the Slocan Lake fault. The open-system kinetic exchange modeling employed in this study suggests that the hydrothermal event related to detachment faulting probably affected these rocks over a duration at least 0.75 Ma, and it could easily have extended to 3.0 Ma or more, particularly in the waning stages of lower temperature deposition of calcite. These times are consistent with the cooling history of the Valhalla complex as determined by Parrish (1995) and Spear and Parrish (1996); in their work a rapid pulse of cooling of the lower plate from ~ 600 °C to ~400 °C can be interpreted to have occurred at the onset of extension ~58-55 Ma. Furthermore, Wernicke (1985) has shown that a plausible 100 °C temperature step related to the rapid movement of the lower plate out from beneath the upper plate will be dissipated by heat conduction within 1.6 Ma. The short-lived hydrothermal system proposed by our modeling is consistent with this short conductive decay time; in fact, the large-scale circulation of hydrothermal fluids may be an important means of advecting heat away from the cooling lower plate if fluid fluxes are sufficiently high (Bickle and Mackenzie, 1987; Connolly and Thompson, 1989). If this were the case, there would be local heating of the upper plate adjacent to the detachment interface.

5.3.7 Fluid Flux Calculations

Because we have a fairly good estimate of the time scales and water/rock ratios involved in this meteoric-hydrothermal event, fluid fluxes can be calculated if a flow path can be assumed. In this fault zone, hot meteoric fluids can in principle be moving either updip, downdip, or laterally. However, given our understanding of the buoyant nature of hot waters under hydrostatic pressure conditions in the crust, together with the framework provided by the regional geology, one can propose specific flow path lengths and geometries for this hydrothermal system (Fyles, 1967; Carr et al., 1987; Parrish et al., 1988; Ghent et al., 1991; Cook et al., 1992). Seismic imaging (Cook et al., 1992) has shown that the Slocan Lake fault has a dip of 30° through the crust down to the Moho. Hornblende geobarometry (Ghent et al., 1991) on rocks from the Nelson batholith imply

6 km rotation and tilting of this batholith during detachment faulting along the Slocan Lake fault. The estimated displacement along the Slocan Lake fault is 20-30 km (Carr et al., 1987). Assuming that the regime of hydrostatic fluid flow extends to the brittle-ductile transition (~350 °C in quartzose rocks; Sibson, 1977), it is plausible that the Slocan Lake fault hydrothermal system was active at depths as great as 15 km, compatible with the suggestions by Nesbitt and Muehlenbachs (1989; 1995) for somewhat analogous situations elsewhere in this region. Taking a 30° dip for the fault, the minimum down-dip path length to the brittle-ductile transition is 30 km.

Given the above conditions, it is plausible that hydrothermal fluid flow could have been in an up-dip direction with westward movement of fluids fed by a recharge zone to the east. Fyles (1967) reports a series of steeply west-dipping normal faults of unknown age between the eastern margin of the Nelson batholith and the north arm of Kootenay Lake. Archibald et al. (1984) report muscovite and whole-rock K-Ar cooling ages of 40-55 Ma in the sillimanite zone of the Kootenay Lake metamorphic high; note that this metamorphic high is in the footwall of these faults and the one muscovite K-Ar cooling age from the hanging wall of these faults is 131 Ma. It is plausible that these faults served as an important bounding structure that separated the hot footwall rocks from the cooler hanging wall rocks, but these structures need more study. The eastern contact of the Nelson batholith dips 20-30° to the west in this zone (Fyles, 1967), and the base of this batholith is estimated to be at 7 km depth at the latitude of the study area (Cook et al., 1992). The structural and thermal evolution of the Valhalla complex and the upper-plate block that contains the Nelson batholith, as well as the Kootenay Lake thermal metamorphic high (see Figures 2.9 and 2.10) suggest that during extension the detached upper-plate block may have been tectonically underlain by rocks hotter than 350 °C, as determined by muscovite K-Ar geochronometry (Archibald et al., 1983; 1984; Carr et al., 1987). There are numerous Ag-Pb-Zn mineral deposits within this zone of faulting east of the Nelson batholith (Fyles, 1967; Beaudoin et al., 1992); and as mentioned before, this area has been subjected to intense meteoric-hydrothermal activity (with water $\delta^{18}O$ as low as –16) during the Eocene (Ohmoto and Rye, 1970; Beaudoin et al., 1992).

Thus, it is useful to examine the following scenario where meteoric waters enter the crust through these steeply dipping faults and flow westward through the relatively permeable rocks beneath the Nelson batholith where they eventually encounter the Slocan Lake fault zone and begin their ascent back to the surface. Estimates of the flow path length for this system could range up to a maximum of 50 km to 100 km, assuming a 30° dip for the Slocan Lake fault and a 60° dip for the steeply dipping faults east of the Nelson batholith.

The flux of water or an aqueous fluid (in moles per unit cross-sectional area per unit time) through an elemental volume of rock (a cube with each side length d in cm) is given by (*e.g.*, Taylor, 1996):

$$(12) \qquad F_{H_2O} = \frac{(\lambda/d)(m)(W/R)}{(d^2)(t)}$$

where W/R is the material-balance open-system water/rock ratio from equation 2 above (in oxygen units), t is the duration of fluid flow in sec, λ/d is the total flow length (λ) divided by the size of each elemental volume, and m is the factor that converts the W/R ratio in oxygen units to moles of H_2O per unit elemental volume. The factor (m) is the ratio of the number of moles of rock oxygen in the elemental volume of rock (calculated by summing the contribution of rock oxygen from each major oxide in the rock sample) to the number of moles of water oxygen per mole of H_2O (*e.g.*, Larson and Zimmerman, 1991). This factor is approximately 0.076 for an elemental volume of 1 cm^3 for a typical granodiorite.

Equation 12 is solved for 10, 30, 50, and 100 km flow paths and arbitrary times of 0.5, 1.0, and 3.0 Ma; these values are tabulated in the upper half of Table 5.2.

By the very nature of this simplistic calculation (*e.g.*, see Taylor, 1977), the fluid flux values given in Table 5.2 can only be minimum estimates, for two main reasons: (1) the infinitesmal packets of H_2O entering the system always have $\delta^{18}O = -15$ (*i.e.*, they haven't suffered any ^{18}O shift whatsoever); and (2) this calculation only counts the water that actually interacts and exchanges oxygen with the rock system (we don't count any of the H_2O that passes through the fracture system without exchanging its oxygen). For example, if one examines the model calculations in Figures 5.10, 5.11, and 5.12, it is clear that during much of the duration of exchange the packets of water are considerably more ^{18}O-rich than –15. In fact, over the specific time period from about 3,000 years to 10,000 years, the ^{18}O-shifted H_2O has a $\delta^{18}O$ as high as –7.5, 2‰ higher than the final, steady-state value. Obviously, the water/rock ratios in the model system from Figure 5.10 will be much higher than in the simple calculation based on equation 2 above. That is the reason why it is useful to carry out the more elaborate calculations using equations 8 to 11. If the normalized flow rate from that model ($u = 10^{-12}\text{sec}^{-1}$) is assumed to be constant, that flow rate can also be converted to a water/rock ratio (W/R) using the equation (Gregory et al., 1989):

$$(13) \qquad \frac{W}{R} = \frac{\left(X_w + \int u \cdot dt\right)}{\left(X_Q + X_F\right)} = \frac{\left(X_w + ut\right)}{\left(X_Q + X_F\right)}$$

In the model, $X_w = 0.02$ and $\left(X_Q + X_F\right) = 0.98$, so to a very good approximation, we have:

$$(14) \qquad \frac{W}{R} = ut$$

Equation 14 can then be substituted into equation 12 to convert the normalized flow rate, u, to fluid flux. That substitution allows t to be cancelled, giving a relationship that is independent of time:

$$(15) \qquad F_{H_2O} = \frac{(\lambda/d)(m)(W/R)}{(d^2)(t)} = \frac{\lambda mu}{d^3}$$

If the elemental volume is assumed to be a 1-cm cube, we have:

$$(16) \qquad F_{H_2O} = \lambda mu$$

These values of fluid flux from the Figure 5.10 model are independent of any arbitrary assumptions about the duration of hydrothermal activity (because those data are built into the model itself, as shown on Figures 5.11 and 5.12). Using equation 16, the fluid flux values calculated from this model are shown in the bottom half of Table 5.2, and it can be seen that they range from an order of magnitude higher than the 500,000-yr fluxes calculated from the simple open-system W/R equation 2, up to two orders of magnitude higher than the 3,000,000-yr fluxes given in Table 5.2. Because the Figure 5.10 model is very detailed, it is likely that the fluxes shown in the bottom half of Table 5.2 are more realistic than those in the top half.

Nevertheless, there is reason to believe that the actual fluid fluxes along the Slocan Lake fault are probably intermediate between the extremes listed in Table 5.2, based on the following reasoning. The model in Figure 5.10 was predicated on the assumption that the

TABLE 5.2. FLUID FLUX CALCULATIONS FOR THE SLOCAN LAKE FAULT HYDROTHERMAL SYSTEM

Calculations Using W/R (1.05) of Lowest-^{18}O Sample MT-324

Flow Path Length (km)		10	30	50	100
Duration (yr)	Units				
500,000	mol/cm^2·sec	5.06×10^{-9}	1.52×10^{-8}	2.53×10^{-8}	5.06×10^{-8}
	m/sec	1.20×10^{-9}	3.64×10^{-9}	6.05×10^{-9}	1.20×10^{-8}
	m/yr	0.04	0.12	0.19	0.38
1,000,000	mol/cm^2·sec	2.53×10^{-9}	7.59×10^{-9}	1.26×10^{-8}	2.53×10^{-8}
	m/sec	6.00×10^{-10}	1.82×10^{-9}	3.03×10^{-9}	6.00×10^{-9}
	m/yr	0.02	0.06	0.09	0.19
3,000,000	mol/cm^2·sec	8.43×10^{-10}	2.53×10^{-9}	4.20×10^{-9}	8.43×10^{-9}
	m/sec	2.00×10^{-10}	6.00×10^{-10}	1.00×10^{-9}	2.00×10^{-9}
	m/yr	0.01	0.02	0.03	0.06
Integrated	mol/cm^2	7.98×10^{4}	2.40×10^{5}	3.98×10^{5}	7.98×10^{5}
Fluid Flux	cm^3/cm^2	1.92×10^{6}	5.75×10^{6}	9.54×10^{6}	1.92×10^{7}

Calculations Using Normalized Flow Rate ($u = 10^{-12} sec^{-1}$) From Model in Figure 5.10

Flow Path Length (km)		10	30	50	100
Duration (yr)	Units				
Independent	mol/cm^2·sec	7.60×10^{-8}	2.28×10^{-7}	3.80×10^{-7}	7.60×10^{-7}
of Duration	m/sec	1.80×10^{-8}	5.40×10^{-8}	9.00×10^{-8}	1.80×10^{-7}
	m/yr	0.58	1.70	2.90	5.80
Integrated	mol/cm^2	1.2×10^{6}	3.6×10^{6}	6.0×10^{6}	1.2×10^{7}
Fluid Flux	cm^3/cm^2	2.9×10^{7}	8.7×10^{7}	1.5×10^{8}	2.9×10^{8}
500,000 yr					
Integrated	mol/cm^2	2.4×10^{6}	7.2×10^{6}	1.2×10^{7}	2.4×10^{7}
Fluid Flux	cm^3/cm^2	5.8×10^{7}	1.7×10^{8}	2.9×10^{8}	5.8×10^{8}
1,000,000 yr					
Integrated	mol/cm^2	7.2×10^{6}	2.2×10^{7}	3.6×10^{7}	7.2×10^{7}
Fluid Flux	cm^3/cm^2	1.7×10^{8}	5.1×10^{8}	8.5×10^{8}	1.7×10^{9}
3,000,000 yr					

minimum feldspar $\delta^{18}O$ in the Slocan Lake area is the lowest measured value of –5.0. However, it is very likely that a more intensive search along the fault would turn up a lower-^{18}O sample (a $\delta^{18}O$ value as low as –7 or –8 would not be unexpected). If such a feldspar were indeed found, and if, as would be expected, it coexisted with a quartz having a lower $\delta^{18}O$ than the +9.1 value in MT-324, one could probably fit an exchange trajectory through both this sample and all the other data points on Figure 5.10, ending up with the horizontal part of the trajectory at –7 or –8 instead of –5. This new exchange trajectory would not have as sharp a bend as that shown on Figure 5.10, and it could be fitted by a smaller normalized flow rate (*e.g.*, $u = 10^{-13}sec^{-1}$). Using that value for u, and applying equation 16, this would give exactly an order of magnitude lower fluid flux than the values tabulated in the bottom half of Table 5.2.

Using the water/rock ratios determined from equation 2 and applying equation 12 to the rock (MT-324) exhibiting the highest water/rock ratio, we obtain fluid fluxes that range from 8.43 x 10^{-10} mol/cm^{2}sec (0.01 m/yr) to 5.06 x 10^{-8} mol/cm^2 (0.38 m/yr). For this model, integrated fluid fluxes of 7.98 x 10^4 mol/cm^2 (1.92 x 10^6 cm^3/cm^2) to 7.98 x 10^5 mol/cm^2 (1.92 x 10^7 cm^3/cm^2) are obtained for flow-path lengths between 10 km and 100 km. Fluid fluxes calculated using equation 16 and assuming a normalized flow rate of 10^{-12}/sec are much higher, between 7.60 x 10^{-8} mol/cm^2 (0.58 m/yr) and 7.60 x 10^{-7} mol/cm^2 (5.80 m/yr). Integrated fluid fluxes calculated from this more quantitative model are also much higher, from 1.2 x 10^6 cm^3/cm^2 to 7.2 x 10^7 cm^3/cm^2.

These two independent models, combined with a range of likely durations and path lengths for the hydrothermal system, provide upper and lower bounds on the fluid fluxes that would plausibly apply to the parts of the Slocan Lake fault hydrothermal system that experienced the greatest degree of interaction with hot meteoric water. A fairly good understanding of possible flow paths for these fluids is constrained by the geological relationships (Fyles, 1967; Carr et al., 1987; Cook et al., 1992). As shown on Figure 5.13, these calculated fluid fluxes and path lengths plot within the domain where both mass (solutes) and heat are being advected by the hydrothermal fluids, based on the model of Bickle and McKenzie (1987). This domain is defined by Bickle and McKenzie (1987) to be that where the Peclet numbers for both heat and solute advection/diffusion are greater than 10 (given by the two diagonal lines on Figure 5.13). The calculations show that these meteoric-hydrothermal fluid fluxes, for comparable path lengths along the detachment faults, are larger by 1-2 orders of magnitude than those thought to be operative during regional metamorphism.

Inasmuch as heat is likely to be advected from the Slocan Lake fault system by these meteoric-hydrothermal fluids, it is not unexpected that this hydrothermal system would be short-lived relative to the total duration of the faulting event (1-3 Ma for hydrothermal activity versus perhaps as much as 9 Ma for faulting; Carr et al., 1987). However, one complication is that the fluid fluxes discussed in the Bickle and McKenzie (1987) and Ferry and Dipple (1991) models were calculated assuming lithostatic fluid pressure. Nevertheless, the domains in Figure 5.13 are probably generally applicable, because the transport equations themselves are independent of pressure, and because the fluid flux is an input into this calculation and can be determined prior to solving the differential equation for either heat transport and/or solute transport through diffusion and advection.

An estimate of the permeabilities for the detachment fault systems can be calculated using Darcy's law (Dullien, 1979). This is again done using sample MT-324, the sample

Figure 5.13 -- Plot showing calculations of path length vs fluid flux for different regimes in the Earth's lithosphere, and their relationship to the principal mechanisms of heat and mass transfer in the continental crust (from an original diagram by Bickle and McKenzie, 1987, as modified by Ferry and Dipple, 1991). From lower left to upper right, the diagram indicates the generalized domains of combined heat and mass diffusion, combined heat diffusion and mass advection, and combined heat and mass advection. Note that both regional and contact metamorphic systems lie generally within the range where mass advection and heat diffusion are the means of transport. Also plotted on the diagram are the generalized values for path length and fluid flux from the Slocan Lake fault hydrothermal models (large black dot); note that these parameters place the Slocan Lake fault system in the domain where advection of both mass and heat take place simultaneously.

Figure 5.13 Mechanisms of Heat and Mass Transfer

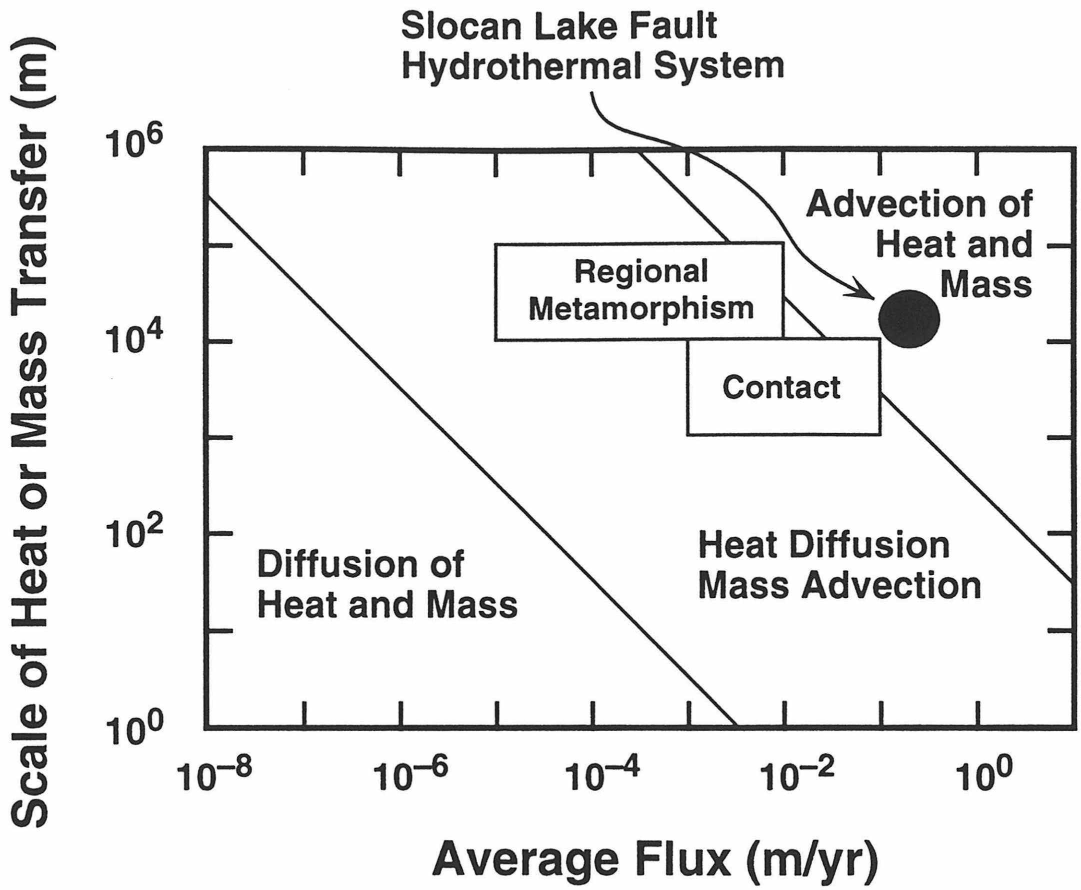

with highest water/rock ratio, in order to place constraints on the maximum plausible permeability for this system according to our data set. Darcy's law is:

$$(17)\quad \upsilon = \frac{-k}{\eta}\nabla P^{*}$$

where υ is the Darcy velocity in cm^3/cm^2sec, k is the permeability in cm^2, η is the fluid viscosity in poise, and P^* is the piezometric pressure in $dynes/cm^2$. The Darcy velocity is related to the calculated flux by the relation:

$$(18)\qquad \upsilon = F_{H_2O}\left(\frac{M}{\rho}\right)$$

with M being equal to the molecular weight of the fluid and ρ is the fluid density. Now we can calculate the permeability of the rock by:

$$(19)\qquad k = -F_{H_2O}\left(\frac{M}{\rho}\right)\left(\frac{\eta}{\nabla P^{*}}\right)$$

This equation is solved using the following parameters: M = 18 g/mol, ρ = 0.75 g/cm^3 (Norton, 1984), and η = 1.0 x 10^{-3} poise. The fluid pressure gradient (∇P^*) is –367.9 $dynes/cm^2$ $\left(=\rho g \sin 30^{o}\right)$ for the fluid being transported upward along a fault dipping 30°. Using these parameters and the calculated flow rates, a range of permeabilities between 3.3 x 10^{-13} cm^2 (0.033 mD) and 5.0 x 10^{-11} cm^2 (5 mD); these values are about two orders of magnitude greater than the values for typical metamorphic rocks calculated by Ferry and Dipple (1991), but are well within the range of many crystalline rocks (see Criss and Taylor, 1986), and in particular are very similar to the values calculated by Norton and Taylor (1979) for the 6 to 8 km-deep meteoric-hydrothermal system that affected the Skaergaard intrusion in east Greenland, which also took place during Eocene time.

5.3.8 $\delta^{18}O$ and $\delta^{13}C$ Systematics of Carbonates

Calcite $\delta^{18}O$ values from late fractures indicate precipitation from CO_2-bearing fluids over a large range of temperatures, most likely between 150° and 300 °C. Low $\delta^{18}O$ calcite (< 0‰) is restricted to the brittle zone and the lowermost 100 m of the granodiorite (Figure 5.8). Rocks proximal to the hot lower plate experienced higher temperatures than those distal to the fault, with this heat from the lower plate being advected away by the convecting fluids. These low-^{18}O calcites could have formed in $^{18}O/^{16}O$ equilibrium with water $\delta^{18}O = -9.8$ at T ~ 250 °C, using the calcite-water $^{18}O/^{16}O$ fractionation factor of O'Neil et al. (1969).

The high-^{18}O calcite hosted in the upper-plate granodiorite either precipitated in $^{18}O/^{16}O$ equilibrium at lower temperature or with more evolved (*i.e.*, more ^{18}O-shifted) meteoric water. The most straightforward interpretation of the uniform $\delta^{13}C$ values of these proximal upper plate rocks and a single sample from the uppermost part of the brittle fault zone is that these calcites formed in equilibrium at a uniform temperature with a fluid uniform in ^{13}C. If these calcites formed at the relatively low temperature indicated by their $\delta^{18}O$ values (*i.e.*, 150 °C), their $\delta^{13}C$ values ought to have been about 1-2‰ higher than their measured values (*i.e.*, they should plot near the lowermost diagonal line on Figure 5.8). Feldspar $\delta^{18}O$ values (+7.0 to +9.0) of these samples imply relatively low water/rock ratios, indicating that these waters probably were higher in ^{18}O than the meteoric waters that interacted with the rocks of the fault zone itself. This contrasts with the isotopic data from calcite veins analyzed by Beaudoin et al. (1992) that plot near the temperature evolution trend calculated for calcite forming in $^{18}O/^{16}O$ equilibrium with a

Figure 5.14 -- $\delta^{13}C$ vs. $\delta^{18}O$ for carbonates hosted in the upper-plate (Nelson batholith) of the Slocan Lake fault. Distal upper plate data (open squares) are late-stage calcite veins associated with Ag-Pb-Zn deposits studied by Beaudoin et al. (1992). All other data (except one sample from the brittle zone) are from the present study. The two diagonal lines indicate calculated $\delta^{13}C$ and $\delta^{18}O$ values for calcite formed in equilibrium with two different aqueous fluids at 125-300 °C, both with $\delta^{18}O = -9.8$, but one having $\delta^{13}C$ of $H_2CO_3 = -1.0$ and one having $\delta^{13}C$ of $H_2CO_3 = -5.0$. The fluid $\delta^{18}O$ of –9.8 is essentially the steady state $\delta^{18}O$ value calculated for the model of Figure 5.10. These curves were calculated using the calcite $^{18}O/^{16}O$ fractionation factor of O'Neil et al. (1969) and the $^{13}C/^{12}C$ fractionation factor of Bottinga (1968). The dashed curve represents a fluid with pH = 8, and provides an approximation of the upward shift in $\delta^{13}C$ of H_2CO_3 (aq) in a fluid initially having $\delta^{13}C = -5.0$ (*i.e.*, primitive mantle carbon) as pH increases from 6 to 8 (from Ohmoto, 1972). These data suggest that precipitation of these calcites occurred in equilibrium with low-^{18}O meteoric waters as these waters became more alkaline. The low-^{13}C and relatively high-^{18}O proximal samples labelled "low W/R" (GH-118, 120, and 122) are probably the result of calcite forming in equilibrium with limited amounts of hot meteoric waters whose $^{18}O/^{16}O$ ratios have been buffered by exchange with the large reservoir of granodiorite.

Figure 5.14 Slocan Lake Fault Carbonates

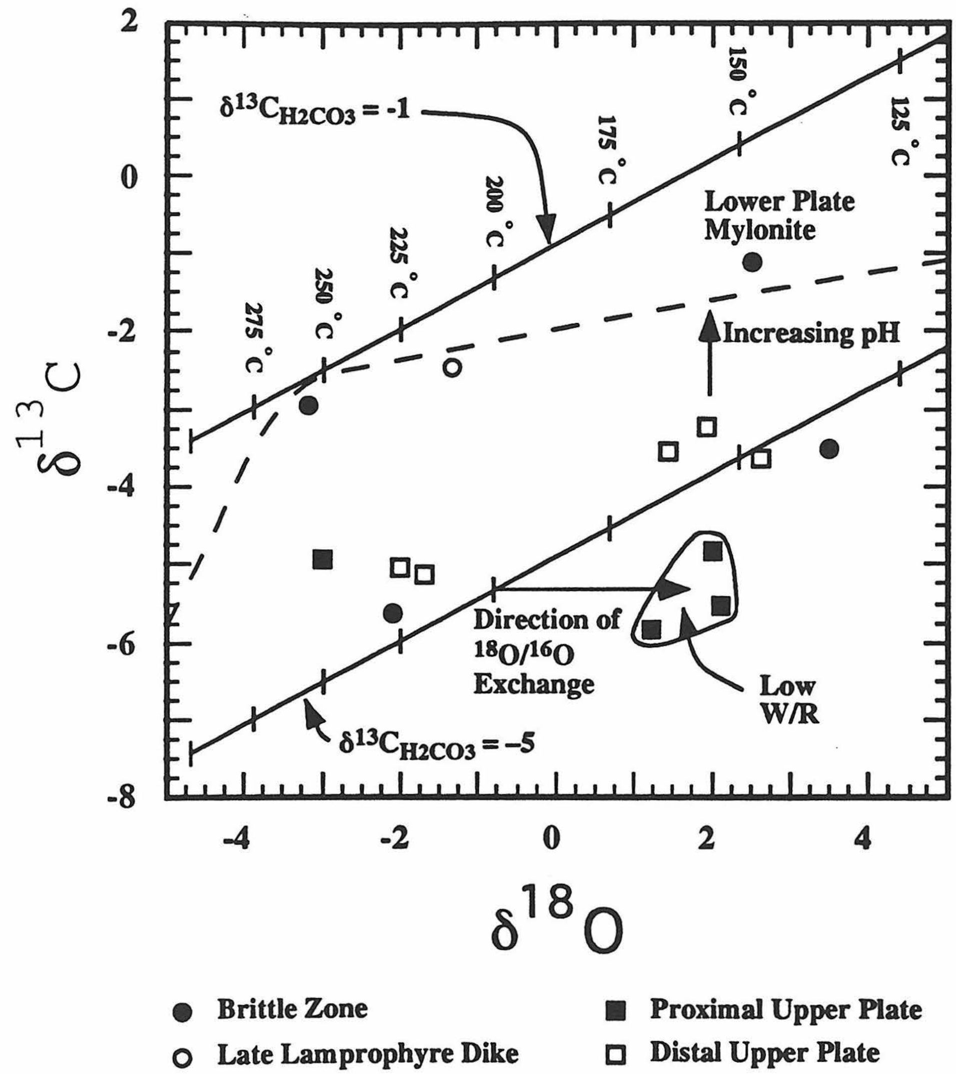

fluid having $\delta^{18}O = -9.8$ and $\delta^{13}C = -5.0$. Trends in those data indicate precipitation of calcite at about 150-225 °C.

The isotopic composition of carbon in hydrothermal carbonates depends not only on the $\delta^{13}C$ of the total carbon in the system and temperature, but also fluid pH, oxygen fugacity, the ionic strength of the fluid, and the total concentration of carbon in the fluid (Ohmoto, 1972). Homogeneous $\delta^{13}C$ values in the upper plate indicate that these samples formed in $^{13}C/^{12}C$ equilibrium with fluid having a uniform $\delta^{13}C = -5.0$, assuming T = 250 °C, and using the carbon isotope fractionation factor for calcite-H_2CO_3 given in Ohmoto (1972). This ^{13}C-uniform fluid can be either a deep-seated ($\delta^{13}C \sim -5$ to -7) fluid from the mantle (or lower crust), or a mixture of low-^{13}C organic fluids ($\delta^{13}C \sim -15$) and those released by the decarbonation of limestone ($\delta^{13}C \sim 0$).

Beaudoin and others (1991, 1992) proposed that the major source of carbon in this system came from the upper mantle, based on the results of the seismic imaging and the finding that the ore-stage siderites from Ag-Pb-Zn deposits were extremely uniform in $^{13}C/^{12}C$ ($\delta^{13}C = -7.1 \pm 0.5$‰) throughout the entire block that comprises the upper plate of the Slocan Lake fault west of Kootenay Lake. This siderite was the first mineral to form during the paragenetic sequence of these mineral deposits (Beaudoin et al., 1992) and probably represents deposition from the earliest fluids to circulate through this system. LITHOPROBE seismic reflection studies indicate that the Slocan Lake fault extends through the crust and roots into the upper mantle (Cook at al., 1992), and this fault may have served as a channelway accommodating the ascent of these deep-seated fluids into the upper crust.

The high $\delta^{13}C$ values from the brittle zone cannot be explained by the fluids having a common source. There are three ways of increasing the $^{13}C/^{12}C$ of these fluids (see Ohmoto, 1972): (1) mixing between a fluid from an organic source and fluids derived from the decarbonation of limestones, marbles, and calc-silicates, (2) increasing the pH of the fluids, and (3) lowering the f_{O_2} of the system in a reducing environment. The large water/rock ratios recorded in this part of the system indicate a water-rich environment, and there is no indication of particularly reducing conditions. The average $\delta^{13}C$ of Paleozoic marbles from this part of the southern Omineca belt is +1.1 ± 1.3‰; the $\delta^{13}C$ of fluid released by decarbonation of such marbles would be ~ +3‰. Nesbitt and Muehlenbachs (1995) argued for mixing between fluids derived from the decarbonation at 300 °C of the limestones, black shales, and argillites that comprise the country rocks of the Nelson batholith.

By way of comparison, in the Arizona metamorphic core complexes, significant potassium metasomatism occurred in the upper plate volcanic rocks as the result of interaction with large amounts of basinal brine (Brooks, 1986; Chapin and Lindley, 1986; Roddy et al., 1988). Roddy et al. (1988) concluded that K-metasomatism occurred in the presence of high-pH fluids. K-feldspar is stable in equilibrium with such high-pH fluids, and as pH decreases, muscovite becomes the stable K-bearing mineral. Ohmoto (1972) has shown that increases in pH can result in an increase in fluid $\delta^{13}C$, and the dashed line on Figure 5.14 indicates the approximate upward shift in $\delta^{13}C$ expected for an increase in 2 pH units.

5.4 The Valkyr Shear Zone

5.4.1 Geologic Setting

The Valkyr shear zone comprises the western boundary of the Valhalla metamorphic core complex (Figure 5.2). This is a very gently west-dipping, east-directed, ductile shear zone that can be projected into the Slocan Lake fault to the east. The footwall is made up of variably deformed Ladybird leucogranite, and the hanging wall consists of Jurassic plutonic rocks similar to those in the Nelson batholith to the east, as well as Cretaceous plutonic rocks and low grade metasedimentary and metavolcanic rocks of the Quesnellia terrane (Carr et al., 1987). Younger, undeformed phases of the Ladybird suite that crosscut this shear zone date the latest movement along it to have been at about 56 Ma (Carr et al., 1987).

5.4.2 Samples Studied

Eight samples of variably deformed Ladybird leucogranite from the Valkyr shear zone were collected from seven outcrops along logging roads that follow Koch Creek and Ladybird Creek. Most samples are biotite + hornblende ± tourmaline quartz monzonite of the Ladybird suite. At locality 309 (see Figure 5.2), samples from a quartz monzonite and a thin, late, crosscutting dike were collected and analyzed. Many samples have biotite altering to chlorite + leucoxene. Highly strained samples contain recrystallized quartz grains that experienced grain-size reduction and have undulatory extinction. Feldspar grains are cut by numerous shear fractures, many of which contain sericite, and there are local occurrences of late epidote. The degree of visible alteration seems to be much less intense than that observed 30 km to the east along the Slocan Lake fault. Deformational style appears to be independent of distance from the mapped trace of the Valkyr shear zone; this is likely due to multiple stages of magma emplacement, much of which occurred after the cessation of deformation along this early shear zone (Carr et al., 1987).

One sample was analyzed from a hydrothermally altered late-stage mafic dike that cuts the Ladybird quartz monzonite. This rock is green in outcrop and contains many thin (~1-3 cm) quartz veins. Sanidine phenocrysts are almost completely altered to calcite+sericite, but biotite phenocrysts are only slightly altered to chlorite.

5.4.3 Results

Quartz and feldspar $\delta^{18}O$ values from the Valkyr shear zone indicate that alteration of these rocks occurred as hot meteoric water interacted with this system. Most samples have quartz $\delta^{18}O = +10.8 \pm 0.2‰$ (N = 6), but two samples have quartz $\delta^{18}O$ values of +9.7 and +7.8. Feldspar $\delta^{18}O$ ranges from +0.2 to +8.8 (N = 6), with the most ^{18}O-depleted samples ($\delta^{18}O$ feldspar = +4.6 and +0.2) corresponding to the two rocks with the lowest quartz $\delta^{18}O$ values. A large range in $\Delta_{Q\text{-}F}$ (2.0-7.6‰) indicates that oxygen isotope disequilibrium was imprinted upon these assemblages during exchange with hot meteoric waters. These data contrast with those from the Slocan Lake fault 30 km to the east in that quartz and feldspar $\delta^{18}O$ values define a much more shallow-sloping array (slope ~5) on a δ-δ plot with quartz $\delta^{18}O$ plotted on the abcissa; this indicates either a longer-lived hydrothermal system (>> 500 ka) than that at the Slocan Lake fault, or that meteoric-hydrothermal water-rock interaction occurred at higher temperatures (~ 450 °C). The rock with the lowest quartz and feldspar $\delta^{18}O$ values has whole rock $\delta^{18}O = +1.0$. One analysis of sphene (S) has $\delta^{18}O = +6.0$ and $\Delta_{Q\text{-}S} = 4.5‰$.

The late mafic dike is the rock with the lowest whole-rock $\delta^{18}O$ value (–5.1) of all rocks studied from the Valhalla complex. This very low $\delta^{18}O$ value is almost the same as that of a similar dike (MT-323b, $\delta^{18}O = -5.3$) that crosscuts the Slocan Lake fault zone along the north shore of Slocan Lake. Alteration calcite from the Valhalla dike has $\delta^{18}O = -1.3$ and $\delta^{13}C = -2.4$. Nesbitt and Muehlenbachs (1995) report a mineral separate δD value of –151 from the Valkyr shear zone area, along with at least two strongly ^{18}O-depleted whole-rock samples ($\delta^{18}O = +1.2$ and +3.4).

5.4.4 Discussion

The hydrothermal system associated with the Valkyr shear zone appears to be independent of tectonic style because there are no apparent correlations between $\delta^{18}O$ values and either intensity or type of deformation. The lowest-^{18}O samples are a post-tectonic quartz monzonite (GH-307), and a mylonitic quartz monzonite (GH-317). A protomylonitic granite (GH-297) appears to be only slightly affected by meteoric-hydrothermal fluids in that it has $\Delta_{Q\text{-}F} = 2.7‰$. The Valkyr shear zone lies within close proximity to the Coryell alkaline intrusions (see Figure 5.2), and it is very likely that the meteoric-hydrothermal system that affected this shear zone was also influenced by the emplacement of these post-tectonic plutons. The most altered sample from this region is the late-stage dike ($\delta^{18}O = -5.1$); this implies that meteoric water entered these rocks late in their deformational history, perhaps during late fracturing associated with final uplift along the Slocan Lake fault; this is similar to the observation that late-stage dikes emplaced at deep levels of the Whipple Mountains metamorphic core complex have interacted with hot meteoric waters at the time of their emplacement (Morrison, 1994). Deformational fabrics are annealed along the Valkyr shear zone, an indication that deformation ceased while the shear zone was still in the ductile regime (Carr et al., 1987) and apparently impermeable to aqueous fluids.

The relatively shallow array in δ-δ space defined by these Valkyr shear zone data (Figure 5.15) can be the result of either a hotter hydrothermal system, a longer-lived hydrothermal system, or both. A comparison of alteration mineralogy indicates that the former explanation is most likely, and this is certainly also supported by the proximity to the "heat engines" of the nearby Coryell alkaline intrusions. In this connection, also note that epidote is the prominent alteration mineral in this area, chlorite is nearly absent, and feldspars are much less altered to sericite. This contrasts with the extreme chloritization and sericitization of feldspar observed near the Slocan Lake fault. Thus, the meteoric-hydrothermal system associated with the Valkyr shear zone very likely was post-tectonic and related to the shallow emplacement of the Coryell plutonic suite to the west. This is similar to observations of large-scale meteoric-hydrothermal activity in the country rocks of most granitic intrusions emplaced at shallow crustal depth elsewhere in the world (*e.g.*, Forester and Taylor, 1979; Criss and Taylor, 1983; Larson and Taylor; 1986).

5.5 The Coryell Plutonic Suite

5.5.1 Geologic Setting

The Coryell plutonic suite is the youngest group of intrusive rocks in the southern Omineca belt. The most voluminous plutons that belong to this group of intrusive rocks are intruded into older plutonic and metasedimentary rocks west of the Valhalla complex (Figure 5.2). These intrusions are synextensional with faulting along the west-dipping detachment faults such as the Okanagan fault, but they postdate the east-dipping detachment faults (Carr et al., 1987). Coryell intrusive rocks along the west shore of southern Arrow Lake and southeast of the Valhalla study area have 51.1 Ma U-Pb zircon ages (Carr et al., 1987; Carr and Parkinson, 1989). The intrusions belonging to this suite that have been investigated in the present study are located west and southwest of the Valhalla complex along Arrow Lake (Figure 5.2), but analogous bodies are found throughout the area between the Okanagan Valley and the western margin of the Valhalla complex (Tempelman-Kluit, 1989; see Figure 2.7). These plutons were emplaced at very shallow depths in the crust. The magmas were of alkaline composition, were alkalic to calc-alkalic in composition, and consisted mainly of pink syenites and quartz-bearing monzonites, along with pink porphyry dikes. Initial $^{87}Sr/^{86}Sr$ (0.7067 to 0.7075), ε_{Nd} (–7.5 to –9.3), $^{206}Pb/^{204}Pb$ (18.426), $^{207}Pb/^{204}Pb$ (15.556), and $^{208}Pb/^{204}Pb$ (38.867) indicate an enriched mantle lithosphere or deep lower crustal source for these magmas (Bevier, 1987; Ghosh, 1995). These alkaline magmas certainly were intruded at higher temperatures than the H_2O-rich leucogranites of the Selkirk Allochthon (see Chapter 4).

5.5.2 Samples Studied

Seven samples of porphyritic syenite were collected from the two large plutons in the vicinity of Arrow Lake along logging roads that traverse the area. These plutons have no names, so for purposes of the discussion that follows, they will be named according to the most prominent geographic or cultural feature in each pluton. The northern pluton is termed the Arrow Lake pluton (samples 586, 868, 793, 791, and 874 on Figure 5.2) and the southern pluton will be referred to as the Renata pluton (samples 780 and 563 on Figure 5.2). These $^{18}O/^{16}O$ data supplement the data from this plutonic suite published by Magaritz and Taylor (1986). The pluton southwest of the town of Castlegar that was studied by Magaritz and Taylor will be called the Nancy Greene pluton (samples MT 331 and 332 on Figure 5.2). Two country rocks from near the Nancy Greene pluton are also considered in this discussion.

The characteristic feature of these rocks is the predominance of K-feldspar megacrysts; these megacrysts are commonly zoned with pink cores and white rims. Matrix feldspar has been altered to deep red color. Hornblende, sphene, and pyroxene are the predominant mafic minerals. Quartz comprises no more than 5 vol. % of these porphyritic rocks. Epidote is the main alteration mineral.

5.5.3 Results

Oxygen isotope analyses of these rocks indicate large-scale meteoric-hydrothermal water-rock interaction associated with the shallow emplacement of these alkaline plutons (Figures 5.15 and 5.16). Even though quartz is a minor mineral in these rocks, quartz $\delta^{18}O$ is homogeneous for the Renata and Arrow Lake plutons at +8.4 ± 0.1‰ (N = 4). The $\delta^{18}O$ values of K-feldspar megacrysts in 2 relatively unaltered samples of syenite porphyry from the core of the Arrow Lake pluton are identical at +7.6. These data indicate that these magmas probably had a uniform source, at least with respect to $^{18}O/^{16}O$. This contrasts with the groundmass feldspar (dominantly plagioclase) in these two plutons, which is highly variable in $\delta^{18}O$ (–1.7 to +6.3); the latter values clearly represent $^{18}O/^{16}O$ disequilibrium, and indicate that these particular rocks exchanged with large amounts of hot meteoric water. There are no analyses of samples containing

TABLE 5.3. $^{18}O/^{16}O$ DATA ON ROCKS AND MINERALS FROM THE CORYELL ALKALINE SUITE

Sample	Rock Type	WR	Qz	Ksp	Plg	Amp	Other
Coryell Alkaline Suite							
Renata Pluton							
GH-563	Coarse Quartz Syenite		8.5		0.2	4.5	3.7s*
GH-780	Fine-Grained Quartz Syenite		8.4		−1.7		
Arrow Lake Pluton							
GH-586	Quartz Syenite		8.4			4.9	
GH-791	Syenite Porphyry			7.6	6.3	5.4	
GH-793	Syenite Porphyry			7.6			−2.6e*
GH-868	Quartz Syenite Porphyry		8.5		5.1		
GH-874	Quartz Syenite Porphyry		8.2				
Nancy Greene Pluton							
MT-331a	Quartz Monzonite	−2.2	5.8#		−4.4		
MT-331b	Quartz Syenite Porphyry w/Xenolith	0.7	6.1#		−3.1		
MT-332	Lamprophyre	−5.0					
Country Rocks							
MT-329	Migmatite			7.1			
MT-330	Diorite	−1.1					

* s = sphene, e = epidote. See Table 5.1 for explanation of other symbols.

\# These two quartz samples were treated with HF prior to $^{18}O/^{16}O$ measurement (see Magaritz and Taylor, 1986).

Figure 5.15 -- Plot of $\delta^{18}O$ quartz versus coexisting $\delta^{18}O$ feldspar for the Valkyr shear zone (solid squares) and the Coryell intrusions (open squares). These data are compared to $\delta^{18}O$ data from the Valhalla lower plate (oval envelope) and the Nelson batholith away from mapped detachment faults (crosses). Within the near-vertical data-point envelope for the Renata and Arrow Lake plutons are two asterisks that indicate samples GH-791 and 793, where only the feldspars were actually analyzed for $\delta^{18}O$; the plotted $\delta^{18}O$ values for the coexisting quartz are inferred to be identical to the characteristic homogeneous $\delta^{18}O$ values of quartz in these plutons (*i.e.*, +8.5). The 45° dashed diagonal lines at Δ=0 and Δ=2 represent the range in normal quartz-feldspar fractionations in granitic rocks. Data are from this study and Magaritz and Taylor (1986).

Figure 5.16 -- Plot of mineral and whole-rock $\delta^{18}O$ data from the Coryell plutonic suite and its country rocks. These data are from three large plutons (here termed the Renata, Arrow Lake, and Nancy Greene plutons) that crop out in the west and southwest parts of the study area; sample locations are plotted on Figure 5.2. $\delta^{18}O$ values are shown for whole-rock (plus signs), quartz (solid dots), K-feldspar (solid squares), plagioclase (open dots), sphene (open squares), epidote (open diamonds), and amphibole (solid diamonds). Data are from this study (GH) and Magaritz and Taylor (MT; 1986). Quartz ($\delta^{18}O$ = +8.4 ± 0.1‰), megacrystic K-feldspar ($\delta^{18}O$ = +7.6), and amphibole ($\delta^{18}O$ = +4.9) from the analyzed samples of the Renata and Arrow Lake plutons are homogeneous in $^{18}O/^{16}O$, whereas groundmass feldspars in some other samples of these plutons have $\delta^{18}O$ from +6.3 to –1.7; this indicates these plutons were locally affected by meteoric-hydrothermal fluids during their emplacement at shallow crustal levels. The Nancy Greene pluton has lower quartz $\delta^{18}O$ (+5.8 to +6.1), and was also affected by similar meteoric-hydrothermal processes, as indicated by the extremely low-^{18}O plagioclase ($\delta^{18}O$ = –4.4 and –3.1) and whole-rock ($\delta^{18}O$ = +0.7 to –5.0).

Figure 5.15 Valkyr Shear Zone Coryell Intrusions

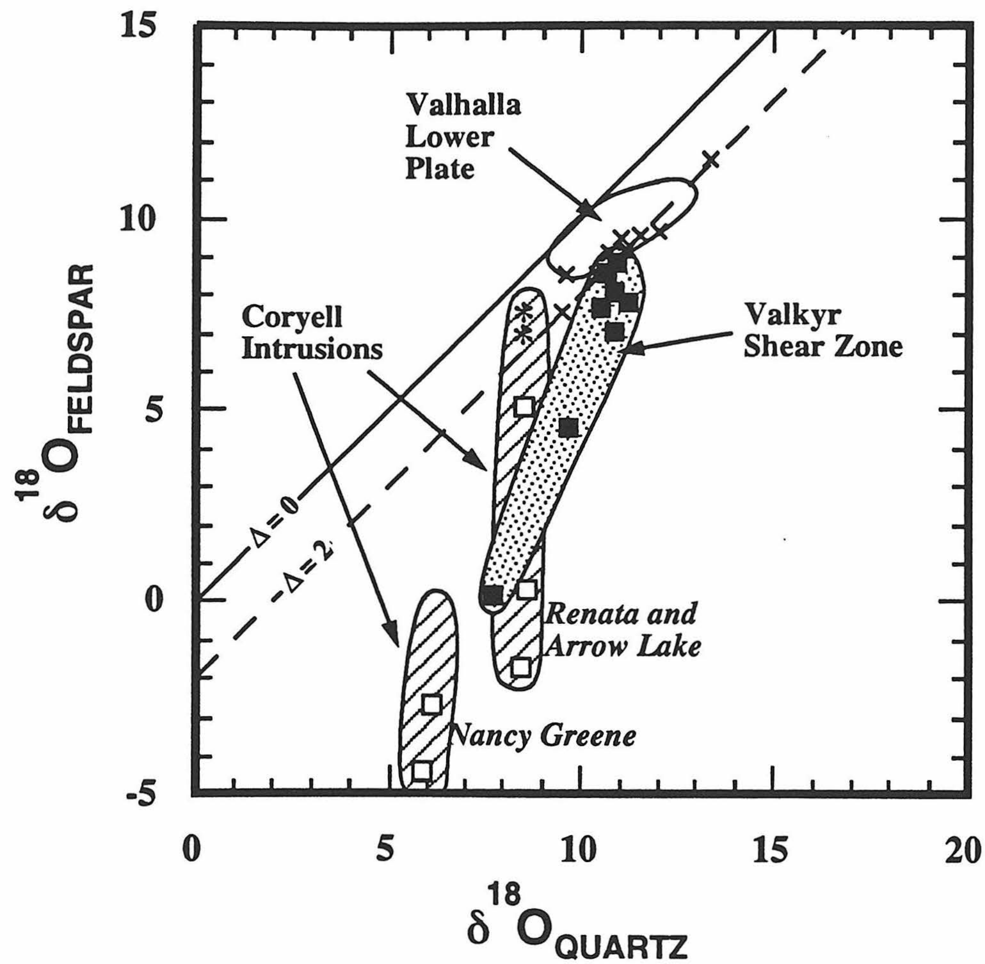

Figure 5.16 Data from the Coryell Plutonic Suite

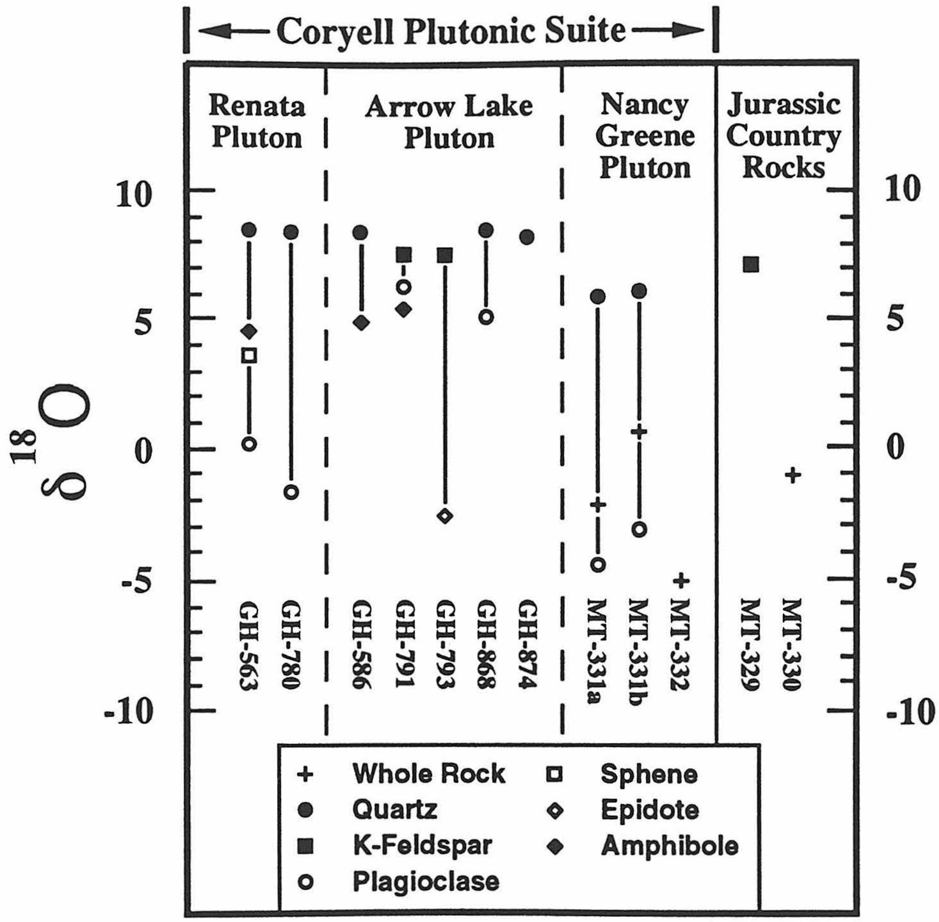

coexisting quartz and K-feldspar, but quartz-plagioclase oxygen isotope fractionations in the Renata and Arrow Lake plutons range from 3.4‰ to 10.1‰, clearly indicating disequilibrium. Inasmuch as the quartz $\delta^{18}O$ values are exceedingly uniform, the data from all three plutons define an array having a near vertical slope on a δ-δ diagram where $\delta^{18}O$ quartz is plotted on the x-axis and coexisting $\delta^{18}O$ feldspar on the y-axis (Figure 5.15). Alteration epidote from the Arrow Lake pluton has $\delta^{18}O = -2.6$, another indication of alteration involving large amounts of hot meteoric water. Amphibole $\delta^{18}O$ values, like those of quartz and K-feldspar, are uniform in ^{18}O ($\delta^{18}O = +4.9 \pm 0.4$‰). One quartz-amphibole oxygen isotope fractionation is 4.0‰, indicating T ~ 600 °C using the fractionation factor of Javoy (1977); this indicates apparent $^{18}O/^{16}O$ equilibrium between these two minerals at near magmatic temperatures. The quartz-sphene fractionation for this sample is 4.8‰ (sphene $\delta^{18}O = +3.7$).

The magma that formed the Nancy Greene pluton probably had a lower $\delta^{18}O$ value than the two plutons discussed above in that it exhibits lower quartz $\delta^{18}O$ values of +5.8 and +6.1, along with lower feldspar $\delta^{18}O$ values of –4.4 to –3.1 (Magaritz and Taylor, 1986), and these data plot as a distinct array with a steep slope offset to the left of the other Coryell plutons. The quartz separates from these two porphyries were analyzed for $^{18}O/^{16}O$ following an HF-stripping treatment (see Magaritz and Taylor, 1976); this indicates that the original, pre-treatment $\delta^{18}O$ values of these quartz separates could have been even lower. Whole-rock $\delta^{18}O$ of three porphyries from this pluton range from –5.5 to +0.7. Migmatitic (feldspar $\delta^{18}O = +7.1$) and dioritic (whole rock $\delta^{18}O = -1.1$) country rocks of this pluton also were lowered in ^{18}O by meteoric fluids associated with the shallow emplacement of this pluton. The δD values of these two samples range from –147 to –162 (Magaritz and Taylor, 1986), yet another indication of the involvement of meteoric waters in this system.

5.5.4 Discussion

These oxygen isotope data from the Coryell Suite contrast with data from other plutonic rocks in this portion of the southern Omineca belt. Quartz $\delta^{18}O$ values from the Renata and Arrow Lake plutons are 3-4‰ lower in $\delta^{18}O$ than the slightly younger Ladybird leucogranites to the north and east at the Thor-Odin complex (quartz $\delta^{18}O$ ~ +12.4) and at the Valhalla complex (quartz $\delta^{18}O$ ~ +11.0), and the quartz $\delta^{18}O$ values from the Nancy Greene pluton are 5-6‰ lower than these leucogranites. These differences can be due to either a large difference in source region, or subsolidus $^{18}O/^{16}O$ exchange between quartz and meteoric-hydrothermal fluids, or both. The $^{18}O/^{16}O$ homogeneity of quartz from the Renata and Arrow Lake plutons indicates that the magmatic quartz $\delta^{18}O$ value may have been preserved. It is noteworthy that the difference between the quartz and megacryst feldspar $\delta^{18}O$ values from this set of analyses gives an apparent $^{18}O/^{16}O$ fractionation of 0.8‰; this fractionation is typical for rapidly quenched volcanic and intrusive rocks (*e.g.*, Larson and Taylor, 1986). This small inferred quartz-K-Feldspar fractionation is further indication that these quartz $\delta^{18}O$ values are primary. It is plausible that these alkaline magmas had a lower crust or enriched mantle lithospheric source, as indicated by their radiogenic isotopic characteristics (Bevier, 1987; Ghosh, 1995). Note also that the inferred primary $\delta^{18}O$ values of these bodies are very similar to those of the large Eocene quartz monzonite plutons that established giant meteoric-hydrothermal systems in the Idaho batholith to the south (Criss and Taylor, 1983).

The origin of the low quartz $\delta^{18}O$ values of the Nancy Greene pluton is inconclusive; these low values could be due to either (1) $^{18}O/^{16}O$ exchange with extremely hot meteoric waters at long time scales, or (2) these are low-^{18}O magmas such as those found at Yellowstone National Park (*e.g.*, Hildreth et al., 1991). These rocks also have the lowest-^{18}O feldspar in the entire set of Coryell analyses. These two different possibilities might be resolved in the future through analyses of minerals known to be refractory to $^{18}O/^{16}O$ exchange under hydrothermal conditions (*e.g.*, sphene).

Except for the Nancy Greene pluton, the Coryell rocks that display the greatest degree of exchange with hot meteoric water are those rocks collected from the shore of Arrow Lake; this is consistent with the widespread occurrence of rocks that have experienced meteoric-hydrothermal metamorphism along the faults that define the major N-trending lakes in Southeastern British Columbia (Magaritz and Taylor, 1986). No major lineament has been mapped at the location of Arrow Lake; however, it is probable that outcrops of this inferred structure have been masked by the waters of Arrow Lake.

5.6 The Columbia River Detachment Fault

5.6.1 Geologic Setting

The Columbia River fault is a moderately east-dipping north-south striking detachment fault that extends 200 km along the Columbia River Valley (CRF on Figure 2.4). This fault forms the eastern margins of both the basement Monashee complex and the middle-crustal southern Thor-Odin – Pinnacles complex, and was active between 58 and 52 Ma (Parrish et al., 1988). Overall displacements on this fault are estimated to be 20-30 km (Lane, 1984; Parrish et al., 1988; Carr, 1991). To the south, this fault probably splays out into many subsidiary faults just to the northwest of the Valhalla Complex (Hyndman, 1968; Read and Brown, 1981). It appears that east-west displacements were probably accommodated by a series of en-echelon north-trending faults that crop out to the south of the southernmost exposure of the Columbia River fault.

5.6.2 Samples Studied

A total of 11 samples from the Columbia River fault zone were analyzed for their carbon and oxygen isotopic composition (Table 5.4; locations are shown on Figures 3.1

and 4.1). These results are supplemented by five Magaritz and Taylor (1986) samples from the Whatshan batholith at the southernmost extremity of the fault (see Figure 5.2). Three rocks from the northern part of this fault near Revelstoke, British Columbia, include a fractured marble and cataclastic granodiorite from the detachment zone, and a lower plate metapelite from the Monashee complex (Figure 3.1). Seven rocks from the southern Thor-Odin area (Figure 4.1) include a highly brecciated and altered leucogranite from a zone equivalent to the brittle zone of the Slocan Lake fault, three lower-plate mylonitic leucogranites, two samples of lower plate calc-silicate mylonitic gneiss, and one marble from the lower plate.

5.6.3 Results

Oxygen isotope analyses of quartz, feldspar, calcite, and whole rocks indicate a similar meteoric-hydrothermal history for fluid-rock interaction along the Columbia River fault as was found at the Slocan Lake fault, but there are a few differences. These altered samples are compared to the lower-plate protolith rocks, namely the Thor-Odin middle crustal zone, the Monashee complex basement, and Cretaceous granodiorite of the Whatshan batholith.

To review, the Thor-Odin middle crustal zone rocks are homogeneous in $\delta^{18}O$ with quartz $\delta^{18}O$ equal to +12.4 (see Chapter 4), and the Monashee complex basement is heterogeneous in $^{18}O/^{16}O$ with quartz $\delta^{18}O$ values that range from +8.0 to +16.4 (see Chapter 3). The distal Whatshan granodiorite samples (Magaritz and Taylor, 1986) unaffected by detachment-related hydrothermal alteration have quartz $\delta^{18}O$ = +9.5 (N = 2) and feldspar $\delta^{18}O$ = +8.0 ± 0.4‰ (N = 2).

Most of the samples involved in detachment faulting show only about a 3‰ variation in quartz $\delta^{18}O$ (+9.5 to +12.6; N = 6); this variation is most likely attributable to initial oxygen isotope heterogeneity in the various lithologies (granodiorite,

Figure 5.17 -- Plot of quartz $\delta^{18}O$ versus coexisting feldspar $\delta^{18}O$ for the Columbia River fault (solid circles), the Spruce Grove Batholith (solid diamonds), the Whatshan batholith (solid squares), and basement rocks near late-stage normal faults (open circles). These data are compared to the $\delta^{18}O$ values of the Thor-Odin leucogranite sheets, the Valhalla lower plate, and the uppermost part of the Monashee basement (labeled as "homogeneous basement"). The 45° dashed diagonal lines at Δ=0 and Δ=2 represent the range in normal quartz-feldspar fractionations in granitic rocks. The data from the Columbia River fault define a steep disequilibrium array much like that observed for the Slocan Lake fault. Note also that the similar, but slightly offest, $^{18}O/^{16}O$ disequilibrium array for the Spruce Grove batholith is probably related to meteoric-hydrothermal effects along the Beavan detachment fault.

Figure 5.18 -- $\delta^{13}C$ vs $\delta^{18}O$ for marble (solid squares), calcsilicate (solid dots), and late-stage calcite (open dots) from the Columbia River fault, the Beavan fault, the Monashee Decollement, and the Okanagan fault. These data are compared to data from the lower plate discussed in Chapter 4 (marbles and calc-silicates) and data from the Slocan Lake fault discussed earlier. Except for the Okanagan fault (Magaritz and Taylor, 1986), all data are from this study. Marbles and calcsilicates from the lower plates of the Columbia River and Beavan faults both show evidence for involvement with meteoric-hydrothermal fluids in the decarbonation of these carbonate materials. Calcsilicates from the lower plate of the Beavan fault provide evidence for the involvement of meteoric-hydrothermal fluids. Data from the Monashee decollement indicate a late-stage incursion of meteoric-hydrothermal fluid into the system (the time of late-stage calcite deposition) after the decarbonation of the calcsilicates. The limited data from the Okanagan fault suggests that fluids there were also dominantly meteoric-hydrothermal.

Figure 5.17 Columbia River Fault

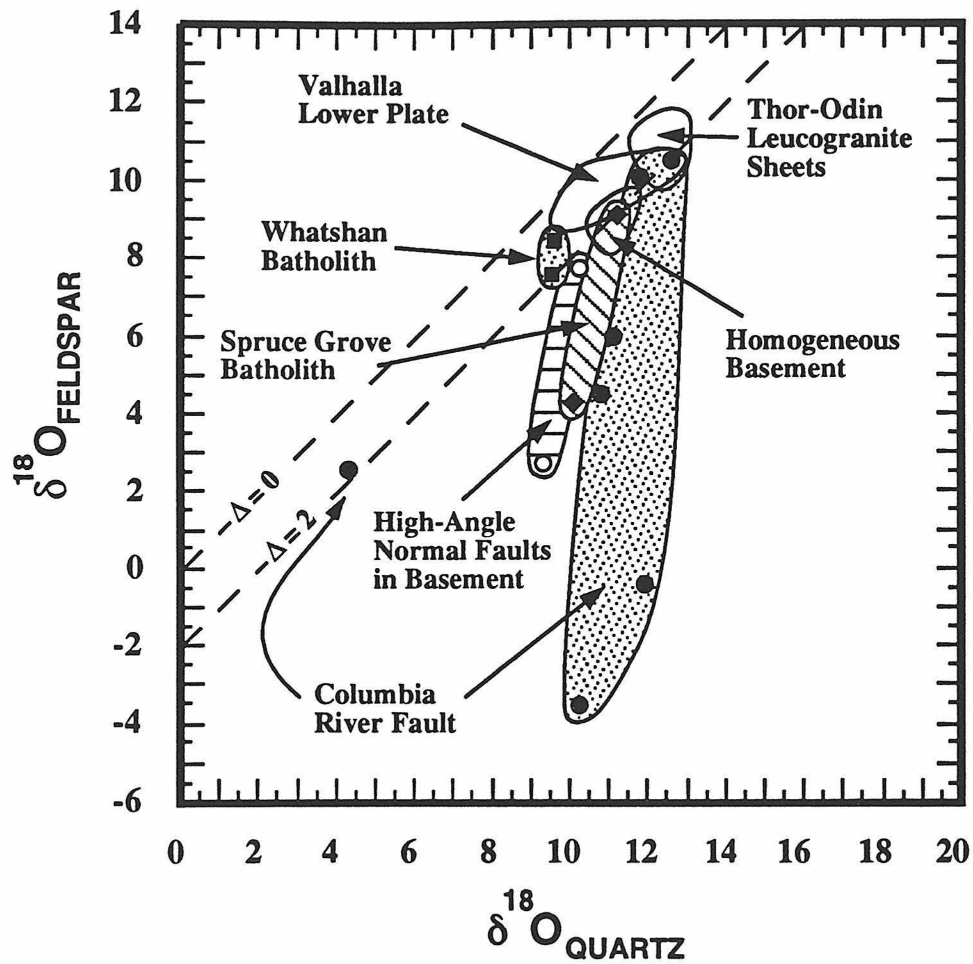

Figure 5.18 Carbonates from Detachment Faults

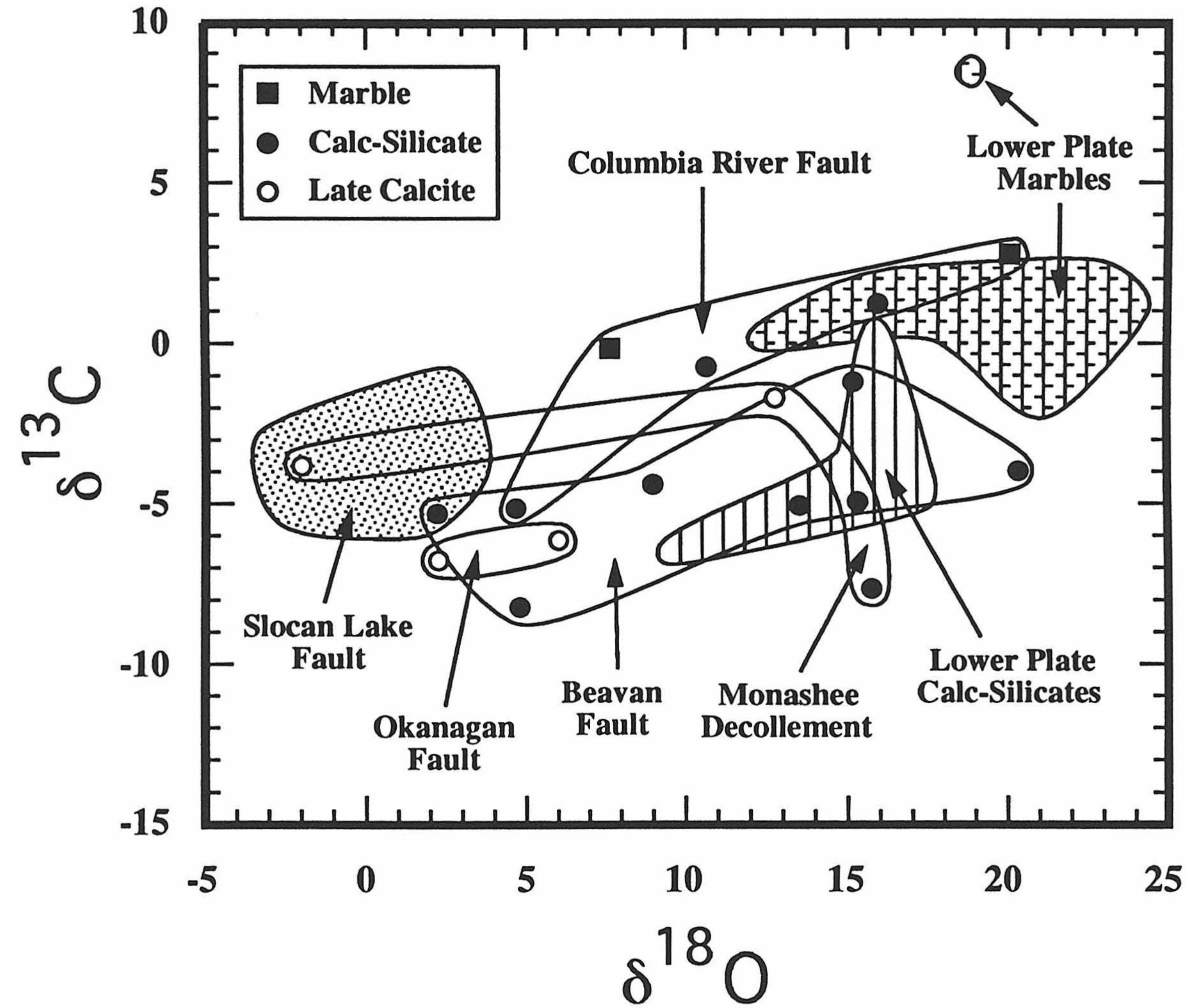

TABLE 5.4. $^{18}O/^{16}O$ DATA ON ROCKS AND MINERALS FROM THE COLUMBIA RIVER FAULT

Sample	Rock Type	WR	Qz	Fs	Other	Cc $\delta^{18}O$	Cc $\delta^{13}C$
Monashee Complex							
GH-31	Marble					7.6	–0.1
GH-66	Granodiorite		10.8	4.5			
GH-74	Metapelite	7.1					
Southern Thor-Odin Complex							
GH-647	Brecciated Leucogranite		4.3	2.6	7.7m*		
GH-660	Mylonitic Leucogranite		12.6	10.5			
GH-663	Marble					15.9	1.3
GH-664	Marble					20.1	2.8
GH-665	Calcite Alteration					4.6	–5.1
GH-672	Mylonitic Leucogranite		11.1	6.0			
GH-813	Calc-Silicate					10.6	–0.7
GH-832	Marble					24.0	1.3
GH-832a	Marble					23.8	1.0
GH-834	Leucogranite		11.9	-0.4	9.2g*		
Whatshan Batholith							
MT-319	Granodiorite		9.5	7.6			
MT-320	Granodiorite		10.2	–3.5			

* g = garnet, m = muscovite; see Table 5.1 for other symbols.

TABLE 5.5. $^{18}O/^{16}O$ DATA ON ROCKS AND MINERALS FROM THE BEAVAN-CHERRYVILLE FAULT

Sample	Rock Type	Qz	Fs	Cc $\delta^{18}O$	Cc $\delta^{13}C$
Spruce Grove Batholith					
MT-315	Granodiorite	11.2	9.1		
Whatshan Batholith					
MT-317	Granodiorite	10.1	4.3		
Vidler Calc-Silicate					
GH-385	Calc-Silicate			4.7	–8.2
GH-386	Calc-Silicate			20.3	–4.0
GH-388	Calc-Silicate			13.5	–5.1
GH-394	Sheared Calc-Silicate			15.2	–1.1
GH-394a	Mafic Calc-Silicate			9.0	–4.4
GH-396	Calc-Silicate			2.1	–5.3
Carbonates Distal to Fault					
GH-390	Marble			17.7	0.7
GH-391	Calc-Silicate			15.9	0.3
GH-392	Calc-Silicate			17.3	–4.7

See Table 5.1 for explanation of symbols.

leucogranite, calc-silicate, pelite) from diverse crustal domains (basement Monashee complex, middle crustal Selkirk allochthon, Cretaceous Whatshan batholith). However, feldspar $\delta^{18}O$ varies by as much as 14‰, from –3.5 to +10.5 (N = 7). Quartz-feldspar $^{18}O/^{16}O$ fractionations ($\Delta_{Q\text{-}F}$ = 1.1‰ to 13.7‰) indicate marked disequilibrium and these values define an array with a slope of ~ 10 in δ-δ space (Figure 5.17). One quartz-garnet $^{18}O/^{16}O$ fractionation ($\Delta_{Q\text{-}G}$ = 2.7‰, garnet $\delta^{18}O$ = +9.2) in a leucogranite indicates apparent equilibrium between quartz and garnet at T ~ 750 °C, using the calibration of Javoy (1977); however, feldspar from this sample has $\delta^{18}O$ = –0.4, indicating that quartz and garnet were essentially inert to exchange during this hydrothermal event. A heavily altered and brecciated muscovite-bearing leucogranite from a zone of brittle fracturing near this detachment fault has quartz and feldspar $\delta^{18}O$ values of +4.3 and +2.6, respectively; however, the coexisting muscovite ($\delta^{18}O$ = +7.7) is way out of equilibrium with the quartz and feldspar, indicating a multi-stage fluid evolution history for this rock. These data are supplemented by a whole-rock $\delta^{18}O$ value of +3.3 for a gneiss in the immediate hanging wall, and a footwall quartzite having whole rock $\delta^{18}O$ = +9.6, both near Revelstoke (Nesbitt and Muehlenbachs, 1995); all of these data require the presence of hot meteoric waters in the evolution of these rocks.

One outcrop of the Whatshan granodiorite provides evidence for fracture-controlled and channelized meteoric-hydrothermal fluid flow in this zone. The host quartz diorite at this locality has quartz $\delta^{18}O$ = +9.6 and feldspar $\delta^{18}O$ = +8.5, along with a cross-cutting aplite dike having $\delta^{18}O$ = +9.2 (Magaritz and Taylor, 1986). These are all essentially primary, unaltered igneous $\delta^{18}O$ values. However, a late-stage lamphyrophyre dike from this same outcrop has whole-rock $\delta^{18}O$ = –5.3. These data indicate that meteoric-hydrothermal fluid infiltration was very local to the fractures that were the conduits that the dikes intruded, and that this occurred during or directly following the emplacement of the dike. The fine grain size of the dike and its internal heat were probably the main factors that localized meteoric-hydrothermal effects in this part of the outcrop.

Carbon and oxygen isotope data from carbonate materials near the Columbia River detachment fault also indicate a complex history of meteoric water infiltration and $^{18}O/^{16}O$ exchange, as well as the probability of some decarbonation along the fault. Marble $\delta^{18}O$ values range from +7.6 to +20.1 (N = 3), with the lowest value almost certainly indicating exchange with hot meteoric waters. $\delta^{13}C$ values are typical of Paleozoic marble, and are between –0.1 and +2.8. The lowest-^{18}O marble is from near the detachment trace and is heavily fractured, analogous to the highly altered rocks immediately above the Slocan Lake fault. Calcsilicates from this detachment fault exhibit a range in carbonate $\delta^{18}O$ similar to that of the marble (+4.6 to +15.9, N = 3), also indicating interaction with hot meteoric waters. For these calcites, $\delta^{13}C$ decreases with $\delta^{18}O$ ($\delta^{13}C$ = +1.3 to –5.1), possibly indicating decarbonation being driven by infiltration of meteoric water (*e.g.*, Valley, 1986).

5.6.4 Discussion

Quartz and feldspar oxygen isotope data from the Columbia River fault indicate that it, like the Slocan Lake fault, underwent meteoric-hydrothermal water-rock interaction during detachment faulting. The fact that these data define a steep array (slope = 10) in δ-δ space (Figure 5.17) indicates that the hydrothermal event that affected this fault zone was short-lived, but of longer duration and/or hotter than the one that affected the Slocan Lake fault. Most of the samples with low-^{18}O feldspars from the Columbia River fault are from the lower plate leucogranites and pelites that are within close proximity to the detachment fault trace, indicating that meteoric waters managed to infiltrate a limited distance into the lower plate of the Columbia River detachment fault.

The small quartz-feldspar $^{18}O/^{16}O$ fractionation (*i.e.*, near-equilibrium) for a low-^{18}O sample (GH-647) from the brittle zone of this fault indicates either that water/rock ratios were very high for this rock, or that it was formed under very high-temperature hydrothermal conditions or from a low-^{18}O magma (see Figure 5.17). However, muscovite from this rock has a higher $\delta^{18}O$ value than either the coexisting feldspar or the quartz. This observation is perplexing, but is definitely an indication of a complex water-rock history involving waters of variable isotopic composition. This coarsely crystalline synkinematic muscovite appears to have formed during the mylonitization event that was superimposed upon the quartz-feldspar assemblages; samples of this muscovite were used to obtain a Rb-Sr isochron age of 59.7 Ma (Parrish et al., 1988).

The lithological diversity in this sample suite means that this locality is unsuitable for the kind of quantitative modeling that was applied above to the Slocan Lake fault; however, it can be shown that the Columbia River fault hydrothermal system was in general quite similar to that which affected the Slocan Lake fault. These two faults are associated with a pulse of extension with movement of the upper-plate to the east between 58 and 52 Ma (Parrish et al., 1988); this indicates that the $\delta^{18}O$ of the meteoric waters involved in hydrothermal metamorphism of these faults should have been similar. However, the most striking similarity is the presence of sheets of Ladybird leucogranite in the immediate footwall for much of the strike-length of both of these two faults, thereby also indicating a similar thermal history. Thus, it is probably no coincidence that the array slopes of quartz and feldspar $\delta^{18}O$ are very steep for both of these faults, because the "heat engines" driving convective circulation of hydrothermal fluids were similar, and both hydrothermal systems were operative at essentially the same time.

These steep δ-δ arrays contrast with the much shallower δ-δ array slopes observed along the western margin of the Valhalla complex (Valkyr shear zone); this latter array was formed by the hydrothermal system associated with the emplacement of the Coryell intrusions (compare Figures 5.15 and 5.17). In the case of the Valkyr shear zone, the hydrothermal systems were longer-lived (58-45 Ma) and/or hotter because there were multiple pulses of heat added to the crust at that location. Also, note that the Coryell intrusions form large, unfloored bodies and probably crystallized at much higher temperatures than the Ladybird leucogranites, which typically form thin sheet-like units. Rocks of the Valkyr shear zone were probably subjected to at least two pulses of meteoric-hydrothermal activity; the first pulse was associated with the first stage of extension and intrusion of the Ladybird suite, while the second pulse was related to the emplacement of the Coryell syenites. The Columbia River fault and the Slocan Lake fault apparently escaped the thermal effects of the Coryell intrusive event. Thus, the ambient thermal state of the lower plate during extension (*i.e.*, presence or absence of coeval plutons, and their respective sizes, temperatures, and shapes) may be a prime factor is determining the durations and temperatures of these kinds of meteoric-hydrothermal water/rock interaction events. It is these factors that mainly control the slopes of the δ-δ arrays on diagrams like those shown in Figures 5.10, 5.15, and 5.17.

5.7 The Beavan-Cherryville Fault System

5.7.1 Geologic Setting

The Beavan-Cherryville fault system separates the middle crustal zone high-grade metasedimentary and metaplutonic terrane from an overlying klippe of upper-crustal middle Jurassic granodiorite of the Spruce Grove batholith and associated low-grade stratified rocks of the Quesnellia terrane (Carr, 1991). The Beavan fault is a moderately dipping (~ 45°) normal fault that has been interpreted as being the breakaway structure for the Okanagan detachment fault that crops out to the west. The Cherryville fault is unexposed, but is an inferred structure that follows the Shuswap River valley and juxtaposes anatectic sillimanite-grade rocks to the west against chlorite-grade rocks to the east. The Beavan and Cherryville faults intersect at Vidler Ridge (see Figure 4.1).

The hanging-wall klippe of this fault system contains a sequence of folded shale, chlorite+biotite-bearing fine-grained schist, intermediate to mafic volcanics, and minor limestone and sandstone; these rocks are interpreted to be correlative with the Upper Triassic Nicola and Slocan groups (Carr, 1992). This stratigraphic sequence is intruded by granodiorites of the Spruce Grove batholith, a 175 Ma (Carr, 1991a) pluton that is part of the Middle Jurassic Nelson plutonic suite.

Plutonic rocks that comprise the footwall are the anatectic leucogranites of the Paleocene-Eocene Ladybird suite and the Late Cretaceous Whatshan batholith. These plutonic rocks are intrusive into a sequence of metasediments correlated with the Milford (Vidler calc-silicate), Kaslo, and Slocan Groups, metamorphosed to staurolite to sillimanite+muscovite zone conditions (Carr, 1991).

5.7.2 Samples Studied

A total of 13 samples from the lower plate, mostly carbonates, comprise the dataset to be discussed in this section. An upper-plate rock from the Spruce Grove batholith and a lower plate rock from the Whatshan batholith analyzed by Magaritz and Taylor (1986) are the only silicates discussed in this section. Six samples of calc-silicates near the Beavan fault at the southern Thor-Odin complex (Figure 4.1) were collected along logging roads that follow the projected trace of this fault. Carbonates distal to the fault were collected along a logging road that follows Sitkum Creek.

The marbles typically contain more than 90% calcite, with diopside, tremolite, and anorthite comprising the remainder of the rock. Calcsilicates have variable bulk composition and mineralogy ranging from quartz-rich to mafic. Most calcsilicates have the stable assemblage quartz+calcite+diopside+tremolite±biotite±plagioclase ±muscovite, and evidence of late mineralogical alteration is essentially limited to calcite and sericite overprinting and replacing diopside and plagioclase, respectively. One sample (GH-385) contains talc (and anthophyllite?) overprinting amphibole and diopside; calcite veins overprint feldspar and diopside in this sample. The development of ribbon textures in some quartz samples indicates that quartz was recrystallized locally where it was subjected to high strain associated with shearing along the Beavan fault.

5.7.3 Results

Oxygen and carbon isotope analyses of granodiorite, marble, and calcsilicate indicate that meteoric-hydrothermal fluids strongly interacted with rocks along the Beavan fault zone. Granodiorites from the Spruce Grove batholith have quartz $\delta^{18}O$ = +11.2 and +10.1, while feldspar $\delta^{18}O$ = +9.1 and +4.3 (Magaritz and Taylor, 1986); the large $\Delta_{Q\text{-}F}$ value of 5.8‰ clearly indicates $^{18}O/^{16}O$ disequilibrium similar to that observed at detachment faults in the region.

Carbonates distal to the fault seem to have escaped the effects of the meteoric hydrothermal system that affected the rocks near the fault. Marble $\delta^{18}O$ = +17.7 to +24.0 (N = 3), with $\delta^{13}C$ = +0.7 to +1.3 (N = 3). Calcsilicate from this zone gives evidence only for decarbonation in the presence of high-^{18}O water, similar to those rocks deeper in the Thor-Odin complex, with $\delta^{18}O$ = +15.9 and +17.7, and $\delta^{13}C$ = +0.3 and –4.7.

Calcsilicates near the fault have a wide range in $\delta^{18}O$ values and all $\delta^{13}C$ values are less than zero, indicating that these assemblages had undergone meteoric-hydrothermal alteration. The calcite $\delta^{18}O$ values range from +2.1 to +20.3 while $\delta^{13}C$ values are between – 1.1 and –8.2. There appears to be a correlation between low $\delta^{18}O$ values (down to +2.1) and the degree of strain experienced by the rock, with rocks having textures indicative of high strain having the lowest $\delta^{18}O$ values.

5.7.4 Discussion

These $^{18}O/^{16}O$ and $^{13}C/^{12}C$ data do not provide evidence one way or the other as to whether the decarbonation experienced by calcsilicates in the footwall of the Beavan-Cherryville fault system at the southern Thor-Odin metamorphic core complex occurred in response to the infiltration of meteoric water during detachment faulting. In principle, the infiltration of large amounts of H_2O into these calcsilicates could produce decarbonation of these rocks at much lower temperatures than if H_2O is absent (*e.g.*, Greenwood, 1967); thus, it is plausible that decarbonation of these rocks could have taken place under the temperatures (~ 300 °C) at which these hot meteoric fluids are interacting with these rocks. However, low $\delta^{13}C$ values (–1.1 to –5.1) from samples having high $\delta^{18}O$ values (+13.5 to +20.3) are also compatible with the major part of the decarbonation process having occurred prior to the introduction of meteoric fluids into this system.

These calcsilicate calcite data contrast to those from deeper parts of the southern Thor-Odin section beneath the South Fosthall pluton (see Figure 4.1) in that they are very heterogeneous in $^{18}O/^{16}O$ ($\delta^{18}O$ = +2.1 to +20.3) with $\delta^{18}O$ values both below and above the homogenized values below the pluton ($\delta^{18}O$ = +15.3). This suggests that the pluton may have served as a boundary separating the zone of $^{18}O/^{16}O$ homogenization below from a zone of $^{18}O/^{16}O$ heterogeneity above. However, this is inconclusive at the moment because more data are needed from the silicate lithologies that comprise the stratigraphic section above this pluton.

This data set, together with a comparable data set from the Monashee Complex, indicates that hot meteoric waters interacted with the shallow part of the continental crust along virtually all types of brittle faults in the region. These high-angle normal faults probably served as major conduits of fluid flow in the extending crust.

5.8 The Okanagan Valley Fault

5.8.1 Geologic Setting

The Okanagan Valley fault is the western bounding structure of the southern Omineca belt. It extends almost 500 km from the western edge of the Monashee complex into northern Washington where it is buried by Miocene flood basalts of the Columbia River sequence. Displacements along this fault are estimated to be as large as 100 km (Templeman-Kluit and Parkinson, 1985). This fault was active at 52 to 45 Ma (Parrish et al., 1988) and accommodated the westward movement of the hanging-wall Okanagan batholith and other plutonic rocks of the Intermontane Superterrane. Coeval with extension is the emplacement of stocks of the Coryell alkaline suite and eruption of the Penticton Group alkaline volcanic rocks (Church, 1973; Bardoux, 1985; Tempelman-Kluit and Parkinson, 1986). The hanging wall of this fault zone is comprised of Jurassic granodiorite, quartz diorite, and granite of the Okanagan (or Similkameen) batholith (Tempelman-Kluit, 1989); these rocks are cut by numerous aplite dikes of unknown age. The footwall is comprised of mylonitic orthogneiss and paragneiss of uncertain age mapped as the Okanagan gneiss (Tempelman-Kluit, 1989); this unit is strongly brecciated and chloritized as the fault zone is approached. Numerous plutonic bodies of Ladybird leucogranite are found in the footwall of this fault (Parrish et al., 1988).

5.8.2 Samples Studied

All data discussed in this section are from Magaritz and Taylor (1986), and sample descriptions are taken from those reported in that paper, from my personal observations of these hand specimens archived at Caltech, and from my own field observations (see Figure 2.12 for locations). This information is used to reinterpret these data, which come from two traverses collected by Magaritz and Taylor (1986; see Figure 2.12 for sample locations); one traverse follows the immediate hanging wall of the fault zone along the west shore of Okanagan Lake, while the other traverse extends westward into the upper plate along the road that runs from Summerland to Jellicoe, British Columbia. The publication of the Magaritz and Taylor (1986) study occurred just prior to the recognition that the faults that occur along most of the north-trending, arcuate lakes in this region are in fact regional-scale detachment faults having great displacements (Parrish et al., 1988).

5.8.3 Results

Oxygen isotope data from the central Okanagan batholith indicate only slight interaction with meteoric water (Figures 5.19 and 5.20). Quartz $\delta^{18}O$ values range from +7.9 to +9.9; all but one of the quartz samples have $\delta^{18}O = +9.3 \pm 0.5$ (N = 7). Oxygen isotopes were measured on both plagioclase and K-feldspar in some of these samples; most K-feldspar $\delta^{18}O$ is between +6.2 and +7.5 (N = 8), but one sample has a red K-feldspar with $\delta^{18}O = +4.0$. Plagioclase $\delta^{18}O$ ranges from +6.4 to +8.6. Quartz-feldspar oxygen isotope fractionations range from $\Delta_{Q\text{-}F} = 1.3$ to 2.2‰ (N = 6) for plagioclase, but these fractionations have a larger range for K-feldspar ($\Delta_{Q\text{-}F} = 1.7$ to 3.9‰; N = 7). δD values from hydrous minerals range from –74 to –138. Most of the samples from the core of the Okanagan batholith appear to have escaped major meteoric water-rock interaction, but five of these samples have low δD values and $\Delta_{Q\text{-}F}$ larger than 2.0‰ indicating limited interaction with hot meteoric waters.

$\delta^{18}O$ and δD of rocks and minerals from the zone proximal to the Okanagan fault along Okanagan Lake provide evidence for very large-scale oxygen isotope exchange between these rocks and hot meteoric waters (Figure 5.19 and 5.20). Granodiorites and quartz diorites from the Okanagan batholith have quartz $\delta^{18}O$ values ranging from +7.1 to +9.8 (N = 5), but it should be noted that analyses of quartz from three samples treated with the HF-stripping method (Magaritz and Taylor, 1986) have quartz $\delta^{18}O = +9.3$

Figure 5.19 -- Plot of mineral and whole rock $\delta^{18}O$ data from the Central Okanagan batholith and the Okanagan Valley fault zone (data from Magaritz and Taylor, 1986). Okanagan Valley fault data are separated into the Okanagan batholith, aplite dikes, Coryell porphyry, a late vein, and a diorite xenolith. $\delta^{18}O$ data are shown for quartz (solid squares), HF-treated quartz (triangles), K-feldspar (solid dots), plagioclase (open dots), whole-rock (open squares), biotite (solid diamonds), amphibole (plus signs), and calcite (open diamonds).

Figure 5.20 -- Plot of quartz $\delta^{18}O$ versus coexisting feldspar $\delta^{18}O$ for the Okanagan fault (solid circles) compared to the central Okanagan batholith protolith rocks (plus signs), and the synextensional Coryell porphyry intrusions (open squares). The 45° diagonal dashed lines at $\Delta = 0$ and $\Delta = 2$ represent the range in normal quartz-feldspar fractionations in most granitic rocks. The steeply-sloped oxygen isotope disequilibrium array for the Okanagan fault is shallower than those from the east-dipping detachment faults (the Slocan Lake and Columbia River faults), but similar to the slope of the array at the Valkyr shear zone, another extensional structure proximal to Coryell intrusions. This indicates longer-lived or higher-temperature hydrothermal systems at these structures that were affected by Coryell-stage plutonism. The steeply-dipping dashed lines connect either data points for different samples from the same outcrop, or they connect the data points representing $\delta^{18}O$ of HF-treated quartz (open circles) and the inferred primary coexisting $\delta^{18}O$ feldspar (see Magaritz and Taylor, 1986) to the actual measured $\delta^{18}O$ quartz and $\delta^{18}O$ feldspar values from the same rock specimens.

Figure 5.19 Okanagan Fault Data

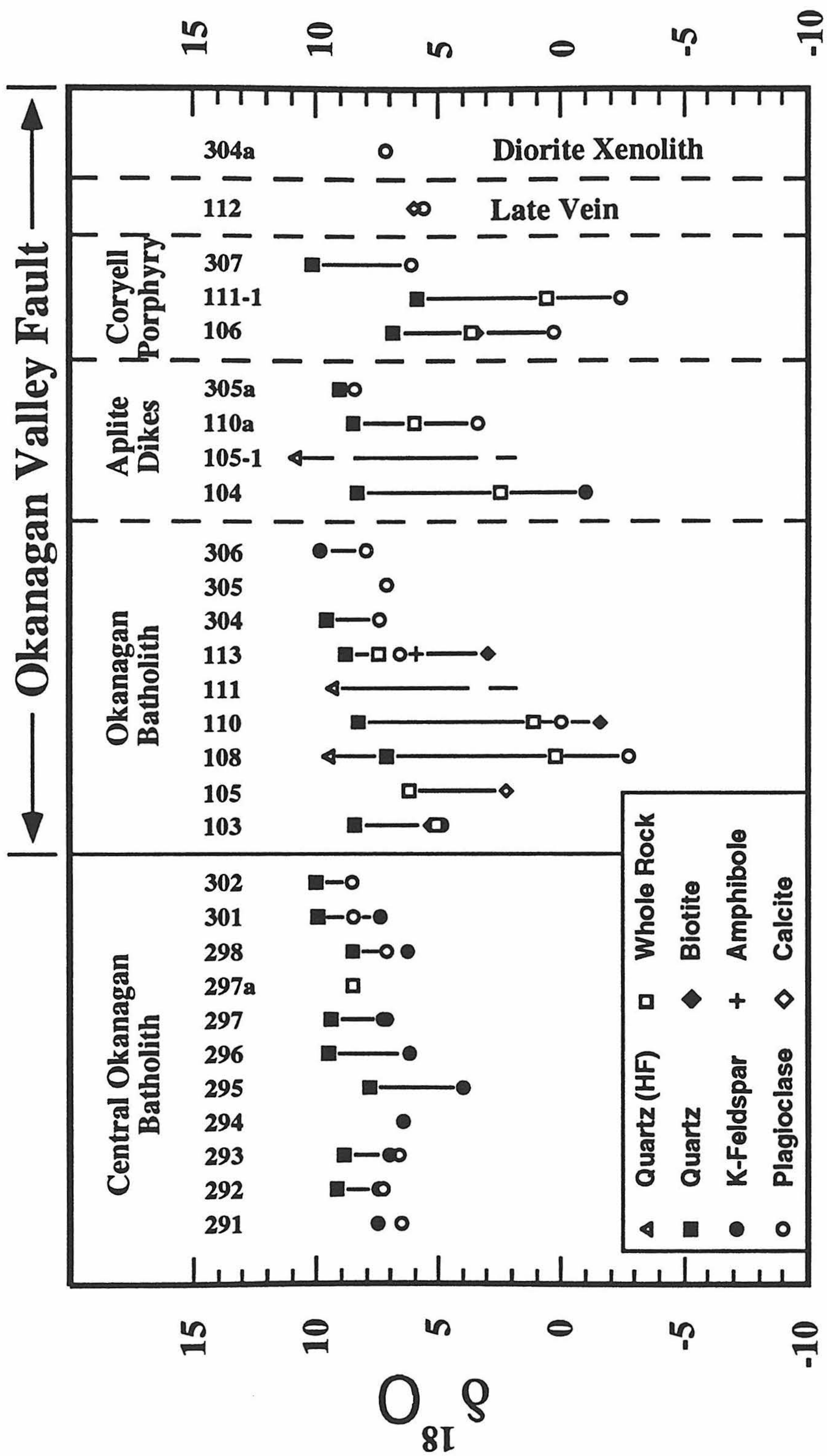

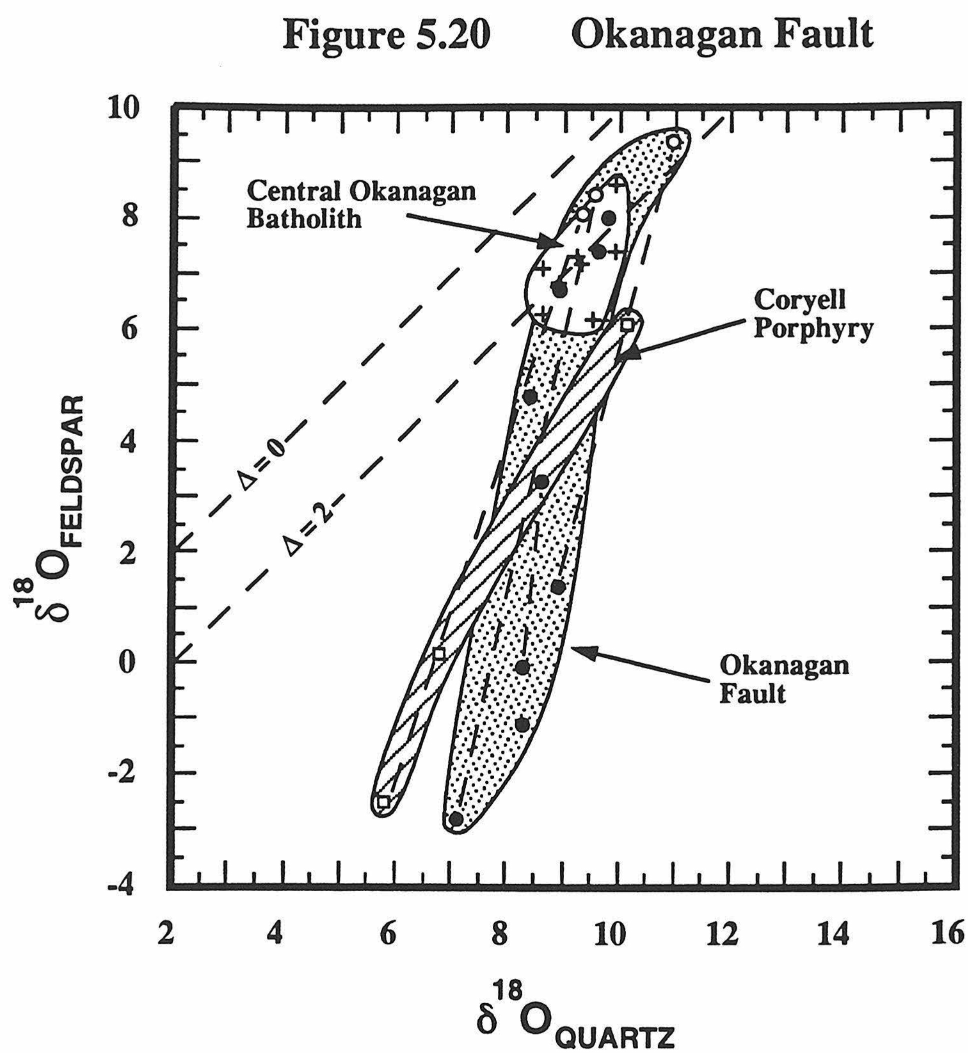
Figure 5.20 Okanagan Fault
Central Okanagan Batholith
Coryell Porphyry
Okanagan Fault
Δ = 0
Δ = 2
$\delta^{18}O_{FELDSPAR}$
$\delta^{18}O_{QUARTZ}$
10
8
6
4
2
0
-2
-4
2
4
6
8
10
12
14
16

to +10.9. Feldspars from these intrusive rocks display a large variation in $\delta^{18}O$ with values ranging from –2.8 to +8.0 (N = 8), a clear indication of oxygen isotope disequilibrium ($\Delta_{Q\text{-}F}$ = 1.8 to 12.4‰) due to meteoric water-rock interaction. This is also reflected in the large variation in whole-rock $\delta^{18}O$ (+0.2 to +7.5; N = 6) and the low δD of mafic hydrous minerals (–103 to –151; N = 9) for these rocks. Biotite $\delta^{18}O$ values from three of these samples range from –1.6 to +5.0, and these data also indicate meteoric-hydrothermal activity at this fault zone.

Three samples of Coryell porphyry (Figures 5.19 and 5.20) have $^{18}O/^{16}O$ systematics much like analogous samples much farther to the east in the vicinity of the Valkyr shear zone. Quartz $\delta^{18}O$ ranges from +5.8 to +10.0, along with feldspar $\delta^{18}O$ values that range from –2.5 to +6.1, indicating a history of meteoric-hydrothermal water-rock interaction for these late porphyries. These coexisting quartz-feldspar pairs are surely not in $^{18}O/^{16}O$ equilibrium (Magaritz and Taylor, 1986). Whole-rock $\delta^{18}O$ values of two of these samples are +0.2 and +3.5. One sample has biotite $\delta^{18}O$ = +3.5 and a $\Delta_{Q\text{-}B}$ value of 3.3‰, indicating an apparent equilibrium temperature of 700 °C, using the calibration of Javoy (1977). However, it should be noted that feldspar from this rock has $\delta^{18}O$ = +0.2, a clear indication of meteoric-hydrothermal water-rock interaction; thus, it is inconclusive as to whether the quartz and/or biotite $\delta^{18}O$ values represent primary magmatic values.

The aplite dikes (Figure 5.19) have relatively homogeneous quartz $\delta^{18}O$ values (+8.3 to +8.9), but HF treatment of one of these samples indicates a much higher magmatic $\delta^{18}O$ value for this sample ($\delta^{18}O$ = +10.9), indicating that these quartz grains underwent some $^{18}O/^{16}O$ exchange with hot meteoric waters. This is consistent with the occurrence of low-^{18}O feldspar ($\delta^{18}O$ = –1.1 to +3.3) and whole-rock ($\delta^{18}O$ = +2.3 to +6.0).

5.8.4 Discussion

δD and $\delta^{18}O$ analyses (Magaritz and Taylor, 1986) from the Okanagan fault zone indicate that this detachment fault was subjected to the greatest degree of meteoric-hydrothermal water-rock interaction observed so far in the southern Omineca belt. Quartz-feldspar $^{18}O/^{16}O$ fractionations ($\Delta_{Q\text{-}F}$ = 1.8 to 9.9‰ for untreated samples) are smaller at this fault than at others in the region for two possible reasons: (1) primary magmatic quartz $\delta^{18}O$ values may have been lower in ^{18}O for those rocks, which are to the west of those previously discussed (Nelson batholith), or (2) their quartz $\delta^{18}O$ values may have undergone $^{18}O/^{16}O$ exchange with hot meteoric waters if a long-lived hydrothermal system was active along this fault, as was probably the case (see below).

Quartz $\delta^{18}O$ data from the relatively unaltered portions of the Okanagan batholith in the distal upper plate are 2-3‰ lower in ^{18}O ($\delta^{18}O$ quartz = +9.3) than the previously mentioned Jurassic intrusive rocks of the Nelson batholith ($\delta^{18}O$ quartz ~ +12); thus the primary $\delta^{18}O$ of the Okanagan batholith is lower in ^{18}O than the analogous rocks that lie to the east. This is consistent with the observed eastward increase in ^{18}O for Mesozoic plutonic rocks throughout the batholithic belt of the North American Cordillera (*e.g.*, Solomon and Taylor, 1989).

It is important to note that $\delta^{18}O$ data on coexisting quartz and feldspar mineral pairs define a shallow-sloping (slope = 4) data-point array in δ-δ space when plotted with feldspar on the y-axis. This is an indication of either prolonged meteoric-hydrothermal activity at ~300 °C, or a shorter pulse of meteoric-hydrothermal metamorphism at a higher temperature (Gregory et al., 1989). Magaritz and Taylor (1986) report that virtually all of the rocks along the west shore of Okanagan Lake are intensely chloritized, and locally these rocks are cut by epidote veins. The presence of abundant epidote and chlorite over such a broad area is compatible with this being a moderately high-temperature system.

If the Okanagan fault actually accommodated as much as 100 km displacement, as proposed by Tempelman-Kluit and Parkinson (1986), then the hanging-wall rocks of this fault would have been in a structural position immediately above the current location of the Arrow Lake pluton and the large Coryell series pluton southwest of it (see Figure 2.7) at 52 Ma. This unnamed large pluton has a U-Pb zircon age of 51.1 Ma (Carr and Parkinson, 1986). Thus, it is plausible that the emplacement of these very large intrusive bodies drove the convective circulation of meteoric-hydrothermal fluids on a massive scale, having immense impact on the hydrothermal evolution of the southern Omineca belt. It is likely that the meteoric-hydrothermal effects observed along the Okanagan fault, the Valkyr shear zone, and in the vicinity of the Coryell intrusions may comprise constituent parts of a single, giant hydrothermal system active during the emplacement of these alkaline plutons at about 51 Ma.

This scenario is analogous to the giant meteoric-hydrothermal systems that are known to have affected the entire eastern half of the Cretaceous Idaho batholith as the result of emplacement of a series of very large Eocene plutons (Taylor and Magaritz, 1978; Criss and Taylor, 1983; Criss and Fleck, 1990). The regional geologic setting of this part of Idaho is very much like that of the southern Omineca belt: (1) The eastern margin of the Idaho batholith is marked by a detachment fault having an Eocene (Ar-Ar cooling ages of 45-41 Ma) deformational history (Criss et al., 1982; House and Hodges, 1994). (2) Meteoric-hydrothermal fluids affected this detachment fault (Kerrich and Hyndman, 1986), much in the same manner as the detachment faults to the northwest in British Columbia. (3) Numerous intrusions that cut older intrusive rocks have Eocene K-Ar cooling ages (~ 44 Ma) of similar age to the detachment fault cooling ages (Criss et al., 1982); one of these plutons, the Casto pluton, has been suggested as having been emplaced as a low-^{18}O magma (Larson and Giest, 1995).

5.9 Summary

Meteoric-hydrothermal systems were active during the formation of all of the studied detachment faults in the southern Omineca belt. The intensity and duration of these episodes of meteoric-hydrothermal water-rock interaction were determined by local thermal conditions, most importantly those in the lower plate at the time of intitiation of detachment faulting. The $^{18}O/^{16}O$ data demonstrate that the presence or absence of magma bodies in the lower plate is important in determining the degree to which the upper plate and the detachment fault are affected by these hot meteoric waters. Important observations concerning these systems are summarized below.

5.9.1 The Slocan Lake Fault System as a Type Example

The Slocan Lake fault provided much insight into how meteoric-hydrothermal systems operate during detachment faulting. At this locality, it is shown that the zone which experienced the greatest degree of interaction with hot meteoric water is the brittle portion of this detachment fault. Only small amounts of meteoric water managed to infiltrate into the lower plate mylonites; the latter rocks were rock-buffered for $^{18}O/^{16}O$, but remained water-buffered for D/H, providing unequivocal evidence for the involvement of small amounts of meteoric water in this part of the system. These structural controls on the hydrothermal system are similar to that proposed by Fricke et al. (1992) for the detachment fault at the Ruby Mountains-East Humboldt Range core complex in Nevada. The calcite $\delta^{18}O$ data show that this meteoric-hydrothermal activity was also active very late in the hydrothermal cycle as the system gradually cooled.

Profound quartz-feldspar $^{18}O/^{16}O$ disequilibrium is a diagnostic feature of these detachment fault-related meteoric-hydrothermal systems. This appears to be a universal feature of this type of system, as quartz-feldspar $^{18}O/^{16}O$ disequilibrium, to variable degrees, is observed at detachment faults throughout the North American Cordillera (Lee et al., 1984; Kerrich and Hyndman, 1986; Kerrich and Rehrig, 1987; Kerrich, 1988; Fricke et al., 1992; Morrison, 1994). The lithologic simplicity of the hanging wall rocks of the Slocan Lake fault allows for semiquantitative modeling of the $^{18}O/^{16}O$ changes that occurred during the duration of this hydrothermal system. Open-system kinetic $^{18}O/^{16}O$ exchange modeling (Criss et al., 1987; Gregory et al., 1989) of the Slocan Lake fault hydrothermal system indicates that meteoric-hydrothermal water-rock interaction probably affected quartz and feldspar oxygen isotope systematics over a period of 0.5 to 3.0 Ma during detachment faulting. Open-system water/rock ratios exceeded 1.0 near the brittle zone of this fault. These water/rock ratios and the results of the exchange modeling were used to constrain fluid fluxes to be approximately 0.05 to 2.0 m/yr, a flux well within the range of that needed for advective heat and mass transport to occur (*e.g.*, Bickle and McKenzie, 1987).

We found no *prima facie* evidence for the involvement of metamorphic or magmatic waters in these detachment fault-related systems. Undoubtedly, these kinds of deeper-seated fluids passed through the detachment fault system, and these detachment faults were the most likely discharge pathways for these fluids to take, but as shown in the previous chapter, the water/rock ratios calculated for that part of the system are on the order of 0.05 oxygen units; this is almost two orders of magnitude less than the calculated water/rock ratio for the sample from the most permeable part of the meteoric-hydrothermal system. Thus, any imprint left on this detachment fault system by the passage of the deep-seated waters would be completely swamped by the large amounts of hot meteoric water that invaded the system once it reached the regime of brittle fracturing in the crust.

However, it should be noted that evidence for the passage of fluids generated by deeper-seated processes has been reported for the South Mountain metamorphic core complex in Arizona (Smith et al., 1991). It should also be noted that the fluid fluxes calculated for the Slocan Lake fault system are two orders of magnitude greater than those advocated for typical metamorphic-hydrothermal systems (*e.g.*, Ferry and Dipple, 1991).

5.9.2 Meteoric-Hydrothermal Interaction Throughout the Southern Omineca Belt

Meteoric-hydrothermal water-rock interaction affected all of the detachment faults studied in this thesis, and the thermal state of the lower plate clearly plays a prominent role in determining the style, duration, and intensity of meteoric-hydrothermal water-rock interaction in these metamorphic core complexes (Figure 5.21). These effects are also found in the zone of imbricate thrusting along the Monashee decollement (see Chapter 4, Figure 4.5). Data that pertain to meteoric-hydrothermal activity can be separated out into three groupings: (1) fault systems with no known Eocene intrusions in the footwall (the Monashee decollement), (2) older, east-dipping detachment faults in which the only plutons in the footwall are synorogenic Ladybird leucogranites (Slocan Lake fault and Columbia River fault), and (3) younger, west-dipping detachment faults (Okanagan fault) with both syntectonic Ladybird and post-tectonic Coryell intrusions in the footwall.

For the Monashee decollement, the effects of meteoric-hydrothermal fluids are limited to the fault zone itself and to areas close to it. Fluid flow along this decollement was probably driven by the ambient thermal gradient at the time of extension along overlying detachment faults (*e.g.*, Columbia River fault). Fractures at this fault may have been reactivated during uplift and extension, providing the avenues of entry for these meteoric-hydrothermal fluids. Quartz $\delta^{18}O$ is variable at the Monashee decollement because these rocks were initially more ^{18}O-rich and heterogeneous in ^{18}O (Figure 5.21).

Meteoric-hydrothermal systems that affected the older, east-dipping detachment faults were short-lived (1-3 Ma) relative to the deformational history of these faults (CRF and SLF on Figure 5.21). Coexisting quartz-feldspar mineral pairs from this set of detachment faults define steep data-point arrays (slope ≥ 10) in δ-δ space where quartz is plotted on the x-axis. Meteoric-hydrothermal activity was of the type observed at the Slocan Lake fault, and is summarized in the previous section.

Meteoric-hydrothermal systems that affected the younger, west-dipping detachment faults were either longer-lived or hotter hydrothermal systems than those described above that preceded this event. Coexisting quartz-feldspar mineral pair $^{18}O/^{16}O$ data from these detachment faults plot as shallower data-point arrays on δ-δ plots where quartz is plotted on the x-axis (Figure 5.21). Syntectonic alkaline Coryell intrusions (Figure 5.22) cut these faults and were the major "heat engines" driving convective circulation of these waters. The Valkyr shear zone was also affected by this kind of hydrothermal event, which apparently occurred after most of the deformation had ceased along this shear zone.

Figure 5.21 -- Summary plot showing generalized data-point envelopes for $\delta^{18}O$ quartz versus coexisting $\delta^{18}O$ feldspar from detachment faults of the southern Omineca belt and the Monashee decollement. SLF = Slocan Lake fault; CRF = Columbia River fault; and VSZ = Valkyr shear zone. The Monashee decollement has no known Eocene intrusions in the footwall, and the effects of meteoric-hydrothermal fluids are limited to the fault zone and areas close to it; fluid flow along the decollement was probably driven by the ambient thermal gradient in these deep-seated rocks at the time of extension along overlying detachment faults (*e.g.*, Columbia River fault). The data-point envelope for the Monashee decollement is wider, and lies to the right of the others, because prior to meteoric-hydrothermal alteration, these basement rocks were more heterogeneous in ^{18}O and also more ^{18}O-rich than were the others (see Chapter 4). Steep data arrays defined by samples from the hanging wall and the uppermost 300 m of the syntectonic, leucogranite-rich footwall at the Slocan Lake and Columbia River faults (early east-dipping detachment faults) indicate that fluid flow was most likely driven by the thermal contrast between the hot (~650 °C) footwall and a much cooler hanging wall (~300 °C). These steep arrays also indicate that the meteoric-hydrothermal events related to detachment faulting are relatively short-lived (~ 1 Ma) relative to the duration of the faulting event. $\delta^{18}O$ values of quartz and feldspar from the Valkyr shear zone and the Okanagan fault zone define shallower arrays in this δ-δ space, indicating either a much longer-lived or much hotter meteoric hydrothermal system affected these areas. The data point labeled CRF(647) denotes a brecciated sample from the brittle zone of the Columbia River fault; this sample is unique among the low-^{18}O samples in having both quartz and feldspar $\delta^{18}O$ values that are approximately in isotopic equilibrium (it either formed from a low-^{18}O magma or it was equilibrated with low-^{18}O meteoric water at very high temperatures or for a very long time).

Figure 5.21 Southern Omineca Belt Faults

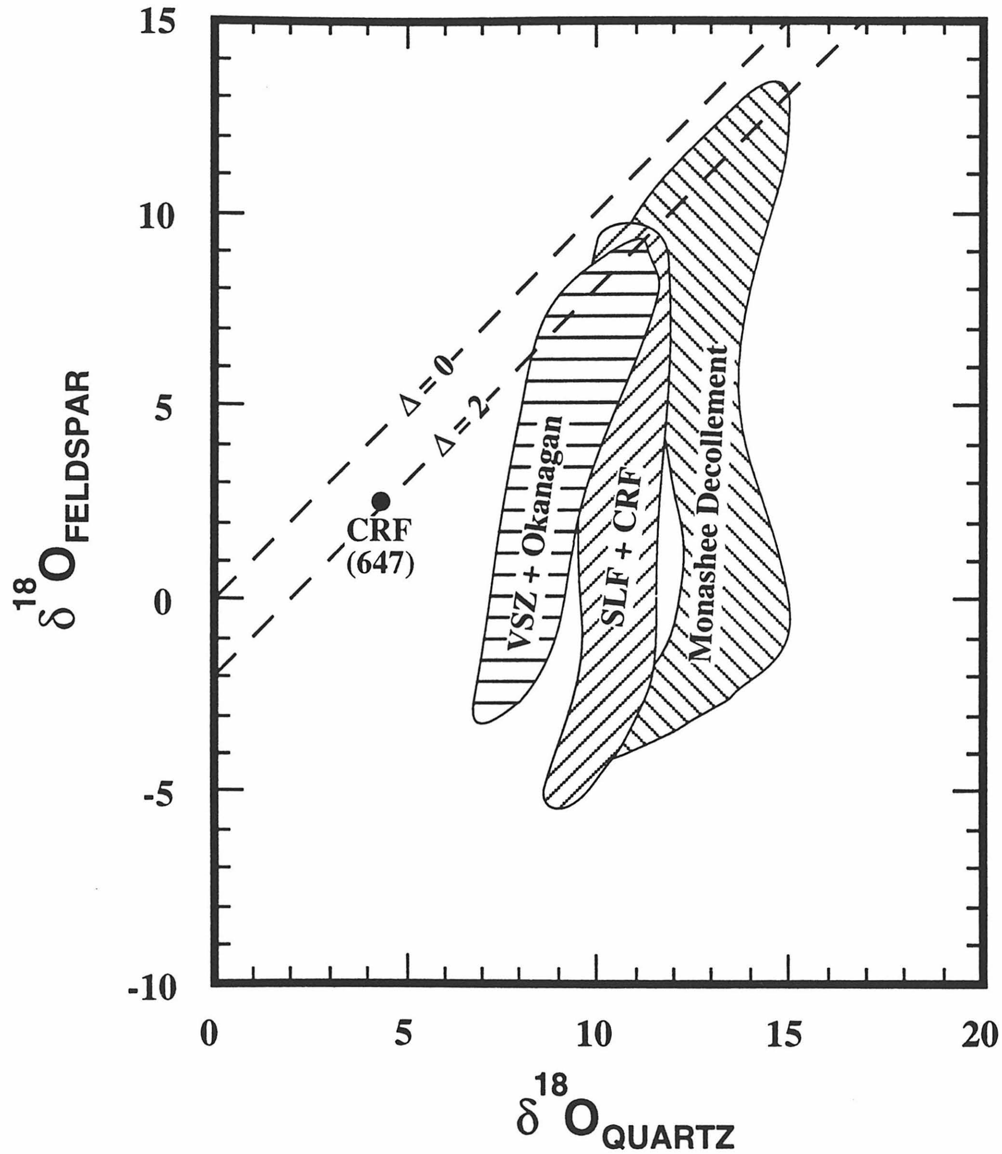

Figure 5.22 -- Summary plot of quartz $\delta^{18}O$ versus coexisting feldspar $\delta^{18}O$ from detachment faults of the southern Omineca belt and the Monashee decollement showing the same data-point envelopes from Figure 5.21, along with the data-points from the late Coryell alkaline intrusions. The Valkyr shear zone and Okanagan fault are both cut by the late-stage Coryell plutonic suite. The overlap between the data from the Coryell intrusions and that of the Valkyr shear zone and the Okanagan fault (see Figure 5.20) indicate that the Coryell intrusions were important in supplying heat to drive more vigorous (and probably hotter) hydrothermal systems at these structures. At the Valkyr shear zone, spatial patterns of meteoric-hydrothermal activity seem to be unrelated to faulting, a definite indication that the intrusion of the Eocene magmas was the prime driving force behind this particular hydrothermal system. Likewise, the Okanagan fault (Figure 5.20) is cut by these late alkaline intrusions and the greatest effects of meteoric-hydrothermal water-rock interaction are found associated with these bodies and the synextensional volcanism. Of the faults discused in this work, only the Okanagan fault is known to have had extensive synextensional volcanism.

Figure 5.22 Southern Omineca Belt Faults

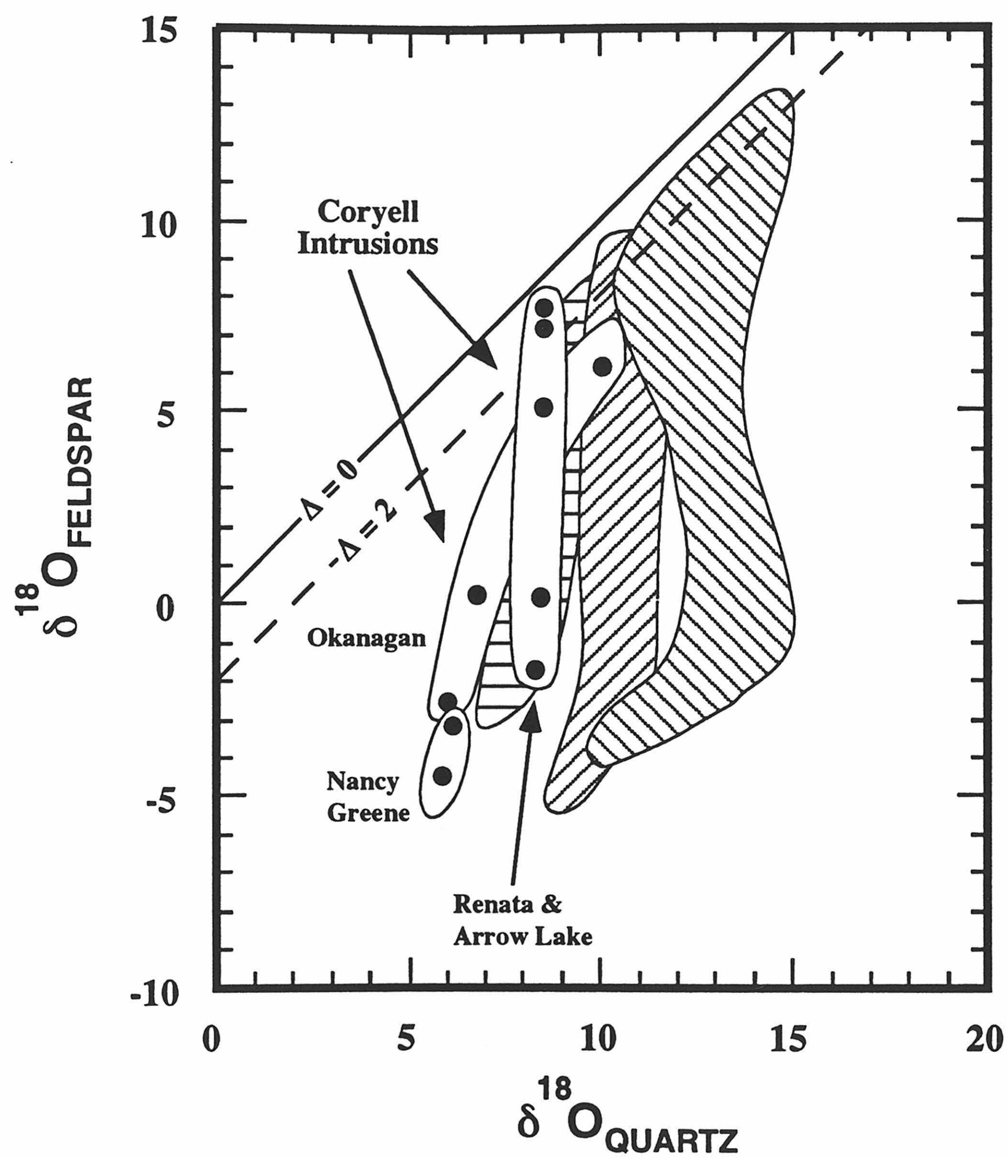

Chapter 6. Summary and Conclusions

In this thesis, I have investigated the oxygen isotope geochemistry of the metamorphic core complexes in the southern Omineca belt, British Columbia. This study was undertaken mainly in order to understand the role of hydrothermal processes and water-rock interaction in the development of this important type of geologic association. This dissertation discusses these hydrothermal processes in some detail, and shows how the $^{18}O/^{16}O$ ratios of rocks and minerals were affected by these processes. Although the water-rock and melt-rock interactions exhibit distinctive features in different portions of the metamorphic core complexes, it can be shown that fluid-rock exchange phenomena affected virtually all levels of the continental crust that were involved in the orogenic activity related to core complex formation. The organization of this thesis is arranged such that the various hydrothermal regimes active during the tectonogenesis of these metamorphic core complexes are discussed in order of structural level, going from deepest to shallowest. The purpose of this summary chapter is to briefly review the conclusions of the previous chapters within the context of the entire fluid-rock history of the metamorphic core complexes in the southern Omineca belt, and to provide an assessment of the questions posed at the beginning of Chapter 1.

6.1 The Monashee Terrane Inverted Metamorphic Sequence

The Paleocene syncompressional metamorphic-hydrothermal event related to inverted metamorphism of the Monashee Terrane occurred under lithostatic pressures during burial of that terrane beneath the 25-km-thick Selkirk Allochthon, simultaneously with thrusting along the Monashee decollement. The zone of intense fluid-rock interaction is localized in a 200-m-thick section immediately beneath the decollement, where it is marked by a striking $^{18}O/^{16}O$ homogeneity of quartz $\delta^{18}O$ values (+11.0 ± 0.3‰) in the highest-grade rocks. The effects of this $^{18}O/^{16}O$ homogenization are observed over a wide area at several localities along the 150-km-long outcrop trace of the Monashee decollement (see Figure 3.1). The isotopic homogeneity in this zone just beneath the thrust plate can be clearly contrasted with the $^{18}O/^{16}O$ heterogeneity (quartz $\delta^{18}O$ = +8.0 to +16.4) in the lower-grade rocks (their protoliths?) that make up the deeper part of the Monashee basement complex in this area. This 200-m-thick zone of $^{18}O/^{16}O$ homogeneity beneath the Monashee decollement correlates beautifully with the observations of Nyman et al. (1995) that these particular rocks underwent as much as 50 vol. % melting during the thrusting event. Thus, it seems clear that the two processes, anatexis and $^{18}O/^{16}O$ homogenization, were produced at the same time and by the same series of events. Also, the $^{18}O/^{16}O$ homogeneity beneath the thrust sheet ($\delta^{18}O$ quartz = +11.0 ± 0.3‰) contrasts sharply with the 1.5‰ higher values in the much thicker zone of

$^{18}O/^{16}O$ homogeneity (quartz $\delta^{18}O = +12.5 \pm 0.5‰$) that makes up the major part of the Selkirk Allochthon above the decollement.

6.2 $^{18}O/^{16}O$ Homogenization and Anatexis of the Selkirk Allochthon

The occurrence of isotopically uniform quartz ($\delta^{18}O = 12.5 \pm 0.5‰$) and feldspar ($10.9 \pm 0.7‰$) throughout a variety of different rock types indicates that much of a 6-km-thick section of the mid-crustal Selkirk Allochthon underwent internally buffered $^{18}O/^{16}O$ homogenization during Paleocene melting and decompression as it moved up the Monashee thrust ramp. Areas of uniform $\delta^{18}O$ are those with the most leucogranite or those subjected to severe anatexis, indicating that the presence of leucogranite is intimately connected with the $^{18}O/^{16}O$ homogenization process. Only locally, in the most impermeable (or refractory) zones did ^{18}O exchange among the rocks, leucogranite melts, and aqueous fluids fail to go to completion (*i.e.*, in the deepest parts of the section, in a marble-rich zone, around some thick amphibolite layers, and in most garnets), namely in just those situations where $^{18}O/^{16}O$ homogenization was *a priori* expected to be much more difficult to attain based on isotopic studies of analogous phenomena elsewhere in the world.

Evidence for $^{18}O/^{16}O$ heterogeneity in the protoliths of these rocks is observed in stratigraphically correlative lower-grade units elsewhere in British Columbia, as well as in garnets that coexist with isotopically homogeneous quartz. In our model, $^{18}O/^{16}O$ homogenization occurred under lithostatic pressures during water-rock and melt-rock interactions that accompanied muscovite dehydration and partial melting of pelites, and this involved only minor influx of external H_2O, followed by release of magmatic H_2O from these anatectic melts (triggering further melting of adjacent feldspathic assemblages) as they were uplifted 20 km during thrusting just prior to onset of detachment faulting. Thus, it is envisioned that the $^{18}O/^{16}O$ homogenization of the Selkirk Allochthon was basically a closed-system phenomenon, with little or no change in the overall bulk $^{18}O/^{16}O$ of the entire section, but with a pronounced smoothing of $^{18}O/^{16}O$ gradients in all but the most impermeable parts of the section.

6.3 Meteoric-Hydrothermal Water-Rock Interaction During Detachment Faulting

Eocene synextensional meteoric-hydrothermal events under hydrostatic pressures affected the shallow crust along all of the major detachment faults in the region, as well as locally along reactivated decollement faults. This was enhanced locally by the simultaneous emplacement of synextensional alkaline intrusions (Coryell plutons). These events are indicated by quartz-feldspar $^{18}O/^{16}O$ disequilibrium brought about by exchange between hot meteoric water ($\delta^{18}O \sim -15$) and mainly feldspar ($\delta^{18}O$ down to -5.0). Open-system kinetic oxygen isotope exchange modeling was done on the Slocan Lake detachment fault at the Valhalla complex to provide some constraints on duration (1-3 Ma) and integrated fluid flux ($\geq 10^7$ $cm^3{}_{H_2O}/cm^2{}_{rock}$) for this hydrothermal metamorphism. All of the detachment faults in this large area show these effects, but these meteoric-hydrothermal systems were hotter and/or longer-lived at sites of synextensional plutonism.

6.4 Concluding Questions

This thesis has made some important observations concerning the hydrothermal evolution of metamorphic core complexes. Eleven questions about the role of

Figure 6.1 -- Schematic west-to-east cross section through the southern Omineca belt (no vertical exaggeration) showing the complex hydrothermal evolution of this region at different levels of the continental crust. The three types of water-rock interaction discussed in this thesis are portrayed in this summary diagram, together with their possible linkages to one another. The thin arrows denote hypothetical flow paths for the lithostatic metamorphic and magmatic fluid regimes active in the crustal sections beneath the detachment faults (Okanagan fault, Valkyr shear zone, and Slocan Lake-Columbia River faults), and the thick arrows denote these flow paths for the much higher aqueous fluid fluxes involved in the detachment fault-related meteoric-hydrothermal systems, which takes place under hydrostatic conditions. The dashed arrows signify limited amounts of deep-seated waters derived from lower crustal-or mantle-derived magmas. It should be emphasized that these episodes of water-rock interaction are separated in space and time, so this hypothetical diagram displays a whole series of events that overlapped in time over the approximate interval 62 Ma to 44 Ma. Episode 1: A dehydration front migrated downward into the deep rocks of the Monashee Complex, driving off fluids of initially variable $\delta^{18}O$ (+7 to +14) that mixed to form a much more uniform fluid with $\delta^{18}O \sim +10$ that produced the homogenized $\delta^{18}O$ values of +11 in the footwall of the Monashee decollement; this triggered anatexis in the high-grade parts of this section just beneath the Monashee decollement. These melts (H_2O-saturated at ~10 wt.% H_2O) intruded into the Selkirk Allochthon hanging wall, where they contributed H_2O to that system as it was undergoing decompression during transport up the Monashee thrust ramp. Within the lower part of the Selkirk Allochthon, massive anatexis of metapelite and arkosic grit took place in response to the dehydration of muscovite and decompression as that package of rocks moved eastward and upward along the Monashee thrust ramp.

Figure 6.1 (Cont.) -- During anatexis, large parts of this middle crustal section were homogenized in $^{18}O/^{16}O$ (producing uniform $\delta^{18}O$ quartz = +12.5 in equilibrium with water $\delta^{18}O$ = +11) as a result of multiple stages of exchange associated with the exsolution of H_2O from the leucogranite magmas as they reached H_2O saturation during decompression and crystallization. This continued with partial melting of lithologies fertile to melting in the presence of the newly released H_2O producing $^{18}O/^{16}O$ homogenization during transport of this H_2O through intervening lithologies that were infertile to melting. This large-scale partial melting of the middle crust served to weaken this crustal layer such that this thick crust was no longer gravitationally stable, resulting in its collapse through detachment faulting. The juxtaposition of the hot, ductile middle-crustal rocks of the anatectic zone against the cold, brittle, heavily faulted rocks of the upper plate caused large-scale circulation of meteoric-hydrothermal fluids ($\delta^{18}O$ ~ –13 to –15) through fractures formed in the upper plate during extension. There were multiple pulses of meteoric-hydrothermal activity in this region: (a) An initial pulse occurred during faulting along the east-dipping detachment faults (Columbia River fault and Slocan Lake fault). Convective circulation of hot meteoric fluids was most likely driven by the temperature contrast between the lower plate at ~ 600-700 °C and the brittle portion of the crust. Fluid-flow was fault controlled and flow paths probably ranged from 10-50 km. Also associated with this stage of meteoric-hydrothermal water-rock interaction was the ingress of meteoric water into the imbricate thrust zone of the Monashee decollement, most likely along extensional structures related to detachment faulting. (b) The second major pulse of meteoric-hydrothermal metamorphism is associated with the intrusion of the Coryell alkaline magmas into shallow levels of the crust during late stages of extension along the west-dipping detachment faults (*e.g.*, the Okanagan fault).

Figure 6.1

Schematic Cross-Section With Hydrothermal Systems

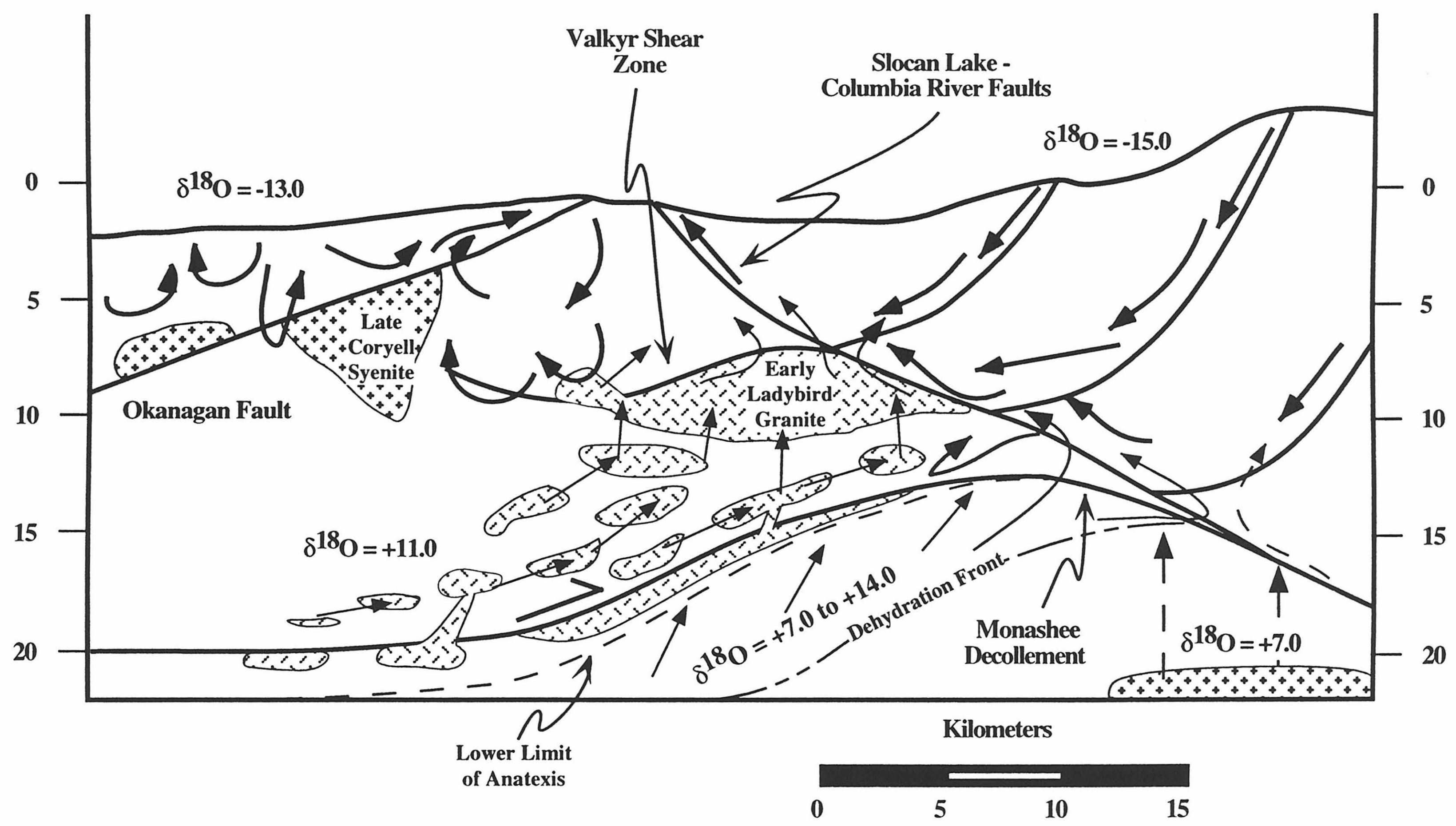

hydrothermal processes in the metamorphic, magmatic, and tectonic evolution of metamorphic core complexes were posed at the beginning of Chapter 1. Listed below are the ways in which this thesis has provided partial answers to these questions.

1. What types of hydrothermal systems developed during the evolutionary history of the core complexes?

Evidence was found for at least three types of hydrothermal systems active during the formation of the metamorphic core complexes that comprise the southern Omineca belt. These are: (1) Metamorphic-hydrothermal water-rock interaction at relatively low water/rock ratios in the inverted metamorphic sequence of the deep-crustal Monashee terrane, just beneath the Monashee decollement. (2) Magmatic-hydrothermal and metamorphic-hydrothermal interactions that produced internally buffered $^{18}O/^{16}O$ homogenization during Paleocene melting and decompression of mid-crustal portions of the Selkirk Allochthon. (3) Extensive meteoric-hydrothermal metamorphism that affected shallow crustal levels during detachment faulting and the emplacement of coeval syntectonic alkaline intrusions.

2. What was the duration and intensity of water-rock interaction at various levels in the crust?

The duration and intensity of water-rock interaction was different at each of the three crustal levels. The basement layer, the Monashee complex, was a metamorphic fluid regime with very low water/rock ratios except perhaps in a 200-m-thick section immediately beneath Monashee decollement. Hydrothermal fluid-flow in this zone was probably triggered by downward dehydration of a 2 km-thick metasedimentary section in the basement complex. The anatectic melt that formed along the Monashee decollement during this process provided a fluid sink, preventing the large-scale recirculation of fluids. This event was probably short-lived because metamorphic inversions are erased within a few million years as the system attains thermal equilibrium (*e.g.*, England and Thompson, 1984).

The middle crustal layer, the Selkirk Allochthon, was another zone of relatively low-water/rock ratios involving metamorphic and magmatic water. The duration of this event is constrained by the time at which the Monashee ramp first formed, and by the time of final crystallization of the leucogranites in this section. In the interval between these events, the time required is defined by the decompressional processes that are so important in $^{18}O/^{16}O$ homogenization and the generation of such large amounts of leucogranite melt, as thrust ramping occurred. The Ladybird leucogranites in this zone apparently crystallized over a period of at least 7 million years (62-55 Ma) at the Valhalla (Carr et al., 1987) and southern Thor-Odin (Carr, 1992) complexes. However, this provides information only about the history of crystallization, and not the entire event; thus, it is plausible that the $^{18}O/^{16}O$ homogenization of the middle crust could have taken place over tens of millions of years as the Monashee thrust ramp was developing.

The most intense episode of true hydrothermal metamorphism in the southern Omineca belt was the meteoric-hydrothermal event associated with the extensional unroofing of these complexes by detachment faulting during the Eocene. Detachment faulting in the southern Omineca belt is constrained to have been active from 58 to 44

Ma, suggesting that these meteoric-hydrothermal systems were active over a period of at least 14 million years. However, when each separate hydrothermal regime is examined as an entity, they appear to have lifetimes of about 1-3 Ma, perhaps being active only during the intitial stages of extension, a time of high thermal gradients between the brittle rocks of the upper plate and the ductile rocks of the lower plate.

3. Is it possible to define the location and depth of the transition from metamorphic/magmatic hydrothermal systems at lithostatic pressure to meteoric systems at hydrostatic pressure?

Although it is clear that the two deep-seated events occurred wholly under lithostatic pressures, and that the bulk of this shallow event occurred under hydrostatic pressures, the actual situation is more complex. This is particularly true in the deeper parts of these systems, or where the fault trace has been invaded by coeval bodies that must have been emplaced under lithostatic conditions (particularly as some of these may have been intruded as low-^{18}O magmas (and such magmas can only be formed if there is an interaction between the lithostatic magma systems and the hydrostatic meteoric-hydrothermal systems; *e.g.*, Taylor, 1986; Hildreth et al., 1991). The data from this study suggest that the transition between the hydrothermal systems operative at lithostatic pressures and those operating under hydrostatic pressures locally may have occurred within the deeper parts of the detachment faults. Evidence discussed in Chapter 5 from the Slocan Lake fault indicates that hot meteoric fluids infiltrated as deep as 800 m beneath the brittle-ductile transition at this detachment fault. The discovery of meteoric-hydrothermal effects along the Monashee decollement at the southern Thor-Odin complex came as a complete surprise, and this event is most likely related to meteoric-hydrothermal metamorphism during re-activation of this fracture system by the episode of extension.

More stable isotopic studies, combined with careful field mapping, are needed to discern the evolution of the lithostatic-hydrostatic boundary in these systems, particularly because in many cases (most cases?) the effects of the meteoric-hydrothermal systems are later imprinted upon the earlier magmatic or metamorphic hydrothermal systems that affected the same rocks. The natural laboratory provided by the Slocan Lake fault may provide a good opportunity for addressing these issues. The exposure at this detachment fault is such that the deformational, magmatic, and hydrothermal evolution of this detachment fault can be mapped in great detail. Thus, detailed mapping of this fault in conjunction with a stable isotope study where each distinct fluid event can be separated out in space and time may provide some critical information about this extremely important transition in the Earth's crust.

4. What is the role of water in the generation of lower-plate syntectonic magmas?

The data from this thesis indicate that water is an extremely important agent with respect to the generation of lower-plate syntectonic magmas, specifically the Ladybird leucogranites. However, the amount of external water actually required to drive this melting is small relative to the amount of metasedimentary protolith being melted, because it has been shown with "the petrologic catalyst model" that internal H_2O (as OH in muscovite) is sufficient to do the job, if such H_2O is: (1) first incorporated into early-formed pelitic melts; (2) released as these melts crystallize because of loss of

H_2O during decompression; and (3) then recycled and used to melt adjacent arkosic grit layers. Other factors, such as decompressional evolution of the system and the fertility (to melting) of the rock units that comprise it, are also important factors in determining the degree of partial melting and isotopic homogenization that takes place within the system. A sufficiently large decompression allows for the multiple use of the same H_2O as it is recycled for $^{18}O/^{16}O$ exchange, as well as triggering further melting of the fertile lithologies (*e.g.*, feldspathic clastic lithologies such as arkosic grit).

5. What was the temperature contrast between the upper and lower plates during the evolution of the core complexes, and specifically during the meteoric-hydrothermal activity?

It is clear that the temperature contrasts between the upper and lower plates of the detachment faults were sufficiently high to drive the hydrothermal circulation of large amounts of hot meteoric fluids in the upper plate. The intensity and duration of this meteoric-hydrothermal event was greatly influenced by the temperature contrast between the upper and lower plate during detachment faulting. The temperature of the lower plate of the east-dipping detachment fault systems (Slocan Lake fault, Columbia River fault) may have been about 650-700 °C at the onset of detachment faulting (Carr, 1995; Parrish, 1995). Assuming that heat advection by hydrothermal fluids keeps the upper plate temperature at about 300 °C at the detachment fault, then the thermal contrast between these two parts of the system will be on the order of 350 °C. However, this upper plate-lower plate temperature contrast diminishes with time as the system quickly evolves to a state approaching thermal equilibrium. The sheet-like leucogranite plutons of the Ladybird suite would cool relatively rapidly during their passive ascent toward the surface in the footwall of these detachment faults. The rate of displacement along the detachment fault also probably plays a role in determining the thermal contrast between these two sections of the Earth's crust.

In the case of the west-dipping detachment faults, the thermal contrast between upper and lower plate was probably larger during detachment faulting and meteoric-hydrothermal activity. The syntectonic emplacement of the alkaline Coryell intrusive rocks could indicate a lower plate temperature >800 °C, and by analogy with the previous discussion, the upper-lower plate thermal contrast then may have been as great as 500 °C. However, this is a difficult parameter to constrain because there are no published compilations of the thermal history of these younger, west-dipping faults. The plutonic bodies being emplaced into the crust at this stage of extension were more massive and hotter than the older Ladybird suite.

6. To what extent did the presence or absence of synextensional lower-plate magmas drive the hydrothermal alteration of the upper plate?

The temperature contrast between the upper and lower plates during extension was a very important factor in determining the style and intensity of meteoric-hydrothermal metamorphism that affected the upper crust and the detachment faults. The size of the "heat engine" is of greatest importance in meteoric-hydrothermal systems. The $^{18}O/^{16}O$ data show that the meteoric-hydrothermal systems associated with the younger, west-dipping detachment faults (*e.g.*, Okanagan fault) were enhanced by the emplacement of late alkaline intrusions (*e.g.*, Coryell plutonic suite), such that these systems were either hotter or longer-lived than those affecting the east-dipping detachment faults (*e.g.*, Columbia River fault and Slocan Lake fault). The lower plates of the east-dipping faults likely were at temperatures of 600-700 °C (Carr, 1995; Parrish, 1995) at the onset of extension whereas the younger, west-dipping detachment faults locally contained alkaline synextensional plutons in the lower plate and may have been as hot as 800-900 °C. Thus, this temperatue contrast was most likely related to the type of magmatism active in the lower plate at the time of extension.

7. Did the earlier compressional history of this terrane have any impact on the various deep-level hydrothermal processes?
8. Are aqueous fluids the primary agent that produced wholesale weakening of the crust in this area, perhaps triggering the development of detachment faults in the middle part of the continental crust?

These two questions are discussed together, because there is no question that the earlier compressional history of the southern Omineca belt was extremely important in determining the subsequent tectonic and hydrothermal evolution of this region. The Cretaceous-Paleocene overthrusting of the Selkirk Allochthon across the Monashee basement upset the thermal gradient in the continental crust, and resulted in the formation of an inverted metamorphic sequence. Dehydration and the transport of aqueous fluids related to this event drove anatexis (Nyman et al., 1995) along the sole of the Monashee decollement. This melting resulted in the wholesale weakening of this thin layer of crust, allowing for the rapid movement (*e.g.*, Hollister, 1993) of the Selkirk Allochthon up the Monashee thrust ramp. This rapid transport of the allochthon provided a means of nearly isothermally decompressing the hot rocks of the Selkirk Allocthon, and this in turn allowed for extensive partial melting and for internally-derived H_2O to be recycled through the leucogranite melts and the rocks that were infertile to melting, thereby producing the massive $^{18}O/^{16}O$ homogenization observed in the mid-crustal layer. The anatexis of the middle crust provided an extensive weak crustal layer from which structures related to collapse could nucleate (*e.g.*, Coney and Harms, 1984; Lister and Baldwin, 1993); also, this extensive partial melting provided an excellent means of accommodating crustal extension by the large-scale flow of middle crustal material from those places that experienced lesser degrees of extension into zones with large magnitudes of extension (*e.g.*, Wernicke, 1992). The role of decompression related to detachment faulting itself cannot be discounted in assessing the hydrothermal processes active in the middle crust; Wernicke's (1992) "rolling hinge" model appears to be an efficient means of driving the style of the decompression-melting observed in the middle crust in these Canadian metamorphic core complexes. The synchronous domino-style fault block rotation model (*e.g.*, Proffett, 1977; Miller et al., 1983) is not such an efficient means of transporting heat from deep levels of the crust toward shallower levels, and an input of magma from below is needed to account for the observed magmatism at these complexes. The stable isotope results from the southern Omineca belt show no evidence for the input of low-^{18}O mantle-derived fluids from below at any of these complexes, until possibly late in the extensional history (*i.e.*, Coryell intrusions). The crustal hydrology of this orogenic terrane is a multi-layered one where the fluids are being supplied internally to the deep-level Monashee complex and deep parts of the mid-crustal Selkirk Allochthon. The $^{18}O/^{16}O$ heterogeneity in the deepest parts of the Monashee terrane indicates that there likely cannot have been any large quantities of external fluid entering the system from below; if that were the case, then we would expect to observe the kind of concurrent $^{18}O/^{16}O$ homogenization and $\delta^{18}O$ lowering that is observed in the East Humboldt Range in Nevada (Wickham and Peters, 1990; Grunder and Wickham, 1991; Peters and Wickham, 1995) and the Whipple Mountains, California (Morrison, 1994). Thus, in this case, the earlier compressional tectonic history set the stage for the subsequent collapse of this orogenic belt, and water-rock interaction was the likely catalyst driving the processes that allowed orogenic collapse of this type to happen.

9. What are the tectonic controls governing the behavior of the various hydrothermal systems?

The style of hydrothermal metamorphism is surely determined by the local tectonic environment in that there are different means of heat advection brought about by the various tectonic processes that have affected this area. First, rapid movements in the compressional regime result in the emplacement of a hot sequence of rocks over a colder sequence of rocks, a "hot-side-up" scenario (*e.g.*, England and Thompson, 1984). Fluid flow in this environment is most likely down-pressure, but up-temperature, and the fluids involved in this type of system are granitic melts and metamorphic dehydration fluids. Rock permeability was very small, but sufficiently large to allow for the transport of enough H_2O to drive melting of the highest grade rocks at the highest position within this regime. In the Selkirk Allochthon, decompression was the main tectonic control in driving fluid flow, but the melting related to this decompression could only have happened if the allochthon system was held at temperatures greater than the wet solidus of granite throughout the decompressive process. The small amounts of water needed to trigger this melting are probably adequately acounted for by dehydration and generation of anatectic melts in the Monashee complex below.

In the detachment faulting regime, the tectonics dictate that the local thermal environment is one where there is a "hot-side-down" configuration, with heat being advected to shallower crustal levels from below. These conditions are prime for the convective circulation of meteoric fluids given a sufficient permeability (*e.g.*, Norton and Taylor, 1979; Norton, 1984). This results in local heating of the upper plate and the advective removal of heat by the circulating hydrothermal fluids in this brittle portion of the crust.

10. How much water is needed to drive decompression-driven dehydration melting of the middle crust?

The question posed here should be: How much decompression-driven dehydration melting should be expected for a given stratigraphic section? The reason for revising the question in this case is because the amount of decompression-driven dehydration melting a metamorphic sequence undergoes is a function of the distribution of lithologies fertile to melting under the temperature and pressure conditions of the system at the time of decompression. The amount of melting a given metamorphic sequence can undergo is determined by the amounts of hydrous minerals available for dehydration and the abundance of phases that can be incorporated into the melt phase once the melting temperature is reached. The rate of decompression is important also, because it is possible for the heat to be lost too rapidly to allow for large-scale anatexis to proceed. If a rock system is lacking hydrous minerals for dehydration, then significant water must be added to the system to drive melting.

11. Was the exsolution and dissolving of aqueous fluids in high-silica partial melt phases an important process in the evolution of these core complexes?

The exsolution and dissolving of aqueous fluids in high-silica melt phases appear to have been important processes in the evolution of the metamorphic core complexes in Southern British Columbia. The portions of the crust that underwent large-scale anatexis also became homogeneous in $^{18}O/^{16}O$. This thesis has shown that thick sequences of the middle crust undergoing decompression melting can be strikingly homogenized in $^{18}O/^{16}O$. One more reason why this process is important is that it allows for the creation of large amounts of melt in the crust that can contribute to its overall weakening, providing the local forces necessary for the initiation of extension as gravitational collapse begins in continental crust built during compressional orogeny.

Appendix A. Analytical Techniques and Development of the Laser Fluorination Apparatus

This appendix describes the analytical techniques employed during the course of this study. These include: (1) conventional silicate oxygen isotope extraction techniques using Ni reaction vessels, (2) laser-assisted oxygen isotope extraction techniques for silicate materials, (3) an acid reaction technique for the extraction of CO_2 from carbonate materials, and (4) mass spectrometry using two different mass spectrometers.

During this time, I was involved in helping to put the new Finnegan MAT 252 mass spectrometer and the Caltech oxygen isotope laser extraction system in operational condition. Mass spectrometry for this project was transferred from the old McKinney-Nier mass spectrometer to the Finnegan MAT 252 instrument in early 1993. Standardization and calibration between these two mass spectrometers is briefly described. The laser system became operational in January, 1995, and a brief description of this system, operational procedures, standards, and calibration to other techniques is given below.

A.1 $^{18}O/^{16}O$ Analytical Procedures for Silicates

The fluorination technique described by Taylor and Epstein (1962) was used to obtain oxygen isotope analyses of silicates. Oxygen isotope extractions from silicate materials were done on the middle vacuum line in room 404 North Mudd (the Penthouse). A diagram showing a vacuum extraction line of this type is shown in Taylor and Epstein (1962). This extraction procedure for six samples generally takes two days, a sample loading day and an extraction day.

A.1.1 Loading Day

Weighed samples (15-25 mg) were loaded into nickel reaction vessels in a dry box containing a P_2O_5-drying agent, located in room 307 North Mudd. Prior to entry into this dry box, the manifold containing six reaction vessels and the weighed samples were put into a chamber and pumped to a rough vacuum. Once rough vacuum was reached, dry N_2 was introduced into the chamber and the manifold was then brought into the dry box. One at a time, the Teflon-ferrule flange to each reaction vessel is then opened. Prior to sample loading, the bottom of the reaction vessel is scraped with a screwdriver to remove any fluoride residue from the previous sample. One by one, six samples are placed into the bottom of the reaction vessels, and the flanges are sealed. The final step is the removal of the manifold from the drybox, and its transfer to the extraction line.

The part of the extraction line that was exposed to the air during sample loading is pumped down to vacuum for one hour. One-third atmosphere of F_2 is then loaded into portions of the vacuum system exposed to air, in order to remove hydrous contaminants

(H_2O) that have adhered to the interior walls of the metal line. These sections are heated with the gas torch. After a few minutes, this waste F_2 is then removed by letting it slowly flow through and react with the waste KBr chamber. The bromine product of this reaction can then be frozen down in a glass trap cooled by liquid N_2 (–195 °C) just downstream of the KBr. The dry N_2 in the reaction vessels is pumped away, and the line is pumped on for another hour. Simply as a precaution, one-third atmosphere of F_2 is loaded into the reaction vessels to react with any adsorbed water (except when feldspars and very fine-grained powders are being analyzed). This waste F_2 is then removed as before, completing the sample clean-up procedure.

The line is pumped by the waste pump for an hour, followed by two hours pumping through the high-vacuum part of the line, after which two-thirds atmosphere F_2 is loaded into each reaction vessel and the metal portion of the extraction line. The reaction vessels are isolated and heated to 550 °C, and left to react overnight. This completes the analytical procedure for the loading day.

A.1.2. Extraction Day

The line is prepared for oxygen extraction by first removing F_2 from the metal part of the line by the procedure mentioned above. This is followed by pumping down to vacuum for one hour first through the waste pump and then via high-vacuum. The O_2 to CO_2 conversion chamber (see below) is heated until the graphite rod glows red and pressure is back to ambient high vacuum levels. This rids the CO_2 converter of any adsorbed water that may have accumulated on it since its last use. Once vacuum is reached, dewar flasks filled with liquid N_2 are put onto the two glass traps immediately downstream of the KBr reaction trap and the two metal traps upstream of the KBr. Now the line is ready for oxygen extraction.

For each sample, the following procedure is followed:

(1) All valves along the line path up to the CO_2 converter are closed.

(2) The Nupro valve separating the reaction vessel from the rest of the line is opened. The sample gas is allowed to slowly expand into the first LN_2 trap. SiF_4 and other volatile products of the fluorination reaction (*e.g.*, HF) freeze out into this trap. Allow one minute for this stage.

(3) The gas is then allowed to slowly expand into the liquid N_2 trap immediately upstream of the KBr trap. Wait one minute.

(4) Crack the valve leading to the KBr reaction chamber. This chamber is kept at 150 °C. Fluorine gas is reacted out by the following reaction:

$$F_{2(g)} + KBr_{(s)} = Br_{2(g)} + KF_{(s)}$$

Br_2 freezes out in the liquid N_2 trap upstream of the KBr chamber. Allow this reaction to proceed until the pressure stops dropping on the Bourdon gauge on the metal portion of the vacuum line (usually about three minutes).

(5) Barely crack the valve just downstream of the KBr chamber to allow the $Br_2 + O_2$ gas mixture to expand into the liquid nitrogen trap just downstream; this is the point at which most of the Br_2 freezes out. Allow about five minutes for the bromine to freeze out.

(6) Open the next downstream stopcock to expand the gas mixture to the next liquid nitrogen trap. This trap freezes residual bromine that escaped the previous trap. The gas now is comprised of O_2 and a tiny amount of N_2 (a trace impurity from the tank F_2).

(7) The next chamber is where an aliquot of O_2 gas is cached for use later in the extraction process. Open the stopcock leading to this chamber and the stopcock

that separates this aliquot storage volume from the rest of the line. Once gas has expanded into the aliquot volume, isolate this volume.

(8) Expand the O_2 gas into the conversion chamber for conversion to CO_2. Record the pressure on the glass ionization gauge. Insert the converter into a dewar of liquid N_2 for CO_2 freezeout. Turn the converter on until the graphite rod glows orange-red (T ~ 1200 °C). Continue while the reaction of O_2 to CO_2 proceeds to completion until pressure stops dropping (usually about 20 minutes). Record the final pressure (which is attributed to the tiny amount of N_2 left over).

(9) Open the stopcock to the stored aliquot to expand that O_2 into the travel path experienced by the sample thus far. This brings in a fresh supply of O_2 to react with any CO that may have formed during conversion (which can cause a spurious analysis, because of the large collision-frequency $^{18}O/^{16}O$ fractionation that accompanies reaction of O_2 with the hot carbon). Continue until pressure stops dropping (usually about five minutes).

(10) Pump the tiny amounts of non-condensable gas (N_2) away through the clean pump until pressure drops to its ambient vacuum level (about one minute).

(11) Isolate the segment of the line leading from the converter to the freezing finger at the manometer. Transport the CO_2 gas from the converter to this freezing finger by inserting a dewar of liquid nitrogen into the freezing finger and removing the dewar that is on the converter. Wait until pressure drops to zero. Isolate the manometer volume.

(12) Replace the liquid N_2 dewar with a dewar filled with an ethanol-dry-ice slush. The CO_2 gas expands into the manometer. Record the pressure difference between the two sides of the manometer and calculate the yield.

(13) Prepare for gas clean-up by opening the circulatory pathway through an Hg-diffusion pump. Expand the sample gas into this volume and allow it to circulate for about five minutes. This insures that all traces of reactive gases (F_2, Br_2, etc.) are removed, so they do not contaminate the mass spectrometer.

(14) Freeze sample down into the sample tube. This completes the extraction process and the sample gas is ready for analysis in the mass spectrometer.

A.1.3 The Caltech Rose Quartz Laboratory Standard

A Rose Quartz standard was run with every manifold of samples. This coarse- to medium-grained, isotopically homogeneous quartz standard is used to determine the analytical precision of the experimental apparatus and to normalize the oxygen isotope data from the samples run in each manifold. The accepted $\delta^{18}O$ value of this standard is +8.45 relative to Standard Mean Ocean Water, based on 40 years of analyses at Caltech. The NBS-28 quartz standard has $\delta^{18}O$ = +9.60 on this scale, based on hundreds of analyses that have been compared to Rose Quartz. Samples of unknown material were loaded into the vacuum line only when analytical precision better than 0.2‰ was assured, based on the Rose Quartz standard (see Appendix B). $\delta^{18}O$ values from analyses of Caltech Rose Quartz on the McKinney-Nier mass spectrometer are shown in Table B.1 and analyses of this standard on the Finnegan 252 mass spectrometer are shown in Table B.2.

A.1.4 Maintenance of the Extraction Line

Numerous maintenance procedures are followed to insure the reliable operation of this system. The Teflon ferrules in the flanges that seal the reaction vessels are replaced every five manifolds. Once a year, the bellows seats of the Nupro values need replacement. Stopcock grease needs replacement and cleaning every three months. Pump oil is changed once a year. Under the conditions of nearly continuous use, KBr was replaced every three years. Graphite rods for the CO_2 conversion chamber typically last 20 manifolds (*i.e.*, 120 samples). Waste bromine is removed from all traps once a week.

The reaction vessels are cleaned every 20 manifolds by sanding and polishing the insides with emery paper to insure the removal of absolutely all fluoride residue. Vessels are then rinsed with distilled water. This is followed up with drying using acetone. The manifold is then loaded onto the extraction line, pumped out, and baked out overnight and reacted with aliquots of waste F_2 at 550 °C to remove hydrous phases. Manifolds of Caltech Rose Quartz standards are then run until reproducibility reaches acceptable levels (usually one or two manifolds).

A.2 $^{18}O/^{16}O$ and $^{13}C/^{12}C$ Analytical Procedures for Carbonate Samples

Carbon dioxide was extracted from carbonates using the H_3PO_4 technique of McCrea (1950). The oxygen isotope composition of this CO_2 gas was corrected using the Calcite-CO_2 fractionation factor of 1.01008 for reaction at 25 °C (Sharma and Clayton, 1965).

Sample loading is a one day process. A glass reaction vessel having a stopcock valve and two lower compartments is utilized in carbonate extractions. Two ml of H_3PO_4 is loaded into one of the lower compartments with a pipet. A 10-25 mg powdered sample is loaded into the other compartment. The reaction vessel is attached to the vacuum line and the back seats of the stopcocks are opened for pumping to vacuum. This configuration is pumped on for two hours. The stopcock seats are then isolated, and one at a time, the reaction chambers are slowly opened to vacuum while taking care not to disturb the powder. The reaction chambers are pumped to vacuum (at least two hours). Upon the attainment of vacuum, the reaction vessels are closed, removed from the line, and set into a metal basket.

The reaction vessels are placed in a constant temperature water bath set at 25 °C, with care taken not to tip the vessels, preventing premature reaction. Once temperature has settled at 25 °C, each vessel is tipped such that the acid moves into the compartment containing the sample. Once the acid and sample meet, the reaction vessel is immediately placed into the water bath. Samples are left to react overnight. The next morning, the reaction vessels are removed from the bath, dried off, and attached to the extraction line along with an equal number of sample tubes. The line is pumped down to vacuum (two hours).

The extraction procedure for carbonates is much simpler than the one previously described for silicates. Once vacuum is reached, all reaction vessels and sample tubes are closed off. For each sample, check the vacuum in the stopcock seat. A liquid N_2 dewar is placed on a glass "U"-tube and the extraction line is isolated from the pump. The reaction vessel is opened and the CO_2 is frozen in the trap (allow five minutes to ensure complete freezedown). Once freezedown is complete, close the stopcock of the reaction vessel and insert an ethanol-dry ice bath onto the "U"-tube; this traps any unwanted water that may have been released during the acid reaction. The sample gas is next frozen down into the manometer freezing finger, noncondensables are pumped away, and the yield is measured on the manometer. This is followed by the collection of the CO_2 into the sample tube for mass spectrometry. The final step is the pumping away of phases left frozen in the ethanol-dry ice bath.

A.3 Standards and Mass Spectrometry

A.3.1 The McKinney-Nier Mass Spectrometer

Mass spectrometry was done on both a McKinney-Nier, 60° sector, double-collecting mass spectrometer and a Finnegan MAT 252 mass spectrometer. These data are presented in the standard form (Craig, 1957):

$$(1) \qquad \delta^{18}O_{sample} = \left[\frac{R_{sample} - R_{s\tan dard}}{R_{s\tan dard}}\right] \times 1000$$

where

$$(2) \qquad R_{sample} = \left(\frac{^{18}O}{^{16}O}\right)_{sample}$$

$$(3) \qquad R_{s\tan dard} = \left(\frac{^{18}O}{^{16}O}\right)_{s\tan dard}$$

The standard is Mean Ocean Water (SMOW) as defined by Craig (1961). Analyses of CO_2 done on the McKinney-Nier mass spectrometer were analyzed relative to the working standard, which is Harding Iceland Spar (HIS) carbon dioxide reference gas. These analyses were then corrected to $\delta^{18}O_{SMOW}$ by the following equation:

$$(4) \qquad \delta^{18}O(SMOW)_{sample} = \left[\delta^{18}O(HIS)_{sample} - \delta^{18}O(HIS)_{RQS}\right] \times A + B$$

where:

$$(5) \qquad A = (1.02162) \times \left(1 + \frac{Background}{2520}\right)$$

$$(6) \qquad B = +8.45‰$$

The fractionation factor between the HIS and SMOW standards is the first term in equation 6 (1.02162). The second factor taken into account is the background CO_2 signal in the source of the mass spectrometer and the leakage between the sample and reference gas inlet valves; this background is measured at the end of the mass spectrometer analysis

Figure A.1 -- Plot of Caltech Rose Quartz mass spectrometer $\delta^{18}O$ analyses, comparing the Finnegan MAT-252 and McKinney-Nier instruments. The $\delta^{18}O$ values for the McKinney-Nier mass spectrometer are relative to the Harding Iceland Spar operating standard while those of the Finnegan are relative to SMOW. The linear best curve fit is shown along with the equation corresponding to it. Rose Quartz $\delta^{18}O(SMOW) = +8.45$ when $\delta^{18}O(HIS) = -13.50$, the average Rose Quartz $\delta^{18}O$ of samples analyzed by the McKinney-Nier mass spectrometer.

Figure A.1 Mass Spectrometer Comparison

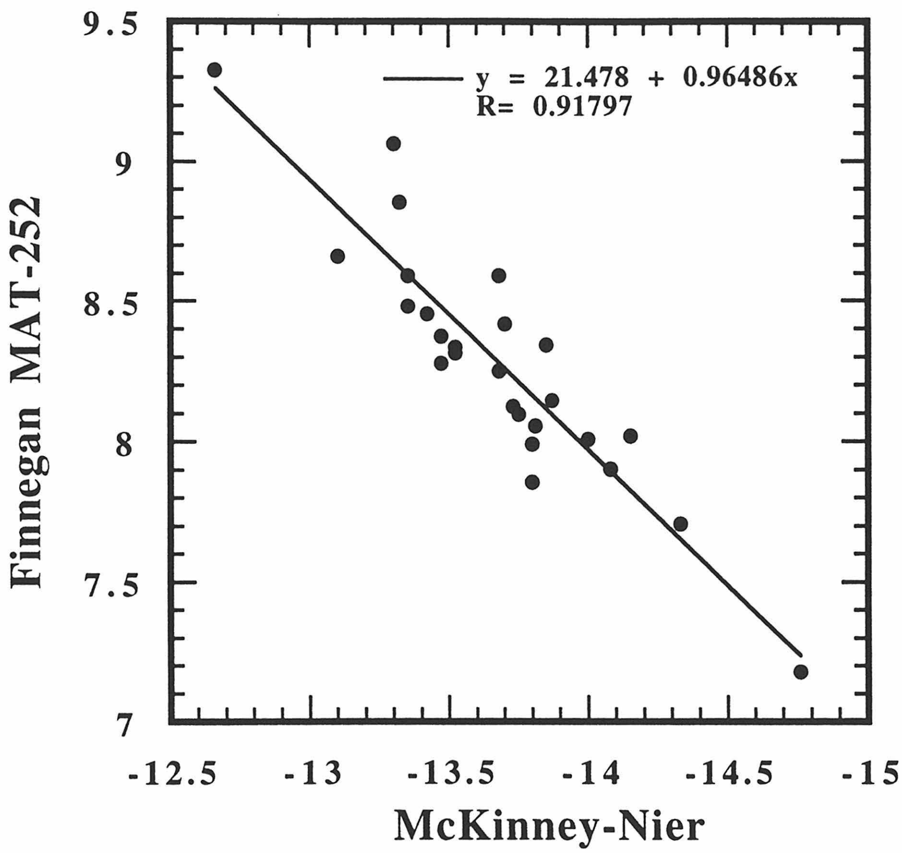

for each sample. Equation 6 is the accepted $\delta^{18}O(SMOW)$ value for the Caltech Rose Quartz standard CO_2.

A.3.2 The Finnegan MAT 252 Mass Spectrometer

The Finnegan MAT 252 mass spectrometer became operational during the fall of 1992. I played a role in calibrating the standard gas to Caltech Rose Quartz by comparing analyses on the Finnegan mass spectrometer to those performed on the McKinney-Nier machine. Up to December, 1995, the working CO_2 gas standard employed by the Finnegan MAT-252 was the OZTECH® gas #CALT-286C with $\delta^{18}O(SMOW) = +42.79$, $\delta^{18}O(PDB) = +1.06$, and $\delta^{13}C(PDB) = -30.08$. In December, 1995, the working standard became OZTECH® gas #CALT-513C with $\delta^{18}O(SMOW) = +14.90$, $\delta^{18}O(PDB) = -25.71$, and $\delta^{13}C(PDB) = -36.44$. Upon loading, each aliquot of mass spectrometer standard gas was checked for accuracy versus CO_2 from the Harding Iceland Spar standard.

The comparison between analyses of the Rose Quartz standard on the two mass spectrometers is shown on Figure A.1; this was done to calibrate results from the two mass spectrometers. The variations in the measured $\delta^{18}O$ values of the Rose Quartz standard have two sources: (1) the vacuum extraction system was having problems at that time, resulting in the overall ~2‰ variation in Rose Quartz $\delta^{18}O$, (2) variation in $^{18}O/^{16}O$ during the lifetime of HIS and OZTECH gas standard aliquots, a variation estimated to be about 0.10‰, and (3) the analytical precision provided by the mass spectrometer, ~ 0.05‰ for the Finnegan and ~0.10‰ for the McKinney-Nier instrument. It was found that the Rose Quartz $\delta^{18}O(HIS)$ value that corresponds to $\delta^{18}O = +8.45$ is -13.50 (Figure A.1). This value is within analytical error of the overall average Rose Quartz $\delta^{18}O(HIS)$ value (-13.55) for standard analyses with close to 100% extraction yield. The conversion of the Rose Quartz $\delta^{18}O$ value from the HIS standard to OZTECH CALT-286C standard utilized the following equation:

$$\text{(7)} \qquad \delta_{RQS-OZTECH} = \left[\left(\frac{\delta_{HIS-OZTECH}}{10^3} \right) \left(\frac{\delta_{RQS-HIS}}{10^3} \right) - 1 \right] \times 10^3$$

yielding $\delta_{RQS-OZTECH} = -34.38$ for $\delta_{RQS-HIS} = -13.50$ and $\delta_{HIS-OZTECH} = -21.17$; this gives a Rose Quartz $\delta^{18}O$(SMOW) value of +8.41, a value well within the analytical precision of our instruments.

A.4 The Caltech Oxygen Isotope Laser Extraction System

A.4.1 Introduction – Laser-Based Techniques for Silicate Oxygen Isotope Analyses

Recent advances in the development of laser ablation techniques for stable isotopes allow for reliable, precise, and accurate oxygen isotope analyses of samples as small as 0.1 mg (Sharp, 1990; Elsenheimer and Valley, 1992; Mattey and Macpherson, 1993; Rumble and Hoering, 1994; Wiechert and Hoefs, 1995). This increase in spatial resolution provides the capability of investigating processes (*e.g.*, diffusive exchange, zoning) that affect petrologic systems on a microscopic scale. This new analytical tool allows for routine, precise, and accurate oxygen isotope analyses of minerals resistant to conventional techniques (*e.g.*, garnet, olivine). These laser techniques have also demonstrated potential for investigating low-temperature biogenic and geologic processes, by allowing the microsampling of carbonate and phosphate materials (Smalley et al., 1989; Powell and Kyser, 1991).

Many problems remain to be solved before these laser-assisted techniques reach their full potential. The most pressing problem is the fractionation of oxygen isotopes during in situ analyses due to partial fluorination and oxygen diffusion occurring at the boundaries of the reaction zone (Sharp, 1992; Elsenheimer and Valley, 1992). Also, hydrous, fine-grained, and reactive minerals may undergo partial fluorination during reaction chamber preparation and while the preceding samples are being processed through the system. Except at Caltech, virtually all laser-assisted silicate oxygen isotope extraction systems elsewhere in the world use BrF_5 or ClF_3 as the fluorinating reagent, adding much complexity and uncertainty to the chemical processes active during the lasing process, a possible source of $^{18}O/^{16}O$ fractionation.

To try to alleviate some of these problems, a laser-assisted fluorination system for silicate oxygen isotope analyses was constructed at Caltech. This system utilizes F_2 gas as a reagent. Fluorine has numerous advantages over BrF_5 for this purpose: (1) The equilibrium vapor pressure of F_2 at –195 °C (liquid N_2 temperture) is 220 torr; BrF_5 is completely frozen at this low temperature. (2) The chemical processes active during the F_2 lasing process are much simpler and better understood than those involving BrF_5. Problems with $^{18}O/^{16}O$ fractionations due to partial reaction and oxygen diffusion during F_2 reactions in Ni vessels are known to be much less serious than those using BrF_5. Thus in situ laser analysis of silicates conceivably might be solved by the simpler chemistry involving F_2 reactions during the lasing process. The low freezing temperature of F_2 makes it possible to operate at very low temperatures (*e.g.*, liquid N_2), effectively retarding problems of partial reaction between the fluorinating agent and hydrous minerals during preliminary sample treatments. This is not possible with BrF_5 because of its relatively high freezing temperature.

The laser-assisted extraction technique is similar to the previously described conventional technique, but the Ni reaction vessel and exterior-heated resistance furnace is replaced with the laser as an internal heat source. Thus, the walls of the reaction chamber remain at room temperature. A 10 watt CO_2 laser beam focusing system, with attached video monitor and microscope, using a 10.6 μm wavelength, was purchased from Merchantek® to serve as the energy source in this system. The frequency of the principal

Si-O stretching in the SiO_4 tetrahedron is similar to that of CO_2-laser radiation; thus the energy transmitted by the laser is a highly efficient means of absorption heating of silicate materials. The beam diameter of most CO_2 lasers is 20-50 μm, providing excellent spatial resolution.

A.4.2 Design and Construction

Design and construction of the Caltech Oxygen Isotope Laser Extraction system with Dr. Michael Palin of the Australian National University and Professor Taylor took place between October, 1994, and February, 1995. The record of all components purchased for this system are held at Caltech by Professor Hugh P. Taylor, Jr. A scaled cartoon of the clean side of the laser extraction system vacuum line is shown on Figure A.2.

This system was designed for the greatest possible flexibility: (1) It is set up to utilize either F_2 or BrF_5 as oxidizing agent, allowing for comparison of results from these two reagents. (2) A pathway is available that allows gas to bypass the CO_2 converter, and a freezing finger is available for a molecular seive for the direct collection of O_2 gas for mass spectrometry (avoiding fractionation problems in the CO_2 converter for very small samples). (3) A port is available for the attachment of a small manifold of Nickel reaction vessels, allowing for a direct comparison between conventional and laser $\delta^{18}O$ values extracted from the same vacuum system. (4) The sample collection port is designed to either collect the sample in a sealed glass tube, or, in the future, to allow for direct introduction into the mass spectrometer inlet.

The vacuum system incorporated numerous other innovations designed for versatility, efficiency, and clean operation. The main components of the glass portion of the line are easily removable for cleaning. All parts of the line encountered by the sample

Figure A.2 -- The rack plan of the vacuum system for the Caltech Oxygen Isotope Laser Extraction System. The metal part of the line is shown in the center, whereas the glass line is on the left. This drawing is to scale with dimensions as shown.

Figure A.2 COILES Rack Plan

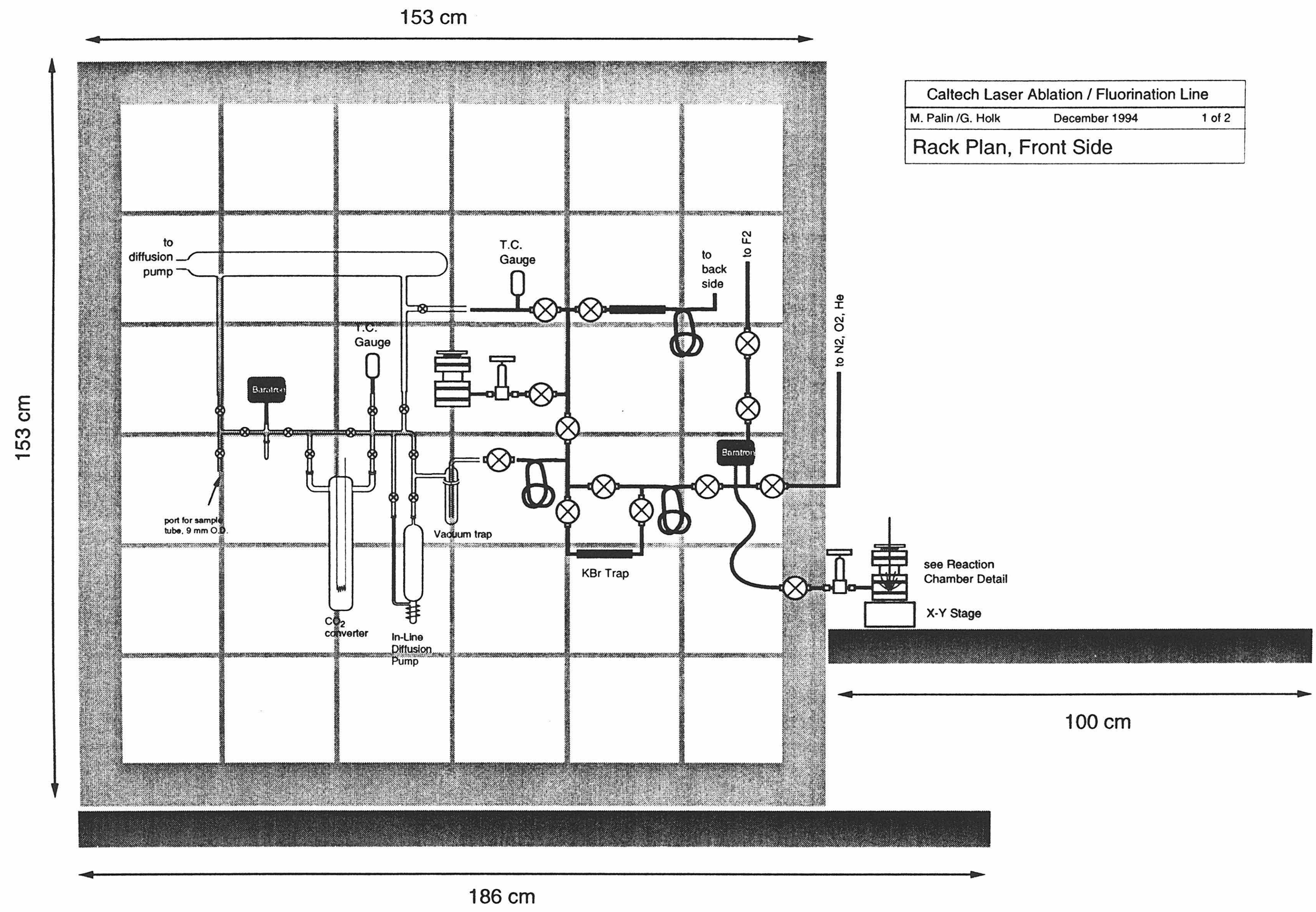

gases are greaseless, thus reducing grease buildup and potential contamination. The KBr chamber is easily removed and replacable, reducing downtime in the event of KBr exhaustion. Snap flow valves are employed on the cooling system in order to isolate parts of this system during their removal from the line without compromising other parts of the line. An extra port for a reaction chamber is included in the metal part of the line, allowing for the preparation of one set of samples while the previous set is still being worked on. A 250 ml fluorine storage volume is incorporated into the metal line; it serves two purposes, as an expansion volume in the event the line gets overpressured with F_2, and as a storage volume for clean F_2 during times of heavy use, providing for continuous use over an entire set of 40 samples.

A reaction chamber was constructed using stainless steel components available from MDC Corporation. This reaction chamber is mounted onto X-Y-Z translation stages that are operated with a joystick controller. A flexible stainless steel tube connects the reaction chamber to the extraction line. This chamber has an opening in the top through which samples are loaded. An optical-grade BaF_2 window is mounted onto a Kelrez® O-ring to insure a good seal. BaF_2 is a material that does not react with F_2, but still transmits CO_2 laser radiation and is optically transparent. The lasing process is observed either with a binocular microscope focused on the sample through the window aperture, and/or on a video monitor connected to the microscope system.

A.4.3 The Fluorine Purification System

Commercially available F_2 gas typically has trace amounts of impurities, of which about 0.3% is O_2. An O_2 blank of this size introduces much uncertainty to the measured $\delta^{18}O$ value of the material being analyzed. We have eliminated this contamination by designing and constructing an on-line fluorine purification system using a Ni reaction vessel and the method of Asprey (1966). This F_2 purification system operates by the following oxidation-reduction reaction:

$$(8) \qquad 2[K_2NiF_6 \cdot KF]\ (s) = 2K_3NiF_6 + F_2\ (g).$$

Equilibrium for this reaction lies to the right at high temperature (25 atm at 400 °C) and is to the left at lower temperature (~ 0.1 atm at 250 °C).

The $K_2NiF_6 \cdot KF$ salt is a very fine powder, and much care must be taken to prevent the escape of this compound into other portions of the extraction apparatus and to ensure efficient delivery of fluorine to the compound. A series of three 1 μm frits are placed between the purification system and the extraction line to keep this powder from entering the line. This component is attached via a VCR fitting, making it possible to attach other components (*i.e.*, conventional reaction vessels) to the line through this port. Efficient fluorine delivery is provided by the placement of a series of four Ni tubes (I.D. = 1/16", O.D. = 1/8") containing 1/16" diameter holes with hole spacing decreasing downward (see Figure A.3). These four tubes are held in place by a Monel capping disk. This apparatus is placed in the Ni reaction vessel and, to prevent contamination, the $K_2NiF_6 \cdot KF$ salt is loaded into a prefluorinated Ni reaction vessel in the dry box described in Section A.1.1 above. The compound in its non-hydrated form is pinkish-violet; it turns a deeper violet color as reaction (8) proceeds to the right.

The purification apparatus is attached to the extraction line and pumped to vacuum at room temperature. The metal part of the line is isolated from the pump and the laser reaction chamber. A dry ice-ethanol bath (–115 °C) is inserted over the metal freezing traps to collect contaminants that are driven off from the $K_2NiF_6 \cdot KF$ compound upon heating. The reaction vessel is heated to 400 °C until pressure > 1000 torr. Then the temperature is lowered to 250 °C to recharge the compound with F_2. Once pressure stops dropping (usually at 100 torr) the temperature is decreased to 225 °C and the non-condensable gases are pumped away. Then, one isolates the purification system and measures the pressure of the gases unfrozen in the freezing traps (mostly HF); these are then pumped away. These steps are repeated until there are no measureable amounts of gas frozen down in the traps. This system routinely produces 99.998 molar % F_2 gas reagent, and 25 grams of this compound is capable of supplying F_2 for 15 analyses each day. This system has been operational for over a year without an observable decrease in efficiency or gas purity. The standard operating procedure followed during the daily operation of the laser system is as follows:

Fluorine gas is usually purified overnight prior to each operating day. First, the purification vessel is set at 250 °C and 3 atm of F_2 is introduced into the metal part of the line. Make sure the reaction chamber is isolated from this part of the line and the large F_2-bearing volume is closed. Return in an hour to check the pressure. If the pressure is below 400 torr, load 3 atm into the system and leave overnight. In the morning, reduce the temperature to 225 °C. Open the large volume to reduce the F_2 pressure in the line, isolate this volume and slowly pump away all non-condensibles through the waste KBr and waste pump. Pump the metal side of the line to vacuum and isolate the purification vessel. Allow the vessel to heat up to 350 °C while the line pumps to vacuum through the clean side. Pure F_2 is ready for delivery to the reaction chamber once vacuum is reached.

A.4.4 Operating Procedure

The routine operation of the laser system can be compartmentalized into fluorine preparation, sample loading and preparation, and sample lasing and gas processing. These operations are discussed separately below.

Figure A.3 -- A schematic drawing of the 4 Ni tubes (1/8" O.D., 5" in length) embedded in a 9/16" diameter monel cap. These 4 Ni tubes contain numerous 1/16" diameter holes, as shown. This apparatus is inserted into a large aliquot (~25g) of the powdered $K_2NiF_6{\cdot}KF$ salt that has been placed in a standard Ni reaction vessel, in order to insure sufficient permeability and porosity so that F_2 gas can readily react with, and be released by, the compound. A threaded rod is inserted into the center of the disk in order to enable the placement of this assembly into the Ni reaction vessel.

Figure A.4 -- Scaled drawing of the 20-sample capacity Monel sample holder (a cylindrical plate). Dimensions are shown. The threaded hole in the center of the plate allows for the insertion and removal of a threaded metal rod; this allows for the placing of this plate onto the base of the reaction chamber through the window aperture, reducing the likelihood of contamination during loading.

Figure A.3 Fluorine Purification System

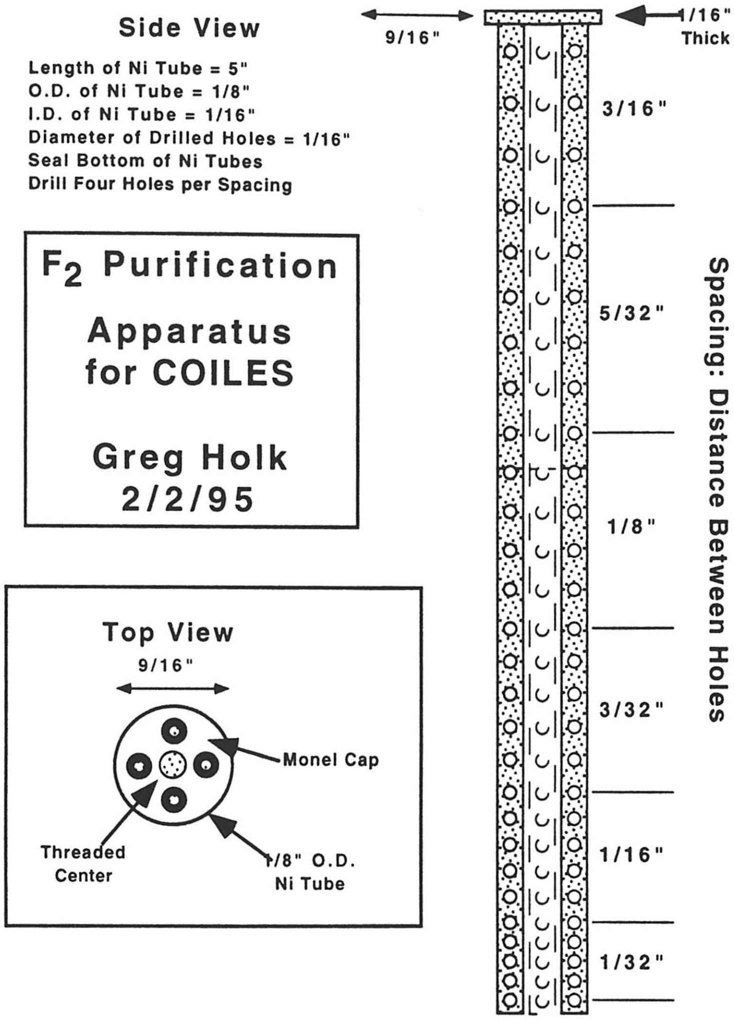

Figure A.4 Sample Holder

COILES
Caltech Oxygen Isotope Laser Extraction System
Sample Holder Schematic 1/27/95
Greg Holk

Thickness of Plate = 0.25 inch
Depth of Holes = 0.18 inch
Diameter of Holes = 0.12 inch
Diameter of Flat Bottom of Holes = 0.04 inch
Spacing Between Holes = 0.06 inch
Threaded Hole in Center of Plate

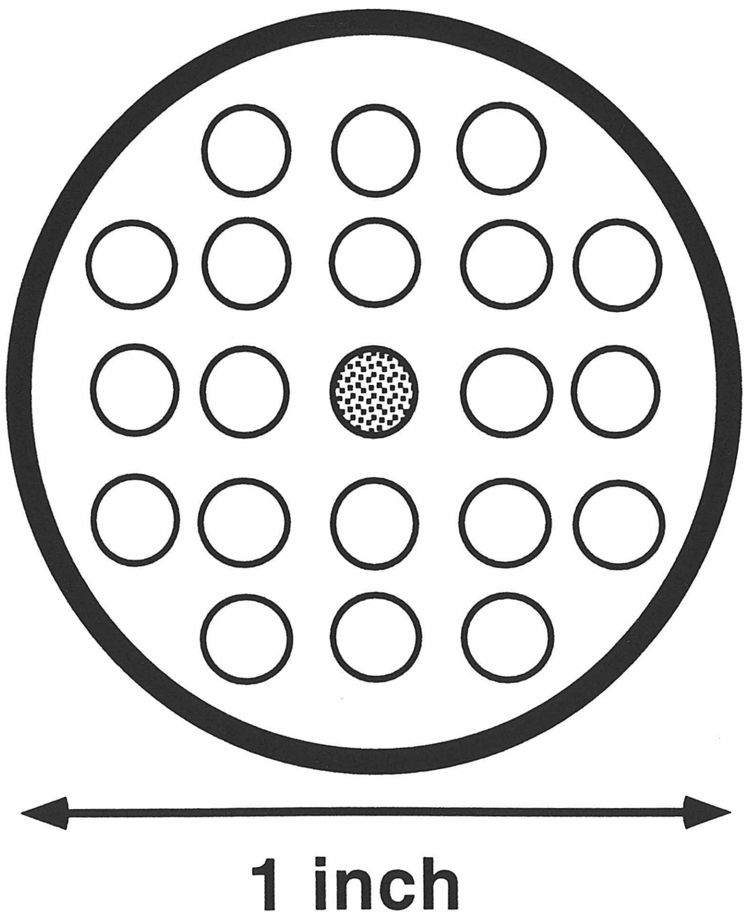

Weighed samples (0.8-2.0 mg) are loaded into the sample holder (see Figure A.4). The sample holder is inserted into the reaction chamber with a removable rod inserted into the threaded center hole. Dry N_2 gas is circulated through the line and kept at pressure >1 atm during the time the reaction chamber is open to the outside. The BaF_2 window is placed onto the opening and centered, and the dry N_2 is closed off from the line. Then that part of the line involved in loading is immediately brought to pressure < 1 atm to seal-off the reaction chamber from the outside. Pumping to vacuum through the waste side commences immediately and the belt furnace encasing the reaction chamber is turned up to 50 $^{\circ}$C to drive off contaminants that may have entered the reaction chamber during loading. After 15 minutes, those parts of the line are isolated and 100 torr F_2 is introduced into them. The line is heated with a heating gun and F_2 is pumped away immediately through the waste pump. This step is repeated, but F_2 is kept in the line for 15 minutes during the second treatment. Once vacuum is reached following the second treatment, the reaction chamber furnace is turned off and the system is opened to high vacuum and pumped for an hour. The reaction chamber is then loaded with 100 torr F_2 and isolated from the rest of the line (very important, see above). The fluorine purification procedure is set up and left overnight (see above).

The line is ready for lasing and sample gas processing once the line is pumped to vacuum and the fluorine purification apparatus is ready. Insert liquid N_2 dewars onto the two traps downstream of the KBr and the trap immediately upstream of it. Turn on the Hg-diffusion pump. The total time to lase and prepare a sample for the mass spectrometer is about 30 minutes. The procedure is as follows:

(1) 350 torr of F_2 is loaded into the line volume containing the metal-side Baratron capacitance manometer.

(2) A dry ice-ethanol bath is inserted onto the freezing trap just upstream of the Baratron, and the pressure is recorded to measure any possible contaminants.

(3) The reaction chamber is opened to the volume containing F_2 and a liquid N_2 bath replaces the dry-ice-ethanol bath. The pressure (~ 100 torr) is measured once it equilibrates. This purpose of putting this trap in liquid nitrogen is two-fold: (a) to freeze out gaseous SiF_4 reaction products during lasing, and (b) to guarantee a net movement of gas into the vacuum system in the event of BaF_2 window breakage during laser fluorination (this prevents the release of F_2 gas into the laboratory).

(4) Lasing begins with the laser optics focused to maximize the beam size on the sample while the microscope optics are still in focus. Laser intensity is set to the level at which fluorination of the sample begins, and is then gradually turned up as fluoride reaction products accumulate in the sample well. The reaction is complete when the sample no longer glows red (this ranges from 90 seconds to 5 minutes) with the laser turned up to its highest level (10 watts). Measure the pressure on the Baratron.

(5) Close all valves between the sample and the converter. Sequentially crack the valves leading into and out of the KBr furnace. F_2 begins to react with the KBr and Br_2 starts freezes into the traps upstream and downstream of the KBr. Very slowly, sequentially open all valves upstream of the KBr. When pressure stops dropping, record it and crack the valve leading to the first glass trap. Allow the O_2 + Br_2 gas to diffuse into this volume. Next, open the valve leading to the small Hg-diffusion pump to react out fluorine missed by the KBr with the hot Hg-vapor. Once this step is complete, the O_2 sample is ready for conversion to CO_2.

(6) Expand gas into the converter, measure pressure, separate and isolate an aliquot of gas into the volume beside the converter, start the converter glowing red, and

insert a liquid N_2 trap over the converter. Adjust the converter such that the reaction proceeds slowly. Rapid conversion can result in CF_4 contamination because the sample gas is sent through the KBr too quickly. Once pressure stops dropping in the conversion chamber, completely open the valve immediately downstream of the KBr. As a precaution, bring the aliquot gas into the conversion chamber for reaction with any CO that may have formed during conversion. The conversion is complete when pressure drops to zero. Start pumping on the parts of the line seen by the sample thus far with a path that goes through the converter. Turn the converter off.

(7) Isolate a path leading from the converter to the manometer volume. Replace the liquid N_2 trap on the converter with a dry-ice-ethanol bath. Freeze the sample in the glass finger and isolate the manometer volume. Remove the trap and allow the sample to expand into the measuring volume as it rises to room temperature. Measure the pressure on the Baratron and calculate the yield. Freeze out the sample into a glass tube and seal. The sample is ready for mass spectrometry.

(8) Isolate the converter plus manometer volumes. Begin pumping on the rest of the line. Remove the dry-ice-ethanol trap from the converter and insert a liquid N_2 trap onto the manometer freezing finger. Once pressure drops to zero, isolate the manometer volume, heat that volume to room temperature and measure the pressure; this is a measure of the amounts of any contaminant (this should be very close to zero) contained in that sample. Open to the pump. The line is now ready to process the next sample.

A.4.5 Standards and Calibration

The precision and accuracy of this laser extraction system was calibrated using the familiar Caltech Rose Quartz standard (Table A.3), a garnet from the Gore Mountain locality in the Adirondack Mountains, New York (Table A.5), and an olivine taken from a large dunite xenolith from the Kaupulehu alkalic basalt flow formed during the 1801 eruption of Hualalai volcano, Hawaii (Table A.4). In these early analyses, a consistent shift of +0.4‰ was noted for Rose Quartz $\delta^{18}O$ ($\delta^{18}O$ = +8.72), the NBS-28 quartz standard ($\delta^{18}O$ = +10.0), and the Washington State University MM-1 quartz ($\delta^{18}O$ = +13.3) standard (see Figures A.5 and A.6); it was later found by comparing these data to conventional Rose Quartz analyses that this shift was caused by lowering of the $\delta^{18}O$ value of the OZCALT-286C mass spectrometer working standard of similar magnitude. All data have been corrected to account for this discrepancy. There is no observable difference in the $\delta^{18}O$ of analyses using F_2 from those using BrF_5. One conventional Rose Quartz analysis on this vacuum system has $\delta^{18}O$ (+8.73), indistinguishable from values obtained with the laser.

It has been shown that sample size can have an effect on laser-assisted $\delta^{18}O$ values with smaller samples having higher $\delta^{18}O$ values, probably due to problems involving the conversion to CO_2 or to absorption in the KBr reaction chamber. Experiments on samples of Hualalai olivine indicate that this shift to pronounced higher $\delta^{18}O$ values (up to 2‰) begins when sample size is less than 15 micromoles. This trend is apparently also true for the garnet and Rose Quartz laboratory standards (see Figure A.5); the shift between 15 and 10 micromoles is approximately 0.4‰. Thus, until these problems with micro samples can be ironed out, the optimum results from the standard operating procedure for this laser system are best obtained using samples larger than 10-15 micromoles (*i.e.*, > 0.5 mg).

Figure A.5 -- Sample size versus raw (*i.e.*, non-normalized) $\delta^{18}O$ values of Caltech Rose Quartz, Hualalai Olivine, Gore Mountain Garnet, NBS-28 Quartz, and the Washington State University quartz standard, as analyzed through May, 1995. During this period, there was a consistent upward shift of ~ 0.4‰ for these materials relative to their accepted $\delta^{18}O$ values. Note the slight increase (~0.3‰) in $\delta^{18}O$ with decreasing sample size.

Figure A.6 -- Sample yield versus raw (non-normalized) $\delta^{18}O$ for the samples shown. The effect of yield on $\delta^{18}O$ is minimal (~0.2‰) for this set of analyses. The uncertainty of the % yield term is > 5% because of the ±0.1 mg analytical precision of the analytical balance in use at that time.

Figure A.7 -- Plot comparing results on laboratory standards from Caltech and the University of Wisconsin silicate oxygen isotope laser fluorination systems. Data from Caltech were collected by 2 operaters whereas 11 operators were employed in Wisconsin analyses. Raw data from the Caltech Rose Quartz (N = 25) and the Hualalai olivine (N = 42) have a 1σ standard deviation of ±0.10‰ for the period 4/26/95 to 9/10/95. Hualalai olivine normalized to Caltech Rose Quartz $\delta^{18}O$ = +8.45 has $\delta^{18}O$ = +5.37 ± 0.06‰. Analyses of NBS-28 quartz (N = 65) and the Wisconsin UWG-2 garnet standard (N = 1081) have a 1σ standard deviation of ±0.20 and ±0.15, respectively (Valley et al., 1995).

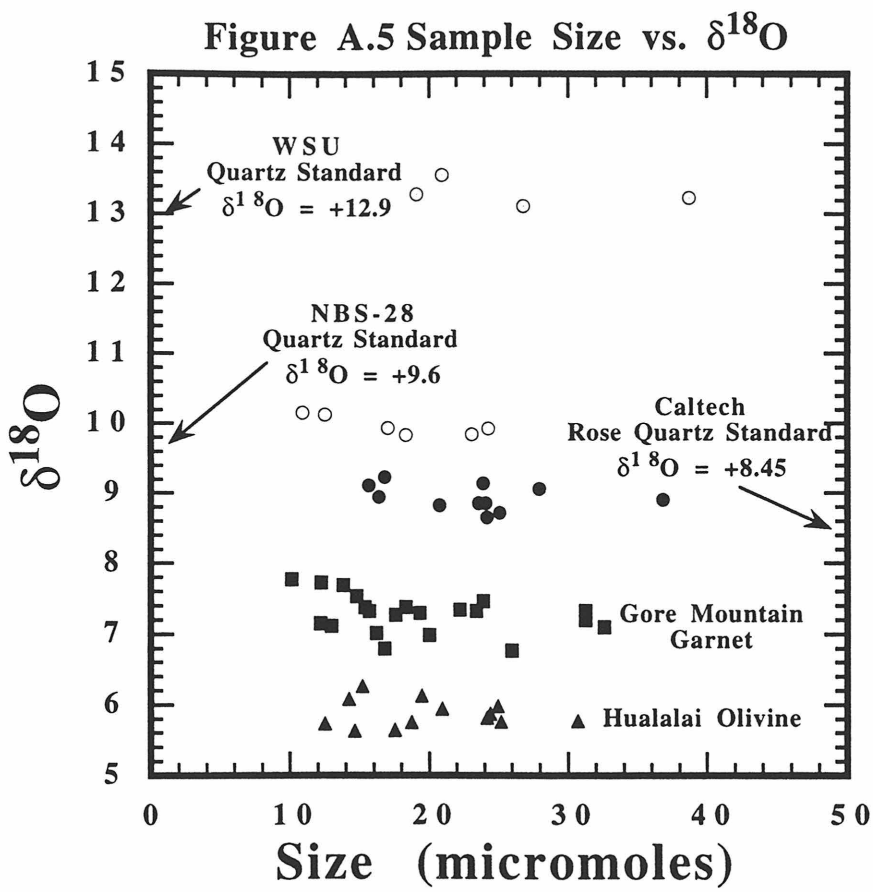
Figure A.5 Sample Size vs. δ18O
δ18O
Size (micromoles)
0
10
20
30
40
50
5
6
7
8
9
10
11
12
13
14
15
WSU
Quartz Standard
δ18O = +12.9
NBS-28
Quartz Standard
δ18O = +9.6
Caltech
Rose Quartz Standard
δ18O = +8.45
Gore Mountain
Garnet
Hualalai Olivine

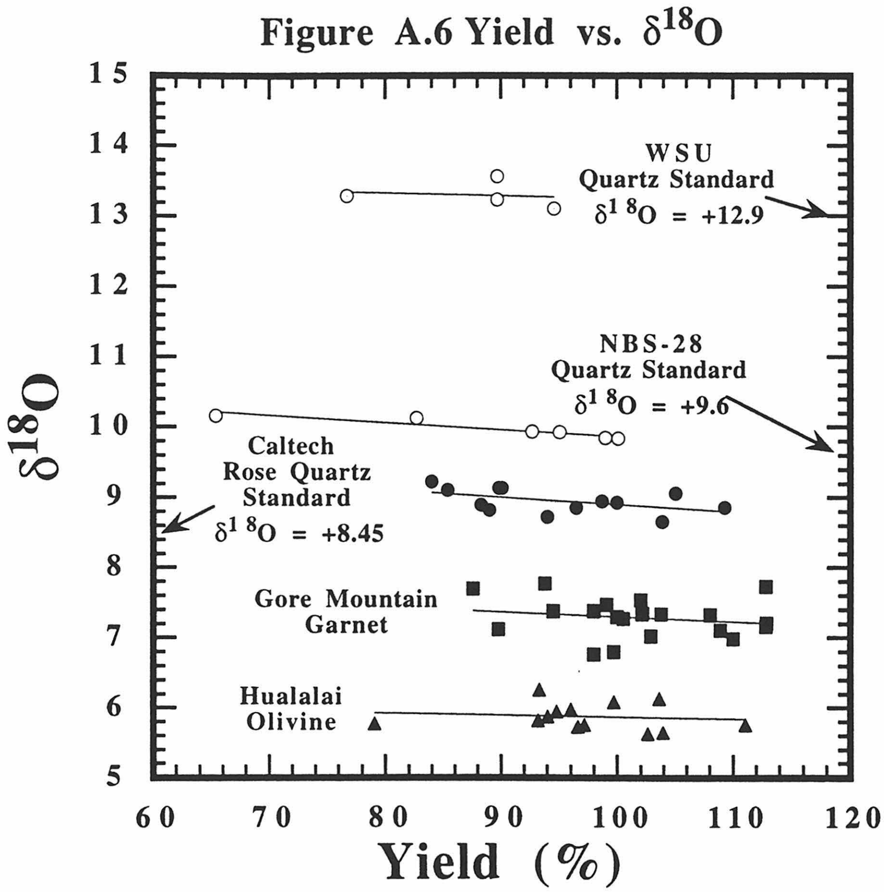
Figure A.6 Yield vs. δ18O
15
14
13
12
11
10
9
8
7
6
5
60
70
80
90
100
110
120
Yield (%)
δ18O
WSU
Quartz Standard
δ18O = +12.9
NBS-28
Quartz Standard
δ18O = +9.6
Caltech
Rose Quartz
Standard
δ18O = +8.45
Gore Mountain
Garnet
Hualalai
Olivine

Figure A.7 Comparison of Caltech Standards to Wisconsin Standards

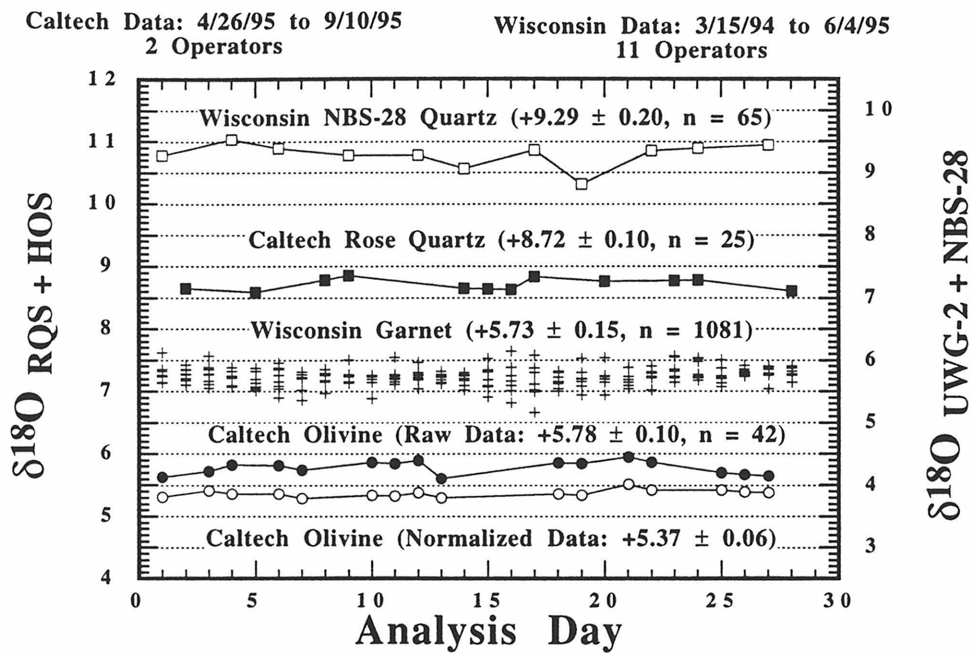

Sample yield appears to have a minimal effect on the analyzed $\delta^{18}O$ values from this laser system (see Figure A.6). Our data indicate no more than a +0.2‰ shift in $\delta^{18}O$ between 80% and 110% yield for Rose Quartz, Hualalai olivine, Gore Mountain garnet, NBS-28 quartz, and MM-1 quartz. It should be noted that at the time of this experiment, the analytical precision of the balance scale was ±0.1 mg, introducing an uncertainty of 5-10% in the yield calculation for these small samples (~1-3 mg). This contrasts with observed large downward shifts in $\delta^{18}O$ (1-2‰) with lowering yield for ClF_3 (Mattey and MacPherson, 1993) and BrF_5 (Kyser, 1995).

Figure A.7 is a comparison of data from laboratory standards from the Caltech and University of Wisconsin (Valley et al., 1995) oxygen isotope laser extraction systems. Raw, uncorrected oxygen isotope data from Caltech Rose Quartz (N = 25) and the Hualalai olivine (N = 42) have a 1σ standard deviation of ±0.10 for the period 4/26/95 to 9/10/95. The $\delta^{18}O$ of Hualalai olivine normalized to Rose Quartz ($\delta^{18}O$ = +8.45) is +5.37± 0.06‰; this value is well within the range of laser $\delta^{18}O$ values of olivine from mantle peridotite ($\delta^{18}O$ = +5.18 ± 0.28‰; Mattey et al., 1994). Hualalai olivine is *a priori* expected to be extremely homogeneous in ^{18}O because it is a cumulate phase crystallized in chemical and isotopic equilibrium with a basaltic melt at 1225-1350 °C (Bohrson and Clague, 1988), making this olivine an excellent candidate for a laboratory standard. To date, olivine from four different xenoliths have been analyzed and all data are homogeneous in $^{18}O/^{16}O$ at the scale of analytical precision. This contrasts with the UWG-2 garnet standard (Valley et al., 1995) which has an apparent ±0.15‰ reproducibility and NBS-28 quartz with a ±0.20‰ reproducibility. Crystallization of garnet is a slow process that takes place over a wide temperature range; this hampers its feasibility as a standard because there will be inherent variations in $^{18}O/^{16}O$ contained within a mineral having this history. This is confirmed by the large variation in the $\delta^{18}O$ (+7.32 ± 0.23‰) of the Gore Mountain garnet sample analyzed in the present study.

Appendix B. Tabulation of all Isotopic Standards Analyzed in the Present Study

TABLE B.1. $^{18}O/^{16}O$ DATA ON CALTECH ROSE QUARTZ ANALYZED ON THE MCKINNEY-NIER MASS SPECTROMETER

Sample #	$\delta^{18}O$	RV	Date Extracted
GH-127	-13.58	1	10/31/91
GH-128	-13.40	2	10/31/91
GH-129	-13.44	3	10/31/91
GH-130	-14.13	4	10/31/91
GH-131	-13.40	5	10/31/91
GH-132	-13.86	6	10/31/91
ave (127-132), 1σ std dev	−13.63 ± 0.30		
GH-137	-13.57	5	11/2/91
GH-142	-14.14	4	11/4/91
GH-148	-14.74	4	11/6/91
GH-153	-13.34	3	11/8/91
GH-162	-13.88	6	11/10/91
GH-164	-14.66	2	11/12/91
ave (137-164), 1σ std dev	−14.06 ± 0.57		
GH-169	-13.75	1	11/15/91
GH-171	-13.17	2	11/15/91
GH-171	-13.56	3	11/15/91
GH-173	-13.46	5	11/15/91
GH-174	-13.20	6	11/15/91
ave (169-174), 1σ std dev	−13.43 ± 0.25		
GH-175	-13.81	1	11/17/91
GH-176	-13.55	2	11/17/91
GH-177	-13.88	3	11/17/91
GH-178	-13.98	4	11/17/91
GH-179	-13.38	5	11/17/91
GH-180	-13.36	6	11/17/91
ave (175-180), 1σ std dev	−13.66 ± 0.27		
GH-185	-13.82	5	11/19/91
GH-187	-13.18	1	11/21/91
GH-188	-13.06	2	11/21/91
GH-189	-13.31	3	11/21/91
GH-190	-13.24	4	11/21/91
GH-191	-13.05	5	11/21/91
ave (187-191), 1σ std dev	−13.17 ± 0.11		
GH-196	-13.90	4	11/24/91
GH-201	-12.86	3	11/26/91
GH-210	-13.17	6	12/2/91
GH-215	-13.40	5	12/4/91
GH-217	-13.48	1	12/6/91
GH-224	-13.67	2	12/8/91
GH-231	-13.88	3	12/10/91
GH-238	-14.40	4	12/12/91
GH-245	-14.39	5	12/14/91
ave (196-245), 1σ std dev	−13.68 ± 0.52		
GH-265	-13.52	1	4/1/92
GH-266	-13.43	2	4/1/92
GH-267	-13.48	3	4/1/92
GH-268	-13.45	4	4/1/92
GH-269	-13.32	5	4/1/92
GH-270	-13.23	6	4/1/92
ave (265-270), 1σ std dev	−13.41 ± 0.11		

Sample #	$\delta^{18}O$	RV	Date Extracted
GH-273	-12.83	3	4/7/92
GH-278	-13.88	2	4/11/92
GH-285	-13.76	3	4/14/92
GH-286	-13.65	4	4/14/92
GH-293	-13.56	5	4/19/92
ave (273-293), 1σ std dev	−13.54 ± 0.41		
GH-295	-11.70	1	6/2/92
GH-296	-13.15	2	6/2/92
GH-297	-13.27	3	6/2/92
GH-298	-13.23	4	6/2/92
GH-299	-12.95	5	6/2/92
GH-300	-12.85	6	6/2/92
ave (296-300), 1σ std dev	−13.09 ± 0.18		
ave (295-300), 1σ std dev	−12.86 ± 0.59		
GH-301	-14.32	1	6/7/92
GH-302	-13.53	2	6/7/92
GH-303	-13.55	3	6/7/92
GH-304	-13.69	4	6/7/92
ave (300-304), 1σ std dev	−13.77 ± 0.37		
GH-307	-12.61	1	6/9/92
GH-311	-12.87	5	6/9/92
ave (307-311), 1σ std dev	−12.74 ± 0.18		
GH-313	-14.77	1	6/17/92
GH-314	-14.40	2	6/17/92
ave (313-314), 1σ std dev	−14.59 ± 0.26		
GH-370	-13.35	2	1/25/93
GH-371	-14.15	3	1/25/93
GH-372	-13.81	4	1/25/93
GH-373	-12.82	5	1/25/93
GH-374	-13.30	6	1/25/93
ave (370-374), 1σ std dev	−13.49 ± 0.51		
GH-375	-14.76	1	1/29/93
GH-376	-13.65	2	1/29/93
GH-377	-14.59	3	1/29/93
GH-378	-14.39	4	1/29/93
GH-379	-15.09	5	1/29/93
GH-380	-13.62	6	1/29/93
ave (375-380), 1σ std dev	−14.35 ± 0.60		
GH-381	-9.49	1	2/2/93
GH-382	-13.10	2	2/2/93
GH-383	-13.32	3	2/2/93
GH-384	-13.53	4	2/2/93
GH-385	-12.13	5	2/2/93
ave (382-385), 1σ std dev	−13.02 ± 0.62		
GH-387	-14.33	1	2/4/93
GH-388	-14.00	2	2/4/93
GH-389	-14.08	3	2/4/93
GH-390	-13.80	4	2/4/93
GH-391	-13.80	5	2/4/93
GH-392	-12.66	6	2/4/93
ave (387-392), 1σ std dev	−13.78 ± 0.58		

Sample #	$\delta^{18}O$	RV	Date Extracted
GH-393	-13.35	1	2/13/93
GH-394	-13.55	2	2/13/93
GH-395	-13.68	3	2/13/93
GH-396	-13.47	4	2/13/93
GH-397	-13.52	5	2/13/93
GH-398	-13.47	6	2/13/93
ave (393-398), 1σ std dev	−13.51 ± 0.11		
GH-399	-13.42	1	2/15/93
GH-401	-13.92	3	2/15/93
GH-405	-13.68	1	2/18/93
GH-406	-13.85	2	2/18/93
GH-411	-13.73	1	2/20/93
GH-414	-13.75	4	2/20/93
GH-421	-13.87	5	2/22/93
ave (399-421), 1σ std dev	−13.75 ± 0.17		
GH-429	-13.70	1	2/26/93
GH-430	-14.77	2	2/26/93
GH-432	-13.80	4	2/26/93
GH-433	-13.74	5	2/26/93
GH-434	-13.52	6	2/26/93
ave (429-434), 1σ std dev	−13.91 ± 0.49		
GH-495	-13.92	1	4/30/93
GH-496	-13.89	2	4/30/93
GH-497	-13.71	3	4/30/93
GH-498	-14.11	4	4/30/93
GH-499	-14.16	5	4/30/93
GH-500	-13.60	6	4/30/93
ave (495-500), 1σ std dev	−13.90 ± 0.22		
GH-544	-14.05	2	6/1/93
GH-545	-13.13	3	6/1/93
GH-546	-13.67	4	6/1/93
GH-547	-13.61	5	6/1/93
ave (544-547), 1σ std dev	−13.61 ± 0.38		
GH-549	-13.46	1	6/6/93
GH-550	-13.49	2	6/6/93
GH-551	-13.33	3	6/6/93
GH-552	-13.52	4	6/6/93
ave (549-552), 1σ std dev	−13.45 ± 0.08		
GH-623	-13.53	1	7/19/93
GH-624	-13.62	2	7/19/93
GH-625	-13.59	3	7/19/93
GH-626	-13.89	4	7/19/93
GH-627	-13.40	5	7/19/93
GH-628	-13.62	6	7/19/93
ave (623-628), 1σ std dev	−13.61 ± 0.16		
GH-630	-14.15	2	7/21/93
GH-635	-13.69	1	7/23/93
GH-642	-13.80	2	7/25/93
ave (630-642), 1σ std dev	−13.88 ± 0.24		
GJH-22	-13.69	4	12/6/93
GJH-29	-13.54	5	12/8/93
GJH-103	-13.82	3	2/7/94
GJH-105	-13.85	5	2/7/94
GJH-152	-13.89	3	3/29/94
GJH-159	-14.02	4	4/8/94
ave (22-159), 1σ std dev	−13.80 ± 0.17		

TABLE B.2. $^{18}O/^{16}O$ DATA ON CALTECH ROSE QUARTZ ANALYZED ON THE FINNEGAN MAT 252 MASS SPECTROMETER

Sample #	$\delta^{18}O$	$\delta^{13}C$	RV	Date Extracted
GH-370	8.48	-26.06	2	1/25/93
GH-371	8.02	-26.00	3	1/25/93
GH-372	8.05	-26.03	4	1/25/93
GH-373	8.59	-26.05	5	1/25/93
GH-374	9.06	-26.05	6	1/25/93
GH-375	7.17	-26.05	1	1/25/93
GH-382	8.66	-26.04	2	2/2/93
GH-383	8.85	-26.04	3	2/2/93
GH-385	9.63	-26.04	5	2/2/93
GH-387	7.71	-26.04	1	2/4/93
GH-388	8.01	-26.04	2	2/4/93
GH-390	7.99	-26.05	4	2/4/93
GH-391	7.86	-26.05	5	2/4/93
GH-389	7.90	-26.02	3	2/4/93
GH-392	9.33	-26.04	6	2/4/93
ave (370-392), 1σ std dev	8.36 ± 0.67	-26.04 ± 0.01		
GH-393	8.59	-26.10	1	2/13/93
GH-395	8.25	-26.01	3	2/13/93
GH-396	8.28	-26.01	4	2/13/93
GH-397	8.32	-26.07	5	2/13/93
GH-398	8.37	-26.05	6	2/13/93
GH-405	8.59	-26.08	1	2/18/93
GH-399	8.46	-26.06	1	2/15/93
GH-406	8.34	-26.03	2	2/18/93
GH-411	8.13	-26.03	1	2/20/93
GH-414	8.10	-25.99	4	2/20/93
GH-421	8.15	-26.18	5	2/22/93
GH-429	8.42	-26.18	1	2/26/93
GH-434	8.34	-26.22	6	2/26/93
ave (393-434), 1σ std dev	8.33 ± 0.16	-26.08 ± 0.07		
GH - 477	8.44	-26.20	1	4/7/93
GH - 478	8.01	-26.15	2	4/7/93
GH - 479	6.90	-26.12	3	4/7/93
GH - 480	6.37	-26.09	4	4/7/93
GH - 481	7.95	-26.05	5	4/7/93
GH - 482	8.63	-26.11	6	4/7/93
ave (477-482), 1σ std dev	7.72 ± 0.89	-26.12 ± 0.05		
GH - 483	10.76	-26.09	1	4/11/93
GH - 484	9.97	-26.10	2	4/11/93
GH - 485	8.90	-26.13	3	4/11/93
GH - 486	8.52	-26.07	4	4/11/93
GH - 487	8.50	-26.21	5	4/11/93
GH - 488	8.77	-26.11	6	4/11/93
ave (483-488), 1σ std dev	9.24 ± 0.92	-26.12 ± 0.05		
ave (477-488), 1σ std dev	8.48 ± 1.17	-26.12 ± 0.05		
GH - 489	9.72	-26.09	1	4/13/93
GH - 490	8.87	-26.11	2	4/13/93
GH - 491	8.88	-26.12	3	4/13/93
GH - 492	9.10	-26.11	4	4/13/93
GH - 493	9.05	-26.10	5	4/13/93
GH - 494	8.79	-26.12	6	4/13/93
ave (483-488), 1σ std dev	9.07 ± 0.34	-26.11 ± 0.01		
ave (477-488), 1σ std dev	8.67 ± 1.00	-26.12 ± 0.04		

Sample #	$\delta^{18}O$	$\delta^{13}C$	RV	Date Extracted
GH - 495	8.07	-26.17	1	4/30/93
GH - 496	8.11	-26.15	2	4/30/93
GH - 497	8.61	-26.10	3	4/30/93
GH - 498	8.15	-26.10	4	4/30/93
GH - 499	8.06	-26.11	5	4/30/93
GH - 500	8.54	-26.11	6	4/30/93
ave (495-500), 1σ std dev	8.26 ± 0.25	-26.12 ± 0.03		
ave (477-500), 1σ std dev	8.57 ± 0.89	-26.12 ± 0.04		
GH - 423	8.50	-26.13	1	5/2/93
GH - 502	8.48	-26.15	2	5/4/93
GH - 509	7.80	-26.13	3	5/7/93
GH - 516	8.50	-26.09	4	5/9/93
GH - 521	8.57	-26.05	3	5/12/93
GH - 525	7.98	-26.07	1	5/14/93
GH - 535	8.46	-26.09	5	5/16/93
ave (423-535), 1σ std dev	8.33 ± 0.30	-26.10 ± 0.04		
GH - 538	7.91	-26.07	2	5/30/93
GH - 539	8.06	-26.08	3	5/30/93
GH - 540	7.72	-26.07	4	5/30/93
GH - 541	7.98	-26.05	5	5/30/93
ave (538-541), 1σ std dev	7.92 ± 0.15	-26.07 ± 0.01		
GH - 543	8.35	-26.06	1	6/1/93
GH - 544	7.99	-26.13	2	6/1/93
GH - 545	8.12	-26.06	3	6/1/93
GH - 546	8.05	-26.07	4	6/1/93
GH - 547	8.20	-26.08	5	6/1/93
ave (543-547), 1σ std dev	8.14 ± 0.14	-26.08 ± 0.03		
ave (538-547), 1σ std dev	8.04 ± 0.18	-26.07 ± 0.02		
GH - 549	8.43	-26.25	1	6/6/93
GH - 550	8.53	-26.22	2	6/6/93
GH - 551	8.62	-26.20	3	6/6/93
GH - 552	8.23	-26.21	4	6/6/93
GH - 553	8.94	-26.19	5	6/7/93
GH - 554	9.03	-26.17	6	6/7/93
GH - 559	8.83	-26.18	5	6/9/93
GH - 560	8.00	-26.21	6	6/9/93
ave (549-560), 1σ std dev	8.58 ± 0.35	-26.20 ± 0.03		
GH - 561	8.26	-26.17	1	6/17/93
GH - 562	8.07	-26.15	2	6/17/93
GH - 563	7.82	-26.11	3	6/17/93
GH - 564	8.04	-26.12	4	6/17/93
GH - 565	7.81	-26.12	5	6/17/93
GH - 566	8.47	-26.14	6	6/17/93
ave (561-566), 1σ std dev	8.08 ± 0.26	-26.14 ± 0.02		
GH - 567	8.53	-26.14	1	6/21/93
GH - 568	8.39	-26.13	2	6/21/93
GH - 569	8.31	-26.13	3	6/21/93
GH - 570	8.22	-26.13	4	6/21/93
GH - 571	8.22	-26.11	5	6/21/93
GH - 572	8.35	-26.11	6	6/21/93
ave (567-572), 1σ std dev	8.34 ± 0.12	-26.13 ± 0.01		
GH - 590	8.42	-26.10	4	6/25/93
ave (567-590), 1σ std dev	8.35 ± 0.11	-26.12 ± 0.01		
				New converter

Sample #	$\delta^{18}O$	$\delta^{13}C$	RV	Date Extracted
GH - 594	7.97	-26.04	2	6/30/93
GH - 595	7.87	-26.02	3	6/30/93
GH - 596	7.62	-26.03	4	6/30/93
GH - 597	7.57	-26.05	5	6/30/93
GH - 598	7.85	-26.06	6	6/30/93
ave (594-598), 1σ std dev	7.78 ± 0.17	-26.04 ± 0.02		
GH - 599	8.14	-26.05	1	7/2/93
GH - 600	7.69	-26.05	2	7/2/93
GH - 602	8.10	-26.00	4	7/2/93
GH - 603	8.07	-25.98	5	7/2/93
ave (599-603), 1σ std dev	8.00 ± 0.21	-26.02 ± 0.04		
GH - 605	8.18	-26.02	1	7/5/93
GH - 606	8.16	-26.03	2	7/5/93
GH - 607	7.63	-26.03	3	7/5/93
GH - 608	8.19	-26.04	4	7/5/93
GH - 609	7.74	-26.02	5	7/5/93
GH - 610	8.08	-26.02	6	7/5/93
ave (605-610), 1σ std dev	8.00 ± 0.25	-26.03 ± 0.01		
GH - 611	8.18	-26.04	1	7/14/93
GH - 612	7.77	-26.05	2	7/14/93
GH - 613	7.88	-26.05	3	7/14/93
GH - 614	7.84	-26.07	4	7/14/93
GH - 615	6.81	-26.05	5	7/14/93
GH - 616	6.78	-26.14	6	7/14/93
ave (611-616), 1σ std dev	7.54 ± 0.60	-26.07 ± 0.04		
GH - 617	7.61	-26.10	1	7/15/93
GH - 618	7.76	-26.04	2	7/15/93
GH - 619	8.19	-26.06	3	7/15/93
GH - 620	8.17	-26.07	4	7/15/93
GH - 622	8.59	-26.08	6	7/15/93
ave (617-622), 1σ std dev	8.06 ± 0.39	-26.07 ± 0.02		
GH - 623	8.71	-26.04	1	7/19/93
GH - 624	8.80	-26.02	2	7/19/93
GH - 625	8.72	-26.04	3	7/19/93
GH - 626	8.30	-26.04	4	7/19/93
GH - 627	8.79	-26.04	5	7/19/93
GH - 628	8.89	-26.04	6	7/19/93
ave (623-628), 1σ std dev	8.70 ± 0.21	-26.04 ± 0.01		
GH - 630	8.21	-26.17	2	7/21/93
GH - 635	8.50	-26.19	1	7/23/93
GH - 642	8.59	-26.14	2	7/25/93
GH - 650	8.11	-26.13	4	7/28/93
GH - 655	8.81	-26.14	3	7/30/93
ave (630-655), 1σ std dev	8.44 ± 0.28	-26.15 ± 0.03		
GH - 659	9.10	-26.11	1	8/26/93
GH - 660	8.93	-26.12	2	8/26/93
GH - 661	8.81	-26.12	3	8/26/93
GH - 662	9.03	-26.15	4	8/26/93
GH - 663	8.50	-26.11	5	8/26/93
GH - 664	8.85	-26.10	6	8/26/93
ave (659-664), 1σ std dev	8.87 ± 0.21	-26.12 ± 0.02		
GH - 665	7.87	-26.23	1	8/28/93
GH - 666	7.71	-26.12	2	8/28/93
GH - 667	8.22	-26.11	3	8/28/93
GH - 668	7.90	-26.11	4	8/28/93
ave (665-668), 1σ std dev	7.93 ± 0.21	-26.14 ± 0.06		

Sample #	$\delta^{18}O$	$\delta^{13}C$	RV	Date Extracted
GH - 669	7.93	-26.10	1	8/30/93
GH - 670	8.11	-26.09	2	8/30/93
GH - 671	8.48	-26.08	3	8/30/93
GH - 672	8.66	-26.05	4	8/30/93
GH - 673	8.43	-26.06	5	8/30/93
GH - 674	7.91	-26.08	6	8/30/93
ave (669-674), 1σ std dev	8.25 ± 0.31	-26.08 ± 0.02		
GH - 675	8.27	-26.08	1	9/1/93
GH - 676	8.17	-26.10	2	9/1/93
GH - 680	8.79	-26.10	6	9/1/93
GH - 686	8.11	-26.10	6	9/4/93
GH - 691	8.39	-26.10	5	9/6/93
GH - 696	8.10	-26.09	4	9/8/93
GH - 702	8.58	-26.09	4	9/9/93
GH - 707	8.40	-25.95	3	9/13/93
GH - 712	8.18	-25.92	2	9/16/93
GH - 718	8.14	-25.89	2	9/18/93
ave (675-718), 1σ std dev	8.31 ± 0.23	-26.04 ± 0.09		
GJH - 2	8.65	-27.44	2	11/29/93
GJH - 3	8.02	-27.53	3	11/29/93
GJH - 4	8.24	-27.50	4	11/29/93
GJH - 5	8.26	-27.53	5	11/29/93
GJH - 6	8.37	-27.55	6	11/29/93
ave (2-6), 1σ std dev	8.31 ± 0.23	-27.51 ± 0.04		
GJH - 7	7.97	-27.56	1	12/2/93
GJH - 8	8.12	-27.56	2	12/2/93
GJH - 15	8.40	-27.57	3	12/4/93
GJH - 22	8.49	-27.60	4	12/6/93
GJH - 29	8.48	-27.64	5	12/8/93
GJH - 36	8.28	-27.64	6	12/9/93
ave (7-36), 1σ std dev	8.29 ± 0.21	-27.60 ± 0.04		
ave (2-36), 1σ std dev	8.30 ± 0.21	-27.56 ± 0.06		
GJH - 50	8.56	-25.99	2	12/17/93
GJH - 57	8.61	-25.99	3	12/19/93
GJH - 64	8.72	-25.99	4	12/21/93
ave (50-64), 1σ std dev	8.63 ± 0.08	-25.99 ± 0.00		
ave (2-64), 1σ std dev	8.36 ± 0.23			
GJH - 69	8.69	-26.03	3	12/30/93
GJH - 70	8.42	-26.05	4	12/30/93
GJH - 71	8.64	-26.06	5	12/30/93
GJH - 72	8.80	-26.04	6	12/30/93
ave (69-72), 1σ std dev	8.64 ± 0.16	-26.05 ± 0.01		
ave (2-72), 1σ std dev	8.43 ± 0.24			
GJH - 77	8.42	-26.07	5	1/1/94
GJH - 84	8.49	-26.02	6	1/5/94
ave (77-84), 1σ std dev	8.46 ± 0.05	-26.05 ± 0.04		
GJH - 103	8.55	-26.00	3	2/7/94
GJH - 104	9.08	-25.99	4	2/7/94
GJH - 105	8.50	-25.89	5	2/7/94
GJH - 106	8.73	-25.92	6	2/7/94
ave (103-106), 1σ std dev	8.72 ± 0.26	-25.95 ± 0.05		

Sample #	$\delta^{18}O$	$\delta^{13}C$	RV	Date Extracted
GJH - 108	8.91	-26.03	1	2/10/94
GJH - 109	8.45	-26.02	2	2/10/94
GJH - 110	8.75	-25.99	3	2/10/94
GJH - 111	8.66	-25.99	4	2/10/94
GJH - 112	8.44	-26.04	5	2/10/94
GJH - 113	9.00	-26.03	6	2/10/94
ave (108-113), 1σ std dev	8.70 ± 0.23	-26.02 ± 0.02		
ave (103-113), 1σ std dev	8.71 ± 0.23	-25.99 ± 0.05		
GJH - 115	8.72	-26.01	2	2/14/94
GJH - 116	8.99	-25.98	3	2/14/94
GJH - 117	8.62	-25.98	4	2/14/94
GJH - 118	8.55	-26.03	5	2/14/94
ave (115-118), 1σ std dev	8.72 ± 0.19	-26.00 ± 0.02		
ave (103-118), 1σ std dev	8.71 ± 0.21	-25.99 ± 0.04		
GJH - 120	8.14	-26.01	1	2/20/94
GJH - 121	8.70	-26.00	2	2/20/94
GJH - 122	8.42	-25.99	3	2/20/94
GJH - 123	9.03	-25.99	4	2/20/94
GJH - 125	8.76	-25.99	6	2/20/94
ave (120-125), 1σ std dev	8.61 ± 0.34	-26.00 ± 0.01		
GJH - 126	8.24	-26.00	1	2/22/94
GJH - 127	8.59	-26.00	2	2/22/94
GJH - 128	8.74	-26.00	3	2/22/94
GJH - 130	7.87	-26.01	5	2/22/94
ave (126-130), 1σ std dev	8.36 ± 0.39	-26.00 ± 0.00		
GJH - 132	8.28	-26.24	1	3/15/94
GJH - 134	8.61	-26.19	3	3/15/94
GJH - 135	8.59	-26.14	4	3/15/94
GJH - 136	8.55	-26.14	5	3/15/94
GJH - 137	8.52	-22.14	6	3/15/94
ave (132-137), 1σ std dev	8.51 ± 0.13	-26.17 ± 0.04		
GJH - 138	8.39	-26.13	1	3/20/94
GJH - 145	8.56	-26.10	2	3/25/94
GJH - 152	8.69	-26.06	3	3/29/94
GJH - 159	8.71	-26.05	4	4/8/94
GJH - 162	8.49	-26.09	1	4/10/94
GJH - 163	8.74	-26.07	2	4/10/94
GJH - 164	8.71	-26.05	3	4/10/94
GJH - 165	8.73	-26.06	4	4/10/94
ave (138-165), 1σ std dev	8.63 ± 0.13	-26.08 ± 0.03		
GJH - 172	8.54	-26.07	6	4/12/94
GJH - 173	8.60	-26.10	1	4/15/94
ave (172-173), 1σ std dev	8.57 ± 0.04	-26.09 ± 0.02		
ave (138-173), 1σ std dev	8.62 ± 0.12	-26.08 ± 0.03		

TABLE B.3. $^{18}O/^{16}O$ DATA ON CALTECH ROSE QUARTZ ANALYZED ON COILES

Sample #	$\delta^{18}O$	$\delta^{13}C$	**Date Extracted**
LS - 2 - 2	9.66	-26.25	1/26/95
LS - 2 - 3	8.98	-26.29	1/26/95
LS - 2 - 4	5.58	-26.25	1/26/95
LS - 2 - 5	9.70	-26.27	1/26/95
ave (2 - 5), 1σ std dev	8.48 ± 1.96	-26.27 ± 0.02	
LS - 3 - 6	8.79	-26.32	2/8/95
LS - 4 - I2 BrF5	8.93	-26.27	2/11/95
Conventional #1	8.78	-26.20	2/12/95
LS - 4 - I1	7.97	-26.24	2/14/95
LS - 4 - O2	9.17	-26.10	2/14/95
ave (3/6 - O2), 1σ std dev	8.73 ± 0.45	-26.23 ± 0.08	
			Purified Fluorine
LS - 6 - I1	9.14	-26.13	2/23/95
LS - 6 - I2	9.24	-26.13	2/23/95
LS - 6 - I3	8.83	-26.12	2/23/95
LS - 6 - I4	8.90	-26.14	2/23/95
LS - 6 - I5	9.06	-26.12	2/23/95
LS - 6 - I6	9.11	-26.18	2/27/95
LS - 6 - I7	8.95	-26.12	2/27/95
LS - 8 - I1	8.93	-26.20	3/2/95
ave (6 - 8), 1σ std dev	9.02 ± 0.14	-26.14 ± 0.03	
LS - 10 - O2	9.14	-26.00	4/25/95
LS - 11 - 5	8.66	-26.22	4/27/95
LS - 12 - I2	8.59	-26.19	4/30/95
LS - 14 - O5	8.73	-26.16	5/7/95
LS - 14 - O6	8.86	-26.20	5/7/95
LS - 16 - O2	8.86	-26.18	5/11/95
ave (10 - 16), 1σ std dev	8.81 ± 0.20	-26.16 ± 0.08	
LS - 22 - I5	8.55	-26.19	7/15/95
LS - 22 - I1	8.74	-26.17	7/15/95
LS - 23 - 4	8.88	-26.17	7/18/95
LS - 24 - I2	8.78	-26.18	7/19/95
LS - 24 - O8	8.90	-26.15	7/27/95
LS - 26 - O11	8.77	-26.20	7/28/95
LS - 27 - 103	8.67	-26.18	8/5/95
LS - 27 - 104	8.89	-26.16	8/5/95
LS - 27 - 121	8.62	-26.20	8/9/95
LS - 27 - 102	8.97	-26.17	8/9/95
ave (22 - 27), 1σ std dev	8.78 ± 0.14	-26.18 ± 0.02	
LS - 28 - O5	8.39	-26.19	9/10/95
LS - 28 - O9	8.50	-26.19	9/10/95
LS - 28 - O8	8.60	-26.19	9/10/95
LS - 28 - O7	8.69	-26.19	9/10/95
ave (28), 1σ std dev	8.55 ± 0.13	-26.19 ± 0.00	
LS - 28 - I3	8.71	-26.20	11/10/95
LS - 28 - I2	8.63	-26.19	11/10/95
LS - 28 - I1	8.94	-26.19	11/10/95
LS - 28 - I3	8.75	-26.20	11/10/95
ave (28), 1σ std dev	8.76 ± 0.13	-26.20 ± 0.01	
LS - 29 - M5	8.86	-26.18	11/15/95
LS - 29 - O13	8.71	-26.17	11/15/95
LS - 29 - I1	8.73	-26.15	11/16/95
LS - 29 - O3	8.69	-26.17	11/17/95
ave (29), 1σ std dev	8.75 ± 0.08	-26.17 ± 0.01	
ave (22 - 29), 1σ std dev	8.73 ± 0.15	-26.18 ± 0.02	

Sample #	$\delta^{18}O$	$\delta^{13}C$	Date Extracted
			New Filament
LS - 28 - O9	9.12	-26.15	11/30/95
LS - 28 - O5	9.17	-25.90	11/30/95
LS - 28 - O8	9.03	-26.18	12/11/95
LS - 28 - O6	9.28	-26.16	12/16/95
ave (29), 1σ std dev	9.15 ± 0.10	-26.10 ± 0.13	
LS - 30 - O10	8.39	-26.20	12/18/95
LS - 30 - I5	9.57	-25.64	12/21/95
LS - 28 - O7	9.27	-26.09	12/21/95
LS - 29 - O18	8.22	-26.22	12/21/95
LS - 29 - M12	8.32	-26.25	12/21/95
LS - 30 - O6	8.85	-26.16	12/22/95
LS - 30 - O2	8.59	-26.17	12/23/95
LS - 31 - 3	8.09	-26.28	12/27/95
LS - 31 - 1	8.43	-26.20	12/27/95
ave (28 - 31), 1σ std dev	8.64 ± 0.50	-26.13 ± 0.19	
LS - 32 - O5	8.18	-26.17	12/28/95
LS - 32 - O6	8.29	-26.22	12/30/95
LS - 33 - I3	8.45	-26.22	1/2/96
LS - 33 - I1	8.01	-26.20	1/3/96
LS - 33 - I2	8.42	-26.14	1/4/96
LS - 33 - I1	8.67	-26.18	1/7/96
LS - 34 - I1	8.09	-26.25	1/8/96
LS - 34 - I2	8.20	-26.20	1/9/96
LS - 35 - I2	7.95	-26.22	1/11/96
ave (32 - 35), 1σ std dev	8.25 ± 0.23	-26.20 ± 0.03	
LS - 36 - O1	7.88	-26.24	1/15/96
LS - 36 - I1	8.08	-26.12	1/16/96
LS - 36 - I2	8.04	-26.21	1/16/96
LS - 36 - O2	8.17	-26.18	1/16/96
ave (36), 1σ std dev	8.04 ± 0.12	-26.19 ± 0.05	
LS - 38 - O7	8.33	-26.13	2/12/96
LS - 38 - O8	8.18	-26.15	2/12/96
ave (36), 1σ std dev	8.26 ± 0.11	-26.14 ± 0.01	
LS - 41 - O4	8.07	-26.17	4/12/96
LS - 42 - O7	8.03	-26.20	4/17/96
LS - 42 - O8	8.11	-26.18	4/18/96
LS - 42 - O10	7.73	-26.15	4/20/96
ave (36), 1σ std dev	8.00 ± 0.15	-26.18 ± 0.02	

TABLE B.4. $^{18}O/^{16}O$ DATA ON HUALALAI OLIVINE ANALYZED ON COILES

Sample #	$\delta^{18}O$	$\delta^{13}C$	Date Extracted
LS - 1 - 3	6.83	-26.07	1/24/95
LS - 1 - 1	6.72	-26.00	1/24/95
LS - 3 - 4	6.64	-26.31	2/8/95
LS - 4 - O7	6.58	-26.20	2/14/95
LS - 4 - O9	6.72	-26.20	2/14/95
ave (1 - 4), 1σ std dev	6.70 ± 0.09	-26.16 ± 0.12	
LS - 4 - I5	7.55	-26.10	2/14/95
ave (1 - 4), 1σ std dev	6.84 ± 0.36	-26.16 ± 0.11	
			Pure Fluorine
LS - 7 - O7	5.95	-26.19	3/3/95
LS - 7 - O8	6.08	-26.17	3/3/95
LS - 7 - O9	5.98	-26.17	3/3/95
LS - 7 - O10	6.27	-26.15	3/4/95
ave (7), 1σ std dev	6.07 ± 0.14	-26.17 ± 0.02	
LS - 11 - 3	5.63	-26.24	4/27/95
LS - 12 - I7	5.71	-26.21	4/28/95
LS - 12 - I8	5.83	-26.17	4/30/95
ave (11 - 12), 1σ std dev	5.72 ± 0.10	-26.21 ± 0.04	
LS - 13 - 3	5.65	-26.19	5/5/95
LS - 13 - 4	5.74	-26.20	5/5/95
LS - 13 - 1	5.76	-26.17	5/5/95
LS - 13 - 5	5.82	-26.16	5/5/95
LS - 13 - 2	5.88	-26.16	5/5/95
LS - 13 - 6	5.77	-26.18	5/5/95
ave (13), 1σ std dev	5.77 ± 0.08	-26.18 ± 0.02	
LS - 18 - O9	6.08	-26.15	6/3/95
LS - 18 - I3	5.92	-26.15	6/3/95
LS - 18 - I2	5.61	-26.15	6/3/95
LS - 18 - I4	5.98	-26.13	6/6/95
LS - 18 - I5	5.85	-26.15	6/6/95
LS - 18 - I8	5.71	-26.16	6/6/95
LS - 18 - O8	5.89	-26.16	6/6/95
LS - 18 - O3	5.84	-26.15	6/7/95
ave (18), 1σ std dev	5.86 ± 0.15	-26.15 ± 0.01	
LS - 20 - O7	5.59	-26.22	6/12/95
LS - 20 - O6	5.68	-26.23	6/12/95
LS - 20 - I8	5.56	-26.19	6/14/95
LS - 20 - O8	5.60	-26.20	6/14/95
LS - 20 - I5	5.45	-26.18	6/14/95
LS - 20 - I6	5.66	-26.22	6/14/95
LS - 20 - I8	5.56	-26.19	6/14/95
ave (20), 1σ std dev	5.59 ± 0.08	-26.20 ± 0.02	
LS - 25 - 1	5.93	-26.15	7/20/95
LS - 25 - 4	5.83	-26.15	7/20/95
LS - 25 - 6	5.82	-26.20	7/20/95
ave (25), 1σ std dev	5.86 ± 0.06	-26.17 ± 0.03	
LS - 26 - I4	5.94	-26.16	7/27/95
LS - 26 - I6	5.75	-26.19	7/27/95
LS - 26 - I5	6.05	-26.14	7/28/95
LS - 26 - O2	5.84	-26.17	7/27/95
LS - 27 - 11	5.87	-26.20	8/4/95
LS - 27 - 12	5.91	-26.16	8/11/95
ave (26 - 27), 1σ std dev	5.89 ± 0.10	-26.17 ± 0.02	

Sample #	$\delta^{18}O$	$\delta^{13}C$	Date Extracted
LS - 28 - I4	5.72	-26.17	9/10/95
LS - 28 - I7	5.80	-26.17	9/10/95
LS - 28 - I3	5.57	-26.19	9/10/95
LS - 28 - I6	5.83	-26.17	9/10/95
LS - 28 - I1	5.66	-26.18	9/10/95
LS - 28 - I2	5.72	-26.18	9/10/95
LS - 28 - I5	5.56	-26.19	9/10/95
ave (28), 1σ std dev	5.69 ± 0.10	-26.18 ± 0.01	
LS - 29 - O10	6.15	-26.14	11/15/95
LS - 29 - M2	5.80	-26.12	11/16/95
ave (29), 1σ std dev	5.98 ± 0.20	-26.13 ± 0.01	
			New Filament
LS - 28 - I6	6.32	-26.24	12/12/95
LS - 28 - I2	6.46	-26.12	12/13/95
LS - 28 - I8	6.78	-26.13	12/20/95
LS - 28 - I1	5.96	-26.15	12/21/95
ave (28), 1σ std dev	6.38 ± 0.34	-26.16 ± 0.03	
LS - 30 - O7	6.06	-26.16	12/23/95
LS - 29 - O2	6.17	-26.09	12/26/95
LS - 29 - O1	5.63	-26.17	12/26/95
LS - 28 - I5	5.77	-26.17	12/27/95
LS - 31 - 4	5.30	-26.23	12/27/95
LS - 31 - 5	5.50	-26.19	12/27/95
LS - 31 - 6	5.63	-26.23	12/27/95
LS - 30 - I6	5.93	-26.20	1/7/96
LS - 30 - O11	6.32	-26.09	1/7/96
ave (28 - 31), 1σ std dev	5.81 ± 0.33	-26.17 ± 0.05	
LS - 32 - O3	5.51	-26.24	12/28/95
LS - 32 - I2	5.44	-26.27	1/7/96
LS - 34 - I4	5.37	-26.15	1/11/96
LS - 35 - I5	5.20	-26.22	1/12/96
LS - 36 - I8	5.29	-26.14	1/15/96
LS - 36 - O11	5.47	-26.16	1/11/96
ave (28 - 31), 1σ std dev	5.38 ± 0.12	-26.20 ± 0.05	

TABLE B.5. $^{18}O/^{16}O$ DATA OF GORE MOUNTAIN GARNET ANALYZED ON COILES

Sample #	$\delta^{18}O$	$\delta^{13}C$	**Date Extracted**
LS - 2 - 1	8.25	-26.25	1/26/95
LS - 3 - 2	7.50	-26.32	2/8/95
LS - 4 - I4	7.17	-26.16	2/11/95
LS - 4 - O4	7.60	-26.20	2/11/95
LS - 4 - O5	7.70	-26.20	2/11/95
LS - 4 - O6	7.74	-26.21	2/14/95
LS - 4 - I3	7.40	-26.22	2/14/95
ave (3 - 4), 1σ std dev	7.52 ± 0.21	-26.22 ± 0.05	
			Pure Fluorine
LS - 6 - O3	7.33	-26.12	2/27/95
LS - 6 - O4	7.47	-26.13	2/27/95
ave (6), 1σ std dev	7.40 ± 0.10	-26.13 ± 0.01	
LS - 7 - 4	7.28	-26.14	3/1/95
LS - 7 - 3	6.77	-26.15	3/1/95
LS - 7 - 1	7.78	-26.17	3/1/95
LS - 7 - 2	7.38	-26.10	3/1/95
LS - 7 - 6	7.20	-26.14	3/2/95
LS - 7 - 5	7.34	-26.16	3/2/95
LS - 8 - I7	7.73	-26.14	3/4/95
LS - 8 - I8	7.33	-26.20	3/5/95
ave (7 - 8), 1σ std dev	7.35 ± 0.31	-26.15 ± 0.02	
LS - 9 - 1	7.54	-26.17	3/31/95
LS - 9 - 2	7.38	-26.15	4/1/95
LS - 10 - I5	7.38	-26.17	4/2/95
ave (9 - 10), 1σ std dev	7.43 ± 0.09	-26.16 ± 0.01	
LS - 10 - I1	7.70	-26.19	4/26/95
LS - 11 - 1	6.99	-26.00	4/26/95
LS - 11 - 2	6.80	-26.21	4/27/95
LS - 12 - I4	7.16	-26.22	4/27/95
LS - 12 - I3	7.02	-26.20	4/27/95
ave (10 - 12), 1σ std dev	7.13 ± 0.34	-26.16 ± 0.09	
LS - 14 - I8	7.11	-26.16	5/6/95
LS - 14 - I7	7.12	-26.20	5/7/95
LS - 15 - 6	7.33	-26.15	5/10/95
ave (14 - 15), 1σ std dev	7.19 ± 0.12	-26.17 ± 0.03	
LS - 27 - 124	7.12	-26.18	8/6/95
LS - 27 - 123	7.27	-26.21	8/7/95
LS - 27 - 122	7.20	-26.18	8/9/95
ave (27), 1σ std dev	7.20 ± 0.08	-26.19 ± 0.02	
			New Filament
LS - 30 - I4	7.23	-26.15	12/21/95
LS - 30 - I8	7.21	-26.12	12/23/95
LS - 30 - O5	7.81	-26.09	12/23/95
LS - 30 - O9	7.03	-26.14	1/7/96
ave (30), 1σ std dev	7.32 ± 0.34	-26.13 ± 0.03	
LS - 41 - O1	6.74	-26.13	4/10/96
LS - 41 - O8	6.81	-26.18	4/11/96
LS - 41 - O11	7.03	-26.11	4/11/96
LS - 41 - O12	6.79	-26.08	4/12/96
LS - 42 - O1	6.66	-26.17	4/17/96
LS - 42 - M11	6.97	-26.15	4/17/96
LS - 42 - O2	7.00	-26.13	4/18/96
LS - 42 - O5	6.57	-26.21	4/19/96
ave (30), 1σ std dev	6.82 ± 0.17	-26.15 ± 0.04	

Appendix C. Locations of Samples Studied in this Thesis

TABLE C.1. SAMPLE LOCATIONS AND $^{18}O/^{16}O$ DATA ON ROCKS AND MINERALS FROM THE MONASHEE COMPLEX AND VICINITY

Sample	Latitude	Longitude	Location	$\delta^{18}O$	
Early Proterozoic Basement Gneiss					
GH-49	51° 02' 04"	118° 21' 02"	Kirkup Creek logging road, first outcrop east of second bridge past 17 km marker.	Qz Fs	10.2 7.7
GH-669	50° 29' 41"	118° 00' 17"	Ledge Creek logging road, 0.3 km upstream of first bridge.	Qz Fs Gr	9.7 8.1 7.1
MC-4	51° 02' 15"	118° 23' 01"	Kirkup Creek logging road, 1.5 km upstream of GH-49.	Qz Fs	9.3 2.7
MC-5	51° 01' 45"	118° 28' 28"	Crazy Creek logging road, 2.0 km east of last bridge.	Qz	12.0
Late Proterozoic Mantling Gneiss					
> 200 m below Monashee Decollement					
GH-76	50° 57' 48"	118° 23' 28"	Trans-Canada Highway, outcrop on westbound roadside near Victor Lake Provincial Park sign.	Qz	14.0
GH-556	51° 22' 58"	118° 42' 34"	Perry River logging road, 0.2 miles west of the first river crossing north of powerlines.	Qz	16.4
MC-2	51° 05' 24"	118° 20' 32"	Hiren Creek logging road, 1.6 km upstream of Jordan River Road junction.	Qz	14.7
MC-2a	51° 05' 24"	118° 20' 32"	See MC-2	Qz Fs	13.6 12.1
MC-2b	51° 05' 24"	118° 20' 32"	See MC-2	Qz	13.4
MC-3a	51° 05' 27"	118° 21' 06"	Hiren Creek logging road, 0.8 km upstream of MC-2	Qz	12.2
MC-3b	51° 05' 27"	118° 21' 06"	See MC-3	Qz	12.2
MC-3c	51° 05' 27"	118° 21' 06"	See MC-3	Qz	14.7
< 200 m below Monashee Decollement					
GH-75	50° 58' 23"	118° 20' 58"	Trans-Canada Highway, 0.5 km east of railroad bridge east of Victor Valley.	WR Qz Fs	10.7 11.0 9.0
GH-552	51° 17' 00"	118° 40' 24"	Perry River logging road, 0.3 mi. north of junction of creek draining the west slope of Schrund Peak and the Perry River.	Qz	10.6
GH-553	51° 17' 40"	118° 40' 30"	Perry River logging road, 1.2 mi. north of junction of creek draining the west slope of Schrund Peak and the Perry River.	Qz Fs	11.6 9.6

TABLE C.1. (Cont.)

Sample	Latitude	Longitude	Location	$\delta^{18}O$
GH-555	51° 22' 11"	118° 41' 56"	Perry River logging road, 2.4 mi. north of last creek crossing before the powerlines.	Qz 11.3
GH-841	50° 38' 50"	118° 01' 44"	Pingston Creek logging road, 1.4 mi. south of the junction at the switchback.	Qz 10.6 Fs 9.0
GH-842	50° 38' 06"	118° 01' 54"	Pingston Creek logging road, 2.5 mi. south of the junction at the switchback.	Qz 11.0 Fs 8.4
GH-843	50° 38' 29"	118° 03' 02"	Pingston Creek logging road, 3.7 mi. south of the junction at the switchback.	Qz 11.1 Fs 9.1
Selkirk Allochthon				
GH-557	51° 22' 22"	118° 48' 32"	Ratchford Creek logging road, 1.2 mi. east of Cotton Creek crosing.	Qz 12.0
GH-77	50° 57' 15"	118° 24' 11"	Trans-Canada Highway, roadcut 0.2 km west of Victor Lake picnic ground.	WR 12.4 Qz 12.4
GH-78	50° 56' 44"	118° 25' 28"	Trans-Canada Highway, 250 m east of the first highway bridge over Eagle River west of Victor Lake.	WR 8.7
GH-81	51° 02' 19"	118° 35' 10"	Crazy Creek logging road, 8 km marker southwest of Eagle Mountain.	WR –1.0
GH-79	50° 57' 45"	118° 30' 00"	Trans-Canada Highway, first outcrop west of first bridge west of Three Valley Gap, north shore of Griffin Lake.	WR 9.6
GH-83	50° 55' 35"	118° 27' 35"	Trans-Canada Highway, 1 km west of Three Valley Gap gift shop.	WR 2.9
GH-80	50° 59' 26"	118° 38' 00"	Trans-Canada Highway, first outcrop west of Griffin Lake.	WR 12.4
GH-190	50° 58' 31"	118° 43' 35"	Trans-Canada Highway, north side of the road at the Last Spike monument.	WR –1.7
Columbia River Fault				
GH-31	51° 18' 24"	118° 17' 06"	Highway 23, first roadcut north of Holditch Creek.	Cc 7.6 $\delta^{13}C$ –0.1
GH-66	51° 01' 06"	118° 12' 35"	Highway 23, north of the Trans-Canada highway, roadcut east of church in Revelstoke.	Qz 10.8 Fs 4.5
GH-74	50° 58' 46"	118° 14' 39"	Trans-Canada Highway, 1.5 km west of bridge over Columbia River.	WR 7.1

Note: The oxygen isotope data are for whole rocks (WR), quartz (Qz), feldspar (Fs), almandine garnet (Gr), and calcite (Cc).

TABLE C.2. SAMPLE LOCATIONS AND $^{18}O/^{16}O$ DATA ON ROCKS AND MINERALS FROM THE THOR-ODIN COMPLEX AND VICINITY

Sample	Latitude	Longitude	Comments	$\delta^{18}O$
Traverse 1			Traverse 1 crosses the imbricate thrust zone of the Monashee Decollement system and Fawn Lake succession (see Reesor and Moore, 1971; and Carr, 1991) from the drop off at Caribou Alp southwest to the tree-line. Samples were collected according to stratigraphic sections published in Reesor and Moore (1971).	
Zone of Imbricate Thrusting			Samples are from the section in Geological Survey of Canada Memoir 197, pages 134-136 (Reesor and Moore, 1971); Caribou Alp from the contact with the Core zone to the intensely folded zone.	
MD-1	50° 31' 51"	118° 11' 27"	Basement gneiss. At Gates Ledge, just below Monashee Decollement.	Qz 13.4 Fs 2.7
MD-2	50° 31' 52"	118° 11' 29"	Quartzite. At Monashee Decollement.	Qz 11.9
MD-3	50° 31' 53"	118° 11' 31"	Unit 1, rusty weathering biotite+feldspar +sillimanite schist.	Qz 13.9
MD-4	50° 31' 51"	118° 11' 32"	Unit 2, white quartzite.	Qz 12.1
MD-5	50° 31' 50"	118° 11' 33"	Unit 3, sillimanite+quartz+feldspar+garnet schist.	Qz 13.1 Fs 4.2
MD-6	50° 31' 49"	118° 11' 35"	Unit 5, rusty weathering sillimanite+garnet +biotite schist with layers of white quartzite.	Qz 12.3 Fs 8.0
MD-6a	50° 31' 49"	118° 11' 35"	Unit 5, aluminous quartz+sillimanite +corundum schist.	Qz 12.9
MD-7	50° 31' 48"	118° 11' 36"	Unit 13, grey weathering biotite+quartz +feldspar gneiss. Collected from base of unit, 385 ft. above MD.	Qz 12.9
MD-14	50° 31' 47"	118° 11' 40"	Unit 8, pure, white quartzite.	Qz 13.5
MD-17	50° 31' 33"	118° 11' 27"	Unit 14, interbedded rusty weathering garnet+sillimanite+biotite schist, quartz-ite, and calcsilicate.	Cc 15.7 $\delta^{13}C$ −7.6
MD-17a	50° 31' 33"	118° 11' 27"	Pegmatite knot cutting schist.	Qz 14.4 Fs 12.9
MD-17b	50° 31' 33"	118° 11' 27"	Quartz vein cutting pegmatite.	Qz 14.2

TABLE C.2. (Cont.)

Sample	Latitude	Longitude	Comments	$\delta^{18}O$
MD-19b	50° 31' 29"	118° 11' 30"	At fault contact between units 19 and 20, 949 ft. above MD. Undeformed dike that cuts contact between rusty weathering paragneiss below from grey weathering basement gneiss above.	Qz 13.2 Fs 4.4
MD-20a	50° 31' 28"	118° 11' 30"	Unit 20, boudins of calcsilicate, material analyzed is quartz vein that cuts boudin.	Qz 13.5
MD-24	50° 31' 22"	118° 11' 44"	Unit 22, grey weathering basement paragneiss, sample collected within 1 m of fault contact 1, 315 ft. above MD.	Qz 11.7 Fs 10.2
MD-26a	50° 31' 20"	118° 11' 46"	Unit 23, rusty weathering quartzitic calcsilicate gneiss.	Qz 16.4 Cc 15.4 $\delta^{13}C$ –4.9
MD-27	50° 31' 19"	118° 11' 47"	Unit 25, biotite+quartz+feldspar paragneiss, collected just below fault contact at 1,450 ft. above MD.	Qz 11.0 Fs 10.0
MD-29	50° 31' 14"	118° 11' 52"	Unit 26, feldspathic quartzite. All units at this outcrop are imbricately folded.	Qz 14.9
MD-29a	50° 31' 14"	118° 11' 52"	Unit 28, layered biotite+quartz+plagioclase paragneiss.	Qz 14.6 Fs –0.9 Bi 4.4
MD-29b	50° 31' 14"	118° 11' 52"	Unit 27, Garnet+plagioclase amphibolite.	Fs 5.5 Ga 8.6 Am 8.8
MD-30	50° 31' 09"	118° 11' 55"	Quartzite with calcite-filled fractures. Just below the intensely folded zone.	Qz 14.7 Cc 12.8 $\delta^{13}C$ –1.7
MD-31	50° 31' 04"	118° 12' 00"	Intensely folded zone. Quartz+feldspar +biotite paragneiss with calcite-filled fractures. Rock is intensely deformed.	Qz 10.2 Fs –3.8 Cc –2.1 $\delta^{13}C$ –7.9
MD-32	50° 31' 00"	118° 12' 02"	Intensely folded zone. Garnet+quartz+plagioclase+biotite paragneiss. Just below thrust contact with Fawn Lake Assemblage.	Qz 12.1 Ga 9.3

TABLE C.2. (Cont.)

Sample	Latitude	Longitude	Comments	$\delta^{18}O$
Amphibolite-Rich Zone			Approximately follows the stratigraphic section compiled by Reesor and Moore (1971, p. 137) measured along the base of the cliffs northeast of the south end of Peters Lake across unit M1 (Fawn Lake Assemblage; Carr, 1991)	
MD-33a	50° 30' 56"	118° 12' 07"	Leucogranite sheet, immediately above contact with imbricate thrust zone.	Qz 12.3 Fs 11.0
MD-35	50° 30' 56"	118° 12' 07"	Quartz+garnet psammitic schist, outcrop located between two small lakes along the creek that passes through Valley of the Moon.	Qz 12.7 Ga 10.3
MD-35a	50° 30' 56"	118° 12' 07"	Leucogranite dike from same outcrop.	Qz 13.4 Fs −3.8
MD-36a	50° 30' 56"	118° 12' 07"	Calcsilicate gneiss between layers of quartzite and marble between two small lakes along the Valley of the Moon creek.	Cc 15.2 $\delta^{13}C$ −3.5
MD-36b	50° 30' 56"	118° 12' 07"	Marble, same outcrop as before, collected from an adjacent layer.	Cc 18.8 $\delta^{13}C$ 8.5
MD-37	50° 30' 56"	118° 12' 07"	Quartz+biotite+garnet schist.	Qz 11.8 Ga 9.1
MD-38	50° 30' 56"	118° 12' 07"	Quartz+K-feldspar+plagioclase+biotite leucogranite sheet.	Qz 12.1 Fs 5.4
MD-38a	50° 30' 56"	118° 12' 07"	Quartz+feldspar+biotite+amphibole gneiss, adjacent layer above previous sample.	Qz 13.3 Fs 11.3 Am 7.5 Bi 7.4
MD-38b	50° 30' 56"	118° 12' 07"	Quartz+feldspar+biotite amphibolite, layer just above the gneiss.	Qz 13.0 Am 10.3 Bi 8.0
MD-39a	50° 30' 56"	118° 12' 07"	Leucogranite sheet, collected from the crest of the ridge between Valley of the Moon and Fawn Lake drainages.	Qz 12.2 Fs 10.8
MD-40	50° 30' 34"	118° 12' 09"	Amphibolite, >80% amphibole, just above the second zero in "6700" foot contour marker northwest fo Fawn Lake.	Fs −0.8 Am 4.3
MD-40a	50° 30' 34"	118° 12' 09"	Leucogranite sheet, collected in layer just above the amphibolite (MD-40).	Qz 11.7 Fs 11.1

TABLE C.2. (Cont.)

Sample	Latitude	Longitude	Comments	$\delta^{18}O$
MD-40b	50° 30' 34"	118° 12' 09"	Quartz+feldspar+biotite pelitic gneiss, layer just above the leucogranite sheet.	Qz 11.8 Fs 9.6 Bi 4.2
MD-41	50° 30' 31"	118° 12' 07"	Quartzite, location is on the southernmost part of the first zero in "6700" contour marker northwest of Fawn Lake.	Qz 12.3
MD-41a	50° 30' 31"	118° 12' 07"	Leucogranite sheet, two layers below the quartzite.	Qz 12.9 Fs 11.5 Ga 9.7
MD-41b	50° 30' 31"	118° 12' 07"	Amphibolite with garnets up to 1 cm in diameter, collected just below leucogranite sheet.	Qz 13.6 Ga 10.0 Am 10.7 Bi 9.7
MD-50	50° 30' 28"	118° 12' 08"	Psammite, ~ 50 m northwest of small peninsula on the west shore of Fawn Lake.	Qz 12.4 Fs 10.9
MD-50a	50° 30' 28"	118° 12' 08"	3-m-thick quartz+feldspar+biotite+garnet leucogranite sheet that cuts the psammite.	Qz 12.7 Fs 11.0 Ga 8.6
MD-49	50° 30' 25"	118° 12' 11"	Quartz+feldspar+biotite+garnet+sillimanite metapelite gneiss, collected from the west shore of Fawn Lake ~ 200 m from drainage outlet.	Qz 12.8 Fs 7.0 Ga 10.5 Bi 4.1
MD-49a	50° 30' 25"	118° 12' 11"	Quartz vein in the paragneiss.	Qz 12.1
MD-48	50° 30' 18"	118° 12' 05"	Quartz+feldspar+biotite+garnet metapelite, southeasternmost shore of Fawn Lake.	Fs 10.9 Ga 8.7
MD-48a	50° 30' 18"	118° 12' 05"	Quartz+biotite+garnet amphibolite, interlayered with metapelite and leucogranite sheets.	Qz 11.9 Ga 8.1 Am 8.1 Bi 6.2
MD-48b	50° 30' 18"	118° 12' 05"	Quartz+feldspar+biotite+garnet pegmatitic leucogranite sheet.	Qz 12.3 Fs 10.0 Ga 8.3 Bi 7.3
MD-47	50° 30' 15"	118° 12' 07"	Quartz+feldspar+garnet paragneiss, east of the first knoll east of the creek draining Fawn Lake.	Qz 10.7 Fs 8.4 Ga 6.7
MD-47a	50° 30' 15"	118° 12' 07"	Garnet amphibolite, probably restite from melting.	Qz 9.7 Ga 6.6

TABLE C.2. (Cont.)

Sample	Latitude	Longitude	Comments	$\delta^{18}O$
MD-46	50° 30' 13"	118° 12' 09"	Quartz+feldspar+garnet+biotite amphibolite, south of the first knoll east of the creek draining Fawn Lake.	Qz 9.7 Fs 8.1 Ga 6.4 Am 7.8 Bi 3.1
MD-46a	50° 30' 13"	118° 12' 09"	Quartz+feldspar+biotite+garnet paragneiss, sharp contact with the amphibolite.	Qz 11.1 Fs 9.8 Ga 8.0
MD-46b	50° 30' 13"	118° 12' 09"	Quartz+garnet-rich leucogranite pegmatitic melt segregation in amphibolite.	Qz 11.7 Ga 7.8
MD-45	50° 30' 08"	118° 12' 08"	Garnet amphibolite, collected from midway point in north-south direction from the ridge that extends from the southeast edge of Fawn Lake.	Qz 13.0 Ga 10.4 Am 9.6
MD-45a	50° 30' 08"	118° 12' 08"	Quartz+feldspar+biotite+garnet leucogranite segregation from the amphibolite.	Qz 12.7 Fs 11.2 Ga 10.2 Bi 9.0
MD-44	50° 30' 05"	118° 12' 10"	Quartz+garnet+diopside calcsilicate gneiss, in the valley between the previously mentioned ridge and the first knoll to the southwest.	Qz 12.9 Ga 10.4
MD-44a	50° 30' 05"	118° 12' 10"	Coarse-grained quartz+feldspar pegmatite segregation.	Qz 12.1 Fs 10.4
MD-43	50° 30' 04"	118° 12' 16"	Quartz+feldspar+garnet leucogranite pegmatite, next valley to the southwest at the base of cliff at the north side of the valley.	Qz 12.3 Fs 11.5
MD-43a	50° 30' 04"	118° 12' 16"	Calcsilicate gneiss from same outcrop.	Qz 13.8
MD-42	50° 30' 02"	118° 12' 20"	Garnet amphibolite at edge of the alpine plateau of Caribou Alp. This lithology comprises the entire outcrop.	Fs 9.1 Ga 6.8 Am 6.3
North Fosthall Creek – Amphibolite-Rich Zone				
NF-3	50° 25' 47"	118° 01' 56"	North Fosthall Creek logging road, 0.1 km upstream of first stream crossing on south side of North Fosthall Creek. Amphibolite with garnets up to 10 cm in diameter.	Qz 12.3 Ga 10.5

TABLE C.2. (Cont.)

Sample	Latitude	Longitude	Comments	$\delta^{18}O$
Traverse 2			This traverse was cut short by poor weather conditions (two-day snowstorm) during the time alloted for sample collection at this part of the Thor-Odin stratigraphic section. This traverse is located in the upper northeast slope of the highland above timberline immediately west of Margie Lake.	
Marble-Rich Zone			Samples were collected from a 250-m-thick section equivalent to the uppermost part of the Hamill Group, the Mohican Formation, and the Badshot Formation; all units are Cambrian in age.	
MD-57	50° 28' 40"	118° 11' 59"	White quartzite, collected at the top of a large talus slope that spills into the Margie Lake valley.	Qz 13.6
MD-57a	50° 28' 40"	118° 11' 59"	Semi-pelitic gneiss.	Qz 13.9 Fs 13.3
MD-57b	50° 28' 40"	118° 11' 59"	Psammitic schist from the same locality.	Qz 14.0
Outcrop MD-58			Outcrop-scale traverse across a 3-m-thick portion of the Mohican Formation. Located at the campsite for this traverse, ~50 m due east of the large cirque lake in the alpine valley drained by Margie Creek. This outcrop is approximately 2150 m above the Monashee Decollement. Order is from lowest-to-highest.	
MD-58	50° 28' 37"	118° 12' 13"	Quartz+feldspar+biotite pelitic gneiss, base of the outcrop, layer is 15 cm thick.	WR 14.0 Qz 14.5 Fs 13.7 Bi 9.6
MD-58a	50° 28' 37"	118° 12' 13"	Thin (10 cm) pegmatitic leucogranite concordant to layering.	WR 14.1 Qz 14.3 Fs 13.9
MD-58b	50° 28' 37"	118° 12' 13"	Psammite, sample collected from uppermost part of unit, layer is 30 cm thick.	WR 14.2 Qz 15.1 Fs 13.7
MD-58c	50° 28' 37"	118° 12' 13"	Lower marble unit, 60 cm thick, >90% calcite, sharp contact with psammite.	Cc 21.0 $\delta^{13}C$ –1.9
MD-58d	50° 28' 37"	118° 12' 13"	Calcsilicate gneiss between two marble layers. Layer is 60 cm thick, sample is from center of unit.	WR 12.1 Qz 12.4 Px 12.4

TABLE C.2. (Cont.)

Sample	Latitude	Longitude	Comments	$\delta^{18}O$	
MD-58e	50° 28' 37"	118° 12' 13"	Upper marble unit, 60 cm thick. See previous marble.	Cc $\delta^{13}C$	18.2 0.9
MD-58f	50° 28' 37"	118° 12' 13"	Thin (13 cm) pegmatitic leucogranite	WR Qz Fs	13.9 15.0 13.3
MD-58g	50° 28' 37"	118° 12' 13"	Quartz+biotite+garnet semipelitic gneiss. Layer is 30-cm-thick.	WR Qz Ga Bi	13.8 15.3 13.2 11.8
MD-58h	50° 28' 37"	118° 12' 13"	White quartzite, ~ 6 m upsection of previous sample.	Qz	13.6
MD-56a	50° 28' 32"	118° 12' 20"	Location is ~125 m due south of the outlet drainage of the cirque lake in Margie Creek drainage. Leucogranite pegmatite immediately adjacent to marble.	Qz Fs	18.8 17.0
MD-56b	50° 28' 32"	118° 12' 20"	Marble, > 90% calcite.	Cc $\delta^{13}C$	20.6 0.3
MD-56c	50° 28' 32"	118° 12' 20"	Pegmatite cutting marble.	Qz Fs	17.4 16.8
MD-55	50° 28' 28"	118° 12' 25"	Semipelitic schist, in valley ~75 m south of Margie Creek.	Qz Fs Ga	13.9 13.2 12.5
MD-54	50° 28' 26"	118° 12' 28"	Marble, >90% calcite, collected from base of the Empress (Badshot Fm.) marble unit. The Empress marble unit at this location is ~100-m-thick.	Cc $\delta^{13}C$	21.7 –0.4
MD-53	50° 28' 25"	118° 12' 29"	White quartzite, middle part of Empress marble unit.	Qz	16.1
MD-53a	50° 28' 25"	118° 12' 29"	Quartz+feldspar+biotite+garnet pelitic schist, immediately above quartzite.	Qz Fs Ga	15.1 13.9 12.4
MD-53b	50° 28' 25"	118° 12' 29"	Pure marble, >90% calcite, next layer above the metapelite.	Cc $\delta^{13}C$	19.3 1.9

TABLE C.2. (Cont.)

Sample	Latitude	Longitude	Comments	$\delta^{18}O$	
MD-51	50° 28' 24"	118° 12' 30"	This sample localitiy is at the base of the cliff that forms Fosthall ridge. The uppermost part of the Empress marble unit was collected here. Quartz-rich calc-silicate. Immediately above highest marble of Empress.	Qz Cc $\delta^{13}C$	15.7 15.2 −4.0
MD-51W	50° 28' 24"	118° 12' 30"	Stratigraphically highest Empress marble sample, but the lowest at the site. Pure marble, >90% calcite. Layer is ~5-m-thick. Whole-rock fraction.	Cc $\delta^{13}C$	21.5 2.3
MD-51C	50° 28' 24"	118° 12' 30"	Coarse calcite fraction of previous sample. Sample has bimodal distribution of calcite grain sizes. Coarse grains are up to 1 cm in diameter.	Cc $\delta^{13}C$	22.0 2.4
MD-51M	50° 28' 24"	118° 12' 30"	Fine calcite fraction of previous sample. Fine grains are ~ 1 mm.	Cc $\delta^{13}C$	21.5 2.2
MD-51a	50° 28' 24"	118° 12' 30"	Calcsilicate gneiss, zoisite-bearing, next layer above the quartzite (MD-51).	Qz Cc $\delta^{13}C$	15.9 15.5 −5.2
MD-51b	50° 28' 24"	118° 12' 30"	Pegmatitic leucogranite, next unit above calcsilicate gneiss.	Qz Fs	16.3 14.2
MD-51c	50° 28' 24"	118° 12' 30"	Thin layer of pure marble, a few meters above previous sample.	Cc $\delta^{13}C$	15.9 2.0
MD-51d	50° 28' 24"	118° 12' 30"	Pelitic schist, in Mount Fosthall Composite unit A (basal Lardeau Group), stratigraph-ically highest unit at outcrop.	Qz Fs Ga	16.2 15.3 13.5
Traverse 3			This east-west traverse is across the alpine zone east of Goat Mountain, mainly along the southern shores of Twin Peaks Lake and Sitkum Lake.		
Leucogranite-Rich Zone			Samples collected are from the section beneath the zone mapped by Reesor and Moore (1971) as being >50% leucogranite. These rocks were correlated by Carr (1991) to the Ordovician Broadview Formation of the Lardeau Group.		
MD-59	50° 25' 52"	118° 14' 57"	Late-stage north-south trending leuco-granite dike. Dike is ~20-m-thick. Southern shore of Twin Peaks Lake east end of north-jutting peninsula at eastern lobe of lake.	Qz Fs	11.1 10.3

TABLE C.2. (Cont.)

Sample	Latitude	Longitude	Comments	$\delta^{18}O$
MD-60a	50° 26' 06"	118° 14' 20"	Leucogranite sheet, outcrop consists of thick layers (~1m) of leucogranite and metapelite. At western edge of the south-facing cirque east of Twin Peaks Lake.	Qz 12.8 Fs 10.7
MD-63	50° 26' 00"	118° 14' 26"	Quartz+feldspar+sillimanite metapelite. ~20 m north of mapped pond east of Twin Peaks Lake.	Qz 13.1 Fs 11.7
MD-63a	50° 26' 00"	118° 14' 26"	Feldspar+garnet amphibolite from same outcrop as previous sample.	Fs 11.7 Ga 10.3 Am 10.1
MD-66	50° 25' 51"	118° 14' 42"	Sillimanite-bearing leucogranite. At the drainage outlet for Twin Peaks Lake, collected from the southern side of creek.	Qz 11.8 Fs 11.1
MD-68	50° 25' 51"	118° 15' 07"	Leucogranite, ~100 m west of sample MD-59.	Qz 12.9 Fs 11.2
MD-70	50° 25' 52"	118° 15' 13"	Leucosome of partially melted garnet amphibolite. Base at the eastern shore of peninsula that separates the lobes of Twin Peaks Lake.	Qz 12.4 Fs 11.4
MD-70a	50° 25' 52"	118° 15' 13"	Melanosome of garnet amphibolite, one garnet is ~6 cm in diameter. Melanosome-leucosome boundary marked by biotite-rich (>90%) zone.	Qz 13.3 Fs 11.6 Ga 10.5 Bi 9.0
MD-71a	50° 25' 52"	118° 15' 18"	Quartz+feldspar+sillimanite+garnet pelitic gneiss. At base of peninsula separating lobes of Twin Peaks Lake, ~50 m east of lakeshore.	Qz 12.3 Ga 9.8
MD-73	50° 25' 45"	118° 15' 35"	Ladybird granite, entire outcrop is granite. On the shore of Twin Peaks Lake ~150 m east of the north-south to east-west bend of the lakeshore.	Qz 11.9 Fs 10.6
MD-74a	50° 25' 51"	118° 15' 43"	Pure (>90% calcite) marble, layer is ~ 3-4 cm. From the top of the small ridge separating Twin Peaks Lake from the lake to the west.	Cc 12.4 $\delta^{13}C$ 0.2
MD-74b	50° 25' 51"	118° 15' 43"	Calcsilicate from same location, at contact with marble.	Cc 9.6 $\delta^{13}C$ −6.4
MD-77a	50° 25' 43"	118° 16' 27"	Metapelite, North end of small lake south of Sitkum Lake.	Qz 11.9 Ga 9.6

TABLE C.2. (Cont.)

Sample	Latitude	Longitude	Comments	$\delta^{18}O$
MD-78	50° 25' 45"	118° 16' 15"	Metapelite, the drainage outlet of Sitkum Lake.	Qz 13.0 Ga 9.8
MD-80a	50° 25' 45"	118° 16' 16"	Metapelite, 100 feet east up the hill from the Sitkum Lake campsite.	Qz 12.3 Ga 10.0
MD-81	50° 25' 42"	118° 16' 09"	Leucogranite, the crest of the ridge between Sitkum Lake and the small lake west of Twin Peaks Lake, ~300 ft. up the ridge from drainage divide.	Qz 11.9 Fs 10.6
South Fosthall Pluton			These samples were collected from outcrops along logging roads that traverse the South Fosthall pluton south and upsection of Traverse 3.	
GH-380	50° 26' 06"	118° 25' 12"	Ladybird leucogranite, Sugar Mountain logging road where the road becomes too rough for driving.	Qz 12.2 Fs 10.5
GH-381	50° 26' 32"	118° 25' 11"	Garnet-bearing Ladybird leucogranite, Sugar Mountain logging road, at the trailhead to Kate Lake.	Qz 12.5 Ga 9.2
GH-389	50° 23' 39"	118° 20' 33"	Ladybird leucogranite, Sitkum Creek logging road, at Sitkum Lake trailhead.	Qz 12.6 Fs 10.8
GH-397	50° 25' 36"	118° 31' 53"	Protomylonitic Ladybird leucogranite, main logging road that follows the Shuswap River, 0.9 mi. north of the intersection between parallel roads that follow the west shore of Sugar Lake, sample collected along the lakeshore.	Qz 12.5 Fs 10.5
GH-401	50° 35' 38"	118° 23' 54"	Ladybird leucogranite, main Shuswap River logging road, 0.2 mi. north of Celig road.	Qz 11.9 Fs 10.1
GH-642	50° 22' 36"	118° 06' 29"	Pegmatitic Ladybird leucogranite, South Fosthall logging road, 0.5 mi. west of Bear Lake turnout.	Qz 11.8 Fs 10.1
Columbia River Fault			Samples are from logging roads along the eastern margin of the Thor-Odin – Pinnacles complex.	
GH-647	50° 26' 18"	117° 53' 04"	Muscovite-bearing Ladybird leucogranite, S-C mylonite. Main logging road along west side of Arrow Lake, at Pingston Creek bridge, sample is from north side of crossing west of the road at the bridge abutment. This is same outcrop as Parrish et al. (1988) sample "Pingston Creek."	Qz 4.3 Fs 2.6 Mu 7.7

TABLE C.2. (Cont.)

Sample	Latitude	Longitude	Comments	$\delta^{18}O$	
GH-660	50° 28' 15"	118° 00' 19"	Mylonitic Ladybird leucogranite. Empress logging road, 0.2 mi. south of Trout Creek bridge	Qz Fs	12.6 10.5
GH-663	50° 27' 38"	118° 01' 25"	Mylonitic marble. Road to Empress Lake, 0.1 mi. south of hairpin turn #4 (going uphill).	Cc $\delta^{13}C$	15.9 1.3
GH-664	50° 27' 29"	118° 01' 29"	Empress marble, pure (>90%), correlated to the Badshot Formation, 0.3 mi. south of hairpin turn #5.	Cc $\delta^{13}C$	20.1 2.8
GH-665	50° 27' 45"	118° 01' 48"	Mylonitic calcsilicate gneiss. Road to Empress Lake, at hairpin turn #6.	Cc $\delta^{13}C$	4.6 –5.1
GH-672	50° 24' 06"	118° 02' 25"	Mylonitic Ladybird leucogranite. Logging road up to the top of the ridge between North and South Fosthall Creeks, 0.3 mi. uphill of first hairpin turn.	Qz Fs	11.1 6.0
GH-813	50° 19' 44"	118° 07' 02"	Calcsilicate gneiss. Plant Creek logging road, 2.1 mi. west of turnout to Plant Creek drainage.	Cc $\delta^{13}C$	10.6 –0.7
GH-832	50° 15' 40"	118° 08' 31"	Pure (>90% calcite) marble. Rioux Creek logging road, 0.6 mi. upsteam of last stream crossing before road becomes impassable.	Cc $\delta^{13}C$	24.0 1.3
GH-832a	50° 15' 40"	118° 08' 31"	Pure (>90% calcite) marble. Same outcrop as before.	Cc $\delta^{13}C$	23.8 1.0
GH-834	50° 31' 30"	117° 56' 59"	Leucogranite gneiss. Main logging road along west shore of Arrow Lake, 0.8 mi. north of Limekiln road.	Qz Fs Ga	11.9 –0.4 9.2
Beavan-Cherryville Fault					
GH-385	50° 23' 37"	118° 28' 49"	Calcsilicate gneiss. Logging road along east shore of Sugar Lake, at junction with Sugar Mountain road.	Cc $\delta^{13}C$	4.7 –8.2
GH-386	50° 23' 34"	118° 28' 07"	Calcsilicate gneiss. Logging road along east shore of Sugar Lake ~ 1.0 km east of GH-385.	Cc $\delta^{13}C$	20.3 –4.0
GH-388	50° 23' 22"	118° 27' 06"	Calcsilicate gneiss. Logging road along east shore of Sugar Lake, where Sitkum Creek drains into Sugar Lake.	Cc $\delta^{13}C$	13.5 –5.1
GH-394	50° 23' 09"	118° 29' 02"	Sheared calc-silicate. Logging road east of Sugar Lake, at junction with upper spur logging road.	Cc $\delta^{13}C$	15.2 –1.1

TABLE C.2. (Cont.)

Sample	Latitude	Longitude	Comments	$\delta^{18}O$
GH-394a	50° 23' 09"	118° 29' 02"	Amphibolite. Same outcrop.	Cc 9.0 $\delta^{13}C$ –4.4
GH-396	50° 22' 06"	118° 32' 04"	Sillimanite+muscovite calcsilicate paragneiss. Main logging road west of Sugar Lake, first outcrop north of turnout to campground.	Cc 2.1 $\delta^{13}C$ –5.3
GH-390	50° 23' 45"	118° 20' 54"	Pure (>90% calcite) marble. Sitkum Creek logging road, first outcrop downstream from the Sitkum Lake trailhead.	Cc 17.7 $\delta^{13}C$ 0.7
GH-391	50° 23' 24"	118° 25' 56"	Quartzose calcsilicate. Sitkum Lake logging road, ~1 mi. east of main logging road that follows east shore of Sugar Lake.	Cc 15.9 $\delta^{13}C$ 0.3
GH-392	50° 23' 35"	118° 27' 44"	Quartzose calcsilicate. East Sugar Lake logging road, 1 mile west of Sitkum Creek intersection.	Cc 17.3 $\delta^{13}C$ –4.7

Note: The oxygen isotope data are for whole rocks (WR), quartz (Qz), feldspar (Fs), almandine garnet (Gr), amphibole (Am), biotite (Bi), clinopyroxene (Px), muscovite (Mu), and calcite (Cc).

TABLE C.3. SAMPLE LOCATIONS AND $^{18}O/^{16}O$ DATA ON ROCKS AND MINERALS FROM THE VALHALLA COMPLEX AND VICINITY

Sample	Latitude	Longitude	Location	$\delta^{18}O$	
Valhalla Core Gneisses					
Hybrid Gneiss					
GH-89	49° 40' 43"	117° 42' 04"	Garnet amphibolite. Hoder Creek logging road, 4.2 km west of intersection with Little Slocan road.	WR Qz	9.0 11.2
GH-89a	49° 40' 43"	117° 42' 04"	Leucogranite sheet from same location.	WR Qz Fs	9.0 10.4 10.2
GH-102a	49° 36' 34"	117° 44' 18"	Calcsilicate gneiss. Little Slocan logging road, 1.9 km north of intersection with Koch Creek logging road.	Qz Fs	12.6 10.5
GH-105	49° 42' 28"	117° 33' 25"	Quartzofeldspathic gneiss. Little Slocan logging road, 2.1 km north of intersection with Bannock Burn logging road.	Qz Fs	12.0 10.0
GH-106	49° 44' 03"	117° 30' 06"	Mylonitic metapelite. Little Slocan logging road, 7.1 km north of Bannock Burn intersection.	Qz	10.7
GH-108	49° 44' 38"	117° 29' 11"	Graphitic calcsilicate. Little Slocan logging road, at the Mulvey Creek bridge.	Qz	16.5
GH-614	49° 34' 21"	117° 44' 08"	Pure (>90% calcite) marble. Boulder logging road, near turnoff from Koch Creek road.	Cc $\delta^{13}C$	20.6 2.2
Airy Quartz Monzonite					
GH-302	49° 37' 40"	117° 48' 22"	Megacrystic quartz monzonite. Koch Creek logging road, 3.4 km east of Grizzly Creek road.	WR Qz Fs	9.2 10.1 9.0
Mulvey Granodiorite Gneiss					
GH-96	49° 42' 54"	117° 38' 10"	Augen melanocratic granodiorite orthogneiss. Bannock Burn logging road, at "Y" in the road where canyon branches out.	WR Qz Fs	8.4 9.8 9.0
Slocan Lake Fault Zone					
Upper Plate Nelson Granodiorite					
GH-118	49° 48' 06"	117° 25' 47"	Undeformed Nelson granodiorite. Ottawa Hill logging road, at about 4500 foot elevation.	WR Qz Fs Cc $\delta^{13}C$	5.5 11.5 7.0 2.0 -4.8

TABLE C.3. (Cont.)

Sample	Latitude	Longitude	Comments	$\delta^{18}O$
GH-120	49° 47' 26"	117° 26' 12"	Undeformed Nelson granodiorite. Ottawa Hill logging road, at Scorpion Creek crossing.	WR 8.4 Qz 12.1 Fs 9.0 Cc 1.2 $\delta^{13}C$ –5.8
GH-122	49° 47' 07"	117° 26' 51"	Fractured Nelson granodiorite, fault gouge zones cut the granite. Ottawa Hill logging road, ~ 150 m southeast of hairpin curve #6 (in uphill direction).	WR 7.9 Qz 11.9 Fs 8.7 Cc 2.1 $\delta^{13}C$ –5.5
GH-123	49° 46' 57"	117° 26' 50"	Heavily fractured and altered Nelson granodiorite. Ottawa Hill logging road, halfway between hairpin turns #5 and #6.	Fs 2.9
GH-124a	49° 46' 46"	117° 26' 45"	Extremely fractured hydrothermally altered Nelson granodiorite. Ottawa Hill logging road, ~50 m northeast of hairpin #5.	WR –0.2 Qz 11.3 Fs –1.4 Cc –3.0 $\delta^{13}C$ –4.9
MT-324	49° 54' 02"	117° 23' 10"	Extremely fractured and hydrothermally altered Nelson granodiorite. British Columbia Highway 6, at the rest stop overlooking Slocan Lake.	Qz 9.1 Fs –5.0
Zone of Brecciation				
GH-125	49° 46' 46"	117° 26' 51"	Heavily sheared carbonate-rich fault gouge zone, Slocan Lake fault. Ottawa Hill logging road, at hairpin #3.	WR 0.2 Cc –2.1 $\delta^{13}C$ –5.6
GH-127	49° 46' 37"	117° 27' 10"	Extremely altered carbonate-rich granitoid. Ottawa Hill logging road, about halfway between hairpin #1 and #2.	WR 0.9 Cc –3.2 $\delta^{13}C$ –2.9
GH-150	49° 49' 20"	117° 26' 29"	Chloritic, heavily altered Nelson granodiorite. British Columbia Highway 6, first outcrop on the east side of the road north of Memphis Creek.	WR 3.3 Qz 11.4 Fs 0.5 Cc 2.5 $\delta^{13}C$ –1.1
Lower Plate Mylonite				
GH-151	49° 49' 14"	117° 26' 49"	Muscovite-bearing mylonitic Ladybird leucogranite with chloritic alteration; late brittle faults are normal to the foliation. Highway 6, along traverse from Memphis Creek to Cape Horn.	WR 7.6 Qz 11.0 Fs 6.6
GH-154	49° 49' 01"	117° 27' 41"	Late brittle fault cutting Ladybird mylonite. ~ 200 m south of the Cape Horn E-W to N-S bend in Highway 6.	WR 5.3

TABLE C.3. (Cont.)

Sample	Latitude	Longitude	Comments	$\delta^{18}O$
GH-155	49° 49' 08"	117° 29' 31"	Ladybird mylonite. Highway 6, at the Cape Horn bend.	WR 10.0 Qz 11.3 Fs 8.9
GH-159	49° 48' 15"	117° 27' 58"	Mylonitic mafic paragneiss; pyrite is common at this outcrop. Highway 6, ~1.6 km south of Cape Horn bend.	Qz 12.6 Fs 10.3
GH-140	49° 46' 24"	117° 27' 56"	Mylonitic leucogranite sheet in the hybrid gneiss. The old road that follows the east shore of Slocan Lake, first outcrop north of Slocan.	WR 9.6 Qz 11.6 Fs 9.1
GH-134	49° 47' 01"	117° 28' 11"	Mylonitic augen gneiss. The old road that follows the east shore of Slocan Lake, near the end of the road.	WR 10.1 Qz 11.2 Fs 8.6
Valkyr Shear Zone				
Ladybird Quartz Monzonite				
GH-297	49° 42' 15"	117° 55' 00"	Protomylonitic Ladybird leucogranite. Koch Creek logging road, 0.7 km north of first bridge beyond the junction with the powerline road.	Qz 10.8 Fs 8.1
GH-307	49° 44' 45"	117° 53' 10"	Undeformed Ladybird leucogranite. Koch Creek logging road, 2.0 km north of junction with Dago Creek logging road.	WR 1.0 Qz 7.8 Fs 0.2
GH-309	49° 45' 56"	117° 51' 56"	Ladybird quartz monzonite. Koch Creek logging road, at the first bridge north of junction with Dago Creek logging road.	Qz 11.2 Fs 7.9
GH-309a	49° 45' 56"	117° 51' 56"	Thin (~2 cm) aplite dike cutting the quartz monzonite. Same outcrop as previous sample.	Qz 10.9 Fs 7.0
GH-311	49° 46' 27"	117° 51' 36"	Ladybird quartz monzonite. Koch Creek logging road, 0,9 km north of first bridge beyond junction with Dago Creek road.	Qz 10.5 Fs 7.7 Sp 6.0
GH-314	49° 37' 10"	117° 54' 18"	Undeformed Ladybird quartz monzonite. Grizzly Creek logging road, 2.4 km southwest of the first bridge.	Qz 10.9 Fs 8.8
GH-316	49° 27' 10"	117° 48' 18"	Undeformed Ladybird leucogranite. Ladybird Creek logging road, at 13 km marker.	Qz 10.8 Fs 8.8
GH-317	49° 26' 54"	117° 46' 54"	Mylonitic Ladybird leucogranite. Ladybird Creek logging road, 2.8 km east of the bridge at the 14 km marker.	Qz 9.7 Fs 4.6

TABLE C.3. (Cont.)

Sample	Latitude	Longitude	Comments	$\delta^{18}O$
Late-Stage Lamphrophyre Dike				
GH-299	49° 40' 08"	117° 52' 47"	Extremely hydrothermally altered, green, lamprophyre dike. Koch Creek logging road, 3.1 km east of the powerline road turnoff.	WR −5.1 Cc −1.3 $\delta^{13}C$ −2.4
The Coryell Intrusive Suite				
Renata Pluton				
GH-563	49° 27' 00"	118° 05' 15"	Coarse-grained Coryell quartz syenite. Logging road along east shore of southern Arrow Lake, 1.2 mi. north of the end of good road.	Qz 8.5 Pl 0.2 Am 4.5 Sp 3.7
GH-780	49° 26' 19"	118° 06' 34"	Fine-grained Coryell quartz syenite. At the Renata ferry port.	Qz 8.4 Pl −1.7
Arrow Lake Pluton				
GH-586	49° 45' 37"	118° 06' 25"	Coryell quartz syenite. Logging road along the east shore of Arrow Lake south of Applegrove, 2.4 mi. south of Applegrove crossing.	Qz 8.4 Am 4.9
GH-791	49° 35' 06"	118° 13' 37"	Megacrystic Coryell syenite porphyry. Main logging road that follows west side of the Christina Range, at Michaud Creek.	Ks 7.6 Pl 6.3 Am 5.4
GH-793	49° 37' 45"	118° 13' 53"	Megacrystic Coryell syenite porphyry. Main logging road that follows west side of the Christina Range, 3.4 mi. north of Michaud Creek.	Ks 7.6 Ep −2.6
GH-868	49° 40' 57"	118° 28' 15"	Coryell quartz syenite porphyry. Burrell Creek logging road, 3.1 mi. south of the "Y" in the road at Burrell Creek.	Qz 8.5 Pl 5.1
GH-874	49° 32' 02"	118° 21' 12"	Coryell quartz syenite porphyry. Burrell Creek logging road, 0.4 mi. south of Nicholl Creek.	Qz 8.2

Note: The oxygen isotope data are for whole rocks (WR), quartz (Qz), feldspar (Fs), plagioclase (Pl), K-Feldspar (Ks), amphibole (Am), epidote (Ep), sphene (Sp), and calcite (Cc).

TABLE C.4. SAMPLE LOCATIONS AND $^{18}O/^{16}O$ DATA ON MISCELLANEOUS SAMPLES FROM THE SOUTHERN OMINECA BELT, BRITISH COLUMBIA

Sample	Latitude	Longitude	Location	$\delta^{18}O$
Low-Grade Windermere Supergroup				
PW-1c	50° 23' 28"	116° 35' 48"	Chlorite-grade arkosic grit, Windermere Supergroup. Jumbo Creek logging road, at the end of the road.	Fs 15.8
PW-4b	50° 34' 24"	116° 17' 11"	Chlorite-grade arkosic pebble conglomerate, Horsethief Creek Group, Windermere Supergroup. Horsethief Creek logging road, first outcrop south of the bridge across Horsethief Creek.	Qz 10.5 Fs 13.0
PW-9a	50° 56' 36"	116° 41' 32"	Feldspathic grit interlayered with shale, Windermere Supergroup. Bobbie Burns logging road, 5.7 km north of junction with Driftwood Creek road.	Qz 10.2
Miscellaneous Marbles				
GH-202	50° 36' 29"	118° 50' 57"	Very coarse-grained (>1cm) phlogopite marble. Mabel Lake road, 0.7 km west of junction with Cooke Creek logging road.	Cc 18.5 $\delta^{13}C$ 4.0
GH-203	50° 35' 08"	118° 52' 40"	Marble with cross-cutting pegmatite. Mabel Lake road,0.7 km west of Falls Creek.	Cc 12.1 $\delta^{13}C$ 1.6
GH-342	49° 29' 38"	117° 23' 43"	Marble with elongated chert nodules. British Columbia Highway 3A-6, first outcrop west of the crossing over the Kootenay River west of Nelson, British Columbia.	Cc 17.9 $\delta^{13}C$ −1.3
GH-887a	49° 06' 19"	118° 27' 52"	Marble from the footwall of a fault in the Granby River valley (Granby fault ?). The paved road along the west side of the Granby Valley, 0.5 km south of Niagara	Cc 14.2 $\delta^{13}C$ 0.8

Note: The oxygen isotope data are for quartz (Qz), feldspar (Fs), and calcite (Cc).

References

Abers, G.A., 1991. Possible seismogenic shallow-dipping normal faults in the Woodlark-D'Entrecasteaux extensional province, Papua New Guinea, *Geology* , **19**, 1205-1208.

Aitken, J.D., and McMechen, M.E., 1991. Middle Proterozoic assemblages, Chapter 5 in, *Geology of the Cordilleran Orogen in Canada*, H. Gabrielse and C.J. Yorath (ed.); *Geological Survey of Canada*, Geology of Canada, no. **4**, p. 97-124.

Allen, T., and Chamberlain, C. P., 1991. Metamorphic evidence for an inverted crustal section, with constraints on the main Karakorum thrust, Baltistan, Northern Pakistan, *Journal of Metamorphic Geology*, **9**, 403-418.

Althaus, E., Karotke, E., Nitsch, K.H., and Winkler, H.G.F., 1970. An experimental re-examination of the upper stability limit of muscovite plus quartz, *N. Jahrbuch fur Mineralogie*, **112**, 324-336.

Anderson, R.E., 1971. Thin skin distension in Tertiary rocks of southeastern Nevada, *Geological Society of America Bulletin*, **82**, 43-58.

Anderson, J.L., Barth, A.P., and Young, E.D., 1988. Mid-crustal Cretaceous roots of Cordilleran metamorphic core complexes, *Geology*, **16**, 366-369.

Archibald, D.A., Glover, J.K., Price, R.A., Farrar, E., and Carmichael, D.M., 1983. Geochronology and tectonic implications of magmatism and metamorphism, southern Kootenay Arc and neighboring regions, Southeastern British Columbia. Part I: Jurassic to mid-Cretaceous, *Canadian Journal of Earth Sciences*, **20**, 1891-1913.

Archibald, D.A., Krogh, T.E., Armstrong, R.L., and Farrar, E., 1984. Geochronology and tectonic implications of magmatism and metamorphism, southern Kootenay Arc and neighboring regions, Southeastern British Columbia. Part II: Mid-Cretaceous to Eocene, *Canadian Journal of Earth Sciences*, **21**, 567-583.

Armstrong, R.L., 1972. Low-angle (denudation) faults, hinterland of the Sevier orogenic belt, Eastern Nevada and Western, Utah, *Geological Society of America Bulletin*, **83**, 1729-1754.

Armstrong, R.L., 1982. Cordilleran metamorphic core complexes – from Arizona to Southern Canada, *Annual Reviews in Earth and Planetary Sciences*, **10**, 129-154.

Armstrong, R.L., 1988. Mesozoic and early Cenozoic magmatic evolution of the Canadian Cordillera, *Geological Society of America Special Paper*, **218**, 55-91.

Armstrong, R.L., and Hansen, E., 1966. Cordilleran infrastructure in the Eastern Great Basin, *American Journal of Science*, **264**, 112-127.

Armstrong, R.L., Parrish, R.R., Van der Heyden, P., Scott, K., Runkle, D., and Brown, R.L., 1991. Early Proterozoic basement exposures in the southern Canadian Cordillera: core gneiss of Frenchman Cap, Unit I of the Grand Forks Gneiss, and the Vaseaux Formation, *Canadian Journal of Earth Sciences*, **28**, 1169-1201.

Armstrong, R.L., and Ward, P., 1991. Evolving geographic patterns of Cenozoic magmatism in the North American Cordillera: the temporal and spatial association of magmatism and metamorphic core complexes, *Journal of Geophysical Research*, **96**, 13201-13224.

Arzi, A.A., 1978. Critical phenomena in the rheology of partially melted rocks, *Tectonophysics*, **44**, 173-184.

Asprey, L.B., 1976. The preparation of very pure fluorine gas, *Journal of Fluorine Chemistry*, **7**, 359-361.

Axen, G.J., 1992. Pore pressure, stress release, and fault weakening in low angle faulting, *Journal of Geophysical Research*, **97**, 8979-8991.

Axen, G.J., and Selverstone, J., 1994. Stress-state and fluid-pressure level along the Whipple detachment fault, California, *Geology*, **22**, 835-838.

Baldwin, S.L., 1993. Thermochronologic constraints on the tectonic evolution of an active metamorphic core complex, D'Entrecasteaux Islands, Papua New Guinea, *Tectonics*, **12**, 611-628.

Bardoux, M., 1985. The Kelowna detachment zone, Okanagan Valley, South-Central British Columbia, *Current Research, Part A, Geological Survey of Canada Paper*, **85-1A**, 333-339.

Bartley, J.M., and Glazner, A.F., 1985. Hydrothermal systems and Tertiary normal faulting in the Southwestern United States, *Geology*, **13**, 562-564.

Beaudoin, G., Roddick, J.C., and Sangster, D.F., 1992. Eocene age for Ag–Pb–Zn–Au vein and replacement deposits of the Kokanee Range, Southeastern British Columbia, *Canadian Journal of Earth Sciences*, **29**, 3-14.

Beaudoin, G., Sangster, D.F., and Godwin, C.I., 1992. Isotopic evidence for complex Pb sources in the Ag–Pb–Zn–Au veins of the Kokanee Range, Southeastern British Columbia, *Canadian Journal of Earth Sciences*, **29**, 418-431.

Beaudoin, G., Taylor, B.E., and Sangster, D.F., 1991. Silver-lead-zinc veins, metamorphic core complexes, and hydrologic regimes during crustal extension, *Geology*, **19**, 1217-1220.

Beaudoin, G., Taylor, B.E., and Sangster, D.F., 1992. Silver-lead-zinc veins and crustal hydrology during Eocene extension, Southeastern British Columbia, Canada, *Geochimica et Cosmochimica Acta*, **56**, 3513-3529.

Beddoe-Stephens, B., 1982. The petrology of the Rossland volcanic rocks, Southern British Columbia, *Geological Society of America Bulletin*, **93**, 585-594.

Beddoe-Stephens, B., and Lambert, R.S.J., 1981. Geochemical, mineralogical, and isotopic data relating to the origin and tectonic setting of the Rossland volcanic rocks, Southeastern British Columbia, *Canadian Journal of Earth Sciences*, **18**, 858-868.

Bergantz, G.W., 1989. Underplating and partial melting: implications for melt generation and extraction, *Science*, **245**, 1093-1095.

Berner, R.A., Lasaga, A.C., and Garrels, R.M., 1983. The carbonate-silicate geochemical cycle and its effect on atmospheric carbon dioxide over the past 100 million years, *American Journal of Science*, **283**, 641-683.

Bevier, M.L., 1987. A Pb isotopic study of the Valhalla complex and its surrounding rocks, Southeastern British Columbia: preliminary interpretations, in *Radiogenic Age and Isotopic Studies: Report 1, Geological Survey of Canada Paper*, **87-2**, 13-20.

Bickle, M.J., and McKenzie, D., 1987. The transport of heat and matter by fluids during metamorphism, *Contributions to Mineralogy and Petrology*, **95**, 384-392.

Blattner, P., 1971. Migmatite by partial fusion and short range hydrothermal transfer, British Columbia, *Schweiz. Min. Petr. Mitt.*, **51**, 155-177.

Block, L.H., and Royden, L.H., 1990. Core complex geometries and regional-scale flow in the lower crust, *Tectonics*, **9**, 557-567.

Bohrson, W.A., and Clague, D.A., 1988. Origin of ultramafic xenoliths containing exsolved pyroxenes from Hualalai volcano, Hawaii, *Contributions to Mineralogy and Petrology*, **100**, 139-155.

Bond, G.C., and Kominz, M.A., 1984. Construction of tectonic subsidence curves for the early Paleozoic miogeosyncline, Southern Canadian Rocky Mountains: Implications for subsidence mechanisms, age of breakup and crustal thinning, *Geological Society of America Bulletin*, **95**, 155-173.

Bosdachin, R., and Harrap, R.M., 1988. Stratigraphy and structure of the Monashee complex and overlying rocks adjacent to the Trans-Canada Highway, west of Revelstoke, B.C., in *Current Research, Part E, Geological Survey of Canada Paper*, **88-1E**, 19-23.

Bottinga, Y., 1969. Calculated fractionation factors for carbon and hydrogen isotopic exchange in the system calcite-carbon dioxide-graphite-methane-hydrogen-water vapor, *Geochimica et Cosmochimica Acta*, **33**, 41-64.

Bowman, J.R., and Ghent, E.D., 1986. Oxygen and hydrogen isotope study of minerals from metapelitic rocks, staurolite to sillimanite zones, Mica Creek, British Columbia, *Journal of Metamorphic Geology*, **4**, 131-141.

Brandon, A.D., and Lambert, R.S.J., 1993. Geochemical characterization of mid-Cretaceous granitoids of the Kootenay Arc in the Southern Canadian Cordillera, *Canadian Journal of Earth Sciences*, **30**, 1076-1090.

Brandon, A.D., and Lambert, R.S.J., 1994. Crustal melting in the Cordilleran interior: the mid-Cretaceous White Creek batholith in the Southern Canadian Cordillera, *Journal of Petrology*, **35**, ???-???.

Brandon, A.D., and Smith, A.D., 1994. Mesozoic granitoid magmatism in Southeast British Columbia: implications for the origin of granitoid belts in the North American Cordillera, *Journal of Geophysical Research*, **99**, 11879-11896.

Brooks, W.E., 1986. Distribution of anomalously high K_2O volcanic rocks in Arizona: Metasomatism at the Picacho Peak detachment fault, *Geology*, **14**, 339-342.

Brown, M., 1994. The generation, segregation, ascent and emplacement of granite magma: the migmatite-to-crustally-derived granite connection in thickened orogens, *Earth Science Reviews*, **36**, 83-130.

Brown, R.L., and Journeay, J.M., 1987. Tectonic denudation of the Shuswap metamorphic terrane of Southeastern British Columbia, *Geology*, **15**, 142-146.

Brown, R.L., Journeay, J.M., Lane, L.S., Murphy, D.C., and Rees, C.J., 1986. Obduction, backfolding, and piggyback thrusting in the metamorphic hinterland of the Southeastern Canadian Cordillera, *Journal of Structural Geology*, **8**, 255-268.

Brown, R.L., and Murphy, D.C., 1982. Kinematic interpretation of mylonitic rocks in part of the Columbia River fault zone, Shuswap terrane, British Columbia, *Canadian Journal of Earth Sciences*, **19**, 456-465.

Brown, R.L., and Read, P.B., 1983. Shuswap terrane of British Columbia: A Mesozoic "core complex," *Geology*, **11**, 164-168.

Brown, R.L., Tippet, C.R., and Lane, L.S., 1978. Stratigraphy, facies changes, and correlations in the Northern Selkirk Mountains, Southern Canadian Cordillera, *Canadian Journal of Earth Sciences*, **15**, 1129-1140.

Brown, R.L., and 5 others, 1992. The Monashee decollement of the southern Canadian Cordillera: a crustal-scale shear zone linking the Rocky Mountain foreland belt to lower crust beneath accreted terranes, in *Thrust Tectonics* (edited by K.R. McClay), Chapman and Hall, London, 357-364.

Burchfiel, B.C., and Royden, L.H., 1985. North-south extension within the convergent Himalayan region, *Geology*, **13**, 679-682.

Carr, S.D., 1991. U-pb zircon and titanite ages of three Mesozoic igneous rocks south of the Thor-Odin – Pinnacles area, Southern Omineca Belt, British Columbia, *Canadian Journal of Earth Sciences*, **28**, 1877-1882.

Carr, S.D., 1991. Three crustal zones in the Thor-Odin - Pinnacles area, Southern Omineca Belt, British Columbia, *Canadian Journal of Earth Sciences*, **28**, 2003-2023.

Carr, S.D., 1992. Tectonic setting and U-Pb geochronology of the early Tertiary Ladybird leucogranite suite, Thor-Odin - Pinnacles area, Southern Omineca belt, British Columbia, *Tectonics*, **11**, 258-278.

Carr, S.D., 1995. The Southern Omineca belt, British Columbia: new perspectives from the Lithoprobe geoscience program, *Canadian Journal of Earth Sciences*, **32**, 1720-1739.

Carr, S.D., and Parkinson, D.L., 1989. Eocene stratigraphy, age of the Coryell batholith, and extensional faults in the Granby Valley, Southern British Columbia, in *Current Research, Part E, Geological Survey of Canada Paper*, **89-1E**, 79-87.

Carr, S.D., Parrish, R.R., and Brown, R.L., 1987. Eocene structural development of the Valhalla complex, Southeastern British Columbia, *Tectonics*, **6**, 175-196.

Carter, E.S., Orchard, M.J., Ross, C.A., Ross, J.R.P., Smith, P.L., and Tipper, H.W., 1991. Part B. Palentological signatures of terranes; in , Chapter 2 of Geology of the Cordilleran Orogen in Canada, H. Gabrielse and C.J. Yorath (eds.); Geological Survey of Canada, Geology of Canada, no. 4, 28-38.

Cathles, L.M., 1983. An analysis of the hydrothermal system responsible for massive sulfide deposition in the Hukoroko basin of Japan, *Economic Geology Monograph*, **5**, 439-487.

Chamberlain, C.P., and Conrad, M.E., 1991. Oxygen isotope zoning in garnet, *Science*, **254**, 403-406.

Chapin, C.E., and Lindley, J.I., 1986. Potassium metasomatism of igneous and sedimentary rocks in detachment terranes and other sedimentary basins: Economic implications, *Arizona Geological Society Digest*, **16**, 118-126.

Cheney, E.S., 1980. Kettle dome and related structures of Northeastern Washington, *Geological Society of America Memoir*, **153**, 463-483.

Church, B.N., 1973. Geology of the White Lake Basin, *British Columbia Department of Mines and Petroleum Resources Bulletin*, **61**, 120p.

Clark, I.D., Fritz, P., Michel, F.A., and Souther, J.G., Isotope hydrogeology and geothermometry of the Mt. Meager geothermal area, *Canadian Journal of Earth Sciences*, **19**, 1454-1473.

Clayton, R.N., and Kieffer, S.W., 1991. Oxygen isotopic thermometer calculations; in: Stable Isotope Geochemistry, *Stable Isotope Geochemistry: A Tribute to Samuel Epstein. Geochemical Society Special Publication:* **No. 3**, 3-10.

Clayton, R.N., O'Neil, J.R., and Mayeda, T.K., 1972. Oxygen isotope exchange between quartz and water, *Journal of Geophysical Research*, **77**, 3057-3067.

Clemens, J.D., and Vielzeuf, D., 1987. Constraints on melting and magma production in the crust, *Earth and Planetary Science Letters*, **86**, 287-306.

Cloos, M., 1985. Thermal evolution of convergent plate margins – Thermal modeling and reevaluation of isotopic Ar-ages for blueschists in the Franciscan complex of California, *Tectonics*, **4**, 421-433.

Cole, D.R., and Ohmoto, H., 1986. Kinetics of isotopic exchange at elevated pressures and temperatures, *Reviews in Mineralogy*, **16**, 41-87.

Coney, P.J., 1973. Non-collision tectogenesis in Western North America, in: *Implications of Continental Drift to the Earth Sciences,* (edited by D.H. Tarling and S.K. Runcorn) Academic Press, New York, 713-727.

Coney, P.J., 1980. Cordilleran metamorphic core complexes: an overview, *Geological Society of America Memoir*, **153**, 7-31.

Coney, P.J., and Harms, T., 1984. Cordilleran metamorphic core complexes: Cenozoic extensional relics of Mesozoic compression, *Geology*, **12**, 550-554.

Coney, P.J., Jones, D.L., and Monger, J.W.H., 1980. Cordilleran suspect terranes, *Nature*, **288**, 329-333.

Connolly, J.A.D., and Thompson, A.B., 1989. Fluid and enthalpy production during regional metamorphism, *Contributions to Mineralogy and Petrology*, **102**, 347-366.

Cook, F.A., and Varsek, J.L., 1994. Orogen-scale decollements, *Reviews in Geophysics*, **32**, 37-60.

Cook, F.A., and 9 others, 1992. Lithoprobe crustal reflection cross section of the Southern Canadian Cordillera, 1, Foreland thrust and fold belt to Fraser River fault, *Tectonics*, **11**, 12-35.

Craig, H., 1957. Isotopic standards for carbon and oxygen and correction factors for mass-spectrometric analysis of carbon dioxide, *Geochimica et Cosmochimica Acta*, **12**, 133-149.

Craig, H., 1961. Isotopic variations in meteoric waters, *Science*, **133**, 1702-1703.

Crawford, M. L., Hollister, L. S., and Woodsworth, G. J., 1987. Crustal deformation and regional metamorphism across a terrane boundary, Coast Plutonic complex, British Columbia, *Tectonics*, **6**, 343-361.

Criss, R.E., and Taylor, H.P. Jr., 1983. An $^{18}O/^{16}O$ and D/H study of Tertiary hydrothermal systems in the southern half of the Idaho Batholith, *Geological Society of America Bulletin*, **94**, 640-663.

Criss, R.E., and Taylor, H.P. Jr., 1986. Meteoric-hydrothermal systems, *Reviews in Mineralogy*, **16**, 373-424.

Criss, R.E., and Fleck, R.J., 1990. Oxygen isotope map of the giant metamorphic-hydrothermal system around the northern part of the Idaho batholith, U.S.A., *Applied Geochemistry*, **5**, 641-655.

Criss, R.E., Fleck, R.J., and Taylor, H.P. Jr., 1991. Tertiary meteoric hydrothermal systems and their relation to ore deposition, Northwestern United States and Southern British Columbia, *Journal of Geophysical Research*, **96**, 13335-13356.

Criss, R.E., Gregory, R.T., and Taylor, H.P. Jr., 1987. Kinetic theory of oxygen isotope exchange between minerals and water, *Geochimica et Cosmochimica Acta*, **51**, 1099-1108.

Criss, R.E., Lanphere, M.A., and Taylor, H.P. Jr., 1982. Effects of regional uplift, deformation, and meteoric-hydrothermal metamorphism on K-Ar ages of biotites in the southern half of the Idaho batholith, *Journal of Geophysical Research*, **87**, 7029-7046.

Crittenden, M.D., 1980. Metamorphic core complexes of the North American Cordillera: summary, *Geological Society of America Memoir*, **153**, 485-490.

Crittenden, M.D., Coney, P.J., and Davis, G.H., 1980. Cordilleran metamorphic core complexes, *Geological Society of America Memoir* **153**.

Crosby, P., 1968. Tectonic, plutonic, and metamorphic history of the central Kootenay Arc, British Columbia, Canada, *Geological Society of America Special Paper*, **99.**

Dalziel, I.W.D., and Brown, R.L., 1989. Tectonic denudation of the Darwin metamorphic core complex in the Andes of Tierra del Fuego, Southernmost Chile: Implications for Cordilleran orogenesis, *Geology*, **17**, 699-703.

Dansgaard, W., 1964. Stable isotopes in precipitation, *Tellus*, **16**, 436-468.

Davis, G.A., and Lister, G.S., 1986. Detachment faulting in continental extension; perspectives from the Southwestern U.S. Cordillera, *Geological Society of America Special Paper*, **218**, 133-159.

Davis, G.H., 1983. Shear-zone model for the origin of metamorphic core complexes, *Geology*, **14**, 342-347.

Davis, G.H., and Coney, P.J., 1979. Geologic development of the Cordilleran metamorphic core complexes, *Geology*, **7**, 120-124.

Devlin, W.J., 1984. Syn-depositional tectonism related to continental break-up in the Hamill Group, Northern Selkirk Mountains, British Columbia, *Geological Association of Canada Program with Abstracts*, **9**, 57.

Dewey, J.F., 1988. Extensional collapse of orogens, *Tectonics*, **7**, 1123-1139.

Dodson, M.H., 1973. Closure temperature in cooling geochronological and petrological systems, *Contributions to Mineralogy and Petrology*, **40**, 259-274.

Douglas, R., and Woodruff, F., 1981. Deep-sea benthic foraminifera, in Emiliani, C., ed., *The Sea* , New York, Wiley Interscience, 1233-1328.

Dullien, F.A.L., 1979. *Porous Media. Fluid Transport and Pore Structure.* (Academic Press, New York.)

Duncan, I.J., 1984. Structural evolution of the Thor-Odin gneiss dome, *Tectonophysics*, **101**, 87-130.

Echtler, H., and Malavieille, J., 1990. Extensional tectonics, basement uplift, and Stephano-Permian collapse basin in a late Variscan metamorphic core complex (Montagne Noire, Southern Massif Central), *Tectonophysics*, **177**, 125-138.

Elsenheimer, D., and Valley, J.W., 1992. In situ oxygen isotope analysis of feldspar and quartz by Nd:YAG laser microprobe, *Chemical Geology*, **101**, 21-42.

England, P.C., and Thompson, A.B., 1984. Pressure-temperature-time paths of regional metamorphism: I. heat transfer during the evolution of regions of thickened continental crust, *Journal of Petrology*, **25**, 929-955.

Eslinger, E.V., and Savin, S.M., 1973. Oxygen isotope geothermometry of the burial metamorphic rocks of the Precambrian Belt Supergroup, Glacier National Park, Montana, *Geological Society of America Bulletin*, **84**, 2549-2560.

Ewing, T.E., 1981. Regional stratigraphy and structural setting of the Kamloops Group, South-Central British Columbia, *Canadian Journal of Earth Sciences*, **18**, 1464-1477.

Ferry, J.M., and Dipple, G.M., 1991. Fluid flow, mineral reactions, and metasomatism, *Geology*, **19**, 211-214.

Forester, R.W., and Taylor, H.P. Jr., 1977. $^{18}O/^{16}O$, D/H, and $^{13}C/^{12}C$ studies of the Tertiary igneous complex of Skye, Scotland, *American Journal of Science*, **277**, 136-177.

Fortier, S.M., and Giletti, B.J., 1989. An empirical model for predicting diffusion coefficients in silicate minerals, *Science*, **245**, 1481-1484.

Fossen, H., and Rykkelid, E., 1992. Post-collisional extension of the Caledonide orogen in Scandanavia: structural expressions and tectonic significance, *Geology*, **20**, 737-740.

Fox, K.F. Jr., 1994. Geology of metamorphic core complexes and associated extensional structures in North-Central Washington, *Washington Division of Energy and Earth Resources, Bulletin*, **80**, 21-47.

France-Lanord, C., Le Fort, P., Pecher, A., and Sheppard, S. M. F., 1988. Evidence for large scale migration of fluids during evolution of Himalaya reverse metamorphism, *EOS Transactions of the American Geophysical Union*, **67**, 399.

France-Lanord, C., and Sheppard, S.M.F., 1988. Large scale infiltration of fluids during regional metamorphism. H and C isotope evidence from Central Nepal, *Chemical Geology*, **70**, 160.

France-Lanord, C., Sheppard, S.M.F., and Le Fort, P., 1986. Hydrogen and oxygen isotope variations in the High Himalaya peraluminous Manaslu leucogranite: evidence for heterogeneous sedimentary source, *Geochimica et Cosmochimica Acta*, **52**, 513-526.

Friedman, I., Redfield, A.C., Schoen, B., and Harris, J., 1964. The variation of the deuterium content of natural waters in the hydrologic cycle, *Reviews in Geophysics*, **2**, 177-224.

Fricke, H.C., Wickham, S.M., and O'Neil, J.R., 1992. Oxygen and hydrogen isotope evidence for meteoric water infiltration during mylonitization and uplift in the Ruby Mountains-East Humboldt Range core complex, Nevada, *Contributions to Mineralogy and Petrology*, **111**, 203-221.

Fritz, W.H., Cecile, M.P., Norford, B.S., Morrow, D., and Geldsetzer, H.H.J., 1991. Cambrian to Middle Devonian Assemblages, Chapter 7; in, *Geology of the Cordilleran Orogen in Canada*, H. Gabrielse and C.J. Yorath (ed.); *Geological Survey of Canada*, Geology of Canada, no. **4**, p. 151-218.

Froese, E., 1970. Chemical petrology of some pelitic gneisses and migmatites from the Thor-Odin area, British Columbia, *Canadian Journal of Earth Sciences*, **7**, 164-175.

Fyles, J.T., 1964. Geology of the Duncan Lake area, Lardeau District, British Columbia, *British Columbia Department of Mines and Petroleum Resources Bulletin*, **49**.

Fyles, J.T., 1967. Geology of the Ainsworth-Kaslo area, British Columbia, *British Columbia Ministry of Energy, Mines and Petroleum Resources Bulletin* , **53**.

Fyles, J.T., 1970. The Jordan River area, British Columbia, *British Columbia Department of Mines and Petroleum Resources Bulletin* , **57**.

Fyles, J.T., and Eastwood, G.E.P., 1962. Geology of the Ferguson area, *British Columbia Department of Mines and Petroleum Resources Bulletin* , **45**.

Gabrielse, H., and Campbell, R.B., 1991. Upper Proterozoic Assemblages, *Geology of the Cordilleran Orogen in Canada*, H. Gabrielse and C.J. Yorath (ed.); *Geological Survey of Canada*, Geology of Canada, no. **4**, p. 125-150.

Gabrielse, H. et al., 1991. Part A. Morphologeological belts, tectonic assemblages, and terranes; in Chapter 2 of*Geology of the Cordilleran Orogen in Canada*, H. Gabrielse and C.J. Yorath (ed.); *Geological Survey of Canada*, Geology of Canada, no. **4**, p. 15-28.

Gabrielse, H. et al., 1991. Structural styles, Chapter 17; in, *Geology of the Cordilleran Orogen in Canada*, H. Gabrielse and C.J. Yorath (ed.); *Geological Survey of Canada*, Geology of Canada, no. **4**, p. 571-675.

Gans, P.B., 1987. An open-system, two-layer crustal stretching model for the Eastern Great Basin, *Tectonics*, **6**, 1-12.

Gans, P.B., Mahood, G.A., and Schermer, E., 1989. Synextensional magmatism in the Basin and Range province: a case study from the Eastern Great Basin, *Geological Society of America Special Paper*, **233**.

Garlick, G.D., Epstein, S., 1966. Oxygen isotope ratios in coexisting minerals of regionally metamorphosed rocks, *Geochimica Cosmochimica Acta*, **31**, 181-214.

Getty, S.R., and Gromet, L.P., 1992. Geochronological constraints on ductile deformation, crustal extension, and doming about a basement-cover boundary, New England Appalachians, *American Journal of Science*, **292**, 359-397.

Ghent, E.D., Nicholls, J., Simony, P.S., Sevigny, J.H., and Stout, M.Z., 1991. Hornblende geobarometry of the Nelson batholith, Southeastern British Columbia, *Canadian Journal of Earth Sciences*, **28**, 1982-1991.

Ghent, E.D., and O'Neil, J.R., 1985. Late Precambrian marbles of unusual carbon-isotope composition, Southeastern British Columbia, *Canadian Journal of Earth Sciences*, **22**, 324-329.

Ghosh, D.K., 1995. U-Pb geochronology of Jurassic to early Tertiary granitic intrusives from the Nelson-Castlegar area, Southeastern British Columbia, *Canadian Journal of Earth Sciences*, **32**, 1668-1680.

Ghosh, D.K., 1995. Nd-Sr isotopic constraints on the interactions of the Intermontane Superterrane with the western edge of North America in the Southern Canadian Cordillera, *Canadian Journal of Earth Sciences*, **32**, 1740-1758.

Giletti, B.J., 1988. Diffusion effects on oxygen isotope temperatures of slowly cooled igneous and metamorphic rocks, *Earth and Planetary Science Letters*, **77**, 218-228.

Goldfarb, R. J., Newberry, R. J., Pickthorn, W. J., and Gent, C. A., 1991. Oxygen, hydrogen, and sulfur isotope studies in the Juneau gold belt, Southeastern Alaska: Constraints on the origin of hydrothermal fluids, *Economic Geology*, **86**, 66-80.

Goldfarb, R.J., Snee, L.W., Miller, L.D., and Newberry, R.J., 1991. Rapid dewatering of the crust deduced from ages of mesothermal gold deposits, *Nature*, **354**, 296-298.

Graham, C.M., and England, P.C., 1976. Thermal regimes and regional metamorphism in the vicinity of overthrust faults: an example of shear heating and inverted metamorphic zonation from Southern California, *Earth and Planetary Science Letters*, **31**, 142-152.

Greenwood, H.J., 1975. Buffering of pore fluids by metamorphic reactions, *American Journal of Science*, **275**, 573-593.

Greenwood, H.J., Woodsworth, G.J., Read, P.B., Ghent, E.D., and Evenchick, C.A., 1991. Metamorphism, *Geology of the Cordilleran Orogen in Canada*, H. Gabrielse and C.J. Yorath (ed.); *Geological Survey of Canada*, Geology of Canada, no. **4**, p. 535-570.

Gregory, R.T., and Taylor, H.P. Jr., 1981. An oxygen isotope profile in a section of Cretaceous oceanic crust, Samial Ophiolite, Oman: evidence for $\delta^{18}O$ buffering of the oceans by deep (>5km) seawater-hydrothermal circulation at mid-ocean ridges, *Journal of Geophysical Research*, **86**, 2737-2755.

Gregory, R.T., Criss, R.E., and Taylor, H.P. Jr., 1989. Oxygen isotope exchange kinetics of mineral pairs in closed and open systems: applications to problems of hydrothermal alteration of igneous rocks and Precambrian iron formations, *Chemical Geology*, **75**, 1-42.

Grunder, A.L., and Wickham, S.M., 1991. Homogenization and lowering of $^{18}O/^{16}O$ in mid-crustal rocks during extension-related magmatism in Eastern Nevada, *Earth and Planetary Science Letters*, **107**, 416-431.

Hansen, V.L., and Goodge, J.W., 1988. Metamorphism, structural petrology, and regional evolution of the Okanogan complex, Northeastern Washington, in *Metamorphism and Crustal Evolution of the Western United States, Rubey Volume VII* (editor, W.G. Ernst), Prentice Hall, Englewood Cliffs, New Jersey, 234-270.

Hildreth, W., Halliday, A.N., and Christiansen, R.L., 1991. Isotopic and chemical evidence concerning the genesis and contamination of basaltic and rhyolitic magma beneath the Yellowstone Plateau volcanic field, *Journal of Petrology*, **32**, 63-138.

Himmelberg, G. R., Brew, D. A., and Ford, A. B., 1991. Development of inverted metamorphic isograds in the western metamorphic belt, Juneau, Alaska, *Journal fofMetamorphic Geology*, **9**, 165-180.

Hitchon, B., and Krouse, H.R., 1972. Hydrogeochemistry of the surface waters of the MacKensie River drainage basin, Canada, III, Stable isotopes of oxygen, carbon, and sulphur, *Geochimica et Cosmochimica Acta*, **36**, 1337-1357.

Hodges, K.V., and Walker, J.D., 1992. Extension in the Cretaceous Sevier orogen, North American Cordillera, *Geological Society of America Bulletin*, **104**, 560-569.

Hoernes, S., and Friedrichsen, H., 1980. Oxygen and hydrogen isotopic composition of Alpine and pre-Alpine minerals of the Swiss Central Alps, *Contributions to Mineralogy and Petrology*, **72**, 19-32.

Holdaway, M.J., 1971. Stability of andalusite and the aluminum silicate phase diagram, *American Journal of Science*, **271**, 97-131.

Holk, G.J., and Taylor, H.P. Jr., 1992. An application of open-system $^{18}O/^{16}O$ exchange kinetics to the Valhalla metamorphic core complex, British Columbia, Canada, *EOS, Transactions of the American Geophysical Union*, **73**, 375.

Holk, G.H., and Taylor, H.P. Jr., 1993. Isotopic evidence for fluid-driven mid-crustal anatexis and late-stage meteoric-hydrothermal activity near the Monashee

Decollement: Thor-Odin metamorphic core complex, S.E. British Columbia, *Geological Society of America Abstracts with Programs*, **25**, 204.

Holk, G.J., and Taylor, H.P. Jr., 1994a. $^{18}O/^{16}O$ data on contrasting crustal-scale aqueous fluid regimes before and during Eocene extension in the southern Omineca crystalline belt, British Columbia, *United States Geological Survey Circular*, **1107**, 140.

Holk, G.H., and Taylor, H.P. Jr., 1994b. Multiple stages of influx and exsolution of H_2O from anatectic melt during adiabatic decompression, a petrologic catalyst responsible for $^{18}O/^{16}O$ homogenization of metamorphic core complexes, *Geological Society of America Abstracts with Programs*, **26**, 280.

Holk, G.J., and Taylor, H.P. Jr., 1995. Crustal-scale aqueous fluid regimes before and during Eocene extension at the southern Thor-Odin metamorphic core complex, British Columbia, *Leon T. Silver 70th Birthday Symposium and Celebration*, Caltech, Division of Geological and Planetary Sciences, 195-199.

Hollister, L.S., 1977. The reaction forming cordierite from garnet, the Khtada Lake Metamorphic complex, British Columbia, *Canadian Mineralogist*, **15**, 217-219.

Hollister, L.S., 1993. The role of melt in the uplift and exhumation of orogenic belts, *Chemical Geology*, **108**, 31-48.

Holtz, F., and Johannes, W., 1994. Maximum and minimum water contents of granitic melts: Implications for chemical and physical properties of ascending magmas, *Lithos*, **32**, 149-159.

House, M.A., and Hodges, K.V., 1994. Limits on the tectonic significance of rapid cooling events in extensional settings: Insights from the Bitterroot metamorphic core complex, Idaho-Montana, *Geology*, **22**, 1007-1010.

Hoy, T., 1977. Big Ledge, in *Geology in British Columbia 1975: British Columbia Department of Mines and Petroleum Resources*, G12-G18.

Hoy, T., 1977. Stratigraphy and structure of the Kootenay Arc in the Riondel area, Southeastern British Columbia, *Canadian Journal of Earth Sciences*, **14**, 2301-2315.

Hoy, T., 1980. Geology of the Riondel area, Central Kootenay Arc, Southeastern British Columbia, *British Columbia Department of Mines and Petroleum Resources Bulletin*, **73**.

Hoy, T., 1988. Geology of the Cottenbelt lead-zinc-magnetite layer, carbonatites and alkalic rocks in the Mount Grace area, Frenchman Cap dome, Southeastern British Columbia, *British Columbia Department of Mines and Petroleum Resources Bulletin*, **80**.

Hubbert, M.K., and Rubey, W.W., 1959. Role of fluid pressure in mechanics of overthrust faulting, *Geological Society of America Bulletin*, **70**, 114-206.

Huerta, A. D., Royden, L. H., and Hodges, K. V., 1996. The interdependence of deformational and thermal processes in mountain belts, *Science*, **273**, 637-639.

Hyndman, D.W., 1968. Petrology and structure of Nakusp map-area, British Columbia, *Geological Survey of Canada Bulletin*, **161**.

Javoy, M., 1977. Stable isotopes and geothermometry, *Journal of the Geological Society of London*, **133**, 609-636.

Johnson, B.J., 1989. Geology of the west margin of the Shuswap terrane near Sicamous: Implications for Tertiary extensional tectonics (82L, M), in *Geological Fieldwork 1988; British Columbia Department of Mines and Petroleum Resources Paper*, **1989-1**, 49-54.

Jones, A.G., 1959. Vernon map-area, British Columbia, *Geological Survey of Canada Memoir*, **296**.

Jones, D.L., Howell, D.G., Coney, P.J., and Monger, J.W.H., 1983. Recognition, character, and analysis of tectonostratigraphic terranes in western North America; in, Accretion Tectonics in the Circum-Pacific region, H. Hashimoto and S. Uyeda (ed.), Terra Scientific Publishing Co., Tokyo, 21-35.

Journeay, J. M., 1988. Relic P-T regimes of the Monashee complex; a record of repeated imbrication and heat transfer, S.E. Omineca belt, *Geological Society of America Abstracts with Programs*, **20** #7, 19.

Journeay, J. M., 1989. The Shuswap thrust; a sole fault to a metamorphic-plutonic complex of late Cretaceous-early Tertiary age, southern Omineca belt, B.C., *Geological Society of America Abstracts with Programs*, **21** #5, 99.

Kerrich, R., 1988. Detachment zones of Cordilleran metamorphic core complexes: thermal, fluid and metasomatic regimes, *Geologische Rundschau*, **77**, 157-182.

Kerrich, R., and Hyndman, D., 1986. Thermal and fluid regimes in the Bitterroot lobe–Sapphire block detachment zone, Montana: evidence from $^{18}O/^{16}O$ and geologic relations, *Geological Society of America Bulletin*, **97**, 147-155.

Kerrich, R., and Rehrig, W., 1987. Fluid motion associated with Tertiary mylonitization and detachment faulting: $^{18}O/^{16}O$ evidence from the Picacho metamorphic core complex, Arizona, *Geology*, **15**, 58-62.

Kerrick, D.M., and Caldiera, K., 1993. Paleoatmospheric consequences of CO_2 released during early Cenozoic regional metamorphism in the Tethyian orogen, *Chemical Geology*, **108**, 201-230.

Kerrick, D.M., and Caldiera, K., 1994. Metamorphic CO_2 degassing and early Cenozoic paleoclimate, *GSA Today*, **4**, 57-63.

Kistler, R.W., and Peterman, Z.E., 1973. Variations in Sr, Rb, K, Na, and initial $^{87}Sr/^{86}Sr$ in Mesozoic granitic rocks and intruded wall rocks in Central California, *Geological Society of America Bulletin*, **84**, 3489-3512.

Klepacki, D.W. and Wheeler, J.O., 1985. Stratigraphic and structural relations if the Milford, Kaslo, and Slocan Groups, Goat Range, Lardeau and Nelson map areas, British Columbia; in Current Research, Part A, *Geological Survey of Canada*, Paper 85-1A, 277-286.

Knoll, A.H., Hayes, J.M., Kaufnam, A.J., Swett, K., Lambert, I.B., 1986. Secular variation in carbon isotope ratios from Upper Proterozoic successions of Svalbard and East Greenland, *Nature*, **321**, 832-838.

Kyser, T.K., 1995. Micro-analytical techniques in stable isotope geochemistry, *The Canadian Mineralogist*, **33**, 261-278.

Kyser, T.K., Ghent, E.D., and Sevigny, J.H., 1994. Petrogenesis of two-mica granites, Northern Monashee Mountains, British Columbia: Evidence from oxygen, hydrogen, and strontium isotopic compositions, *Geological Society of America Bulletin*, **106**, 1531-1537.

Lane, L.S., 1984. Brittle deformation in the Columbia River fault zone near Revelstoke, Southeastern British Columbia, *Canadian Journal of Earth Sciences*, **21**, 584-598.

Lane, L.S., Ghent, E.D., Stout, M.Z., and Brown, R.L., 1989. P-T history and kinematics of the Monashee decollement near Revelstoke, British Columbia, *Canadian Journal of Earth Sciences*, **26**, 231-243.

Larson, P.B., and Taylor, H.P. Jr., 1986. $^{18}O/^{16}O$ ratios in ash-flow tuffs and lavas erupted from the Central Nevada caldera complex and the Central San Juan caldera complex, Colorado, *Contributions to Mineralogy and Petrology*, **92**, 146-156.

Larson, P.B., and Taylor, H.P. Jr., 1986. An oxygen isotope study of hydrothermal alteration in the Lake City caldera, San Juan Mountains, Colorado, *Journal of Volcanology and Geothermal Research*, **30**, 47-82.

Larson, P.B., and Zimmerman, B.S., 1991. Variations in $\delta^{18}O$ values, water/rock ratios, and water flux in the Rico paleothermal anomaly, Colorado, In: Stable Isotope Geochemistry, *Stable Isotope Geochemistry: A Tribute to Samuel Epstein. Geochemical Society Special Publication:* **No. 3**, 463-469.

Larson, P.B., and Geist, D.J., 1995. On the origin of low-^{18}O magmas: Evidence from the Casto Pluton, Idaho, *Geology*, **23**, 909-912.

Latin, D., and White, N., 1990. Generating melt during lithospheric extension: Pure shear vs. simple shear, *Geology*, **18**, 327-331.

Lee, D.E., Friedman, I., and Gleason, J.D., 1982. The oxygen isotope composition of granitoid and sedimentary rocks of the Southern Snake Range, Nevada, *Contributions to Mineralogy and Petrology*, **79**, 150-158.

Lee, D.E., Friedman, I., and Gleason, J.D., 1984. Modification of δD values in eastern Nevada granitoid rocks spatially related to thrust faults, *Contributions to Mineralogy and Petrology*, **88**, 288-298.

Lister, G.S., Banga, G., and Feenstra, A., 1984. Metamorphic core complexes of Cordilleran type in the Cyclades, Aegean Sea, Greece, *Geology*, **12**, 221-225.

Lister G.S., and Baldwin, S.L., 1993. Plutonism and the origin of metamorphic core complexes, *Geology*, **21**, 607-610.

Little, H.W., 1960. Nelson map-area, west half, British Columbia, *Geological Survey of Canada Memoir*, **308**.

Little, H.W., 1983. Geology of the Greenwood map-area, British Columbia, *Geological Survey of Canada Paper*, **79-29**, 37p.

Little, H.W., 1984. Geology of the Rossland-Trail map area, British Columbia, *Geological Survey of Canada Paper*, **79-26**, 39p.

Luth, W.C., Jahns, R.H., and Tuttle, O.F., 1964. The granite system at pressures of four to ten kilobars, *Journal of Geophysical Research*, **69**, 759-773.

Margaritz, M., and Taylor, H.P. Jr., 1976. $^{18}O/^{16}O$ and D/H studies along a 500 km traverse across the Coast Range batholith and its country rocks, Central British Columbia, *Canadian Journal of Earth Sciences*, **13**, 1514-1536.

Magaritz, M., and Taylor, H.P. Jr., 1986. Oxygen 18/Oxygen 16 and D/H studies of plutonic granitic and metamorphic rocks across the Cordilleran batholiths of Southern British Columbia, *Journal of Geophysical Research*, **91**, 2193-2217.

Mattey, D., and MacPherson, C., 1993. High-precision oxygen isotope microanalysis of ferromagnesium minerals by laser-fluorination, *Chemical Geology*, **105**, 305-318.

Mattey, D.P., Lowry, D., and MacPherson, C.G., 1994. Oxygen isotope composition of mantle peridotite, *Earth and Planetary Science Letters*, **128**, 231-241.

Matthews, W.H., 1981. Early Cenozoic resetting of potassium-argon dates and geothermal history of North Okanagan area, British Columbia, *Canadian Journal of Earth Sciences*, **18**, 1310-1319.

Matthews, W.H., 1983. Early Tertiary resetting of potassium-argon dates in the Kootenay Arc, Southeastern British Columbia, *Canadian Journal of Earth Sciences*, **20**, 867-872.

McCaig, A.M., Wickham, S.M., and Taylor, H.P. Jr. 1991. Deep fluid circulation in alpine shear zones Pyrenees, France: field and oxygen isotope studies, *Contributions to Mineralogy and Petrology*, **106**, 41-60.

McKenzie, D., and Bickle, M.J., 1988. The volume and composition of melt generated by extension of the lithosphere, *Journal of Petrology*, **29**, 625-679.

McClelland, W.C., Gehrels, G.E., and Saleeby, J.B., 1992. Upper Jurassic-Lower Cretaceous basinal strata along the Cordilleran margin: Implications for the accretionary history of hte Alexander-Wrangellia-Peninsular terrane, *Tectonics*, **11**, 823-835.

McCrea, J.M., 1950. On the isotopic chemistry of carbonates and a paleotemperature scale, *Journal of Chemical Physics*, **18**, 849-857.

McMechan, M.E., 1981. The Middle Proterozoic Purcell Supergroup in the southwestern Rocky and southeastern Purcell Mountains, British Columbia and the initiation of the Cordilleran miogeocline, Southern Canada and adjacent United States, *Bulletin of Canadian Petroleum Geology*, **29**, 583-621.

McMechan, M.E., Hoy, T., and Price, R.A., 1980. Van Creek and Nicol Creek Formations (New): A revision of the stratigraphic nomenclature of the Middle Proterozoic Purcell Supergroup, Southeastern British Columbia, *Bulletin of Canadian Petroleum Geology*, **28**, 542-558.

McMechan, M.E., and Thompson, R.I., 1989. Structural style and history of the Rocky Mountain fold and thrust belt: in, Ricketts, B.D. (ed.), Western Canada Sedimentary Basin: A Case History; Calgary, Alberta, Canadian Society of Petroleum Geologists, 47-69.

McMillan, W.J., 1971. Petrology and structure of the west flank, Frenchman's Cap dome, near Revelstoke, British Columbia, *Geological Survey of Canada Paper*, **71-29**.

McMillan, W.J., 1985. Geology and ore deposits of the Highland Valley Camp: in, *Geological Association of Canada, Mineral Deposits Division Field Guide and Reference Manual Series*, **1**, 121p.

McNicoll, V.J., and Brown, R.L., 1995. The Monashee decollement at Cariboo Alp, southern flank of the Monashee complex, Southern British Columbia, Canada, *Journal of Structural Geology*, **17**, 17-30.

Medford, G.A., 1975. K-Ar and fission track geochronometry of an Eocene thermal event in the Kettle River (west half) map-area, Southern British Columbia, *Canadian Journal of Earth Sciences*, **12**, 836-843.

Medford, G.A., Armstrong, R.L., and Osatenko, M.J., 1983. Rb-Sr dating of Paleozoic (?), Mesozoic, and Cenozoic intrusive rocks, Okanagan Lake region, Southern British Columbia, Canada, *Canadian Journal of Earth Sciences*, **20**, 1579-1585.

Miller, C.F., and Bradfish, L.J., 1980. An inner Cordilleran belt of muscovite-bearing plutons, *Geology*, **8**, 412-416.

Miller, E.L., Gans, P.B., and Garing, J., 1983. The Snake Range Decollement: an exhumed mid-Tertiary ductile-brittle transition, *Tectonics*, **2**, 239-263.

Miller, E.L., Gans, P.B., Wright, J.E., and Sutter, J.F., 1988. Metamorphic history of the East-Central Basin and Range province: Tectonic setting and relationship to magmatism: in, *Metamorphism and Crustal Evolution of the Western United States,* *Rubey Volume VII* (editor, W.G. Ernst), Prentice Hall, Englewood Cliffs, New Jersey, 649-682.

Miller, E.L., and Gans, P.B., 1989. Cretaceous crustal structure and metamorphism in the hinterland of the Sevier thrust belt, western U.S. Cordillera, *Geology*, **17**, 59-62.

Misch, P., 1960. Regional structural reconnaissance in Central-Northeast Nevada and some adjacent areas: observations and interpretations, *Intermountain Association of Petroleum Geologists Guidebook for 11th Annual Field Conference*, 17-42.

Molnar, P., and England, P., 1990. Temperatures, heat flux, and frictional stress near major thrust faults, *Journal of Geophysical Research*, **95**, 4833-4856.

Monger, J.W.H., 1977. Upper Paleozoic rocks of the Western Canadian Cordillera and thier bearing on Cordilleran evolution, *Canadian Journal of Earth Sciences*, **14**, 1832-1859.

Monger, J.W.H., 1993. Canadian Cordilleran tectonics: from geosynclines to crustal collage, *Canadian Journal of Earth Sciences*, **30**, 209-231.

Monger, J.W.H., and Berg, H.C., 1984. Lithotectonic terrane map of western Canada and southeastern Alaska, Lithotectonic Terrane Map of the North American Cordillera, edited by N.J. Silberling and D.L. Jones, *United States Geological Survey OPen File Report*, **84-523**, B1-B31.

Monger, J.W.H., Price, R.A., and Tempelman-Kluit, D.J., 1982. Tectonic accretion and the origin of the two major metamorphic and plutonic welts in the Canadian Cordillera, *Geology*, **10**, 70-75.

Monger, J.W.H. and 9 others, 1991. Part B. Cordilleran Terranes; in, Upper Devonian to Middle Jurassic assemblages, Chapter 8 of *Geology of the Cordilleran Orogen in Canada*, H. Gabrielse and C.J. Yorath (ed.); *Geological Survey of Canada*, Geology of Canada, no. **4**, p. 281-327.

Moores, E.M., Scott, R.B., and Lumsden, W.W., 1968. Tertiary tectonics of the White-Pine-Grant Range region, East-Central Nevada, and some regional implications, *Geological Society of America Bulletin*, **79**, 1703-1726.

Morrison, J. 1994. Meteoric water-rock interaction in the lower plate of the Whipple Mountain metamorphic core complex, California, *Journal of Metamorphic Geology*, **12**, 827-840.

Nesbitt, B.E., and Muehlenbachs, K., 1989. Origins and movement of fluids during deformation and metamorphism in the Canadian Cordillera, *Science*, **245**, 733-736.

Nesbitt, B.E., and Muehlenbachs, K., 1991. Stable isotopic constraints on the nature of the syntectonic fluid regime of the Canadian Cordillera, *Geophysical Research Letters*, **18**, 963-966.

Nesbitt, B.E., and Muehlenbachs, K., 1995a. Geochemical studies of the origins and effects of synorogenic crustal fluids in the Southern Omineca Belt of British Columbia, *Geological Society of America Bulletin*, **107**, 1033-1050.

Nesbitt, B.E., and Muehlenbachs, K., 1995b. Geochemistry of syntectonic, crustal fluid regimes along the Lithoprobe Southern Canadian Cordillera transect, *Canadian Journal of Earth Sciences*, **32**, 1699-1719.

Nesbitt, B.E., Mendoza, C.A., and Kerrick, D.M., 1995. Surface fluid convection during Cordilleran extension and the generation of metamorphic CO_2 contributions to Cenozoic atmospheres, *Geology*, **23**, 99-101.

Nesbitt, B.E., Muehlenbachs, K., and Murowchick, J.B., 1989. Genetic implications of stable isotope characteristics of mesothermal Au deposits and related Sb and Hg deposits in the Canadian Cordillera, *Economic Geology*, **84**, 1489-1506.

Newton, R.C., Smith, J.V., and Windley, B.F., 1980. Carbonic metamorphism, granulites, and crustal growth, *Nature*, **288**, 45-50.

Nguyen, K.K., Sinclair, A.J., and Libby, W.G., 1968. Age of the northern part of the Nelson batholith, *Canadian Journal of Earth Sciences*, **5**, 955-957.

Norton, D.L., 1984. Theory of hydrothermal systems, *Annual Reviews of Earth and Planetary Science*, **12**, 155-177.

Norton, D., and Taylor, H.P. Jr., 1979. Quantitative simulation of the hydrothermal systems of crystallizing magmas on the basis of transport theory and oxygen isotope data: An analysis of the Skaergaard Intrusion, *Journal of Petrology*, **20**, 421-486.

Nyman M.W., Pattison, D.R.M., and Ghent, E.D., 1995. Melt extraction during formation of K-feldspar + sillimanite migmatites, west of Revelstoke, British Columbia, *Journal of Petrology*, **36**, 351-372.

O'Neil, J.R., Clayton, R.N., and Mayeda, T.K., 1969. Oxygen isotope fractionation in divalent metal carbonates, *The Journal of Chemical Physics*, **51**, 5547-5558.

O'Neil, J.R., and Ghent, E.D., 1975. Stable isotope study of coexisting metamorphic minerals from the Esplanade Range, British Columbia, *Geological Society of America Bulletin*, **86**, 1708-1712.

O'Neil, J.R., and Taylor, H.P. Jr., 1967. The oxygen isotope and cation exchange chemistry of feldspars, *American Mineralogist*, **52**, 1414-1437.

Ohmoto, H., 1972. Systematics of sulfur and carbon isotopes in hydrothermal ore deposits, *Economic Geology*, **67**, 551-578.

Ohmoto, H., and Rye, R.O., 1970. The Bluebell mine, British Columbia. I. Mineralogy, paragenesis, fluid inclusions, and the isotopes of hydrogen, oxygen, and carbon, *Economic Geology*, **65**, 417-437.

Okulitch, A.V., 1984. The role of the Shuswap metamorphic complex in Cordilleran tectonism: a review, *Canadian Journal of Earth Sciences*, **21**, 1171-1193.

Okulitch, A.V., 1985. Paleozoic plutonism in Southeastern British Columbia, *Canadian Journal of Earth Sciences*, **22**, 1409-1424.

Parkinson, D., 1991. Age and isotopic character of early Proterozoic basement gneisses in the Southern Monashee Complex, Southeastern British Columbia, *Canadian Journal of Earth Sciences*, **28**, 1159-1168.

Parrish, R.R., 1981. Geology of the Nemo Lakes belt, Northern Valhalla Range, Southeast British Columbia, *Canadian Journal of Earth Sciences*, **18**, 944-958.

Parrish, R.R., 1984. Slocan Lake fault: a low angle fault zone bounding the Valhalla gneiss complex, Nelson map-area, Southern British Columbia, in *Current Research, Part A, Geological Survey of Canada Paper*, **84-1A**, 323-330.

Parrish, R.R., 1991. Precambrian basement rocks of the Canadian Cordillera, Chapter 4 in, *Geology of the Cordilleran Orogen in Canada*, H. Gabrielse and C.J. Yorath (ed.); *Geological Survey of Canada*, Geology of Canada, no. **4**, p. 87-96.

Parrish, R.R., 1992. U-Pb ages of Jurassic-Eocene plutonic rocks in the vicinity of Valhalla Complex, Southeast British Columbia: in, *Radiogenic Age and Isotopic Studies: Report 5; Geological Survey of Canada Paper*, **91-2**, 115-134.

Parrish, R.R., 1995. Thermal evolution of the Southeastern Canadian Cordillera, *Canadian Journal of Earth Sciences*, **32**, 1618-1642.

Parrish, R.R., Carr, S.D., and Parkinson, D.L., 1988. Eocene extensional tectonics and geochronology of the Southern Omineca belt, British Columbia and Washington, *Tectonics*, **7**, 181-212.

Patino Douce, A.E., Humphreys, E.D., and Johnston, A.D., 1990. Anatexis and metamorphism in tectonically thickened continental crust exemplified by the Sevier hinterland, Western North America, *Earth and Planetary Science Letters*, **97**, 290-315.

Peacock, S. M., 1987. Creation and preservation of subduction-related inverted metamorphic gradients, *Journal of Geophysical Research*, **92B**, 12763-12781.

Peacock, S.M., 1988. Inverted metamorphic gradients in the westernmost Cordillera: in, *Metamorphism and Crustal Evolution of the Western United States, Rubey Volume VII* (editor, W.G. Ernst), Prentice Hall, Englewood Cliffs, New Jersey, 953-975.

Pell, J., and Simony., P.S., 1987. New correlations of Hadrynian strata, South-Central British Columbia, *Canadian Journal of Earth Sciences*, **24**, 302-313.

Peters, M.T., and Wickham, S.M., 1995. On the causes of ^{18}O-depletion and $^{18}O/^{16}O$ homogenization during regional metamorphism, the East Humboldt range core complex, Nevada, *Contributions to Mineralogy and Petrology*, **119**, 68-82.

Peto, P., 1973. Petrochemical study of the Similkameen batholith, British Columbia, *Geological Society of America Bulletin*, **84**, 3977-3984.

Podladchikov, Y.Y., and Wickham, S.M., 1994. Crystallization of hydrous magmas: Calculation of associated thermal effects, volatile fluxes, and isotopic alteration, *Journal of Geology*, **102**, 25-45.

Poulton, T.P., and Simony, P.S., 1980. Stratigraphy, sedimentology, and regional correlation of the Horsethief Creek Group (Hadrynian, late Precambrian) in the Northern Purcell and Selkirk Mountains, British Columbia, *Canadian Journal of Earth Sciences*, **17**, 1708-1724.

Powell, M.D., and Kyser, T.K., 1991. Analysis of $\delta^{13}C$ and $\delta^{18}O$ in calcite, dolomite, rhodochrosite, and siderite using a laser extraction system, *Chemical Geology*, **94**, 55-66.

Price, R.A., 1964. The Precambrian Purcell system in the Rocky Mountains of Southern Alberta and British Columbia, *Bulletin of Canadian Petroleum Geology*, **12**, 399-426.

Price, R.A., 1986. The Southeastern Canadian Cordillera: thrust faulting, tectonic wedging, and delamination of the lithosphere, *Journal of Structural Geology*, **8**, 239-254.

Price, R.A., and Carmichael, D.M., 1986. Geometric test for Late Cretaceous-Paleogene intracontinental transform faulting in the Canadian Cordillera. *Geology*, **14**, 468-471.

Price, R.A., and Mountjoy, E.W., 1970. Geologic structure of the Canadian Rocky Mountains between Bow and Athabaska Rivers – A progress report, *Geological Association of Canada Special Paper*, **6**, 7-25.

Proffett, J.M. Jr., 1977. Cenozoic geology of the Yerington District, Nevada, and implications for the nature and origin of Basin and Range faulting, *Geological Society of America Bulletin*, **88**, 247-266.

Raeside, R.P., and Simony, P.S., 1983. Stratigraphy and deformational history of the Scrip nappe, Monashee Mountains, British Columbia, *Canadian Journal of Earth Sciences*, **20**, 639-650.

Raeside, R.P., and Ghent, E.D., 1986. The migmatization of Hadrynian sedimentary rocks, Mica Creek, British Columbia, *Canadian Mineralogist*, **24**, 547-556.

Read, P.B., 1979. Relationship between the Shuswap metamorphic complex and Kootenay Arc, Vernon east-half, Southern British Columbia, *Geological Survey of Canada Paper*, **79-1A**, 37-40.

Read, P.B., and Brown, R.L., 1981. Columbia River fault zone: southeastern margin of the Shuswap and Monashee complexes, Southern British Columbia, *Canadian Journal of Earth Sciences*, **18**, 1127-1145.

Read, P.B., and Okulitch, A.V., 1977. The Triassic unconformity of South-Central British Columbia, *Canadian Journal of Earth Sciences*, **14**, 606-638.

Read, P.B., and Wheeler, J.O., 1977. Geology Lardeau, west-half map area and marginal notes, revised edition, *Geological Survey of Canada Open File*, **432**, 1:125,000 scale map.

Read, P.B., Woodsworth, G.J., Greenwood, H.J., Ghent, E.D., and Evenchick, C.A., 1991. Metamorphic map of the Canadian Cordillera, *Geological Survey of Canada Map*, **1714A**, 1:2000000 scale.

Reesor, J.E., 1958. Dewar Creek map-area with special emphasis on the White Creek batholith, British Columbia, *Geological Survey of Canada Memoir*, **292**.

Reesor, J.E., 1965. Valhalla gneiss complex, *Geological Survey of Canada Bulletin*, **129**.

Reesor, J.E., 1973. Geology of the Lardeau map-area, east half, British Columbia, *Geological Survey of Canada Memoir*, **369**.

Reesor, J.E., 1983. Nelson map-area, east half, British Columbia, *Geological Survey of Canada, Open File*, **929**.

Reesor, J.E., and Moore, J.M., 1971. Petrology and structure of the Thor-Odin gneiss dome, Shuswap metamorphic complex, British Columbia, *Geological Survey of Canada Bulletin,* **197**.

Reynolds, S.J. and Lister, G.S., 1987. Structural aspects of fluid-rock interactions in detachment zones, *Geology*, **15**, 362-366.

Rhodes, B.P., and Hyndman, D.W., 1988. Regional metamorphism, structure, and tectonics of northeastern Washington and northern Idaho: in, *Metamorphism and Crustal Evolution of the Western United States, Rubey Volume VII* (editor, W.G. Ernst), Prentice Hall, Englewood Cliffs, New Jersey, 272-295.

Ricketts, B.O. (ed.), 1989. Western Canada Sedimentary Basin: A Case History; Calgary, Alberta, Canadian Society of Petroleum Geologists, 320.

Roddick, J.A., 1983. Geophysical review and composition of the Coast Plutonic Complex south of latitude 55 °N: in, Circumpacific Plutonic Terranes, J.A. Roddick (ed.), *Geological Society of America Memoir*, **159**, 195-211.

Roddy, M.S., Reynolds, S.J., Smith, B.M., and Ruiz, J., 1988. K-metasomatism and detachment-related mineralization, Harcuvar Mountains, Arizona, *Geological Society of America Bulletin*, **100**, 1627-1639.

Ross, J.V., 1973. Mylonitic rocks and flattened garnets in the Southern Okanagan of British Columbia, *Canadian Journal of Earth Sciences*, **10**, 1-17.

Rubin, C.M., Saleeby, J.B., Cowan, D.S., Brandon, M.J., and McGroder, M.F., 1990. Regionally extensive mid-Cretaceous west-vergent thrust system in the Northwestern Cordillera: Implications for continent-margin tectonism, *Geology*, **18**, 276-280.

Rumble, D. III, and Hoering, T.C., 1994. Analysis of oxygen and sulfur isotope ratios in oxide and sulfide minerals by spot heating with a carbon dioxide laser in a fluorine atmosphere, *Accounts of Chemical Research*, **27**, 237-241.

Rye, R.O., Schuiling, R.D., Rye, D.M., and Jansen, J., 1976. Carbon, hydrogen, and oxygen isotope studies of the regional metamorphic complex at Naxos, Greece, *Geochimica Cosmochimica Acta*, **40**, 1031-1049.

Saleeby, J.B., 1983. Accretionary tectonics of the North American Cordillera, *Annual Review of Earth and Planetary Sciences*, **15**, 45-73.

Sandiford, M., and Powell, R., 1986. Deep crustal metamorphism during continental extension: modern and ancient examples, *Earth and Planetary Science Letters*, **79**, 151-158.

Satir, M., and Friedrichsen, H., 1986. Geochronological and stable isotope investigations on poly-metamorphic rocks from the Eastern Alps (western Tauern Window, Austria), *Neues Jahrbuch Mineral. Abh.*, **154**, 313-334.

Scammell, R.J., and Brown, R.L., 1990. Cover gneisses of the Monashee terrane: a record of synsedimentary rifting in the North American Cordillera, *Canadian Journal of Earth Sciences*, **27**, 712-726.

Schiarizza, P., and Preto, V.A., 1984. Geology of the Adams Plateau-Clearwater area, British Columbia Ministry of Energy, Mines, and Petroleum Resources, *Preliminary Map*, **56.**

Selverstone, J., 1988. Evidence for east-west crustal extension in the Alps: implications for the unroofing history of the Tauern Window, Eastern Alps, *Tectonics*, **7**, 87-105.

Selverstone, J., and Chamberlain, C.P., 1990. Apparent isobaric cooling paths from granulites: Two counterexamples from British Columbia and New Hampshire, *Geology*, **18**, 307-310.

Sevigny, J.H., and Parrish, R.R., 1993. Age and origin of late Jurassic and Paleocene granitoids, Nelson batholith, Southern British Columbia, *Canadian Journal of Earth Sciences*, **30**, 2305-2314.

Sevigny, J.H., Parrish, R.R., and Ghent, E.D., 1989. Petrogenesis of peraluminous granites, Monashee Mountains, Southeastern Canadian Cordillera, *Journal of Petrology*, **30**, 557-581.

Sevigny, J.H., Parrish, R.R., Donelick, R.A., and Ghent, E.D., 1990. Northern Monashee Mountains, Omineca Crystalline belt, British Columbia: timing of metamorphism, anatexis, and tectonic denudation, *Geology*, **18**, 103-106.

Sharma, T., and Clayton, R.N., 1965. Measuremant of O^{18}/O^{16} ratios of total oxygen of carbonates, *Geochimica Cosmochimica Acta*, **29**, 1347-1353.

Sharp, Z.D., 1990. A laser-based microanalytical method for the in situ determination of oxygen isotope ratios of silicates and oxides, *Geochimica Cosmochimica Acta*, **54**, 1353-1357.

Sharp, Z.D., 1992. In situ laser microprobe analyses for stable isotope analysis, *Chamical Geology*, **101**, 3-20.

Sheppard, S.M.F., 1986. Characterization and isotopic variations in natural waters, in Stable Isotopes in High Temperature Geological Processes: *Reviews in Mineralogy* (editors J. W. Valley, H. P. Taylor Jr., and J.R. O'Neil), **16**, 165-181.

Shieh, Y.N., and Schwarcz, H.P., 1974. Oxygen isotope studies of granite and migmatite, Grenville province of Ontario, Canada, *Geochimica et Cosmochimica Acta*, **38**, 21-45.

Sibson, R.H., 1977. Fault rocks and fault mechanisms, *Journal of the Geological Society of London*, **133**, 191-213.

Sibson, R.H., 1987. Earthquake rupturing as a mineralizing agent in hydrothermal systems, *Geology*, **15**, 701-704.

Sibson, R.H., Moore, J.M.M., and Rankin, A.H., 1975. Seismic pumping - hydrothermal fluid transport mechanism, *Journal of the Geological Society of London*, **131**, 653-659.

Simony, P.S., Ghent, E.D., Craw, D., Mitchell, W., and Robbins, D.B., 1980. Structural and metamorphic evolution of northeast flank of Shuswap complex, southern Canoe River area, British Columbia, *Geological Society of America Memoir*, **153**.

Simpson, C., and Schmid, S.M., 1983. An evaluation of criteria to deduce the sense of movement in sheared rocks, *Geological Society of America Bulletin*, **94**, 1281-1288.

Smalley, P.C., Stijfhoorn, D.E., Raheim, A., Johansen, H., and Dickson, J.A.D., 1989. The laser microprobe and its application to the study of C and O isotopes in calcite and aragonite, *Sedimentary Geology*, **65**, 211-221.

Smith, B.M., Reynolds, S.J., Day, H.W., and Bodnar, R.J., 1991. Deep-seated fluid involvement in ductile-brittle deformation and mineralization, South Mountains metamorphic core complex, Arizona, *Geological Society of America Bulletin*, **103**, 559-569.

Smith, M.T., and Gehrels, G.E., 1992. Structural geology of the Lardeau Group near Trout Lake, British Columbia: implications for the structural evolution of the Kootenay Arc, *Canadian Journal of Earth Sciences*, **29**, 1305-1319.

Solomon, G.C., and Taylor, H.P. Jr., 1989. Isotopic evidence for the origin of Mesozoic and Cenozoic granitic plutons in the Northern Great Basin, *Geology*, **17**, 591-594.

Souther, J.G., 1991. Volcanic regimes, Chapter 14: in, *Geology of the Cordilleran Orogen in Canada*, H. Gabrielse and C.J. Yorath (ed.); *Geological Survey of Canada*, Geology of Canada, no. **4**, p. 457-490.

Spear, F.S., 1995. P-T-t evolution of the Valhalla complex, British Columbia, Canada, *Mineralogical Magazine*, **58A**, 868-869.

Spear, F.S., and Parrish, R.R., 1996. Petrology and cooling rates of the Valhalla complex, British Columbia, Canada, *Journal of Petrology*, **37**, 733-765.

Spencer, J.E., 1984. Role of tectonic denudation in uplift and warping of low-angle normal faults, *Geology*, **12**, 95-98.

Spencer, J.E., 1985. Miocene low-angle normal faulting and dike emplacement, Homer Mountain and surrounding areas, Southeastern California and Southernmost Nevada, *Geological Society of America Bulletin*, **96**, 1140-1155.

Spencer, J.E., and Welty, J.W., 1986. Possible controls on base- and precious-metal mineralization associated with Tertiary detachment faults in the lower Colorado River trough, Arizona and California, *Geology*, **14**, 195-198.

Stewart, J.H., 1972. Initial deposits of the Cordilleran geosyncline: Evidence of a Late Precambrian (<850 M.y.) continental separation, *Geological Society of America Bulletin*, **83**, 1345-1360.

Striuk, L.C., 1986. Imbricated terranes of the Cariboo gold belt with correlations and implications for tectonics in Southeastern British Columbia, *Canadian Journal of Earth Sciences*, **23**, 1047-1061.

Suzouki, T., and Epstain, S., 1976. Hydrogen isotope fractionation between OH-bearing minerals and water, *Geochimica Cosmochimica Acta*, **40**, 1229-1240.

Taylor, H.P. Jr., 1974. The application of oxygen and hydrogen isotope studies to problems of hydrothermal alteration and ore deposition, *Economic Geology*, **69**, 843-883.

Taylor, H.P. Jr., 1977. Water/rock interactions and the origin of H_2O in granitic batholiths, *Journal of the Geological Society of London*, **133**, 509-558.

Taylor, H.P. Jr., 1986. Igneous rocks: II. Isotopic case studies of circumpacific megmatism, *Reviews in Mineralogy*, **22**, 273-318.

Taylor, H.P. Jr., 1988. Oxygen, hydrogen, and strontium isotope constraints on the origin of granites, *Transactions of the Royal Society of Edinburgh: Earth Sciences*, **79**, 317-388.

Taylor, H.P. Jr., 1996. Oxygen and hydrogen isotope relationships in hydrothermal mineral deposits, Chapter in *Geochemistry of Hydrothermal Ore Deposits,* ed., H.L. Barnes (Wiley and Sons, New York). In press.

Taylor, H.P. Jr., and Epstein, S., 1962. Relationship between $^{18}O/^{16}O$ ratios in coexisting minerals of igneous and metamorphic rocks, Part I: principles and Experimental Results, *Geological Society of America Bulletin*, **73**, 461-480.

Taylor, H.P. Jr., and Forester, R.W., 1979. An oxygen and hydrogen isotope study of the Skaergaard intrusion and its country rocks: a description of a 55-M.Y. old fossil hydrothermal system, *Journal of Petrology*, **20**, 355-419.

Taylor, H.P., Jr., and Magaritz, M., 1978. Oxygen and hydrogen isotope studies of the Cordilleran batholiths of Western North America: in, *Stable Isotopes in the Earth Sciences (Rafter Volume)*, edited by B.W. Robinson, *Bulletin of the New Zealand Dep. Sci. Ind. Res.*, **220**, 151-173.

Taylor, H.P. Jr., Magaritz, M., and Wickham, S.M., 1991. Application of stable isotopes in identifying a major Hercynian synplutonic rift zone and its associated meteoric-hydrothermal activity, Southern Schwarzwald, Germany, *Stable Isotope Geochemistry: A Tribute to Samuel Epstein. Geochemical Society Special Publication:* **No. 3**, 355-371.

Taylor, H.P. Jr., and Sheppard, S.M.F., 1986. Igneous Rocks: I. Processes of Isotopic Fractionation and Isotope Systematics, *Reviews in Mineralogy*, **16**, 227-272.

Tempelman-Kluit, D., 1989. Geology, Penticton, British Columbia, *Geological Survey of Canada, Map,* **1736A**, scale 1:250000.

Templeman-Kluit, D., and Parkinson, D., 1986. Extension across the Eocene Okanagan crustal shear in Southern British Columbia, *Geology*, **14**, 318-321.

Thompson, A.B., and Algor, J.R., 1977. Model systems for anatexis of pelitic rocks, *Contributions in Mineralogy and Petrology*, **63**, 247-269.

Tuttle, O.F., and Bowen, N.L., 1958. Origin of granite in the light of experimental studies in the system $NaAlSi_3O_8$-$KAlSi_3O_8$-SiO_2-H_2O, *Geological Society of America Memoir*, **74**.

Valley, J.W., 1986. Stable isotope geochemistry of metamorphic rocks, in Stable Isotopes in High Temperature Geological Processes: *Reviews in Mineralogy* (editors J. W. Valley, H. P. Taylor Jr., and J.R. O'Neil), **16**, 445-490.

Valley, J.W., and O'Neil, J.R., 1984. Fluid heterogeneity during granulite facies metamorphism in the Adirondacks: stable isotope evidence, *Contributions to Mineralogy and Petrology*, **85**, 158-173.

Valley, J.W., Bohlen, S.R., Essene, E.J., and Lamb, W., 1990. Metamorphism in the Adirondacks: II. The role of fluids, *Journal of Petrology*, **31**, 555-596.

Valley, J.W., Kitchen, N., Kohn, M.J., Niendorf, C.R., and Spicuzza, M.J., 1995. UWG-2, a garnet standard for oxygen isotope ratios: Strategies for high precision and accuracy with laser heating, *Geochimica Cosmochimica Acta*, **59**, 5223-5231.

Veizer, J., and Hoefs, J., 1976. The nature of $^{18}O/^{16}O$ and $^{13}C/^{12}C$ secular trends in sedimentary carbonate rocks, *Geochimica et Cosmochimica Acta*, **40**, 1387-1395.

Vielzeuf, D., and Holloway, J.R., 1988. Experimental determination of the fluid-absent melting relations in the pelitic system, *Contributions to Mineralogy and Petrology*, **98**, 257-276.

Walther, J.V., and Orville, 1982. Volatile production and transport in regional metamorphism, *Contributions to Mineralogy and Petrology*, **79**, 252-257.

Walther, J.V., and Wood, B.J., 1984. Rate and mechanism in prograde metamorphism, *Contributions to Mineralogy and Petrology*, **88**, 246-259.

Wanless, R.K., and Reesor, J.E., 1975. Precambrian zircon age of orthogneiss in the Shuswap metamorphic complex, British Columbia, *Canadian Journal of Earth Sciences*, **12**, 326-331.

Wernicke, B., 1981. Low-angle normal faults in the Basin and Range province: nappe tectonics in an extending orogen, *Nature*, **291**, 645-648.

Wernicke, B., 1985. Uniform-sense normal simple shear of the continental lithosphere, *Canadian Journal of Earth Sciences*, **22**, 108-125.

Wernicke, B., 1990. The fluid crustal layer and its implications for continental dynamics, in *Exposed Cross-Sections of the Continental Crust*, (edited by M.H. Salisbury and D.M. Fountain) Kluwer, Dordrecht, 559-544.

Wernicke, B., 1992. Cenozoic extensional tectonics of the U.S. Cordillera: in, *Geology of North America*, **3**, *Cordilleran Orogen: Conternimous U.S.*, edited by B.C. Burchfiel, P.W. Lipman, and M.L. Zoback, 553-582, Geological Society of America, Boulder, Colorado.

Wernicke, B., and Axen, G.J., 1988. On the role of isostasy in the evolution of normal fault systems, *Geology*, **16**, 848-851.

Wheeler, J.O., 1964. Big-Bend map-area, British Columbia, *Geological Society of Canada Paper*, **64-32**.

Wheeler, J.O. and McFeely, P., 1991. Tectonic Assemblage Map of the Canadian Cordillera and adjacent parts of the United States of America; *Geological Survey of Canada,* Map 1712A, scale 1:2,000,000.

Wheeler, J.O., Brookfield, A.J., Gabrielese, H., Monger, J.W.H., Tipper, H.W., and Woodsworth, G.J., 1991. Terrane map of the Canadian Cordillera. *Geological Survey of Canada.*

Whitney, J.A., 1988. The origin of granite: The role and source of water in the evolution of granitic magmas, *Geological Society of America Bulletin*, **100**, 1971-1980.

Wickham, S.M., 1987. The segregation and emplacement of granitic magmas, *Journal of the Geological Society of London*, **144**, 281-297.

Wickham, S.M., 1987. Crustal anatexis and granite petrogenesis during low-pressure regional metamorphism: the Trois Seigneurs Massif, Pyrenees, France, *Journal of Petrology*, **28**, 127-169.

Wickham, S.M., and Oxburgh, E.R., 1985. Continental rifts as a setting for regional metamorphism, *Nature*, **318**, 330-333.

Wickham, S.M., and Peters, M.T., 1990. An oxygen isotope discontinuity in high-grade rocks of the East Humboldt Range, Nevada, *Nature*, **345**, 150-153.

Wickham, S.M., and Peters, M.T., 1992. Oxygen and carbon isotope profiles in metasediments from Lizzies Basin, East Humboldt Range, Nevada: constraints on mid-crustal metamorphic and magmatic volatile fluxes, *Contributions to Mineralogy and Petrology*, **112**, 46-65.

Wickham, S.M., and Peters, M.T., 1993. High $\delta^{13}C$ Neoproterozoic carbonate rocks in Western North America, *Geology*, **21**, 165-168.

Wickham, S.M., and Taylor, H.P. Jr., 1985. Stable isotopic evidence for large-scale seawater infiltration in a regional metamorphic terrane; the Trois Seigneurs Massif, Pyrenees, France, *Contributions to Mineralogy and Petrology*, **91**, 122-137.

Wickham, S.M., and Taylor, H.P., 1987. Stable isotope constraints on the origin and depth of penetration of hydrothermal fluids associated with Hercynian regional metamorphism and crustal anatexis in the Pyrenees, *Contributions to Mineralogy and Petrology*, **95**, 255-268.

Wickham, S.M., Peters, M.T., Fricke, H.C., and O'Neil, J.R., 1993. Core complex plumbing systems: identification of magmatic and meteoric fluid sources and upward and downward moving infiltration fronts, *Geology*, **21**, 81-84.

Wickham, S.M., Taylor, H.P., Snoke, A.W., and O'Neil, J.R., 1991. An oxygen and hydrogen isotope study of high-grade metamorphism and anatexis in the Ruby Mountains-East Humboldt Range core complex, Nevada, *Stable Isotope Geochemistry: A Tribute to Samuel Epstein. Geochemical Society Special Publication:* **No. 3**, 373-389.

Wiechert, U., and Hoefs, J., 1995. An eximer laser-based micro analytical preparation technique for in-situ oxygen isotope analysis of silicate and oxide minerals, *Geochimica et Cosmochimica Acta*, **59**, 4093-4101.

Winston, D., Woods, M., and Steckler, M.S., 1984. The case for an intracratonic Belt-Purcell basin: tectonic, stratigraphic, and stable isotopic considerations: in, Montana Geological Survey, *1984 Field Conference and Symposium* , J.D. McBane and P.B. Ganson (ed.), 103-118.

Woodsworth, G.J., Anderson, R.G., and Armstrong, R.L., 1991. Plutonic Regimes, Chapter 15: in, *Geology of the Cordilleran Orogen in Canada*, H. Gabrielse and C.J. Yorath (ed.); *Geological Survey of Canada*, Geology of Canada, no. **4**, p. 491-531.

Wyllie, P. J., 1977. Crustal anatexis: An experimental review, *Tectonophysics*, **43**, 41-71.

Yapp, C.J., and Epstein, S., 1982. A reexamination of cellulose carbon-bound hydrogen δD measurements and some factors affecting plant-water D/H relationships, *Geochimica et Cosmochimica Acta*, **46**, 955-965.

Yin, A., 1989. Origin of regional, rooted low-angle normal faults: a mechanical model and its tectonic implications, *Tectonics*, **8**, 469-482.

Yin, A., 1991. Mechanisms for the formation of domal and basinal detachment faults: a three dimensional analysis, *Journal of Geophysical Research*, **96**, 14577-14594.

Zanzwig, H.V., 1973. Structural transitions between the foreland zone and the core zones of hte Columbian orogen, Selkirk Mountains, British Columbia; Ph.D. thesis, Queens University, Kingston, Ontario.

Zartman, R.E., Peterman, Z.E., Obradovich, J.D., Gallego, M.D., and Bishop, D.T., 1982. Age of the Crossport C sill near Eastport, Idaho: in, Society of Economic Geologists Coeur d'Alene Field Conference, Idaho, R.R. Reid and G.A. Williams editors, *Idaho Bureau of Mines and Geology Bulletin*, **24**, 61-69.